frontiers | Research Topics

Rock avalanche, landslide and debris flow hazards in mountainous areas

Edited by
Xiaojun Guo, Marcel Hürlimann, Changdong Li and Wen Zhang

Published in
Frontiers in Earth Science

ISSN 1664-8714
ISBN 978-2-83251-310-1
DOI 10.3389/978-2-83251-310-1

About Frontiers

Frontiers is more than just an open access publisher of scholarly articles: it is a pioneering approach to the world of academia, radically improving the way scholarly research is managed. The grand vision of Frontiers is a world where all people have an equal opportunity to seek, share and generate knowledge. Frontiers provides immediate and permanent online open access to all its publications, but this alone is not enough to realize our grand goals.

Frontiers journal series

The Frontiers journal series is a multi-tier and interdisciplinary set of open-access, online journals, promising a paradigm shift from the current review, selection and dissemination processes in academic publishing. All Frontiers journals are driven by researchers for researchers; therefore, they constitute a service to the scholarly community. At the same time, the *Frontiers journal series* operates on a revolutionary invention, the tiered publishing system, initially addressing specific communities of scholars, and gradually climbing up to broader public understanding, thus serving the interests of the lay society, too.

Dedication to quality

Each Frontiers article is a landmark of the highest quality, thanks to genuinely collaborative interactions between authors and review editors, who include some of the world's best academicians. Research must be certified by peers before entering a stream of knowledge that may eventually reach the public - and shape society; therefore, Frontiers only applies the most rigorous and unbiased reviews. Frontiers revolutionizes research publishing by freely delivering the most outstanding research, evaluated with no bias from both the academic and social point of view. By applying the most advanced information technologies, Frontiers is catapulting scholarly publishing into a new generation.

What are Frontiers Research Topics?

Frontiers Research Topics are very popular trademarks of the *Frontiers journals series*: they are collections of at least ten articles, all centered on a particular subject. With their unique mix of varied contributions from Original Research to Review Articles, Frontiers Research Topics unify the most influential researchers, the latest key findings and historical advances in a hot research area.

Find out more on how to host your own Frontiers Research Topic or contribute to one as an author by contacting the Frontiers editorial office: frontiersin.org/about/contact

Rock avalanche, landslide and debris flow hazards in mountainous areas

Topic editors

Xiaojun Guo — Institute of Mountain Hazards and Environment, Chinese Academy of Sciences (CAS), China

Marcel Hürlimann — Universitat Politecnica de Catalunya, Spain

Changdong Li — China University of Geosciences Wuhan, China

Wen Zhang — Jilin University, China

Citation

Guo, X., Hürlimann, M., Li, C., Zhang, W., eds. (2023). *Rock avalanche, landslide and debris flow hazards in mountainous areas*. Lausanne: Frontiers Media SA.

doi: 10.3389/978-2-83251-310-1

Table of contents

frontiers | Frontiers in Earth Science

ORIGINAL RESEARCH
published: 08 June 2022
doi: 10.3389/feart.2022.908078

Numerical Simulation and Hazard Analysis of Debris Flows in Guxiang Gully, Tibet, China

Jinbo Tang[1,2†], *Chen Liu*[1,2,3], *Jiajie Mao*[1,2,4] *and Hao Wang*[1,2*]

[1]Key Laboratory of Mountain Hazards and Earth Surface Processes, Chinese Academy of Sciences, Chengdu, China, [2]Institute of Mountain Hazards and Environment, Chinese Academy of Sciences, Chengdu, China, [3]School of Energy and Power Engineering, Xihua University, Chengdu, China, [4]College of Water Conservancy and Hydropower Engineering, Sichuan Agriculture University, Ya'an, China

Guxiang Gully, located in Bome county in southwest Tibet, China, is a right-bank tributary of the Purlung Tsangpo River. Hanging glaciers are widely distributed upstream of the gully, and a large number of moraines can cause debris flows triggered by run-offs generated by the rainstorm and melting water of glaciers deposited in this gully. The debris flow in the Guxiang Gully can frequently pose a serious threat to the Sichuan–Tibet highway. Due to the lack of field observation data, in this study, the flood discharge method combining the run-off generated by rainstorms and melting water of glaciers was employed to determine the magnitudes of debris flows under once-in-a-century, once-in-two-century, and once-in-three-century flood return periods. Furthermore, a numerical simulation is implemented to determine the maximum flow depth and velocity of the debris flow in each grid cell and the inundated debris flow area in Guxiang Gully with different return periods. Subsequently, each grid cell's maximum flow depth and velocity are used to assess buried hazards and impact hazards, respectively. The integrated hazard could be calculated by combining the buried hazard and the impact hazard. The result shows that the hazard of the top of the fan and Purlung Tsangpo River affected by the debris flow is highest, and the debris flow is likely to block the Purlung Tsangpo River.

Keywords: Guxiang Gully, debris flows, flood discharge method, numerical simulation, hazard analysis

OPEN ACCESS

Edited by:
Changdong Li,
China University of Geosciences (Wuhan), China

Reviewed by:
Nazir Bazai,
Institute of Mountain Hazards and Environment (CAS), China
Yifei Cui,
Tsinghua University, China

***Correspondence:**
Hao Wang
hgoodspeed2008@163.com

†These authors share first authorship

Specialty section:
This article was submitted to Geohazards and Georisks, a section of the journal Frontiers in Earth Science

Received: *30 March 2022*
Accepted: *27 April 2022*
Published: *08 June 2022*

Citation:
Tang J, Liu C, Mao J and Wang H (2022) Numerical Simulation and Hazard Analysis of Debris Flows in Guxiang Gully, Tibet, China. Front. Earth Sci. 10:908078. doi: 10.3389/feart.2022.908078

1 INTRODUCTION

The mountainous region southeast of the Qinghai–Tibet Plateau is one of the most crucial areas in China for natural disasters such as landslides and debris flows (Du and Zhang, 1981). Once a debris flow occurs, it causes significant damage to the buildings of settlements and transportation infrastructure (Takahashi, 2007; Cui et al., 2015). Modern glaciers, especially marine glaciers, are widely distributed in this region. Due to the influence of the southwest monsoon from the Indian Ocean and the complex geological and geomorphological environment, debris flows are initiated frequently by run-offs generated by the coupling of frequent heavy precipitation with glacier meltwater during summer (Liu and Cheng, 2015). Generally, run-off is generated only when glacier meltwater has difficulty initiating debris flows due to a relatively small discharge. However, when there is a condition of heavy precipitation, rainfall can lead to largely accelerated glacier melt and form a relatively large discharge and then trigger debris flows. This type of debris flow is typically termed as glacier–rainfall mixed debris flows.

It is necessary to analyze the hazard of debris flows to reduce their risks. Luo et al. (2020) proposed a framework for vulnerability analysis to generate a physical-vulnerability model of sequential and

concurrent hazards based on the interaction mechanism between debris flows and buildings, in which the cumulative damage effects of sequential debris flows were analyzed. Paudel et al. (2020) used a GIS model by coupling the hazard areas of debris flows with rainfall frequency to assess the hazard of debris flows. Bonetto et al. (2021) established an open geographic database to quantitatively and rapidly assess the hazard of debris flows based on the independent parameters in the region. Jiang et al. (2021) proposed an empirical model (Flow-R model) to assess the debris flows' hazard class on the flow paths and spreading areas of debris flows at the regional scale with basic information on debris flows. However, traditional hazard analysis is based mainly on the empirical formula, which can only calculate parameters such as runout distance but cannot describe the buried area of debris flows (Wei et al., 2006).

In recent years, with the development of dynamic theory and numerical simulation technology for debris flows, hazard analysis based on the dynamic process of debris flows has also made many achievements (O'Brien et al., 1993; Liu and Tang, 1995; Iverson, 1997; Guo et al., 2022). Based on the determination of the magnitudes of the debris flows in 12 creeks in Bíldudalur over 10 years, Glade (2005) compared the input of the sediment requirement model for debris flows and estimated sediment reproduction from both the suction and rock wall retreat models. Wei et al. (2006) applied the momentum partition method to analyze the hazard, but it did not involve disasters caused by burying the protected object. Liu et al. (2008) derived the magnitude–frequency (MF) relationship by expressing the observed live debris flows and runoff (i.e., total volume) distributions over the last 40 years. It is critical for debris flow prediction. However, they did not fully consider the reliability and authenticity of the data. Zou et al. (2016) proposed a method to describe the integrated hazard of debris flows by summing up the depth and kinetic energy of debris flows. Because the depth implied the disaster caused by burying the protected object and the kinetic energy represented the hazard caused by impacting the protected subjects, the risk of debris flows seems to be considered adequately in the method proposed by Zou et al. (2016). However, the depth and kinetic energy have separate physical dimensions, and summing them can lead to the problem of dimensional dissonance. Gao et al. (2019) analyzed 178 debris flow events by regression analysis in Jiang Jia Gully from 1987 to 2004. The MCF relationship for high-frequency debris flows is consistent with the power-law equation, but there are differences in the regression coefficients in the equation. Fan et al. (2020) proposed to evaluate the hazard of loose material on post-earthquake slopes by comparing multi-temporal landslide and hydro-topographic parameters. However, Fan et al. (2020) did not try to distinguish the association between different types of hydro-topographic parameters and multi-temporal landslide inventories. Dash et al. (2021) performed a 3D numerical simulation of the Himalayas based on the Voellmy model and conducted a hazard assessment. It is advantageous to the region where data integrity is incomplete. But the study fails to consider the hydrogeological and other conditions upstream which cause debris flows. Therefore, the numerical simulation of the long time scale for rainfall, dynamic, and high altitude for glacial debris flow is urgently needed.

In this study, a method to describe the integrated hazard of debris flows is proposed by employing numerical simulation techniques and is used for the integrated hazard analysis of debris flows in Guxiang Gully. After this review of the literature (**Section 1**), the overview of Guxiang Gully is described in **Section 2**. **Section 3** introduces the method used to determine the magnitude of the Guxiang Gully debris flows. **Section 4** describes the numerical techniques used in this study. In **Section 5**, a numerical technique is used to simulate debris flows in Guxiang Gully with different frequency scales, and then the integrated hazard of debris flows is analyzed by combining the maximum flow depth and the maximum flow velocity head. Finally, conclusions are drawn in **Section 6**.

2 OVERVIEW OF THE STUDY AREA

Guxiang Gully, located in Bomi county, Tibet Autonomous Region, China, is a right-bank tributary of the Parlung Tsangpo valley (As **Figure 1A**), where moraines controlled by modern marine glaciers are widespread in this region (Gao et al., 2018). As a typical glacial debris flow that threatens the safety of the Sichuan–Tibet highway, the debris flows in the Guxiang Gully have a high velocity with a powerful impact and buried destruction on the downstream roads (Cheng et al., 1997; You et al., 1997). It is vital to analyze the motility and hazard of debris flows in Guxiang Gully to ensure the safety of the Sichuan–Tibet Highway (Wei et al., 2006).

The Guxiang Gully area watershed is 25.2 km^2, and the main channel has a length of 6 km and a longitudinal mean gradient of 256‰, as shown in **Figure 1B**. The steep slopes can supply potential energy for debris flow initiation. The six hanging glaciers are developed in the source area of this gully, and large moraines that supply the material sources for debris flow initiation accumulated in this gully (Zhu et al., 1997). Guxiang Gully is situated in the suture zone of Yarlung Tsangpo (King et al., 2016), and intense geological activity induced plenty of loose disperse debris, which can contribute to material sources for debris flow initiation. In addition, due to thaw and freeze weathering, rock crevices developed, which were vulnerable to avalanches (IMHE (Chengdu Institute of Mountain Hazards and Environment), 1995; Zhang, 2008). Overall, these conditions resulted in tremendous amounts of loose sediment, which can initiate large-magnitude debris flows.

In addition, the marine glaciers in the region play an important role in enlarging the magnitude of debris flows (IMHE (Chengdu Institute of Mountain Hazards and Environment), 1995). Due to the influence of radiation by solar and heavy precipitation, the meltwater volume for the glacier of Guxiang Gully is the largest in July and August every year and accounts for more than 70% of the year in the rainy season (Liu et al., 2013; Zhang and Lin, 2016). The Indian monsoon can transport large amounts of warm humid airflow along the Brahmaputra–Yarlung Tsangpo River into the Parlung Tsangpo valley (Deng et al., 2017). Under the influence of the

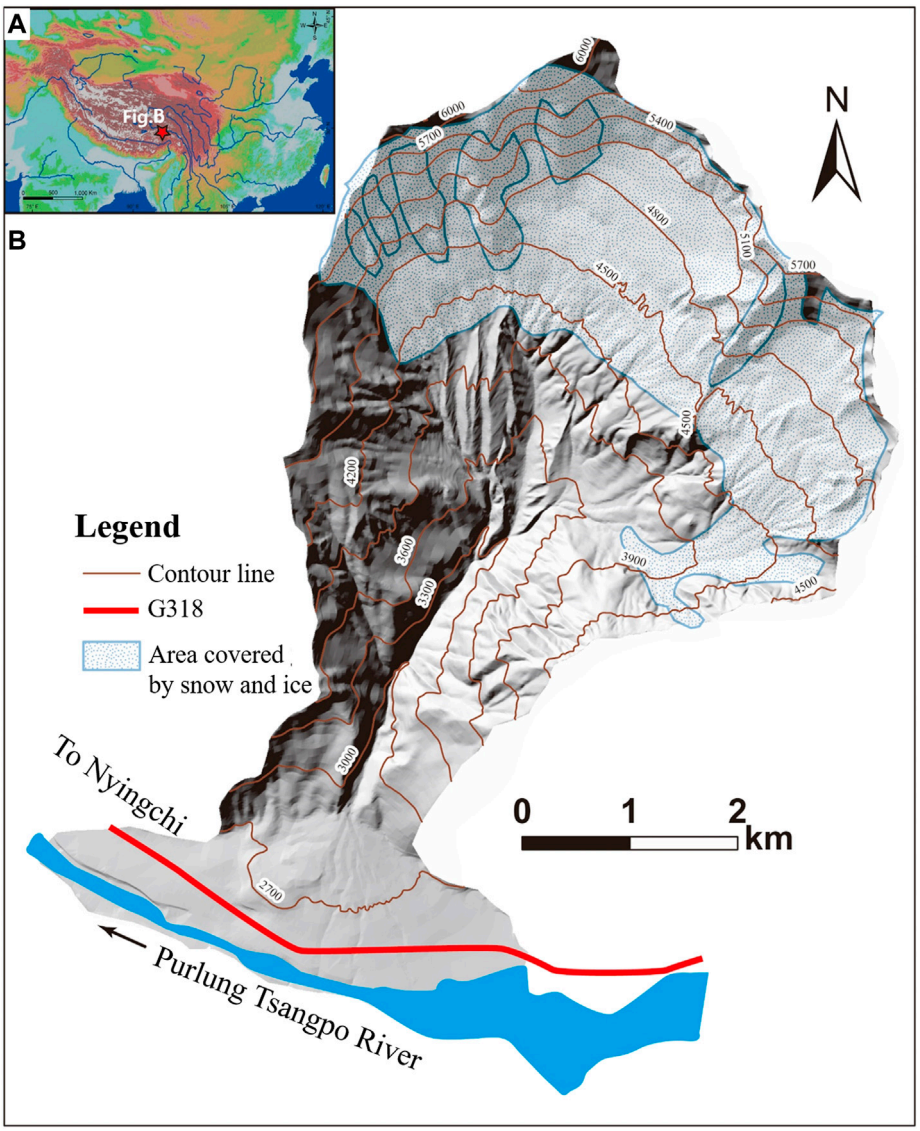

FIGURE 1 | Overview map of the Guxiang Gully watershed.

southwest monsoon, the rainy season lasts for approximately 6 months and has enough precipitation for debris flow initiation. In addition, due to the presence of modern glaciers at the source, meltwater increases the existing run-off discharge caused by precipitation due to the increase in ambient temperature, which provided sufficient hydrodynamic conditions for the formation of debris flows in the region (Cui et al., 2015).

In September 1953, a large-scale debris flow with a peak discharge of 28,600 m^3/s occurred in the Guxiang Gully as a result of heavy precipitation, which lasted for more than 4 h. Vast amounts of sediments, approaching 11 million m^3, were transported to the 1.5–3.5-km wide and 2-km long downstream fan. A single granite gneiss 20 m × 8 m × 12 m size boulder was found in the depositional fan. A large body of sediments was transported into and blocked the Purlung Tsangpo River and then formed a dammed lake where the water level upstream of the dammed lake rose 40 m, causing backwater flooding more than 70 km upstream. In 1963, other large-scale debris flows occurred again in the Guxiang Gully, and the sediments rushed into the Purlung Tsangpo River and squeezed the cross-section of the channel of the Purlung Tsangpo River. The backwater associated with the second event flooded approximately 12 m upstream (Shi et al., 1964). In addition to these large-scale debris flows, these events caused massive physical and economic losses; additionally, these debris flows in the Guxiang Gully could occur from May to September every year. Although the scales of these debris flows were small, they had a very high frequency, sometimes occurring more than hundreds of times a year. Before 1953, the area of the debris flow fans in

Guxiang Gully was 1.5 km^2 and increased to 3.7 km^2 in 1964, 4.23 km^2 in 1973, and 4.25 km^2 at present (You, 2001).

According to the results of Zhu et al. (1997), the longest branch before 1950 in the Guxiang Gully source area was a small-scale shallow gully. Due to the effect of the Medog earthquake, the strength of the moraine dropped. Moreover, due to rainfall and infiltration of glacier meltwater, saturated instability of the soil, and gravity unloading, numerous landslides occurred in the source area. The moraine also provided abundant material sources for the large debris flows that occurred in 1953. In the 1960s, landslides collapsed 5–6 times per hour in the catchment (Shi et al., 1964). However, after the 1990s, the moraine in the source area of the Guxiang Gully gradually stabilized, and the frequency and scale of debris flows also decreased, transforming into dilute debris flows and hyperconcentrated flows (Zhu et al., 1997).

3 DETERMINATION OF THE MAGNITUDE OF GUXIANG GULLY DEBRIS FLOWS

The initiation mechanism of the debris flow is very complex, which can be initiated by landslide transformation, glacial lake outburst floods (GLOFs), ice-rock avalanches, and glacial debris flows (Kääb et al., 2018; Shugar et al., 2021). Since hydrological data in this area are not available, in this study, the flood discharge method combining the run-off generated by the rainstorm and by melting water of glaciers was employed to determine the magnitude of debris flows. This method has been widely applied and has played a pivotal role in the hydrological calculation in the areas where hydrological data are not available in Tibet (IHME (Chengdu Institute of Mountain Hazards and Environment), 1995; Looper and Vieux, 2012; Kim and Choi, 2015; Banasik et al., 2016; Vasil'eva et al., 2019; Deng et al., 2020).

In this study, the run-off generated by rainfall can be calculated by the following formula (IMHE (Chengdu Institute of Mountain Hazards and Environment), 1995):

$$Q_0 = \begin{cases} 0.278\left(\frac{S_p}{\tau^n} - \mu\right)F, & t_c \geq \tau, \\ 0.278\frac{nS_p t_c^{1-n}}{\tau}F, & t_c < \tau, \end{cases} \quad (1)$$

where Q_0 is the peak discharge of flood (m^3/s); μ is the flood runoff coefficient; S_p is the rain intensity, i.e., the maximum hourly rain intensity (mm/h); τ is the confluence time (h) in the catchment; n is the rain attenuation index; F is the confluence area in the catchment (km^2), and the time of the run-off generation t_c is calculated as follows:

$$t_c = \left[\frac{(1-n)S_p}{\mu}\right]^{1/n}. \quad (2)$$

The time of hydrological confluence in the catchment can be calculated as follows:

TABLE 1 | Values of the watershed and rainfall parameters used in **Eqs 1**, **6**.

F (km^2)	F_1 (km^2)	θ_0 (°)	S_p (mm/h)	n (/)
25.2	18.19	32.00	57.4	0.5

$$\tau = \frac{0.278L}{mJ^{1/3}Q_0^{1/4}}, \quad (3)$$

where $\mu = 3.6F^{-0.19}$is the runoff coefficient; $m = 0.278\theta^{0.204}$ is the confluence coefficient; and $\theta = L/(J^{1/3}F^{1/4})$ is the characteristic coefficient of the catchment.

In addition, when the glacier area accounts for 10%–30% of the catchment, glacier meltwater plays a pivotal role in the formation of run-off in the catchment where the integrated effect of heavy rainfall and glacier melting needs to be simultaneously considered. To determine the peak discharge of floods in glacier–rainfall mixed debris flows gullies, the peak discharge of glacier melting Q_1 needs to be calculated using the following formula (IMHE (Chengdu Institute of Mountain Hazards and Environment), 1995):

$$Q_1 = F_1(0.05H + 2.1), \quad (4)$$

where F_1 is the area covered by glaciers and snow (km^2), and H is the total rainfall for individual debris flow events (mm).

Combining the peak discharge generated by rainfall with that by glacier meltwater, the peak discharge of glacier-rainfall mixed debris flows can be calculated as follows:

$$Q_d = (Q_0 + Q_1)(1 + \varphi_d)D, \quad (5)$$

where Q_d is the peak flood discharge of glacier-rainfall mixed debris flows; and Q_0 and Q_1 can be determined by **Eq. 1** and **Eq. 4**, respectively. $\varphi_d = (\gamma_d - \gamma_w)/(\gamma_s - \gamma_d)$ is the correction coefficient due to the presence of sediment in debris flows, γ_d is the bulk density of debris flows, γ_w is the inherent density of water and is taken as 1,000 kg/m^3, γ_s is the inherent density of particles in debris flows and is taken as 2,650 kg/m^3, and D is the scale amplification coefficient due to the presence of glaciers and can be calculated as follows:

$$D = 1 + 7.6\left(\frac{F_1}{F}\right) + 0.05\theta_0, \quad (6)$$

where F_1 is the area covered by glaciers and snow; F is the total area of the catchment (km^2); and θ_0 is the surface angel of the glacier relative to the horizontal plane (°).

According to the duration of debris flows T and the maximum flow Q_d, the total volume V_t of a debris flow process can be calculated by the following formula:

$$V_t = 0.26TQ_d. \quad (7)$$

In this study, catchment and rainfall parameters were used from IMHE (Chengdu Institute of Mountain Hazards and Environment), (1995) and are listed in **Table 1**. The peak flood discharges and total magnitudes of debris flows in Guxiang Gully under once-in-a-century, once-in-two-century,

TABLE 2 | Determination of the values of run-off in **Eqs 4**, **5** and the total magnitude of debris flows calculated by **Eq. 7**.

Frequency (/)	H (mm)	Q_0 (m^3/s)	Q_1 (m^3/s)	Q_d (m^3/s)	V_t ($10^4 m^3$)
Once-in-a-century	144.65	154.49	169.76	6405.38	912.77
Once-in-two-centuries	160.15	176.42	183.85	8303.15	1183.20
Once-in-three-centuries	168.76	187.26	191.68	13,100.16	1866.77

and once-in-three-century flood frequency conditions were calculated from **Eq. 1** to **Eq. 7** and are listed in **Table 2**.

4 NUMERICAL SIMULATIONS OF DEBRIS FLOW MOVEMENTS

As a special kind of solid and liquid two-phase fluid, the dynamics of debris flows are very sophisticated (Wang et al., 1998). According to the joint efforts of many debris flow scholars at home and abroad, kinetic equations that can describe the movement of debris flows have been developed to a certain extent (Iverson and Denlinger, 2001; Pitman and Le, 2005; Pudasaini and Mergili, 2019). The movement of debris flows is an enormously complex dynamic process, and it is almost impossible to find an analytical solution for debris flow channels in real terrain based on fluid dynamics, so it can only be solved with the help of numerical calculation methods (Iverson, 1997). In this study, based on the basic hydrodynamic equation, the dynamic control equation of viscous debris flows is derived and developed as follows:

$$\frac{\partial h}{\partial t} + \frac{\partial p}{\partial x} + \frac{\partial q}{\partial y} = 0, \tag{8}$$

$$\frac{\partial p}{\partial t} + \frac{\partial}{\partial x}\left(\frac{p^2}{h}\right) + \frac{\partial}{\partial y}\left(\frac{pq}{h}\right) = -gh\frac{\partial (z_b + h)}{\partial x} - S_{fx}, \tag{9}$$

$$\frac{\partial q}{\partial t} + \frac{\partial}{\partial x}\left(\frac{pq}{h}\right) + \frac{\partial}{\partial y}\left(\frac{q^2}{h}\right) = -gh\frac{\partial (z_b + h)}{\partial y} - S_{fy}, \tag{10}$$

where $p = hu$ and $q = hv$ are the discharges per width in the x and y directions, respectively; u and v are the debris flow velocity in the x and y directions, respectively; h is the debris flow depth; Z_b is the bottom altitude; $g = 9.8$ m/s^2 is the acceleration of gravity; and S_{fx} and S_{fy} are the bottom resistances of debris flows in the x and y directions, respectively. According to Iverson's study, the resistance to debris flow movement includes liquid-phase constituent and solid-phase particle motion friction resistance (O'Brien et al., 1993) adding, which can be expressed as follows:

$$S_{fx} = (1 - C_s)\left(\frac{p}{\sqrt{p^2 + q^2}}\frac{\tau_B}{\rho} + \eta\frac{p}{\rho h^2}\right) + \frac{p}{\sqrt{p^2 + q^2}}\frac{C_s gh\left(\rho_s - \rho_f\right)\tan\left(\psi\right)}{\rho}, \tag{11}$$

$$S_{fy} = (1 - C_s)\left(\frac{q}{\sqrt{p^2 + q^2}}\frac{\tau_B}{\rho} + \eta\frac{q}{\rho H^2}\right) + \frac{q}{\sqrt{p^2 + p^2}}\frac{C_s gh\left(\rho_s - \rho_f\right)\tan\left(\psi\right)}{\rho}, \tag{12}$$

where C_s is the volumetric concentration of the solid phase, τ_B is the yield stress of debris flows in the liquid phase, η is the dynamic viscosity coefficient of the liquid phase of the debris flows, ρ is the density of debris flows, ρ_f is the liquid-phase fluid density, ρ_s = 2,650 kg/m^3 is the density of particles, and ψ is the friction angle between the particles and the bed surface in the debris flow mass. According to the study of Wei et al.(2006), in this study, these parameters could be taken as C_s = 0.46, ρ_f = 1,450 kg/m^3, ρ = 2,000 kg/m^3, τ_B = 55.20 Pa, η = 0.086 Pa·s, and ψ = 18.5°.

In this study, the numerical software proposed by Zhang and Lin (2016) was employed to numerically simulate the motion of debris flows. As listed in **Table 2**, under once-in-a-century, once-in-two-century, and once-in-three-century flood return periods, the magnitudes of debris flows in Guxiang Gully are approximately 9.1277 million m^3, 11.8320 million m^3, and 18.6677 million m^3, respectively. According to the 1:10,000 topographic map of Guxiang Gully, the digital elevation model (DEM) of the catchment area of Guxiang Gully was established. The numerical simulation of the debris flows of Guxiang Gully was implemented under the conditions of 100-year frequency, 200-year frequency, and 300-year frequency, and the final deposition area and depth distribution of the debris flows are shown in **Figure 2**. The maximum depths of the accumulation were 27.50 m and 31.63 m, the maximum accumulation depths were 27.50 m, 31.63 m, and 47.60 m, and the maximum accumulation depth was located in the main river area of the Purlung Tsangpo River affected by the debris flows.

5 HAZARD ANALYSIS

Traditionally, statistical methods were mainly employed to assess the risk of debris flows that involve the runout and deposition area but cannot consider the dynamical characteristics of debris flows, such as the distribution of depth and velocity (Guzzetti et al., 2005; Zou et al., 2016). To precisely evaluate the hazard of debris flows, more details on the dynamical characteristics of debris flows are essential. In this study, to analyze the hazard based on the results of numerical simulations, the maximum flow depth and maximum velocity were extracted at each grid cell during debris flow movement, which can be described as follows:

$$h_{i,j}^{\max} = \max_{0 \le t \le T}\left(h_{i,j}^{t+\Delta t}, h_{i,j}^{t}\right), \tag{13}$$

$$U_{i,j}^{\max} = \max_{0 \le t \le T}\left(U_{i,j}^{t+\Delta t}, U_{i,j}^{t}\right), \tag{14}$$

where $U = (u^2 + v^2)^{1/2}$ is the resultant velocity of the debris flows; u and v are the x- and y-component velocity debris flows, respectively; Δt is the numerical time step; T is the total time of debris flow simulation; and the subscripts i and j represent the

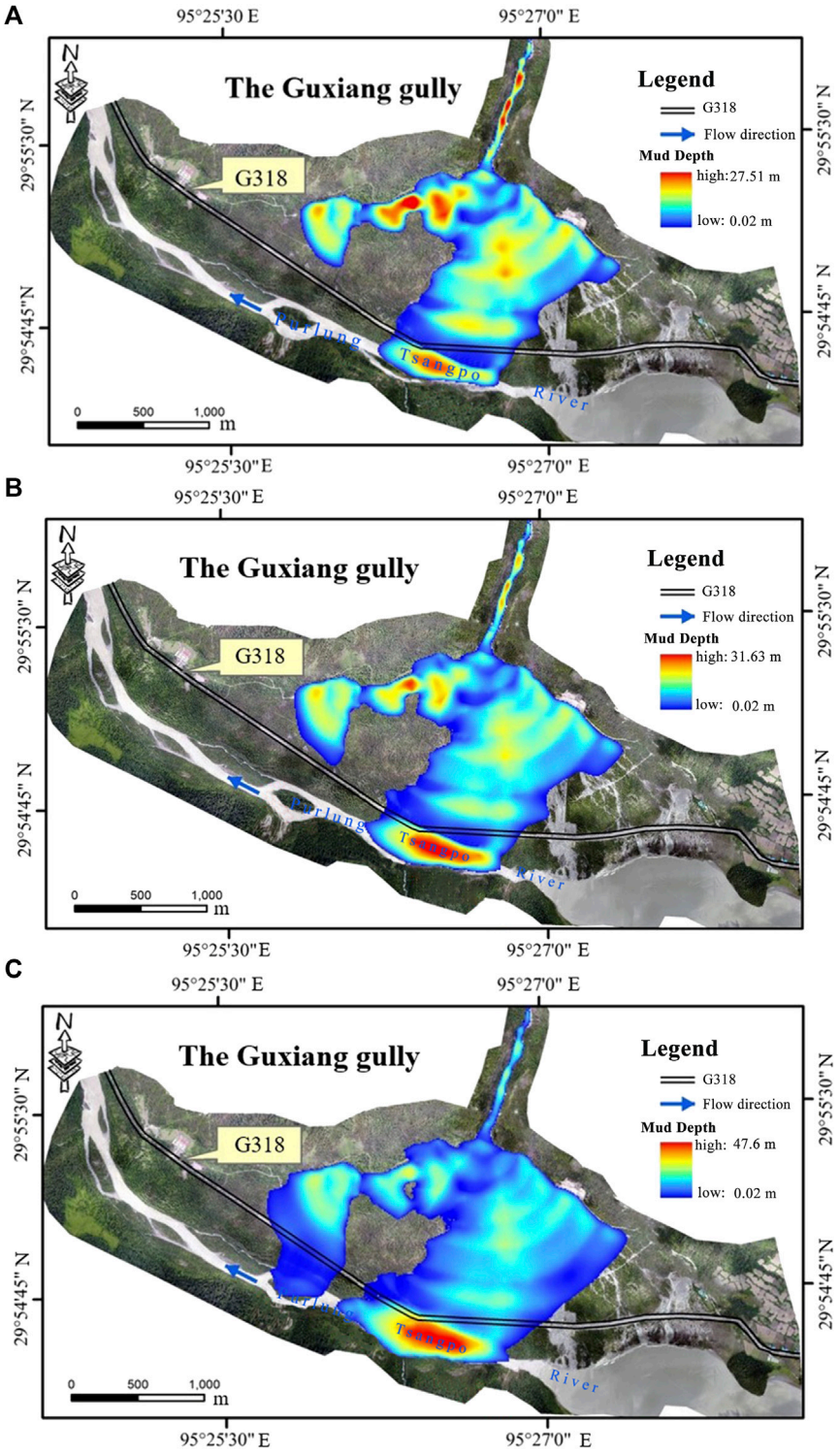

FIGURE 2 | Deposition area of debris flows with different return periods: **(A)** 100-year frequency, **(B)** 200-year frequency, and **(C)** 300-year frequency.

i-th and *j*-th grid cells along the *x*-direction and *y*-direction, respectively, in the computational domain.

In the process of numerical simulation, the maximum flow depth distribution and maximum velocity distribution of debris flows at different frequencies were extracted by **Eqs 13**, **14** and are shown in **Figure 3**. The numerical simulation results indicated that after the debris flows ran out from the outlet of the Guxiang Gully, the debris flows spread rapidly

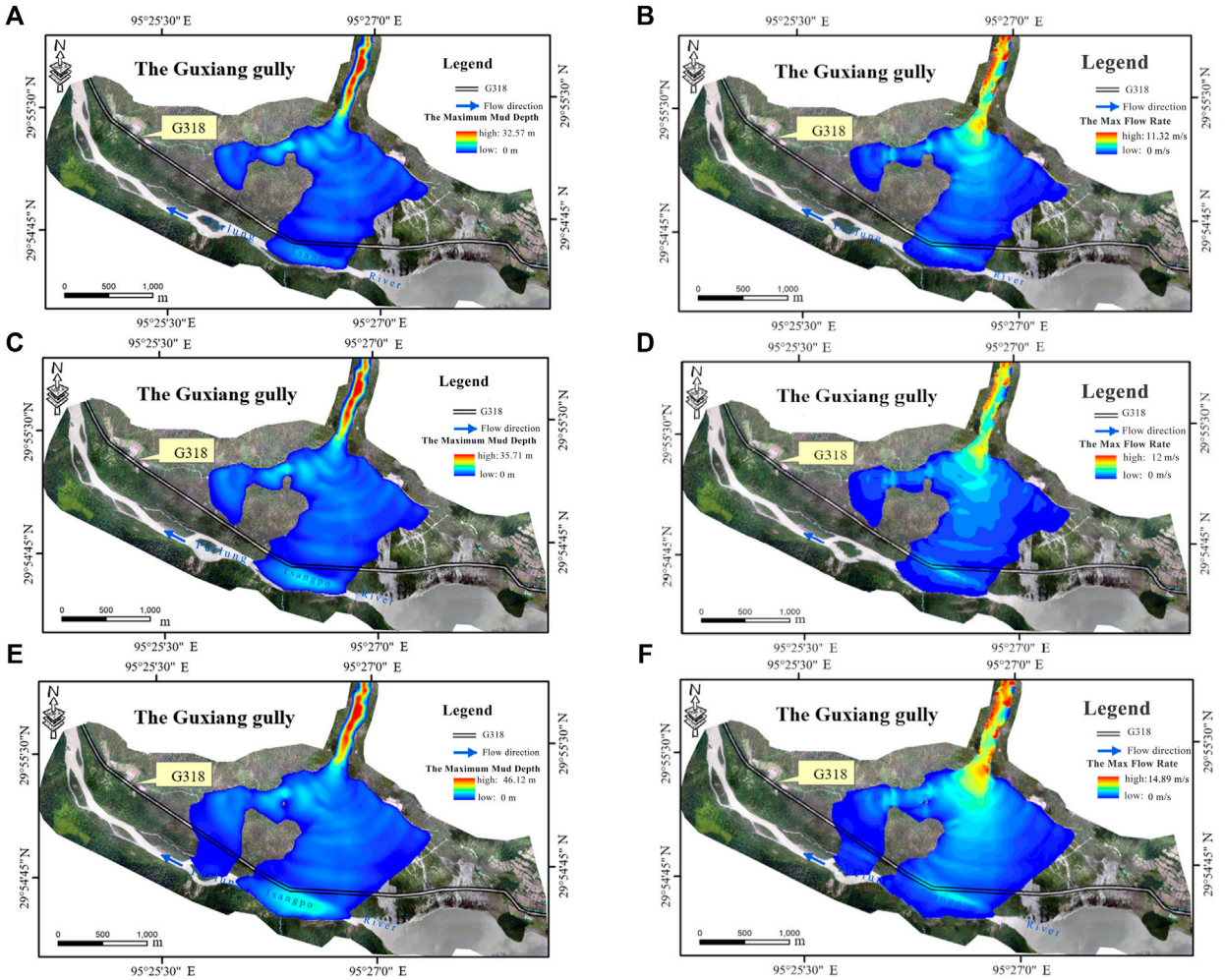

FIGURE 3 | Maximum depth of debris flows with different return periods. **(A)** 100-year frequency. **(C)** 200-year frequency. **(E)** 300-year frequency. The maximum velocity distribution of debris flows with the different return periods. **(B)** 100-year frequency. **(D)** 200-year frequency. **(F)** 300-year frequency.

over the depositional fan. Under the condition of a once-in-a-century frequency, the maximum flow depth and the maximum flow velocity of debris flows were 32.57 m and 11.32 m/s, respectively, in the whole computational domain. The maximum depth of debris flows is distributed at the main river area of the Purlung Tsangpo river and is equal to 27.5 m, where the maximum flow velocity is 4.32 m/s. Under the conditions of a once-in-two-century frequency, the maximum flow depth and the maximum flow velocity of debris flows were 35.71 m and 12.00 m/s, respectively, in the whole computational domain. The maximum depth of debris flows is distributed at the main river area of the Purlung Tsangpo river and is equal to 31.63 m, where the maximum flow velocity is 5.63 m/s; under the condition of a once-in-three-century frequency, the maximum flow depth and the maximum flow velocity of debris flows were 46.12 m and 14.89 m/s, respectively, in the whole computational domain. The maximum depth of debris flows is distributed at the main river area of the Purlung Tsangpo River and is equal to 47.60 m, where the maximum flow velocity is 7.54 m/s.

Furthermore, according to the hazard characteristics of debris flows, the hazard of debris flows in the movement process is mainly reflected by burying and impacting caused by debris flows (Hu et al., 2012; Zhu et al., 2021). In this study, the maximum depth of debris flows at each grid-cell was regarded as the hazard by burying the protected objects caused by debris flows. In addition, the impact force of debris flows is usually expressed as $p = K\rho U^2$ (Tang et al., 2013). Therefore, the maximum flow velocity head $U^2/(2\,g)$ at each grid cell was employed to represent a hazard caused by impacting the protected objects, where U is the resultant flow velocity, and g is the gravity acceleration. Summing up the hazard of debris flows caused by burying and impacting protected objects, the integrated hazard of debris flows can be described as follows:

$$H_{ij} = h_{i,j}^{\max} + \frac{\left(U_{i,j}^{\max}\right)^2}{2g}, \tag{15}$$

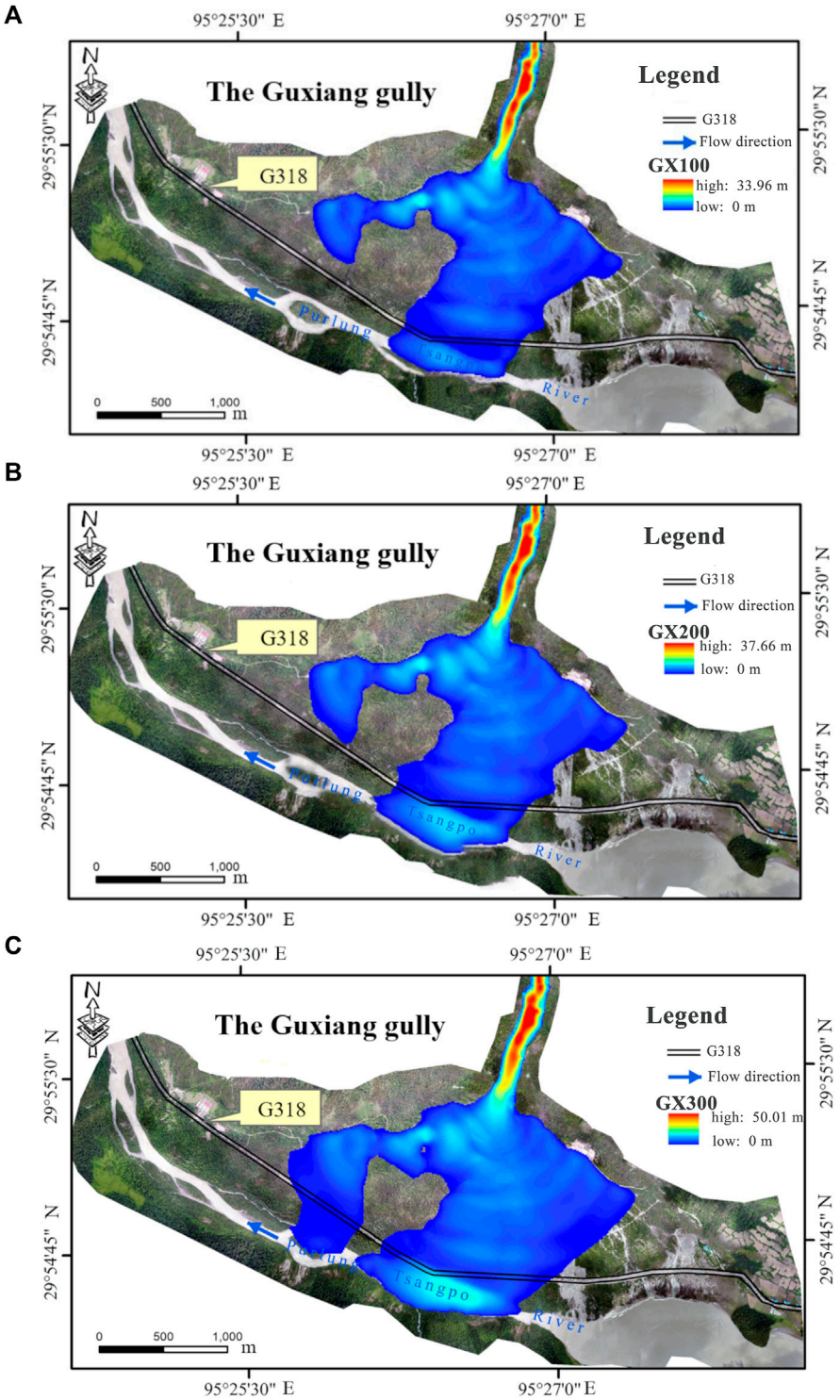

FIGURE 4 | Distribution of debris flow hazards for different return periods. **(A)** 100-year frequency. **(B)** 200-year frequency. **(C)** 300-year frequency.

where H_{ij} represents the integrated hazard of debris flows at the i-th and j-th grid cells in the computational domain, which have dimensions of length (m).

In this study, based on the numerical results, **Eq. 15** is employed to determine the integrated hazard distribution of debris flows under once-in-a-century, once-in-two-century,

and once-in-three-century flood frequency conditions, as shown in **Figure 4**. The numerical simulation results showed that under once-in-a-century, once-in-two-century, and once-in-three-century flood frequency conditions, the areas with the highest hazard of debris flows were distributed at the outlet of Guxiang Gully, which were 33.96 m, 37.66 m, and 50.01 m for different frequencies, respectively. In addition, under the conditions of these frequencies, the debris flows in Guxiang Gully have obvious implications of blocking the Purlung Tsangpo River. Once the debris flows block the Purlung Tsangpo river, it forms a dam. As the debris flow dam collapses, it may lead to a debris flow-blocking-failure and flood disaster chain.

6 CONCLUSION

The magnitude of the debris flows is one of the major control factors in assessing debris flow hazards. The debris flows in Guxiang Gully were initiated by the run-off of rainfall and meltwater from glaciers. The integrated effect of heavy rainfall and glacier meltwater needs to be fully considered as determining the magnitude of the debris flows. In this study, the flood discharge method combining the run-off generated by rainstorms and by the melting water of glaciers was employed to determine the magnitudes of debris flows for the once-in-a-century, once-in-two-century, and once-in-three-century return periods.

Furthermore, the motions of debris flow in Guxiang Gully with once-in-a-century, once-in-two-century, and once-in-three-century flood frequency conditions were numerically simulated. The integrated debris flow hazard is proposed by combining the maximum flow depth and the maximum flow velocity head, where the maximum flow depth of debris flows at each grid cell implies the hazard of debris flows caused by burying the protected objects, and for the hazard of debris flows caused by impacting the protected objects, the flow velocity head was employed.

Based on the numerical simulation results, the integrated hazards of debris flows in Guxiang Gully with once-in-a-century, once-in-two-century, and once-in-three-century flood frequency conditions were analyzed. The results showed that the high-hazard area caused by debris flows in Guxiang Gully is mainly distributed at the outlet of the gully and the main river area of the Purlung Tsangpo River downstream, and the debris flows have the apparent risk of blocking the river under once-in-a-century, once-in-two-century, and once-in-three-century flood frequency conditions. If debris flows block the Purlung Tsangpo river, the dam caused by debris flows can fail, which likely leads to a debris flow blocking the river and flood disaster chain as the dam fails.

DATA AVAILABILITY STATEMENT

The original contributions presented in the study are included in the article further inquiries can be directed to the corresponding author.

AUTHOR CONTRIBUTIONS

JT: conceptualization, methodology, data curation, writing—original draft, and formal analysis. CL: conceptualization, methodology, and formal analysis. JM: conceptualization, methodology, and formal analysis. HW: conceptualization, methodology, and formal analysis.

FUNDING

This work was supported by the Key Research Program of Frontier Sciences, CAS (Grant No. QYZDY-SSW-DQC006), National Natural Science Foundation of China (Grant Nos. 41941017 and U20A20112), and the support from the Sichuan Science and Technology Program 2021YFH0009 is gratefully acknowledged.

REFERENCES

Banasik, K., Hejduk, L., Woodward, D. E., and Banasik, J. (2016). Flood Peak Discharge vs. Various CN and Rain Duration in a Small Catchment. *Rocz. Ochr. Srodowiska* 18, 201–212.

Bonetto, S., Mosca, P., Vagnon, F., and Vianello, D. (2021). New Application of Open Source Data and Rock Engineering System for Debris Flow Susceptibility Analysis. *J. Mt. Sci.* 18 (12), 3200–3217. doi:10.1007/s11629-021-6814-3

Chen, N., Zou, Q., Su, F., Cui, P., and Zhang, Y. (2015). Risk Assessment and Disaster Reduction Strategies for Mountainous and Meteorological Hazards in Tibetan Plateau. *Chin. Sci. Bull.* 60, 3067–3077. doi:10.1360/N972015-00849

Cheng, Z. L., Liu, L. J., and You, Y. (1997). *Debris Flow Velocity of Guxiang Ravine, Xizang*. Chengdu, China: Mountain Research, 04, 293–295.

Dash, R. K., Kanungo, D. P., and Malet, J. P. (2021). Runout Modelling and Hazard Assessment of Tangni Debris Flow in Garhwal Himalayas, India. *Environ. Earth Sci.* 80. doi:10.1007/s12665-021-09637-z

Deng, P., Xu, G., Bing, J., Xu, C., and Jia, J. (2020). Evaluation Method of Rain-Flood Resource Utilization Availability and its Application in the Hanjiang River Basin. *Water Supply* 20, 3557–3575. doi:10.2166/ws.2020.251

Du, R. H., and Zhang, S. C. (1981). Characteristics of Glacial Mud-Flow in South-Eastern Qinhai-Xizang Plateau. *J. Glaciol. Geocryol.* (03), 10–16. (in Chinese).

Fan, X., Yunus, A. P., Scaringi, G., Catani, F., Siva Subramanian, S., Xu, Q., et al. (2021). Rapidly Evolving Controls of Landslides after a Strong Earthquake and Implications for Hazard Assessments. *Geophys. Res. Lett.* 48. doi:10.1029/2020GL090509

Gao, Y.-c., Chen, N.-s., Hu, G.-s., and Deng, M.-f. (2019). Magnitude-frequency Relationship of Debris Flows in the Jiangjia Gully, China. *J. Mt. Sci.* 16 (6), 1289–1299. doi:10.1007/s11629-018-4877-6

Glade, T. (2005). Linking Debris-Flow Hazard Assessments with Geomorphology. *Geomorphology* 66, 189–213. doi:10.1016/j.geomorph.2004.09.023

Guo, J., Cui, Y., Xu, W., Yin, Y., Li, Y., and Jin, W. (2022). Numerical Investigation of the Landslide-Debris Flow Transformation Process Considering Topographic and Entrainment Effects: a Case Study. *Landslides* 19, 773–788. doi:10.1007/s10346-021-01791-6

Guzzetti, F., Reichenbach, P., Cardinali, M., Galli, M., and Ardizzone, F. (2005). Probabilistic Landslide Hazard Assessment at the Basin Scale. *Geomorphology* 72, 272–299. doi:10.1016/j.geomorph.2005.06.002

Hu, K. H., Cui, P., and Ge, Y. G. (2012). Building Destruction Patterns by August 8, 2010 Debris Flow in Zhouqu, Western China. *Mt. Res.* 30 (04), 484–490. doi:10.16089/j.cnki.1008-2786.2012.04.020

IMHE (Chengdu Institute of Mountain Hazards and Environment) (1995). *Mountain Disasters and Prevention Countermeasures on the South Line of Sichuan - Tibet Highway (In Tibet)*. Beijin: Science Press.

Iverson, R. M., and Denlinger, R. P. (2001). Flow of Variably Fluidized Granular Masses across Three-Dimensional Terrain: 1. Coulomb Mixture Theory. *J. Geophys. Res.* 106, 537–552. doi:10.1029/2000JB900329

Iverson, R. M. (1997). The Physics of Debris Flows. *Rev. Geophys.* 35, 245–296. doi:10.1029/97RG00426

Jiang, N., Su, F., Li, Y., Guo, X., Zhang, J., and Liu, X. (2021). Debris Flow Assessment in the Gaizi-Bulunkou Section of Karakoram Highway. *Front. Earth Sci.* 9, 660579. doi:10.3389/feart.2021.660579

Kääb, A., Leinss, S., Gilbert, A., Bühler, Y., Gascoin, S., Evans, S. G., et al. (2018). Massive Collapse of Two Glaciers in Western Tibet in 2016 after Surge-like Instability. *Nat. Geosci.* 11, 114–120. doi:10.1038/s41561-017-0039-7

Kim, E. S., and Choi, H. I. (2015). A Method of Flood Severity Assessment for Predicting Local Flood Hazards in Small Ungauged Catchments. *Nat. Hazards* 78 (3), 2017–2033. doi:10.1007/s11069-015-1817-4

Liu, J., Cheng, Z., and Li, Q. (2013). Meteorological Conditions for Frequent Debris Flows from Guxiang Glacier, Mount Nyenchen Tanglha, China. *Mt. Res. Dev.* 33, 95–102. doi:10.1659/MRD-JOURNAL-D-12-00053.1

Liu, J. J., Li, Y., Su, P. C., and Cheng, Z. L. (2008). Magnitude-frequency Relations in Debris Flow. *Environ. Geol.* 55 (6), 1345–1354. doi:10.1007/s00254-007-1083-1

Liu, X. L., and Tang, C. (1995). *Evaluation of Debris-Flow Risk*. Beijin: Science Press.

Looper, J. P., and Vieux, B. E. (2012). An Assessment of Distributed Flash Flood Forecasting Accuracy Using Radar and Rain Gauge Input for a Physics-Based Distributed Hydrologic Model. *J. Hydrology* 412-413, 114–132. doi:10.1016/j.jhydrol.2011.05.046

Luo, H., Zhang, L., Wang, H., and He, J. (2020). Multi-hazard Vulnerability of Buildings to Debris Flows. *Eng. Geol.* 279, 105859. doi:10.1016/j.enggeo.2020.105859

O'Brien, J., Julien, P., and Fullerton, W. (199319932). Two-dimensional Water Flood and Mudflow Simulation. *J. Hydraulic Eng.* 119119, 2. doi:10.1061/(ASCE)0733-942910.1061/(asce)0733-9429(1993)119:2(244)

Pitman, E. B., and Le, L. (2005). A Two-Fluid Model for Avalanche and Debris Flows. *Phil. Trans. R. Soc. A* 363, 1573–1601. doi:10.1098/rsta.2005.1596

Pudasaini, S. P., and Mergili, M. (2019). A Multi-Phase Mass Flow Model. *J. Geophys. Res. Earth Surf.* 124, 2920–2942. doi:10.1029/2019JF005204

Shi, Y. F., Yang, Z. H., Xin, Z. C., and Du, R. H. (1964). Glacier Debris Flow in Guxiang Area, Tibet. *Chin. Sci. Bull.* (06), 542–544. (in Chinese).

Shugar, D. H., Jacquemart, M., Shean, D., Bhushan, S., Upadhyay, K., Sattar, A., et al. (2021). A Massive Rock and Ice Avalanche Caused the 2021 Disaster at Chamoli, Indian Himalaya. *Science* 373 (6552), 300–306. doi:10.1126/science.abh4455

Takahashi, T. (2007). *Debris Flow: Mechanics, Prediction and Countermeasures*. London: Taylor and Francis Group, 35–38.

Tang, J. B., Hu, K. H., Zhou, G., Chen, H., Zhu, X. H., and Ma, C. (2013). Debris Flow Impact Pressure Signal Processing by the Wavelet Analysis. *J. Sichuan Univ. Eng. Sci. Ed.* 45 (1), 8–13. doi:10.15961/j.jsuese.2013.01.003

Vasil'eva, E., Aleksyuk, A., Belyakova, P., Fedorova, T., and Belikov, V. (2019). Numerical Modeling of the Behavior of a Destructive Rain Flood on a Mountain River. *Water Resour.* 46, S43–S55. doi:10.1134/S0097807819070169

Wang, G. Q., Sao, S. D., and Fei, X. J. (1998). Debris Flow Simulation: I-Model. *J. Sediment Res.* (03), 9–15. doi:10.16239/j.cnki.0468-155x.1998.03.002

Wei, F. Q., Hu, K. H., Lopez, J. L., and Cui, P. (2003). The Method of Momentum Zoning of Debris Flow Hazard and its Application. *Chin. Sci. Bull.* (03), 298–301. (in Chinese).

You, Y., Cheng, Z. L., Hu, P. H., and He, S. F. (1997). A Study on Model Testing of Debris Flow in GuXiang Gully, Tibet. *J. Nat. Disasters* (01), 54–60.

You, Y. (2001). Transporting Characteristics of Debris Flow at Guxiang Accumulation Fan in Tibet Autonomous Region. *Bull. Soil Water Conservation* (02), 28–30. doi:10.13961/j.cnki.stbctb.2001.02.007

Zhang, B. B. (2008). *Study on Debris Flow Characteristics in Temperate Glacier Area of Pallon Tsanggpo*, Master's Thesis. [CHINA(SC)]. Sounthwest Jiaotong University.

Zhang, Y., and Lin, P. (2016). An Improved SWE Model for Simulation of Dam-Break Flows. *Proc. Institution Civ. Eng. - Water Manag.* 169 (6), 260–274. doi:10.1680/wama.15.00021

Zhu, L., He, S., Qin, H., He, W., Zhang, H., Zhang, Y., et al. (2021). Analyzing the Multi-Hazard Chain Induced by a Debris Flow in Xiaojinchuan River, Sichuan, China. *Eng. Geol.* 293, 106280. doi:10.1016/j.enggeo.2021.106280

Zhu, P. Y., Luo, F. D., and Kou, Y. Z. (1997). *Debris Flow Development Trend of Guxiang Ravine, Tibet*. Chendu, China: Mountain research, 04, 296–299.

Zou, Q., Cui, P., Zeng, C., Tang, J., and Deep Regmi, A. (2016). Dynamic Process-Based Risk Assessment of Debris Flow on a Local Scale. *Phys. Geogr.* 37 (2), 132–152. doi:10.1080/02723646.2016.1169477

Conflict of Interest: The authors declare that the research was conducted in the absence of any commercial or financial relationships that could be construed as a potential conflict of interest.

Publisher's Note: All claims expressed in this article are solely those of the authors and do not necessarily represent those of their affiliated organizations, or those of the publisher, the editors, and the reviewers. Any product that may be evaluated in this article, or claim that may be made by its manufacturer, is not guaranteed or endorsed by the publisher.

frontiers | Frontiers in Earth Science

METHODS
published: 17 June 2022
doi: 10.3389/feart.2022.921706

Assessment of Debris Flow Activity in Response to an Earthquake Using the Sediment Connectivity Index

Yanji Li[1,2], Kaiheng Hu[1], Xiaopeng Zhang[1,2], Xudong Hu[3], Lan Ning[1,2] and Hao Li[1,2]*

[1]Key Laboratory of Mountain Hazards and Earth Surface Processes/Institute of Mountain Hazards and Environment, Chinese Academy of Sciences, Chengdu, China, [2]University of Chinese Academy of Sciences, Beijing, China, [3]College of Civil Engineering & Architecture, China Three Gorges University, Yichang, China

Large earthquakes can trigger landslides and collapses, which not only increase the mass of loose solid materials but also change the topography of catchments. Debris flow activity in response to earthquakes is of widespread concern; however, most studies have focused on the material conditions and flow property variations prior to and after earthquakes. In this study, we investigate temporal variations in the debris flow activity in a typical catchment in the Wenchuan Earthquake area via the sediment connectivity index (IC), which reflects the sediment delivery efficiency in the catchment. The IC values in different tributaries and during different time periods were calculated to determine their spatial distribution and temporal variations. The results show that high IC values are distributed in downstream tributaries near the main fault. The IC values decreased significantly following a 2008 Wenchuan Earthquake, indicating a continuous decrease in the sediment transfer ability. The debris flow history and loose solid material amounts were also investigated via field surveys. The debris flow activity is closely related to variations in the solid material source amounts and the IC values in the catchment. This study provides a new insight into the assessment of debris flow activity with respect to its close relationship with the distribution of loose solid materials and the sediment connectivity.

Keywords: debris-flow activity, sediment connectivity, material source, Wenchuan Earthquake, geomorphometry

OPEN ACCESS

Edited by:
Wen Zhang,
Jilin University, China

Reviewed by:
Haijun Qiu,
Northwest University, China
Baofeng Di,
Sichuan University, China

***Correspondence:**
Kaiheng Hu
khhu@imde.ac.cn

Specialty section:
This article was submitted to Geohazards and Georisks, a section of the journal Frontiers in Earth Science

Received: *16 April 2022*
Accepted: *30 May 2022*
Published: *17 June 2022*

Citation:
Li Y, Hu K, Zhang X, Hu X, Ning L and Li H (2022) Assessment of Debris Flow Activity in Response to an Earthquake Using the Sediment Connectivity Index. Front. Earth Sci. 10:921706. doi: 10.3389/feart.2022.921706

1 INTRODUCTION

Earthquakes that occur in mountains can instantaneously change landscapes, release massive amounts of energy, and trigger large numbers of landslides as sources of debris flows. Earthquakes play an important role in increasing erosion, sediment transport, and deposition (Pearce and Watson, 1983; Pearce and Watson, 1986; Guo et al., 2016; Fan et al., 2019a; Hu et al., 2019). For example, an earthquake that occurred on May 12, 2008, in Wenchuan County, Sichuan Province, China, triggered more than 56,000 landslides and collapses (Parker et al., 2011; Fan et al., 2019a), with abundant loose solid materials retained in channels and on hillslopes. Debris flows subsequently occurred very frequently in the following years, especially in the rainy seasons in neighboring catchments close to the epicenter (Cui et al., 2009; Guo et al., 2015; Guo et al., 2016; Fan et al., 2019a). The influence of an earthquake is estimated to last more than 20 years (Dadson et al., 2004; Tang et al., 2009; Guo et al., 2016). Therefore, it is necessary, both scientifically and practically, to assess the debris flow activity and its temporal evolution.

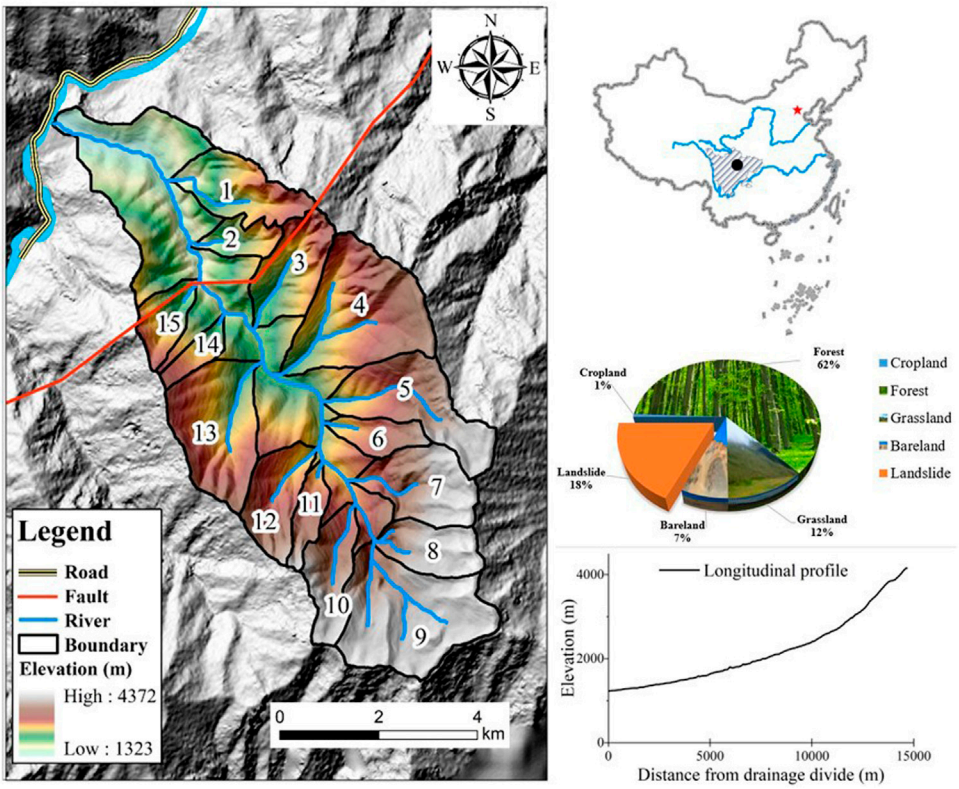

FIGURE 1 | Topography, land use, and channel profile of the Qipangou Valley.

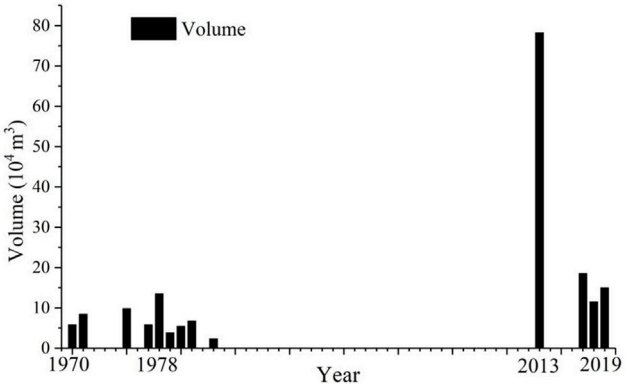

FIGURE 2 | Recorded debris flow occurrences and volumes in Qipangou Valley since 1970.

Earthquakes influence debris flows by creating numerous material sources for debris flows and by changing the topography of the slopes and channels, both of which need to be considered in evaluations of post-earthquake debris flows. Previous studies have indicated that there are temporal variations in the post-earthquake debris flow activity; for example, Fan et al. (2019a) proposed spatial and temporal patterns of enhanced mass wasting based on multi-temporal inventories of coseismic landslides and collapses. Guo et al. (2021) proposed variations in the characteristics of debris flows using actual monitoring data and presented increased triggering conditions after analyzing the hydrological process of debris flow formation. However, the effect of topographic variations is rarely considered.

Connectivity is a concept that represents the materials and energy transfer in a catchment system. It can be expressed at different spatio-temporal scales and is widely used in fields such as hydrology, geomorphology, geography, and landscape ecology (Michaelides and Chappell, 2009). Connectivity represents the linkage of sediment transfer in different parts of a catchment (e.g., the progress of sediment from sources thorough the catchment to the outlet) and is crucial to sediment redistribution over a landscape (Bracken et al., 2015; Najafi et al., 2021). It also provides a constructive framework to describe both the erosion and deposition processes of sediment transport with respect to the spatio-temporal variability of a catchment (Wainwright et al., 2011) and reflects the pathways of runoff and sediment at a given time as an effective concept for sediment management (Heckmann and Vericat, 2018).

Debris flows represent a special type of sediment transfer behavior in a catchment, involving a large amount material movement in a very short period. High connectivity indicates that a debris flow can be easily transferred downstream from its source in a catchment. Nevertheless, the sediment connectivity

FIGURE 3 | Field investigation and remote sensing images in Qipangou valley **(A,B)** photography of Qipangou valley **(C,D)** Ikonos images and UAV images of Qipangou valley.

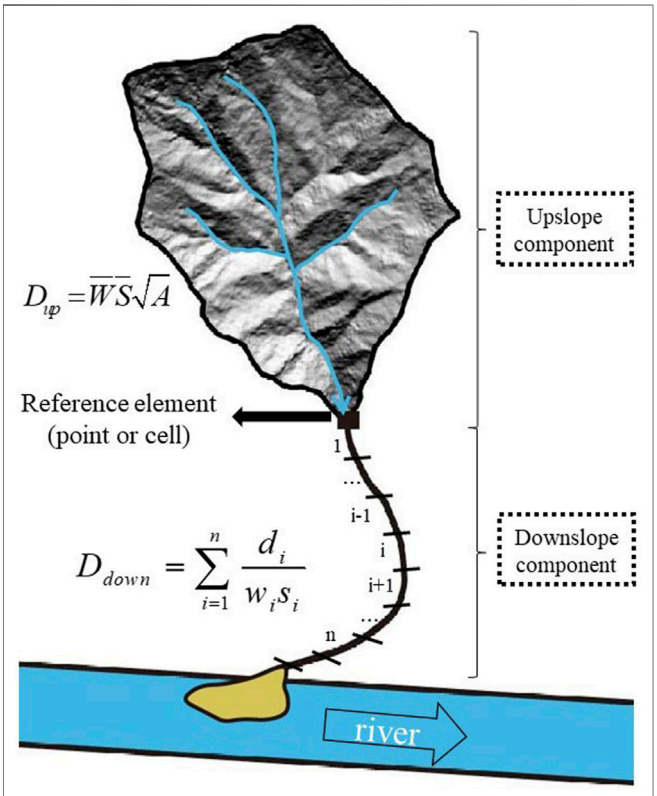

FIGURE 4 | Definition of the sediment connectivity index (IC; Borselli et al., 2008).

is not static; changes in the connectivity not only usually affect the development process of a debris flow, such as the addition of materials and the efficiency of sediment delivery, but can also be used as an index with which to assess the debris flow activity.

As a proxy variable, sediment connectivity is not measured directly. Various indices, existing models, and graph theories have been proposed and employed to quantify the sediment connectivity (Borselli et al., 2008; Hoffmann, 2015; Cossart and Fressard, 2017; Sadeghi et al., 2017; Zanandrea et al., 2019; Pearson et al., 2020; Najafi et al., 2021). In general, it is expressed by the sediment connectivity index (IC), which is calculated using factors affecting the sediment yield and transport, such as topographic characteristics and the vegetative cover (Foerster et al., 2014; Lisenby and Fryirs, 2017; Zanandrea et al., 2021). A model for calculating the IC value on a slope and in a small headwater catchment has been proposed (Borselli et al., 2008; Cavalli et al., 2013) based on the topographic characteristics of the catchment.

The debris flows are a special sediment transfer in a catchment. Debris flows strongly control sediment transfer patterns in mountainous catchments and their frequent and geomorphic changes are rapid. Recently, sediment connectivity method has been used in debris flows transfer (Abatti et al., 2021) and the high IC values have a superposition with debris flows path. So, sediment connectivity could be used to describe the potential transfer path for debris flows. It is a linkage of materials movements, no matter the materials come from general sediment transfer or debris flows. Here, we use this approach to investigate how the connectivity and topographic variations in a debris flow catchment, which has more extensive and complex sediment transfer behavior than a single slope, correspond to the debris flow activity in

TABLE 1 | Potential debris flow sources in the catchment.

River	Area (km2)	Length (km)	Average Slope (‰)	Potential Source (m3)
Main stream	54.2	14.5	170	323.1 × 104
1	2.58	3.22	530	--
2	1	1.13	588	11.25 × 104
3	2.52	1.46	271	1.6 × 104
4	5.49	3.05	263	2.25 × 104
5	3.81	4.26	470	--
6	1.13	0.97	537	1.8 × 104
7	2.88	2.86	590	--
8	1.91	0.94	550	--
9	5.57	2.57	600	--
10	2.09	3.24	470	--
11	0.96	2.76	560	--
12	2.19	1.82	560	--
13	4.18	1.15	222	0.65 × 104
14	0.75	0.66	670	--
15	1.29	1.32	600	8.6 × 104

that catchment. We investigate how the variation in the loose solid materials and the sediment connectivity of a debris flow is influenced by an earthquake. Both the spatial distribution and the temporal variation of the loose solid materials and sediment connectivity were analyzed in a catchment to study the effect of an earthquake on the debris flow activity in the 2008 Wenchuan Earthquake area.

2 STUDY SITE

The Qipangou Valley was selected to assess the debris flow activity in response to an earthquake. This valley is situated in Wenchuan County in Sichuan Province, southwestern China, approximately 44 km from the epicenter of the 2008 Wenchuan Earthquake. It is a tributary of the Minjiang River and covers an area of 54.2 km^2. The elevation ranges from 1320 m at the basin outlet to 4360 m at the mountain ridge. The channel is 15.8-km long and the channel gradient is approximately 180‰. Mid-alpine mountains and deep canyon landforms characterize the catchment. It hosts a variety of glacial-erosion geomorphic structures, including a horn, cirque, and hanging valley above 3000 m. In contrast, in the main channel, the catchment is characterized by a deep-cutting V-shaped valley.

The average annual mean precipitation is 530 mm. The catchment is situated in the southern part of the Jiudingshan Cathaysian tectonic belt and is a part of the interstitial fold subsystem of the Ganzi-Songpan geosynclinal belt and the Yangtze Platform. The lithology is principally composed of dolomite, diorite, and granite, which have developed rock joints and fissures over time. As a result of the hard rocks and the stable vegetation, the primary sediment source for debris flows prior to 2008 was shallow slope sediments near the outlet. Debris flows occurred with low frequency and contained small amounts of sediment as a result of the dry climate conditions and limited source materials.

The catchment was significantly affected by the 2008 Wenchuan Earthquake, which caused large-scale collapses and landslides; for example, earthquake-related landslides occurred over 22% of the area in 2010 (**Figure 1**). The most disastrous debris flows event occurred on July 11, 2013; this event was triggered by a storm with 118 mm of rainfall and resulted in eight deaths and six missing, caused infrastructure destruction, and blocked the Minjiang River, forming a dammed lake. Associated debris flows are still currently active, indicating the necessity of assessing the debris flow activity in this region (**Figure 2**). From 2014 to 2021, we took many field investigations in Qipangou valley, and many data have been acquired, especially the real-time distribution of landslides and collapses after the 2008 Wenchuan Earthquake. Therefore, Qipangou valley is the best for this research.

3 DATA SOURCES AND METHODS

3.1 Data Acquisition

The geographic information data used for this study consisted of digital elevation models (DEMs) and remote-sensing images. The studied time period was divided into periods before 2008, from 2008 to 2013, and after 2013, based on two catastrophic events: the Wenchuan Earthquake on May 12, 2008, and the debris flow on July 11, 2013. The DEM derived from the SRTM data in 2008 with a resolution of 30 m × 30 m, ALOS PALSAR data collected in 2010 with a horizontal accuracy of 12.5 m × 12.5 m, and an unmanned aerial vehicle DEM with a resolution of 12.5 m × 12.5 m were used for the topographic analyses in the different time periods. The aerial photographs from Landsat-4/5 on June 30, 2000, with a resolution of 30 m × 30 m, Ikonos on May 23, 2008, with a resolution of 1 m × 1 m, and an unmanned aerial vehicle on July 13, 2013, with a resolution of 1 m × 1 m, were used to determine the land use and analyze the debris flow sources in the different time periods (**Figure 3**).

3.2 Methods to Identify IC

In this study, we use IC to represent the potential debris flows transfer pathway and to describe the storage capacity of a debris flow catchment. IC is a dimensionless parameter that has upslope and downslope components and is therefore used to express the sediment transport and the potential connectivity between units

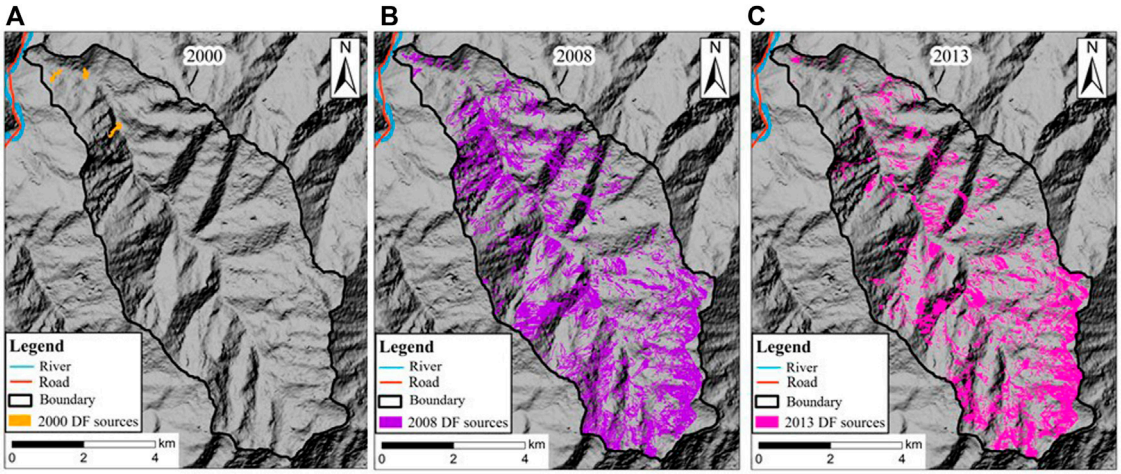

FIGURE 5 | Distribution of loose source materials for debris flows. **(A)** Debris flow sources in 2000, prior to the 2008 Wenchuan Earthquake. **(B)** Debris flow sources in 2008, just after the earthquake. **(C)** Debris flow sources in 2013, after a catastrophic debris flow.

(**Figure 4**). It is calculated using **Eq. 1** (Crema and Cavalli, 2018), which describes the sediment changes over an entire catchment. The upslope component describes the main distribution of the sediment yield, and the amount of loose solid materials is related to the slope and the area. Sediment transfer primarily takes places in the channels in the downslope component and is influenced by the runoff length and the channel slope. The ratio of the upslope and downslope sediments could represent the sediment transfer efficiency from upslope to downslope.

$$IC = \log_{10}\left(\frac{D_{up}}{D_{down}}\right) = \log_{10}\left(\frac{\bar{w}\bar{s}\sqrt{A}}{\sum_i \frac{d_i}{w_i s_i}}\right) \quad (1)$$

Here, D_{up} and D_{down} are the upslope and downslope components, respectively, of the connectivity in the catchment; s indicates the slope in D_{up} and D_{down} [m/m]; A is the upslope contributing area [m^2]; and w is the weighing factor for the upslope and downslope. In this paper, sediment connectivity is mainly expressed the potential sediment transfer pathway, which influenced by terrain characteristics. So that w is replaced with the roughness in this paper, which is the impedances for sediment transfer and computed as the standard deviation of the residual topography at a scale of few meters. (Cavalli et al., 2013). d_i is the length of each cell along the sediment transfer pathway [m]; w_i is the weight of each cell, which represent the roughness in this paper; and s_i is the slope gradient of each cell [m/m]. IC is computed using the two slope components and is defined in the range of $[-\infty, +\infty]$.

4 RESULTS

4.1 Debris Flow Sources in the Catchment

4.1.1 Amount and Distribution of Debris Flow Sources in the Catchment

According to field investigations and the remote-sensing interpretation, shallow slope failures, landslides, and loose solid accumulations in the channels are the main sources of the debris flows. Of these, slope sources, including landslides and shallow failures, can potentially increase the sediment connectivity, whereas solid materials in channels can decrease the connectivity (Zhou et al., 2022).

Landslides and collapses are the main source types on hillslopes in the headwater regions and along the main channel. These sources generally occur on steep slopes of 20–40°. An earthquake can devastate the vegetation (forest, shrub, and grass) on the original slopes and increase the slope surface runoff, which can increase the slope erosion. The surface runoff may deeply cut the slope surface and form a channel on the slope, transferring material from the upper slope to the toe of the slope. In addition, an earthquake may cause multiple cracks on the heads of hillslopes, which increases the potential for post-earthquake landslides. These types of slope failures increase the sediment connectivity from the slopes to the channels.

There are several types of channel materials. For example, deposits from coseismic landslides may accumulate in the channels and increase the roughness. Shallow slope deposits on both sides of the channels may partially block the channels and increase their curvature. Compared with natural landslides, individual deposits may be smaller in amount but occur in larger numbers. Shallow rills formed on the slopes also contribute materials to debris flows during rainstorms. These accumulations greatly raise the channel bed; for example, the field survey indicated that the main channel was uniformly raised by approximately 3 m after the debris flow in 2013. Accumulations also change the slope gradient and increase the impedance for debris flows, which decreases the sediment connectivity in the channels.

To quantify the amount of source materials, remote-sensing images were used to analyze the distribution and areas of the slope sources. Then, **Eqs 2**, **3** (Larsen et al., 2010; Li et al., 2014)

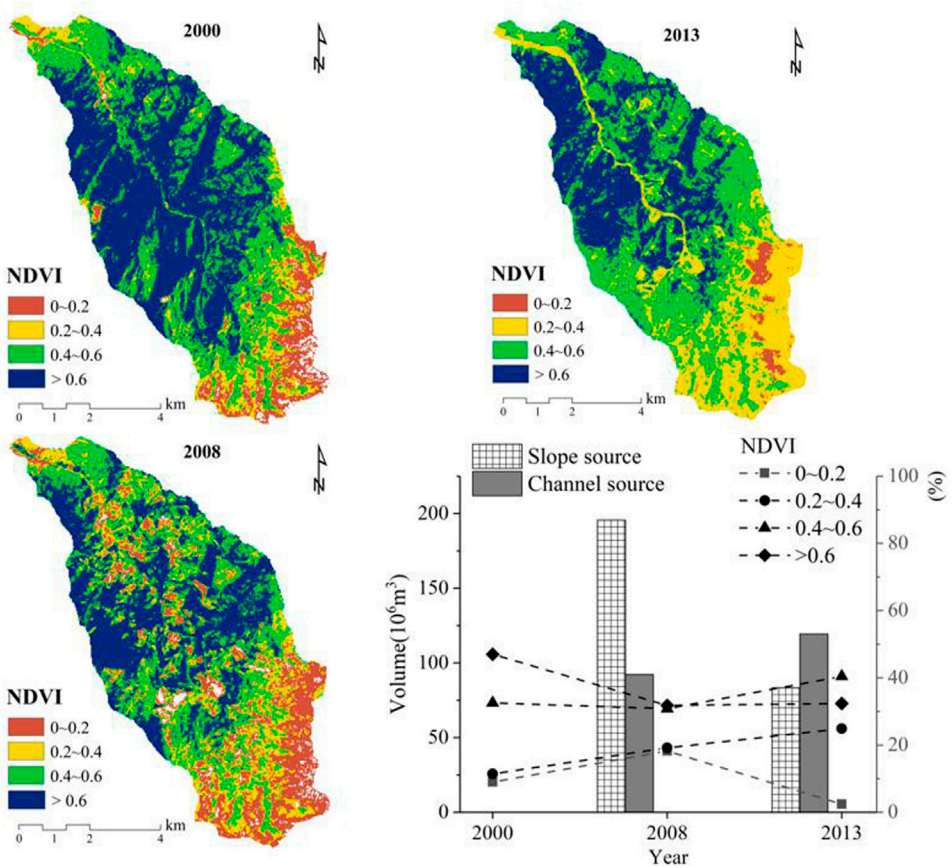

FIGURE 6 | Spatio-temporal distribution of the normalized difference vegetation index (NDVI) in 2000, 2008, and 2013. Green represents areas with high vegetative cover, and red represents areas with low or no vegetative cover.

were used to calculate the volumes of the loose solid materials on the slopes and in the channel, respectively.

$$V = \alpha A^{\gamma} \quad (2)$$

$$V = Ah \quad (3)$$

In **Eq. 2**, V is volume of the landslide on the slope; A is area of the landslide; α is the intercept, and γ is a scaling exponent. Researchers set α to 0.146 and γ to 1.332, which computed by collecting a large number of landslides all over the world. In **Eq. 3**, V is the volume of sediment in the main channel, A is area of deposits in the channel, and h is the average thickness of the sediment in the channel. In this paper, h is set to 3 by the field survey.

The calculated amounts of loose materials in the catchment are listed in **Table 1**. Shortly after the earthquake in 2008, the loose materials were primarily distributed in the tributaries in the middle part of the catchment; this may reflect the close proximity of this region to the active fault (**Figure 1**). The amounts of potential solid materials in tributaries 2, 3, and 4, all of which have areas of approximately 1 km^2 on the right-hand side of the main channel, were found to be 11.25×10^4 m^3, 1.6×10^4 m^3, and 2.25×10^4 m^3, respectively. Tributary 15 contributed the largest amount of material sources on the left-hand side of the main channel and is also close to the fault. The total volume of material sources was found to be 8.6×10^4 m^3 (**Table 1**).

4.1.2 Temporal Variations in the Debris Flow Source Material Amounts

The loose materials resulting from the Wenchuan Earthquake were transferred in the years following the earthquake. Therefore, the variation in the potential sources is of great interest. Accordingly, the spatial distribution and amounts of loose solid materials in different periods need to be determined.

The total area of landslides and collapses was 1.4×10^4 m^2; the volume of 1.1×10^4 m^3 calculated in 2000 represents the conditions prior to the earthquake (**Figure 5A**). The sources were primarily landslides and collapses on the hillslopes in the middle of the catchment and downstream. This amount was not sufficient to form large-scale debris flows.

The 2008 Wenchuan Earthquake triggered multiple landslides on the hillslopes, which then subsequently accumulated in the channels. Therefore, the amount of source materials for debris flows increased significantly. Remote-image interpretation indicates that the earthquake triggered 983 coseismic

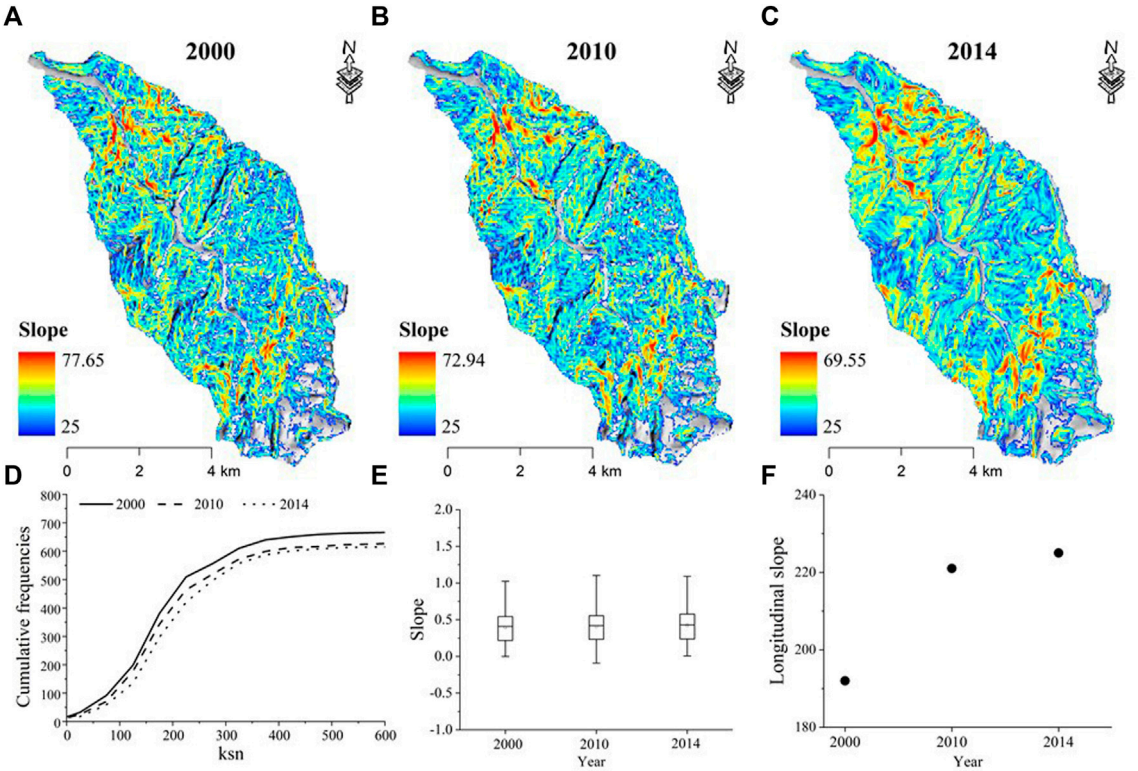

FIGURE 7 | Topographic variation in response to the earthquake **(A–C)** Slope variation in 2000, 2008, and 2014, respectively. **(D)** Channel steepness index variation in the Qipangou catchment. **(E)** Average slope of the main channel in 2000, 2010, and 2014. **(F)** Main stream longitudinal slope gradient in 2000, 2010, and 2014.

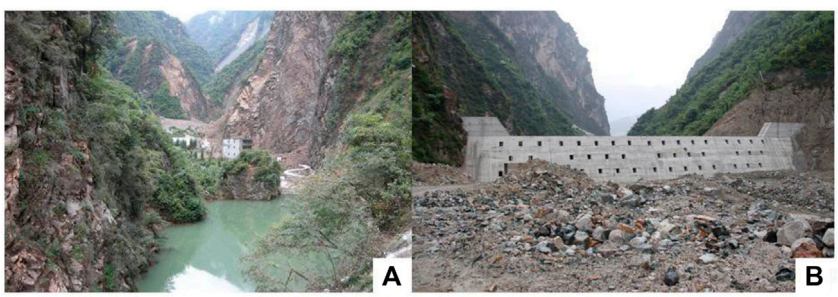

FIGURE 8 | (A) Dammed lake formed by the earthquake and **(B)** artificial dam in the catchment.

landslides and a large amount of loose deposits in the catchment, with a total landslide area of 1307×10^4 m^2, covering 24.3% of the catchment. The volumes of loose solid materials were 125.6×10^6 m^3 and 70.2×10^6 m^3 on the slopes and in the channels, respectively (**Figure 5B**).

The available source materials definitely increased the debris-flow frequency and scale. However, these materials were then transported out of the catchment in the form of debris flows and other fluvial mechanisms (e.g., hyper-concentration flows and debris floods). In addition, the natural vegetative recovery decreased the areas and the volumes of the landslides. In 2013, the landslide area was calculated to be 901.46×10^4 m^2, consisting of 603.36×10^4 m^2 on the hillslope and 298.1×10^4 m^2 in the main channel (**Figure 5C**). The volume of sources on the slope was 83.3×10^6 m^3, less than the volume in 2008, and the volume in the channel was 62.9×10^6 m^3, 10.4% less than the volume in 2008.

The variation in the normalized difference vegetation index (NDVI) reveals the variation in the vegetation and the landslide

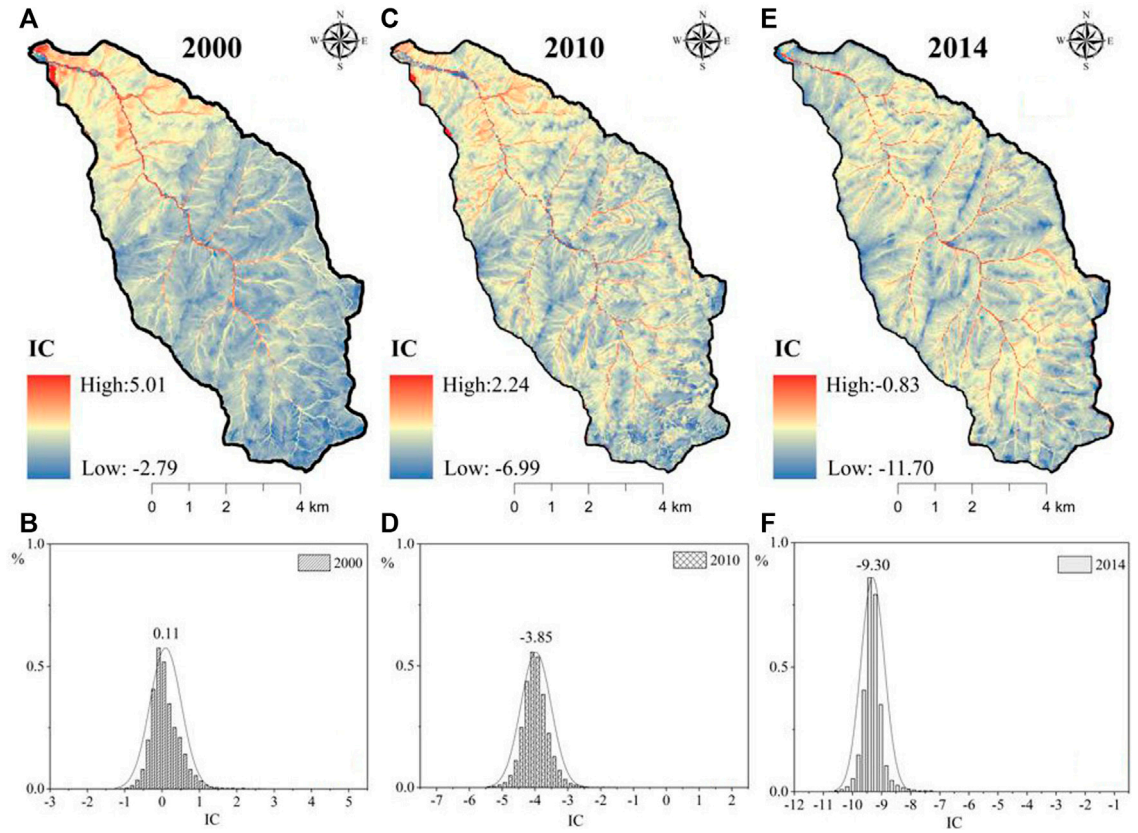

FIGURE 9 | Distribution of the IC values. **(A)** Sediment connectivity in 2000, prior to the 2008 earthquake. **(C)** Sediment connectivity in 2010. **(E)** Sediment connectivity in 2014 **(B,D,F)** IC values with Gaussian distributions. The expectation values are used to describe the variation in the IC values.

TABLE 2 | Sediment connectivity index (IC) values in 2000, 2010, and 2014.

River	IC Value								
	2000			2010			2014		
	Max	min	Mean	Max	Min	Mean	Max	min	Mean
Main river	5.01	−2.79	0.11	2.24	−6.99	−3.85	−0.83	−11.70	−9.30
1# tributary	2.22	−0.55	0.57	1.26	−4.96	−3.67	−2.56	−10.48	−9.20
2# tributary	1.92	−0.39	0.41	−1.80	−4.92	−3.80	−7.30	−10.41	−9.18
3# tributary	1.23	−0.84	0.08	−0.04	−5.20	−3.96	−7.76	−10.37	−9.27
4# tributary	1.45	−0.79	−0.04	1.98	−5.23	−4.01	−1.86	−10.80	−9.37
5# tributary	1.47	−0.95	−0.04	2.07	−5.85	−4.02	−1.55	−10.73	−9.29
6# tributary	1.44	−0.80	−0.05	−2.67	−4.77	−3.94	−8.06	−10.03	−9.27
7# tributary	1.24	−0.86	−0.02	−2.27	−5.19	−4.00	−0.83	−10.56	−9.23
8# tributary	1.13	−0.97	−0.12	1.72	−6.49	−4.04	−1.34	−11.02	−9.35
9# tributary	1.00	−2.79	−0.24	1.69	−6.99	−4.25	−1.81	−11.18	−9.43
10# tributary	1.06	−1.06	0	2.24	−6.22	−3.96	−1.21	−10.37	−9.20
11# tributary	5.01	−0.63	−0.05	1.89	−5.02	−4.04	−8.09	−10.16	−9.30
12# tributary	1.08	−0.87	−0.04	1.24	−5.40	−4.09	−7.87	−10.67	−9.33
13# tributary	1.26	−0.78	0.02	1.59	−6.36	−4.05	−7.78	−10.65	−9.35
14# tributary	0.98	−0.78	0.15	−3.05	−5.07	−4.11	−8.32	−10.58	−9.36
15# tributary	1.25	−0.19	0.33	1.94	−4.56	−3.72	−7.98	−10.16	−9.28

area in the catchment. Prior to the earthquake, areas with NDVI >0.4, representing high vegetative cover, dominated the catchment, accounting for 80% of the total area. Meanwhile, in 2008, this area decreased to 62.6% and areas with NDVI <0.2, which represents nearly bare land, accounted for 18.25% of the total area. In 2013, the area with NDVI >0.4 recovered to 72.8% and areas with NDVI <0.2 accounted for 2.3% of the total area (**Figure 6**).

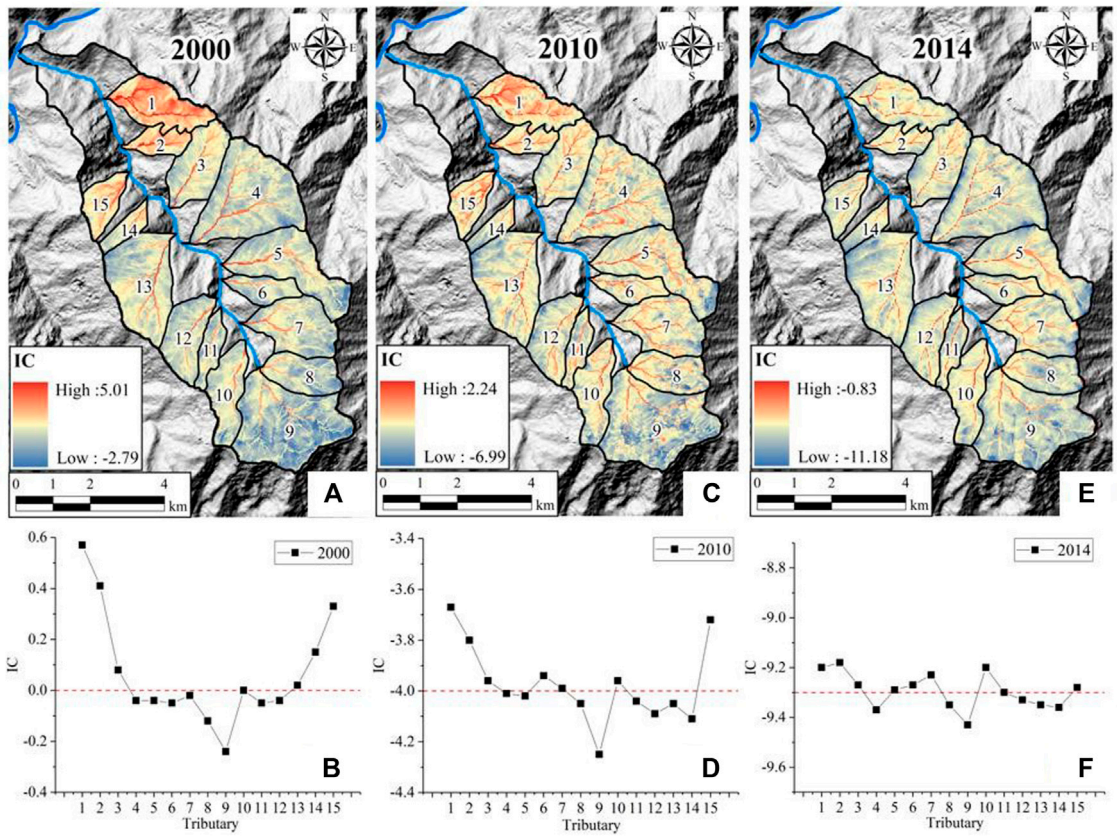

FIGURE 10 | Distribution of the IC values in the 15 tributaries. **(A)** Sediment connectivity in 2000, prior to the 2008 Wenchuan Earthquake. **(B)** Mean IC values of the 15 tributaries in 2000. **(C)** Sediment connectivity in 2010. **(D)** Mean IC values of the 15 tributaries in 2010. **(E)** Sediment connectivity in 2014. **(F)** Mean IC values of the 15 tributaries in 2014.

TABLE 3 | IC values in the channels and on the slopes.

Site		IC Value								
		2000			2010			2014		
		Max	min	Mean	Max	min	Mean	Max	min	Mean
Whole catchment	channel	3.86	2.41	0.73	0.71	6.99	–3.33	7.22	10.76	–9.16
	slope	5.01	2.79	0.07	2.24	6.83	–4.00	0.83	11.70	–9.31
1# tributary	channel	2.22	0.02	1.07	1.67	4.64	–2.98	7.22	10.15	–8.90
	slope	1.63	0.55	0.55	2.40	4.96	–3.69	7.86	10.48	–9.20
9# tributary	channel	1.00	1.15	0.24	2.61	6.99	–3.85	9.08	10.76	–9.38
	slope	0.83	2.79	-0.26	1.69	6.83	–4.26	1.81	11.18	–9.43

4.2 Topographic Variation in Response to the Earthquake

The local topography in the catchment also changed significantly as a result of the earthquake and the following sediment transformation activities.

As previously mentioned, debris flows in the tributaries have a significant influence on the main channel by not only suppling sediment accumulation to the main channel but also by changing the local terrain. The maximum slope in the catchment decreased from 77.2° in 2000 to 72.9° in 2010 and 69.6° in 2014. However, the area with slope >40° increased with time. The area was 139.4×10^4 m^2, accounting for 2.57% of the total area prior to 2000. The earthquake triggered landslides and mass movements on the slope, which caused the slope to steepen; the area with slope >40° increased to 142.3×10^4 m^2, accounting for 2.63% of the total area in 2008, shortly after the earthquake. This area increased further to 161.64×10^4 m^2, accounting for 3.0% of the total area in 2014. This can be attributed to repeated erosion events on the

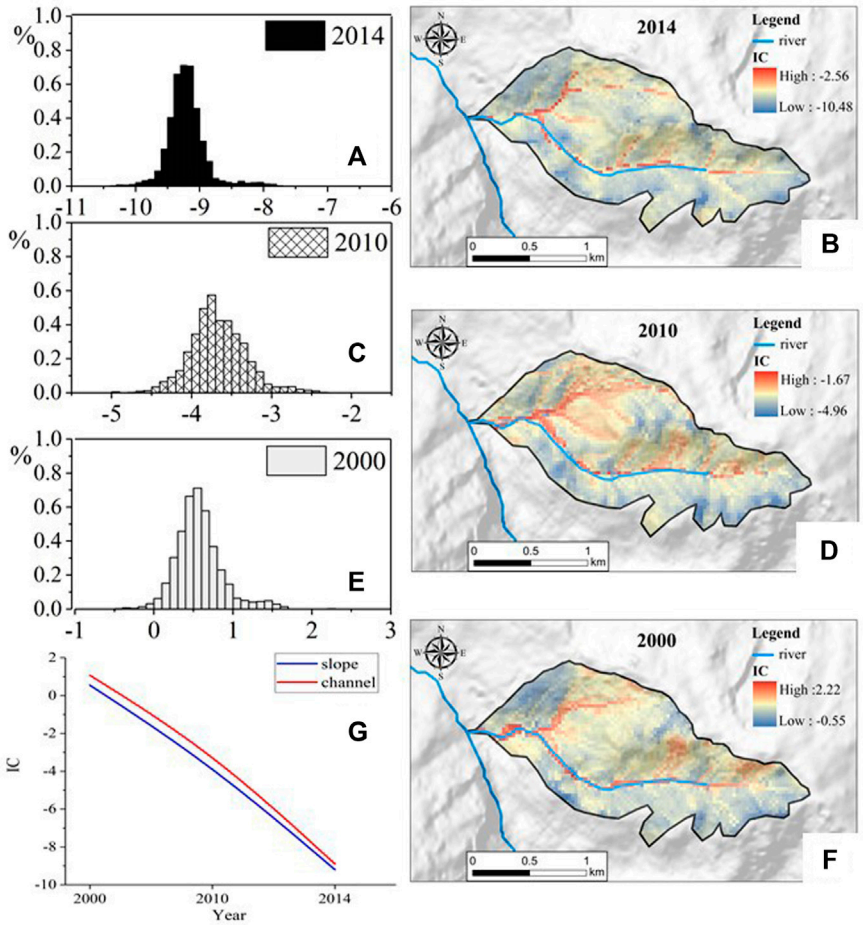

FIGURE 11 | Distribution of the IC values in tributary 1 near the outlet.

slopes caused by rainfall, increasing the local gradient of slope, as well as the failure of the slope toe triggered by the channel runoff, which induced additional landslide events and increased the slope gradient (**Figures 7A–C**).

The channel steepness index reflects the steepness of the entire channel profile (Trauerstein et al., 2013). Affected by the 2008 Wenchuan Earthquake, the high steepness of the main river decreased. Before and after the earthquake, the change was quick, while from 2008 to 2014, the rate of change slowed down (**Figure 7D**). The average slope of the main Qipangou River changed slowly (**Figure 7E**), and the longitudinal slope gradient of the main stream increased; this is an important factor affecting the hydrodynamic conditions in the river (**Figure 7F**). After the earthquake, large amounts of loose solid materials were deposited in the channel and the riverbeds that were steep prior to the earthquake were filled after the earthquake. The main river was therefore relatively gentle. However, the debris flows scrapped the channel after the earthquake, such that the average groove gradient then increased.

The local channel topography has also changed with time. First, the loose materials triggered by the earthquake accumulated in the channels causing the channel beds to raise. Second, the deposits of debris flows in tributary 2 blocked the main stream and generated a quake lake (**Figure 8A**), which suffered an outburst in 2009. In 2010, dams were built downstream, which intercepted the debris flow movements (**Figure 8B**). Initially, the dams decreased the smoothness of the channel, further decreasing the sediment connectivity. However, later, debris flows may fill up the dams and raise the main channel.

4.3 Spatio-Temporal Variation in the Sediment Connectivity of the Debris Flows

4.3.1 Temporal Variations in IC

The material transformation process occurs from the slope to the channel and then to the outlet of the catchment. Therefore, topographic variations influence the sediment connectivity in this catchment. The IC values in the total catchment and in the 15 tributaries in 2000, 2010, and 2014 were calculated using **Eq. 1**. In each time period, the values in the 15 tributaries are found to fit a Gaussian distribution, which provides a method to obtain a mean value to represent the characteristics of the sediment connectivity

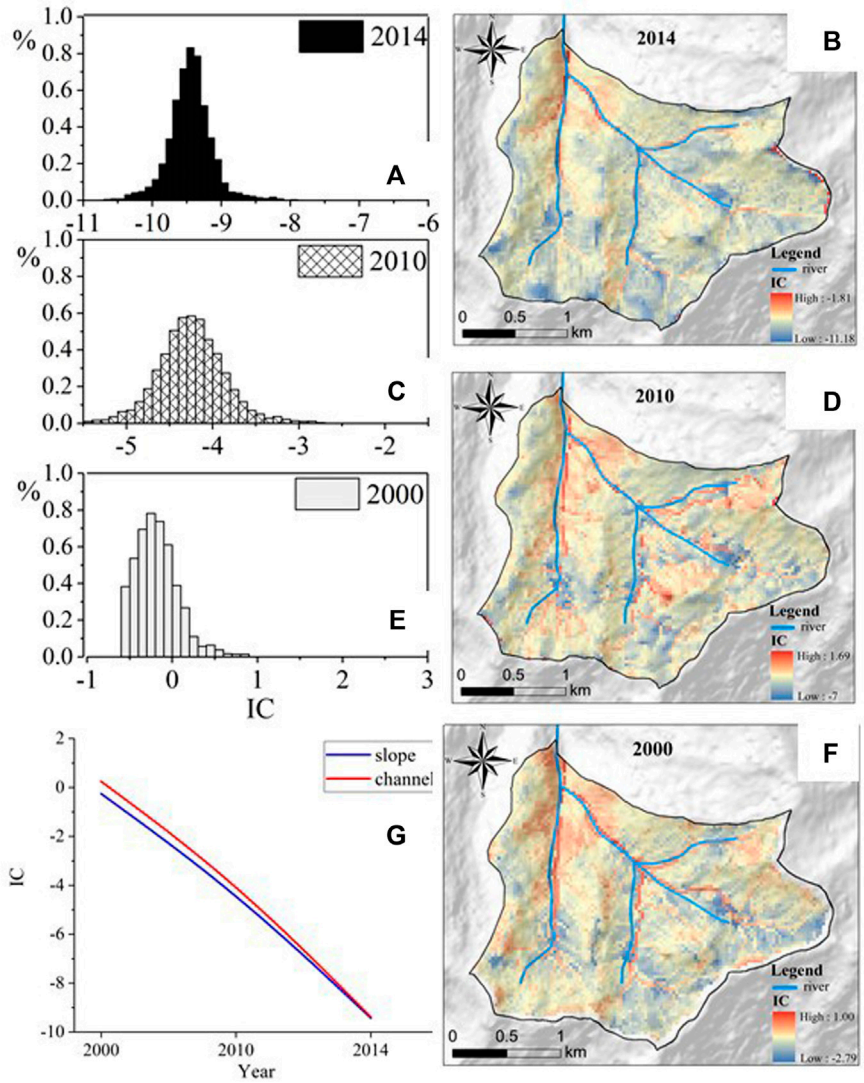

FIGURE 12 | Distribution of the IC values in tributary 9 near the outlet.

of the catchment (**Figure 9**). The derived values are listed in **Table 2**.

The IC values ranged from −2.79 to 5.01, with a mean value of 1.11 in 2000 prior to the earthquake (**Figure 9A**). The high sediment connectivity regions were distributed in the downstream region of the catchment and along the runoff pathway in the channels; the mean IC value in the channel was 0.73, and that on the slope was 0.07.

In 2010, the IC values ranged from 2.24 to −6.99, with a mean value of −3.85. The mean IC values were −4.00 and −3.33 on the slopes and in the channels, respectively; both values were lower than those in 2000. This indicates that the sediment connectivity of the debris flows decreased. The IC value decreased on the hillslopes because landslides and collapses destroyed the ground cover, such that boulders were stored on the slope, increasing the impedance for sediment movement. In the channels, the IC value decreased because of the abundant materials accumulated from the landslides, collapses, and slope failures of other forms triggered by the earthquake and because the debris flow deposits from the tributaries partially blocked the main channel.

In 2014, the IC values ranged between −0.83 and −11.7, with a mean value of −9.30. The mean IC values on the slopes and in the channels were −9.31 and −9.16, respectively, both values being lower than those in 2010. On the slopes, the vegetative recovery increased the roughness, therefore decreasing the connectivity. In the channels, the decreasing values were primarily a result of the formation of debris flow dams, which significantly blocked the transportation of materials.

4.3.2 Spatial Distributions of IC

The IC value is not evenly distributed in the catchment, as shown in **Figure 10**. Prior to the earthquake, the IC values in the tributaries close to the catchment outlet (downstream) were higher than those in other tributaries; however, the earthquake

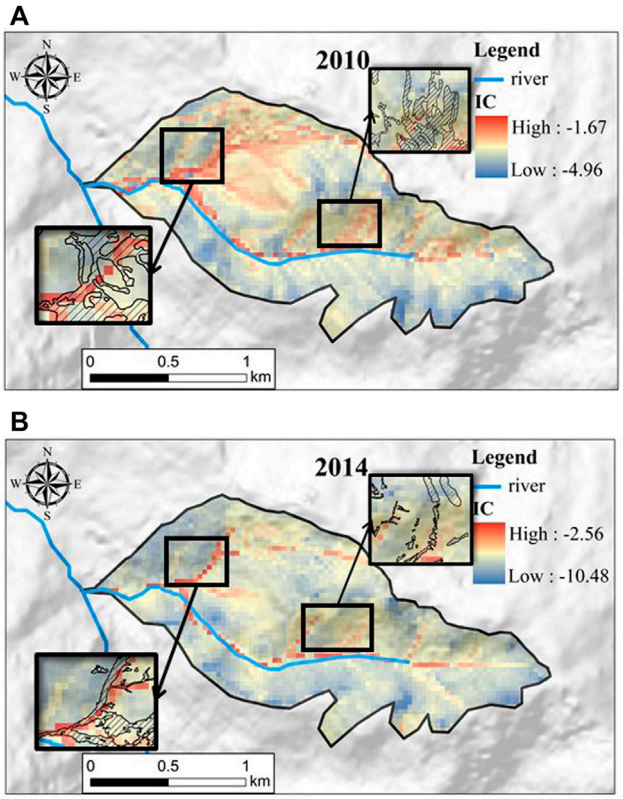

FIGURE 13 | Comparing the distribution of landslides and collapses with the distribution of the sediment connectivity in tributary 1 in **(A)** 2010 and **(B)** 2014. In 2010, the distribution of landslides and collapses is consistent with distribution of high IC values. In 2014, the areas of landslide and collapses are decreasing, as are the areas with high IC values.

caused the IC values to become more evenly distributed throughout the catchment. As **Figure 9** shows, the standard deviation in the values in all 15 tributaries is decreasing and homogeneous after the earthquake.

Tributaries 1 and 9, which are located in the downstream and upper stream regions of the catchment, respectively, are taken as examples (**Figures 11**, **12**). Prior to the earthquake, the mean IC value in tributary 1 was 0.57; this decreased to −3.67 and −9.20 in 2010 and 2014 (**Figures 11A–F**), respectively. In tributary 9, the mean value in 2000 was 0.57; this decreased to −4.25 and −9.43 in 2010 and 2014 (**Figures 12A–F**), respectively. The values decreased temporally in both tributaries after the earthquake, and the degree of the decrease in tributary 1 was much higher than that in tributary 9 (4.42 and 4.01, respectively) (**Figures 11G**, **12G**). This indicates that the earthquake affected the connectivity unevenly throughout the catchment.

As shown in **Table 3**, the IC values in the main channel are constantly higher than those on the slopes, both before and after the earthquake, indicating that it is easier to transport sediment in the channels than on the slopes.

In each tributary, the IC values decreased both on the slope and in the channel. For example, the mean value decreased from 0.07 in 2000 to −4.00 in 2010 and to −9.31 in 2014 on the slopes, while in the channels, the IC value decreased from 0.73 to −3.33 and then to −9.16. This decrease reflects the effects of landslides and collapses on the slopes and the blocking effect of the abundant loose materials, which increased the roughness in the channels from 2000 to 2010. Meanwhile, in the following years, the deceases in the IC values occurred because of vegetative recovery on the slopes and the building of dams in the channels; similar processes occurred throughout the entire catchment. In some tributaries, such as tributary 9, even though there were no dams built, the IC value decreased in the channel because the mean gradient was smoother and sediment deposition occurred in the channel bed raising the main channel of the catchment.

The earthquake affected the connectivity in the channels more than that on the slopes. In tributary 1, the mean channel and slope IC values were 1.07 and 0.55, respectively, in 2000 prior to the earthquake, showing an evident difference; however, the mean IC values of the two regions were later much closer, −2.98 and −3.69, respectively, in 2010 and −8.90 and −9.20, respectively, in 2014. This indicates that the earthquake caused the connectivity to become more even in each tributary. Even though the overall IC decrease in tributary 9 is 9.19, which is lower than the value of 9.77 in tributary 1, the connectivity became more even during the same period (**Figures 11**, **12**).

5 DISCUSSION

The time scale over which an earthquake affects debris flows is an issue of great interest (Guo et al., 2016; Fan et al., 2019b). Previous studies examined the temporal variations in post-earthquake debris flow activity primarily by analyzing the variation in the material amounts and via actual monitoring (Fan et al., 2019a; Guo et al., 2021). In this study, we examined this issue from the perspective of the loose solid materials distribution and the sediment transfer conditions to explain the spatio-temporal variation in the debris flow activity in response to an earthquake. Despite the influences of the amount of movable materials, the triggering rainfall and/or runoff conditions, and the composition of the soil particles, the topographic conditions of the slopes and channels and the sediment connectivity also considerably influenced the debris flows.

Earthquakes change the local landscape and vegetation, which affect the sediment distribution and debris flow movement. However, it is also interesting to compare the distribution of the landslides and collapses with the distribution of the sediment connectivity in the catchment, even though no significant general similarities were observed in this study, that is, the areas with landslides and collapses do not necessarily correspond to the areas with high IC values. In most cases, conversely, the channels accumulating abundant loose solid materials have higher values and, with decreasing amounts of loose solid materials, the sediment connectivity decreases (**Figure 13**) as does the debris flow activity. The sediment connectivity also influences the frequency of the debris flows.

The loose solid materials and sediment connectivity are two main factors which influenced the debris flows activity. In this work, we consider the mount of sediment and its transfer

pathway to represent debris flows activity affected by the earthquake, which gives a new method for debris flows activity in respond to an earthquake. This is simple and easy to compute. But, limiting by the data, some details are imperfect, they need to be improved in the future.

6 CONCLUSION

Debris flow activity is linked to the loose solid material conditions and sediment transfer capacity in a catchment. In this study, we used the IC to evaluate the sediment transfer capacity and, combining this with an analysis of the material amount variations, assessed the debris flow activity in a typical catchment affected by the 2008 Wenchuan Earthquake.

The earthquake triggered the significant generation of loose materials in the catchment. Prior to the earthquake, loose materials constituted an area of only $1.1 \times 10^4\ m^3$ and were unevenly distributed throughout the catchment. However, this area increased to $195.8 \times 10^6\ m^3$ in 2008 and then decreased to $146.2 \times 10^6\ m^3$ in 2013, indicating a tendency of the amount of loose material to increase as a result of an earthquake and then gradually decrease.

The local topography, including the slope and channel gradient, varied as a result of the effect of the earthquake and the manual debris flow-control works. This resulted in variations in the sediment connectivity in the catchment. Prior to the earthquake in 2000, the mean value of the sediment connectivity was 1.11, which was favorable to sediment transfer. However, the 2008 Wenchuan Earthquake changed the terrain and the sediment connectivity in the Qipangou valley. After the earthquake, the sediment connectivity decreased. The mean values of the sediment connectivity were −3.85 in 2010 and −9.30 in 2014, both of which are lower than the mean value prior to the earthquake.

The debris flow activity is influenced by changes in sources volume and sediment connectivity. From 2008 to the present, the activity of debris flows in Qipangou valley was increasing firstly and then decreasing. At first, tremendous mounts of loose solid materials controlled the activity of debris flows mainly. Only very weak sediment connectivity was required, the debris flows were happened. Subsequently, the debris flows transferred lots of sources from upslopes and deposited in the channels. So that the sediment connectivity in the channel decreased more than that on the hillslopes and the values in the downstream regions had a higher variation than those in the upstream regions. Ultimately, the debris flow activity decreased because of the variations in the loose materials and the sediment connectivity. Accordingly, this study provides a new insight into evaluations of debris flow activity.

DATA AVAILABILITY STATEMENT

The original contributions presented in the study are included in the article/Supplementary Material, further inquiries can be directed to the corresponding author.

AUTHOR CONTRIBUTIONS

YL, write this paper KH, guildance XZ, programming LN, data analysis HL, data analysis, XH, guildance.

FUNDING

This study is supported by the Second Tibetan Plateau Scientific Expedition and Research Program (2019QZKK0902), the National Natural Science Foundation of China (41790434), and K.C. Wong Education Foundation.

REFERENCES

Abatti, B. H., Zanandrea, F., Rodolfo Paul, L., and Michel, G. P. (2021). *Relationship between Sediment Connectivity and Debris Flow in a Mountain Catchment*. Vienna, Austria: EGU.

Borselli, L., Cassi, P., and Torri, D. (2008). Prolegomena to Sediment and Flow Connectivity in the Landscape: A GIS and Field Numerical Assessment. *Catena* 75 (3), 268–277. doi:10.1016/j.catena.2008.07.006

Bracken, L. J., Turnbull, L., Wainwright, J., and Bogaart, P. (2015). Sediment Connectivity: a Framework for Understanding Sediment Transfer at Multiple Scales. *Earth Surf. Process. Landforms* 40 (2), 177–188. doi:10.1002/esp.3635

Cavalli, M., Trevisani, S., Comiti, F., and Marchi, L. (2013). Geomorphometric Assessment of Spatial Sediment Connectivity in Small Alpine Catchments. *Geomorphology* 188, 31–41. doi:10.1016/j.geomorph.2012.05.007

Cossart, É., and Fressard, M. (2017). Assessment of Structural Sediment Connectivity within Catchments: Insights from Graph Theory. *Earth Surf. Dynam.* 5 (2), 253–268. doi:10.5194/esurf-5-253-2017

Crema, S., and Cavalli, M. (2018). SedInConnect: a Stand-Alone, Free and Open Source Tool for the Assessment of Sediment Connectivity. *Comput. Geosciences* 111, 39–45. doi:10.1016/j.cageo.2017.10.009

Cui, P., Zhu, Y.-y., Han, Y.-s., Chen, X.-q., and Zhuang, J.-q. (2009). The 12 May Wenchuan Earthquake-Induced Landslide Lakes: Distribution and Preliminary Risk Evaluation. *Landslides* 6 (3), 209–223. doi:10.1007/s10346-009-0160-9

Dadson, S. J., Hovius, N., Chen, H., Dade, W. B., Lin, J.-C., Hsu, M.-L., et al. (2004). Earthquake-triggered Increase in Sediment Delivery from an Active Mountain Belt. *Geol* 32 (8), 733. doi:10.1130/g20639.1

Fan, X., Scaringi, G., Domènech, G., Yang, F., Guo, X., Dai, L., et al. (2019a). Two Multi-Temporal Datasets that Track the Enhanced Landsliding after the 2008 Wenchuan Earthquake. *Earth Syst. Sci. Data* 11 (1), 35–55. doi:10.5194/essd-11-35-2019

Fan, X., Scaringi, G., Korup, O., West, A. J., Westen, C. J., Tanyas, H., et al. (2019b). Earthquake-Induced Chains of Geologic Hazards: Patterns, Mechanisms, and Impacts. *Rev. Geophys.* 57 (2), 421–503. doi:10.1029/2018rg000626

Foerster, S., Wilczok, C., Brosinsky, A., and Segl, K. (2014). Assessment of Sediment Connectivity from Vegetation Cover and Topography Using Remotely Sensed Data in a Dryland Catchment in the Spanish Pyrenees. *J. Soils Sediments* 14 (12), 1982–2000. doi:10.1007/s11368-014-0992-3

Guo, X., Cui, P., Chen, X., Li, Y., Zhang, J., and Sun, Y. (2021). Estimation of Discharges of Water Flows and Debris Floods in a Small Watershed. *Earth Surf. Process. Landforms* 46 (3), 642–658. doi:10.1002/esp.5053

Guo, X., Cui, P., Li, Y., Ma, L., Ge, Y., and Mahoney, W. B. (2016). Intensity-duration Threshold of Rainfall-Triggered Debris Flows in the Wenchuan Earthquake Affected Area, China. *Geomorphology* 253, 208–216. doi:10.1016/j.geomorph.2015.10.009

Guo, X., Cui, P., Li, Y., Zhang, J., Ma, L., and Mahoney, W. B. (2015). Spatial Features of Debris Flows and Their Rainfall Thresholds in the Wenchuan

Earthquake-Affected Area. *Landslides* 13 (5), 1215–1229. doi:10.1007/s10346-015-0608-z

Heckmann, T., and Vericat, D. (2018). Computing Spatially Distributed Sediment Delivery Ratios: Inferring Functional Sediment Connectivity from Repeat High-Resolution Digital Elevation Models. *Earth Surf. Process. Landforms* 43 (7), 1547–1554. doi:10.1002/esp.4334

Hoffmann, T. (2015). Sediment Residence Time and Connectivity in Non-equilibrium and Transient Geomorphic Systems. *Earth-Science Rev.* 150, 609–627. doi:10.1016/j.earscirev.2015.07.008

Hu, X.-d., Hu, K.-h., Zhang, X.-p., Wei, L., and Tang, J.-b. (2019). Quantitative Assessment of the Impact of Earthquake-Induced Geohazards on Natural Landscapes in Jiuzhaigou Valley. *J. Mt. Sci.* 16 (2), 441–452. doi:10.1007/s11629-018-5240-7

Larsen, I. J., Montgomery, D. R., and Korup, O. (2010). Landslide Erosion Controlled by Hillslope Material. *Nat. Geosci.* 3 (4), 247–251. doi:10.1038/ngeo776

Li, G., West, A. J., Densmore, A. L., Jin, Z., Parker, R. N., and Hilton, R. G. (2014). Seismic Mountain Building: Landslides Associated with the 2008 Wenchuan Earthquake in the Context of a Generalized Model for Earthquake Volume Balance. *Geochem. Geophys. Geosyst.* 15 (4), 833–844. doi:10.1002/2013gc005067

Lisenby, P. E., and Fryirs, K. A. (2017). 'Out with the Old?' Why Coarse Spatial Datasets Are Still Useful for Catchment-scale Investigations of Sediment (Dis)connectivity. *Earth Surf. Process. Landforms* 42 (10), 1588–1596. doi:10.1002/esp.4131

Michaelides, K., and Chappell, A. (2009). Connectivity as a Concept for Characterising Hydrological Behaviour. *Hydrol. Process.* 23 (3), 517–522. doi:10.1002/hyp.7214

Najafi, S., Dragovich, D., Heckmann, T., and Sadeghi, S. H. (2021). Sediment Connectivity Concepts and Approaches. *Catena* 196, 104880. doi:10.1016/j.catena.2020.104880

Parker, R. N., Densmore, A. L., Rosser, N. J., de Michele, M., Li, Y., Huang, R., et al. (2011). Mass Wasting Triggered by the 2008 Wenchuan Earthquake Is Greater Than Orogenic Growth. *Nat. Geosci.* 4 (7), 449–452. doi:10.1038/ngeo1154

Pearce, A. J., and Watson, A. (1983). Medium-term Effects of Two Landsliding Episodes on Channel Storage of Sediment. *Earth Surf. Process. Landforms* 8, 29–39. doi:10.1002/esp.3290080104

Pearce, A. J., and Watson, A. J. (1986). Effects of Earthquake-Induced Landslides on Sediment Budget and Transport over a 50-yr Period. *Geology* 14 (1), 52–55. doi:10.1130/0091-7613(1986)14<52:eoelos>2.0.co;2

Pearson, S. G., Prooijen, B. C., Elias, E. P. L., Vitousek, S., and Wang, Z. B. (2020). Sediment Connectivity: A Framework for Analyzing Coastal Sediment Transport Pathways. *J. Geophys. Res. Earth Surf.* 125 (10). doi:10.1029/2020jf005595

Sadeghi, S. H., Najafi, S., and Bakhtiari, A. R. (2017). Sediment Contribution from Different Geologic Formations and Land Uses in an Iranian Small Watershed, Case Study. *Int. J. Sediment Res.* 32 (2), 210–220. doi:10.1016/j.ijsrc.2017.02.002

Tang, C., Zhu, J., Li, W. L., and Liang, J. T. (2009). Rainfall-triggered Debris Flows Following the Wenchuan Earthquake. *Bull. Eng. Geol. Environ.* 68 (2), 187–194. doi:10.1007/s10064-009-0201-6

Trauerstein, M., Norton, K. P., Preusser, F., and Schlunegger, F. (2013). Climatic Imprint on Landscape Morphology in the Western Escarpment of the Andes. *Geomorphology* 194, 76–83. doi:10.1016/j.geomorph.2013.04.015

Wainwright, J., Turnbull, L., Ibrahim, T. G., Lexartza-Artza, I., Thornton, S. F., and Brazier, R. E. (2011). Linking Environmental Régimes, Space and Time: Interpretations of Structural and Functional Connectivity. *Geomorphology* 126 (3-4), 387–404. doi:10.1016/j.geomorph.2010.07.027

Zanandrea, F., Michel, G. P., Kobiyama, M., and Cardozo, G. L. (2019). Evaluation of Different DTMs in Sediment Connectivity Determination in the Mascarada River Watershed, Southern Brazil. *Geomorphology* 332, 80–87. doi:10.1016/j.geomorph.2019.02.005

Zanandrea, F., Michel, G. P., Kobiyama, M., Censi, G., and Abatti, B. H. (2021). Spatial-temporal Assessment of Water and Sediment Connectivity through a Modified Connectivity Index in a Subtropical Mountainous Catchment. *Catena* 204, 105380. doi:10.1016/j.catena.2021.105380

Zhou, W., Qiu, H., Wang, L., Pei, Y., Tang, B., Ma, S., et al. (2022). Combining Rainfall-Induced Shallow Landslides and Subsequent Debris Flows for Hazard Chain Prediction. *Catena* 213, 106199. doi:10.1016/j.catena.2022.106199

Conflict of Interest: The authors declare that the research was conducted in the absence of any commercial or financial relationships that could be construed as a potential conflict of interest.

Publisher's Note: All claims expressed in this article are solely those of the authors and do not necessarily represent those of their affiliated organizations, or those of the publisher, the editors and the reviewers. Any product that may be evaluated in this article, or claim that may be made by its manufacturer, is not guaranteed or endorsed by the publisher.

frontiers | Frontiers in Earth Science

ORIGINAL RESEARCH
published: 30 June 2022
doi: 10.3389/feart.2022.916805

The Tension-Shear and Compression-Shear Joint Strength Model for Unsaturated Clay and Its Application to Slopes

Xiaoang Kong, Yongfeng Cheng, Binbin Zhao, Yi Liu and Jingshan Han*

China Electric Power Research Institute, Beijing, China

The capillary component and adsorptive component of matric suction differently impact the soil strength. Due to the cavitation effects of pore water, the adsorption effect dominates the behavior of soil when matric suction exceeds the cavitation tension. Based on the binary medium theory, a compression-shear strength model for unsaturated soils considering both capillary effect and adsorption effect is established. Compared with test data, the proposed compression-shear strength model has better prediction performance on the compression-shear strength of soil over a range of wide suction. The soil failure depends both on tension-shear stress and compression-shear stress. The tension-shear coupling mechanism in the soil is first investigated. A concept of closed stress point is introduced to divide the two zones of tension-shear coupling stress and compression-shear stress. According to the compression-shear strength model and tension-shear failure mechanism, the tension-shear and compression-shear joint strength model applicable to plane stress conditions is then established. Compared with test data, the proposed model in this article can better predict the nonlinear strength characteristics of clays and has better applicability. Finally, using the user material subroutine (UMAT), the secondary development of the joint strength model is conducted in ABAQUS and then applied to the slope stability analysis. The calculation results show that the established strength model presents a reasonable description of the development of the tension-shear coupling plastic zone in slope and gives an accurate safety factor.

Keywords: unsaturated soil, adsorption effect, tension-shear, compression-shear, joint strength

OPEN ACCESS

Edited by:
Xiaojun Guo,
Institute of Mountain Hazards and Environment (CAS), China

Reviewed by:
Yuanjun Jiang,
Institute of Mountain Hazards and Environment (CAS), China
Xiaomeng Shi,
Beijing Jiaotong University, China

****Correspondence:***
Xiaoang Kong
kongxiaoang@epri.sgcc.com.cn

Specialty section:
This article was submitted to Geohazards and Georisks, a section of the journal Frontiers in Earth Science

Received: *10 April 2022*
Accepted: *18 May 2022*
Published: *30 June 2022*

Citation:
Kong X, Cheng Y, Zhao B, Liu Y and Han J (2022) The Tension-Shear and Compression-Shear Joint Strength Model for Unsaturated Clay and Its Application to Slopes. Front. Earth Sci. 10:916805. doi: 10.3389/feart.2022.916805

INTRODUCTION

Due to the existence of suction, unsaturated soils have more complicated properties than saturated soils. Thus, considering the influence of suction or degree of saturation on shear strength in a reasonable way is the key to studying the shear strength of unsaturated soils. Many scholars have proposed formulas that can directly or indirectly predict the shear strength of unsaturated soils by means of the soil–water characteristic curve (SWCC) and shear strength parameters of saturated soil in recent years, such as Khalili and Khabbaz (1998), Tarantino and Tombolato (2005), Garven and Vanapalli (2006), Lu et al. (2010), and Sheng et al. (2011). It is worth noting that, however, most existing strength formulas have no difference in essence and can all be expressed in the forms of Bishop-type (Bishop and Blight, 1963) or Fredlund-type (Fredlund et al., 1978) strength formulas. The different mathematical forms and parameters involved in these strength formulas determine

their ability to predict the strength characteristics of different soils. In general, strength formulas with more parameters have better fitting performance.

The matric suction is directly defined as $s = u_a - u_w$ in major research on unsaturated soils, where u_a is the pore gas pressure and u_w is the pore water pressure. By this definition, the matric suction depends only on the negative pore-water pressure generated by capillarity. In fact, however, besides the capillarity, the other factors such as adsorption, osmosis, temperature, and gravity can also contribute to the change of total suction. Tuller et al. (1999), Baker and Frydman (2009), and Zhao et al. (2016) pointed out that the matric suction in soil generally comprises capillary components and adsorptive components when ignoring the effects of osmosis, temperature, gravity, and other factors. The two components of matric suction have different mechanisms and differently influence the mechanical behavior of soils. Ignoring the effect of the adsorptive component of matric suction, the existing strength theories fail to accurately describe the strength characteristics under high suction (or the low degree of saturation). Very few shear strength formulas consider the effects of both components of matric suction.

The mutual changes between the states of tensile stress and compressive stress occur during the failure process of soil under natural conditions. Accordingly, the soil failure is affected both by tension-shear coupling stress and compression-shear stress, especially in clay slopes, embankments, and impervious layers of landfills. It has always been a key issue in the strength theory of soil, that is, how to comprehensively consider the tension-shear and compression-shear characteristics and establish a joint strength model considering both coupling stresses. This is mainly because the issue is seemingly simple but actually complex in the intrinsic mechanism. After years of research, some beneficial results of the joint strength theory have been obtained, such as the Griffith strength criterion (Margolin, 1984; Singh and Zimmerman, 2014), the hyperbolic joint strength criterion (Abbo and Sloan, 1995; Li R. J. et al., 2014; Li et al., 2016) and the Griffith–Mohr strength criterion (Vesga, 2009; Zhang et al., 2010). However, most existing research adopts some simplified methods to describe the tension-shear coupling strength owing to the unclear strength mechanism of soil under tension-shear coupling stress. Presently, it has not yet established a unified coupling strength theory of soil. Therefore, establishing a tension-shear and compression-shear joint strength model that reasonably considers the tension-shear coupling mechanism is of great significance to accurately describe the tension-shear coupling failure and compression-shear failure of soils and the relationship between them.

Aiming at the problems in current theory, this article first establishes a compression-shear strength model that comprehensively considers the effects of the capillary component and adsorptive component of matric suction.

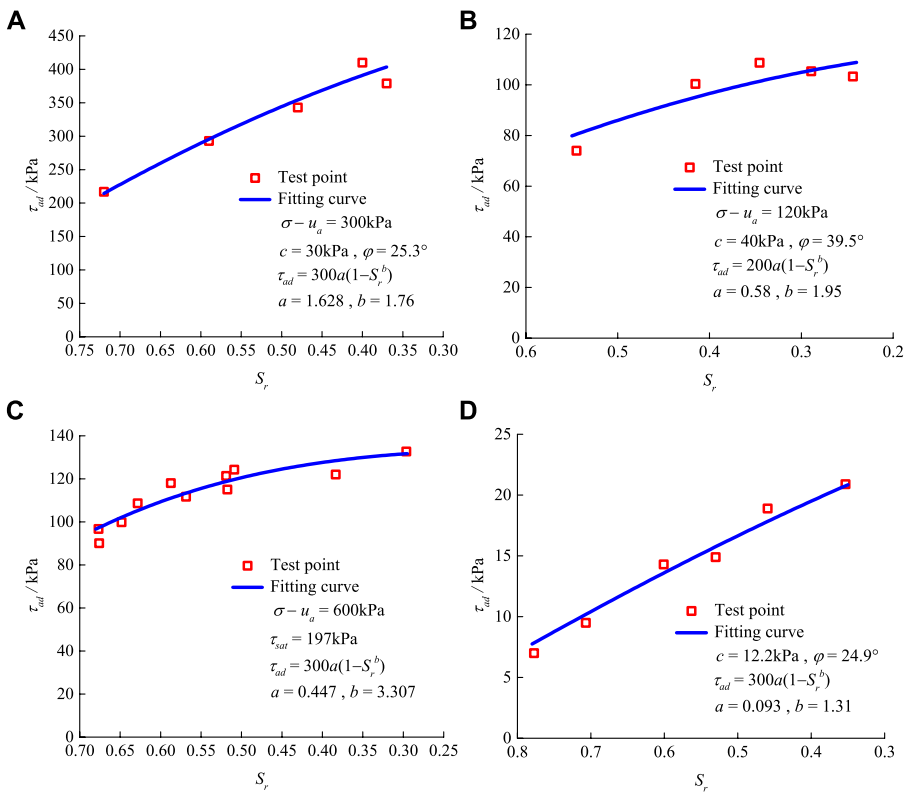

FIGURE 1 | Data fitting of different clays: **(A)** Madrid clay (Escario and Saez, 1986), **(B)** Madrid sandy clay (Escario and Saez, 1986), **(C)** kaolin clay (Tarantino and Tombolato, 2005), and **(D)** silty clay (Shen et al., 2007).

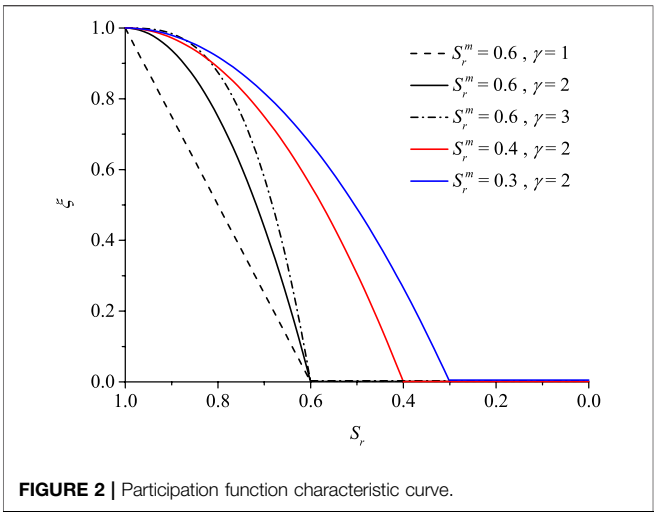

FIGURE 2 | Participation function characteristic curve.

Taking the tension-shear coupling mechanism into account, a tension-shear and compression-shear joint strength model is then proposed. Finally, the established joint strength model is numerically implemented in ABAQUS, which is then applied to the stability analysis of unsaturated slopes, and its validity and accuracy are discussed.

THE COMPRESSION-SHEAR STRENGTH MODEL CONSIDERING ADSORPTION EFFECT

The capillary component of matric suction in the soil is capillary suction with its value of $u_a - u_w$, which results from the surface tension at the gas–liquid interface and is related to the free water in pore water. The adsorptive component of matric suction is generated by the physicochemical actions between liquid water and soil particles, including long-range electrostatic force (such as electric double-layer force), van der Waals force, cementation force, and other forces, which are related to the bound water in pore water (Gens, 2010). The action mechanisms of these two components on soil strength are significantly different and their action effects depend on soil type and water content. Capillarity tends to dominate in non-cohesive soils or in soils with a higher degree of saturation, while the adsorption effect tends to dominate in clays with higher plasticity indices or in soils with a low degree of saturation (Zhao et al., 2016).

To consider capillarity and adsorption effect in soil, the method of binary medium theory (Liu and Zhang, 2013; Li R. J. et al., 2014) is introduced. The soil is abstracted as a medium consisting of two ideal elements that can be quantitatively described (that is, capillary element and adsorption element). The ideal capillary strength and ideal adsorption strength for capillary element and adsorption element are formulated, respectively. Then, these two ideal strength formulas are rationally combined, and a compression-shear strength model involving the adsorption effect is thus proposed.

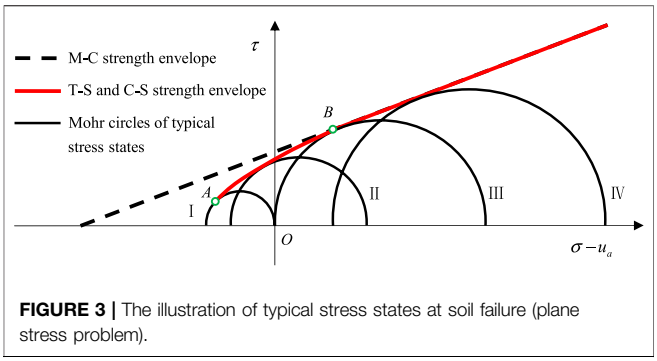

FIGURE 3 | The illustration of typical stress states at soil failure (plane stress problem).

Ideal Capillary Strength

In the capillary element, the soil strength is assumed to be independent of physicochemical action and only related to capillarity. Accordingly, the ideal capillary strength conforms to the strength theory established on account of the macroscopic capillary phenomenon, and can be expressed as follows:

$$\tau_f^c = c' + (\sigma - u_a)\tan\varphi' + (u_a - u_w)S_r \tan\varphi'', \quad (1)$$

where τ_f^c is the ideal capillary strength, σ is the normal stress, c' is the effective cohesion, φ' is the effective angle of internal friction, S_r is the degree of saturation, and φ'' is the friction angle corresponding to capillarity and can be simplified as $\tan\varphi'' = \tan\varphi'$ (Fredlund et al., 1996; Chaney et al., 1997).

Ideal Adsorption Strength

Because of the cavitation effects of pore water in practical soil, tensile stress in pore water cannot be larger than a limiting value s_m (i.e., cavitation tension), typically in the range of 100~400 kPa, at which the water is transformed from liquid to vapor (Baker and Frydman, 2009; Lu, 2016). When matric suction exceeds s_m, the cavitation of pore water occurs, and the capillarity fails. Thus, the adsorption effect controls the mechanical behavior of soil under this situation, whose influence on strength can be reflected by the degree of saturation.

In the adsorption element, the soil strength is assumed to be dependent only on physicochemical interaction between liquid water and soil particles and independent of capillarity. Accordingly, the ideal adsorption strength can be expressed as follows:

$$\tau_f^{ad} = c' + (\sigma - u_a)\tan\varphi' + \tau_{ad}, \quad (2)$$

where τ_f^{ad} is the ideal adsorption strength and τ_{ad} is the additional strength due to the adsorption effect, which relates to s_m and S_r (Zhao et al., 2016), and can be expressed as follows:

$$\tau_{ad} = s_m \zeta(S_r), \quad (3)$$

where $\zeta(S_r)$ is a function dependent on S_r.

Based on the strength test results of different types of clay with low degrees of saturation (Escario and Saez, 1986; Tarantino and Tombolato, 2005; Shen et al., 2007), the evolution law of the additional strength due to the adsorption effect with the degree of saturation was fitted and analyzed, as illustrated in **Figure 1**. It

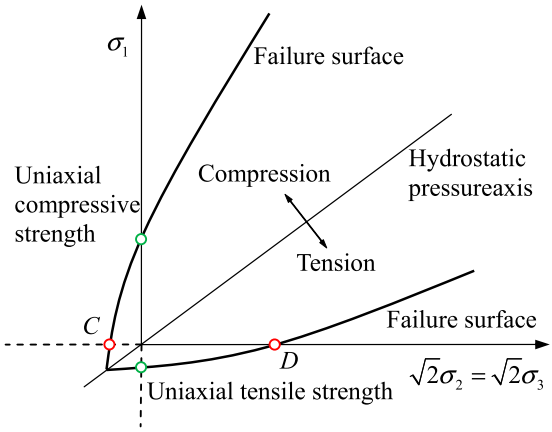

FIGURE 4 | Schematic diagram of failure states in the triaxial plane.

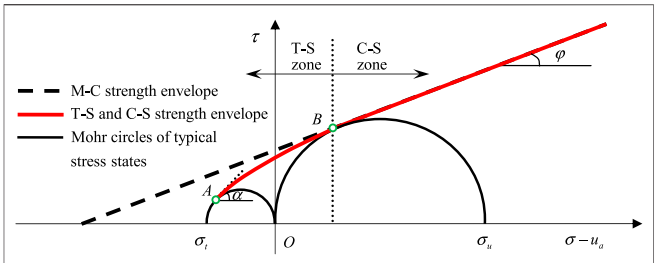

FIGURE 5 | Failure envelopes of unsaturated clay under tension-shear and compression-shear stresses (note: the T-S zone and C-S zone mean the compression-shear action zone and tension-shear coupling action zone, respectively).

can be found from **Figure 1** that with the decrease in the degree of saturation, the additional strength due to the adsorption effect increases nonlinearly and its growth rate decreases continuously, which approaches a constant at a very low degree of saturation. According to the data fitting of the tests, $\zeta(S_r)$ can be obtained as follows:

$$\zeta(S_r) = a\left(1 - S_r^b\right), \tag{4}$$

where a and b are the fitting parameters. $\zeta(S_r)$ has a tendency toward a with the decrease of degree of saturation.

Therefore, the formula of ideal adsorption strength can be written as follows:

$$\tau_f^{ad} = c' + (\sigma - u_a)\tan\varphi' + s_m a\left(1 - S_r^b\right), \tag{5}$$

The Binary-Medium Compression-Shear Strength Model

According to the binary medium theory, the practical unsaturated soil is idealized as a medium composed of the capillary element and the absorption element. The compression-shear strength of soil can be expressed as follows:

$$\tau_f = \xi\tau_f^c + (1 - \xi)\tau_f^{ad}, \tag{6}$$

where ξ is the participation function and represents the proportion of the capillary element in the practical soil.

Experimental studies have shown that the degree of saturation impacts the mechanics and hydraulic behavior of unsaturated soils, in turn affecting their behavioral characteristics (Li J. et al., 2014). Therefore, ξ is related to the degree of saturation and can be expressed as follows:

$$\xi = \left\langle 1 - \left(\frac{1 - S_r}{1 - S_r^m}\right)^{\gamma} \right\rangle, \tag{7}$$

where $\langle \cdot \rangle$ is the McCauley bracket, $\langle x \rangle = x$ when $x > 0$ and $\langle x \rangle = 0$ when $x \le 0$; S_r^m is the degree of saturation corresponding to the cavitation tension s_m and can be called cavitation saturation; and γ is the fitting parameter, reflecting the degree of influence of the degree of saturation change on the participation function. The characteristic curve of the participation function ξ is shown in **Figure 2**. ξ gradually decreases with the degree of saturation and decreases to 0 at the cavitation saturation. As the parameter γ increases, the characteristic curve of the participation function presents an upward convex, and the degree of curvature increases gradually. The range of the descending section of the characteristic curve increases with the cavitation saturation S_r^m decreasing.

Combining **Eqs. 1**,**5**–**7** with **Eq. 6**, the formula of binary-medium compression-shear strength can be expressed as follows:

$$\tau_f = c' + (\sigma - u_a)\tan\varphi' + \left[\xi(u_a - u_w)S_r\tan\varphi'' + (1 - \xi)s_m a\left(1 - S_r^b\right)\right], \tag{8}$$

Parameters in the Compression-Shear Strength Model

The compression-shear strength model contains eight material parameters, c', φ', φ'', s_m, S_r^m, a, b, and γ, which can be determined by the following methods.

(1) Shear strength parameters of saturated soil: effective cohesion c' and effective internal friction angle φ'. They can be determined by the triaxial shear test of saturated soil.
(2) Friction angle corresponding to capillarity, φ''. It can be determined by the shear strength test under the condition of a high degree of saturation (near-saturation state). φ'' is simplified as $\varphi'' = \varphi'$ in this article.
(3) Cavitation tension s_m and cavitation saturation S_r^m. The existing research on the cavitation tension is too insufficient to directly obtain its value. Based on the existing research results (Baker and Frydman, 2009; Lu, 2016), we compared the SWCC of types of soil and obtained corresponding cavitation tension s_m by analogy. The cavitation saturation S_r^m is then determined by SWCC.
(4) Parameters in the ideal adsorption strength formula: a and b. They can be determined according to the shear strength test at low degrees of saturation or high suctions.

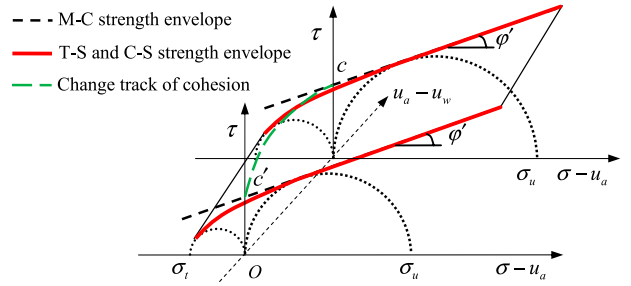

FIGURE 6 | Failure surfaces of unsaturated clay under tension-shear and compression-shear stresses.

TABLE 1 | Model parameters of clays.

Soil sample	c′/kPa	φ′/(°)	s_m/kPa	S_r^m	*a*	*b*	*γ*
Madrid clay	30	25.3	300	0.814	1.628	1.76	0.5
Kaolin clay	14.8	16.89	300	0.766	0.447	3.307	2.0

(5) Parameter in participation function: γ. The parameter γ is the prediction parameter of the compression-shear strength model, through which the prediction effect of the model is controlled.

The Tension-Shear and Compression-Shear Joint Strength Model for Unsaturated Clay

The strength theory that can describe both tensile failure and shear failure is generally called joint strength theory. The theoretical research on the joint strength of soil mainly focuses on plane stress conditions and clay and can be roughly divided into two categories. One category is that the joint strength formula is established by using an empirical curve from strength test data (Abbo and Sloan, 1995; Li et al., 2016); the other category is that the joint strength formula is derived by using soil strength index (c, φ, and σ_t) based on some assumptions (Vesga, 2009; Zhang et al., 2010). c is the cohesion of unsaturated soil, φ is the compression-shear internal friction angle of unsaturated soil, and σ_t is the uniaxial tensile strength. However, none of these studies have revealed the tension-shear failure mechanism of soil properly. This section first analyzes the failure mechanism of soil under tension-shear coupling stress and then investigates the establishment of tension-shear and compression-shear joint strength models under plane stress conditions.

Mechanism of Tension-Shear Coupling Strength

Under compression-shear stress, the traditional M-C strength theory gives an accurate description of soil strength. Under tension-shear coupling stress, however, the linear M-C strength theory tends to significantly overestimate the soil strength

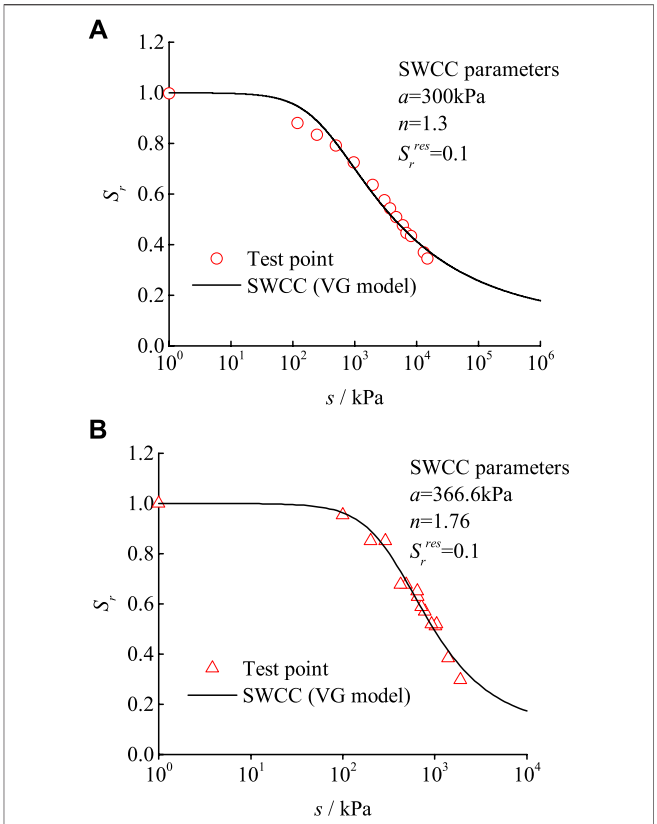

FIGURE 7 | SWCC of clays: **(A)** Madrid clay and **(B)** kaolin clay.

exhibiting typical nonlinearity. Several typical failure stress states of soil are shown in **Figure 3**. Stress state I is the Mohr circle of uniaxial tensile failure, stress state II is the Mohr circle of tension-shear coupling failure, stress state III is the Mohr circle of uniaxial compressive failure, and stress state IV is the Mohr circle of triaxial shear failure. Point A and point B in **Figure 3** are the uniaxial tensile failure point and uniaxial compressive failure point, respectively. It should be noted that the practical soil is in a three-dimensional stress space and is under three-dimensional stress. Only under the equal tensile stress in three directions is the soil without shear stress completely controlled by the tensile stress. Under the uniaxial tensile stress, however, the soil bears both tensile stress and shear stress and the tension-shear coupling failure occurs. Therefore, the strength envelope under plane stress conditions has the following characteristics: 1) the multidirectional tensile strength of soil cannot be described, which needs to be discussed in the three-dimensional stress space; 2) the strength envelope is tangential to the Mohr circle of uniaxial tensile failure at the failure point instead of simply intersecting with the effective stress axis at the uniaxial tensile strength point; and 3) the strength envelope is not closed.

The mechanism of tension-shear coupling failure applies not only to the traditional triaxial tensile test (or triaxial extension test) with constant confining pressure and reduced axial compression, but also to the triaxial compression-shear test associated with tension-shear coupling strength. That is, the

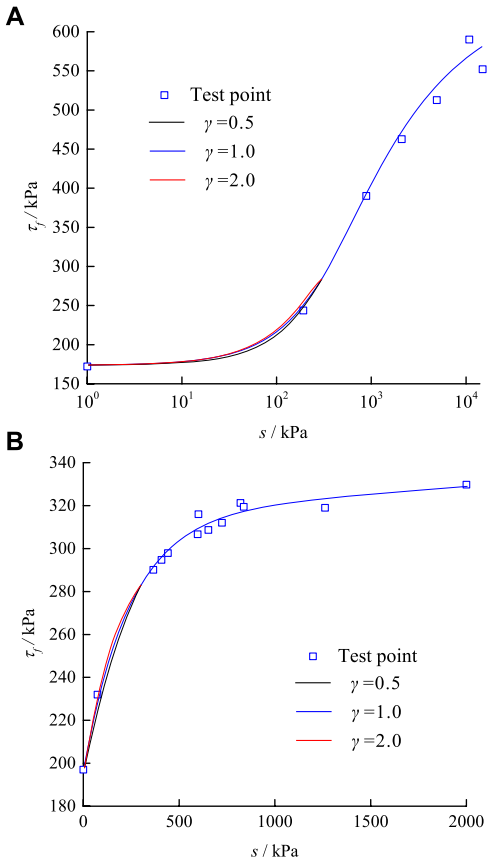

FIGURE 8 | The predictions of the compression-shear strength model: **(A)** Madrid clay and **(B)** kaolin clay.

TABLE 2 | Model parameters of unsaturated soil sample.

Soil sample	c/kPa	φ/(°)	σ_t/kPa	σ_u/kPa	χ
Kaolin clay	374.0	25.0	402	1,114	1.4
Dam clay	54.1	23.5	48	199	1.5

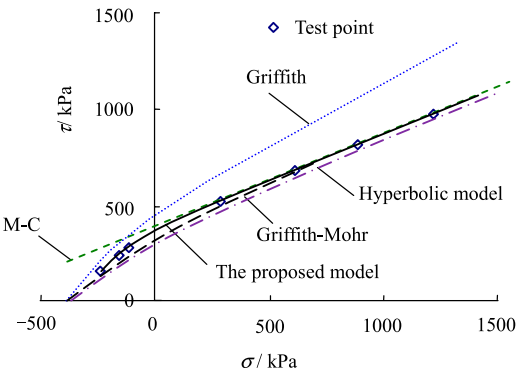

FIGURE 9 | Predictions by different strength models for kaolin clay.

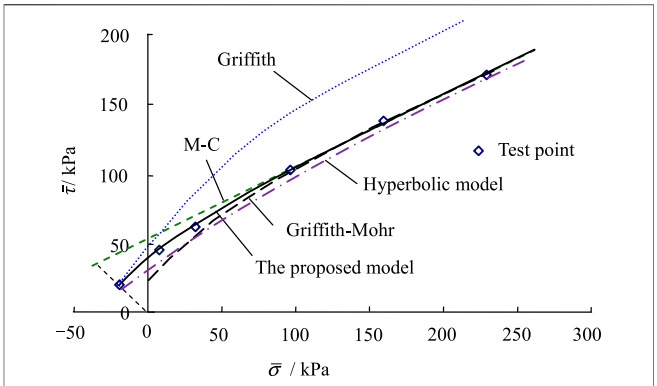

FIGURE 10 | Predictions by different strength models for dam clay.

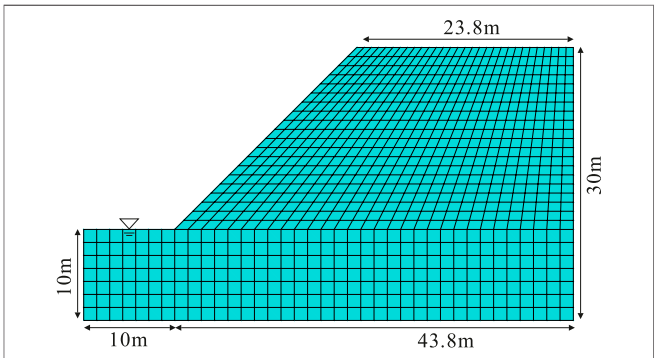

FIGURE 11 | Finite element model of the slope.

mechanism of tension-shear coupling failure can be used for both triaxial tension conditions and triaxial compression conditions. The following points need special attention: 1) Under triaxial compression, the stress state on Mohr circle I is that the confining pressure is negative and the failure axial pressure is zero (as shown by point C in **Figure 4**). This stress state is difficult to achieve experimentally, but it differs little from the uniaxial tensile stress state under plane stress, which thus can be simply viewed as the stress state at uniaxial tensile failure. Mohr circle III represents the stress state at uniaxial compression failure. 2) Under triaxial tension, Mohr circle I represents the stress state at uniaxial tensile failure, and the stress state on Mohr circle III is characterized by confining pressure being positive and failure axial pressure being zero (as shown by point D in **Figure 4**).

Tension-Shear and Compression-Shear Joint Strength

Based on the tension-shear coupling failure mechanism, we used for reference the concept of a closed stress point (Murrell and Digby, 1970) and define it as the dividing point between the zones of the tension-shear and compression-shear stresses. The failure functions within the two zones smoothly connected at the closed stress points are then established, respectively. The uniaxial

TABLE 3 | Geotechnical properties of soil.

Elastic modulus E/MPa	10	Dry unit weight γ_d/(kN/m^3)	14	
Poisson's ratio ν	0.3	Saturated unit weight γ_{sat}/(kN/m^3)	19	
Effective internal friction angle φ'/(°)	30	Saturated permeability coefficient k_s/(m/s)	2×10^{-6}	
Effective cohesion c'/kPa	15	Parameters in VG model	α/(1/m)	0.02
Initial void ratio e_0	1		n	3

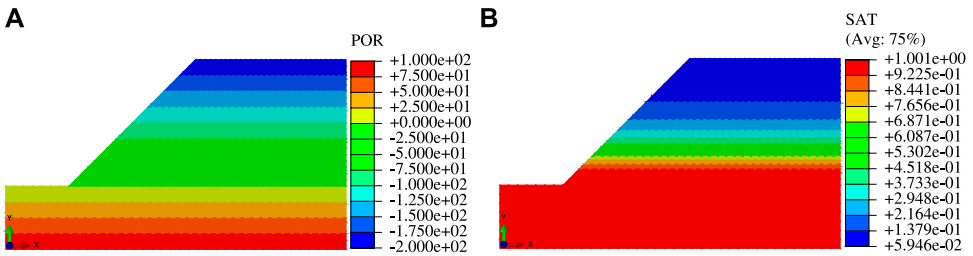

FIGURE 12 | Nephogram of pore pressure and effective degree of saturation at the initial state: **(A)** Pore pressure and **(B)** effective degree of saturation.

compression failure point is by definition selected as the closed stress point, which gives this point specific physical meaning. **Figure 5** illustrates the failure envelopes of unsaturated clay under tension-shear coupling stress and compression-shear stress at a certain suction.

The shear stress of soil in the compression-shear action zone satisfies the M-C strength criterion, but the shear stress in the tension-shear coupling action zone exhibits characteristics of typical nonlinear strength. Therefore, the soil strength can be described by the quadratic curve function, and be expressed as follows:

$$\sigma - u_a = A'\tau^2 + B'\tau + C', \tag{9}$$

where A', B', and C' are the coefficients, which can be deduced by using three characteristic parameters ($A(\sigma_t^{'}, \tau_t^{'})$, $B(\sigma_b, \tau_b)$, and φ) and the geometric continuity requirements:

$$\begin{cases} \tau\big|_{\sigma-u_a=\sigma_t^{'}} = \tau_t^{'} \\ \tau\big|_{\sigma-u_a=\sigma_b} = \tau_b \\ \tau'\big|_{\sigma-u_a=\sigma_b} = \tan\varphi \end{cases} \Rightarrow \begin{cases} A' = -m \\ B' = \cot\varphi + 2\tau_b m \\ C' = \sigma_b - \tau_b\cot\varphi - \tau_b^2 m \end{cases}, \tag{10}$$

where:

$$\begin{cases} m = \left[\sigma_b - \sigma_t^{'} - \cot\varphi\left(\tau_b - \tau_t^{'}\right)\right] \Big/ \left(\tau_b - \tau_t^{'}\right)^2 \\ \sigma_b = \sigma_u(1-\sin\varphi)/2 \\ \tau_b = \sigma_u\cos\varphi/2 \\ \sigma_t^{'} = -\sigma_t(1+\sin\alpha)/2 \\ \tau_t^{'} = \sigma_t\cos\alpha/2 \end{cases}, \tag{11}$$

Where σ_u is the uniaxial compressive strength, and $\alpha = \chi\varphi$ is the tension-shear internal friction angle (Mitachi and Kitago, 1976; Mayne, 1985) with χ (= 1 ~ 1.5) being the physical parameter related to the tension-shear coupling stress action. The compression-shear internal friction angle φ can be taken as the effective internal friction angle φ'. In simplifying calculation, σ_t and σ_u can be expressed as $\sigma_t = 2c\cos\varphi/(1+\sin\varphi)$ and $\sigma_u = 2c\cos\varphi/(1-\sin\varphi)$.

Combining **Eqs. 8**, **9**, the complete tension-shear and compression-shear joint strength formulas can be obtained as:

$$\begin{cases} A'\tau^2 + B'\tau = (\sigma - u_a) - C' & (\sigma - u_a) < \sigma_u\left(1-\sin\varphi'\right)\Big/2 \\ \tau = c + (\sigma - u_a)\tan\varphi' & (\sigma - u_a) \geq \sigma_u\left(1-\sin\varphi'\right)\Big/2 \end{cases}, \tag{12}$$

The failure surfaces of unsaturated clay under tension-shear and compression-shear stress are shown in **Figure 6**, which consists of a series of failure envelopes at different suctions.

PREDICTION AND VERIFICATION

Prediction and Verification of the Compression-Shear Strength Model

The compression-shear strength model considering the adsorption effect was first verified using the strength test results of kaolin clay (Tarantino and Tombolato, 2005) and Madrid clay (Escario and Saez, 1986). Model parameters can be determined by test data, which are shown in **Table 1**. In this article, the Van Genuehten (VG) model (Genuchten, 1980) is used to convert the degree of saturation of unsaturated soil into the corresponding suction. The variation of suction with the degree of saturation is illustrated in **Figure 7**.

The predictions of the compression-shear strength model are shown in **Figure 8**. Through comparison, it can be found from **Figure 8** that the proposed model has accurate prediction performances on the compression-shear strength of soil over a range of wide suction. The strength increases nonlinearly with matric suction, whose growth rate decreases continuously (this law is not directly reflected in logarithmic coordinate), and almost remains unchanged with large enough matric suction. The influences of the parameter γ being 0.5, 1.0, and 2.0 in turn on soil strength are also analyzed. The strength increases gradually γ, but its variation only focuses on a relatively small

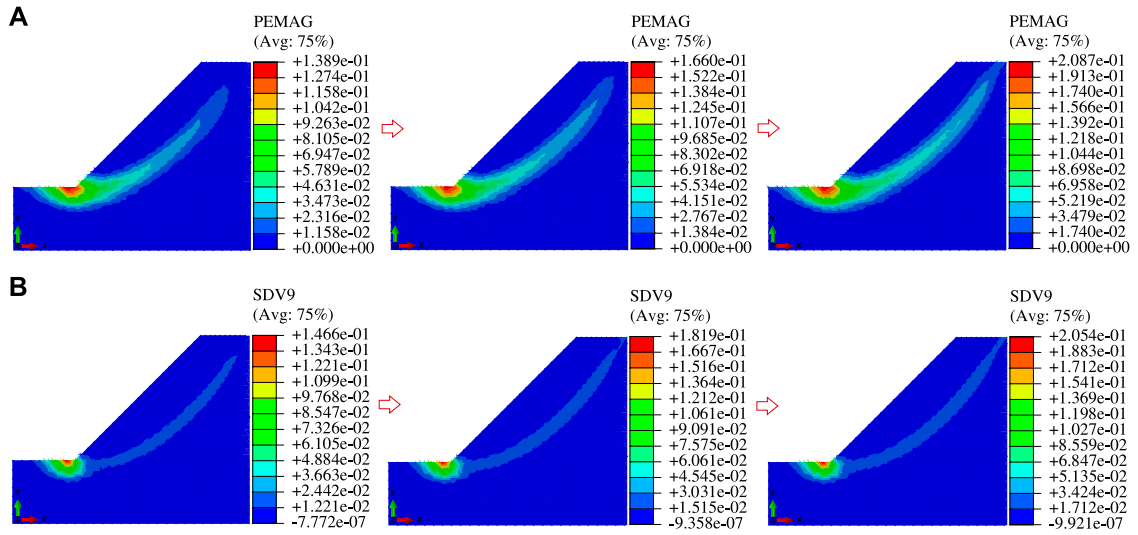

FIGURE 13 | Development of the equivalent plastic strain zone of a progressively unstable slope: **(A)** M-C yield criterion and **(B)** tension-shear and compression-shear joint yield criterion.

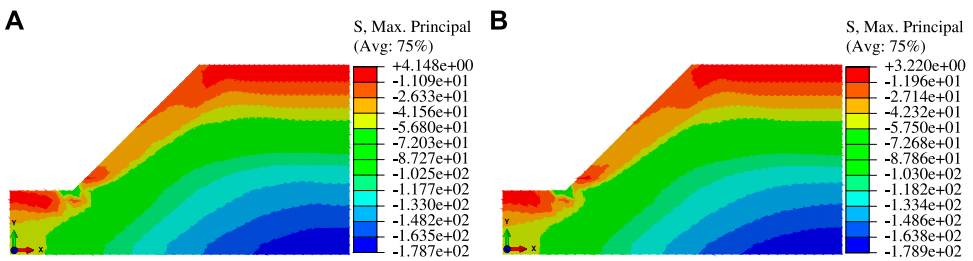

FIGURE 14 | Maximum principal stress nephograms of unstable slopes: **(A)** M-C yield criterion and **(B)** tension-shear and compression-shear joint yield criterion.

zone where capillarity coexists with the adsorption effect. This is mainly because the contribution of capillarity to soil strength increases with y, and the interaction zone of capillarity and adsorption effect is relatively small due to the cavitation effect.

Prediction and Verification of the Tension-Shear and Compression-Shear Joint Strength Model

The triaxial tension-shear tests from Vesga (2009) and Zhang et al. (2010) are used to verify the tension-shear and compression-shear joint strength model. The soil samples selected by Vesga and Zhang et al. are kaolin clay and dam clay, respectively, with their specific gravity being 2.59 and 2.71, water content being 15 and 15%, the liquid limit being 44, and 33.4%, and plastic limit being 26 and 19.6%. The model parameters of the two clays are shown in **Table 2**. **Figures 9,10** show the predictions of our strength model and other models for the two clays. Through comparison and analysis, it can be found that the prediction of the M-C strength criterion is significantly larger than the test data in the tension-shear coupling zone. In addition, the Griffith strength criterion (Singh and Zimmerman, 2014) markedly overestimates the soil strength in all zones and thus is inapplicable to clay materials. Meanwhile, the hyperbolic strength criterion (Li R. J. et al., 2014) and the Griffith–Mohr strength criterion (Zhang et al., 2010) underestimate the strength of soil under tension-shear stress. These happen mainly because the above models fail to well describe the tension-shear failure mechanism. The tension-shear and compression-shear joint strength model established in this article gives good predictions for both unsaturated clays and makes accurate descriptions of the nonlinear strength of clay.

APPLICATION OF THE MODEL TO SLOPE STABILITY ANALYSIS

The tension-shear and compression-shear joint strength model is numerically implemented by using ABAQUS which provides a

secondary developmental user material subroutine (UMAT). A UMAT subroutine is programmed by means of the implicit integral algorithm (Sutharsan et al., 2017; Sabetamal et al., 2021; Singh et al., 2021) in this article and is then applied to the slope stability analysis. The instability and failure of the slope are finally discussed by adopting the finite element strength reduction method.

A general soil slope (Jiang et al., 2018) is selected to analyze the stability of the unsaturated slope. The calculation model and grid partition are illustrated in **Figure11**. As shown in **Figure11**, the grid cell CPE4P is used in the finite element model of the slope and the water table is located at the toe. The boundary conditions of the left and right sides below the water table are the pressure conditions with the hydrostatic pore water pressure increasing linearly with the depth. In the calculation, the soil is regarded as an ideal elastic-plastic material and the associated flow law is adopted. In addition to the tension-shear and compression-shear joint model yielding the criterion established in this article, the M-C yield criterion is also taken as the yield criterion. The material parameters of soil are shown in **Table 3**.

The role of the static water table is first analyzed. Some initial conditions (pore water pressure, effective degree of saturation, and stress distribution) of the slope can be obtained as the initial states of the subsequent slope stability analysis. The initial distributions of pore water pressure and effective degree of saturation are illustrated in **Figure 12**. It can be seen from **Figure 12A** that the initial pore water pressure presents a linear distribution with its value at slope bottom being 100kPa, its value at slope top being −200kPa, and its value at the water table being 0. As shown in **Figure 12B**, the initial effective degree of saturation below the water table remains one and the initial effective degree of saturation above the water table decreases with height.

Based on the initial states of the slope, the stability of the unsaturated slope is then analyzed by using the finite element strength reduction method. The developments of the equivalent plastic strain zone of a progressively unstable slope are shown in **Figure 13** (three calculation steps are selected during slope instability from the near instability to the final instability). When the M-C yield criterion is used, the equivalent plastic zone develops upward from the toe and extends to the slope top, resulting in the generation of a plastic penetration zone. When the tension-shear and compression-shear joint yield criterion is used, an obvious tension-shear coupling plastic zone generates from the top of the slope, which gradually develops downward, and finally connects with the equivalent plastic zone that develops upward from the slope toe. Taking the penetration of the plastic zone as the standard, the slope safety factors calculated based on the two yield criteria are 1.516 and 1.504, respectively. **Figure 14** shows the maximum principal stress nephograms of the unstable slope. It can be seen from **Figure 14** that the ranges of the tensile stress region are essentially the same in cases of different yield criteria, but the maximum value of the tensile stress region in the case of the tension-shear and compression-shear joint yield criterion (3.220 kPa) is smaller than that in the case of the M-C yield criterion (4.148 kPa).

The calculation results in the cases of the two yield criteria indicate that the M-C yield criterion overestimates the tension-shear coupling strength of soil and gives a larger safety factor (dangerous result), but the tension-shear and compression-shear joint yield criterion presents a reasonable description of the strength characteristics of soil under tension-shear coupling stress and gives a smaller safety factor. Therefore, the influence of tension-shear coupling stress should be included in the stability analysis of unsaturated slopes. The use of the tension-shear and compression-shear joint yield criterion can avoid some dangerous results.

CONCLUSION

(1) The existing strength theories on unsaturated soils almost focus only on the macroscopic capillarity and ignore the effect of the adsorptive component of matric suction, which fails to well describe the soil strength. The unsaturated soil is idealized as a medium consisting of two elements that can be quantitatively described, that is, the capillary element and the adsorption element. The strength formulas for each element are first proposed successively and then a compression-shear strength model considering the adsorption effect is established based on the binary medium theory.

(2) The action mechanism of tension-shear strength not revealed in current research on joint strength theory is systematically analyzed. The multi-directional tensile strength of soil cannot be described by the failure envelope under plane stress conditions and thus needs to be investigated in three-dimensional stress space. Under the uniaxial tensile stress, the soil bears both tensile stress and shear stress and the tension-shear coupling failure occurs.

(3) Based on the established compression-shear strength model for unsaturated clays and the tension-shear coupling mechanism, the closed point is introduced to properly divide the zones affected by tension-shear stress and compression-shear stress. A tension-shear and compression-shear joint strength model applicable to plane stress conditions is established.

(4) According to the test data from types of clays, the compression-shear strength model considering the adsorption effect can well describe the compression-shear strength of soils with different suctions. Compared with several existing joint strength models, the tension-shear and compression-shear joint strength models established in this article can better predict the strength characteristics of soil and have better applicability.

(5) The tension-shear and compression-shear joint strength model is numerically implemented by programming a UMAT subroutine in ABAQUS, which is then applied to the slope stability analysis. The calculation results show that the established strength model presents a reasonable description of the development of the tension-shear coupling plastic zone in slope and gives an accurate safety factor.

DATA AVAILABILITY STATEMENT

The raw data supporting the conclusion of this article will be made available by the authors, without undue reservation.

AUTHOR CONTRIBUTIONS

XK contributed to the conception and investigation of the study and wrote the first draft of the manuscript. All authors contributed to manuscript revision, read, and approved the submitted version.

FUNDING

This study was funded by the National Key Research and Development (R&D) Program of China, grant number 2018YFC0809400.

REFERENCES

Abbo, A. J., and Sloan, S. W. (1995). A Smooth Hyperbolic Approximation to the Mohr-Coulomb Yield Criterion. *Comput. Struct.* 54 (3), 427–441. doi:10.1016/0045-7949(94)00339-5

Baker, R., and Frydman, S. (2009). Unsaturated Soil Mechanics. *Eng. Geol.* 106 (1-2), 26–39. doi:10.1016/j.enggeo.2009.02.010

Bishop, A. W., and Blight, G. E. (1963). Some Aspects of Effective Stress in Saturated and Partly Saturated Soils. *Géotechnique* 13 (3), 177–197. doi:10.1680/geot.1963.13.3.177

Chaney, R., Demars, K., Øberg, A., and Sällfors, G. (1997). Determination of Shear Strength Parameters of Unsaturated Silts and Sands Based on the Water Retention Curve. *Geotech. Test. J.* 20 (1), 40–48. doi:10.1520/gtj11419j

Escario, V., and Sáez, J. (1986). The Shear Strength of Partly Saturated Soils. *Géotechnique* 36 (3), 453–456. doi:10.1680/geot.1986.36.3.453

Fredlund, D. G., Morgenstern, N. R., and Widger, R. A. (1978). The Shear Strength of Unsaturated Soils. *Can. Geotech. J.* 15 (3), 313–321. doi:10.1139/t78-029

Fredlund, D. G., Xing, A., Fredlund, M. D., and Barbour, S. L. (1996). The Relationship of the Unsaturated Soil Shear Strength to the Soil-Water Characteristic Curve. *Can. Geotech. J.* 33 (3), 440–448. doi:10.1139/t96-065

Garven, E. A., and Vanapalli, S. K. (2006). "Evaluation of Empirical Procedures for Predicting the Shear Strength of Unsaturated Soils", in: Fourth International Conference on Unsaturated Soils, Portugal, Lisbon. 19-10-2020 - 21-10-2020. 2570–2592. doi:10.1061/40802(189)219

Gens, A. (2010). Soil-environment Interactions in Geotechnical Engineering. *Géotechnique* 60 (1), 3–74. doi:10.1680/geot.9.P.109

Jiang, M., Liu, J., and Shen, Z. (2018). Investigating the Shear Band of Methane Hydrate-Bearing Sediments by FEM with an Elasto-Plastic Constitutive Model. *Bull. Eng. Geol. Environ.* 77 (3), 1015–1025. doi:10.1007/s10064-017-1109-1

Khalili, N., and Khabbaz, M. H. (1998). A Unique Relationship for χ for the Determination of the Shear Strength of Unsaturated Soils. *Géotechnique* 48 (5), 681–687. doi:10.1680/geot.1998.48.5.681

Li, J., Zhao, C., Cai, G., and Guo, Y. (2014a). A Model Considering Solid-Fluid Interactions Stemming from Capillarity and Adsorption Mechanisms in Unsaturated Expansive Clays. *Chin. Sci. Bull.* 59 (26), 3314–3324. doi:10.1007/s11434-014-0411-6

Li, R. J., Liu, J. D., Yan, R., Zheng, W., and Shao, S. J. (2014b). Characteristics of Structural Loess Strength and Preliminary Framework for Joint Strength Formula. *Water Sci. and Eng.* 7 (3), 319–330. doi:10.3882/j.issn.1674-2370.2014.03.007

Li, R., Liu, J., Wang, Z., Luo, J., and Mu, H. (2016). Modifying Algorithm for the Failure Stress According to the Joint Strength Formula. *J. Comput. Theor. Nanosci.* 13 (2), 1153–1157. doi:10.1166/jctn.2016.5026

Liu, E., and Zhang, J. (2013). "Binary Medium Model for Rock Sample," in *Constitutive Modeling of Geomaterials* (Berlin, Heidelberg: Springer), 341–347. doi:10.1007/978-3-642-32814-5_47

Lu, N. (2016). Generalized Soil Water Retention Equation for Adsorption and Capillarity. *J. Geotech. Geoenviron. Eng.* 142 (10), 04016051. doi:10.1061/(ASCE)GT.1943-5606.0001524

Lu, N., Godt, J. W., and Wu, D. T. (2010). A Closed-form Equation for Effective Stress in Unsaturated Soil. *Water Resour. Res.* 46 (5), 567–573. doi:10.1029/2009WR008646

Margolin, L. G. (1984). A Generalized Griffith Criterion for Crack Propagation. *Eng. Fract. Mech.* 19 (3), 539–543. doi:10.1016/0013-7944(84)90010-9

Mayne, P. W. (1985). Stress Anisotropy Effects on Clay Strength. *J. Geotechnical Eng.* 111 (3), 356–366. doi:10.1061/(asce)0733-9410(1985)111:3(356)

Mitachi, T., and Kitago, S. (1976). Change in Undrained Shear Strength Characteristics of Saturated Remolded Clay Due to Swelling. *Soils and Found.* 16 (1), 45–58. doi:10.3208/sandf1972.16.45

Murrell, S. A. F., and Digby, P. J. (1970). The Theory of Brittle Fracture Initiation under Triaxial Stress Conditions--II. *Geophys. J. Int.* 19 (5), 499–512. doi:10.1111/j.1365-246X.1970.tb00155.x

Sabetamal, H., Salgado, R., Carter, J. P., and Sheng, D. (2021). A Two-Surface Plasticity Model for Clay; Numerical Implementation and Applications to Large Deformation Coupled Problems of Geomechanics. *Comput. and Geotechnics* 139, 104405. doi:10.1016/j.compgeo.2021.104405

Shen, X. Z., Guan, X. J., and Lan, Y. (2007). Calculation of Effective Strength Indexes of Unsaturated Low Liquid Limit Clay. *Rock and Soil Mech.* 28, 207–210.

Sheng, D., Zhou, A., and Fredlund, D. G. (2011). Shear Strength Criteria for Unsaturated Soils. *Geotech. Geol. Eng.* 29 (2), 145–159. doi:10.1007/s10706-009-9276-x

Singh, G., and Zimmerman, R. W. (2014). Modification of Griffith-McClintock-Walsh Model for Crack Growth under Compression to Incorporate Stick-Slip along the Crack Faces. *Int. J. Rock Mech. and Min. Sci.* 72, 311–318. doi:10.1016/j.ijrmms.2014.09.020

Singh, V., Stanier, S., Bienen, B., and Randolph, M. F. (2021). Modelling the Behaviour of Sensitive Clays Experiencing Large Deformations Using Non-local Regularisation Techniques. *Comput. and Geotechnics* 133, 104025. doi:10.1016/j.compgeo.2021.104025

Suits, L. D., Sheahan, T. C., and Vesga, L. F. (2009). Direct Tensile-Shear Test (DTS) on Unsaturated Kaolinite Clay. *Geotech. Test. J.* 32 (5), 101563–102409. doi:10.1520/GTJ101563

Sutharsan, T., Muhunthan, B., and Liu, Y. (2017). Development and Implementation of a Constitutive Model for Unsaturated Sands. *Int. J. Geomechanics* 17 (11), 4017103. doi:10.1061/(ASCE)GM.1943-5622.0001004

Tarantino, A., and Tombolato, S. (2005). Coupling of Hydraulic and Mechanical Behaviour in Unsaturated Compacted Clay. *Géotechnique* 55 (4), 307–317. doi:10.1680/geot.2005.55.4.307

Tuller, M., Or, D., and Dudley, L. M. (1999). Adsorption and Capillary Condensation in Porous Media: Liquid Retention and Interfacial Configurations in Angular Pores. *Water Resour. Res.* 35 (7), 1949–1964. doi:10.1029/1999wr900098

van Genuchten, M. T. (1980). A Closed-form Equation for Predicting the Hydraulic Conductivity of Unsaturated Soils. *Soil Sci. Soc. Am. J.* 44 (5), 892–898. doi:10.2136/sssaj1980.03615995004400050002x

Zhang, Y., Zhang, B., Sun, X., and Li, G. (2010). Experimental Study on Triaxial Tensile Property of Compacted Clay. *J. Hydroelectr. Eng.* 29 (6), 172–177. CNKI:SUN:SFXB.0.2010-06-030.

Zhao, C. G., Liu, Z. Z., Shi, P. X., Li, J., Cai, G. Q., and Wei, C. F. (2016). Average Soil Skeleton Stress for Unsaturated Soils and Discussion on Effective Stress. *Int. J. Geomechanics* 16 (6), D4015006. doi:10.1061/(asce)gm.1943-5622.0000610

Conflict of Interest: The authors declare that the research was conducted in the absence of any commercial or financial relationships that could be construed as a potential conflict of interest.

Publisher's Note: All claims expressed in this article are solely those of the authors and do not necessarily represent those of their affiliated organizations, or those of the publisher, the editors, and the reviewers. Any product that may be evaluated in this article, or claim that may be made by its manufacturer, is not guaranteed or endorsed by the publisher.

frontiers | Frontiers in Earth Science

ORIGINAL RESEARCH
published: 04 July 2022
doi: 10.3389/feart.2022.901889

SBAS-InSAR-Based Landslide Susceptibility Mapping Along the North Lancang River, Tibetan Plateau

Jiajia Zhang[1,2]*, *Bo Gao*[2], *Hai Huang*[2], *Long Chen*[2], *Yuanling Li*[2] and *Dongxu Yang*[2]

[1]School of Earth Science, Chengdu University of Technology, Chengdu, China, [2]Institute of Exploration Technology, Chinese Academy of Geological Sciences, Chengdu, China

Landslides pose huge challenges to the economic activities in mountainous areas at present, while large numbers of landslide disasters have developed in the Hengduan Mountains area in the eastern part of the Tibetan Plateau. Accurate landslide susceptibility mapping (LSM) serves as a critical measure to predict the serious risks that may be encountered in engineering activities. However, previous landslide susceptibility assessment can only play a limited role in the real-time analysis of current activities of slopes. In this study, the deformation rates of the slopes along the Lancang River were determined using the SBAS-InSAR technique. Meanwhile, the landslide susceptibility along the north Lancang River was assessed using the frequency ratio (FR), random forest and FR-RF models, and the precision of the assessment results was verified according to receiver operating characteristic curves (ROCs). Finally, a refined landslide susceptibility map was developed by integrating the deformation rates and landslide susceptibility indexes (LSIs) using a contingency matrix. As indicated by the deformation rates calculated using the SBAS-InSAR technique according to ascending and descending data show that the RADARSAT-2 descending data yielded more precise deformation results. The area-under-the-curve (AUC) values of the three assessment models were 0.866, 0.897, and 0.916, respectively, indicating that the assessment results obtained with the FR-RF model are the most precise. In the upgraded landslide susceptibility map, the areas with high and very high landslide susceptibility increased by 2.97%. Meanwhile, a total of 563,430 grid cells showed an increase in landslide susceptibility, accounting for 11.15% of all the grid cells. Most especially, the Xueru and Ritong areas exhibited a significant increase in landslide susceptibility, and it has been verified by remote sensing images and field surveys that both areas are subject to landslide risks. Therefore, the upgraded landslide susceptibility map has a better prediction performance and can provide valuable support for the decision making in the construction of major engineering facilities and the prevention and remediation of landslides.

Keywords: landslide susceptibility mapping, SBAS-InSAR, FR-RF, Lancang River, Tibetan Plateau

OPEN ACCESS

Edited by:
Marcel Hürlimann, Universitat Politecnica de Catalunya, Spain

Reviewed by:
Jianqi Zhuang, Chang'an University, China
Chong Xu, Ministry of Emergency Management, China

***Correspondence:**
Jiajia Zhang
jimjia2008@163.com

Specialty section:
This article was submitted to Geohazards and Georisks, a section of the journal Frontiers in Earth Science

Received: *22 March 2022*
Accepted: *13 June 2022*
Published: *04 July 2022*

Citation:
Zhang J, Gao B, Huang H, Chen L, Li Y and Yang D (2022) SBAS-InSAR-Based Landslide Susceptibility Mapping Along the North Lancang River, Tibetan Plateau. Front. Earth Sci. 10:901889. doi: 10.3389/feart.2022.901889

1 INTRODUCTION

Landslides are the major challenges of the economic activities in mountainous areas at present. In many countries, landslides have a greater influence on the society and economy than any other natural disasters (Glade 1998; Wallemacq et al., 2018) and have seriously affected the operation and management of engineering facilities of humankind (Turner 2018; Wei et al., 2018; Celik et al., 2021). In China, the most severe landslides occur in mountainous areas and plateaus (Shi. 2016), which will become more notable with the aggravation of climate change (Turner 2018; Pánek 2019). The Hengduan Mountains area in the eastern part of the Tibetan Plateau (where Jinsha, Lancang, and Nujiang rivers flow together) features high mountains and canyons, large numbers of loose cuttings, and sudden heavy rainfall. As a result, a series of serious and frequent geo-hazards have struck the area, such as rock collapse, high-elevation landslides, glacier-related debris flows, cutting creep, soil creep, and rate avalanches (Dai and Deng 2020; Zhang et al., 2011; Chen et al., 2013; Wang et al., 2017; Dai and Deng 2020; Lyu et al., 2021; Hu et al., 2021). In 2018, the landslide occurring in Baige village even directly blocked the Jinsha River and broke the ridge over the river, causing huge economic losses for the lower reaches (Xiong et al., 2020; An et al., 2021). All these geo-hazards have greatly damaged the engineering facilities of humankind and the surrounding environment. The Sichuan-Tibet Railway is a major railway project under planning in China, along which the terrain, landform, and geological tectonic conditions are extremely complex and landslides and other geo-hazards are extremely developed (Lu and Cai, 2019; Guo et al., 2021). Therefore, it is highly important to assess the landslide susceptibility along the major rivers around the Tibetan Plateau, especially the susceptibility to geo-hazards at the upper and lower reaches of the railway. LSM is used to describe the spatial distribution of the occurrence probabilities of landslides in a certain area according to the geographical environment and is considered a common countermeasure against the effects of landslides (Huang and Zhao 2018; Merghadi et al., 2020). To obtain more accurate LSM, this study employed the FR, RF, and FR-RF models to assess the landslide susceptibility along the north Lancang River where the Sichuan-Tibet railway passes. However, since traditional assessment models take historical landslide data as input, inaccurate historical landslide data tend to cause classification errors in LSM. Therefore, a method is required to improve the reliability of LSM.

The interferometric synthetic aperture radar (InSAR) technique serves as a reliable way to improve the identification and monitoring of landslides. Most especially, it can provide valuable information on the current activity of regional landslides (Dong et al., 2017; Introeri et al., 2017; Zhang et al., 2021). It has attracted increasing attention and has been applied to landslide identification (Bürgmann et al., 2000; Rott and Nagler,2006; Altamira 2017; Yao et al., 2017; Ge et al., 2019; Xu et al., 2019) and establish optimized landslide assessment models (Ciampalini et al., 2016; Zhao et al., 2019; Dimitris and Skevi Perdikou 2021) in the past 20 years. However, this method has not been used in the big rivers along the Sichuan-Tibet Railway, where the high-locality slope deformation information is very important, for the reason that the steep terrain is more prominent. In addition, the previous research always used one InSAR data source along the north Lancang River (Yao et al., 2020), but for the canyon area, multi-source data of ascending and descending orbits are very necessary, which is the advantages of this study compared with previous studies.

On-site mapping and monitoring of landslide susceptibility are complex and time-consuming and involve the collection and analysis of field data. Therefore, it is considered being impractical to obtain the latest changes of landslides through regular and repeated field surveys, especially on a large scale. Given this, the small baseline subset interferometric synthetic aperture radar (SBAS-InSAR) was used in this study to obtain the activity of slopes along the Lancang River, which is an indicator for susceptibility assessment. This technique can overcome the limitation of temporal incoherence and avoid the decoherence induced by too large intervals of SAR data, spatial incoherence, and atmospheric effects of traditional interferometry, thus producing more continuous spatial-temporal deformation results of lands (Berardino et al., 2002; Lanari et al., 2004). The SBAS-InSAR technique is applicable to the monitoring of long-sequence slow linear and nonlinear deformation and has been widely used in the identification and monitoring of land subsidence, earthquakes, active faults, and slope instability such as creep and landslides (Lanari et al., 2007; Qu et al., 2013; Chen et al., 2018; Li et al., 2018; Zhang et al., 2018).

To sum up, this study assessed the application of LSM in the north Lancang River using the FR, RF, and FR-RF models. Then it verified the accuracy of assessment results according to the AUC values of ROC curves and selected the most accurate assessment results for LSI refining. Specifically, the LSI was refined according to the deformation results of the study area from 2018 to 2020 obtained by the SBAS-InSAR method. As a result, the upgraded LSM can provide more reliable bases for the construction of major projects and the prevention and remediation of landslides.

2 STUDY AREA

The Sichuan-Tibet Railway and the Lancang River—one of the main rivers in a north-south direction in the Hengduan Mountains area—intersect in Changdu City, Tibet Autonomous Region. The study area spans 160 km in the north-south direction between the upper and lower reaches of the Lancang River section of the Sichuan-Tibet Railway and 10 km in the east-west direction around the two banks of the main stream of the Lancang River, which is the most intensive area of human activity (**Figure 1**). It is located in the middle-upper reach of the Lancang River and lies in the Changdu City overall. In terms of tectonic position, it is a part of the Hengduan Mountains in the eastern part of the Tibetan Plateau and belongs to the Jinsha River-Lancang River-Nujiang River tectonic belt. The outcrops in the study area primarily include Triassic and Jurassic sandstones and mudstones, as well as a small number of magmatic rocks and limestones. The hugely thick Triassic and Jurassic sandstone and

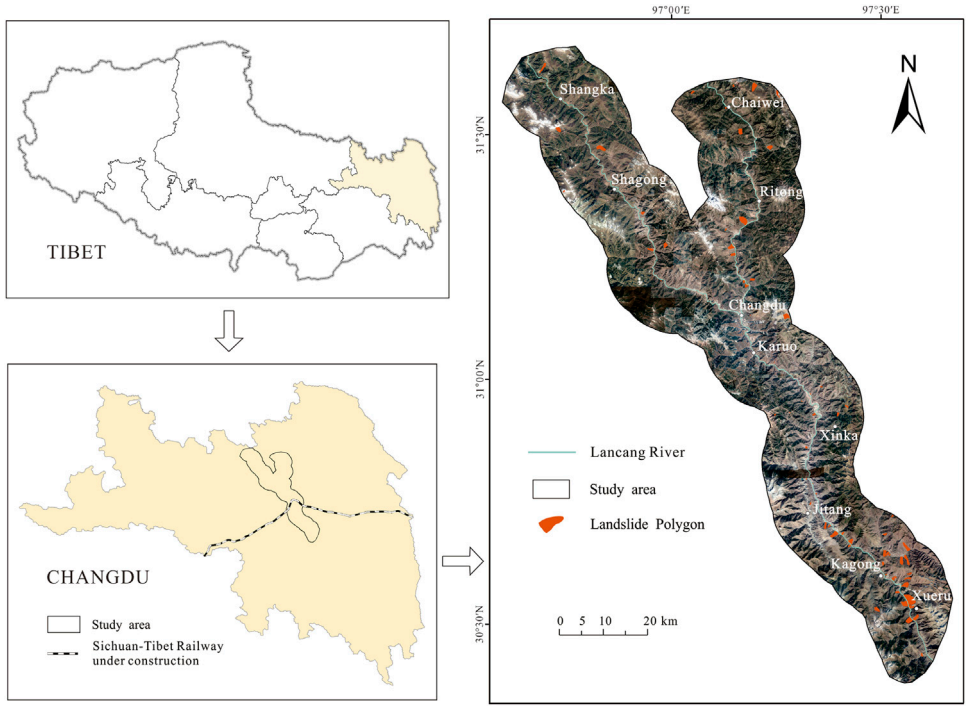

FIGURE 1 | Geographical location and landslide distribution of the study area.

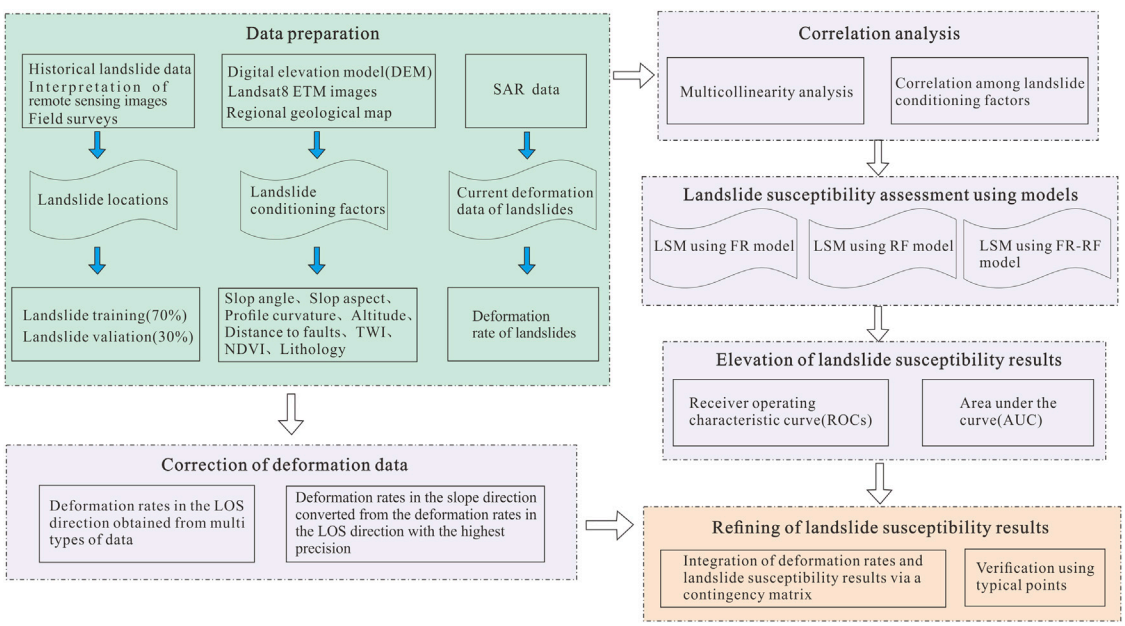

FIGURE 2 | Research method.

mudstone strata constitute multiple NW-SE-trending folds, and the faults in the study area are also mainly in the NW-SE trending. The study area is at an elevation of 2500–4500 m and is a typical area with high mountains and canyons due to the development of medium-high mountains, widely distributed gullies, and deep valleys. These provide favorable terrain conditions for the occurrence of slope-related geo-hazards such as landslides and collapse. Owing to the high elevation,

the study area has a relatively dry climate, with annual precipitation of less than 500 mm (70% occurring from July to September). Meanwhile, it has a low vegetation coverage, which is predominated by bushes.

3 DATA AND METHOD

As shown in **Figure 2**, the research method mainly consists of six steps: 1) preparation of data including historical landslide inventory, landslide conditioning factors, and the InSAR interpretation of current landslide deformation; 2) correlation analysis, mainly involving the correlation among landslide conditioning factors; 3) landslide susceptibility assessment using the FR, RF, and FR-RF models; 4) verification of landslide susceptibility assessment results according to ROCs; 5) correction of slope deformation information, processing of multi-source data, and conversion to the deformation rates in the slope direction; 6) optimization of landslide susceptibility assessment results, including refining the susceptibility assessment results according to slope deformation rates and the verification using typical points.

3.1 Data and Variables

3.1.1 Landslide Inventory

In this study, a total of 82 landslides were confirmed in the study area based on field survey data as well as remote sensing images and historical data and are present in the form of polygons in GIS. They are dominated by small-medium-scale shallow landslides but also include huge-scale deep rock landslides. Their minimum and maximum volume are $5 \times 10^2\,m^3$ and $1.8 \times 10^8\,m^3$, respectively. The 82 landslide polygons were divided into 46,458 grid cells (valued as 1) under the resolution of 30 m. Meanwhile, the same number of non-landslide grid cells (valued as 0) were randomly selected (i.e., a total of 92,916 grid cells were used for model training). These grid cells were randomly divided into a training and test data set at a ratio of 7:3 (Tien et al., 2016). That is, the training and the test data sets include 65,042 and 27,874 grid cells, respectively.

3.1.2 Landslide Conditioning Factors

There are no available general criteria for the selection of independent variables of landslide susceptibility, while the variables should be selected on the principle that they must be operable, inconsistent, measurable, and non-redundant (Lulseged and Yamagishi, 2005). According to the geological environment characteristics of the study area, the landslide susceptibility variables selected in this study include elevation, slope, aspect, profile curvature, terrain humidity index (TWI), normalized difference vegetation index (NDVI), lithology, and distance from a fault. The data sources of this study mainly include: 1) SRTM digital elevation model (DEM) with a resolution of 30 m, used to extract geomorphic parameters and hydrological environmental factors such as terrain humidity; 2) 1:250,000 geologic maps, used to extract the data on lithology and faults; 3) remote sensing images with a resolution of 30 m (images from paths/rows of 134/38 and 134/39 of Landsat 8 OLI_TIRS on August 13, 2013), based on which NDVI values were extracted using software ENVI. All conditioning factors were mapped as the grid cells with a resolution of 30 m.

The multicollinearity among landslide conditioning factors can be determined according to the variance inflation factor (VIF) and tolerance (TOL; Bai et al., 2010; Tien et al., 2011; Colkesen et al., 2016). VIF values of greater than 10 or TOL values of less than 0.1 indicate potential significant multicollinearity (O'brien 2007; Tien et al., 2011). The multicollinearity diagnosis was performed using the software SPSS, and the VIF and TOL values obtained are shown in **Table 1**. According to data analysis, the maximum VIF and the minimum TOL were 2.842 and 0.956, respectively, indicating no multicollinearity among the eight landslide conditioning factors. The eight variables were classified using the method of Jenks natural breaks. They were present in layers and assigned to the training data set to facilitate the operation of the susceptibility model (**Figure 3**).

3.2 Landslide Susceptibility Assessment Models

3.2.1 Frequency Ratio Model

The FR model is used to analyze the spatial relationships between landslide distribution and various environmental factors. It can be summarized as the ratio of two percentages, namely the percentage of the landslide grid cells corresponding to a classification interval of a certain factor accounting for all landslide grid cells and the percentage of all the grid cells corresponding to a classification interval of a certain factor accounting for all grid cells in the study area (Li et al., 2017; Aditian et al., 2018; Guo et al., 2019), as shown in **Formula (1)**:

$$\mathrm{FR} = \frac{\mathrm{NLS}_{pix} \Big/ \sum_{i=1}^{n} \mathrm{NLS}_{pix}}{\mathrm{NC}_{pix} \Big/ \sum_{i=1}^{n} \mathrm{NC}_{pix}} \tag{1}$$

Where, n is the number of all classification intervals of a certain factor; NLS_{pix} is the number of the landslide grid cells corresponding to a classification interval of a certain factor; NC_{pix} is the number of the grid cells corresponding to a classification interval of a certain factor. Ratios greater than 1 indicate that the classification interval of a certain factor is favorable for the occurrence of landslides. Otherwise, the classification interval of a certain factor is unfavorable of the occurrence of landslides.

3.2.2 Random Forest Model

RF is an integrated learning method for prediction, in which the bagging method is employed to generate multiple independent sample sets and multiple classification and regression trees (CARTs), and the results are determined by the highest or average votes (Breiman 2001). The main idea behind the RF model is that multiple weak classifiers are combined according to a certain strategy to form an integrated model that has a better prediction performance than a single classifier. This model has well been applied in landslide susceptibility assessment (Youssef et al., 2015). In this study, the RF model in the R language and

TABLE 1 | Diagnosis results of Multicollinearity among landslide conditioning factors.

Conditioning factor	TWI	Elevation	Distance from faults	Lithology	NDVI	Profile curvature	Slope	Aspect
TOL	0.352	0.710	0.956	0.829	0.928	0.423	0.705	1.015
VIF	2.842	1.409	1.046	1.207	1.073	2.364	1.419	0.985

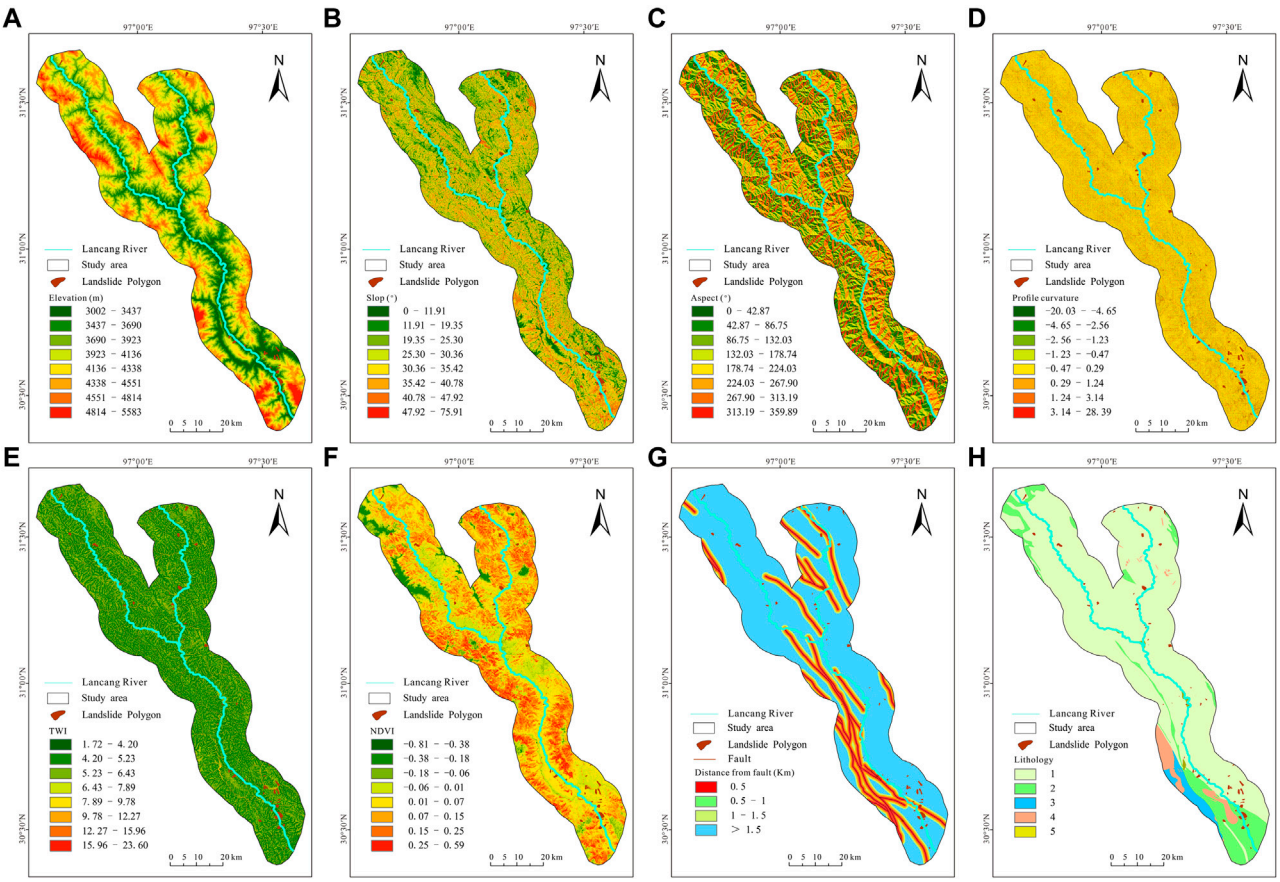

FIGURE 3 | Landslide conditioning factors: **(A)** elevation, **(B)** slope, **(C)** aspect, **(D)** profile curvature, **(E)** TWI, **(F)** NDVI, **(G)** distance from a fault, **(H)** lithology. Note: for the legends in **(H)**, "1" represents the conglomerate, sandstone, and mudstone with bedding developing; "2" represents limestone, slate, dolomite, and marble; "3" represents gneiss, granulite, and quartz schist; "4" represents blocky granite, diorite, and magmatic dike, and "5" represents loose gravel, sand, and detritus soil.

environment was adopted to assess the landslide susceptibility, flowchart was shown as **Figure 4**. Dependent variables were present in the form of landslide probability pixels on the landslide susceptibility map and the bagging technique was employed to conduct RF feature selection. At each node of the CARTs, samples of variables and observation were randomly incorporated into the training data set for model calibration. Since the random selection of the training data set may affect the results of the model, multiple trees were adopted to balance the model. Meanwhile, unselected cases (outside the bags) were used to calculate the error of the model (OOB Error), which is equal to the standard deviation between predicted and observed values.

3.2.3 Frequency Ratio-Random Forest Model

The FR and RF models were superimposed by replacing the values of the influencing factors with the FRs calculated using **Formula (1)**. Specifically, the FRs of each independent variable factor obtained using the FR model were input into the RF model under the R language and environment for learning. Then the FR-RF model was adoped to predict the landslide susceptibility of the whole study area to obtain the landslide susceptibility index (LSI) values.

3.2.4 Verification of Model Accuracy

ROCs were adopted to verify and compare the performance of the three models. In a ROC, the y-axis represents the true positive

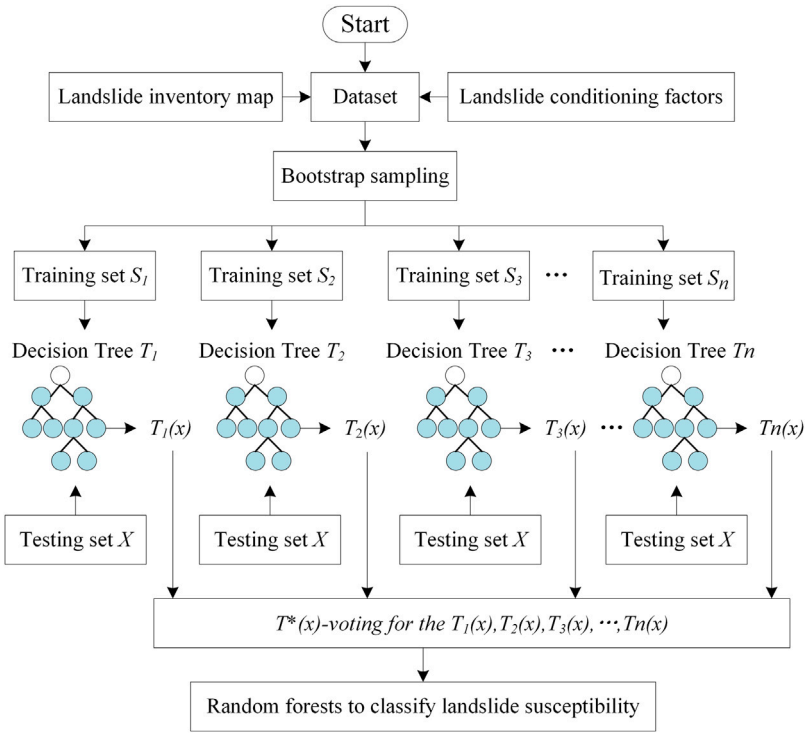

FIGURE 4 | Flowchart of the random forest method.

TABLE 2 | Basic parameters of the satellite-based SAR images.

Parameter		Orbital direction	Waveband	Radar wavelength/cm	Spatial resolution/m	Revisit cycle	Angle of incidence/°	Image time	Image number/phase
SAR sensor	RADARSAT-2	Descending	C	5.6	5	24	35.6	201808–202002	10
	Sentinel-1	Ascending	C	5.6	5*20	12	33.9	201808–202002	45

rate (sensitivity), which is used to characterize the percentage of correctly predicted landslide grid units, and the x-axis denotes the false positive rate (1-Specificity), which is utilized to characterize the percentage of wrongly predicted landslide grid cells (Van et al., 2006). Therefore, the closer the ROC to the upper left corner of the graph, the more accurate the test results. The area under the ROC is the AUC value, which varies in the range of 0.5–1. The higher the AUC value, the more accurate the model.

3.3 SBAS-InSAR

Given the average development degree of the vegetation in the study area, interpretation was individually conducted using 10 phases of RADARSAT-2 (descending) data and 45 phases of Sentinel-1 (ascending) data of C-band from August 2018 to February 2020. The basic parameters of the two types of data are shown in **Table 2**. The interpretation results of the two types of data were compared and those with higher precision were taken as the final deformation results. The data of SRTM1 DEM with a resolution of 30 m were used as external data to eliminate the terrain-contributed interference phases.

Data processing was conducted using the open-source software StamPS (Hooper et al., 2012), SBAS-InSAR processing flow was consistent with Yang et al., 2022. For RADARSAT-2 data, the spatial and temporal baselines were set at 300 m and 96 days, respectively, obtaining 14 interferometric pairs in total (**Figure 5A**). For Sentinel-1 data, the spatial and temporal baselines were set at 150 m and 24 days, respectively, obtaining 80 interferometric pairs in total (**Figure 5B**). Afterward, the interferometric pairs obtained through filtering using a Goldstein filter were filtered again to improve the signal-to-noise ratio and to further improve the precision of phase unwrapping and prediction results. Phase unwrapping was conducted using the minimum cost flow (MCF) algorithm. To avoid the effects of the unwrapping errors of low-coherence areas on the final results, the coherence value threshold was set at 0.35 (i.e., phase

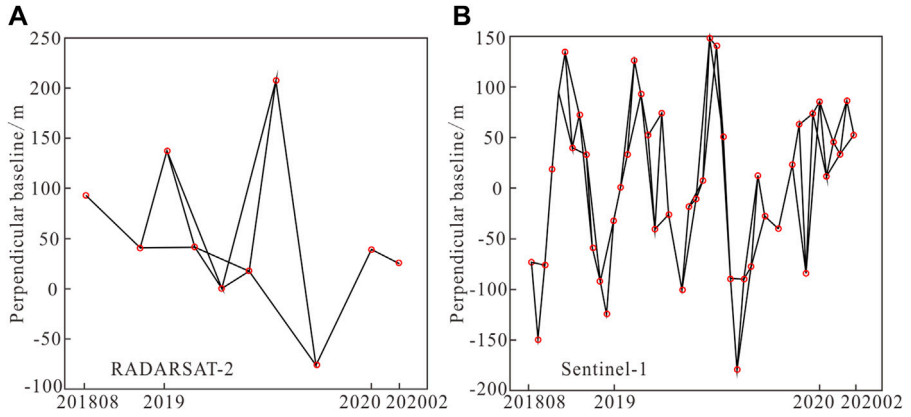

FIGURE 5 | Temporal and spatial baseline of interferometric radar images pairs.

unwrapping was only performed for the areas with coherence values higher than 0.35). After that, ground control points (GCPs) were adopted to refine the interferometric pairs to remove orbit-induced residual errors. The GCPs were selected from the stable areas that are far away from deformation and have coherence values higher than 0.7 (Zhu et al., 2011; Gaber et al., 2017). Furthermore, a three-order inversion model was adopted to remove terrain-induced residual phases. In this way, the initial deformation information was obtained. To eliminate atmosphere-induced residual errors, the thresholds of the low- and high-pass filters of the atmosphere were set at 1000 m and 365 days, respectively. Finally, the time-series nonlinear line-of-sight (LOS) deformation was estimated using the least square solution determined by the method of singular-value decomposition (Lanari et al., 2007).

The deformation rates in the LOS direction (*Vlos*) were converted into those in the slope direction (*Vslope*) using **Formula (2)**. To prevent extremely high absolute values from occurring during the conversion of *Vlos* into *Vslope*, Herrera et al. took the empirical value index = ± 0.3 as fixed thresholds (Zhang et al., 2018). In detail, Index was set at −0.3 in the case of −0.3 < index < 0 and at 0.3 in the case of 0 < index < 0.3. Then deformation points with non-negative deformation rates in the slope direction were removed from the results obtained. In this way, the deformation rates in the slope direction were determined.

$$Vslop = \frac{Vlos}{\text{Index}} \tag{2}$$

TABLE 3 | Integration of landslide susceptibility and deformation rates.

		V_{slop} (mm/a)				
		0–13	13–26	26–39	39–80	>80
Susceptibility grade	1	0	+1	+2	+3	+4
	2	0	0	+1	+2	+3
	3	0	0	0	+1	+2
	4	0	0	0	0	+1
	5	0	0	0	0	0

$$\text{Index} = n_{los} \cdot n_{slope}$$

$$n_{los} = (\sin\theta \sin\alpha s, -\sin\theta \cos\alpha, -\cos\theta)$$

$$n_{los} = (\sin\alpha \cos\varphi, -\cos\alpha \cos\varphi, -\sin\varphi)$$

Where:

$Vslop$—deformation rate in slope direction;
V_{los}—deformation rate in LOS direction;
α—direction of slop (°);
φ—slope (°);
θ—incident angle of radar beam (°);
α_S—the angle between the direction of satellite orbit and the true north.

3.4 Refining

The deformation results were integrated and refined by establishing a contingency matrix between the LSI values and the deformation rates obtained by the SBAS-InSAR method (**Table 3**). The computation of the contingency matrix was carried out in GIS. In detail, the deformation rates were spatially connected with the LSM obtained using the FR-RF model and then the contingency matrix was calculated using a field calculator. As a result, the refined landslide susceptibility map was exported. In the contingency matrix, the deformation rate intervals were determined according to the standard deviation of the deformation rates (δ = −13 mm/a; Zhao et al., 2019), and the susceptibility grades of LSI from 1 to 5 represent very low, low, moderate, high, and very high susceptibility, respectively. Based on this, the deformation obtained by the SBAS-InSAR method was classified into different zones according to susceptibility grades. Meanwhile, the susceptibility grades corresponding to the original LSI values were increased by 1–4 according to the deformation rates. The higher the deformation rates, the higher the landslide susceptibility and the susceptibility grades shall not be greater than 5. Slopes are highly active when their deformation rates exceed a certain value according to field survey results. In this case, the landslide susceptibility grades should be high and very

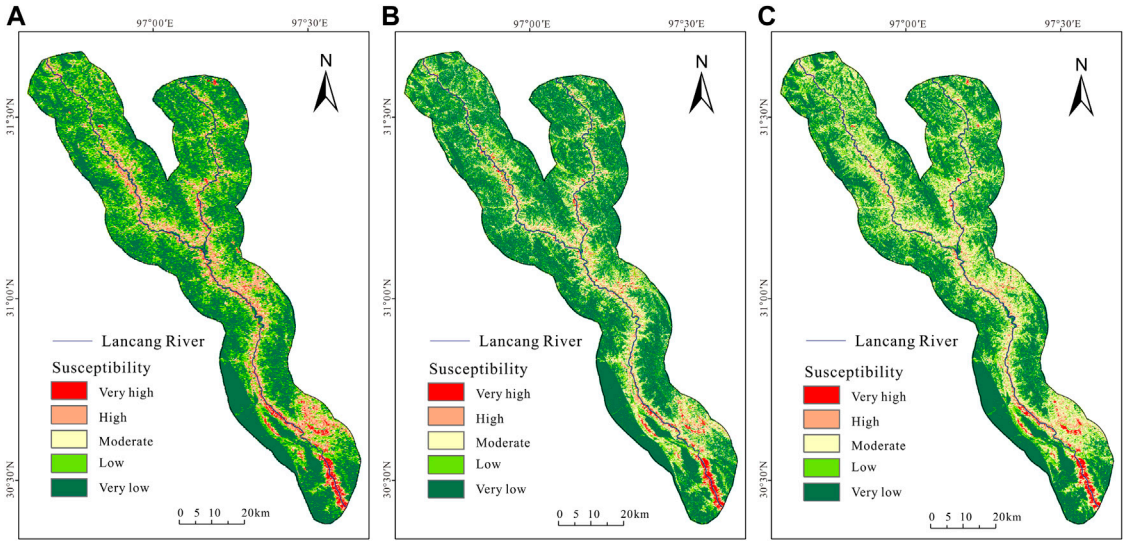

FIGURE 6 | Landslide susceptibility maps obtained using the three models. **(A)** FR model; **(B)** RF model; **(C)** FR-RF model.

high. The above integration helps to reduce misclassification probability. Meanwhile, for areas that have low susceptibility but are subject to landslides soon, their susceptibility can be corrected to a high grade after the integration (**Table 2**).

4 RESULTS

4.1 Results of the Frequency Ratio Model

The FRs of all groups of the landslide conditioning factors of the study area were calculated using **Formula (1)**, as shown in **Supplementary Table S1**. Based on this, the weight of each landslide conditioning factor was determined. Then LSI of the study area was calculated using the Raster Calculator tool in the ArcGIS, which fell within the range of 1.43–17.02. The higher the LSI, the higher the occurrence probability of landslides, and vice versa. The LSI range was divided into five intervals by the method of Jenks natural breaks, namely [1.43, 3.82), [3.82, 4.98), [4.98, 6.10), [6.10, 7.68), and [7.68, 17.02], corresponding to the very low, low, moderate, high, and very high susceptibility grades, respectively. Based on this, the landslide susceptibility map was formed, as shown in **Figure 6A**. According to this figure, the areas with very low and low susceptibility are the largest, with area percentages of 30.46 and 26.21%, respectively. In contrast, the areas with moderate, high, and very high susceptibility are smaller, with area percentages of 18.15, 17.23, and 7.95%, respectively. The accuracy of the model was verified using 14,416 landslide grid cells in the test data set. Among them, 11,465 grid cells (79.53%) fell in the scope of high and very high susceptibility.

4.2 Results of the Random Forest Model

The LSI of the study area obtained using the RF model varied in the range of 0–0.98. Similarly, the LSI range was divided into five

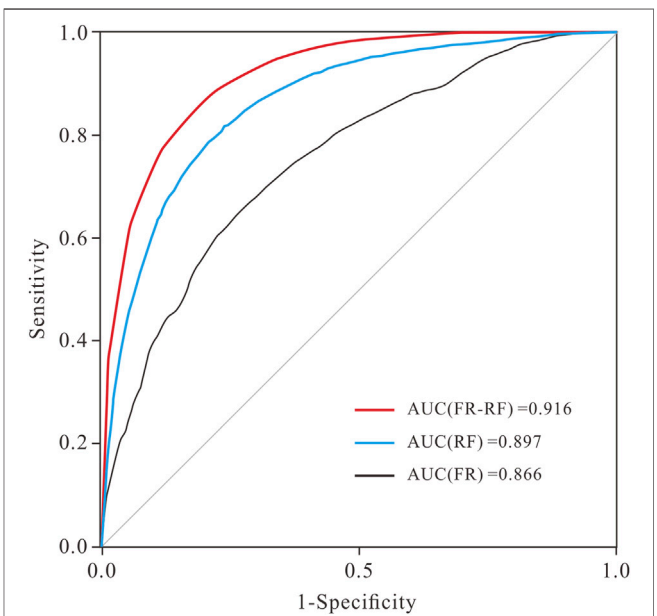

FIGURE 7 | ROCs of the FR, RF, and FR-RF models.

intervals by the method of Jenks natural breaks, namely [0, 0.14), [0.14, 0.28), [0.28, 0.45), [0.45, 0.63), and [0.63, 0.98], which correspond to the very low, low, moderate, high, and very high susceptibility, respectively. The landslide susceptibility map formed is shown in **Figure 6B**. According to this figure, the areas with very low, low, moderate, high, and very high susceptibility have area percentages of 40.25, 21.76, 18.82, 12.13, and 7.04%, respectively. The accuracy of the model was verified using the remaining 14,416 landslide grid cells in the test

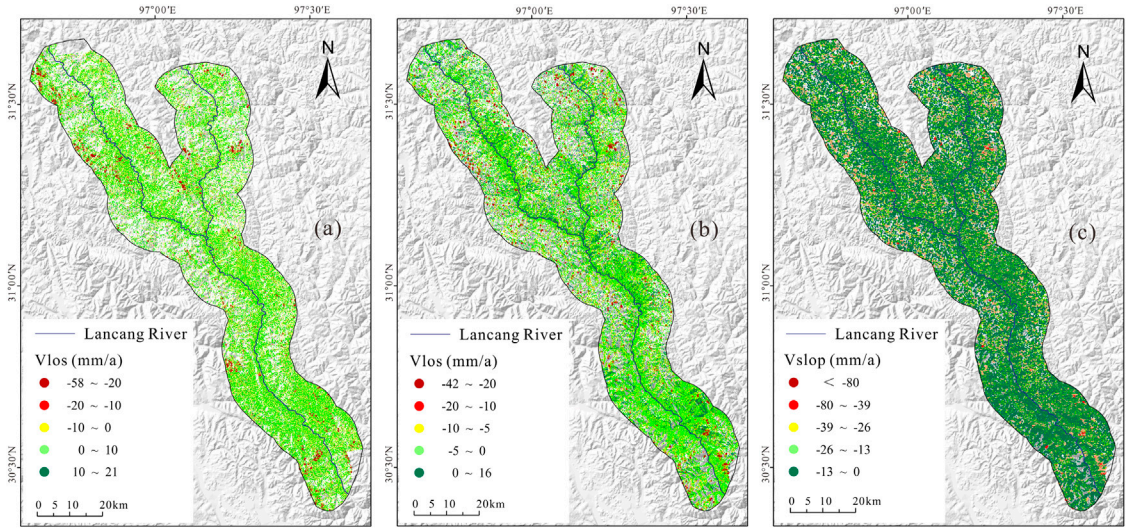

FIGURE 8 | (A) Deformation results in LOS direction obtained using Sentinel-1 data; **(B)** Deformation results in LOS direction obtained using RADARSAT-2 data; **(C)** Deformation results in slope direction after conversion.

data set. Among them, 12,484 grid cells (86.60%) fell in the scope of high and very high susceptibility.

4.3 Results of the Frequency Ratio-Random Forest Model

The FRs obtained using the FR model were taken as input data of the RF model. Then the landslide susceptibility assessment of the whole study area was also conducted using the R language, obtaining the LSI of the study area. The results show that the LSI fell within the range of 0–1. Similarly, the LSI range was divided into five intervals by the method of Jenks natural breaks, namely [0, 0.15), [0.15, 0.31), [0.31, 0.53), [0.53, 0.77), and [0.77, 1], corresponding to the very low, low, moderate, high, and very high susceptibility grades, respectively. The landslide susceptibility map formed is shown in **Figure 6C**. According to this figure, the areas with very low, low, moderate, high, and very high susceptibility have area percentages of 35.90, 25.06, 18.74, 13.73, and 6.57%, respectively. Similarly, the accuracy of the model was verified using the remaining 14,416 landslide grid cells in the test data. Among them, 13,875 grid cells (96.25%) fell in the scope of high and very high susceptibility.

With the landslide probability predicted using the FR, RF, and FR-RF models as the LSI and based on the verification of these models using the remaining 30% landslide test data, the ROCs of the prediction results of all the models were plotted (**Figure 7**) and their AUC values were calculated. Based on this, the prediction precision of all the models was compared. According to **Figure 7**, the final AUC values of the prediction results of the FR, RF, and FR-RF models were 0.866, 0.897, and 0.916, respectively. Therefore, the FR-RF model possesses the highest prediction precision. Meanwhile, it was verified by existing landslides that the FR-RF model had the highest accuracy. Therefore, the assessment results of the FR-RF model were taken as the final susceptibility results and were further optimized.

4.4 SBAS-InSAR Results

For the slopes in the study area, the deformation rates in the LOS direction obtained using the Sentinel-1 ascending data varied in the range of −58–21 mm/a (**Figure 8A**). Then they were converted into the deformation rates in the slope direction, obtaining 2,392,676 coherent points in total. In contrast, the deformation rates in the LOS direction obtained using the RADARSAT-2 descending data varied in the range of −42–16 mm/a and a total of 5,787,774 coherent points were obtained after conversion (**Figure 8B**). The descending data obviously yielded a higher density of interference points and can present more details of hidden hazards. Therefore, the descending data were utilized to identify the slope deformation and identification results as follows. The average density of deformed points was 3687.19/km^2, which was higher than other studies previously considered high density (Meisina et al., 2008; Zhao et al., 2019), shows the density is acceptable. The maximum deformation rate in the slope direction was up to −128 mm/a (the critical stable interval: −13–0 mm/a; **Figure 8C**). The deformation results obtained by the SBAS method failed to cover the whole study area since ice, snow, and water are locally distributed in the study area.

With the standard deviation (−13 mm/a) of RADARSAT-2 data as the threshold of stable points, the areas with statistically reliable deformation obtained by the SBAS method accounted for 54.22% of the entire study area. Through remote sensing interpretation and field verification of the deformation results, a total of 113 points with hidden landslide hazards were delineated and after excluding land subsidence points in flat areas and a few points denoting snow and ice movements, field verification confirms the reliability of InSAR interpretation results (Zhang et al., 2021). According to the map of

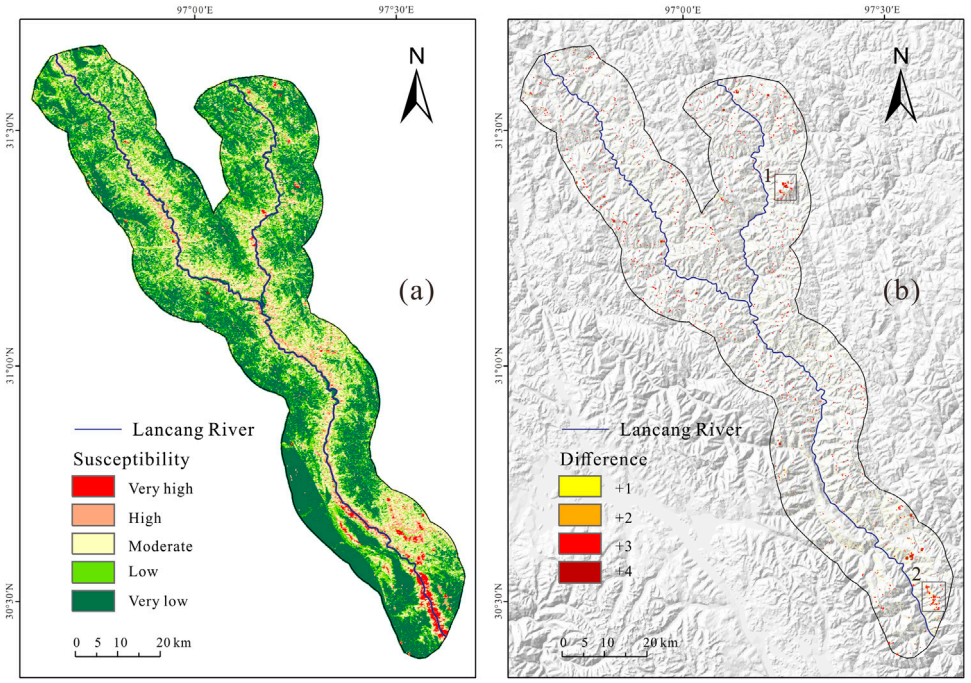

FIGURE 9 | (A) landslide susceptibility assessment results after processing using a correction matrix; **(B)** differences between the unrefined and refined landslide susceptibility grades of each grid cell. Notes: the rectangular areas marked with 1 and 2 denote the Ritong and Xueru areas, respectively.

TABLE 4 | Comparison of landslide susceptibility grades obtained from the FR-RF model and RLSM.

Susceptibility grade	LSM		RLSM		Increment	
/	Cell number	%	Cell number	%	Susceptibility grade	Cell number
1	1,814,040	35.90	1,566,700	31.01	0	4,488,810
2	1,265,862	25.06	1,341,370	26.55	+1	412,563
3	946,683	18.74	968,514	19.17	+2	113,775
4	693,815	13.73	790,170	15.64	+3	36,986
5	331,840	6.57	385,486	7.63	+4	106

slope deformation rates, there exist multiple deformation centers in the study area. In detail, continuous high deformation values are visible on the left bank of the Lancang River in Kagong area in the southern section of the study area, multiple abnormal deformation areas exist on the left bank of the Lancang River in the Chaiwei-Ritong areas in the northern section of the study area, and there are abnormal deformation areas on the right bank of the Lancang River near the Shagong area. As shown by the statistical results, only 39.24% of landslides newly identified by the SBAS method and the FR-RF model feature high or very high landslide susceptibility. Therefore, the results are reliable and can be used to optimize the landslide susceptibility assessment results.

4.5 Refining of Assessment Results

The refined landslide susceptibility map is shown in **Figure 9A**. Compared with the susceptibility results before refining, the landslide susceptibility of multiple areas was notably increased, especially in the Ritong and Xueru areas (**Figure 9B**). **Table 4** shows the changes in the number percentages of the grid cells of all grades before and after the optimization. According to this table, the grid cells with susceptibility grades of 1, 2, 3, 4, and 5 after refining accounted for 31.01, 26.55, 19.17, 15.64, and 7.63%, respectively. By comparison with unrefined assessment results, the areas with high and very high susceptibility increased by 2.97% in the refined assessment results. Meanwhile, 563,430 grid cells showed changes in landslide susceptibility, accounting for 11.15% of the total grid cells. Among them, the landslide susceptibility of 412,563, 113,775, 36,985, and 106 grid cells increased by one, two, three, and four grades, respectively.

4.6 Research Results of Typical Areas

A detailed analysis was carried out on two areas with the greatest changes in landslide susceptibility (marked with 1 and 2 in **Figure 9B**). Area No. 1 lies in the Ritong area in the northern part of the study area. In addition to Jurassic sandstones and

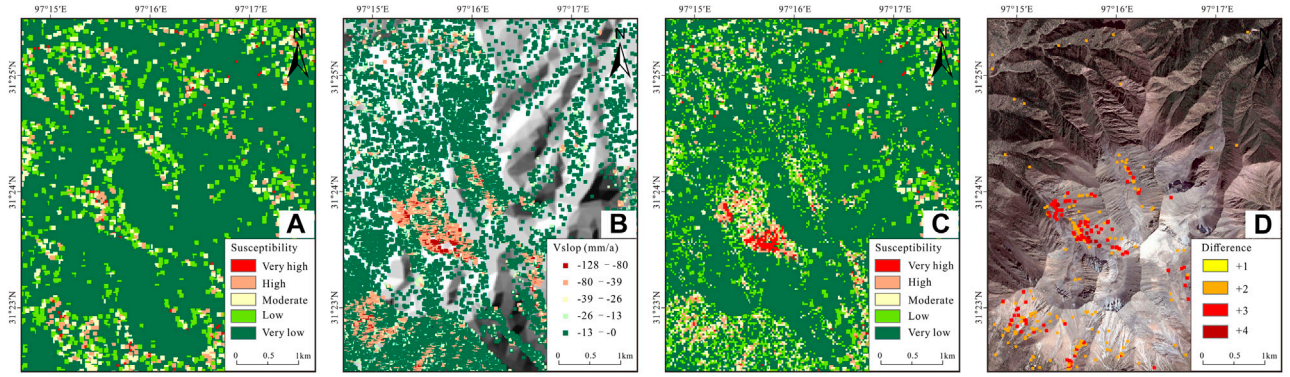

FIGURE 10 | Landslide assessment results of area No. 1 (Ritong area). **(A)** landslide susceptibility assessment results obtained using the FR-RF model. **(B)** deformation rates in the slope direction obtained by the SBAS-InSAR method. **(C)** optimized landslide susceptibility assessment results. **(D)** changes in landslide susceptibility grades before and after refining.

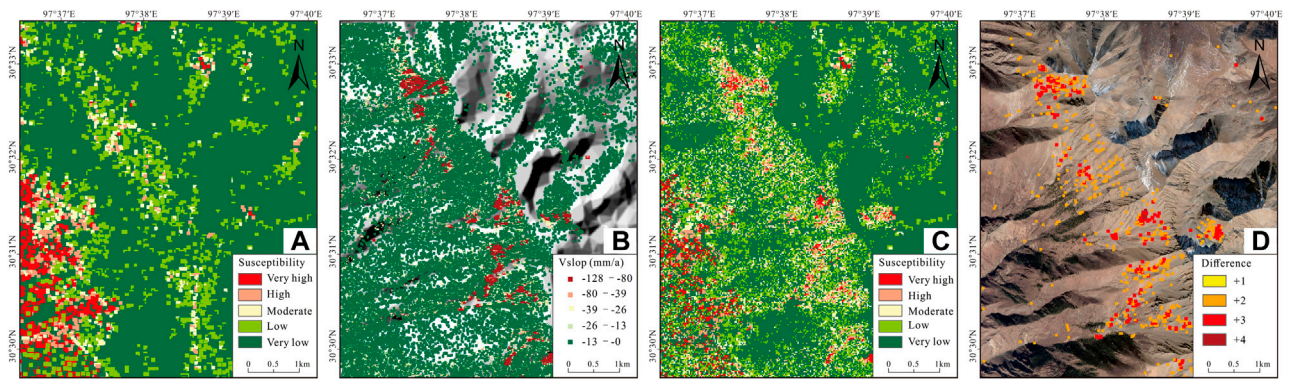

FIGURE 11 | Landslide assessment results for area No. 2 (Xueru area). **(A)** landslide susceptibility assessment results obtained using the FR-RF model. **(B)** Deformation rates in the slope direction obtained by the SBAS-InSAR method. **(C)** optimized landslide susceptibility assessment results. **(D)** changes in landslide susceptibility grades before and after refining.

mudstones, magmatic rocks such as island-shaped Paleogene granite porphyries and ordinary porphyries have developed in the area. Owing to differential weathering, the magmatic rock masses formed convex and isolated peaks with a slope greater than 50°. Furthermore, their strength decreased as a result of long-term weathering and denudation, posing the risks of instability and collapse. Field surveys show that clastic materials accumulated due to the weathering of high-elevation rock masses may cause landslides or other instability events, thus endangering the roads and villages at the slope foot. This possibility was revealed by the deformation information obtained by the SBAS-InSAR method. Meanwhile, the RLSM also shows a significant increase in the landslide susceptibility of this area compared to the LSM (**Figure 10**).

Area No. 2 is located in the Xueru area on the eastern side of the Lancang River in the southern part of the study area. In terms of lithology, the strata in this area consist of schists and slates of the Carboniferous Kagong Formation in the tectonic melanges of the Lancang River. Meanwhile, the Lancang River fault zone runs through this area. Therefore, the rock masses in area No. 2 are relatively broken and show high susceptibility to high-elevation collapse and landslides. However, since this area lies in a high and steep slope on the eastern side of the Lancang River, its adverse high-elevation geological phenomena tend to be ignored. According to the latest SBAS-InSAR interpretation results, multiple areas with high deformation rates exist in the middle-upper part of the slope and they are prone to landslides. The RLSM shows the differences of area No. 2 before and after optimization and meanwhile, some areas with low susceptibility were corrected into areas with high susceptibility (**Figure 11**).

5 DISCUSSION

In this study, the FR, RF, and FR-RF models were adopted to evaluate the application of LSM along the north Lancang River. The purpose is to compare the accuracy of mathematical models and machine learning models and to further obtain more accurate

landslide susceptibility assessment results. Therefore, it is highly necessary to verify the accuracy of the results. To this end, a test data set is required to verify the ability of the models to identify new samples, and then the test errors are taken as the approximation of generalization error. It is generally assumed that the collection of samples for verification is independent of the true distribution of samples. In addition, the test and training data sets should be mutually exclusive as much as possible. However, they should be determined in such a way that their data distribution should be kept consistent as far as possible to avoid the effects of data segmentation on the final results. In this study, 70% of the samples were used for training, while the rest were used for testing.

In this study, both the Sentinel-1 data and the RADARSAT-2 data were utilized for deformation monitoring by the InSAR method. They are ascending and descending data, respectively and have the same monitoring duration. Their advantages and disadvantages were assessed according to the deformation point density that was finally calculated using analytical data. The purpose was to avoid errors that may be caused by a single data source. Finally, the RADARSAT-2 data were selected. Since RADARSAT-2 has a revisit cycle of 14 days, the InSAR method is only applicable to slow and very slow ground surface movements but can only yield average effects in monitoring quick ground surface movements such as collapse and rockfalls. There is no perennial cover of snow and ice and the vegetation coverage is low in the study area. Therefore, the C-band data of RADARSAT-2 are fit for the InSAR interpretation of the study area.

In this study, the LSM was performed using the FR, RF, and FR-RF models. However, the results obtained were limited by the data quality related to each landslide conditioning factor and the quality of landslide samples, which may lead to classification errors. For the data quality related to each landslide conditioning factor, regional susceptibility assessment tends to be carried out using the terrain and landform data with a resolution of 90 m or even higher and the lithologic fault data mostly sourced from 1: 500,000 regional geologic maps (Li et al., 2017; Zhao et al., 2019). Owing to the limited area of the study area, the terrain and landform data used in this study have a resolution of 30 m and the lithologic fault data are on a scale of 1:250,000, thus ensuring the data quality of landslide conditioning factors to the highest extent. For the quality of landslide samples, it is a common practice to use historical landslide data in landslide susceptibility assessment (Alkhasawneh et al., 2014; Wang et al., 2015; Tsangaratos and Ilia 2016; Chen et al., 2017). However, the evidence of landslide activities may be lost due to landslide evolution, erosion process, vegetation growth, and the effects of human activities. Historical landslides can be effectively supplemented through the timely identification of active landslides. In this way, the accuracy of LSM can be improved. Furthermore, the landslides in this study area mostly occur in low-elevation areas due to the landform consisting of high mountains and canyons of the Lancang River. This causes the lack of samples of high-elevation landslides, which tend to be inaccessible in traditional surveys, thus leading to serious classification errors in the LSM. The comparison of results before and after InSAR refining also reveals that the slopes with great changes in landslide susceptibility grades are mostly located in high-altitude areas. This indicates the advantages of InSAR refining in this study and the necessity of optimizing the LSM by the InSAR method.

It should be noted that, for the deformation results determined by LSM along with InSAR, there are fewer errors that the areas subject to slope deformation are wrongly classified as the areas with very low and low sensitivity. In contrast, the LSM based on traditional models only presents the regional distribution of the landslides predicted and cannot provide the dynamic deformation process of slopes. However, the evolution of landslides with time is the greatest concern for decision makers (Xie et al., 2017). RLSM allows the current state of landslides to be revealed and can be applied to the preliminary landslide surveying and mapping and quantitative risk management on a regional scale (Chalkias et al., 2014).

To sum up, landslide susceptibility assessment and its mapping serve as a major step in the research of landslide risks and can be used to assess the risks in areas prone to landslides and areas with infrastructures. It has been proposed that the Sichuan-Tibet Railway under planning run through the study area in the form of a bridge. Therefore, it is obvious that more accurate LSM can better serve the planning and risk control of the Sichuan-Tibet Railway. The deformation results obtained using LSM and InSAR individually can both achieve required goals, while the combination of them can further optimize and refine LSM. Compared with the landslide susceptibility maps obtained using traditional models, the landslide susceptibility map refined using the InSAR results yielded more accurate sorting of landslide susceptibility along Lancang River. Therefore, it is believed that the refined landslide susceptibility map will be valuable for effective land use management and project planning in the Lancang River region.

6 CONCLUSION

In this study, the FR, RF, and FR-RF models were adopted to evaluate the application of the LSM along the north Lancang River. The ascending and descending data of satellites were individually adopted to calculate the deformation rates of slopes using the SBAS-InSAR method. As a result, more accurate deformation results obtained with RADARSAT-2 data were selected to optimize the LSM through a contingency matrix, thus improving the precision of the LSM. The above technologies were combined to further improve the accuracy of the susceptibility assessment results by considering the current deformation state of slopes and accordingly to reduce potential landslide risks.

The LSI values were obtained using the FR, RF, and FR-RF models. They were divided into five grades, namely very low, low, moderate, high, and very high. The AUC values of the assessment results obtained with FR, RF, and FR-RF models were 0.866, 0.897, and 0.916, respectively. Meanwhile, it was verified by existing landslides that the FR-RF model had the highest accuracy. Therefore, the FR-RF model was selected for LSM optimization. Afterward, a contingency matrix was established according to LSI values and the deformation rates in the slope

direction were converted. Based on this, the susceptibility results obtained using the traditional model were updated. As a result, the areas with high and very high susceptibility increased by 2.97% and 563,430 grid cells showed changes in landslide susceptibility, accounting for 11.15% of all grid cells. Most especially, the Xueru and Ritong areas showed more notable increases in landslide susceptibility than other areas, and it has been verified by remote sensing images and field surveys that landslide risks exist in both areas.

This study is greatly significant for the refining of LSM, especially for areas where the SBAS-InSAR method is applicable. The refined landslide susceptibility map can provide valuable support for the decision making in the disaster prevention and mitigation and the management of major engineering facilities in the upper reaches of the Lancang River.

DATA AVAILABILITY STATEMENT

The original contributions presented in the study are included in the article/**Supplementary Material**, further inquiries can be directed to the corresponding author.

AUTHOR CONTRIBUTIONS

JZ designed the model and the computational framework and analysed the data. LC and YL carried out the historical landslide data collecting and field suverys. BG and JZ carried out the InSAR interpretation. JZ and HH wrote the manuscript with input from all authors. HH and DY helped supervise the project.

FUNDING

This study was funded by China Geological Survey Project (No. DD20221741), the Second Tibetan Plateau Scientific Expedition and Research (STEP) Program (Grant No. 2019QZKK0902) and Key laboratory of Deep-Earth Dynamics of Ministry of Natural Resources Open Project (No. J1901).

ACKNOWLEDGMENTS

The Sentinel-1 images, geologic maps, and landsat8 images used in this study were provided by the European Space Agency (ESA), the China Geological Survey, and the National Aeronautics and Space Administration of the United States of America (NASA), respectively.

SUPPLEMENTARY MATERIAL

The Supplementary Material for this article can be found online at: https://www.frontiersin.org/articles/10.3389/feart.2022.901889/full#supplementary-material

REFERENCES

Aditian, A., Kubota, T., and Shinohara, Y. (2018). Comparison of GIS-Based Landslide Susceptibility Models Using Frequency Ratio, Logistic Regression, and Artificial Neural Network in a Tertiary Region of Ambon, Indonesia. *Geomorphology* 318 (1), 101–111. doi:10.1016/j.geomorph.2018.06.006

Alkhasawneh, M. S., Tay, L. T., Ngah, U. K., Al-Batah, M. S., and Mat Isa, N. A. (2014). Intelligent Landslide System Based on Discriminant Analysis and Cascade-Forward Back-Propagation Network. *Arab. J. Sci. Eng.* 39 (7), 5575–5584. doi:10.1007/s13369-014-1105-8

An, H., Ouyang, C., and Zhou, S. (2021). Dynamic Process Analysis of the Baige Landslide by the Combination of DEM and Long-Period Seismic Waves. *Landslides* 18, 1625–1639. doi:10.1007/s10346-020-01595-0

Bai, S., Wang, J., Lü, G., Zhou, P., Hou, S., and Xu, S. (2010). GIS-based Logistic Regression for Landslide Susceptibility Mapping of the Zhongxian Segment in the Three Gorges Area, China. *Geomorphology* 115 (1), 23–31. doi:10.1016/j.geomorph.2009.09.025

Berardino, P., Fornaro, G., Lanari, R., and Sansosti, E. (2002). A New Algorithm for Surface Deformation Monitoring Based on Small Baseline Differential SAR Interferograms. *IEEE Trans. Geosci. Remote Sens.* 40, 2375–2383. doi:10.1109/tgrs.2002.803792

Breiman, L. (2001). Random Forests. *Mach. Learn.* 45 (1), 5–32. doi:10.1023/a:1010933404324

Bui, D. T., Lofman, O., Revhaug, I., and Dick, O. (2011). Landslide Susceptibility Analysis in the Hoa Binh Province of Vietnam Using Statistical Index and Logistic Regression. *Nat. Hazards* 59 (3), 1413–1444. doi:10.1007/s11069-011-9844-2

Bürgmann, R., Rosen, P. A., and Fielding, E. J. (2000). Synthetic Aperture Radar Interferometry to Measure Earth's Surface Topography and its Deformation. *Ann. Rev. Earth Planet* 28, 169–209.

Çelik, S., Özyazıcıoğlu, M., Şahin, R., Uysal, R., Çakıcı, F. Z., Kalkan, E., et al. (2021). The Destruction of Erzurum Ski-Jumping Complex by a Landslide: Evaluation of an Engineering Design Failure. *Nat. Hazards* 107, 475–496. Available at: http://377.rm.cglhub.com/10.1007/s11069-021-04591-2.

Chalkias, C., Ferentinou, M., and Polykretis, C. (2014). Gis-based Landslide Susceptibility Mapping on the Peloponnese Peninsula, Greece. *Geosciences* 4, 176–190. doi:10.3390/geosciences4030176

Chen, G., Zhang, Y., Zeng, R., Yang, Z., Chen, X., Zhao, F., et al. (2018). Detection of Land Subsidence Associated with Land Creation and Rapid Urbanization in the Chinese Loess Plateau Using Time Series Insar: A Case Study of Lanzhou New District. *Remote Sens.* 10, 270. doi:10.3390/rs10020270

Chen, J., Dai, F., Lv, T., and Cui, Z. (2013). Holocene Landslide-Dammed Lake Deposits in the Upper Jinsha River, SE Tibetan Plateau and Their Ages. *Quat. Int.* 298, 107–113. doi:10.1016/j.quaint.2012.09.018

Chen, W., Pourghasemi, H. R., and Naghibi, S. A. (2017). A Comparative Study of Landslide Susceptibility Maps Produced Using Support Vector Machine with Different Kernel Functions and Entropy Data Mining Models in China. *Bull. Eng. Geol. Environ.*, 1–18. doi:10.1007/s10064-017-1010-y

Ciampalini, A., Raspini, F., Lagomarsino, D., Catani, F., and Casagli, N. (2016). Landslide Susceptibility Map Refinement Using PSInSAR Data. *Remote Sens. Environ.* 184, 302–315. doi:10.1016/j.rse.2016.07.018

Colkesen, I., Sahin, E. K., and Kavzoglu, T. (2016). Susceptibility Mapping of Shallow Landslides Using Kernel-Based Gaussian Process, Support Vector Machines and Logistic Regression. *J. Afr. Earth Sci.* 118, 53–64. doi:10.1016/j.jafrearsci.2016.02.019

Dai, F. C., and Deng, J. H. (2020). Development Characteristics of Landslide Hazards in Three-Rivers Basin of Southeast Tibetan Plateau. *Adv. Eng. Sci.* 52 (5), 3–15.

Dimitris, K., and Skevi, P. (2021). The Application of DInSAR and Bayesian Statistics for the Assessment of Landslide Susceptibility. *Nat. hazards* 105, 2957–2985.

Dong, J., Zhang, L., Li, M., Yu, Y., Liao, M., Gong, J., et al. (2017). Measuring Precursory Movements of the Recent Xinmo Landslide in Mao County, China with Sentinel-1 and ALOS-2 PALSAR-2 Datasets. *Landslides* 15 (1), 135–144. doi:10.1007/s10346-017-0914-8

Gaber, A., Darwish, N., and Koch, M. (2017). Minimizing the Residual Topography Effect on Interferograms to Improve Dinsar Results: Estimating Land Subsidence in Port-Said City, Egypt. *Remote Sens.* 9, 752. doi:10.3390/rs9070752

Ge, D. Q., Dai, K. R., Guo, Z. C., and Li, Z. H. (2019). Early Identification of Serious Geological Hazards with Integrated Remote Sensing technologies:Thought and and Recommendations. *Geomatics Inf. Sci. Wuhan Univ.* 44 (7), 949–956.

Glade, T. (1998). Establishing the Frequency and Magnitude of Landslide-Triggering Rainstorm Events in New Zealand. *Environ. Geol.* 35 (2–3), 160–174. doi:10.1007/s002540050302

Guo, C. B., Wu, R. A., Jiang, L. W., Zhong, N., Wang, Y., and Wang, D. (2021). Typical Geohazards and Engineering Geological Problems along the Ya'an-Linzhi Section of the Sichuan-Tibet Railway, China. *Geoscience* 35 (1), 1–17.

Guo, Z. Z., Yin, K. L., and Huang, F. M. (2019). Evaluation of Landslide Susceptibility Based on Landslide Classification and Weighted Frequency Ratio Model. *Chin. J. Rock Mech. Eng.* 38 (2), 287–300.

Hooper, A., Bekaert, D., Spaans, K., and Arıkan, M. (2012). Recent Advances in SAR Interferometry Time Series Analysis for Measuring Crustal Deformation. *Tectonophysics* 514-517, 1–13. doi:10.1016/j.tecto.2011.10.013

Hu, M. M., Wu, Z. H., Reicherter, K., Ali, S., Huang, X. L., and Zuo, J. M. (2021). A Historical Earthquake-Induced Landslide Damming Event at the Qiaojia Reach of the Jinsha River, SE Tibetan Plateau: Implication for the Seismic Hazard of the Xiaojiang Fault. *Front. Earth Sci.* 9. doi:10.3389/feart.2021.649543

Huang, Y., and Zhao, L. (2018). Review on Landslide Susceptibility Mapping Using Support Vector Machines. *Catena* 165, 520–529. doi:10.1016/j.catena.2018.03.003

Intrieri, E., Raspini, F., Fumagalli, A., Lu, P., Del Conte, S., Farina, P., et al. (2017). The Maoxian Landslide as Seen from Space: Detecting Precursors of Failure with Sentinel-1 Data. *Landslides* 15 (1), 123–133. doi:10.1007/s10346-017-0915-7

Lanari, R., Casu, F., Manzo, M., and Lundgren, P. (2007). Application of the Sbas-Dinsar Technique to Fault Creep: A Case Study of the Hayward Fault, California. *Remote Sens. Environ.* 109, 20–28. doi:10.1016/j.rse.2006.12.003

Lanari, R., Mora, O., Manunta, M., Mallorqui, J. J., Berardino, P., and Sansosti, E. (2004). A Small-Baseline Approach for Investigating Deformations on Full-Resolution Differential SAR Interferograms. *IEEE Trans. Geosci. Remote Sens.* 42, 1377–1386. doi:10.1109/tgrs.2004.828196

Li, J., Li, Z.-w., Wu, L.-x., Xu, B., Hu, J., Zhou, Y.-s., et al. (2018). Deriving a Time Series of 3d Glacier Motion to Investigate Interactions of a Large Mountain Glacial System with its Glacial Lake: Use of Synthetic Aperture Radar Pixel Offset-Small Baseline Subset Technique. *J. Hydrology* 559, 596–608. doi:10.1016/j.jhydrol.2018.02.067

Li, L. P., Lan, H. X., and Guo, C. B. (2017). Geohazard Susceptibility Assessment along the Sichuan-Tibet Railway and its Adjacent Area Using an Improved Frequency Ratio Method. *Geosciences* 31 (5), 911–929.

Liu, W., Yan, S., and He, S. (2018). Landslide Damage Incurred to Buildings: A Case Study of Shenzhen Landslide. *Eng. Geol.* 247, 69–83. doi:10.1016/j.enggeo.2018.10.025

Lu, C., and Cai, C. (2019). Challenges and Countermeasures for Construction Safety during the Sichuan-Tibet Railway Project. *Engineering* 5 (5), 833–838. doi:10.1016/j.eng.2019.06.007

Lulseged, A., and Yamagishi, H. (2005). The Application of Gis-Based Logistic Regression for Landslide Susceptibility Mapping in the Kakuda-Yahiko Mountains, Central Japan. *Geomorphology* 65, 15–31.

Lyu, L. Q., Xu, M. Z., Wang, Z. Y., Qi, L. J., and Li, X. (2021). Impact of Densely Distributed Debris Flow Dams on River Morphology of the Grand Canyon of the Nu River (Upper Salween River) at the East Margin of the Tibetan Plateau. *Landslides* 18 (5), 979–991. doi:10.1007/s10346-020-01536-x

Meisina, C., Zucca, F., Notti, D., Colombo, A., Cucchi, A., Savio, G., et al. (2008). Geological Interpretation of PSInSAR Data at Regional Scale. *Sensors* 8, 7469–7492. doi:10.3390/s8117469

Merghadi, A., Yunus, A. P., Dou, J., Whiteley, J., ThaiPham, B., Bui, D. T., et al. (2020). Machine Learning Methods for Landslide Susceptibility Studies: a Comparative Overview of Algorithm Performance. *Earth-Science Rev.* 207, 103225. doi:10.1016/j.earscirev.2020.103225

O'brien, R. M. (2007). A Caution Regarding Rules of Thumb for Variance Inflation Factors. *Qual. Quantity* 41 (5), 673–690.

Pánek, T. (2019). Landslides and Quaternary Climate Changes-The State of the Art. *Earth-Science Rev.* 196, 102871. doi:10.1016/j.earscirev.2019.05.015

Qu, C., Zhang, G., Shan, X., Zhang, G., Song, X., and Liu, Y. (2013). Coseismic Deformation Derived from Analyses of C and L Band SAR Data and Fault Slip Inversion of the Yushu Ms7.1 Earthquake, China in 2010. *Tectonophysics* 584, 119–128. doi:10.1016/j.tecto.2012.05.011

Rott, H., and Nagler, T. (2006). The Contribution of Radar Interferometry to the Assessment of Landslide Hazards. *Adv. Space Res.* 37, 710–719. doi:10.1016/j.asr.2005.06.059

Shi, P. J. (2016). *Natural Disasters in China*. doi:10.1007/978-3-662-50270-9Natural Disasters in China

Tien Bui, D., Tuan, T. A., Klempe, H., Pradhan, B., and Revhaug, I. (2016). Spatial Prediction Models for Shallow Landslide Hazards: a Comparative Assessment of the Efficacy of Support Vector Machines, Artificial Neural Networks, Kernel Logistic Regression, and Logistic Model Tree. *Landslides* 13 (2), 361–378. doi:10.1007/s10346-015-0557-6

Tre, A. (2017). *Data in Focus: Precursor of Maoxian Landslide Measured from Space*. Available at: http://tre-altamira.com/news/datafocus-precursor-maoxian-landslide-measured-space.

Tsangaratos, P., and Ilia, I. (2016). Comparison of a Logistic Regression and Naïve Bayes Classifier in Landslide Susceptibility Assessments: The Influence of Models Complexity and Training Dataset Size. *CATENA* 145, 164–179. doi:10.1016/j.catena.2016.06.004

Turner, A. K. (2018). Social and Environmental Impacts of Landslides. *Innov. Infrastruct. Solut.* 3, 70. doi:10.1007/s41062-018-0175-y

Van Den Eeckhaut, M., Vanwalleghem, T., Poesen, J., Govers, G., Verstraeten, G., and Vandekerckhove, L. (2006). Prediction of Landslide Susceptibility Using Rare Events Logistic Regression: a Case-Study in the Flemish Ardennes (Belgium). *Geomorphology* 76, 392–410. doi:10.1016/j.geomorph.2005.12.003

Wallemacq, P., Below, R., and McLean, D. (2018). *Economic Losses, Poverty and Disasters 1998–2017, United Nations Office for Disaster Risk Reduction (UNDRR) and Centre for Research on the Epidemiology of Disasters*. (CRED) publications.

Wang, L.-J., Guo, M., Sawada, K., Lin, J., and Zhang, J. (2015). Landslide Susceptibility Mapping in Mizunami City, Japan: A Comparison between Logistic Regression, Bivariate Statistical Analysis and Multivariate Adaptive Regression Spline Models. *Catena* 135, 271–282. doi:10.1016/j.catena.2015.08.007

Wang, P., Chen, J., Dai, F., et al. (2017). Chronology of Relict Lake Deposits Around the Suwalong Paleo Landslide in the Upper Jinsha River, SE Tibetan Plateau: Implications to Holocene Tectonic Perturbations. *Geomorphology* 217, 193–203.

Xie, Z., Chen, G., Meng, X., Zhang, Y., Qiao, L., and Tan, L. (2017). A Comparative Study of Landslide Susceptibility Mapping Using Weight of Evidence, Logistic Regression and Support Vector Machine and Evaluated by SBAS-InSAR Monitoring: Zhouqu to Wudu Segment in Bailong River Basin, China. *Environ. Earth Sci.* 76, 313. doi:10.1007/s12665-017-6640-7

Xiong, Z., Feng, G., Feng, Z., Miao, L., Wang, Y., Yang, D., et al. (2020). Pre- and Post-failure Spatial-Temporal Deformation Pattern of the Baige Landslide Retrieved from Multiple Radar and Optical Satellite Images. *Eng. Geol.* 279, 105880. doi:10.1016/j.enggeo.2020.105880

Xu, Q., Dong, X. J., and Li, W. L. (2019). Integrated Space-Airground Early Detection, Monitoring and Warning System for Potential Catastrophic Geohazards. *Geomatics Inf. Sci. Wuhan Univ.* 44 (7), 957–966.

Yang, F., Jiang, Z. R., and Ren, J. Q. (2022). *Monitoring, Prediction, and Evaluation of Mountain Geological Hazards Based on InSAR Technology*, 2022. Scientific Programming, 2022. doi:10.1155/2022/2227049

Yao, X., Deng, J. H., Liu, X. H., Zhou, Z. K., Yao, J. M., and Dai, F. C. (2020). Primary Recognition of Active Landslides and Development Rule Analysis for Pan Three-River-Parallel Territory of Tibet Plateau. *Adv. Eng. Sci.* 52 (5), 16–37. doi:10.15961/j.jsuese.202000529

Yao, X., Li, L., Zhang, Y., Zhou, Z., and Liu, X. (2017). Types and Characteristics of Slow-Moving Slope Geo-Hazards Recognized by TS-InSAR along Xianshuihe

Active Fault in the Eastern Tibet Plateau. *Nat. Hazards* 88 (3), 1727–1740. doi:10.1007/s11069-017-2943-y

Youssef, A. M., Pourghasemi, H. R., Pourtaghi, Z. S., and Al-Katheeri, M. M. (2015). Landslide Susceptibility Mapping Using Random Forest, Boosted Regression Tree, Classification and Regression Tree, and General Linear Models and Comparison of Their Performance at Wadi Tayyah Basin, Asir Region, Saudi Arabia. *Landslides* 13, 839–856. doi:10.1007/s10346-015-0614-1

Zhang, J. J., Gao, B., liu, J. K., Chen, L., Huang, H., and Li, J. (2021). Early Landslide Detection in the Lancangjiang Region along the Sichuan-Tibet Railway Based on SBAS-InSAR Technology. *Geosciences* 35 (1), 64–73.

Zhang, Y., Meng, X., Jordan, C., Novellino, A., Dijkstra, T., and Chen, G. (2018). Investigating Slow-Moving Landslides in the Zhouqu Region of China Using Insar Time Series. *Landslides* 15, 1299–1315. doi:10.1007/s10346-018-0954-8

Zhang, Y., Meng, X., Jordan, C., Novellino, A., Dijkstra, T., and Chen, G. (2018). Investigating Slow-Moving Landslides in the Zhouqu Region of China Using InSAR Time Series. *Landslides* 15 (7), 1299–1315. doi:10.1007/s10346-018-0954-8

Zhang, Y., Zhao, X., Lan, H., and Xiong, T. (2011). A Pleistocene Landslide-Dammed Lake, Jinsha River, Yunnan, China. *Quat. Int.* 233 (1), 72–80. doi:10.1016/j.quaint.2010.10.020

Zhao, F., Meng, X., Zhang, Y., Chen, G., Su, X., and Yue, D. (2019). Landslide Susceptibility Mapping of Karakorum Highway Combined with the Application of SBAS-InSAR Technology. *Sensors* 19 (12), 2685. doi:10.3390/s19122685

Zhu, W., Zhang, Q., Ding, X. L., Zhao, C. Y., Zhang, J., and Qu, F. F. (2011). Surface Deformation Analysis of Xi'an (China) in 2009 Carried Out with Refined Sbas-Dinsar. *Proc. SPIE* 8286, 82861H:36.

Conflict of Interest: The authors declare that the research was conducted in the absence of any commercial or financial relationships that could be construed as a potential conflict of interest.

Publisher's Note: All claims expressed in this article are solely those of the authors and do not necessarily represent those of their affiliated organizations, or those of the publisher, the editors and the reviewers. Any product that may be evaluated in this article, or claim that may be made by its manufacturer, is not guaranteed or endorsed by the publisher.

frontiers | Frontiers in Earth Science

ORIGINAL RESEARCH
published: 04 July 2022
doi: 10.3389/feart.2022.917447

Morphology Evolution of Three-Dimensional Scours Under Submerged Jets

Ke-ling Chen, Wang-ru Wei and Jun Deng*

State Key Laboratory of Hydraulics and Mountain River Engineering, Sichuan University, Chengdu, China

Through physical model tests, the three-dimensional morphological features and their scale changes with time were measured and comparatively analyzed during the scouring of a homogeneous granular bed surface using submerged oblique jets. The effects of various flow velocities and water cushion depths on the depth, length, and width of the scour hole were studied. At the early stage of scour formation, the morphological scales changed more dramatically, and the jet impact flow velocity had a more significant effect on the scour hole relative to the depth of the water cushion; for the final scales in all three directions of the scour, the scour depth developed at a more significant rate relative to the length and width of the scour. The correlation between the depth, length, and width of scour hole formation was achieved based on the time-domain variation pattern of scour hole scales. As the jet velocity increased and the depth of the water cushion decreased, the scour gradually developed from a wide-shallow morphology to a narrow-deep morphology; the impact of three-dimensional morphological features of the scour on hole depth gradually became obvious, appearing to inhibit the development of scour depth. The results of the present experimental tests offered an exploratory study of the effect of three-dimensional morphological features on the formation of jet scours, having constituted the basis for more rational analysis and evaluation of energy dissipation for the hydraulic operation in water conservancy projects.

Keywords: scour evolution, three-dimensional morphology, impingement jet, time domain process, hydraulic model

OPEN ACCESS

Edited by:
Xiaojun Guo,
Institute of Mountain Hazards and Environment (CAS), China

Reviewed by:
Cheng Yang,
North Minzu University, China
Md Nazmul Azim Beg,
Tulane University, United States
Jiangang Chen,
Institute of Mountain Hazards and Environment (CAS), China

****Correspondence:***
Wang-ru Wei
weiwangru@scu.edu.cn

Specialty section:
This article was submitted to Geohazards and Georisks, a section of the journal Frontiers in Earth Science

Received: *11 April 2022*
Accepted: *25 May 2022*
Published: *04 July 2022*

Citation:
Chen K-l, Wei W-r and Deng J (2022) Morphology Evolution of Three-Dimensional Scours Under Submerged Jets. Front. Earth Sci. 10:917447. doi: 10.3389/feart.2022.917447

INTRODUCTION

Jet scours in river beds are a common hydraulic issue in the fields of geomorphology and hydraulic engineering applications (in **Figure 1**). Insufficient understanding of hydraulic scours and improper treatment may cause destructive actions, such as dam breaks and river bed erosion (Boniforti et al., 2015; Yao and Wu, 2020; Qian et al., 2021). Mason showed the effects of jet aeration and discharge conditions on the final two-dimensional scour and proposed a formula for the scour depth calculations (Manson, 1989). Based on a series of experimental tests, the two-dimensional scour geometry was depicted by Canepa and Hager (2003). Their experimental results described the primary definition to account for the effects of aerated jets on scour generation. Using two sine functions, the axial scour profile was determined with non-dimensional parameters. The jet scour involved a complex hydraulic phenomenon, from upstream impact to tailwater conditions. The laboratory experimental tests were an effective way to describe the scour process due to the complexity of the scour mechanism (Lenzi et al., 2002; Gaudio and Marion, 2003), and some estimation equations were proposed for the equilibrium scour depth with

FIGURE 1 | Field sampling of water scouring.

its temporal evolution (Meftah and Mossa, 2006; Liu et al., 2018; Wang et al., 2018; Wang et al., 2020). Considering the jet diffusion theory of an empirical nature, a methodology with grade control structures and steady flow conditions was proposed to overcome some limitations in the scour generation (Beltaos and Rajaratnam, 1973; Bormann and Julien, 1991; Li et al., 2017).

In recent years, many studies have focused on the problem of hydraulic scour evolution. Dey and Barbhuiya (2005) conducted jet scour experiments to determine the time variation and equilibrium of scour depths for uniform and non-uniform sediments. Pagliara et al. (2006) summarized the time-domain evolution process of the two-dimensional scour for different incident angles, jet shape, velocity, aeration, and tailwater conditions, concluding that the relative jet impingement intensity was the important factor in scour evolution. They first investigated the three-dimensional plunge pool scour, and the temporal evolution process of scour depth was described (Pagliara et al., 2016; Pagliara and Palermo, 2017; Pagliara et al., 2020). The temporal scour profile development for dry conditions was measured by laboratory experiments, and the simple logarithmic relationship was given between developing and developed scour holes (Canepa and Hager, 2003; Pagliara et al., 2008). These relative research studies emphasized that the developing scour phase was mainly affected by the turbulent features, and it was different to assess the scour generation without the dynamic process. A complex morphological scour compared to the two-dimensional scour was obtained experimentally. Many researchers investigated the flow structures in the equilibrium scour stage (Liu et al., 1998; Adduce and Rocca, 2006; Guan et al., 2014). Dey and Sarkar (2008) studied the flow structure variations with time in a scour hole. A simplified model was proposed for the scours at various typical instants, which inevitably introduced disturbance in the flow velocity fields (Hill and Younkin, 2006). Bombardelli et al. (2018) used the optical principle to study the temporal evolution of a jet with an incident angle under different downstream conditions, and they confirmed that the temporal evolution of the scour can be divided into developing and developed shapes. Therefore, it is necessary to study the scour evolution of the three-dimensional morphology. Detailed experiments about three-dimensional morphological features on the formation of jet scours are needed for further understanding of the jet-solid interactions and predictions.

For the natural process of jet scouring, the scour hole has a typical three-dimensional morphology and a time-domain evolution process. In this study, the three-dimensional scour scales with time development were measured experimentally under different submerged jet and water cushion depth conditions. Detailed analysis of the relationships among the scour depth, length, and width was conducted to provide insight into the scour morphological features. Moreover, a comparison between the two-dimensional and three-dimensional scour holes was discussed to obtain the general difference on the scour evolution process.

TEST METHODS AND HYDRAULIC CONDITIONS

The model scour test was performed in a 1.50-m-long, 1.00-m-wide, 0.75-m-high glass water tank using a circulating water supply and return system. The test layout is shown in **Figure 2** and principally consists of a supply tank, a jet lead section, a scour area, and a backwater area. The test flow was measured using a triangular thin-walled measuring weir located downstream of the scour area. The approach jet was controlled by a rectangular nozzle section, where the nozzle thickness b = 3 cm, the nozzle length W = 6.7 cm, and the incident angle of the jet θ = 60°; the nozzle outlet was submerged approximately 3 cm below the free surface. The inflow water velocity was regulated in that order. The depth T of the water cushion above the scour bed surface was controlled at 0.42, 0.47, and 0.52 m. The bed scour material was made of granular crushed gravels with a density ρ_s of approximately 2.2 g/cm^3. The suitable granular sands were screened out, and almost uniform sands were used for the present experiment with an average particle size of d = 3.0 mm. For the hydraulic scour test study, as it involved the scour resistance characteristics of the sediment, the sediment Froude number Fr_d was used as the hydraulic parameter to evaluate the impact and effect of water flow,

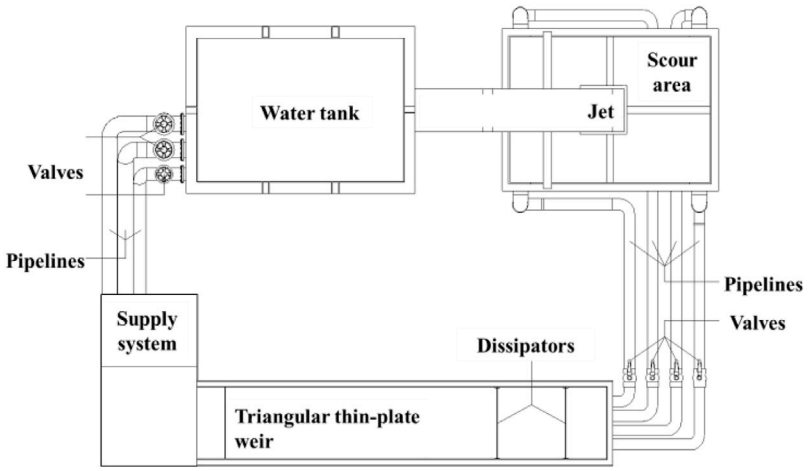

FIGURE 2 | Experimental apparatus.

TABLE 1 | Test programs.

No.	*V* (m/s)	*Q* (L/s)	Fr_d (-)	*T* (m)
1	1.0	2.0	5.3	0.42
2	1.3	2.6	6.9	0.42
3	1.5	3.0	8.0	0.42
4	1.8	3.6	9.6	0.42
5	2.2	4.4	11.7	0.42
6	1.0	2.0	5.3	0.47
7	1.3	2.6	6.9	0.47
8	1.5	3.0	8.0	0.47
9	1.8	3.6	9.6	0.47
10	2.2	4.4	11.7	0.47
11	1.0	2.0	5.3	0.52
12	1.3	2.6	6.9	0.52
13	1.5	3.0	8.0	0.52
14	1.8	3.6	9.6	0.52
15	2.2	4.4	11.7	0.52

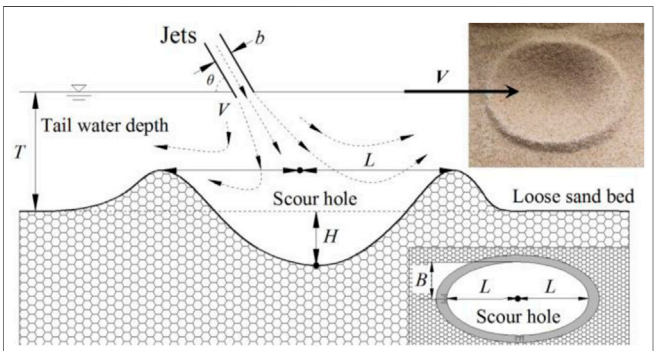

FIGURE 3 | Definition scheme with notations.

defining $Fr_d = V/(g'd)^{0.5}$, where $g' = g\,[\rho_s\text{-}\rho]/\rho$ (Canepa and Hager, 2003); g represents the acceleration of gravity; and ρ_s and ρ denote the densities of sediment and water, respectively; the test conditions are shown in **Table 1**.

Since the start of the scour test, the deepest part of the scour, the side of the mound, and the farthest downstream position were observed and measured with a point gauge. The three-dimensional morphological data on the depth, width, and length of the scour hole were obtained every 5 min. The jet scour time was so determined that the rate of change in the size of the scour hole over five consecutive measurements was less than 0.5%. The three-dimensional morphological generalized characteristics of the jet scour are shown in **Figure 3**, with the difference in elevation between the deepest point and the bed surface as scour depth H, with the farthest longitudinal distance of the hole depth point from the downstream mound as the affected length of scour L, and with the farthest lateral distance from the lateral mound as the affected width of scour B. Upon final stabilization, the three-dimensional scales of the scour hole were H_u, L_u, and B_u, and the relative scales of the scour hole over time were defined as H/H_u, L/L_u, and B/B_u.

TIME-DOMAIN PROCESS ANALYSIS OF JET SCOURS

Figure 4A illustrates the typical course of variation in the depth, length, and width of the two sets of scour holes over time with water cushion depth $T = 0.42$ m, $Fr_d = 6.9$, and $Fr_d = 11.7$; since the onset of scouring ($T = 0$), the increase was significant in all three directions; as the scour continued to develop, the gradient of scale variation in all three directions diminished and gradually reached a stable final state; moreover, the three-dimensional scales were relatively consistent over time, and the depth, length, and width of the scour substantially reached a relatively stable state in the same period; the relative stabilization time for the scour process ranged from approximately 30 min to over 60 min. According to the test result of different flow rates and water cushion conditions, the final stabilization time t_u was less influenced by the depth of the water cushion for each condition and gradually increased with the

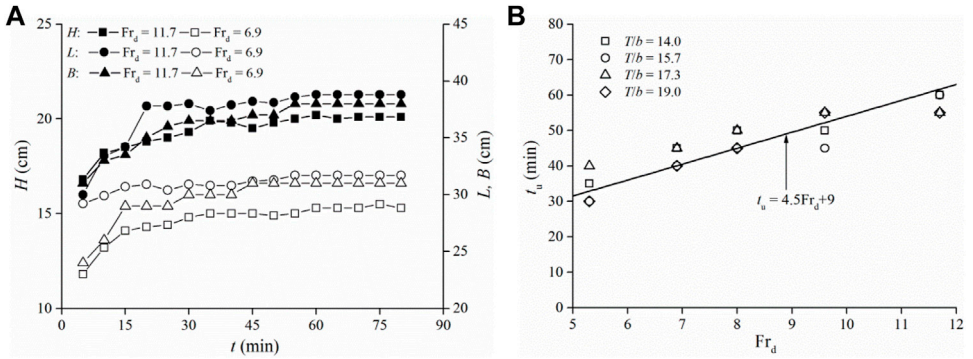

FIGURE 4 | Time-domain processes of scour morphology: **(A)** size scale variation; **(B)** final time t_u.

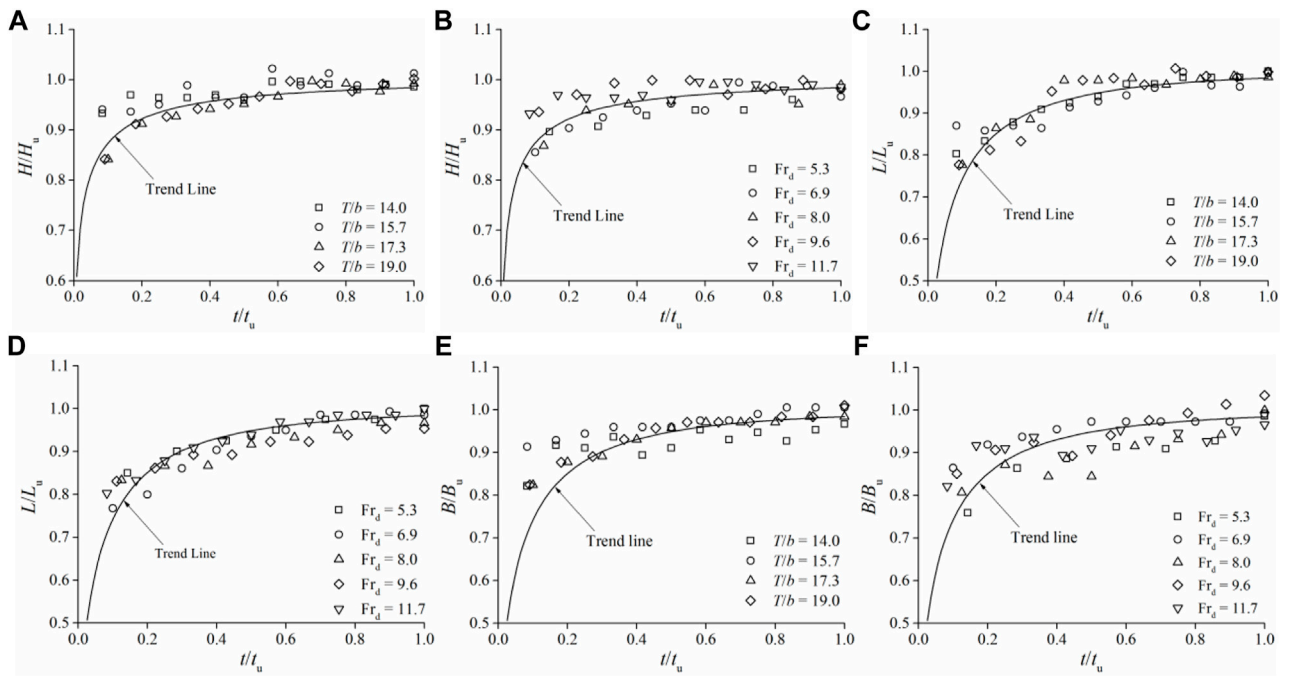

FIGURE 5 | Effects of jet impingement on the time-domain scour process. **(A)** $H/H_u(t/t_u)$, **(B)** $H/H_u(t/t_u)$, **(C)** $L/L_u(t/t_u)$, **(D)** $L/L_u(t/t_u)$, **(E)** $B/B_u(t/t_u)$ and **(F)** $B/B_u(t/t_u)$ with (—) is trend line.

increase in water flow Fr_d. As shown in **Figure 4B**, the variation approximately obeyed a linear relationship, provided by $t_u = 4.5Fr_d+9$. To further analyze the pattern of relative changes in the three-dimensional scale during the development of the scour, this fit equation was used to determine the scour time required for the relative stability of scour development under conditions where Fr_d and T are constant.

Figure 5 shows the relative scale variation of the scour depth, length, and width over time with reference to the relative stability time and three-dimensional stability scale. The relative development processes of the depth, length, and width of the jet scour were principally at the beginning of scour hole formation, while the development of the length and width lagged behind that of the scour length; here, t/t_u = 0.1–0.2, L/L_u and B/B_u were approximately 0.70–0.80 or more, while the depths of all holes were more than 80% of the stable scour depth; as the scour continued to develop when t/t_u = 0.3–0.4, the scour depth substantially approached the final depth, i.e., $H/H_u > 0.90$; when $t/t_u > 0.5$, L/L_u and B/B_u progressively approached over 90% of the final scale of the scour hole. According to the comparative analysis of the hyperbolic tangent function curve and test data points, the relative time-domain processes of three-dimensional scales demonstrated a self-similar pattern for different water cushion depths T and scour Froude number Fr_d. The same formal curves were used to compare the relative lengths and widths of scour holes. During the development of scours and their morphological stabilization, the relative development of the hole morphology on both sides was generally consistent with the time-

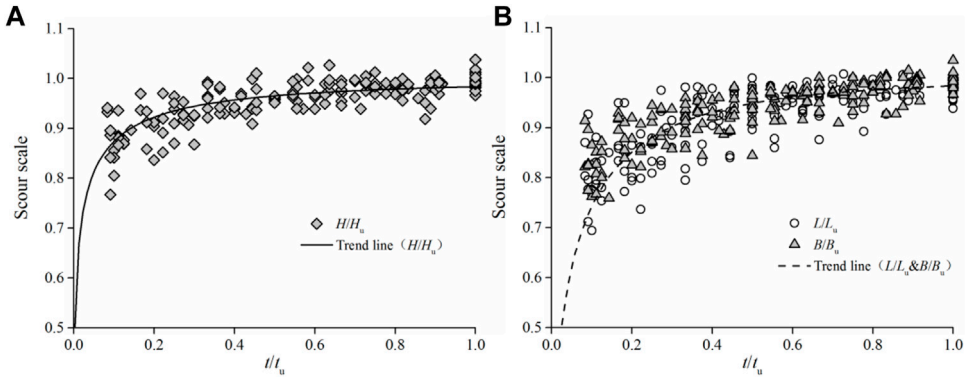

FIGURE 6 | Prediction of the time-domain scour process: **(A)** H/H_u; **(B)** L/L_u and B/B_u.

domain process. Analysis suggested that as the scour depth directly reflected the scouring capacity of the jet, it was principally influenced by the water transport capacity and the granular morphological stability during the stable formation in the two-dimensional directions of length and width, and the pattern adjustment could result in a longer period being required in the development of the scour when compared with the final stable morphology.

The relative scales, i.e., H/H_u, L/L_u, and B/B_u, among the time-domain process data at the three-dimensional scale of the scour were hyperbolic tangent to the relative time t/t_u, which is expressed as

$$H/H_u = \tanh\left[2.4\left(t/t_u\right)^{0.25}\right], \quad (1)$$

$$L/L_u = B/B_u = \tanh\left[2.4\left(t/t_u\right)^{0.40}\right]. \quad (2)$$

In such a case, the applicable conditions for water flow and the scour hole are as follows: $5.3 < Fr_d < 11.7$ and $14.0 < T/b < 19.0$. The comparison of the predicted time-domain processes on the relative morphological scour scale with test data is illustrated in **Figure 6**. The time-domain process curve substantially reflects the pattern of development of the jet scour on a three-dimensional scale to stable formation. Notably, these affecting factors such as hydrodynamic impact, sediment transport, and scour morphology adjustment at the initial stage of jet impingements resulted in the highly discrete fit analysis outcome at the early stage of scour formation. At $t/t_u = 0.2$, the H/H_u can reach 0.9, and the plane scales of the scour hole H/H_u and B/B_u increase to 0.7–0.8. As the developing period exceeds over a half of the entire process with $t/t_u > 0.5$, all scour hole scales get fully developed, and the relative error decreases as the hole gradually develops and stabilizes.

THREE-DIMENSIONAL MORPHOLOGY OF JET SCOUR

When the jet scour development became relatively stable, the test could identify the final three-dimensional scales of scour holes and their correlations by employing the depth H_u, length L_u, and width B_u. **Figure 7** illustrates the effects of Fr_d and T/b conditions on H_u, L_u, and B_u scales. As Fr_d increased, the hydrodynamic scouring intensity progressively increased, as shown by a gradual increase in the scour scale in all directions. The scour depth decreased as the cushion depth increased and gradually increased with the scour length; when T/b increased from 14.0 to 19.0, the scour depth decreased from 0.094 to 0.063 m, while the length L_u increased from 0.200 to 0.282 m. In the meantime, the effect of cushion depth on the scour width was not obvious. It could, thus, be seen that the water cushion during the decrease in the hydraulic scour and the development of the scour depth were principally accompanied by an increase in the affected area of scour along the direction of water flow. The analyses suggest that the impact effects in the scour depth direction decreases after water flows through the water cushion energy dissipation area. The effect of the impingement jet flow on the scour hole depth is principally reflected in the fact that the particle transport of sediment in the direction of water flow dominates the extent of the wall attachment area.

The comparison of scale differences in the three-dimensional directions of the scour indicates that the hole scale in its length and width directions is significantly greater than that of the scour depth. With depth H_u as a reference, **Figure 8** illustrates the scaling relationship of the hole length and width relative to its depth and indicates its variation pattern with water flow conditions. Under weak scouring ($Fr_d = 5.3$) and a deeper water cushion ($T/b = 19.0$), the weaker hydrodynamic impact and enhanced energy dissipation of water cushion results in a decrease in the hole depth. Ultimately, the morphological length of the scour depth may reach more than four times the hole depth, and the hole width may reach more than 3-fold the depth. Moreover, as the hole depth continues to develop under strong scouring ($Fr_d > 9$–10) and a shallow water cushion ($T/b = 14.0$), the length-to-depth ratio L_u/H_u and the width-to-depth ratio B_u/H_u decreases progressively for the hole morphology, which shows a convergence of both to approx. 1.0–2.0.

With respect to the planar features of the jet scour, as shown in **Figures 9A**, a stronger hydraulic scouring capacity is obtained in the case of a shallow water cushion ($T/b = 14$). In terms of length and width, the morphology of the scour was substantially

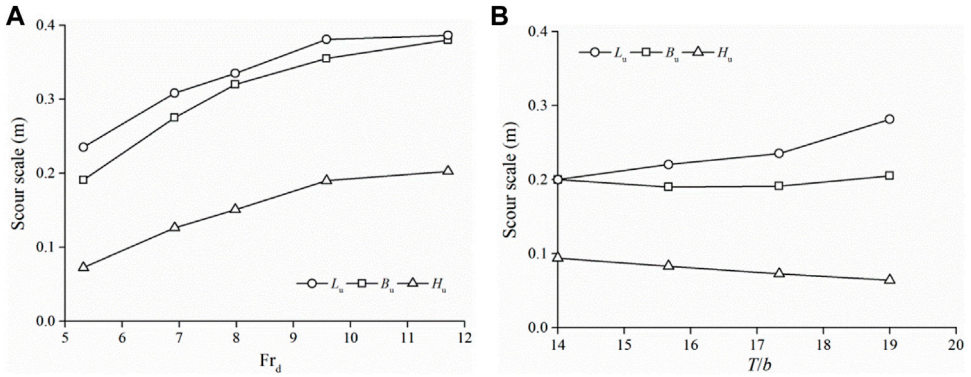

FIGURE 7 | Effects of jet impact on three-dimensional scour scales: **(A)** T/b = 17.3; **(B)** Fr_d = 5.3.

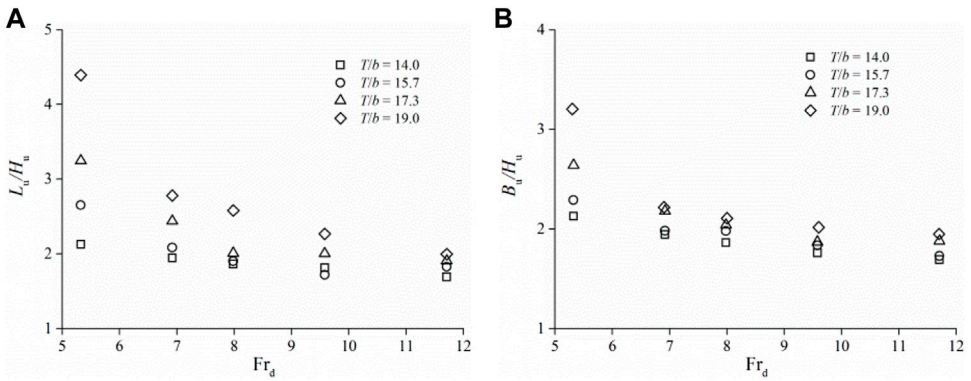

FIGURE 8 | Effects of jet impact on scour morphology: **(A)** L_u/H_u; **(B)** B_u/H_u.

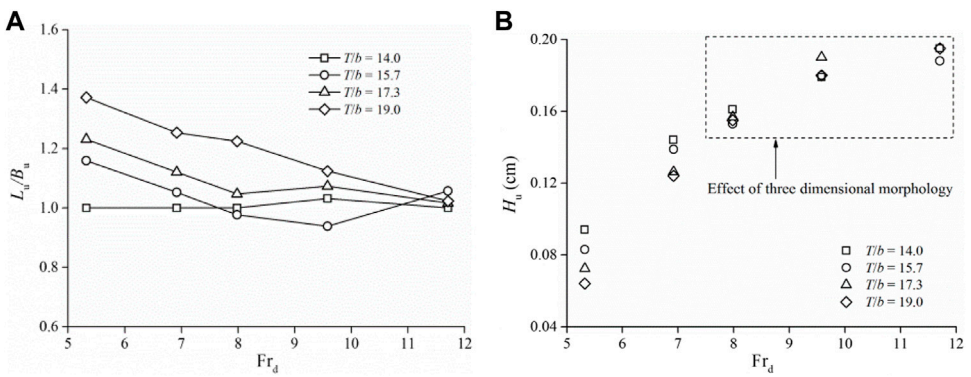

FIGURE 9 | Effects of jet impact on scour morphology: **(A)** planar features; **(B)** three scale effects.

constant. The effect of Fr_d on scour intensity was not significant, which behaved as though L_u/B_u was approximately 1.0. As the water cushion depth increased, the scour length varied more significantly than the scour width under low scouring intensity, which appeared as the length increased from 14.0 to 19.0 with T/b, while the length-to-width ratio increased to 1.40. As the scouring intensity of water increased, L_u/B_u gradually decreased to 1.0, indicating that the scour development in the width direction became increasingly significant as the scouring capacity increased. The test result shows that this three-dimensional morphological feature of the scour hole had a certain effect on the scour depth prediction as the scour

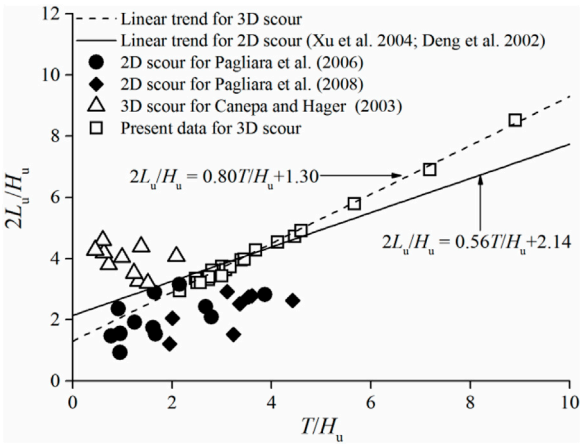

FIGURE 10 | Comparison of morphology between three- and two-dimensional scours.

developed and changed in the depth direction, along with the dramatic change in planimetric extent. As illustrated in **Figure 9B**, under low scour intensity (e.g., Fr_d = 5.3 or Fr_d = 6.9), the pattern change is more pronounced with increasing water cushion, leading to a progressively decreasing scour depth. However, with increasing scour intensity (when Fr_d > 8.0), the change in scour depth was not significant as the water cushion depth increased, indicating that the inhibiting effect of the change in the three-dimensional scales on the scour development was gradually manifested. At low jet flow velocity, the extent of the scour was small and the morphology was predominantly wide and shallow (L_u/H_u and B_u/H_u shown in **Figure 8** are significantly greater than 2.0), while the impact resistance in the direction of the scour depth was dominated by the energy dissipating effect of the water cushion. But as the jet flow velocity increased, the scale of the hole depth increased in and above the plane. Moreover, the broad and shallow morphology of the scour progressively diminished, which led to the gradual significant energy dissipation in the scour hole, which behaved as though the scour depth did not vary remarkably with water cushion energy dissipation. From this point of view, the three-dimensional morphological characteristics of the scour had a substantial impact on the accurate determination of the final scour depth.

DEPTH COMPARISON BETWEEN TWO-DIMENSIONAL AND THREE-DIMENSIONAL SCOURS

The length-depth correlation was compared with the study of the two-dimensional scour in terms of three-dimensional scour morphology in the present test (**Figure 10**). Compared to the previous related experimental studies (Deng et al., 2002; Xu et al., 2004), the lengths of two-dimensional and three-dimensional scours increased linearly with the increasing water cushion depth. In the case of water cushion depth (T/H_u > 5), however, the three-dimensional scours are longer than two-dimensional scours. These scour morphology differences can also be observed from the other literature data, with different jet angles (Pagliara et al., 2006), impinging and submerged jet patterns (Canepa and Hager, 2003; Pagliara et al., 2008). In addition to the effects of the jet angle and impingement pattern on the jet velocity attenuation and the scour capacity, the scour morphology featured by three-dimensional scales is practically the same. The three-dimensional scour has a wider sediment range during the decrease in the scour depth by water cushion. The impact of water flow on the scour is principally manifested in the transportation of sediment in the direction of flow within the area of wall attachment, and this effect is even more pronounced in the case of a three-dimensional scour. Consequently, it is accompanied by the stable morphological feature of a gradually increasing length-to-width ratio in the longitudinal scour. The granular material size may contribute to the specific differences among the three-dimensional scours. The sand size for Canepa and Hager (2003) ranges from 0.010 to 0.019 m. The anti-flushing capacity for granular beds is stronger than the present condition. Thus, the scour development in the depth is weakened relatively, and the plane sand transportation is amplified, resulting in a larger L_u/H_u than that of the present measurement results.

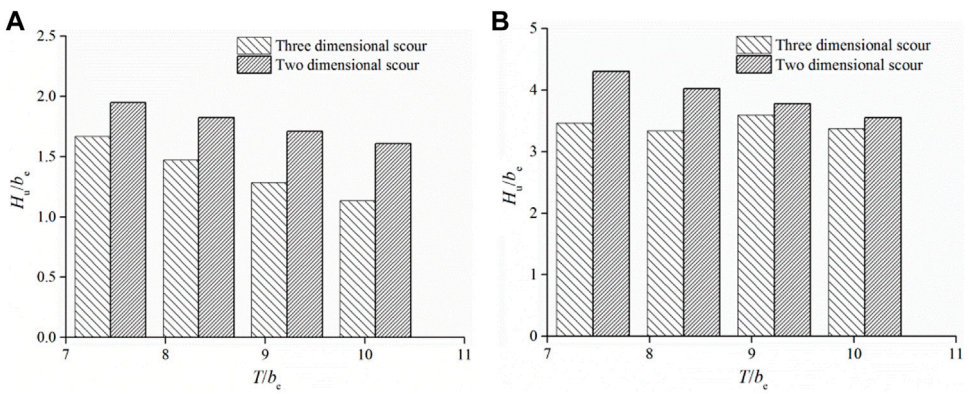

FIGURE 11 | Comparison between two-dimensional and three-dimensional scour depths: **(A)** Fr_d = 5.3; **(B)** Fr_d = 11.7.

Pagliara et al. (2006) systematically studied the prediction of two-dimensional scour depth by considering the effect of hydraulic conditions such as the jet impingement velocity (Fr_d), impact angle (θ), flow aeration (β), water cushion depth (T), and sediment particle size (d) on the scour depth, having proposed the empirical formula

$$H_u/b_e = f(\mathbf{Fr_d}) \cdot f(\theta) \cdot f(\beta) \cdot f(T) \cdot f(d). \quad (3)$$

With consideration of relevant scour hydraulic conditions in the present experimental study, the corresponding two-dimensional scour depth is calculated as follows:

$$H_u/b_e = 1.77 \cdot \mathbf{Fr_d} \cdot [0.12 \ln(1/T) + 0.45] \cdot \sin(\theta + 22.5^o), \quad (4)$$

where b_e represents the equivalent dimension of the jet flow; for rectangular sections, $b_e = (4bW/\pi)^{0.5}$. Under the conditions where Fr_d = 5.3 and Fr_d = 11.7, **Figure 11** indicates that the three-dimensional scour depth is significantly smaller than that of the two-dimensional scour depth. In conditions where Fr_d = 5.3 and T/b_e = 10.1, this difference amounts to approximately 30%. However, under high Fr_d, because of the extensive scour morphology, the change in the scour depth with water cushion depth under three-dimensional conditions is regularly different from that of the two-dimensional scour depth, which reduces the effect of water cushion depth on the reduction of the hole depth.

According to previous studies, the sediment transportation capacity during the scour generation process is correlated with the jet flow velocity (Stein et al., 1993; Jia et al., 2001). As the jet flow velocity decays, gradually impacting the solid surface of the scour hole, most sediment portions are carried out of the hole in the early scour generation period by the major roller in the axial jet zone (Si et al., 2018). As the jet velocity decreases, the sediment amount uplifted by the scour development reduces significantly. This is in accordance with the present research that the scour hole depth stops developing in the early stage. The secondary sediment movements include sediments moving and recirculating upstream, and other sediments entrained downstream but falling back to the scour hole. The main difference between the two- and three-dimensional scour depths indicates that in addition to the effect of jet velocity attenuation on the scour sediment, the three-dimensional scour may improve the scour hole sediment's remaining capacity in the scour. The data analysis results in a distinction between the two- and three-dimensional scour generations, providing a new insight into the three-dimensional scour evolution. All data relationships are obtained from the laboratory experiment measurements, which are limited to the test conditions. The present investigation is a potential step toward the understanding of the morphology and evolution of three-dimensional scours. Therefore, this work suits an appreciation of the temporal scour evolution of geological and hydraulic engineering applications.

CONCLUSION

Based on physical model tests, the present study measured the time-domain process of three-dimensional morphological scours generated by submerged jet impingements. The results suggested that the scour depth, length, and width varied dramatically at the initial stage of jet scour formation; the time-domain development processes in all directions of the scour exhibited self-similarity; the relative development rate of the scour length and width lagged behind that of the scour depth. For the scales in each direction under relatively stable scour development, as the jet velocity increased and the water cushion depth decreased, the scour scales increased in plane and elevation with increasing jet impingement intensity, while the energy dissipation in the scour hole gradually became substantial. The depth variation of the scour hole with the water cushion energy dissipation was insubstantial. The comparison with the two-dimensional scour scale suggested that the three-dimensional scour morphology had a certain inhibitory effect on the development of scour depth. The decrease in scour depth was accompanied by an increase in the scour length. The present experimental results offered an exploratory study on the three-dimensional morphological features of the jet scour formation, having to constitute the basis for more rational analysis and evaluation of hydraulic operations in water conservancy projects.

DATA AVAILABILITY STATEMENT

The original contributions presented in the study are included in the article/supplementary material; further inquiries can be directed to the corresponding author.

AUTHOR CONTRIBUTIONS

K-LC and WW conducted the experimental tests and data analysis. The main text was written by WW and K-LC. Jun Deng provided detailed guidance about the hydraulic model tests.

FUNDING

This work was supported by the National Natural Science Foundation of China (Grant Nos. 51979183 and 51939007).

REFERENCES

Adduce, C., and La Rocca, M. (2006). Local Scouring Due to Turbulent Water Jets Downstream of a Trapezoidal Drop: Laboratory Experiments and Stability Analysis. *Water Resour. Res.* 42 (2), W02405. doi:10.1029/2005WR004139

Beltaos, S., and Rajaratnam, N. (1973). Plane Turbulent Impinging Jets. *J. Hydraulic Res.* 11, 29–59. doi:10.1080/00221687309499789

Ben Meftah, M., and Mossa, M. (2006). Scour Holes Downstream of Bed Sills in Low-Gradient Channels. *J. Hydraulic Res.* 44, 497–509. doi:10.1080/00221686.2006.9521701

Bombardelli, F. A., Palermo, M., and Pagliara, S. (2018). Temporal Evolution of Jet Induced Scour Depth in Cohesionless Granular Beds and the

Phenomenological Theory of Turbulence. *Phys. Fluids* 30, 085109. doi:10.1063/1.5041800

Boniforti, M. A., Guercio, R., and Magini, R. (2015). Effects of Submerged Sheet Pile Vanes on Mobile River Beds. *J. Zhejiang Univ. Sci. A* 16, 182–193. doi:10.1631/JZUS.A1400336

Bormann, N. E., and Julien, P. Y. (1991). Scour Downstream of Grade-Control Structures. *J. Hydraulic Eng.* 117, 579–594. doi:10.1061/(asce)0733-9429(1991)117:5(579)

Canepa, S., and Hager, W. H. (2003). Effect of Jet Air Content on Plunge Pool Scour. *J. Hydraul. Eng.* 128, 358–365. doi:10.1061/(asce)0733-9429(2003)129:5(358)

Deng, J., Xu, W. L., Qu, J. X., and Yang, Y. Q. (2002). Influence of Aeration on Scouring. *Shuili Xuebao* 10, 8–13. (in Chinese). doi:10.3321/j.issn:0559-9350.2002.10.002

Dey, S., and Barbhuiya, A. K. (2005). Time Variation of Scour at Abutments. *J. Hydraul. Eng.* 131, 11–23. doi:10.1061/(asce)0733-9429(2005)131:1(11)

Dey, S., and Sarkar, A. (2008). Characteristics of Submerged Jets in Evolving Scour Hole Downstream of an Apron. *J. Eng. Mech.* 134 (11), 927–936. doi:10.1061/(asce)0733-9399(2008)134:11(927)

Gaudio, R., and Marion, A. (2003). Time Evolution of Scouring Downstream of Bed Sills. *J. Hydraulic Res.* 41, 271–284. doi:10.1080/00221680309499972

Guan, D., Melville, B. W., and Friedrich, H. (2014). Flow Patterns and Turbulence Structures in a Scour Hole Downstream of a Submerged Weir. *J. Hydraul. Eng.* 140 (1), 68–76. doi:10.1061/(ASCE)HY.1943-7900.0000803

Hill, D. F., and Younkin, B. D. (2006). PIV Measurements of Flow in and Around Scour Holes. *Exp. Fluids* 41 (2), 295–307. doi:10.1007/s00348-006-0156-3

Jia, Y., Kitamura, T., and Wang, S. S. Y. (2001). Simulation of Scour Process in Plunging Pool of Loose Bed-Material. *J. Hydraul. Eng.* 127 (3), 219–229. doi:10.1061/(ASCE)0733-9429(2001)127:3(219)

Lenzi, M. A., Marion, A., Comiti, F., and Gaudio, R. (2002). Local Scouring in Low and High Gradient Streams at Bed Sills. *J. Hydraulic Res.* 40, 731–739. doi:10.1080/00221680209499919

Li, J.-n., Zhang, J.-m., and Peng, Y. (2017). Characterization of the Mean Velocity of a Circular Jet in a Bounded Basin. *J. Zhejiang Univ. Sci. A* 18, 807–818. doi:10.1631/jzus.A1600761

Liu, P., Gao, J., and Li, Y. (1998). Experimental Investigation of Submerged Impinging Jets in a Plunge Pool Downstream of Large Dams. *Sci. China Ser. E-Technol. Sci.* 41 (4), 357–365. doi:10.1007/BF02917007

Liu, Q.-s., Tang, H.-w., Wang, H., and Xiao, J.-f. (2018). Critical Velocities for Local Scour Around Twin Piers in Tandem. *J. Hydrodyn.* 30, 1165–1173. doi:10.1007/s42241-018-0122-6

Mason, P. J. (1989). Effects of Air Entrainment on Plunge Pool Scour. *J. Hydraulic Eng.* 115, 385–399. doi:10.1061/(ASCE)0733-9429(1989)115:3(385)

Pagliara, S., Hager, W. H., and Minor, H.-E. (2006). Hydraulics of Plane Plunge Pool Scour. *J. Hydraul. Eng.* 132, 450–461. doi:10.1061/(ASCE)0733-9429(2006)132:5(450)

Pagliara, S., Hager, W. H., and Unger, J. (2008a). Temporal Evolution of Plunge Pool Scour. *J. Hydraul. Eng.* 134, 1630–1638. doi:10.1061/(ASCE)0733-9429(2008)134:11(1630)

Pagliara, S., Mahmoudi Kurdistani, S., Palermo, M., and Simoni, D. (2016). Scour Due to Rock Sills in Straight and Curved Horizontal Channels. *J. Hydro-environment Res.* 10, 12–20. doi:10.1016/j.jher.2015.07.002

Pagliara, S., and Palermo, M. (2008b). Plane Plunge Pool Scour with Protection Structures. *J. Hydro-environment Res.* 2, 182–191. doi:10.1016/j.jher.2008.06.002

Pagliara, S., Palermo, M., and Roy, D. (2020). Experimental Investigation of Erosion Processes Downstream of Block Ramps in Mild Curved Channels. *Environ. Fluid Mech.* 20, 339–356. doi:10.1007/s10652-019-09681-1

Pagliara, S., and Palermo, M. (2017). Scour Process Caused by Multiple Subvertical Non-crossing Jets. *Water Sci. Eng.* 10, 17–24. doi:10.1016/j.wse.2017.03.010

Qian, S.-t., Zhang, Y., Xu, H., Wang, X.-s., Feng, J.-g., and Li, Z.-x. (2021). Effects of Surface Roughness on Overflow Discharge of Embankment Weirs. *J. Hydrodyn.* 33, 773–781. doi:10.1007/s42241-021-0068-y

Si, J.-H., Lim, S.-Y., and Wang, X.-K. (2018). Flow Structures in Evolving Scour Holes Caused by a Plunging Jet Downstream of a Weir. *J. Hydraul. Eng.* 144 (6), 04018018. doi:10.1061/(ASCE)HY.1943-7900.0001452

Stein, O. R., Julien, P. Y., and Alonso, C. V. (1993). Mechanics of Jet Scour Downstream of a Headcut. *J. Hydraulic Res.* 31 (6), 723–738. doi:10.1080/00221689309498814

Wang, L., Melville, B. W., Guan, D., and Whittaker, C. N. (2018). Local Scour at Downstream Sloped Submerged Weirs. *J. Hydraul. Eng.* 144, 04018044. doi:10.1061/(ASCE)HY.1943-7900.0001492

Wang, L., Melville, B. W., Whittaker, C. N., and Guan, D. (2020). Temporal Evolution of Clear-Water Scour Depth at Submerged Weirs. *J. Hydraul. Eng.* 146, 06020001. doi:10.1061/(ASCE)HY.1943-7900.0001712

Xu, W., Deng, J., Qu, J., Liu, S., and Wang, W. (2004). Experimental Investigation on Influence of Aeration on Plane Jet Scour. *J. Hydraul. Eng.* 130, 160–164. doi:10.1061/(ASCE)0733-9429(2004)130:2(160)

Yao, L., and Wu, J.-h. (2020). Local Scour by Multiple Slit-type Energy Dissipaters. *J. Hydrodyn.* 32, 1221–1224. doi:10.1007/s42241-020-0068-3

Conflict of Interest: The authors declare that the research was conducted in the absence of any commercial or financial relationships that could be construed as a potential conflict of interest.

Publisher's Note: All claims expressed in this article are solely those of the authors and do not necessarily represent those of their affiliated organizations, or those of the publisher, the editors, and the reviewers. Any product that may be evaluated in this article, or claim that may be made by its manufacturer, is not guaranteed or endorsed by the publisher.

frontiers | Frontiers in Earth Science

ORIGINAL RESEARCH
published: 06 July 2022
doi: 10.3389/feart.2022.921716

Small-Scale Flume Investigation of the Performance of Step-Baffle Drainage Channels in Mitigating Debris Flows

Shuai Li[1,2], *Xiaoqing Chen*[1,2,3], *Jiangang Chen*[1,2,3]*, *Hui Tang*[4], *Yong You*[1,2], *Huayong Chen*[1,2], *Wanyu Zhao*[1] and *Xueyu Geng*[5]

[1]Key Lab. of Mountain Hazards and Earth Surface Process, Institute of Mountain Hazards and Environment, Chinese Academy of Sciences (CAS), Chengdu, China, [2]College of Resources and Environment, University of Chinese Academy of Sciences, Beijing, China, [3]CAS Center for Excellence in Tibetan Plateau Earth Sciences, Beijing, China, [4]German Research Centre for Geosciences (GFZ), Helmholtz Centre Potsdam, Potsdam, Germany, [5]School of Engineering, University of Warwick, Coventry, United Kingtom

Drainage channels are widely used for discharging debris flows into deposition basins or rivers. However, the current drainage channel designs for guiding rapid debris flows downstream do not account for the variations of the gullies' gradient and debris flow energy. In this study, we evaluated the performance of different step-baffle geometries (square, triangle, and trapezoid) in regulating debris flows. Specifically, their effects on the flow patterns, sediment transport, energy dissipation, and impact pressure are investigated using flume experiments. Results here showed that the square baffles promote highly turbulent flows which in turn result in the highest lift height relative to the triangular and trapezoidal baffles. Maximum sediment interception and highest energy dissipation are obtained using the trapezoidal baffle, whereas the triangular baffle exhibits minimal solid interception and the lowest energy dissipation. Trapezoidal baffles generally experience the greatest impact forces relative to both square and triangular baffles. However, when only the first baffle in the channel is considered, it is the square baffles that experience the largest impact forces. The present work improves the understanding of the effectiveness of step-baffle drainage channels in mitigating debris flows.

Keywords: drainage channel, debris flow, flume test, energy dissipation, impact-resisting

OPEN ACCESS

Edited by:
Wen Zhang,
Jilin University, China

Reviewed by:
Xinghua Zhu,
Chang'an University, China
Ding Mingtao,
Southwest Jiaotong University, China

****Correspondence:***
Jiangang Chen
chenjg@imde.ac.cn

Specialty section:
This article was submitted to Geohazards and Georisks, a section of the journal Frontiers in Earth Science

Received: *16 April 2022*
Accepted: *30 May 2022*
Published: *06 July 2022*

Citation:
Li S, Chen X, Chen J, Tang H, You Y, Chen H, Zhao W and Geng X (2022) Small-Scale Flume Investigation of the Performance of Step-Baffle Drainage Channels in Mitigating Debris Flows. Front. Earth Sci. 10:921716. doi: 10.3389/feart.2022.921716

INTRODUCTION

A drainage channel is an engineering mitigation measure designed to protect residents, facilities, and infrastructures from debris flows. Generally, it works in association with the channel control works (Chen X. et al., 2015; Ozturk et al., 2018; Bernard et al., 2019; Marchi et al., 2019). Drainage channels are widely implemented in the basins of downstream areas (VanDine 1996) with the primary goal of discharging the debris flows. Due to its relevance to disaster mitigation, several works have been dedicated to the improvement of debris flow drainage channel design.

Debris flows were previously treated as sand-carrying floods or hyper-concentrated flows. Hence, civil engineers have designed debris-flow drainage channels similar to spillways in hydropower dams. In most cases, the debris flow drainage channels were designed according to the general flood magnitude of flows along flat-bottomed trapezoidal or rectangular cross sections. However, since the solid content in debris flows is much larger than that of floods or hyper-concentrated flows, there is significant scouring, impact, and abrasion on the channel. To minimize the damage due to erosion and abrasion, two debris flow drainage channels were proposed, i.e., Dongchuan-type and V-type drainage channels (**Figures 1A,B**),

FIGURE 1 | Different types of debris flow drainage channels **(A)** Dongchuan-type; **(B)** V-type; **(C)** SIS-type; **(D)** OSS-type; **(E)** PRCB-type.

which became widely adopted between the 1960s and 1980s in China. The Dongchuan-type drainage channels are characterized by a series of sills that are embedded in the soil. The sills minimize the erosion of the valley bed. When debris flows, mixed with the sediment soil, interact with the sills, flow energy is dissipated, thereby protecting the downstream area. This type of drainage channel is suitable for terrains having slopes of 5–20% (Li, 1997; Huang et al., 2009). However, at gentler slopes (less than 5%), debris flows tend to deposit due to having low velocities and high basal resistance. To overcome this limitation, the V-type drainage channels were proposed and applied in the Laogan gully, Yunnan province (You and Liu, 2008; You et al., 2011). The full section of concrete included in this design reduces the roughness of the drainage channel, which increases the flow velocity and discharge capacity, thereby alleviating siltation.

External perturbations resulting from large earthquakes (e.g. 12 May 2008 Wenchuan M_S 8.0 earthquake) can alter local geographic and geomorphic conditions in mountain areas which in turn change local debris flow characteristics. The steeper slopes (more than 20%) and smaller watersheds (less than 5 km^2), which may result from the large earthquake events, increase debris flow velocities and bulk densities (Cui et al., 2010). In these situations, it is necessary to explore new technologies and drainage channel designs that improve energy dissipation and resistance from wearing (erosion).

In the past decade, three representative debris flow drainage channels with energy dissipation structures were proposed: 1) staggered indented sills (SIS) (Chen et al., 2014) (**Figure 1C**), 2) oblique symmetrical sills (OSS) (Wang et al., 2018) (**Figure 1D**), and 3) pre-fabricated reinforced concrete boxes (PRCBs) (**Figure 1E**) (Chen et al., 2016; Chen J. et al., 2017). Compared to the Dongchuan-type and the V-type drainage channels, the SIS-type and OSS-type drainage channels increase the bed friction and improve the velocity reduction ratios by a factor of two, thereby increasing the energy dissipation. The PRCB-type drainage channel can effectively enhance the flow resistance and relieve bed erosion when the debris flow passes over the concrete boxes. Energy is dissipated through the strong interactions between the debris flow and the rocks in the box structure. The maximum energy dissipation ratio of the PRCB-type drainage channel may be more than 50%, as suggested by Chen et al. (2016). Although the abovementioned debris flow drainage channels have been studied and used in practice for more than 60 years, universal drainage channel designs are still not available. The continuous variation of geological settings induced by large earthquakes and extreme rainfall results in abundant sediment sources and steeper valleys which subsequently promotes larger and more frequent debris flows (Cui et al., 2010). These variabilities force us to design new types of drainage channels that are able to accommodate current debris flow characteristics.

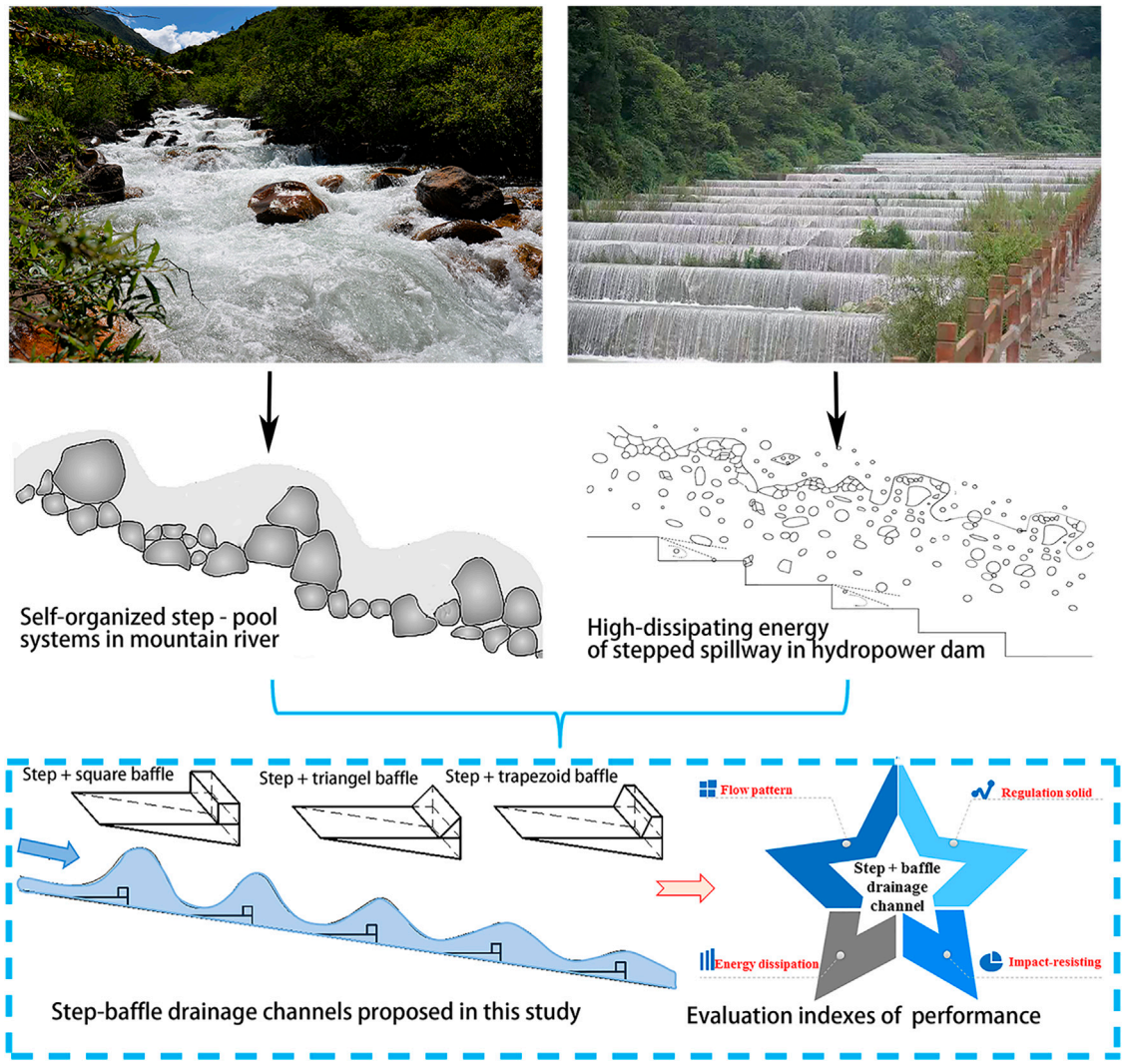

FIGURE 2 | Overview of the inspiration for the present topic.

Step-pool geomorphologic systems are a common phenomenon in steep mountain terrains (3–30%) (**Figure 2A**). This self-organized bed configuration can enhance channel resistance, decrease velocity, and extensively dissipate flow energy (Chin 2002; Comiti et al., 2009; Wilcox et al., 2011; Golly et al., 2019; Saletti and Hassan 2020; Zimmermann et al., 2022). In addition, stepped cascades (**Figure 2B**) are known to significantly dissipate hydraulic energy in hydraulic engineering (Chanson 2001; Matos and Chanson 2006; Bung et al., 2012; Felder et al., 2019; Zhang et al., 2019). Inspired by these two naturally occurring structures, a similar system, step-baffle drainage channels were introduced to mitigate debris flows (**Figure 2C**). This type of drainage channel is composed of a sequence of steps and baffles, resembling a staircase.

The goal of this study was to systematically investigate the performance of the new step-baffle drainage channel in terms of four evaluation indexes (**Figure 2D**). Previous works have shown that debris flow velocity has a positive relationship with channel gradients (Chen et al., 2014). Averaged velocities decreased by 14.2–51.1%, 28–40%, and 27.3–39.3% for OSS-type drainage channels (Wang et al., 2018), step-pool configurations (Chen X. et al., 2017), and energy dissipation baffles (Wang et al., 2017), respectively. Particularly, the energy dissipation in step-pool channels increases gradually with the length and width of the channel (Wang et al., 2012; Chen J. et al., 2015; Chen X. et al., 2015). Other key parameters, such as the step height, pool length, and step-pool gradient were investigated by Abrahams et al. (1995), Chin (1999), Chartrand and Whiting (2000), and Wooldridge and Hickin (2002). Chen et al. (2018) recommended an expression to calculate the roughness coefficient of a drainage channel with an energy dissipation structure. The work of Chen X. et al. (2017) proposed design guidelines for the shape and total length of a single step-pool configuration, as well as the slope of the step. Li et al. (2020) systematically studied the impact pressure on steps and

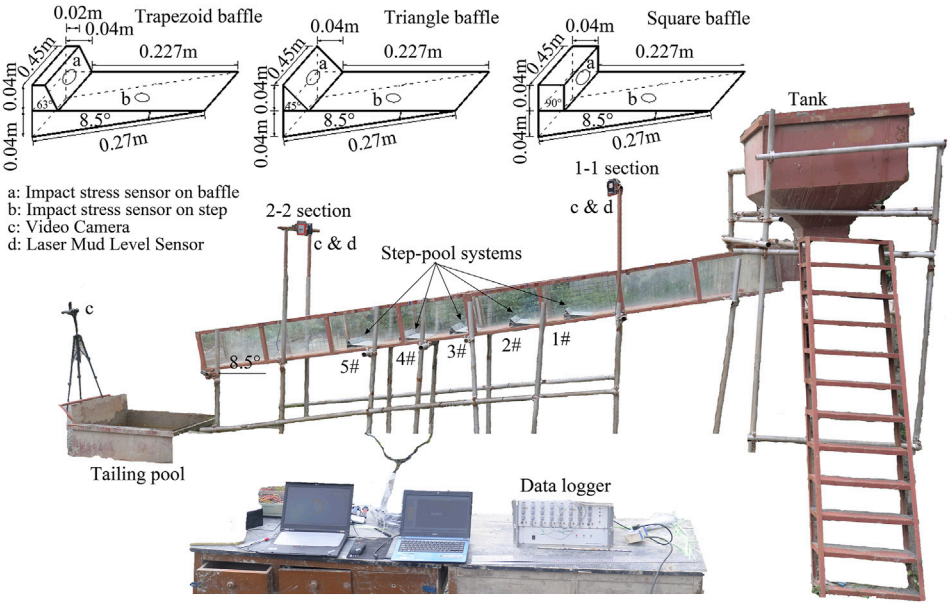

FIGURE 3 | Schematic diagram of the test equipment, baffle configurations and impact pressure measurement points.

baffles based on the stability of the drainage channel and recommended an expression to predict impact pressure by considering the baffle shape.

The abovementioned works have only considered one variable or aspect of debris flow drainage channels, and very few of them incorporate sediment transportation, energy dissipation, and impact pressure to make a comprehensive performance evaluation of drainage channel designs. There has also been no research that has focused explicitly on debris flow drainage channels with step-baffles.

In the present study, the authors reported detailed experimental tests on drainage channels with baffles having three geometric shapes (square, triangle, and trapezoid). Using these experiments, we investigated the relationships between baffle geometry and their regulation efficiency, specifically on **(1)** the variation of longitudinal debris flow patterns along with the step-baffle sequences; 2) the variation of the solid fraction in debris flows across the drainage channel; 3) the efficiency of step-baffles in dissipating debris flow energy; and 4) the performance of impact-resisting baffles. Finally, we briefly discussed the development of debris flow drainage channels, their applicability, and recommendations for different drainage channel designs.

EXPERIMENTAL SETUP

The experimental tests are carried out in the Dongchuan Debris Flow Observation and Research Station (DDFORS), Chinese Academy of Sciences, in Yunnan Province, China. The experimental flume used for modeling is composed of a sequence of steps and baffles, resembling a staircase. The configurations and dimensions of the experimental tests are shown in **Figure 3**. The angle of inclination of the flume is fixed (θ = 8.5°, 0.45 m width, 0.40 m depth, and 6.0 m length). Debris flow materials are stored and released from a tank upstream, while a tailing pool is situated downstream. Five artificial step-pool sequences (from 1# to 5#) are installed starting at 1.8 m from the tank entrance with an interval of 0.27 m along the flume. The wall of the flume is in glass, which allows for observation of the flowing processes. The baffles used in this study have three shapes: square (0.04 m × 0.04 m×0.45 m), triangle (0.04 m × 0.04 m×0.45 m), and trapezoid (0.04 m bottom length, 0.02 m top length, 0.04 m height, and 0.45 m width), which come into contact with the debris flows with faces inclined at β = 90°, 63°, and 45°, respectively (**Figure 3**). At the start of each experiment, the debris flow samples are released onto the flume by a manual gate at the bottom of the tank and are collected at the end of the flume. To prevent sedimentation of the materials in the tank, a hand-held electric mixer continuously stirs the samples before the release of the mixture. The repeatability of manual operation is checked within an error of ±0.05s.

Instrumentation

Five impact stress sensors (LH-Y127B, 2000 Hz, with a range of 0–100 N, and accuracy of ±1.0 %) with a diameter of 25 mm are used to record the impulsive force on stationary load frames (Pa1-Pa5) placed on the center of the baffles along the flume (**Figure 3**). Other measuring devices are installed in two sections (i.e., 1-1 and 2–2), which are mounted near the start (1.5 m) and close to the end of the flume (1.0 m), respectively. The equipment set includes two mud level laser sensors (Leuze, ODSL 30/V-30M-S12, 10 Hz) with a resolution of ±1.0 mm to measure the temporal variations of debris flow depth. Three video cameras (SONY FDR-AX40, 1,440 × 1,080 pixels, 25 fps) are installed to capture the debris flow process and the debris flow impacts on the step-baffles. To measure the velocity of the debris flow front, we marked reference

TABLE 1 | Characteristic parameters of debris flow samples.

Series	Mass (kg)	Density, ρ (kg/M^3)	Solid volume fraction (Cs)	Yield stress (Pa)	Dynamic viscosity (Pa s)	Froude number F_r
M1	280	1,833	0.48	14.35	0.0689	3.34
M2	270	1,891	0.51	18.81	0.0903	3.29
M3	260	1,959	0.55	25.66	0.1231	3.26
M4	250	2,037	0.59	36.88	0.1770	3.18
M5	240	2,129	0.65	49.57	0.2379	2.89

Note: Rheological parameters are measured using a rheometer. The yield stress was determined by the extrapolation of the flow curve (shear stress versus shear rate) to a shear rate of zero.

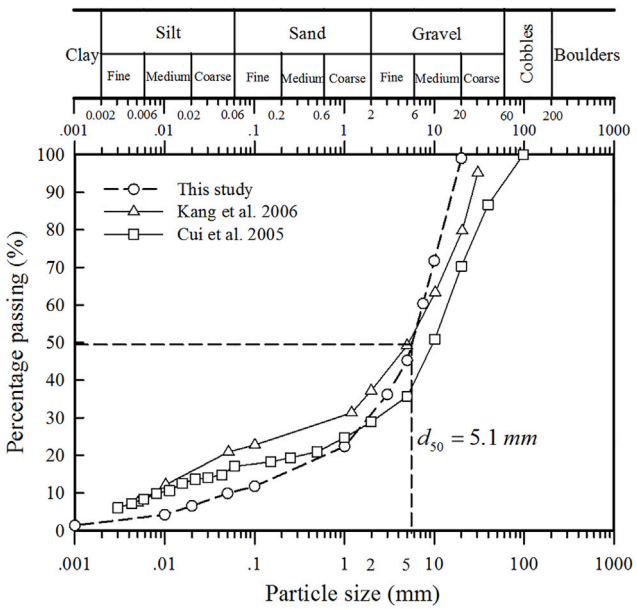

FIGURE 4 | The cumulative grain size distribution of the debris-flow materials adopted in this study and datasets from Jiangjia Gully (cf. Cui et al. 2005 and Kang et al. 2006).

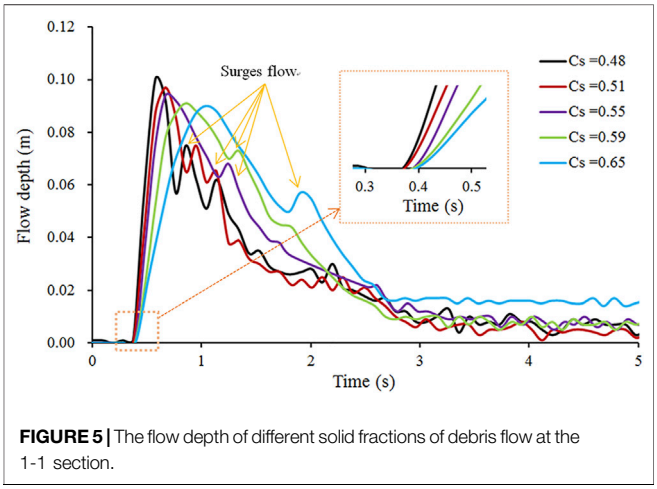

FIGURE 5 | The flow depth of different solid fractions of debris flow at the 1-1 section.

lines with an interval of 0.1 m at the bottom of the flume in sections 1-1 and 2–2. The debris flow velocity can be estimated (within an error of about ±0.1 m/s) from the video recordings of the motion of the flow front with respect to the reference lines.

Source Materials

The experimental mixture materials are prepared based on water combined with solid particles obtained from natural debris flow deposits in the Jiangjia Ravine, China, which has a bulk density of 2,680 kg/m^3. The mass of dry sediment is kept constant at 200 kg, while the water content is varied. Material densities are controlled by varying the water content, namely, high water contents (or low solid volume fraction) correspond to bulk materials with low debris flow density (see **Table 1**). For each type of baffle, five source material sets (M1–M5) are used (i.e., 15 experimental tests in total). The sediment grain size ranges from 0.001 to 20 mm, with d_{50} = 5.1 mm. The maximum used grain diameter of 20 mm was defined in accordance with the maximum height of the baffles (40 mm), as well as the size of the impact area of each aluminum device (diameter equals 25 mm) within the force plate. **Figure 4** shows the cumulative grain size distribution (GSD) curve of the granular materials. A summary of the source material properties (density, solid volume fraction, yield stress, and dynamic viscosity) and Froude numbers of debris flow at the 1-1 section is listed in **Table 1**.

Scaling

Directly measuring the regulation of drainage channels on debris flows in the field or in large-scale experiments usually does not require scaling considerations. However, it is difficult to obtain direct measurements in the field due to the infrequent, unpredictable, and destructive features of debris flow events, and large-scale experiments are costly. For these reasons, small-scale flume experiments are preferred for studying debris flows (Zhou and Ng 2010; Iverson 2015).

To ensure that debris flow experiments are representative of their larger natural counterparts, certain similarity criteria need to be taken into account. In this study, we do not consider the geometric similarity because our work does not represent a specific real-world scenario. The kinematic similarity is characterized by the Froude number, F_r, which represents the ratio of bulk inertia to the gravitational forces acting on the flowing mass, i.e., $F_r = v/(gh)^{0.5}$, where v is the flow velocity, g is the acceleration due to gravity, and h is the flow depth. F_r governs the dynamic behavior of mass flow in

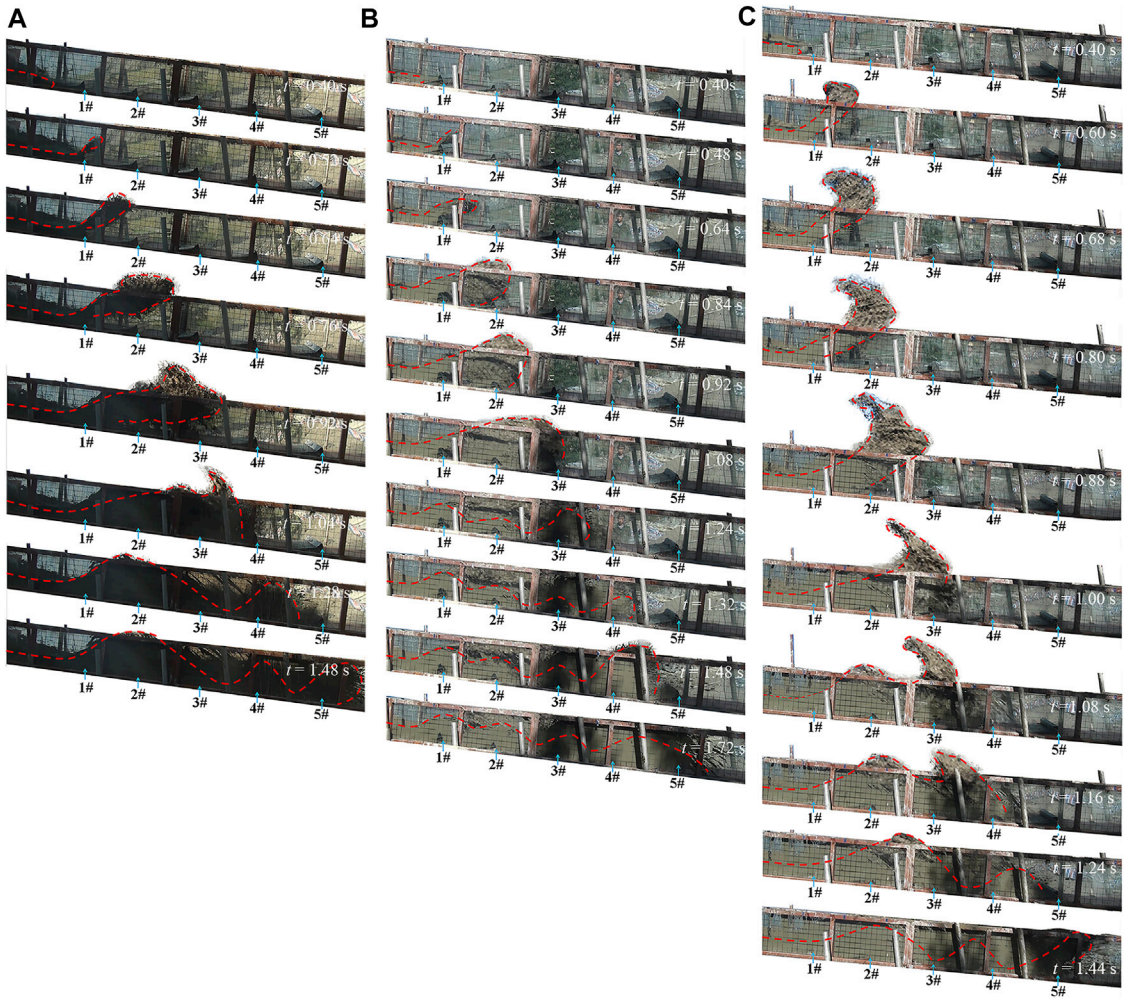

FIGURE 6 | The evolution of debris flow profiles (C_s = 0.55) in the drainage channel: **(A)** step + triangular baffle; **(B)** step + trapezoidal baffle; and **(C)** step + square baffle.

open channels, which has been identified and validated as a major parameter for scaling debris-structure interactions (Hübl et al., 2009; Armanini et al., 2011). The F_r used in the experiments is made similar to natural debris flow events which are usually less than 5.0 (Hübl et al., 2009; Cui et al., 2015). In this study, the flow velocities and depths measured in section 1-1 range from 2.8 to 3.4 (see **Table 1**) and are therefore representative of natural debris flows.

RESULTS

Flow Patterns in the Step-Baffle Channel

The debris flow pattern is one of the fundamental indicators used to evaluate the performance of step-baffle systems. The measurement time starts (t = 0 s) when the source material is released from the storage tank. The flow surface profiles of the five debris flow densities in section 1-1, before they make contact with the first baffle, are shown in **Figure 5**. The flow depth prior to coming into contact with the first baffle is generally similar in the different tests: it initially rapidly increases until it reaches a peak value after which it slowly decreases with several small magnitude surges. The peak flow depth slightly decreases with the increase in the solid volume fraction. It is also observed that the debris flow front arrives at section 1-1 after ~ 0.4 s for all cases, with a slight delay for those with high solid volume fractions. This may be attributed to the difference in viscosity in debris flows since flows with a high solid fraction exhibit more evident viscous behavior which then results in greater internal resistance and lower velocity.

The evolution of debris flow surface profiles for the three types of baffles in drainage channels for a typical debris flow having a solid volume fraction of Cs = 0.55 is shown in **Figure 6**. When the debris flow front impacts the first baffle, the flowing material is propelled sharply into the air, which later drops onto the

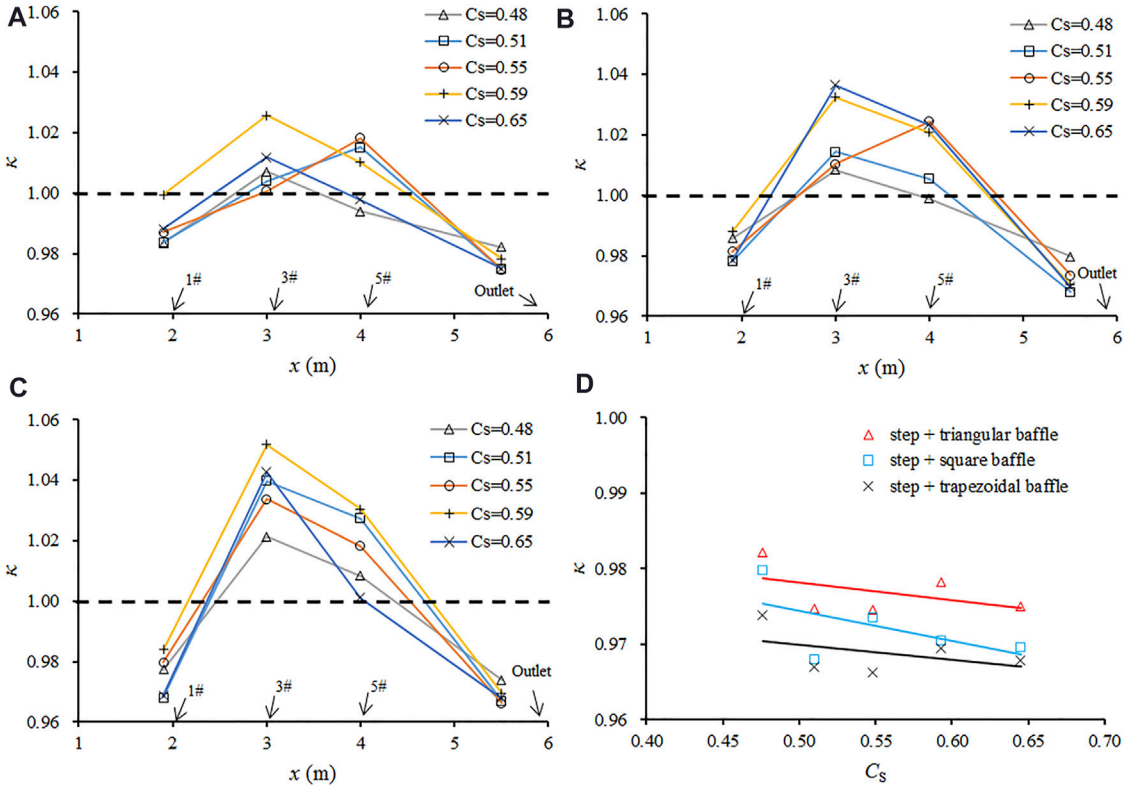

FIGURE 7 | The sediment-trapping ratio for the **(A)** triangular baffle; **(B)** square baffle; **(C)** trapezoidal baffle; and **(D)** channel outlet.

downstream step-baffles. The downstream baffles in turn lift the debris flow materials again until they eventually reach the end of the flume. The maximum lift height is observed after the first baffle for all three types of step-baffle channels. Generally, the debris flows in the step-baffle drainage channel are similar to wave-like flows with very chaotic flow surface patterns. Also, the wavy flow is induced by step-baffle systems, which in turn increases the debris flow height.

It is also observed in **Figure 6** that the maximum heights of the flows propelled upon impacting the square, triangle, and trapezoidal baffles exceed the height of the sidewalls by 0.6, 0.35, and 0.2 m, respectively. These results indicate that a higher sidewall may be needed to avoid the debris splashing out for the step-baffle drainage channel. The position associated with the maximum lift height is closer to the second baffle in the square baffle system than it is for the triangle and trapezoidal systems in which they fall between the second and third baffles. These results are due to the different inclination angles of the upwind face of baffles (**Figure 2**). The upwind face of the square baffle, inclined at 90°, results in a greater and more abrupt change of the flow direction than the trapezoidal (60°) and triangular (45°) systems.

Regulation of the Step-Baffle Channel

A natural consequence of step-baffle channels is step pools which trap portions of the sediments in debris flows. The remaining debris and water mixture will continue to move downstream. The regulatory performance of the step-baffle channel varies with the geometry of the baffle and the property of incoming debris flows. In this study, the sediment-trapping ratio, κ, is used to quantify the regulatory performance of step-baffle channels on debris flows. The ratio κ is formally written as follows:

$$\kappa = \frac{\mathrm{Cs}}{\mathrm{Cs}_{\mathrm{ori}}}, \tag{1}$$

where $\mathrm{Cs}_{\mathrm{ori}}$ is the solid fraction of the source mixture, and Cs is the solid fraction collected behind each step-baffle. When $\kappa < 1$, Cs of the trapped volume is less than that of the source material. On the other hand, $\kappa > 1$ indicates relatively larger amounts of sediments confined behind a baffle.

The sediment-trapping ratio κ at the different types of baffles as well as at the outlet of the channel is shown in **Figure 7**. Generally, the sediment-trapping ratio is less than 1.0 at the first step-baffle and at the channel outlet, whereas $\kappa > 1$ at the 3rd and 5th step-baffles (**Figures 7A–C**). In other words, less amount of sediments are trapped in the 1st step-baffle; however, since the trapping is highly efficient at the middle baffles, very little solid material is transported downstream. The sediment-trapping ratio at the outlet of the channel is less than 1.0 (in the range of 0.96–0.98, see **Figure 7D**), which confirms that the solid fraction is decreased after the regulation by step-baffle systems. This consequently results in the reduction of damage caused by

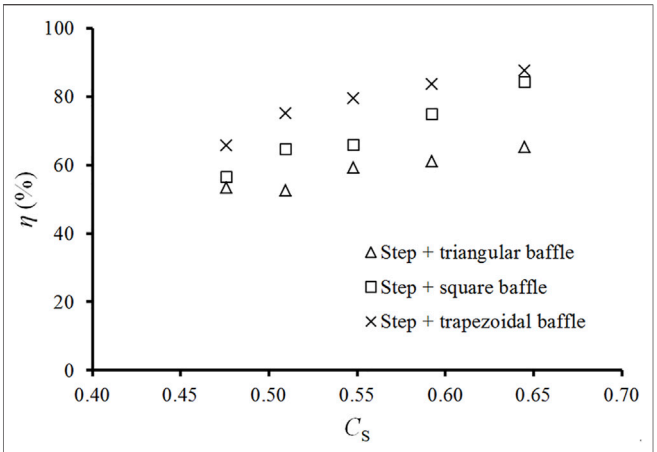

FIGURE 8 | Variation of the energy dissipation ratio κ with solid fraction of the with incoming debris-flow.

solids in debris flows. These results indicate that all three types of baffles are able to regulate debris flows well. The value of κ at the channel outlet decreases with the increase in Cs_{ori} (**Figure 7D**). This implies that the regulatory performance of the step-baffle channel is better when the incoming debris flow becomes viscous.

It can also be observed from the values of κ in the 3rd and 5th step-baffles in **Figure 7** that a trapezoidal design results in the most efficient trapping of sediments. This is followed by the square baffles and the triangular baffles. This is somewhat surprising since one would expect the design with the steepest face angle would be more effective in stopping and trapping flowing sediments. The reason for this is not clear, but it may be related to the maximum height of the propeller flow.

Energy Dissipation of the Step-Baffle Channel

The primary purpose of drainage channels is to quickly discharge debris flows downstream. However, high-speed debris flows with immense energy may cause severe damage to the downstream area. Therefore, the drainage channel should be able to dissipate as much energy as it is discharging the debris flow. In this study, the addition of step-baffle systems in the conventional drainage channel is to dissipate debris flow energy.

The energy dissipation principle of the step-baffle drainage channel lies in two aspects. 1) Due to the drop space between the upper and lower steps, a cavity is often formed there. Under the shear of the high-speed debris flow in the upper part of the cavity, the debris flow inside the cavity is driven to form a strong turbulent vortex in the cavity. The cyclic shear in the vortex cavity reduces the energy of debris flow. 2) The baffles and steps roughen the channel bed and provide resistance to the debris flows and effectively consume the debris flow energy.

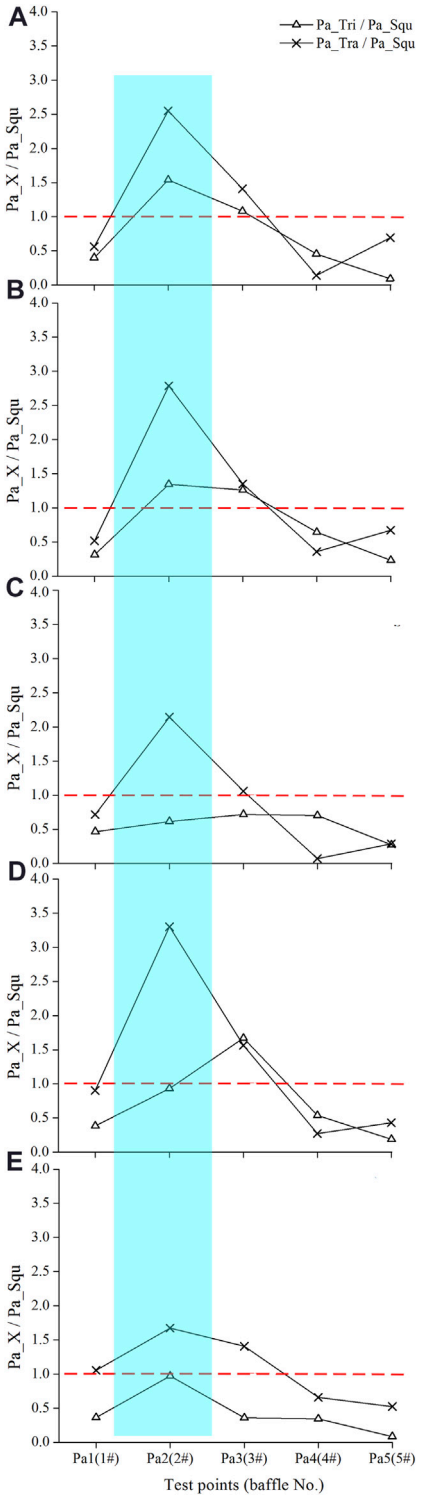

FIGURE 9 | Variation of the peak pressure attenuation on baffles along the channel for **(A)** C_s = 0.48; **(B)** C_s = 0.51; **(C)** C_s = 0.55; **(D)** C_s = 0.59; **(E)** C_s = 0.65. The red dashed line means the impact force on the triangle or trapezoid baffles is equal to that on the square baffles.

Debris flows are special fluids; therefore, the energy balance governing the debris flow in the flume experiments from initiation to end can be described in terms of fluid mechanics. The energy balance approach is commonly used to calculate the energy dissipation in debris flow drainage channels (Chen J. et al., 2015; Choi et al., 2015; Chen X. et al., 2017). It is assumed that the movement of debris flows in a flume is similar to uniform flows. Then, the total energies at the cross sections 1–1 and 2–2 (**Figure 3**) are as follows:

$$E_1 = \Delta z + h_1 \cos\theta + \alpha_1 v_1^2/2g, \quad (2)$$

$$E_2 = h_2 \cos\theta + \alpha_2 v_2^2/2g. \quad (3)$$

Hence, the expression of the energy dissipation ratio, η, can be calculated as follows:

$$\eta = \frac{E_1 - E_2}{E_1} = 1 - \frac{h_2 \cos\theta + \alpha_2 v_2^2/2g}{\Delta z + h_1 \cos\theta + \alpha_1 v_1^2/2g}, \quad (4)$$

where Δz is the potential energy difference between sections 1-1 and 2–2; θ is the channel slope; h_1 and h_2 are debris flow depths, and v_1 and v_2 are the time-averaged surface velocities of debris flows at sections 1-1 and 2–2, respectively; α_1 and α_2 are the kinetic energy correction factors ($\alpha_1 = \alpha_2 \approx 1.0$); g is gravity acceleration.

Figure 8 shows that the energy dissipation ratio η clearly increases with the debris flow solid friction C_s for different types of baffles. This implies that the step-baffle channel dissipates more energy when debris flows hold a higher solid fraction (i.e., viscous debris flow). The most surprising result in **Figure 8** is that the energy dissipation ratio in the trapezoidal baffle is the largest, while that of the triangular baffle is the smallest.

Impact Resistance of the Step-Baffle Channel

The impact force of debris flows quantifies its destructive potential toward structures. A good step-baffle channel should have a strong impact-resisting ability. The baffle, being the key component in step-pool systems, is the most vulnerable to the impacts of debris flows and ought to be the pivotal object to study.

Generally, the peak impact pressure is the critical factor causing structural damage to baffles. Therefore, the ratio of the peak impact pressure (R) on each baffle's upstream face is adopted to evaluate the performance of step-baffles to resist the impact of debris flows. Here, R can be expressed as follows:

$$R = \text{Pa\_X/Pa\_Squ}, \quad (5)$$

where Pa_X and Pa_Squ are the peak impact pressure on each baffle for X type (X represents the triangular and trapezoidal baffles) and square baffles, respectively. The square baffles were adopted as the standard for comparison in accordance with the common baffle shape used in practice engineering. $R > 1$ means the peak impact pressure on the baffle is larger than that on the square baffle (i.e., the impact resistance of this baffle is much higher).

The ratio of the peak impact pressure on triangular and trapezoidal baffles over the peak impact pressure on the square baffles, i.e., "Pa_Tri/Pa_Squ" and "Pa_Tra/Pa_Squ," is shown in **Figure 9**. Generally, the value of "Pa_Tra/Pa_Squ" is greater than the value of "Pa_Tri/Pa_Squ" for all tests. This implies that the impact resistance of trapezoidal baffles is larger than the triangular counterparts. It is also observed that the value of R on the 2nd and 3rd baffles (the blue shaded area) is greater than 1.0 (represented by the red dashed line, where the impact force is equal to that on the square baffles), whereas at the other three baffles (1st, 4th, and 5th), it is less than 1.0. These results mean that the impact pressure on the 2nd and 3rd square baffles is smaller than that on both triangular and trapezoidal baffles, while it is larger on the 1st, 4th, and 5th square baffles. This may be caused by the differences in the inclinations of the upwind faces of the baffles (45°, 63°, and 90° for the triangular, trapezoidal, and square baffles, respectively). For square baffles (90°), the 1st baffle plays a major role in blocking the incoming flow (see the highest lift height of debris flow in **Figure 6**) and experiences the maximum impact. Thus, the impact pressure on the 1# square baffle is the largest among the three types of baffles. However, for triangular (45°) and trapezoidal baffles (63°), the first baffle becomes a ramp over which the debris flow is lifted. The whole jet front or the main jet then falls onto the region between the 2nd and 3rd baffle and induces the largest peak impact pressure. These results indicate that changing the angle of the upwind face may have a notable difference in the impact pressure. This implies that the impact resistance of step-baffle systems is highly dependent on the inclination of the baffle surface.

DISCUSSION

Debris flow drainage channels play a significant role in mitigating debris flow hazards at the headwaters of the deposit fan, where communities, highways, railways, and infrastructures are highly vulnerable to debris flows. Basically, the main purpose of drainage channels is to discharge the debris flow safely, quickly, and smoothly to protect the downstream areas.

Effective and efficient step-baffle drainage channels should be able to transport debris flows downstream while minimizing the solid material content, maximizing the dissipated energy of debris flow, and maintaining its strong impact resistance, thereby ensuring their long-term operation. Considering the debris flow patterns in the drainage channel, the step-baffles lift the debris flow and cause a flow wave in the drainage channel until the movement of the debris flow eventually ceases (**Figure 6**). The wave-like flow is induced by the step-baffle system, which in turn increases the debris-flow depth. The experiment results indicate that the square baffle requires the highest sidewalls, whereas the trapezoidal baffle requires the lowest sidewalls among the three types of step-baffle drainage channels. This result may be attributed to the difference in the angle of the upwind faces. As shown in **Figure 10**, the inclinations of the upwind face of the triangular, trapezoidal, and square baffles are 45°, 63°, and 90°, respectively. The square baffle, having the steepest upwind inclination, provides the strongest blocking effect and induces an abrupt vertical uplift of the debris flow. Although the upstream-facing angle of the trapezoidal baffle is larger, the streamline of the debris flow is smoother when passing over the triangular baffle, resulting in a relatively greater lifting height. However, this conjecture is based only on the observation of flow

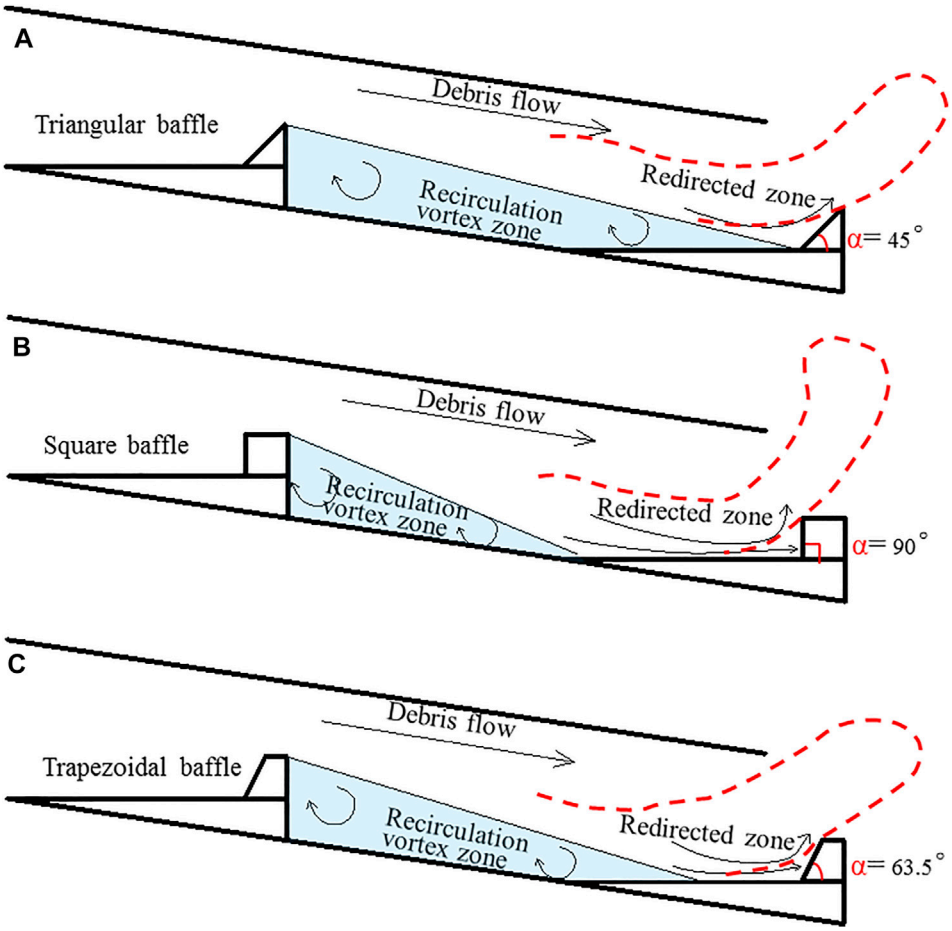

FIGURE 10 | Sketch of the flow structure of debris flows passing over **(A)** triangular **(B)** square and **(C)** trapezoidal baffles.

patterns and needs to be further verified using experiments involving strongly turbulent flows in the step-baffle channels.

In step-baffle drainage channels, the magnitude of energy dissipation decreases from the trapezoidal baffles to the square baffles with the lowest being the triangular baffles (see **Figure 8**). We attempt to explain these results using generalized diagrams of the flow structure in step-baffle systems, as illustrated in **Figure 10**. The debris flow structure between the adjacent step-baffles is divided into two regions: the recirculation vortex zone characterized by eddies and vortices and the redirected zone that re-adjusts the flow toward the main flow. The energy dissipation mainly occurs in two regions. However, the recirculation vortex zone plays a minimal role in dissipating energy, while the redirected zone dissipates considerable energy, especially for skimming debris flow. The energy dissipation for the redirected zone depends mainly on the momentum transfer. Among the reasons why square baffles dissipate more energy than the triangular baffles is that the area of the redirected zone is greater for the square baffle configuration. Although, the area of the redirected zone for square baffles (**Figure 10A**) is larger than that of trapezoidal baffles (**Figures 10B,C**), the influence of the baffle shape (90° of upwind stream face) in adjusting the flow toward the main flow is too strong and instead propels the debris high into the air. These will result in high additional potential energy which later contributes to the increase in momentum, compensating for the reduction in energy.

The effectiveness of the step-baffle drainage channel to regulate the solid phase in debris flows can be ranked according to trapezoidal, square, and triangular baffles (see **Figure 7D**). The trapezoidal baffles experience greater impact forces than triangular baffles, and at least for the first baffle in the channel, it is the square baffles that experience the greatest impact force (see **Figure 9**). In other words, in a step channel with square baffles, it is the first baffle that will most likely be damaged by the debris flow impact, while it is the second baffle in both triangular and trapezoidal baffles that are likely to be destroyed by debris flow impacts.

In practice, it is difficult to guarantee that all the evaluation indices of any type of baffle are optimal at the same time. It is recommended that for a specific creek valley, field surveys and measurements of the topography, scale, and velocity of possible

debris flow events should be conducted in advance from which suitable types of drainage channels can be designed.

CONCLUSION

In this study, the flume model is adopted to study the mitigation of step-baffle drainage channels on debris flows. A series of tests with varying source material densities and baffle shapes (triangular, trapezoidal, and square) are carried out to demonstrate the performance of each baffle type in terms of the induced flow pattern, sediment transportation, energy dissipation, and impact pressure. The conclusions are summarized as follows:

1) The flow pattern in the step-baffle drainage channel is a very complex wave-like flow. The lifting height of debris flows induced by square baffles is the largest, whereas the lowest lifting heights are recorded for trapezoidal baffles.
2) Trapezoidal baffle systems trap the largest volume of sediments whereas triangular baffles trap the least. Similarly, trapezoidal baffles also dissipate the most energy while the triangular baffles dissipate the least.
3) The impact forces experienced by trapezoidal baffles are larger than those of triangular baffles. The impact on the first baffle in square systems is the largest among the three geometries under similar flow conditions, while the impact pressure on the second baffle of both triangular and trapezoidal baffle systems is greater than that on square baffles. The results give insight into potential strategies for designing debris-resisting barriers in debris flow drainage channels.

DATA AVAILABILITY STATEMENT

The original contributions presented in the study are included in the article/Supplementary Material; further inquiries can be directed to the corresponding author.

AUTHOR CONTRIBUTIONS

SL and XC made substantial contributions to the conception, validation, project administration, and funding acquisition. JC and YY made substantial contributions to the methodology, supervision, and writing—original draft preparation. HC and WZ made substantial contributions to the resources, data curation, and investigation. HT made substantial contributions to reviewing and editing. XG polished the English, reviewed the results and approved the manuscript.

ACKNOWLEDGMENTS

The authors would like to thank the funding supported by the National Natural Science Foundation of China (Grant Nos. 42007270 and 41925030), the Strategic Priority Research Program of the Chinese Academy of Sciences (Grant No. XDA23090403), the Sichuan Science and Technology Program (Grant No. 2019YJ0009), the Youth Innovation Promotion Association CAS (Grant No. 2022379), and the Helmholtz-OCPC Postdoc Program fellowship (ZD2019042).

REFERENCES

Abrahams, A. D., Li, G., and Atkinson, J. F. (1995). Step-pool Streams: Adjustment to Maximum Flow Resistance. *Water Resour. Res.* 31 (10), 2593–2602. doi:10.1029/95wr01957

Armanini, A., Larcher, M., and Odorizzi, M. (2011). "Dynamic Impact of a Debris Flow Front against a Vertical Wall," in Proceedings of the 5th International Conference on Debris-Flow Hazards, Mitigation, Mechanics, Prediction and Assessment, Padua, Italy (Rome: Casa Editrice Universita` La Sapienza), 1041–1049.

Bernard, M., Boreggio, M., Degetto, M., and Gregoretti, C. (2019). Model-based approach for design and performance evaluation of works controlling stony debris flows with an application to a case study at Rovina di Cancia (Venetian Dolomites, Northeast Italy). *Sci. total Environ.* 688, 1373–1388. doi:10.1016/j.scitotenv.2019.05.468

Bung, D. B., Sun, Q., Meireles, I., Viseu, T., and Matos, J. S. (2012). "USBR Type III Stilling Basin Performance for Steep Stepped Spillways," in *Proc. 4th Intl. IAHR Symposium on Hydraulic Structures*. Editors J. Matos, S. Pagliara, and I. Meireles. (Porto, Portugal: Portuguese Water Resources Association). (CD-ROM).

Chanson, H. (2001). *The Hydraulics of Stepped Chutes and Spillways*. Lisse, the Netherlands: Balkema Publishers.

Chartrand, S. M., and Whiting, P. J. (2000). Alluvial Architecture in Headwater Streams with Special Emphasis on Step-Pool Topography. *Earth Surf. Process. Landforms* 25 (6), 583–600. doi:10.1002/1096-9837(200006)25:6<583::aid-esp92>3.0.co;2-3

Chen, J.-G., Chen, X.-Q., Chen, H.-Y., and Zhao, W.-Y. (2016). Characteristics of Viscous Debris Flow in a Drainage Channel with an Energy Dissipation Structure. *J. Mt. Sci.* 13 (2), 223–233. doi:10.1007/s11629-014-3290-z

Chen, J., Chen, X., Li, Y., and Wang, F. (2015). An Experimental Study of Dilute Debris Flow Characteristics in a Drainage Channel with an Energy Dissipation Structure. *Eng. Geol.* 193, 224–230. doi:10.1016/j.enggeo.2015.05.004

Chen, J., Chen, X., Zhao, W., and You, Y. (2018). Debris Flow Drainage Channel with Energy Dissipation Structures: Experimental Study and Engineering Application. *J. Hydraul. Eng.* 144 (10), 06018012. doi:10.1061/(asce)hy.1943-7900.0001523

Chen, J., Chen, X., Zhao, W., Yu, X., and Wang, X. (2017). Experimental Study on the Characteristics of a Debris-Flow Drainage Channel with an Energy Dissipation Structure. *Bull. Eng. Geol. Environ.* 76 (1), 341–351. doi:10.1007/s10064-016-0860-z

Chen, X.-q., You, Y., Chen, J.-g., Huang, K., and Li, D.-j. (2014). Characteristics of a Drainage Channel with Staggered Indented Sills for Controlling Debris Flows. *J. Mt. Sci.* 11 (5), 1242–1252. doi:10.1007/s11629-013-2917-9

Chen, X., Chen, J., Zhao, W., Li, Y., and You, Y. (2017). Characteristics of a Debris-Flow Drainage Channel with a Step-Pool Configuration. *J. Hydraul. Eng.* 143 (9), 04017038. doi:10.1061/(asce)hy.1943-7900.0001352

Chen, X., Cui, P., You, Y., Chen, J., and Li, D. (2015). Engineering Measures for Debris Flow Hazard Mitigation in the Wenchuan Earthquake Area. *Eng. Geol.* 194, 73–85. doi:10.1016/j.enggeo.2014.10.002

Chin, A. (1999). The Morphologic Structure of Step–Pools in Mountain Streams. *Geomorphology* 27 (3-4), 191–204. doi:10.1016/s0169-555x(98)00083-x

Chin, A. (2002). The Periodic Nature of Step-Pool Mountain Streams. *Am. J. Sci.* 302 (2), 144–167. doi:10.2475/ajs.302.2.144

Choi, C. E., Ng, C. W. W., Law, R. P. H., Song, D., Kwan, J. S. H., and Ho, K. K. S. (2015). Computational Investigation of Baffle Configuration on Impedance of Channelized Debris Flow. *Can. Geotech. J.* 52 (2), 182–197. doi:10.1139/cgj-2013-0157

Comiti, F., Cadol, D., and Wohl, E. (2009). Flow Regimes, Bed Morphology, and Flow Resistance in Self-Formed Step-Pool Channels. *Water Resour. Res.* 45 (4), 1–18. doi:10.1029/2008wr007259

Cui, P., Zeng, C., and Lei, Y. (2015). Experimental Analysis on the Impact Force of Viscous Debris Flow. *Earth Surf. Process. Landforms* 40 (12), 1644–1655. doi:10.1002/esp.3744

Cui, P., Zhuang, J. Q., Chen, X. C., Zhang, J. Q., and Zhou, X. J. (2010). Characteristics and Countermeasures of Debris Flow in Wenchuan Area after the Earthquake. *J. Sichuan Univ. Eng. Sci. Ed.* 42 (5), 10–19. (In Chinese). doi:10.15961/j.jsuese.2010.05.004

Felder, S., Geuzaine, M., Dewals, B., and Erpicum, S. (2019). Nappe Flows on a Stepped Chute with Prototype-Scale Steps Height: Observations of Flow Patterns, Air-Water Flow Properties, Energy Dissipation and Dissolved Oxygen. *J. Hydro-environment Res.* 27, 1–19. doi:10.1016/j.jher.2019.07.004

Golly, A., Turowski, J. M., Badoux, A., and Hovius, N. (2019). Testing Models of Step Formation against Observations of Channel Steps in a Steep Mountain Stream. *Earth Surf. Process. Landforms* 44 (7), 1390–1406. doi:10.1002/esp.4582

Huang, H., Ma, D. T., and Wang, X. L. (2009). Experimental Study on the Relationship between the Velocity of Debris Flow and Structure of the Dongchuan Debris Flow Channel. *J. Mt. Sci.* 27 (5), 551–556. (In Chinese).

Hübl, J., Suda, J., and Proske, D. (2009). "Debris Flow Impact Estimation," in the 11th international symposium on water management and hydraulic engineering conference. Ohrid, Macedonia: University of Ss Cyril and Methodius, Faculty of Civil Engineering, Skopje, Macedonia, 1–4.

Iverson, R. M. (2015). Scaling and Design of Landslide and Debris-Flow Experiments. *Geomorphology* 244, 9–20. doi:10.1016/j.geomorph.2015.02.033

Li, D. J. (1997). *Debris Flow Mitigation Theory and Practices*. Beijing: Science Press, 132–148. (In Chinese).

Li, S., Peng, C., Wu, W., Wang, S., Chen, X., Chen, J., et al. (2020). Role of Baffle Shape on Debris Flow Impact in Step-Pool Channel: an SPH Study. *Landslides* 17, 2099–2111. doi:10.1007/s10346-020-01410-w

Marchi, L., Comiti, F., Crema, S., and Cavalli, M. (2019). Channel Control Works and Sediment Connectivity in the European Alps. *Sci. total Environ.* 668, 389–399. doi:10.1016/j.scitotenv.2019.02.416

Matos, J., and Chanson, H. (2006). "Hydraulic Structures: a Challenge to Engineers and Researchers," in *Proceedings of the International Junior Researcher and Engineer Workshop on Hydraulic Structures (IJREWHS'06)* (Montemor-o-Novo: Division of Civil Engineering, University of Queensland. Hydraulic Model Report No. CH61/06, Div. of Civil Engineering.

Ozturk, U., Wendi, D., Crisologo, I., Riemer, A., Agarwal, A., Vogel, K., et al. (2018). Rare Flash Floods and Debris Flows in Southern Germany. *Sci. total Environ.* 626, 941–952. doi:10.1016/j.scitotenv.2018.01.172

Saletti, M., and Hassan, M. A. (2020). Width Variations Control the Development of Grain Structuring in Steep Step-pool Dominated Streams: Insight from Flume Experiments. *Earth Surf. Process. Landforms* 45 (6), 1430–1440. doi:10.1002/esp.4815

VanDine, D. F. (1996). *Debris Flow Control Structures for Forest Engineering*. Victoria, B.C.: Research Branch, B.C. Ministry of Forests. (Working Paper 08/1996).

Wang, F., Chen, X., Chen, J., and You, Y. (2017). Experimental Study on a Debris-Flow Drainage Channel with Different Types of Energy Dissipation Baffles. *Eng. Geol.* 220, 43–51. doi:10.1016/j.enggeo.2017.01.014

Wang, T., Chen, X., Li, K., Chen, J., and You, Y. (2018). Experimental Study of Viscous Debris Flow Characteristics in Drainage Channel with Oblique Symmetrical Sills. *Eng. Geol.* 233, 55–62. doi:10.1016/j.enggeo.2017.11.024

Wang, Z. Y., Qi, L., and Wang, X. (2012). A Prototype Experiment of Debris Flow Control with Energy Dissipation Structures. *Nat. Hazards* 60 (3), 971–989. doi:10.1007/s11069-011-9878-5

Wilcox, A. C., Wohl, E. E., Comiti, F., and Mao, L. (2011). Hydraulics, Morphology, and Energy Dissipation in an Alpine Step-Pool Channel. *Water Resour. Res.* 47 (7), W07514. doi:10.1029/2010WR010192

Wooldridge, C. L., and Hickin, E. J. (2002). Step-pool and Cascade Morphology, Mosquito Creek, British Columbia: a Test of Four Analytical Techniques. *Can. J. Earth Sci.* 39 (4), 493–503. doi:10.1139/e01-087

You, Y., and Liu, J. F. (2008). The Optimum Cross-Section Design on the V-Shaped Drainage Channel of Debris Flow. *J. Mt. Sci.* 26 (2), 218–222. (In Chinese)

You, Y., Pan, H., Liu, J., and Ou, G. (2011). The Optimal Cross-Section Design of the "Trapezoid-V" Shaped Drainage Canal of Viscous Debris Flow. *J. Mt. Sci.* 8 (1), 103–107. doi:10.1007/s11629-011-1023-0

Zhang, C., Xu, M., Hassan, M. A., Chartrand, S. M., Wang, Z., and Ma, Z. (2019). Experiment on Morphological and Hydraulic Adjustments of Step-pool Unit to Flow Increase. *Earth Surf. Process. Landforms* 45, 280–294. doi:10.1002/esp.4722

Zhou, G. G. D., and Ng, C. W. W. (2010). Dimensional Analysis of Natural Debris Flows. *Can. Geotech. J.* 47 (7), 719–729. doi:10.1139/t09-134

Zimmermann, A. E., Saletti, M., Zhang, C., and Hassan, M. A. (2022). "Step-pool Channel Features," in *Treatise on Geomorphology*. 2nd edition. Elsevier Inc., 6, 565–586. doi:10.1016/b978-0-12-818234-5.00004-3

Conflict of Interest: The authors declare that the research was conducted in the absence of any commercial or financial relationships that could be construed as a potential conflict of interest.

Publisher's Note: All claims expressed in this article are solely those of the authors and do not necessarily represent those of their affiliated organizations, or those of the publisher, the editors, and the reviewers. Any product that may be evaluated in this article, or claim that may be made by its manufacturer, is not guaranteed or endorsed by the publisher.

frontiers | Frontiers in Earth Science

TYPE Original Research
PUBLISHED 25 August 2022
DOI 10.3389/feart.2022.973528

OPEN ACCESS

EDITED BY
Changdong Li,
China University of Geosciences
Wuhan, China

REVIEWED BY
Shenghua Cui,
Chengdu University of Technology,
China
Ming Zhang,
China University of Geosciences
Wuhan, China

*CORRESPONDENCE
Hufeng Yang,
yanghf@swjtu.edu.cn

SPECIALTY SECTION
This article was submitted to
Geohazards and Georisks,
a section of the journal
Frontiers in Earth Science

RECEIVED 20 June 2022
ACCEPTED 25 July 2022
PUBLISHED 25 August 2022

CITATION
Yang H, Xing B, He J, Jiang H and
Cheng Q (2022), The formation
mechanism and failure mode of a talus
slope induced by rockfalls in Nayong
County, Southwest China.
Front. Earth Sci. 10:973528.
doi: 10.3389/feart.2022.973528

The formation mechanism and failure mode of a talus slope induced by rockfalls in Nayong County, Southwest China

Hufeng Yang[1]*, Bencong Xing[1], Jiangkun He[1], Hu Jiang[2] and Qiang Cheng[3]

[1]Faculty of Geosciences and Environmental Engineering, Southwest Jiaotong University, Chengdu, China, [2]Kunming Survey, Design and Research Institute Co, Ltd. of CREEC, Kunming, China, [3]Sichuan Highway Planning, Survey, Design and Research Institute Ltd, Chengdu, China

Hillslope processes and mass movement are key issues in the analysis and evaluation of geological disasters in mountainous regions. A rockfall-dominated talus slope exhibits a typical outcrop–talus slope system as the product of detached boulders and rock fragments. The Zongling rockfall zone is one of the most active outcrop–talus slope systems in southwest China, and it provides a representative case study on the assessment of rockfall hazards at the base of talus slopes. In this article, the formation mechanism and failure mode of this rock-talus system were studied using field investigation, remote sensing image analysis, and numerical simulation. The findings reveal that the lithology and rock mass structure of the study site are controlling factors for outcrop retreat and the progressive development of talus deposits. This process is intensified by rainfall and mining activities. Boulder accumulation on the platform at the middle section of the talus slope serves as top loading for the slope mechanical system. During the boulder–ground interaction, the rockfall impact acts as toe cutting to change the geometry and mechanical balance of the talus slope. It was found that toe cutting significantly influenced the slope stability, which led to a decrease in the antisliding force of the slope. The slope failure induced by rockfalls occurred with the combined effect of top loading and toe cutting on this talus slope. During rockfall prevention and mitigation in this region, the government and residents should consider the geodisaster chain, as this relates to the impact of rockfall on talus slopes, in addition to the risk of damage due to the rockfall trajectory.

KEYWORDS

rockfall, talus slope, formation mechanism, failure mode, geodisaster chain

Introduction

A rockfall-dominated talus slope exhibits a typical outcrop–talus slope system as the product of detached boulders and rock fragments from the outcrop in mountains. The evaluation of the talus slope is one of the most important slope surface processes on the exposed hard rocks in mountainous regions (Statham, 1976; Evans and Hungr, 1993; De Blasio and Sæter, 2015). Recently, research on rockfall activity in outcrop–talus slope systems has been conducted mainly for the European Alps (Jomelli and Francou, 2000; McCarroll et al., 2001; Otto and Sass, 2005; Sanders, 2010; Sanders et al., 2014; Colucci et al., 2016; Vehling et al., 2017; Messenzehl et al., 2018; Hendrickx et al., 2020), the Japanese Alps (Imaizumi et al., 2020), and some mountains in the UK (Curry and Morris, 2004), North America (Veilleux et al., 2020; Collins et al., 2022), and the Tibetan Plateau (Wan et al., 2021).

Generally, talus slope instability is the result of slope angle evaluation when the slope angle is beyond the natural angle of repose for rock fragments. However, external factors also influence slope stability, such as rainfall, freezing–thawing, and dynamic load from earthquakes or engineering activities (Matsuoka and Sakai, 1999; Zhang et al., 2010; Xing et al., 2019; Imaizumi et al., 2020). Rockfalls from the outcrop are the source material for the formation of talus slopes. Additionally, rockfall impact plays an important role in changes to slope geometry and slope instability (Gerber and Scheidegger, 1974; Statham, 1976; Sass and Krautblatter, 2007; Hale et al., 2009; De Blasio and Sæter, 2015). For example, on 6 May 2011, a 5,800 m^3 rockfall of dolostone detached from the flank of a gorge in the upper part of a mountain in Austria (Central Alps) and triggered a medium-scale avalanche on the talus slope (Sanders et al., 2014). Considering the global climate change, the assessment of rockfall hazards at the base of talus slopes in outcrop–talus slope systems has become a research hotspot in high-altitude and high-latitude regions.

The Zongling rockfall zone is one of the most active outcrop–talus slope systems in southwest China (Gong and Zhao, 2009). There are 12 rockfall-dominated talus slopes in this rockfall zone, which is located in western Nayong County (Figure 1). Since 2000, there have been more than 20 occurrences of rockfall geodisaster events in this rockfall zone (Cheng et al., 2019). One such instance was a catastrophic landslide that occurred in Zuojiaying village on 3 December 2004, resulting in 39 casualties and five missing persons (Liu et al., 2004; Chen et al., 2006; Wu et al., 2006). In another occurrence in the early morning of 6 June 2015, a large-scale rockfall occurred at Zuojiaying, resulting in three casualties (Cheng et al., 2019). For the mechanism and risk assessment of rockfalls in Zongling Town, several scholars have carried out field investigations and numerical analyses. In 2013, Tan (2013) evaluated the deformation failure mechanism and stability of a high slope at Zongling Town and proposed the toppling failure mode. Subsequently, Jiao (2015) delimited the maximum influence range of rockfalls based on the analysis of a typical collapse zone. Since then, Cheng et al. (2019) have divided rockfall zones into accumulation areas, severely affected areas, and evacuation areas. Shi (2019) has used Zongling Town as an example to conduct the risk assessment of geological hazards for rural areas. Wang (2019) qualitatively analyzed the slope deformation induced by a mined-out area (coal mining) at the bottom of the Mazongling slope.

Recently, most research has focused on rockfall events in the Zongling rockfall zone but not specifically on the talus slope dominated by rockfalls. This study focuses on the instability of a talus slope induced by rockfalls: rockfall-dominated talus slope No. 11 (Figure 1). The formation mechanism and failure mode of this rock-talus system were studied by field investigation, remote

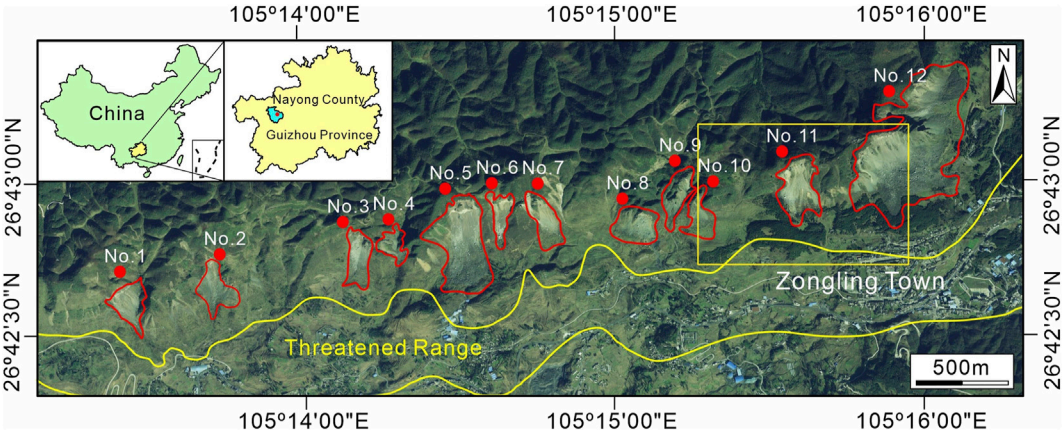

FIGURE 1
Distribution of 12 rockfall-dominated talus slopes in the Zongling rockfall zone (image source: Google Earth).

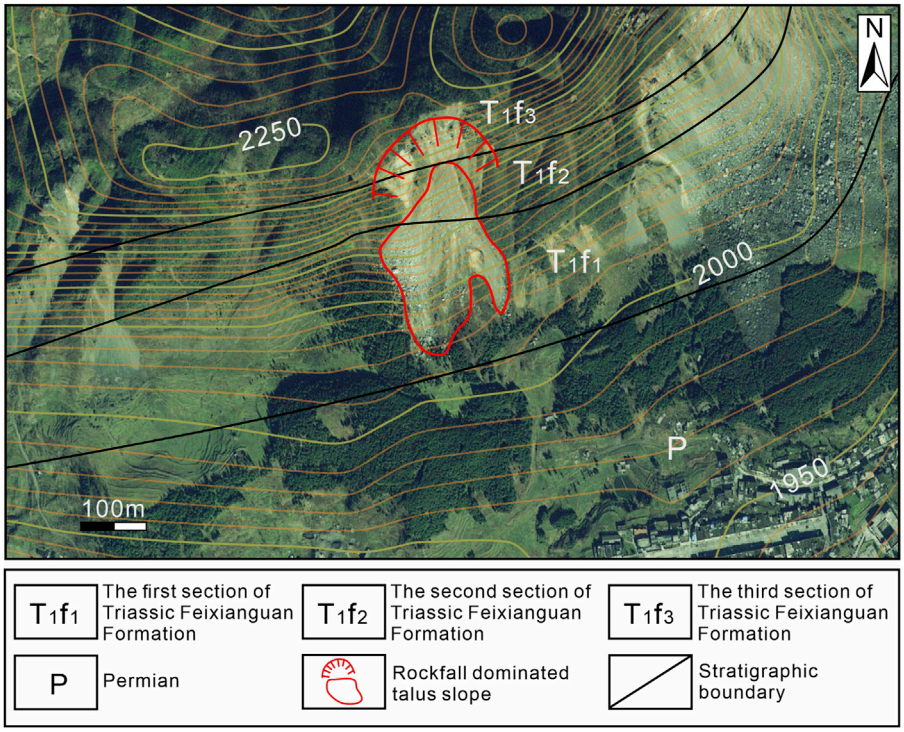

FIGURE 2
Topographic and stratigraphic map of the study site (image source: Google Earth).

sensing image analysis, and numerical simulation. The results indicate that the main reasons for talus slope failure are top loading from boulder accumulation on the slope top, and toe cutting by rockfall impact at the slope toe. Finally, a failure mode for the rockfall-dominated talus slopes was developed in a way that considers the coupling effect of top loading and toe cutting from rockfall. The findings and proposed mode introduced by this study are of practical significance for the prevention and mitigation of rockfall geodisasters in this region.

Geological environmental conditions of the study site

Geomorphology

The Zongling rockfall zone presents with a northeastern trend, with its slope facing south. The terrain is generally high in the east and low in the west, with an altitude of 1,623–2,000 m. The highest point is in the east. To the north of the cliff, the mountains are undulating: the terrain is generally high in the south and low in the north, with an altitude of 2,100–2,334.5 m. The steep cliff has a slope of 50–80° and a height of 100–300 m. The lower slope of the steep cliff becomes gentle, with a slope of about 30–45°. Hilly farmland and local villagers are mostly distributed along the foot of the gentle slope or by the flat mountain highland (Shen and Li, 2015). The study site is located 500 m northwest of Zongling Town. Here, the rockfall source area is a steep cliff with a slope angle of 60–80°, and the talus slope becomes gentler with a slope angle of 35–45°. The relative height difference between the source area and slope toe was about 240 m (Figure 2).

Lithology

Permian and Triassic strata were exposed from south to north in the study area (Figure 2). The Permian Longtan Formation (P_2lt) is composed of gray medium-thick mudstone sandwiched with green–gray medium-thick lithic sandstone, siltstone, dark gray limestone, and siliceous sandstone. The overlying strata consist of the lower Triassic Feixianguan Formation, which are mainly distributed in the foothills of Zongling Town. The rock formation attitude is 330°∠32°. There are two sections of the Triassic Feixianguan Formation. The first section (T_1f_1) is composed of medium-thick chlorotic siltstone (gray–green and dark purple), argillaceous calcareous siltstone, and mudstone (purple and gray–green) interbedded with silty mudstone, which is mainly

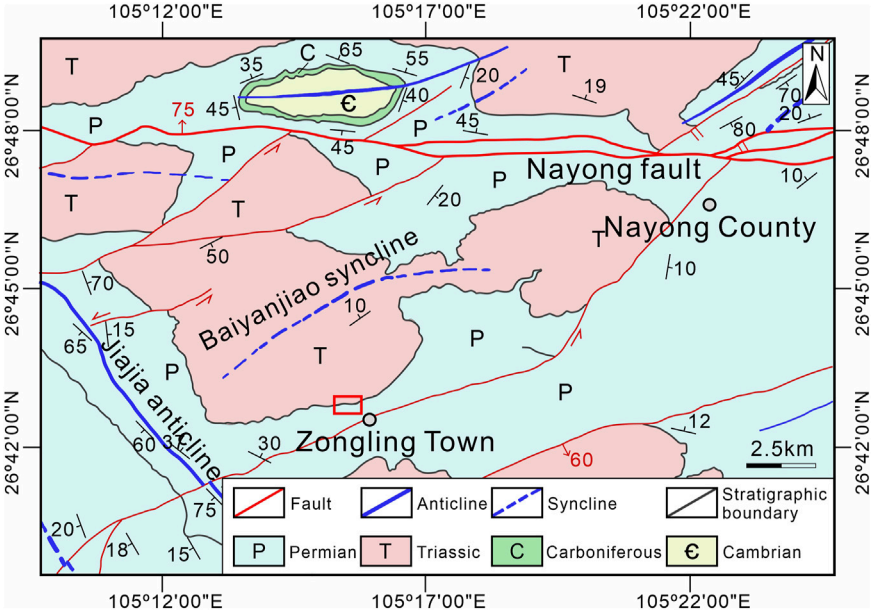

FIGURE 3
Regional tectonic and lithology map (modified from the work of Wu et al., 2019).

distributed in the middle upper cliff. The second section (T_1f_2) consists of thin–thick fine sandstone (gray–purple and green), calcareous sandstone, and basaltic lithic sandstone sandwiched with mudstone (purple), silty mudstone, thin–thick siltstone, tuff feldspar siltstone, silty limestone, and marl.

Regional tectonics

Folds and faults dominate the regional geological structures of the study site (Wu et al., 2019). The investigation area is located in the northeast wing of the Jiajia anticline and the south wing of the Baiyanjiao syncline, which belong to the northeast trending tectonic deformation area in the Bijie of Yangtze paraplatform. Northeast–southwest strike–slip faults are developed in the intermontane basin south of the rockfall. The Nayong fault is located about 13 km to the northwest (Figure 3). Due to the influence of tectonic activity, joints and fissures are developed in the limestone, and Figure 4A shows the scratches and steps left by tectonic action after a joint had been filled with calcite. Two groups of fissures are developed mainly in the western region, with attitude of 200–253°∠52–70° and 53–145°∠70–80° and a fracture rate of 1–4/m. Two groups of fractures are developed mainly in the eastern region, with the occurrence rates of 200–315°∠60–80°and 50–145°∠55–85° and fracture rates of 1–7/m. The two groups of joints in the east and west cut the limestone into vertical blocks, causing the formation of dominant open fractures near the outcrop (Shen and Li, 2015; Cheng et al., 2019; Wu et al., 2019).

Human activity

The main human activity related to the geodisaster at the study site was coal mining (Xiao et al., 2018). Along the rockfall zone in Zongling Town, there were more than 10 licensed coal mines (Tan, 2013). In 2004, 44 people were killed during the Zuojiaying landslide in the Zongling rockfall zone. Mining activity was the major triggering factor for this catastrophic landslide, and there were five coal mines near the landslide: Zhongling Mine, Zuojingying Mine, Sunxiao Mine, Xingyi Mine, and Huangjiagou Mine (Chen et al., 2006). Recently, these coal mines were shut down due to the continuous deformation and failure of slopes (Figure 4). However, large previously mined-out areas will continue to affect the integrity of the mountain structure in this area.

Meteorological and hydrographic characteristics

The study region is located in the subtropical warm and humid zone. It has an average annual temperature of 13.6°C and an average annual precipitation of 1,243.5 mm, mainly

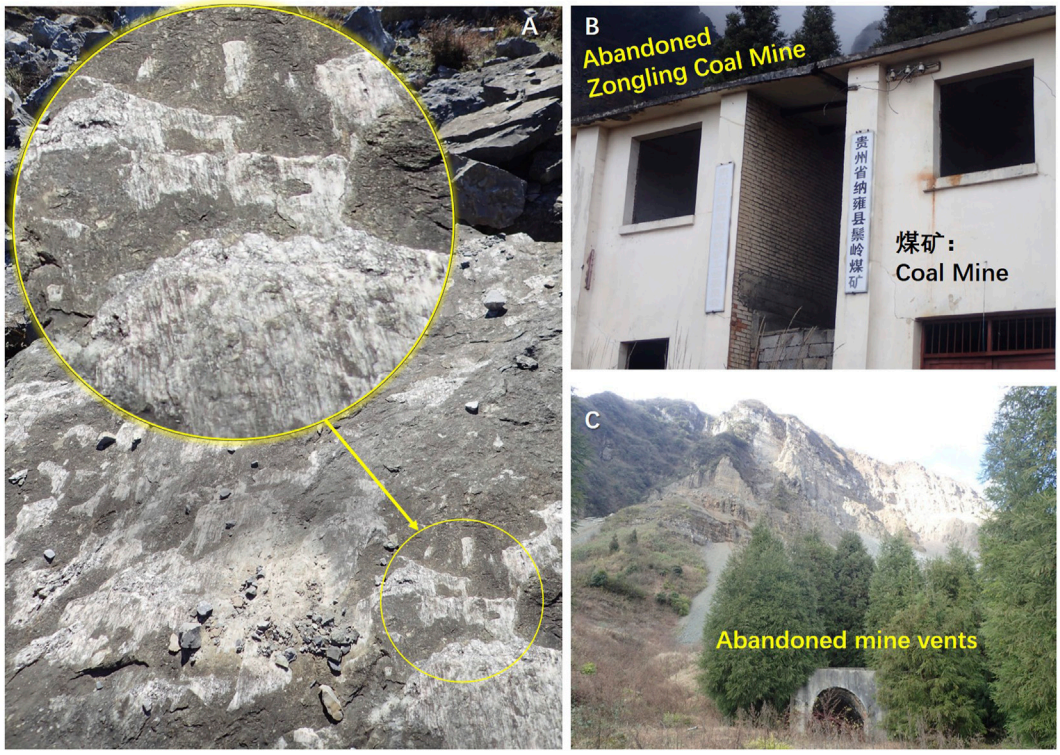

FIGURE 4
Tectonic indications **(A)** and human activity (**(B)** and **(C)**) at the study site.

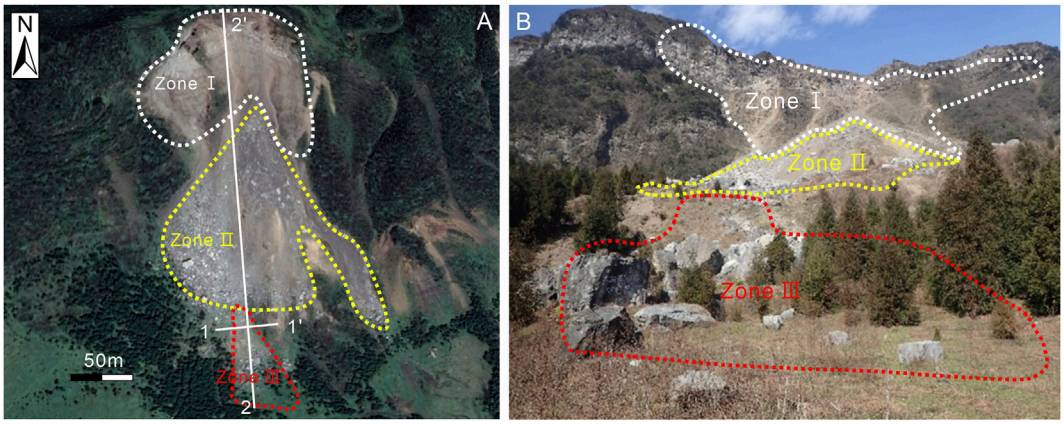

FIGURE 5
Overall features of the rockfall-dominated talus slope: **(A)** plane view (image source: Google Earth) and **(B)** front view.

from May to October, which accounts for about 70% of the annual precipitation (Cheng et al., 2019). The study site is located in the north and west of the Guizhou Plateau, which belongs to the Wujiang River basin in the Yangtze River system (Shen and Li, 2015). The main condition of groundwater is fissures water. Rainfall is the main groundwater recharge at this specific study site. In the upper part of the slope, with a larger topographic cut

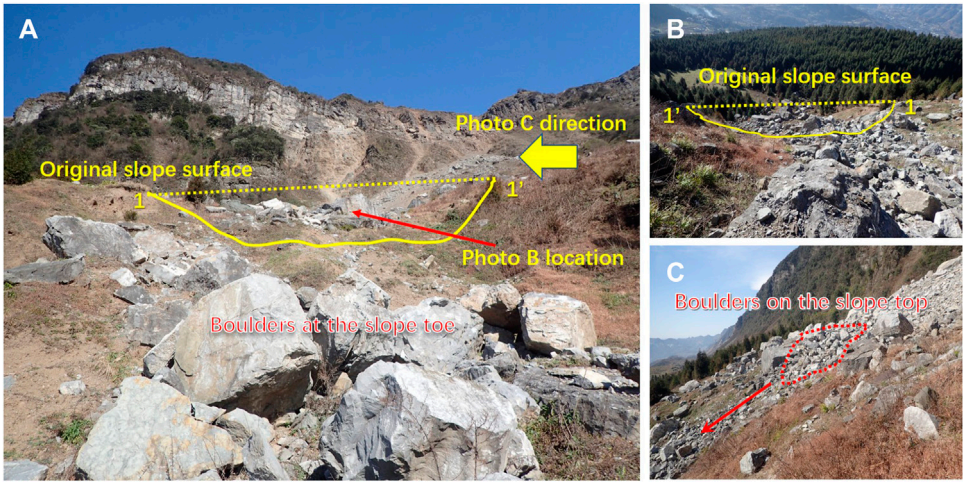

FIGURE 6
Detailed geomorphic features and boulder distribution of the failure area (Zone III). **(A)** overview of failure area, **(B)** boulders in the landslide trough, and **(C)** boulders on the slope top.

depth, the recharge, runoff, and discharge of groundwater alternate quickly, and the connection between the aquifers is poor.

Rockfall-dominated talus slope

The general morphology of this rockfall-dominated talus slope is fan-shaped in the plane. It is about 400 m long from north to south and 240 m wide from east to west. The orientation of the collapse direction is south-forward. Based on its morphology and material composition, this outcrop–talus system can be divided into the outcrop area (Zone I), talus slope (Zone II), and failure area (Zone III) (Figure 5).

Zone I is located at a cliff with a height of 50 m (Figure 5A). The bedrock at the lower cliff is gray–green, medium-thick siltstone interbedded with thin mudstone. The bedrock at the upper cliff is gray–green, medium-thick, fine sandstone interbedded with marl. The stratum inclines into the slope. The rock mass is cut into blocks of different sizes by joints.

Zone II is below the outcrop area. The height of the talus slope is about 120 m. The width of dispersion was about 180 m from west to east (Figure 5B). The slope angle is about 40° in the middle and upper parts. Gradually, the slope angle is reduced to 10° in the lower part. A platform is connected to the toe of the talus slope. The cone is mainly composed of gravel and residual soil with certain sorting properties. It presents fine debris at the top of the slope cone and boulders on the platform.

The failure area (Zone III) is below the platform of the talus slope (Figure 5) with a southern sliding direction. Figure 6 shows the detailed geomorphic features of the collapse area. The photo in Figure 6A was taken at the slope toe. The dotted line area represents the original slope surface before slope failure. Then, there is a landslide trough with an average depth of 3 m after the slope failure. The width of the sliding body was about 15 m. The length of the sliding mass was about 100 m. The western boundary of the landslide shows a steep slope with a slope angle of 55° and a height of 2 m, while the eastern boundary presents a steep shape. A large volume of boulders can be seen deposited at the slope toe. In Figure 6B, taken from the slope top to the slope toe along the sliding direction, it is evident that boulders were distributed in the landslide. Figure 6C indicates the western orientation at the slope top, where there are a few large boulders (delineated by the red dotted line). Those missing large boulders are situated in the landslide trough and at the toe of the slope in Figure 6A.

Due to differential weathering, there is a cavity below the unstable rock mass in the source area (Figure 7A). The stereographic projection analysis of rock mass in the source area of collapse was carried out using the occurrence data (Table 1) of the rock strata and joints obtained from the investigation. The rock layer has been cut into blocks by J_1, J_2, J_3, and J_4 joints. The intersecting lines of J_2 and P_1 and of J_4 and P_1, which are the main controlling structural planes, tend toward the outside of the slope, and their inclination is less than the slope angle. The intersection lines of the other combinations tend toward the inside of the slope. Thus, although the rock mass in the source area is relatively fragmented, the whole rock mass is in a stable state, and only some boulders close to the slope are unstable. In extreme cases, such as earthquakes and torrential rain, fractures may expand the trend, and the dangerous rock mass may slide and collapse downward.

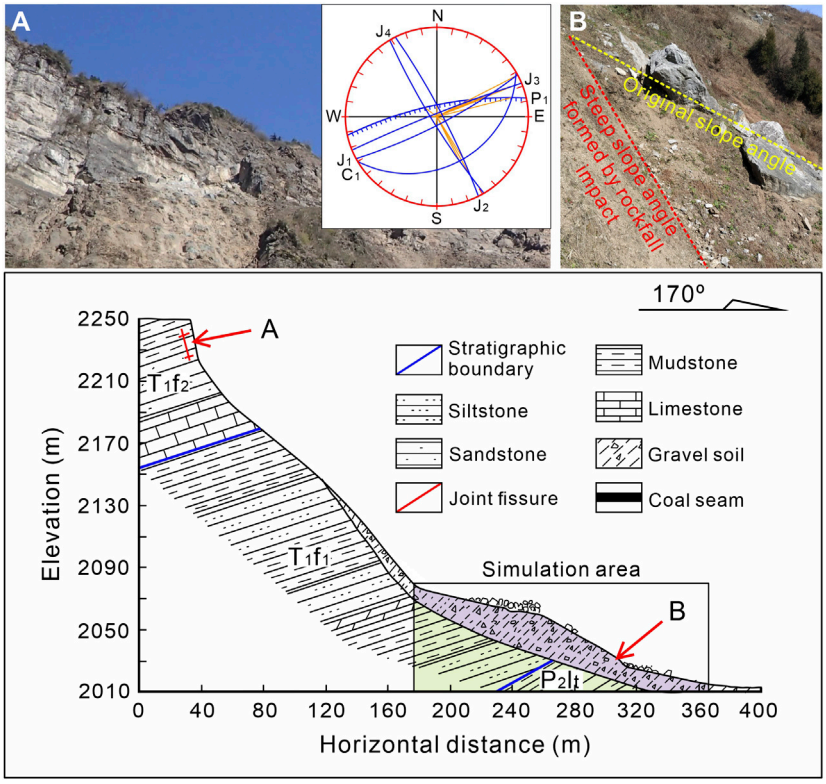

FIGURE 7
Profile section 2-2′ of this rockfall-dominant talus slope. **(A)** source area and **(B)** slope toe cutting by rockfall impact.

TABLE 1 Parameters for stereographic projection.

Notation	Structural plane	Dip direction (°)	Dip angle (°)
P_1	Slope surface	168	75
C_1	Bedding plane	330	32
J_1	Joint 1	59	83
J_2	Joint 2	332	83
J_3	Joint 3	243	83
J_4	Joint 4	158	86

About 5 m west of the western boundary of the collapse area, there is an impact trace formed by a recent rockfall. The fallen boulder was 2.5 m long, 2 m wide, and 2.3 m high. The upper slope angle of the slope body was about 35°. The lower slope angle of the slope body was about 60°, and the development of a small slope was about 2.5 m high (Figure 7B). Based on the rockfall trajectory, it appears that the slope change was caused mainly by the impact, scraping, and pushing of the lower part of the slope body when the rockfall impacted the toe of slope.

Figure 8 shows the ground traces located near the slope toe of the collapse area after the rockfall impact. The green zone indicates a long trench created by the boulder scraping action, the blue zone highlights the sidewall of the long trench, and the red zone shows a steep main scarp near the ground traces. It is evident that the geometry of the slope changed after the rockfall impact, so it may be concluded that frequent rockfall events induce toe cutting, which contributes to slope instability.

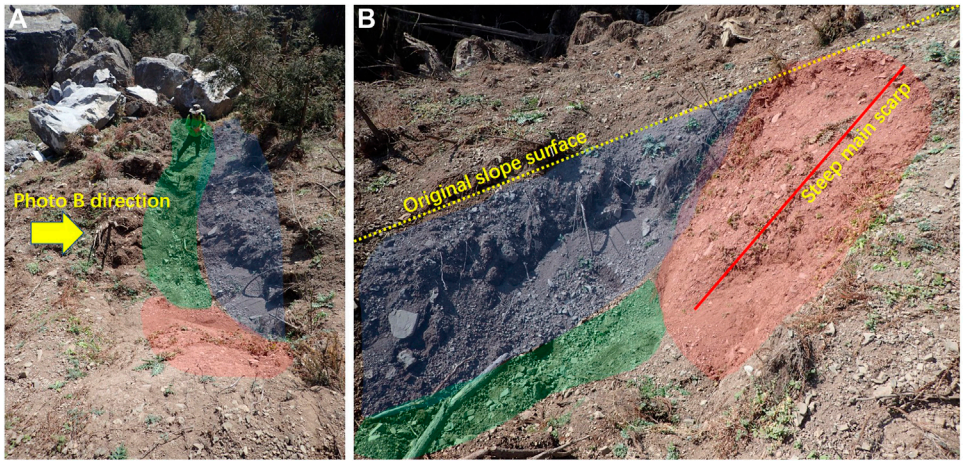

FIGURE 8
Slope toe cutting by rockfall impact: **(A)** view toward slope toe and **(B)** side view.

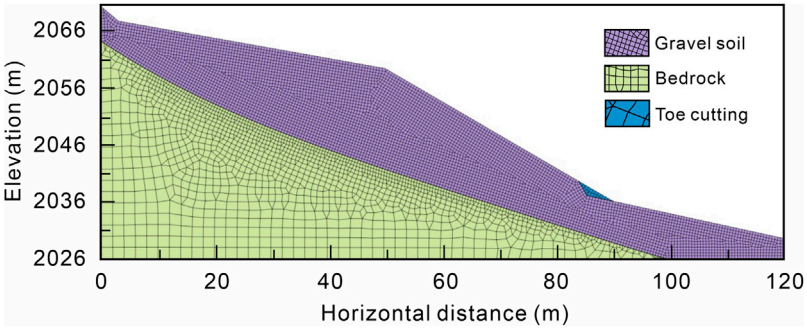

FIGURE 9
Numerical model for SRM.

Effects of top loading and toe cutting on slope stability

One objective of the study was to analyze how boulder load at the top of the slope and slope cutting at the slope toe contribute to landslide formation. Thus, the failure area (see Figure 7), including the platform and toe of the talus slope, was selected as the geological model for numerical simulation. To reduce the influence of boundary range conditions on calculation errors and to improve the calculation accuracy, the size of the model (Figure 9) was set as the distance from the slope toe to the left edge at 1.5 times the slope height, the distance from the top to the right edge was set to 2.5 times the slope height, and the total height of the upper and lower edges was set to no less than two times the slope height (Zhao et al., 2002; Zheng et al., 2002). MIDAS/GTS software was used to carry out the slope stability analysis under the following conditions: a) without top loading and toe cutting, b) top loading, c) toe cutting, and d) top loading and toe cutting. The numerical model (Figure 9) was established based on the field investigations and previous research on the Zongling rockfall (Chen et al., 2006). The slope material structure can be divided into two layers: the upper is gravel soil and the lower is bedrock. The basic physical and strength parameters of the gravel soil and bedrock, shown in Table 2, were obtained from a comprehensive review of field geological surveys, laboratory tests, and relevant regional experience (Chen et al., 2006; Cheng et al., 2019). The slope stability was analyzed using the finite element strength reduction method (SRM).

TABLE 2 Physical and mechanical parameters of soil and rock martials.

Parameters	Unit weight, γ (kN/m^3)	Elasticity modulus, E (MPa)	Poisson's ratio, ν	Cohesion c, (kPa)	Internal friction angle, φ (°)
Gravel soil	21.2	60	0.31	10.5	22.1
Bedrock	25	650	0.4	32	59

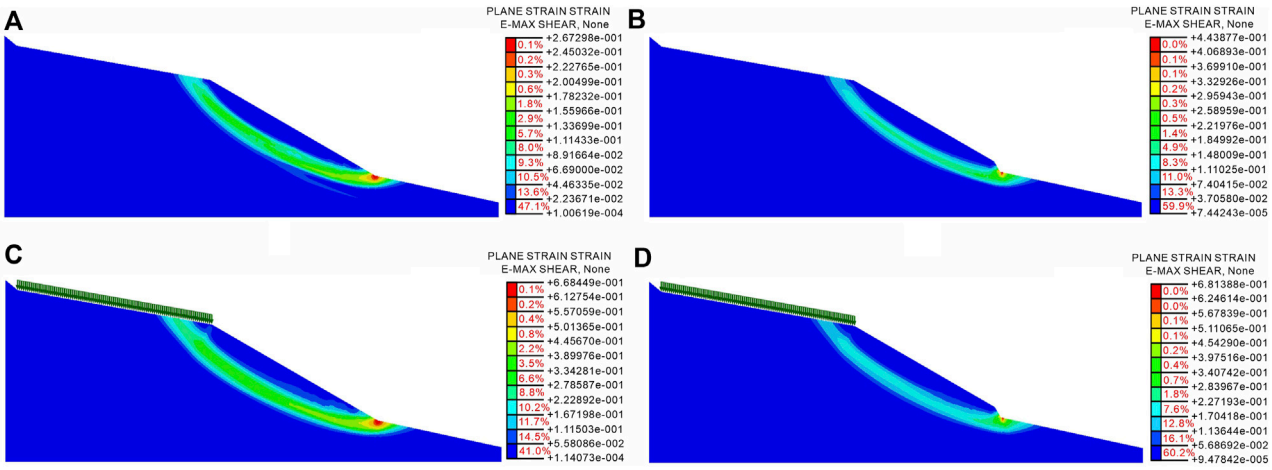

FIGURE 10
Maximum shear strain for four conditions: **(A)** without top loading and toe cutting, **(B)** toe cutting, **(C)** top loading, and **(D)** top loading and toe cutting.

The top loading simulation was located at the top of the slope. The density of the overlying boulders was 2,200 kg, and the thickness was 2 m. Therefore, the linear uniform load can be calculated as 43.12 kN/m. The toe cutting state simulates the phenomenon of slope cutting caused by rockfalls impacting the slope toe, as observed in the lower part of the collapse zone. The slope angle after cutting the slope was set to 60°. All materials were subjected to the Mohr–Coulomb failure criteria.

The numerical simulation results show that the maximum plastic deformation is concentrated at the toe of the slope for four simulation conditions (Figure 10). The safety factors of the slopes under conditions A, B, C, and D were 1.11, 1.06, 1.10, and 1.04, respectively. Theoretically, the slope is stable. However, in engineering practice, to make sure the slope has enough of a safety reserve, it is generally considered that the slope with a safety factor of Fs = 1.1–1.5 is stable. Therefore, the slopes in these four states are near the critical state of instability. The safety factor of the slope for the top loading condition was 0.01 smaller than that for the non-top loading and non-toe cutting conditions. The results indicate that boulders loading on the top of the slope has some influence on the stability of the slope, but that effect is not significant. The safety factor of slope for toe cutting condition was 0.05 smaller than that for the non-top loading and non-toe cutting conditions. Here, the results indicate that the rockfall impact at the toe of the slope has a significant influence on the stability of the slope. The effect of toe cutting on slope stability was greater than that of top loading. The safety factor of the slope under the combined action of top loading and toe cutting was 0.07 smaller than for the non-top loading and non-toe cutting conditions. This result indicates that the slope becomes more unstable under the combined action of rockfalls.

Formation mechanism and failure mode

The lithology and rock mass structure of the study site are the controlling factors for outcrop retreat and the progressive development of talus deposits. The upper part of the outcrop slope is limestone, and the lower part is siltstone and mudstone with the overall structure of the slope being hard at the top and soft at the bottom. Siltstone and mudstone can occur the differential weathering during the wetting and drying cycles due to rainfall and Sun exposure (Chen et al., 2006; Lo, 2015).

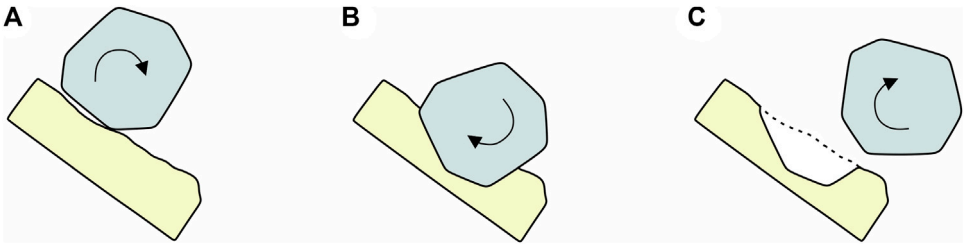

FIGURE 11
Process diagram of the rockfall impact on the talus slope **(A)** contact, **(B)** impact, and **(C)** rebound.

Differential weathering appeared on the outcrop (Figure 7A), and regional tectonics, such as the Baiyanjiao syncline and the Jiajia anticline, controlled the development of joints and fissures on the slope. Due to the long-term geological action, cracks in the rock mass were gradually connected and enlarged to separate the slope surface rock mass from the bedrock. At the same time, weathering, dissolution, and surface water infiltration along the fissure also cause the fissure to expand further and gradually extend downward to form a complete fissure.

Rainfall and human activity are the main external influencing factors on slope stability (Dong et al., 2015; Cheng et al., 2019). The rainfall in the study area was relatively concentrated. On one hand, precipitation infiltration into the unloading cracks causes an increase in water pressure. On the other hand, the rock mass itself presents a structure that is hard at the top and soft at the bottom, and the infiltration of precipitation results in a decrease in the lower, weaker rock stratum's falling strength. Due to the dual action of water filling the unloading fissure and softening the base, the stability of the rock mass is eventually reduced. The slope deformation was further aggravated by long-term mining engineering. The ground collapse and mountain cracking in this area are mainly caused by large goaf areas, long mining times, and shallow buried mining areas (Tan, 2013). The cracks at the top of the mountain have opened about 1–2 m wide, and some blocks have been separated and even became isolated from the bedrock. More importantly, the cracks in the mountain show a developing trend, which may progress quite easily and cause a large-scale mountain collapse. When mining reaches a certain scale, a large area of goaf deformation occurs. The blast loading and mining collapse of human activity eventually degrade the integrity of the rock mass (Xiao et al., 2018). Thus, because the buried depth is shallow, the deformation zone will affect the surface rock mass, and the slope will crack accordingly.

The detached boulders and fragments provide a continuous source of materials for the evolution of this talus slope and gradually change the slope geometry over time. The boulders accumulated on the top of the slope for a long time and continued to load in the upper part of the slope, resulting in creeping deformation of the slope body. In addition, a large boulder on the talus slope reduced the angle of the slope (Evans and Hungr, 1993). Moreover, slope microtopography affected the movement characteristics of the rockfall (Imaizumi et al., 2020; Collins et al., 2022). The relatively flat terrace (Figure 7B) in the middle section of the talus slope increases the jump height of the boulders. The collision process between the beginning of the rockfall and its terminus can be divided into several stages (Dorren et al., 2004; Lu et al., 2019). Figure 11 illustrates the process diagram of the rockfall impact on the talus slope, which

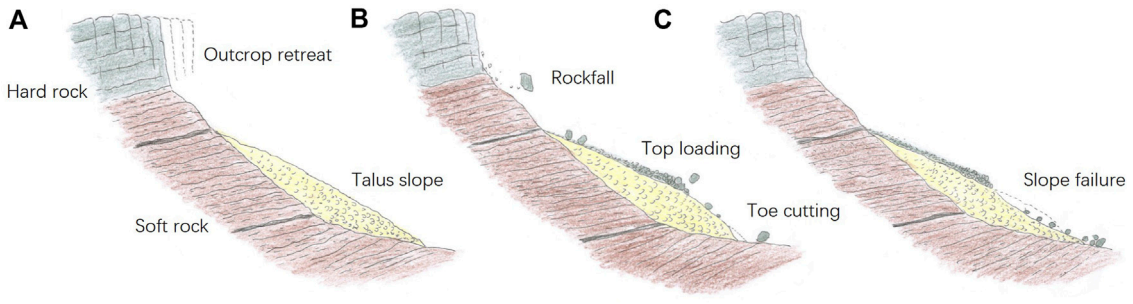

FIGURE 12
Schematic diagram of the formation mechanism and failure mode of a talus slope induced by rockfalls. **(A)** outcrop retreat, **(B)** top loading and toe cutting, **(C)** slope failure.

includes the contact, impact, and rebound stages. After the last stage, the rolling boulder remains as a trace on the slope and functions as a toe cutting (Figure 8). According to the numerical simulation analysis, toe cutting has a great influence on slope stability.

The failure mode of the talus slope induced by rockfalls at this study site is illustrated in Figure 12. The regional tectonic activities control the development of rock joints and fissures. The lithology—hard upper and soft lower at the outcrop—leads to differential weathering. External factors, such as goaf deformation and rainfall, aggravate the development of rock fissures. Frequently, the boulders detach, and these fragments cause the outcrop to retreat, along with the progressive development of talus deposits (Figure 12A). The boulders deposit on the platform in the middle section of the talus slope, which then serves as top loading for the slope mechanical system (Figure 12B). During the boulder–ground interaction of a rolling boulder with a high jump, the rockfall impact functions as a form of toe cutting to change the geometry of the talus slope. The mechanical balance of the slope changes at the same time, which causes a decrease in the antisliding force of the slope. Finally, on this talus slope, slope failure occurred due to the combined effect of top loading and toe cutting (Figure 12C). It is therefore evident that the prevention and mitigation efforts in this region should pay close attention to the role of rockfall impact in the geodisaster chain that affects talus slopes, while also considering the more commonly understood rockfall trajectory.

Conclusion

(1) The Zongling rockfall zone is one of the most active outcrop–talus slope systems in southwest China. The lithology and rock mass structure of the study site are the controlling factors for the outcrop retreat and the progressive development of talus deposits. The external influencing factors of rainfall and human activities enhance this process.
(2) Boulder accumulation on the platform in the middle section of the talus slope functions as top loading for the slope mechanical system. During the boulder-ground interaction, the rockfall impact causes toe cutting to change the geometry and mechanical balance of the talus slope. It was found that toe cutting has a significant influence on slope stability, which then leads to a decrease in the antisliding force of the talus slope. The slope failure induced by rockfalls then occurs due to the combined effect of top loading and toe cutting on this talus slope.
(3) In this region, a rockfall geodisaster event may trigger a large-scale slope failure as one outcome of the geodisaster chain. Therefore, the prevention and mitigation efforts in this region should pay close attention to the role of rockfall impact in the specific geodisaster chains that affect talus slopes, while also considering the more commonly understood rockfall trajectory.

Data availability statement

The original contributions presented in the study are included in the article/Supplementary Material. Further inquiries can be directed to the corresponding author.

Author contributions

HY: conceptualization, methodology, data curation, writing—original draft, and formal analysis. BX: conceptualization, methodology, and formal analysis. JH: conceptualization, methodology, and formal analysis. HJ: conceptualization, methodology, and formal analysis. QC: conceptualization, methodology, and formal analysis.

Funding

This work was supported by the Sichuan Science and Technology Program (Grant No. 2022YFG0141) and National Natural Science Foundation of China (Grant No. 41807248).

Conflict of interest

Author HJ was employed by the company Kunming Survey, Design, and Research Institute Co., Ltd., of CREEC. Author QC was employed by the company Sichuan Highway Planning, Survey, Design, and Research Institute Ltd.

The remaining authors declare that the research was conducted in the absence of any commercial or financial relationships that could be construed as a potential conflict of interest.

Publisher's note

References

Chen, Z. F., Kong, J. M., and Wang, C. H. (2006). Characteristics of the falling-slide type landslide in Nayong in Guizhou Province and the lessons learned for disaster mitigation in other areas. *Chin. J. Geol. Hazard Control* 17, 32–35. doi:10.3969/j.issn.1003-8035.2006.03.008

Cheng, Y., Zhang, J., Chen, J., and Long, J. (2019). Analysis on stability and hazard zone of dangerous rock mass in zongling Town, Nayong of Guizhou Province. *Chin. J. Geol. Hazard Control* 30 (4), 9–15. doi:10.16031/j.cnki.issn.1003-8035.2019.04.02

Collins, B. D., Corbett, S. C., Horton, E. J., and Gallegos, A. J. (2022). Rockfall kinematics from massive rock cliffs: Outlier boulders and flyrock from whitney portal, California, rockfalls. *Environ. Eng. Geosci.* 28 (1), 3–24. doi:10.2113/EEG-D-21-00023

Colucci, R. R., Boccali, C., Žebre, M., and Guglielmin, M. (2016). Rock glaciers, protalus ramparts and pronival ramparts in the south-eastern Alps. *Geomorphology* 269, 112–121. doi:10.1016/j.geomorph.2016.06.039

Curry, A. M., and Morris, C. J. (2004). Lateglacial and holocene talus slope development and rockwall retreat on mynydd du, UK. *Geomorphology* 58 (1–4), 85–106. doi:10.1016/S0169-555X(03)00226-5

De Blasio, F. V., and Sæter, M. B. (2015). Dynamics of grains falling on a sloping granular medium: Application to the evolution of a talus. *Earth Surf. Process. Landforms* 40, 599–609. doi:10.1002/esp.3655

Dong, X. J., Pei, X. J., and Huang, R. Q. (2015). The longchangzhen collapse in kaili, Guizhou: Characteristics and failure causes. *Chin. J. Geol. Hazard Control* 26 (3), 3–9. doi:10.16031/j.cnki.issn.1003-8035.2015.03.02

Dorren, L. K. A., Maier, B., Putters, U. S., and Seijmonsbergen, A. C. (2004). Combining field and modelling techniques to assess rockfall dynamics on A protection forest hillslope in the European Alps. *Geomorphology* 57 (3–4), 151–167. doi:10.1016/S0169-555X(03)00100-4

Evans, S. G., and Hungr, O. (1993). The assessment of rockfall hazard at the base of talus slopes. *Can. Geotech. J.* 30 (4), 620–636. doi:10.1139/t93-054

Gerber, E., and Scheidegger, A. E. (1974). On the dynamics of scree slopes. *Rock Mech.* 6 (1), 25–38. doi:10.1007/bf01238051

Gong, X. X., and Zhao, X. (2009). Type, causation and prevention of geologic disaster hidden danger in Nayong county. *Guizhou Geol.* 26 (3), 235–237. doi:10.3969/j.issn.1000-5943.2009.03.019

Hale, A. J., Calder, E. S., Loughlin, S. C., Wadge, G., and Ryan, G. A. (2009). Modelling the lava dome extruded at soufriere hills volcano, Montserrat, august 2005-may 2006 Part II: Rockfall activity and talus deformation. *J. Volcanol. Geotherm. Res.* 187 (1–2), 69–84. doi:10.1016/j.jvolgeores.2009.08.014

Hendrickx, H., Lars, D. S., Cornelis, S., Reynald, D., Jan, N., and Amaury, F. (2020). Talus slope geomorphology investigated at multiple time scales from high-resolution topographic surveys and historical aerial photographs (sanetsch pass, Switzerland). *Earth Surf. Process. Landforms* 45 (14), 3653–3669. doi:10.1002/esp.4989

Imaizumi, F., Trappmann, D., Matsuoka, N., Cánovas, J. A. B., Yasue, K., and Stoffel, M. (2020). Interpreting rockfall activity on an outcrop–talus slope system in the southern Japanese Alps using an integrated survey approach. *Geomorphology* 371, 107456. doi:10.1016/j.geomorph.2020.107456

Jiao, W. (2015). Analysis on Stopping area and influencing Factors of typical dangerous rock collapse, *master's thesis*. Guiyang, China: Guizhou University.

Jomelli, V., and Francou, B. (2000). Comparing the Characteristics of Rockfall Talus and Snow Avalanche Landforms in an Alpine Environment Using a New Methodological Approach: Massif des Ecrins, French Alps. *Geomorphology* 35 (3–4), 181–192. doi:10.1016/S0169-555X(00)00035-0

Liu, C. Z., Guo, Q., and Chen, H. Q. (2004). Preliminary analysis on the cause of dangerous rock collapse in yanjiaozhai, Nayong county, Guizhou Province. *Chin. J. Geol. Hazard Control* 15, 123+144. doi:10.3969/j.issn.1003-8035.2004.04.029

Lo, C. M. (2015). Cliff retreat and progressive development of talus deposits in hungtsaiping rockfall area, NanTou, taiwan. *Landslides* 12, 29–54. doi:10.1007/s10346-013-0459-4

Lu, G., Caviezel, A., Christen, M., Demmel, S. E., Ringenbach, A., Bühler, Y., et al. (2019). Modelling rockfall impact with scarring in compactable soils. *Landslides* 16, 2353–2367. doi:10.1007/s10346-019-01238-z

Matsuoka, N., and Sakai, H. (1999). Rockfall activity from an alpine cliff during thawing periods. *Geomorphology* 28 (3-4), 309–328. doi:10.1016/S0169-555X(98)00116-0

McCarroll, D., Shakesby, R. A., and Mattews, J. A. (2001). Enhanced rockfall activity during the little ice age: Further lichenometric evidence from a Norwegian talus. *Permafr. Periglac. Process.* 12 (2), 157–164. doi:10.1002/ppp.359

Messenzehl, K., Viles, H., Otto, J. C., Ewald, A., and Dikau, R. (2018). Linking rock weathering, rockwall instability and rockfall supply on talus slopes in glaciated hanging valleys (Swiss Alps). *Permafr. Periglac. Process.* 29 (3), 135–151. doi:10.1002/ppp.1976

Otto, J. C., and Sass, O. (2005). Comparing geophysical methods for talus slope investigations in the turtmann valley (Swiss Alps). *Geomorphology* 76 (3–4), 257–272. doi:10.1016/j.geomorph.2005.11.008

Sanders, D. (2010). Sedimentary facies and progradational style of a pleistocene talus-slope succession, northern calcareous Alps, Austria. *Sediment. Geol.* 228 (3–4), 271–283. doi:10.1016/j.sedgeo.2010.05.002

Sanders, D., Widera, L., Ostermann, M., and Baas, J. (2014). Two-layer scree/snow-avalanche triggered by rockfall (eastern Alps): Significance for sedimentology of scree slopes. *Sedimentology* 61 (4), 996–1030. doi:10.1111/sed.12083

Sass, O., and Krautblatter, M. (2007). Debris flow-dominated and rockfall-dominated talus slopes: Genetic models derived from GPR measurements. *Geomorphology* 86 (1–2), 176–192. doi:10.1016/j.geomorph.2006.08.012

Shen, T. Q., and Li, J. Y. (2015). Study on formation mechanism of collapse in zongling Town, Guizhou Province. *Technol. Innov. Appl.* 35, 19–20.

Shi, Y. S. (2019). Risk Assessment and Management of Rockslide in the rural area - a case Study in zongling Town, Guizhou, *master's thesis*. China, Sichuan, Chengdu: Chengdu University of Technology. doi:10.26986/d.cnki.gcdlc.2019.000412

Statham, I. (1976). A scree slope rockfall model. *Earth Surf. Process.* 1 (1), 43–62. doi:10.1002/esp.3290010106

Tan, N. (2013). Failure Mechanism and stability Evaluation of the zhongling high slope Deformation on mine Area in Nayong county, *master's thesis*. China, Sichuan, Chengdu: Chengdu University of Technology.

Vehling, L., Baewert, H., Glira, P., Moser, M., Rohn, J., and Morche, D. (2017). Quantification of sediment transport by rockfall and rockslide processes on a proglacial rock slope (kaunertal, Austria). *Geomorphology* 287, 46–57. doi:10.1016/j.geomorph.2016.10.032

Veilleux, S., Bhiry, N., and Decaulne, A. (2020). Talus slope characterization in tasiapik valley (subarctic québec): Evidence of past and present slope processes. *Geomorphology* 349, 106911. doi:10.1016/j.geomorph.2019.106911

Wan, Y. H., Zhao, X. Y., Ling, S. X., Li, J., Zeng, C. Y., and Bernd, W. (2021). Directional arrangement of phyllite fragments in phyllite talus slope at the eastern margin of the Tibetan plateau. *J. Mt. Sci.* 18 (11), 3069–3081. doi:10.1007/s11629-020-6605-2

Wang, J. (2019). Study on Damage and Deformation of slope rock mass Caused by underground goaf, *master's thesis*. China, Sichuan, Chengdu: Chengdu University of Technology. doi:10.26986/d.cnki.gcdlc.2019.000827

Wu, C. Y., Qiao, J. P., Wang, C. H., Kong, J. M., and Chen, Z. F. (2006). Analysis on "12·3" super large-scaled landslide in zongling, Nayong, Guizhou. *Res. Soil Water Conserv.* 13 (6), 100–102. doi:10.3969/j.issn.1005-3409.2006.06.031

Wu, K. B., Jiang, K. Y., Huang, W. J., Yue, L. H., and Zhang, D. M. (2019). Tectonic formation features and its evolution in nayong-shuicheng area of northwest Guizhou. *Guizhou Geol.* 36 (2), 165–172. doi:10.3969/j.issn.1000-5943.2019.02.009

Xiao, R. H., Chen, H. Q., Leng, Y. Y., Wei, Y. J., and Wang, W. P. (2018). Preliminary analysis on the failure process and mechanism of the august 28 collapse in Nayong county Guizhou Province. *Chin. J. Geol. Hazard Control* 29 (1), 3–9. doi:10.16031/j.cnki.issn.1003-8035.2018.01.02

Xing, H. F., Liu, L. L., and Luo, Y. (2019). Water-induced changes in mechanical parameters of soil-rock mixture and their effect on talus slope stability. *Geomech. Eng.* 18 (4), 353–362. doi:10.12989/gae.2019.18.4.353

Zhang, Y. C., Huang, R. Q., Fu, R. H., and Pei, X. J. (2010). Experimental research on dynamic failure mechanism of large-scale talus slope. *Chin. J. Rock Mech. Eng.* 29 (1), 65–72.

Zhao, S. Y., Zheng, Y. R., Shi, W. M., and Wang, J. L. (2002). Analysis on safety factor of slop by strength reduction FEM. *Chin. J. Geotech. Eng.* 24 (3), 343–346. doi:10.3321/j.issn:1000-4548.2002.03.017

Zheng, Y. R., Zhao, S. Y., and Zhang, L. Y. (2002). Slope stability analysis by strength reduction FEM. *Eng. Sci.* 4, 57–61+78. doi:10.3969/j.issn.1009-1742.2002.10.011

frontiers | Frontiers in Earth Science

TYPE Original Research
PUBLISHED 26 August 2022
DOI 10.3389/feart.2022.973205

OPEN ACCESS

EDITED BY
Xiaojun Guo,
Institute of Mountain Hazards and Environment (CAS), China

REVIEWED BY
Aiguo Xing,
Shanghai Jiao Tong University, China
Jiewei Zhan,
Chang'an University, China

*CORRESPONDENCE
Qiangong Cheng,
chengqiangong@swjtu.edu.cn

SPECIALTY SECTION
This article was submitted to Geohazards and Georisks, a section of the journal Frontiers in Earth Science

RECEIVED 19 June 2022
ACCEPTED 12 July 2022
PUBLISHED 26 August 2022

CITATION
Yang H, Xing B, Jiang H and Cheng Q (2022), Analogical model tests on repeated surficial failure of dry granular slopes confined by retaining walls. *Front. Earth Sci.* 10:973205. doi: 10.3389/feart.2022.973205

Analogical model tests on repeated surficial failure of dry granular slopes confined by retaining walls

Hufeng Yang[1], Bencong Xing[1], Hu Jiang[2] and Qiangong Cheng[1]*

[1]Faculty of Geosciences and Environmental Engineering, Southwest Jiaotong University, Chengdu, China, [2]Kunming Survey, Design and Research Institute Co, Ltd of CREEC, Kunming, China

In alpine and gorge regions, surficial failure of granular slopes has seriously affected infrastructure construction and the safe operation of transportation networks. This research focuses on dry granular slopes confined by retaining walls. Repeated surficial failure of granular slopes has been explored through indoor physical model tests. The results show that surficial failure presents low frequency and large scale for granular slopes dominated by coarse particles. The mass of debris that crosses retaining walls indicates activity level of granular slopes. When this mass for each surficial failure gradually decreases, it is highly likely that large-scale surficial failure will occur. As the amount of debris deposited on the slope increases, it is probable that the debris mass falling during a massive sliding event will be many times that of the previous sliding event. In engineering practice, it is necessary during road cleaning processes to record the volume of debris accumulated on the road. A continuous increase in the slope angle indicates a high probability of large-scale surficial failure. For each granular slope with a unique particle composition, there is a critical change rate for early warning of surficial failure, which can be determined by long-term monitoring.

KEYWORDS

analogical model test, surficial failure, granular slope, fractal dimension, activity level

Introduction

Granular slopes are widespread in dry-hot valleys, high altitude environments, high latitude regions, and high seismic activity zones (Gerber and Scheidegger, 1974; Statham, 1976; Curry and Morris, 2004; Pudasaini and Hutter, 2007; Sass and Krautblatter, 2007; Davies and McSaveney, 2009; Otto et al., 2009; Takagi et al., 2011; Luckman, 2013; Ye et al., 2019; de Sanjosé-Blasco et al., 2020; Xue et al., 2021). In a natural granular slope, with continual debris supply from the source area, volume of the granular slope will continue to increase during the extension phase (Figure 1). When debris accumulation reaches the source area, the slope is in the consolidation-and-stabilization phase (Figure 1A). In contrast to the natural granular slope, granular slope evolution leads

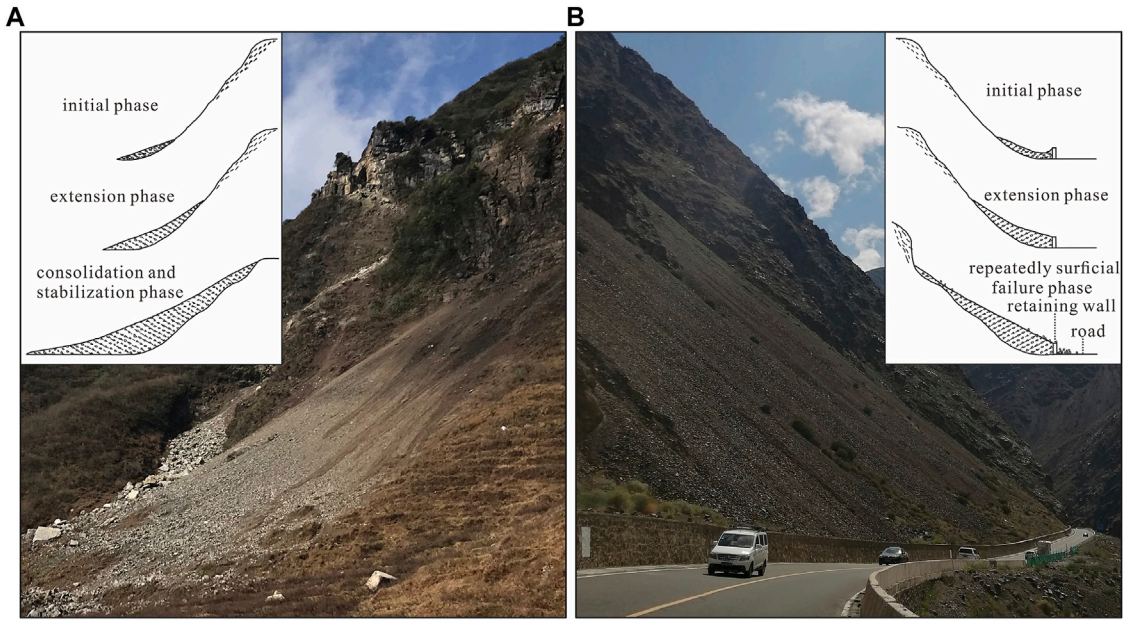

FIGURE 1
Natural granular slope **(A)** and granular slope confined by the retaining wall **(B)**.

to repeated surficial failure, due to the slope toe being confined by a retaining wall (Figure 1B). Generally, the mass of a single surficial failure is not very large. However, repeated surficial failure threatens construction and operation of roads and railways (Luo et al., 2018; Xing and Wang, 2019).

Generally, the granular slope remains mostly stable with the natural angle of repose (Curry and Morris, 2004; Bu et al., 2016; Zheng et al., 2019). The angle of repose is a key parameter for describing the motion state of granular systems and can be used as the boundary angle to distinguish the dynamic and static transformations of granular systems (Carson, 1977; Mehta and Barker, 1994; Liu et al., 2005). Surficial failure occurs when the slope angle of granular material accumulation is greater than the angle of repose (Kleinhans et al., 2011; Beakawi Al-Hashemi and Baghabra Al-Amoudi, 2018).

A model test is the main research method for studies on the process of granular slope failure (De Blasio and Sæter, 2009; Chen et al., 2011; Takagi et al., 2011). Generally, model test research on granular slopes does not conform to a strict geometric similarity with the prototype of slope in the field. However, an analogical model test is appropriate for the study of the evolution and failure process of granular slopes (De Blasio and Sæter, 2015). Most of the physical tests carried out in laboratories are simplified scale simulations, so the real failure characteristics cannot be reflected in terms of volume (Iverson et al., 2011; Bryant et al., 2015; Kesseler et al., 2018). However, the model test results can establish a close relationship between the experimental scale and realistic disaster behavior characteristics. According to the failure process emerging from analogical model tests, many failure models were proposed, such as retrogressive failure, progressive failure, and translational failure (Que et al., 2003; Wang et al., 2007; Zhang et al., 2008). Some failure models were proposed after considering inducing factors. These include the progressive supply-induced failure model, slope excavation-induced failure model, rockfall impact-induced failure model, and surface erosion-induced failure model (Zhang and Shu, 2017).

Activity level and surficial failure scale of granular slopes are the main factors in geo-disaster susceptibility and risk assessment. Therefore, this research focuses on granular slope confined by retaining walls. Based on the simulation of continuous debris supply from the source area as the result of physical weathering, accumulation processes of granular slopes were explored through indoor physical model tests. Repeated surficial failures of granular slopes composed of different particles were compared and analyzed to determine risk assessment and early warning ability for active granular slopes.

Model tests

Equipment design

The model test equipment was designed based on the general accumulation phases of granular slopes confined by retaining

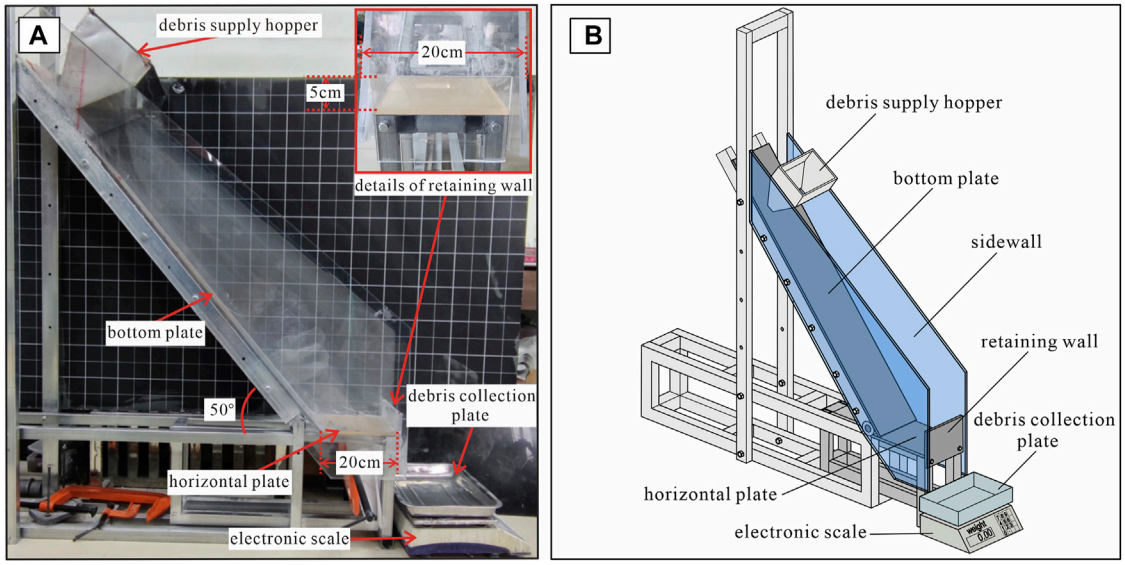

FIGURE 2
Model test equipment **(A)** photograph; **(B)** schematic diagram.

walls (Figure 1B), and followed previous model tests for granular slopes (De Blasio and Sæter, 2009; Takagi et al., 2011; He et al., 2012). The equipment included the following: debris supply hopper, inclined flume, horizontal flume, and debris collection plate (Figure 2). The debris supply hopper is designed to simulate the debris supply from the source area. A debris collection plate is used to collect debris across the retaining wall during surficial failure. The length of the horizontal flume and the height of the retaining wall are adjustable, in order to obtain different volumes of granular slopes. Based on the general geological model of granular slopes confined by a retaining wall in the field (Figure 1), a slope scale was designed with a 5-cm high retaining wall and a 20-cm long horizontal flume (Figure 2B).

Granular material

For preparation of the granular material for model tests, previous studies attempted to collect original granular material from the field to simulate the actual granular slope by conducting large-scale model tests (Wang et al., 2007; Zhang et al., 2008; He et al., 2012). However, a limited amount of granular materials cannot adequately replicate characteristics of the entire slope in the field. The process of rock weathering involves fractal dynamics. The defect structure of rock presents fractal characteristics (Bagde et al., 2002; Tu et al., 2005; Crosta et al., 2007). The evolution of rock fragmentation and weathering is essentially a fractal development process of rock damage and fragmentation. Therefore, fractal dimensions can be used to characterize the degree of rock damage and fracture (Tu et al., 2005). In the field, granules always present fractal features as weathering products from the source area of the granular slope (He et al., 2012). Therefore, in this research, the grain composition of the granule material used for the model test is based on the characteristics of the fractal self-similarity law.

Based on the mass-frequency fractal analysis of granular materials, the empirical relationship between grain size and frequency obeys the Weibull distribution (Turcotte, 1986) as shown in Eq. 1.

$$\frac{m(<r)}{m_t} = 1 - \exp\left[-\left(\frac{r}{\delta}\right)^n\right] \tag{1}$$

where m ($<r$) is mass of grain size$<r$, m_t is the total mass of granules, δ is a constant related to the mean size of grain, and n is an exponential constant.

Based on the description of δ by maximum limit particle size r_l, Tyler and Wheatcraft (1992) obtained the relation between m and r, with the introduction of fractal dimension (D).

$$\frac{m(<r)}{m_t} = \left(\frac{r}{r_l}\right)^{3-D} \tag{2}$$

With the same density of the granule, the m ($<r$) can be calculated under different fractal dimensions (D) as shown below:

$$m(<r) = m_t\left(\frac{r}{r_l}\right)^{3-D} \tag{3}$$

Usually, the fractal dimension of granules for landslides or granular slopes is between 0 and 3. For example, Crosta et al. (2007) described the fractal dimension as between 1.3 and 3.2. He

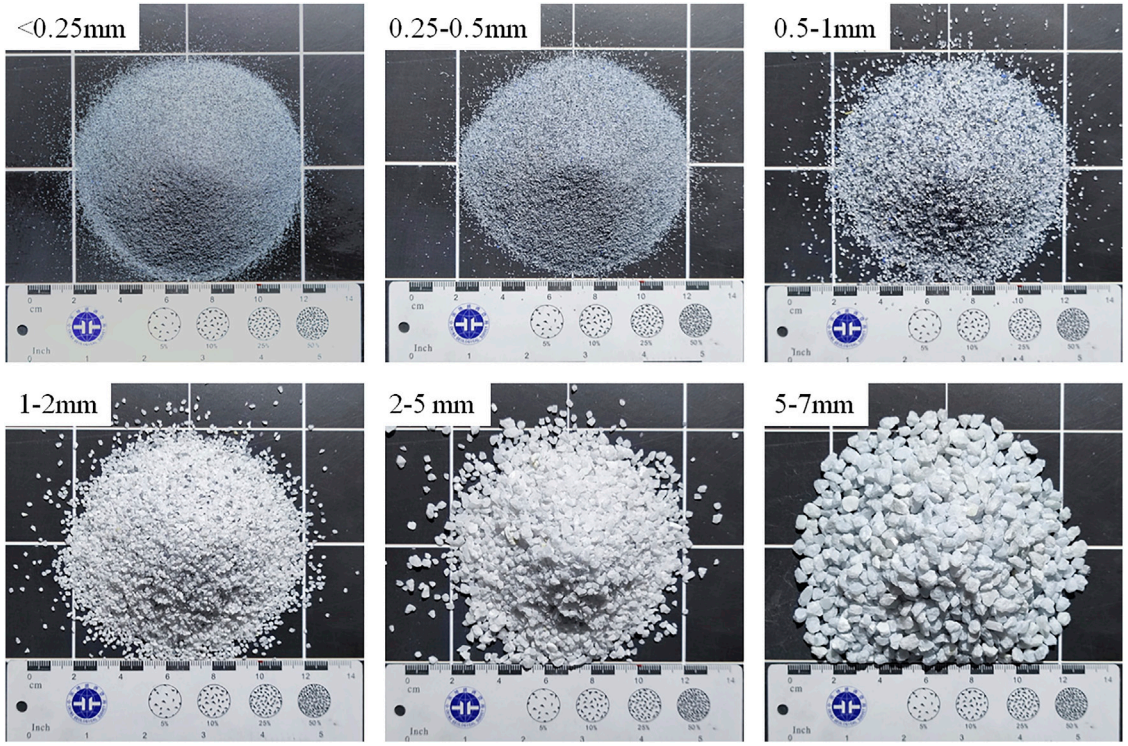

FIGURE 3
Different grain sizes of granular materials.

TABLE 1 Grain mass of each grain size with different fractal dimensions.

Grain size (mm)	Grain mass with different fractal dimensions (D) (g)			
	D = 1.5	D = 1.9	D = 2.3	D = 2.7
<0.25	270.0	1023.7	3881.9	14720.2
0.25–0.5	493.6	1170.7	2424.3	3402.5
0.5–1	1396.2	2509.4	3938.3	4188.9
1–2	3949.0	5379.1	6397.7	5157.2
2–5	18038.4	17543.2	14963.8	8690.6
5–7	15852.8	12373.9	8394.0	3840.6
Total	40000 g	40000 g	40000 g	40000 g

et al. (2012) observed that the fractal dimension of granular slopes is between 2 and 3 in Wenchuan County, Sichuan Provence, China. Therefore, model tests in this study focused on four values of fractal dimensions: D =1.5, 1.9, 2.3 and 2.7.

Quartz sand was selected for the granular material of the model test for the following reasons: (1) The irregular shape of calcium sand produced by mechanical crushing is generally similar to debris resulting from physical weathering. (2) Physical properties of calcium sand, such as density and natural angle of repose, are similar to debris originating from calcareous sandstone and granite in the field. According to the size of slope model, there are six kinds of grain size: <0.25 mm, 0.25–0.5 mm, 0.5–1 mm, 1–2 mm, 2–5 mm, and 5–7 mm (Figure 3).

For the preparation of granular material with different fractal dimensions, the grain mass of each grain size (<0.25 mm, 0.25–0.5 mm, 0.5–1 mm, 1–2 mm, 2–5 mm, and 5–7 mm) was calculated according to Eq. 3. Table 1 shows the mass of each

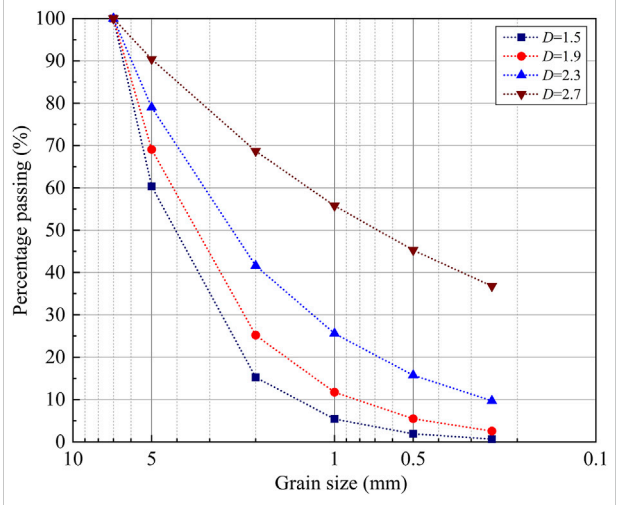

FIGURE 4
Grain size distribution curve of different fractal dimensions.

grain size per 40 kg of granular material with different fractal dimensions. The grain size distribution curves of the different fractal dimensions are shown in Figure 4. The fractal dimension represents the power law relationship between number-size and mass-size in granular systems (Bak et al., 1987, 1988; Tyler and Wheatcraft, 1992). A small fractal dimension means a high coarse particle size content and a low fine particle content in the system. On the other hand, when the fractal dimension is large, the content of coarse particles is low, and that of fine particles is high. Fundamentally, the fractal dimension controls the degree of self-similarity of the system through particle size. The purpose for this element of material preparation is to apply the new findings to the granular slope with similar fractal features.

Test procedure

This study focuses on the surficial failure of dry granular slopes with different fractal dimensions. First, the model test equipment was fixed as the design of the slope scale (Figure 2A). Then, fully blended grains with designed fractal dimensions (D) were supplied through a hopper at the top of the slope to simulate debris supply by rock weathering at the source area. Debris accumulated at the toe of the inclined flume, and then the space behind the retaining wall was filled with granules. With a continuous supply of debris, the granular slope will extend upward until the slope angle reaches the natural angle of repose (Figure 5). The purpose of the accumulation process was to simulate the formation of a granular slope in the field.

The granular slope will be in a critical state when the slope angle reaches the natural angle of repose. The continuous supply of granules triggered surficial failure. The first obvious surficial failure was defined as the initial state for model tests. Then, the mass of the debris supply was measured during continuous debris supply through the hopper. Surficial failure was recorded using a camera.

To compare the geometric features of granular slopes before and after surficial failure, the 3D slope surface was built based on the oblique photogrammetry method for representative model tests of four types of slope grain composition (D = 1.5, 1.9, 2.3, and 2.7). First, photographs of slope surface from multiple orientations were taken with a single CCD camera. Then, these photos were imported into the automatic 3D photogrammetry software ContextCapture 4.0 for aerial triangulation to reconstruct the 3D topography of the slope surface. Various data formats, such as digital surface models (DSMs) and 3D point clouds, were generated from the reconstructed 3D models, allowing the acquisition of surface morphologies, isopach maps, and geometric parameters (Li et al., 2021). With its high resolution at the subpixel level, the accuracy of this method in all tests was within 2 mm. Debris running over the retaining wall was collected during each surficial failure using a pallet placed on an electronic scale. The mass of the granular material was recorded at the end of the surficial failure when the reading was stable. The measurements and observations were repeated more than 60 times in order to reveal the general features of repeated surficial failure of the granular slope. It is important to emphasize that the measurements and observations were repeated more than 90 times for the granular slope with D = 1.5, due to the longer interval period of large-scale surficial failure.

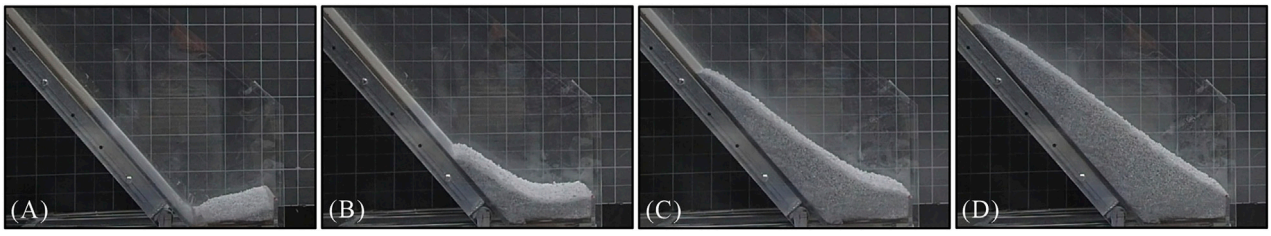

FIGURE 5
Development processes of a granular slope confined by a retaining wall **(A)** debris accumulation behind the wall; **(B)** debris accumulation on the slope; **(C)** granular slope extension; **(D)** critical slope angle.

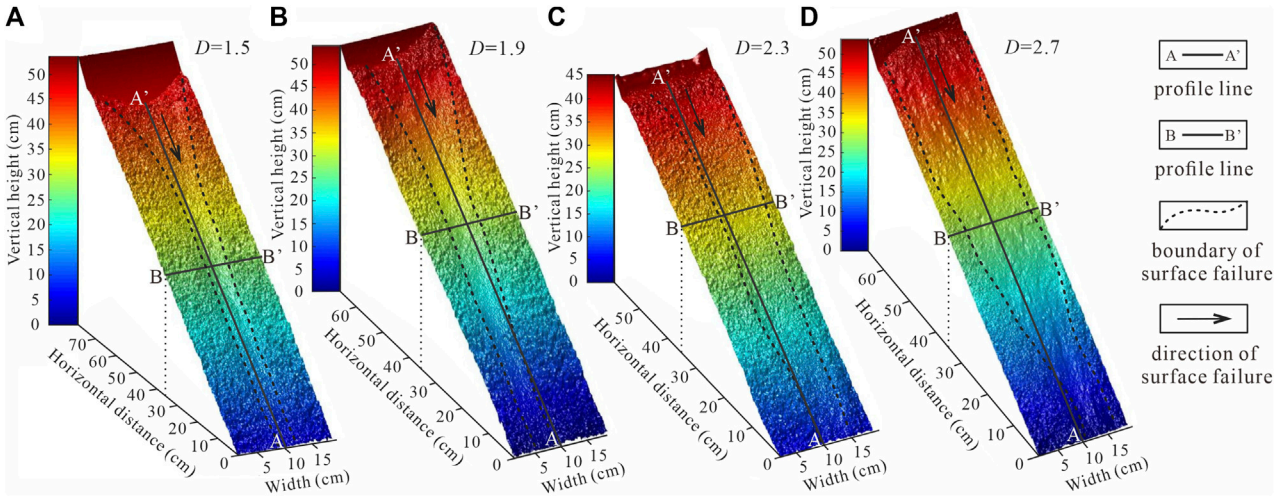

FIGURE 6
Surficial failure of granular slopes with different fractal dimensions **(A)** D = 1.5; **(B)** D = 1.9; **(C)** D =2.3; **(D)** D = 2.7.

Results

Features of surficial failure

Figure 6 shows the 3D slope surface was built based on the oblique photogrammetry method for representative model tests of four kinds of slope grain composition (D = 1.5, 1.9, 2.3, and 2.7). For the granular slopes with a small fractal dimension (D = 1.5 and 1.9), most of the remaining debris accumulated at the upper part of the slope. In contrast, the spatial distribution of grains was relatively uniform on the entire slope surface for the granular slopes with large fractal dimensions (D = 2.3 and 2.7) (Figure 7). The locations of the longitudinal sections (A-A') are presented in Figure 6. The continuous increase of top load for the granular slopes with small fractal dimensions (D = 1.5 and 1.9) induced sudden surficial failure. The translational failure is more general for granular slopes with large fractal dimensions (D = 2.3 and 2.7).

After the sudden occurrence of surficial failure, sliding channels appeared on the slope surface for the granular slopes with small fractal dimensions (D = 1.5 and 1.9) (Figure 6). The morphological characteristic of channels presented as funnel shapes with wide tops and narrow bottoms. The width of the channel also increased gradually with an increase in fractal dimension. The surficial failure of granular slopes with large fractal dimensions (D = 2.3 and 2.7) resulted in a shallow sliding of the entire slope surface. Figure 8 shows the transverse sections (B-B') for granular slopes with different fractal dimensions, which were located at a horizontal distance of 35 cm behind the retaining wall. Generally, the roughness of the granular slope decreases with an increase in fractal dimension. This result is related to the proportion of fine particles. Since fine particles are the main part of the granular slope with large fractal dimensions, they can fill and level the jagged surface to reduce roughness.

The roughness of the channel bottom significantly decreased after surficial failure (Figure 8). Therefore, debris supplied for the source area easily slid downward along the channel. In the beginning, the slope was without accumulation ability. During the channel flow of grains, the width and depth of the channel continued to increase due to lateral and vertical erosion. Finally, granular flow fingering appeared on the slope surface, due to its low roughness. In this phase, more and more debris accumulated on the slope surface, resulting in changes in slope topography. Surficial failure of the granular slope was the result of the evolution process of slopes, with continuous accumulation of debris on the slope surface. When the slope angle reached the repose of the angle, the slope reached a critical state. In that condition, even a small amount of continuous debris accumulation will trigger surficial failure. Numerous particles flowed downward and the slope angle decreased by 1–3°.

Surficial failure mass

Surficial failure of the granular slope will suddenly occur with continuous debris supply from the source area. Figure 9 shows the mass of the surficial failure of granular slopes with different fractal dimensions. The horizontal axis indicates the sequence of surficial failures. Each number presents one obvious surficial failure during an entire test process. The vertical axis indicates the mass of grains that crossed the retaining wall during surficial failure. Material sliding during surficial failure of the granular slope leads to different areas of collapse, which can be expressed

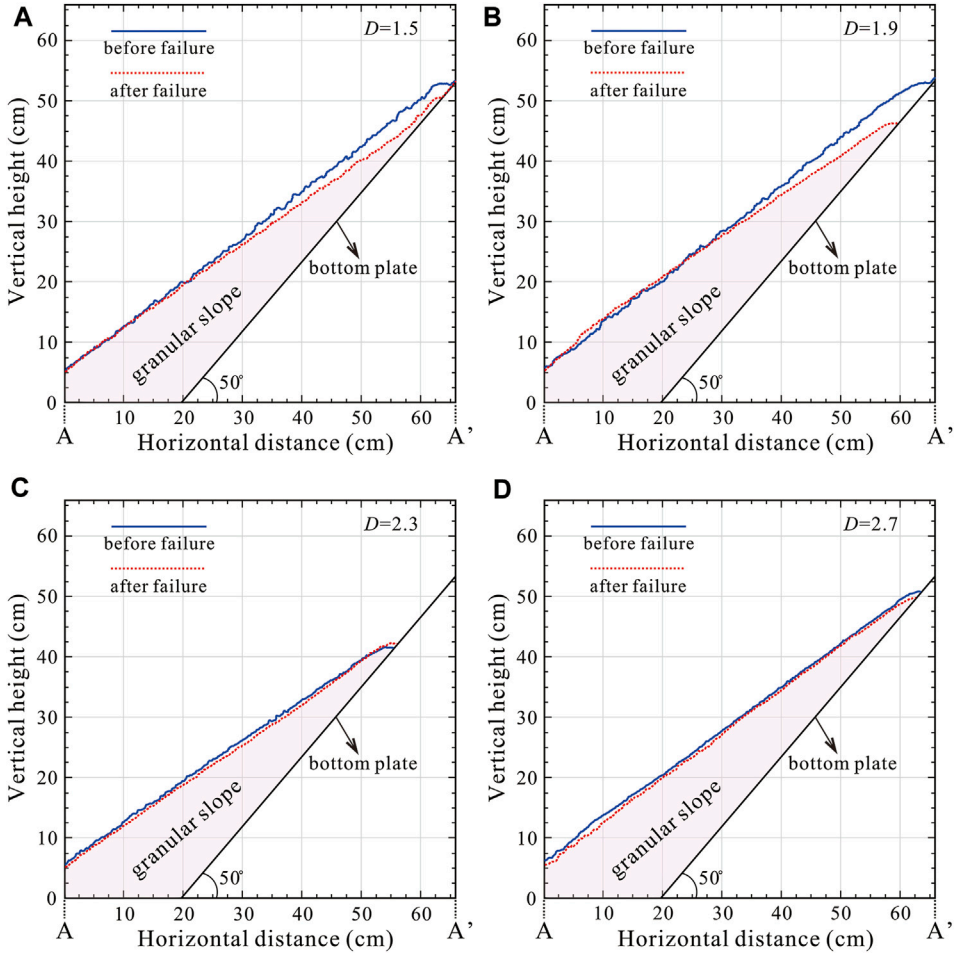

FIGURE 7
Longitudinal sections for granular slopes with different fractal dimensions before and after surficial failure **(A)** D = 1.5; **(B)** D = 1.9; **(C)** D =2.3; **(D)** D = 2.7.

by scale or area, both of which are related to the mass of surficial failure. Large scale, or large area, usually corresponds to a greater mass of surficial failure. In Figure 9, peak values represent relatively large-scale surficial failures of the granular slope. Meanwhile, low values at the bottom of the curve represent the small-scale surficial failures. Therefore, repeated surficial failures can be observed based on fluctuation of the curve.

For the granular slope with D = 1.5, there were several large-scale surficial failures. The maximum mass of surficial failure reached 3150 g. After a large-scale surficial failure, the granular slope is mainly dominated by a small-scale surficial failure. Small-scale surficial failure occurs approximately 20 times between two occurrences of relatively large-scale surficial failure.

For the granular slope with D = 1.9, the frequency of relatively large-scale surficial failures increased compared with the granular slope with D = 1.5. However, the peak values were smaller; that is, the sliding scale of surficial failure became smaller. Small-scale surficial failure occurred approximately 10 times between two incidents of relatively large-scale surficial failure.

For granular slopes with D = 2.3 and 2.7, the frequency of surficial failures demonstrably increased compared with the granular slopes with D = 1.5 and 1.9. Granular slopes were mainly dominated by small-scale surficial failures (peak values were less than 1260 and 630 g, respectively).

Slope angle

Fluctuation of the slope angle of granular slopes with different fractal dimensions is shown in Figure 9. For the granular slopes with D = 1.5 and 1.9, the fluctuation of the slope angle is consistent with the mass of surficial failure. The slope angle continuously increased before the occurrence of

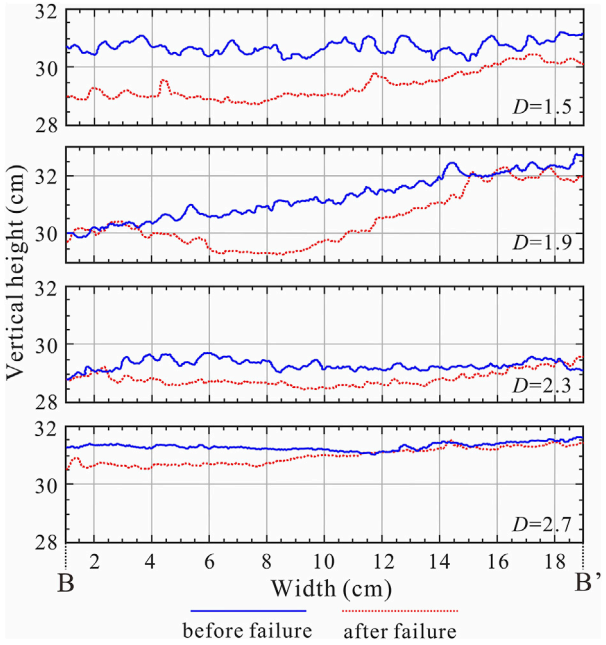

FIGURE 8
Transverse sections for granular slopes with different fractal dimensions before and after surficial failure.

large-scale surficial failure. After surficial failure, the slope angle became smaller. When the slope angle began to increase again, it indicated that the next large-scale slope failure would occur soon. The fluctuation range of the granular slope with D = 1.5 was larger than the slope with D = 1.9. The fluctuation ranges of the slope angle were 3.3° and 2.1°, respectively.

However, for the granular slopes with D = 2.3 and 2.7, the fluctuation of the slope angle did not consistently correspond to the mass of surficial failure. The fluctuation range of the slope angle was significantly less than the granular slopes with small fractal dimensions. The fluctuation ranges of the slope angle for granular slopes with D = 2.3 and 2.7 were 1.3° and 0.7°, respectively.

Mass accumulation

The mass of accumulation is defined as the mass of the debris supply minus the mass of surficial failure, that is, the net mass of debris accumulation on the slope surface. When the mass of accumulation is a positive value, it means that more granules deposit on the slope surface; that is, the total volume of granular slope increases. Conversely, a negative value means that more

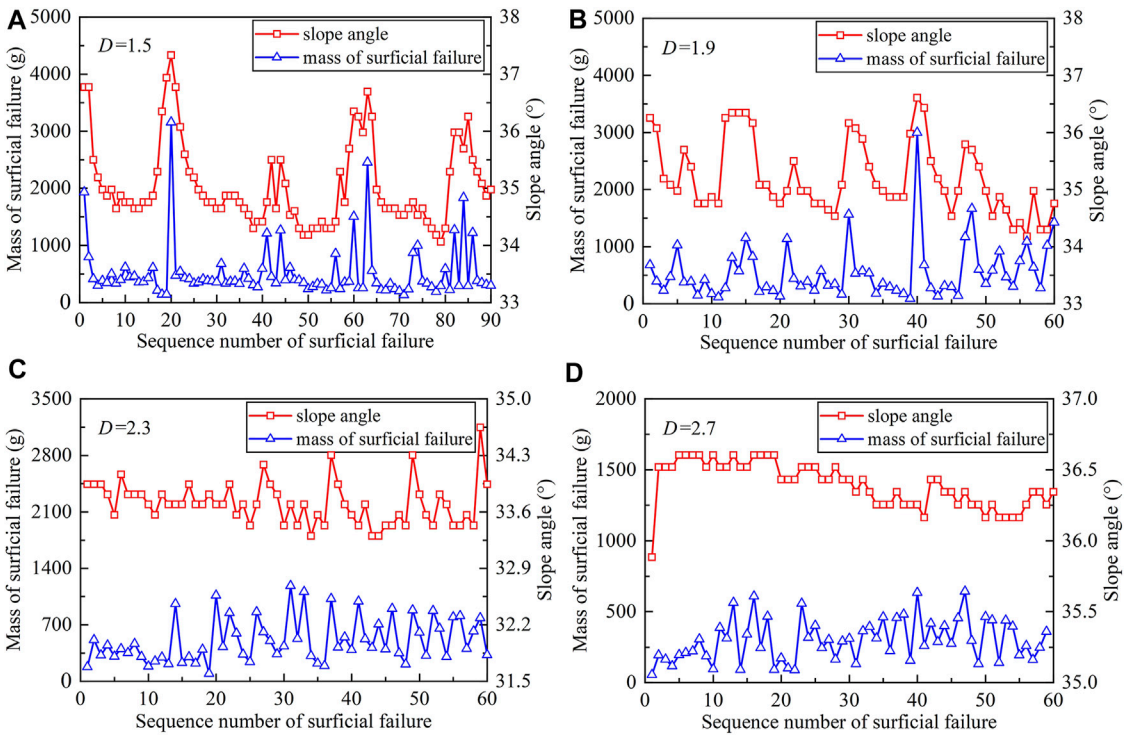

FIGURE 9
Mass of surficial failure and fluctuation of the slope angle for granular slopes with different fractal dimensions **(A)** D = 1.5; **(B)** D = 1.9; **(C)** D =2.3; **(D)** D = 2.7.

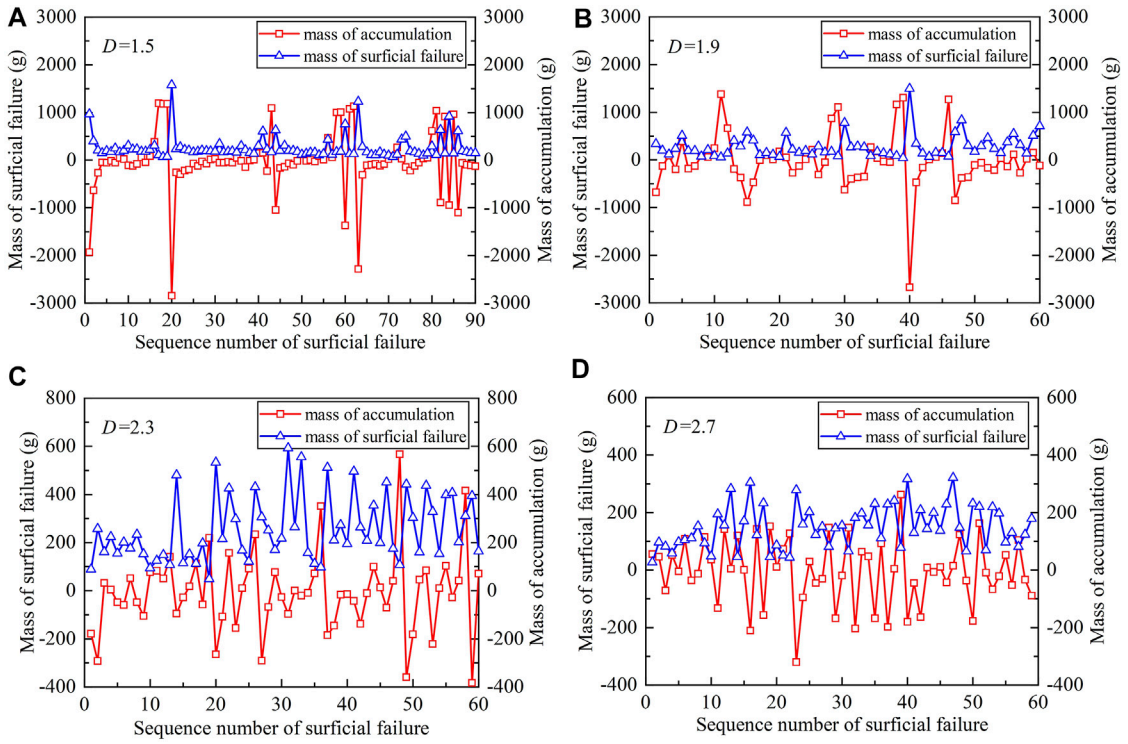

FIGURE 10
Mass of accumulation and surficial failure for granular slopes with different fractal dimensions **(A)** D = 1.5; **(B)** D = 1.9; **(C)** D =2.3; **(D)** D = 2.7.

granules cross over the retaining wall, that is, the total volume of the granular slope decreases.

When the mass of accumulation becomes a negative value, the value is less than −100 g, and it is defined as one occurrence of surficial failure. For the granular slope with D = 1.5, a relatively large-scale surficial failure occurred five times out of 90 total surficial failures. The interval mass of grain supply between these five times of relatively large-scale surficial failure was 10247.5, 10143.5, 10801.5, and 11232.5 g, respectively. For the granular slope with D = 1.9, relatively large-scale surficial failure occurred seven times during 60 total surficial failures. The interval mass of grain supply for these seven times of relatively large-scale surficial failure were 2278.0, 5111.0, 2688.5, 5146.5, 4853.0, 4288.5, and 7292.5 g, respectively. For the granular slopes with D = 2.3 and 2.7, the interval mass of grain supply was significantly reduced. Generally, the interval mass of the grain supply decreased with the increase of fractal dimensions (Figure 10). This indicates that the capacity of grain accumulation for the granular slope with a large fractal dimension is limited, resulting in a high frequency of small-volume surficial failure.

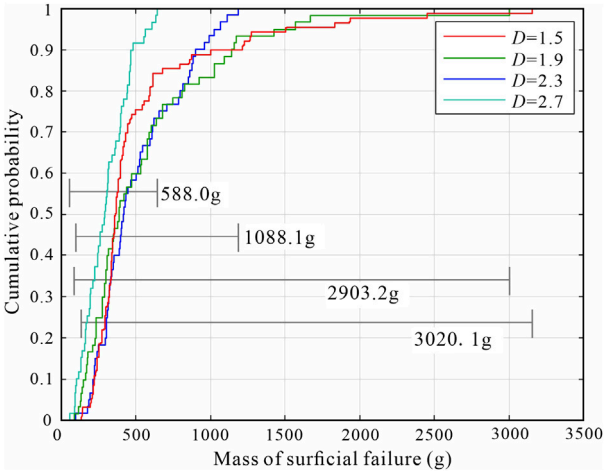

FIGURE 11
Cumulative distribution probability of the mass of surficial failure.

Discussion

Correlation between particle size and surficial failure mass

The cumulative distribution probability of a mass of surficial failure presents the variation of debris mass during surficial failure and the probability of surficial failure for various granular slope debris compositions (Figure 11). The minimum mass in surficial failure was about 100 g for four kinds of granular slopes (D = 1.5, 1.9, 2.3, and 2.7). As seen, the difference in debris composition did not affect the debris mass of small-scale surficial failure. However, the maximum debris mass of surficial failure decreased from 3155.3 to 643.4 g, which was negatively correlated with the increase in fractal dimension. In addition, when slope fractal dimension D is 1.5, 1.9, 2.3, and 2.7, the mass range of surficial failure was 3020.1, 2903.2, 1088.1, and 588.0 g, respectively. The fractal dimension obviously controls the dispersion degree of slip failure. With the increase in slope fractal dimension, the dispersion degree of slip mass decreased significantly, and the probability of a mass collapse event also decreased.

Energy is transferred and consumed by friction and collision between granular particles (Drake, 1990; Campbell, 2006; Forterre and Pouliquen, 2008). Surficial failure is the accumulation and release process of particles on the slope surface. Therefore, based on the change in particle size, the reason for the difference in surficial failure mass can be explained from the perspective of energy dissipation. Particle size obviously controls particle flow behavior, such as shear rate, flow velocity, and vibration state (Iverson, 1997; Hsu et al., 2014; Dai et al., 2022). In these mode tests, the change in particle size significantly changed the range of transverse failure of the slope body in the sliding process, and the width of the sliding groove expanded laterally with the increase in fine particle content (Figure 6). This shows that particle size is an important factor in determining failure mode. The smaller the particle size, the smaller the vibration of the particles in the vertical direction when flow occurs. In the particle contact process, because the oscillation penetrates fewer particles inside the flow layer, less energy is consumed when moving the same distance, so fine particle flow has higher mobility (Cagnoli and Romano, 2010, 2012; Li et al., 2021). The experimental results are in line with the theoretical explanation. When the slope fractal dimension is large, fine particles dominate the failure mode of the slope body. In this state, particles have better fluidity and higher mobility. The high frequency of surficial failure leads to the slope being unable to accumulate the debris-bearing large mass, resulting in a small mass of surficial failure. With the decrease in fractal dimension, the main composition of the granular slope changes from fine particles to coarse particles. The fluidity and mobility of particles decrease gradually, so that the slope can carry more mass debris, the surficial failure mass range can be continuously expanded, and the probability of mass failure increases.

The reason for the mass difference in surficial failure can also be explained from a mechanics viewpoint. When the fractal dimension D is 1.5, 1.9, 2.3, and 2.7, the corresponding maximum load mass was 3155.3, 2995.5, 1186.4, and 643.4 g, respectively. With the increase in fractal dimension, the maximum debris mass that the slope can carry decreases; that is, the maximum shear strength of the slope decreases gradually with the increase in the composition of fine particles. This means that the increase of fine particles reduces the contact shear behavior between particles, so that the shear strength in the slope decreases with the increase of fractal dimension, resulting in a decrease in the mass range of slippage debris on the slope surface. According to studies by scholars in the field, the shear strength inside particles decreases with the increase in fractal dimension (Lai et al., 2021), which accounts for the difference in slip quality from the variation characteristics of shear strength.

Evaluation of the activity level of granular slopes based on the mass of surficial failure

The accumulation curve is obtained by adding the mass of each surficial failure (Figure 12). Fluctuation in the accumulation curve presents three different characteristics: steady increasing stage, slowdown increasing stage, and sudden increasing stage.

The steady increasing stage presents a similar mass of debris crossing the retaining wall for each surficial failure. The slope of the accumulative curve is basically unchanged. This phenomenon is reflected in the actual slope, as the volume of debris accumulated on the road does not change significantly for each surficial failure.

The slowdown increasing stage shows that debris crossing the retaining wall in each surficial failure gradually decreased, and the slope of the accumulative curve decreased and presented a convex shape. At this stage, the particles on the slope surface have a relative movement trend under the force of gravity, which led the particles to closely occlude. Granular debris aggregated on the slope surface to form an arch bulge. The slope angle exceeded the natural angle of repose. In the process of an arch forming on the slope surface, surficial failure occurred in the non-arch part or part of the arch body due to reaching critical stress. However, the scale of failure and the mass of slippery debris on the slope surface are usually smaller than before because the arching effect bears part of the stress. This indicates that debris was increasingly deposited on the slope surface. Corresponding to the continuous negative process of slip debris in Figure 10, it is also an indication of large-scale surficial failure on the granular slope.

The sudden increasing stage led to a large-scale surficial failure of the granular slope. The accumulative curve is characterized by a sudden increase in debris mass

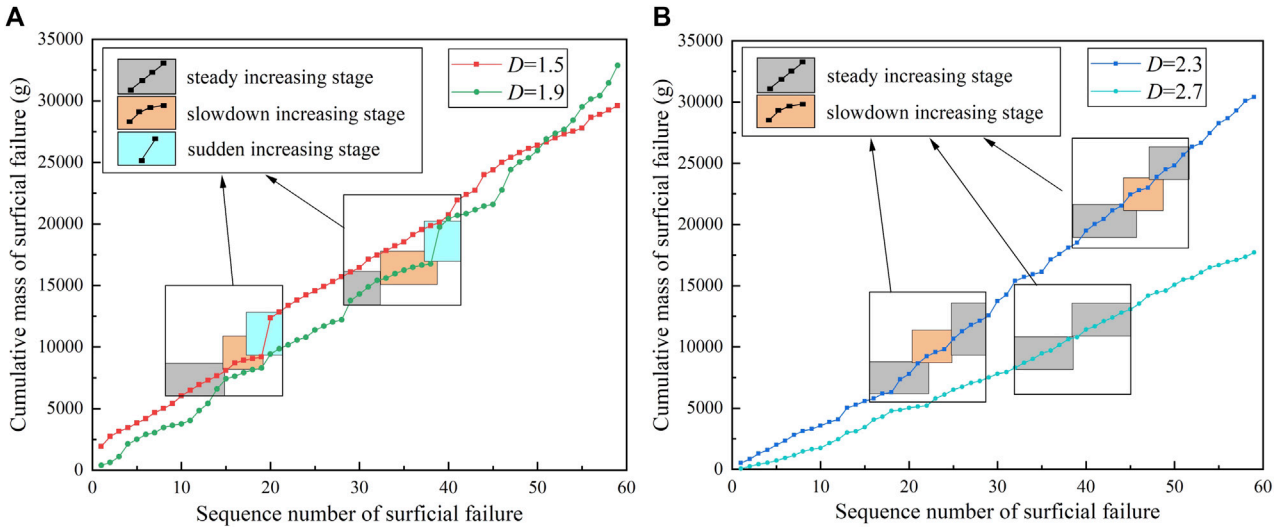

FIGURE 12
Cumulative curve of the mass of surficial failure **(A)** D = 1.5 and 1.9; **(B)** D =2.3 and 2.7.

(Figure 12A). In the process of large-scale surficial failure, there will be strong collision and shear between particles, which will increase vertical vibration (Cruden and Hungr, 1986; Chen et al., 2014; Wang et al., 2015). This vibration action also provides space for particle migration. In the vertical direction, slope particles are sorted to form the reverse grain sequence of the accumulation body. After the sliding event, a slippage groove formed by a layer of fine particles can be observed in the middle of the slope surface (Figure 6). Due to the vertical sorting of particles, the fine particles formed in the middle of the slope become the soft surface on the slope, which reduces the shear strength of the slope as a whole and promotes the occurrence of a large-scale sliding phenomenon.

The failure mode of the granular slope dominated by fine particles obviously differs from that of the one dominated by coarse particles. In the failure process, the events in the large-scale surficial failure disappear, the slip weakening stage is gradually shortened, and the slip stage gradually changes from the original three stages to the steady increasing stage (Figure 12B). Symptoms of the destruction phenomenon gradually disappeared, and the slip gradually turned into a high-frequency event.

Therefore, the mass of debris crossing the retaining wall indicates the activity level of the granular slope, especially for one with a small fractal dimension. In engineering practice, recording the volume date of debris accumulated on the road during the road-cleaning process is required. When the mass of debris for each surficial failure gradually decreases, it is highly likely that large-scale surficial failure will occur. As the amount of debris deposited on the slope increases, it is highly likely that the mass of debris falling during massive slides will be many times that of the previous slide.

Evaluation of activity level of granular slopes based on slope angle

Slope angle increases gradually in successive small-scale slides before large-scale surficial failure of the granular slope occurs. After surficial failure, the slope surface is in an unstable, easily disturbable state, and the slope angle gradually decreases. As seen if Figure 9A, slope angle was continuous (Figure 9A). Therefore, the increase in slope angle means that the probability of the next large-scale surficial failure is greater, and the continuous increase in the slope angle indicates that the mass of surficial failure from the slip event is also larger. Here, the variation characteristics of the slope angle behavior can be studied by analyzing the rate of slope angle change, which is defined as the change value of the slope angle in two adjacent slip failure events (Figure 13).

When coarse particles dominate the slope surface sliding failure mode, such as fractal dimension D = 1.5, the rate of slope angle change has obvious periodicity, showing the alternating characteristics of weak and strong fluctuation periods (Figure 13A). In the weak fluctuation period, the rate of slope angle change fluctuated slightly up and down around zero, slope was relatively stable, the scale of surface slides was small, and there was not significantly different in debris quality each time. The strong fluctuation period was composed of single or multiple abrupt fluctuation periods, in which the fluctuation range of the rate of slope angle change increased several times that of the weak fluctuation period, and slope angle activity increased greatly. The entire process was accompanied by the occurrence of large-scale slides, which is the most dangerous stage of slope surficial failure.

The single strong fluctuation cycle of the slope angle can be divided into four stages: rapid growth period, growth-and-

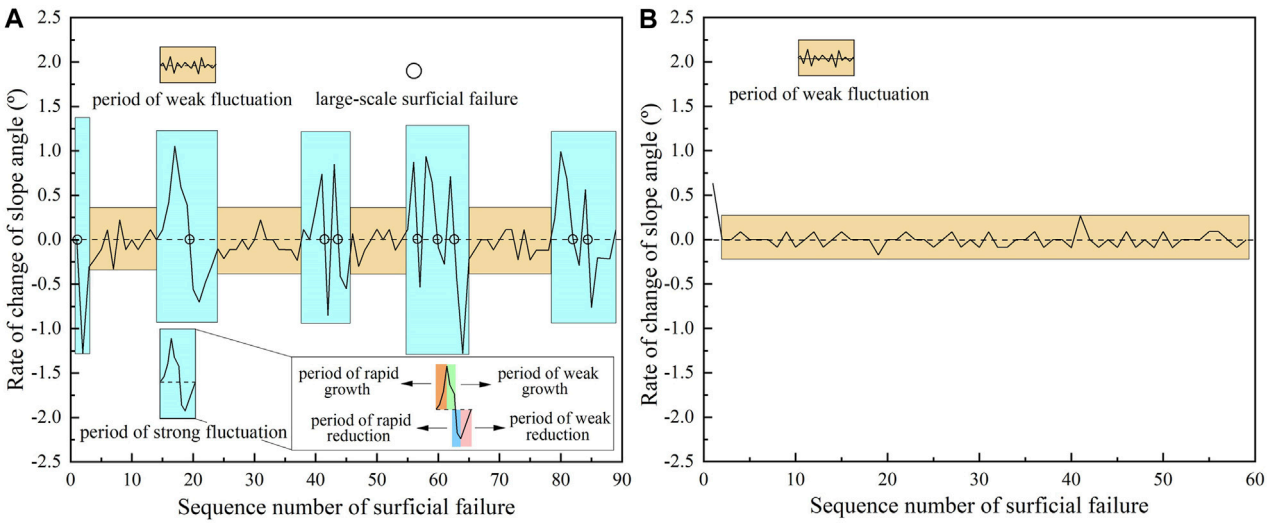

FIGURE 13
Rate of slope angle change **(A)** D = 1.5; **(B)** D = 2.7.

decline period, rapid decrease period, and decrease-and-decline period. The rapid growth period corresponds to the rapid increase in the slope angle during the early formation of slope surface arch. In the weak growth period, the increasing speed of the slope angle gradually decreases, and the accumulation state of the slope surface gradually approaches the critical state. When the rate of slope angle change drops to zero, it reaches the limit state of the slope surface, which is usually the node where large-scale slip events occur. After large-scale surficial failure, the rate of slope angle change enters a period of rapid decrease, which is also related to the fine particle layer generated on the slope surface due to sorting. From the foregoing discussion, we know that fine particles increase with the decrease in the shearing strength of the surface of the particle layer of the particle migration rate. The fine particle layer disappeared gradually with the addition of debris at the top of the slope, and the sliding stage entered the weakening stage. The rate of slope angle change increases with a negative value, and the decreasing rate of slope angle slows to zero. Then, the slope surface reaches a stable state and starts to accumulate particles again, and the rate of slope angle change repeats into the next weak fluctuation cycle.

Compared with the slope surface slide failure dominated by coarse particles, the one dominated by fine particles had only a weak fluctuation period, and the rate of slope angle change only fluctuated around the zero value, without a sudden increase or decrease (Figure 13B). The decrease in coarse particles in the slope structure is the main reason for the disappearance of a strong fluctuation period, which causes the bearing capacity of the slope to decrease and leads to the accumulation of large debris, and a small amount of debris will lead to slip failure. Therefore, surficial failure dominated by fine particles occur most frequently.

The aforementioned analysis demonstrates that the change rate of the slope angle for the granular slope has a natural periodic law. Monitoring the slope angle can determine the state of the granular slope and help prevent and/or provide early warning of surface failure. For example, in the slope structure composed mainly of coarse particles, it can be inferred that the slope of coarse particles is in a period of strong fluctuation, according to the change in slope angle. Growth and weakness periods during strong fluctuation predict the occurrence of large-scale events, and corresponding inducing measures can be taken in advance to avoid or reduce the disastrous impact of slides.

Conclusion

This research focuses on dry granular slopes confined by retaining walls. Based on the simulation of continuous debris supply from the source area as a result of physical weathering, repeated surficial failure of granular slopes with different fractal dimensions was compared and analyzed to understand failure features and evaluate their activity level, which can be summarized as follows:

1) Repeated surficial failure showed different features for granular slopes with different particle compositions. When fine particles dominated the granular slope, surficial failure presented high frequency and small scale. On the other hand, surficial failure presented low frequency, and large scale, for granular slopes dominated by coarse particles.

2) Mass of debris crossing the retaining wall indicated activity level of the granular slope, especially for the one dominated by coarse particles. When mass of debris for each surficial failure gradually decrease, it is highly likely that large-scale surficial failure will occur. As the amount of debris deposited on the slope increases, it is highly probable that the mass of debris falling during a massive slide will be many times that of the previous slide. In engineering practice, it is necessary to record the volume of debris accumulated on the road during road cleaning.
3) It is possible to have early warning of repeated surficial failures of granular slopes, based on monitoring the change rate of the slope angle, especially for granular slopes dominated by coarse particles. Continuous increase in slope angle indicates a high probability of large-scale surficial failure. For each granular slope with a unique particle composition, there is a critical change rate for early warning of surficial failure, which can be obtained by long-term monitoring.

Data availability statement

The original contributions presented in the study are included in the article/supplementary material. Further inquiries can be directed to the corresponding author.

Author contributions

HY: conceptualization, methodology, data curation, writing—original draft, and formal analysis. BX: conceptualization, methodology, and formal analysis. HJ: conceptualization, methodology, and formal analysis. QC: conceptualization, methodology, and formal analysis.

Funding

This work was supported by the Second Tibetan Plateau Scientific Expedition and Research (STEP) program (Grant No. 2019QZKK0905) and the National Natural Science Foundation of China (Grant Nos. 41941017, 41877226, and 41807248).

Conflict of interest

Author HJ is employed by Kunming Survey, Design and Research Institute Co., Ltd. of CREEC.

The remaining authors declare that the research was conducted in the absence of any commercial or financial relationships that could be construed as a potential conflict of interest.

Publisher's note

References

Bagde, M. N., Raina, A. K., Chakraborty, A. K., and Jethwa, J. L. (2002). Rock mass characterization by fractal dimension. *Eng. Geol.* 63 (1–2), 141–155. doi:10.1016/S0013-7952(01)00078-3

Bak, P., Tang, C., and Wiesenfeld, K. (1988). Self-organized criticality. *Phys. Rev. A* 38 (1), 364–374. doi:10.1103/physreva.38.364

Bak, P., Tang, C., and Wiesenfeld, K. (1987). Self-organized criticality: An explanation of the 1/f noise. *Phys. Rev. Lett.* 59 (4), 381–384. doi:10.1103/physrevlett.59.381

Beakawi Al-Hashemi, H. M., and Baghabra Al-Amoudi, O. S. (2018). A review on the angle of repose of granular materials. *Powder Technol.* 330, 397–417. doi:10.1016/j.powtec.2018.02.003

Bryant, S. K., Take, W. A., and Bowman, E. T. (2015). Observations of grain-scale interactions and simulation of dry granular flows in a large-scale flume. *Can. Geotech. J.* 52 (5), 638–655. doi:10.1139/cgj-2013-0425

Bu, X. H., Fu, R. H., Li, J. D., and Huang, Y. (2016). Internal factors of the failure of granular mixtures slope. *J. Yangtze River Sci. Res. Inst.* 33 (9), 116–120. doi:10.11988/ckyyb.20150606

Cagnoli, B., and Romano, G. P. (2010). Effect of grain size on mobility of dry granular flows of angular rock fragments: An experimental determination. *J. Volcanol. Geotherm. Res.* 193 (1–2), 18–24. doi:10.1016/j.jvolgeores.2010.03.003

Cagnoli, B., and Romano, G. P. (2012). Granular pressure at the base of dry flows of angular rock fragments as a function of grain size and flow volume: A relationship from laboratory experiments. *J. Geophys. Res.* 117, B10202. doi:10.1029/2012JB009374

Campbell, C. S. (2006). Granular material flows – an overview. *Powder Technol.* 162 (3), 208–229. doi:10.1016/j.powtec.2005.12.008

Carson, M. A. (1977). Angles of repose, angles of shearing resistance and angles of talus slopes. *Earth Surf. Process.* 2, 363–380. doi:10.1002/esp.3290020408

Chen, R. H., Kuo, K. J., Chen, Y. N., and Ku, C. W. (2011). Model tests for studying the failure mechanism of dry granular soil slopes. *Eng. Geol.* 119 (1-2), 51–63. doi:10.1016/j.enggeo.2011.02.001

Chen, T. C., Lin, M. L., and Wang, K. L. (2014). Landslide seismic signal recognition and mobility for an earthquake-induced rockslide in tsaoling, taiwan. *Eng. Geol.* 171, 31–44. doi:10.1016/j.enggeo.2013.11.018

Crosta, G. B., Frattini, P., and Fusi, N. (2007). Fragmentation in the val pola rock avalanche, Italian alps. *J. Geophys. Res.* 112, F01006. doi:10.1029/2005JF000455

Cruden, D. M., and Hungr, O. (1986). The debris of the frank slide and theories of rockslide–avalanche mobility. *Can. J. Earth Sci.* 23 (3), 425–432. doi:10.1139/e86-044

Curry, A. M., and Morris, C. J. (2004). Lateglacial and holocene talus slope development and rockwall retreat on mynydd du, UK. *Geomorphology* 58 (1–4), 85–106. doi:10.1016/S0169-555X(03)00226-5

Dai, B. B., Wu, F. Y., Zhong, W. T., Shi, Y. H., Qin, J. T., Yang, J. J., et al. (2022). Particle sorting in scree slopes: Characterization and interpretation from the micromechanical perspective. *JGR. Earth Surf.* 127 (5), e2021JF006372. doi:10.1029/2021JF006372

Davies, T. R., and McSaveney, M. J. (2009). The role of rock fragmentation in the motion of large landslides. *Eng. Geol.* 109 (1–2), 67–79. doi:10.1016/j.enggeo.2008.11.004

De Blasio, F. V., and Sæter, M. B. (2009). Small-scale experimental simulation of talus evolution. *Earth Surf. Process. Landforms* 34, 1685–1692. doi:10.1002/esp.1861

De Blasio, F. V., and Sæter, M. B. (2015). Dynamics of grains falling on a sloping granular medium: Application to the evolution of a talus. *Earth Surf. Process. Landforms* 40 (5), 599–609. doi:10.1002/esp.3655

de Sanjosé-Blasco, J. J., López-González, M., Alonso-Pérez, E., and Serrano, E. (2020). Modelling and terrestrial laser scanning methodology (2009–2018) on debris cones in temperate high mountains. *Remote Sens. (Basel).* 12, 632. doi:10.3390/rs12040632

Drake, T. G. (1990). Structural features in granular flows. *J. Geophys. Res.* 95 (B6), 8681. doi:10.1029/JB095iB06p08681

Forterre, Y., and Pouliquen, O. (2008). Flows of dense granular media. *Annu. Rev. Fluid Mech.* 40 (1), 1–24. doi:10.1146/annurev.fluid.40.111406.102142

Gerber, E., and Scheidegger, A. E. (1974). On the dynamics of scree slopes. *Rock Mech.* 6 (1), 25–38. doi:10.1007/bf01238051

He, N., Fu, R. H., Bu, X. H., Wang, L. Y., Li, C., Deng, M. W., et al. (2012). An experimental study on movement and accumulation characteristics of the sand-sliding slope. *J. Geol. Hazard. Environ. Preserv.* 23 (1), 50–53. doi:10.3969/j.issn.1006-4362.2012.01.010

Hsu, L., Dietrich, W. E., and Sklar, L. S. (2014). Mean and fluctuating basal forces generated by granular flows: Laboratory observations in A large vertically rotating drum. *J. Geophys. Res. Earth Surf.* 119 (6), 1283–1309. doi:10.1002/2013JF003078

Iverson, R. M., Reid, M. E., Logan, M., LaHusen, R. G., Godt, J. W., Griswold, J. P., et al. (2011). Positive feedback and momentum growth during debris-flow entrainment of wet bed sediment. *Nat. Geosci.* 4 (2), 116–121. doi:10.1038/ngeo1040

Iverson, R. M. (1997). The physics of debris flows. *Rev. Geophys.* 35 (3), 245–296. doi:10.1029/97RG00426

Kesseler, M., Heller, V., and Turnbull, B. (2018). A laboratory-numerical approach for modelling scale effects in dry granular slides. *Landslides* 15 (11), 2145–2159. doi:10.1007/s10346-018-1023-z

Kleinhans, M. G., Markies, H., de Vet, S. J., in't Veld, A. C., and Postema, F. N. (2011). Static and dynamic angles of repose in loose granular materials under reduced gravity. *J. Geophys. Res.* 116, E11004. doi:10.1029/2011JE003865

Lai, Z. Q., Chen, D., Jiang, E. H., Zhao, L. J., Vallejo, L. E., Zhou, W., et al. (2021). Effect of fractal particle size distribution on the mobility of dry granular flows. *AIP Adv.* 11 (9), 095113. doi:10.1063/5.0065051

Li, K., Wang, Y. F., Lin, Q. W., Cheng, Q. G., and Wu, Y. (2021). Experiments on granular flow behavior and deposit characteristics: Implications for rock avalanche kinematics. *Landslides* 18 (5), 1779–1799. doi:10.1007/s10346-020-01607-z

Liu, X. Y., Specht, E., and Mellmann, J. (2005). Experimental study of the lower and upper angles of repose of granular materials in rotating drums. *Powder Technol.* 154 (2-3), 125–131. doi:10.1016/j.powtec.2005.04.040

Luckman, B. (2013). "Talus slopes," in *The encyclopedia of quaternary science* (Elsevier), 3, 566–573.

Luo, L. G., Pei, X. J., Pei, Z., Yang, B., and Jing, X. (2018). Distribution characteristics and susceptibility of talus slopes in the northern piedmont of tian-Shan mountain. *J. Catastrophol.* 33 (2), 200–205. doi:10.3969/j.issn.1000-811X.2018.02.035

Mehta, A., and Barker, G. C. (1994). The dynamics of sand. *Rep. Prog. Phys.* 57 (4), 383–416. doi:10.1088/0034-4885/57/4/002

Otto, J., Schrott, L., Jaboyedoff, M., and Dikau, R. (2009). Quantifying sediment storage in a high alpine valley (turtmanntal, Switzerland). *Earth Surf. Process. Landf.* 34, 1726–1742. doi:10.1002/esp.1856

Pudasaini, S. P., and Hutter, K. (2007). *Avalanche dynamics: Dynamics of rapid flows of dense granular avalanches*. Berlin: Springer. doi:10.1007/978-3-540-32687-8

Que, Y., Wang, C. H., and Zhang, X. G. (2003). Formative mechanism and control of typical sand-sliding slope along sichuan-tibet highway. *Mt. Res.* 21 (5), 595–598. doi:10.3969/j.issn.1008-2786.2003.05.012

Sass, O., and Krautblatter, M. (2007). Debris flow-dominated and rockfall-dominated talus slopes: Genetic models derived from GPR measurements. *Geomorphology* 86, 176–192. doi:10.1016/j.geomorph.2006.08.012

Statham, I. (1976). A scree slope rockfall model. *Earth Surf. Process.* 1 (1), 43–62. doi:10.1002/esp.3290010106

Takagi, D., McElwaine, J. N., and Huppert, H. E. (2011). Shallow granular flows. *Phys. Rev. E* 83, 031306. doi:10.1103/PhysRevE.83.031306

Tu, X. B., Wang, S. J., and Yue, Z. Q. (2005). Fractal fragmentation of weathered rock and its application in engineering geology. *Chin. J. Rock Mech. Eng.* 24 (4), 587–595. doi:10.3321/j.issn:1000-6915.2005.04.008

Turcotte, D. L. (1986). Fractals and fragmentation. *J. Geophys. Res.* 91 (B2), 1921. doi:10.1029/JB091iB02p01921

Tyler, S. W., and Wheatcraft, S. W. (1992). Fractal scaling of soil particle-size distributions: Analysis and limitations. *Soil Sci. Soc. Am. J.* 56 (2), 362–369. doi:10.2136/sssaj1992.03615995005600020005x

Wang, C. H., Zhang, X. G., Que, Y., and He, S. M. (2007). Formation and basic characteristics of sand-sliding slope composed of granular clasts: Part I of sand-sliding slope series. *Rock Soil Mech.* 28 (1), 29–35. doi:10.16285/j.rsm.2007.01.006

Wang, Y. F., Cheng, Q. G., and Zhu, Q. (2015). Surface microscopic examination of quartz grains from rock avalanche basal facies. *Can. Geotech. J.* 52 (2), 167–181. doi:10.1139/cgj-2013-0284

Xing, J., and Wang, J. B. (2019). Development mechanism of the sand-sliding slope at a tunnel exit in qinghai-tibet expressway. *Chin. J. Geol. Hazard. Control.* 30 (2), 1–8. doi:10.16031/j.cnki.issn.1003-8035.2019.02.01

Xue, Y. G., Kong, F. M., Li, S. C., Zhang, Q. S., Qiu, D. H., Su, M. X., et al. (2021). China starts the world's hardest "Sky-High Road" project: Challenges and countermeasures for Sichuan-Tibet railway. *Innovation* 2 (2), 100105. doi:10.1016/j.xinn.2021.100105

Ye, T. J., Xie, Q., and Wang, Y. (2019). Stability evaluation and classification of debris slopes in eastern tibet section of G318 highway. *J. Eng. Geol.* 27 (4), 914–922. doi:10.13544/j.cnki.jeg.2018-058

Zhang, J., and Shu, Z. P. (2017). Research on failure mode of sand-sliding slope by progressive replenishment and countermeasure. *J. Chengdu Univ.* 36 (4), 434–437. doi:10.3969/j.issn.1004-5422.2017.04.025

Zhang, Y. C., Fu, R. H., and Huang, R. Q. (2008). Experimental study on dynamical and fractal characteristic of sand-sliding slope on Tianshan Highway. *J. Disaster Prev. Mitig. Eng.* 28 (2), 219–222. doi:10.3969/j.issn.1672-2132.2008.02.016

Zheng, H., Wang, D., and Behringer, R. P. (2019). Experimental study on granular biaxial test based on photoelastic technique. *Eng. Geol.* 260, 105208. doi:10.1016/j.enggeo.2019.105208

frontiers | Frontiers in Earth Science

TYPE Original Research
PUBLISHED 12 September 2022
DOI 10.3389/feart.2022.980919

OPEN ACCESS

EDITED BY
Marcel Hürlimann,
Universitat Politecnica de Catalunya, Spain

REVIEWED BY
Aiguo Xing,
Shanghai Jiao Tong University, China
Bo Zhao,
Institute of Mountain Hazards and Environment, (CAS), China

*CORRESPONDENCE
Yu-Feng Wang,
wangyufeng@home.swjtu.edu.cn

SPECIALTY SECTION
This article was submitted to Geohazards and Georisks, a section of the journal Frontiers in Earth Science

RECEIVED 29 June 2022
ACCEPTED 18 August 2022
PUBLISHED 12 September 2022

CITATION
Wang Y-F, Cheng Q-G, Lin Q-W, Li K and Ji Y-D (2022), Insights into the differential fragmentation processes in rock avalanche emplacement from field investigation and experimental study. *Front. Earth Sci.* 10:980919. doi: 10.3389/feart.2022.980919

Insights into the differential fragmentation processes in rock avalanche emplacement from field investigation and experimental study

Yu-Feng Wang[1,2]*, Qian-Gong Cheng[1,2,3], Qi-Wen Lin[1], Kun Li[1] and Yan-Dong Ji[1]

[1]Department of Geological Engineering, Southwest Jiaotong University, Chengdu, Sichuan, China, [2]Key Laboratory of High-Speed Railway Engineering, Ministry of Education, Chengdu, Sichuan, China, [3]State-Province Joint Engineering Laboratory of Spatial Information Technology of High-Speed Rail Safety, Chengdu, Sichuan, China

Fragmentation is a universal phenomenon associated with rock avalanches, resulting in an abundance of complex sedimentological structures. If studied in detail, these structures can provide insights into rock avalanche emplacement processes. Here, six typical avalanche cases are carefully analyzed in conjunction with an analogue experiment. Findings reveal the carapace facies is characterized by clast-supported structures composed of large blocks with sedimentological structures that include retained stratigraphic sequences, imbricate structures, and jigsaw structures. The body facies presents a high degree of fragmentation, with block-rich zones, fine matrix-rich zones, jigsaw structures, and inner shear zones. The basal facies displays the highest degree of fragmentation, however, it is mainly composed of millimeter grains with thin shear strips. Consistent with the field investigations, differential fragmentation is also observed in the analogue tests, with the vertical dimension of the carapace facies mainly fragmented along the lines of pre-existing structures; the body facies fragmented with an abundance of new fractures; and the basal facies fragmented into fine grains. Meanwhile, layer sequences preserved in longitudinal and vertical profiles are also observed in the analogue tests, indicating a low disturbance in the propagation. We, therefore, propose that a process characterized by a sparse state, dominated by collisions, minor disturbance, and pervasive dynamic fragmentation likely occurs in the carapace facies, with fragmentation mainly controlled by the breakage of pre-existing, fully-persistent structures. The body facies is mainly controlled by the fracturing of the weak, less-persistent structures, and the basal facies displays the highest degree of fragmentation with an abundance of new fractures. In the entire propagation, the avalanche mass displays low-disturbance laminar flow.

KEYWORDS

rock avalanche, sedimentological structures, differential fragmentation, analogue study, emplacement kinematics

Introduction

The occurrence of rock avalanches has increased significantly in recent years and with sometimes catastrophic results, due to large volumes (>1 × 10^6 m^3), extremely high velocities (>20 m/s), and long runouts (>1 km) (Evans et al., 2007; Sun et al., 2011; Huang et al., 2012; Pudasaini and Miller, 2013; Lucas et al., 2014; Iverson et al., 2015; Zhu et al., 2019; Friele et al., 2020; Zhang et al., 2020; Zhao et al., 2020). A typical example of such a disaster is the Xinmocun rock avalanche that occurred in China on June 24, 2017 (Fan et al., 2017). The detached mass transformed into a highly fragmented debris avalanche with a volume of 4.5×10^6 m^3, which traveled downwards rapidly with a runout of up to 4.1 km within 110 s, burying the whole of Xinmocun downstream and killing about 100 people. It was calculated that the maximum velocity of the detached mass was over 50 m/s, thus presenting extremely high mobility (Fan et al., 2017). To explain the hypermobility of rock avalanches, some hypotheses have been proposed, including the frictional heating mechanism (Habib, 1975; He et al., 2015; Wang et al., 2017; Hu et al., 2019), dynamic fragmentation (Davies et al., 1999; Davies and McSaveney, 2009), substrate entrainment (Hungr and Evans, 2004; Iverson and Ouyang, 2015; Aaron and McDougall, 2019; Pudasaini and Krautblatter, 2021), shear induced fluidization (Melosh, 1979; Davies, 1982; Wang et al., 2015), and momentum transfer (Heim, 1932; Van Gassen and Cruden, 1989). Moreover, many studies focusing on field investigations (Hewitt et al., 2008; Weidinger et al., 2014; Dufresne et al., 2016a; Strom and Abdrakhmatov, 2018; Wang et al., 2018, 2019; Dufresne and Geertsema, 2020), laboratory experiments (Iverson et al., 2004; Shea and Vries, 2008; Manzella and Labiouse, 2009; Zhang and McSaveney, 2017; Li et al., 2021, 2022), and numerical simulations (Pudasaini and Hutter, 2007; Cagnoli and Piersanti, 2015; Mergili et al., 2018) have also been conducted to enable better understanding of the emplacement of rock avalanches.

Pervasive fragmentation in rock avalanches, as revealed by their deposits, has been commonly reported and is attracting increasing scientific attention (Hewitt, 2002; Locat et al., 2006; Crosta et al., 2007; Zhang et al., 2016; Dufresne and Dunning, 2017; Zhao et al., 2017; Ghaffari et al., 2019; Knapp and Krautblatter, 2020; Lin et al., 2020, 2021). With the occurrence of dynamic fragmentation in emplacement, crude inverse grading is a diagnostic feature in avalanche deposits, with three facies divided from bottom to top: basal facies, body facies, and carapace facies (Cruden and Hungr, 1986; Blair, 1999; Dunning, 2006; Dufresne et al., 2016b; Wang et al., 2018, 2019, 2020). In each facies, certain unique characteristics are well developed and widely distributed (Dufresne et al., 2016b). The basal facies is mainly composed of angular fine particles less than a centimeter in diameter with common entrainment of the substrate. In this facies, some minor internal sedimentological structures have been reported, such as diapiric structures, small-scale faults, and thin shear strips (Dufresne et al., 2016b; Wang et al., 2019). The body facies mainly consists of highly-fragmented angular clasts, ranging in diameter from micrometer to decimeter scale. This facies is the main part of an avalanche deposit and is usually characterized by more internal sedimentological structures, such as block-rich zones, jigsaw structures, and inner shear zones. Because of the distribution of these structures in the vertical dimension, the body facies can be further divided into subfacies (Pollet and Schneider, 2004; Dufresne et al., 2016b). The carapace facies is the coarsest zone, with an abundance of angular blocks, characterized by a clast-supported structure with preserved source stratigraphy and jigsaw structures (Wang et al., 2019, 2020).

A better understanding of the fragmentation processes of these facies provides knowledge of the emplacement of rock avalanches and facilitates the evaluation of potential hazards. Focusing on the three facies outlined above, various studies have reported differential fragmentation (Davies et al., 1999; Strom, 1999; Pollet and Schneider, 2004; Dufresne et al., 2016b; Dufresne and Dunning, 2017; Strom and Abdrakhmatov, 2018). Furthermore, shear-related dynamical fluidization mechanisms have been proposed to explain the hypermobility of rock avalanches (Melosh, 1979; Davies, 1982; Davies and McSaveney, 2009; De Blasio and Crosta, 2015; Wang et al., 2015; Haug et al., 2016). However, studies focused on the differential fragmentation found in avalanche deposits remain limited and further work is needed to understand rock avalanche emplacement. To address this need, first, the surficial and internally deposited features of several typical cases were investigated in detail. An analogue study was then designed and conducted to reproduce the differential fragmentation processes of avalanche masses. Finally, a comparison of the field investigations and the analogue study was carried out, to understand the emplacement processes of rock avalanches from the viewpoint of differential fragmentation. A further aim is to provide sufficient field evidence and analogue data for use in future analogue and numerical studies of rock avalanches.

Regional geological setting

The study focuses on the Tibetan plateau, which formed ~55 Ma and resulted from the intensive and ongoing plate collision of India with Eurasia (Larson et al., 1999). The Tibetan plateau is the youngest and highest mountainous region in the world, characterized by a wide variety of geologies, geomorphologies, and climates. Global positioning system (GPS) data indicate that convergence is still occurring in the plateau, with numerous earthquakes generated (Larson et al., 1999; Tapponnier et al., 2001; Zhang et al., 2004). In just the past 100 years, there have been 36 events with Ms > 7, as reported by the Advanced National Seismic System (Figure 1).

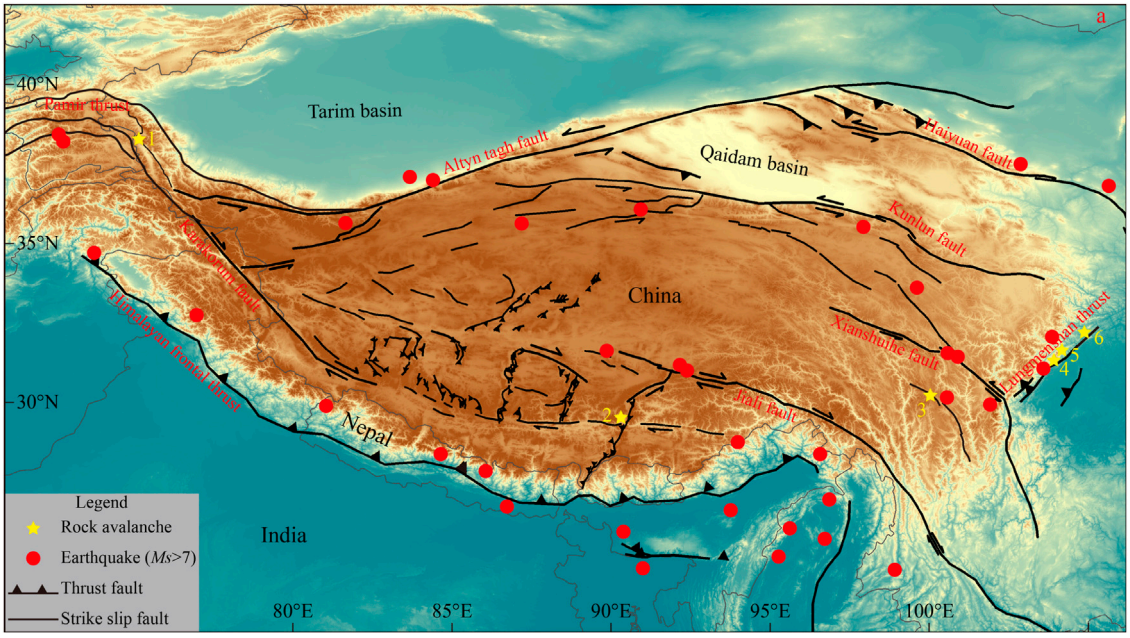

FIGURE 1
Geological map of the Tibetan plateau with the locations of the studied rock avalanches marked.

TABLE 1 Details of the studied rock avalanches.

No.	Name	Main lithology	Volume	Runout	Drop height	Fahrböschung	References
1	Tagarma rock avalanche	Gneiss	~96 × 10^6 m^3	5.4 km	1,500 m	0.28	Wang et al. (2020)
2	Nyixoi Chongco rock avalanche	Biotite monzonitic granite	~28 × 10^6 m^3	4.6 km	885 m	0.19	Wang et al. (2019)
3	Luanshibao rock avalanche	Biotite granodiorite	~28 × 10^6 m^3	4.1 km	820 m	0.2	Wang et al. (2018)
4	Xiejiadianzi rock avalanche	Granite and granodiorite	~3.5 × 10^6 m^3	1.7 km	700 m	0.41	Wang et al. (2015)
5	Daguangbao rock avalanche	Carbonate rocks and siltstone	~7.5 × 10^8 m^3	4.3 km	1,300 m	0.30	Huang et al. (2012)
6	Donghekou rock avalanche	Slate and carbonate rocks	~10 × 10^6 m^3	2.0 km	500 m	0.25	Sun et al. (2011)

Owing to the effects of intense tectonic activity and long-term weathering, intensely fractured bedrock is widely distributed with high topographic relief, which is thought to be particularly favorable for the generation of catastrophic bedrock landslides (Strom and Abdrakhmatov, 2018; Wang et al., 2018, 2019, 2020). Many massive rock avalanches have been reported in this area, and are increasingly attracting scientific attention (Yuan et al., 2013; Weidinger et al., 2014; Reznichenko et al., 2017; Strom and Abdrakhmatov, 2018; Wang et al., 2018, 2019, 2020). Figure 1 shows the locations of the rock avalanches investigated in this study, with three located along the Longmenshan thrust in the southeastern margin of the Tibetan plateau, and triggered by the Wenchuan earthquake in 2008. The remaining are prehistoric cases, with the Luanshibao rock avalanche in the Maoyaba basin along the Litang-Dewu fault system, the Nyixoi Chongco rock avalanche in the Yadong-Gulu rift in the South Tibetan normal fault system, and the Tagarma rock avalanche in the Tarim basin of the Pamir-western Himalayan syntaxis. Table 1 lists some details of these cases. In Table 1, the Fahrböschung is defined as the ratio of the drop height (H) to the horizontal runout (L) between the crown and top, as proposed by Heim (1932) to quantify the hypermobility of rock avalanches.

Figure 2 shows the plan views of the studied rock avalanches, exhibiting the stereographic projections of the preferred structures developed in their source areas. As revealed in Figure 2, most of the cases studied are crossed by faults at the toes of their source areas, except for the Daguangbao and Donghekou rock avalanches, with faults nearly parallel to their flanks. Longitudinally, the topographies of their source

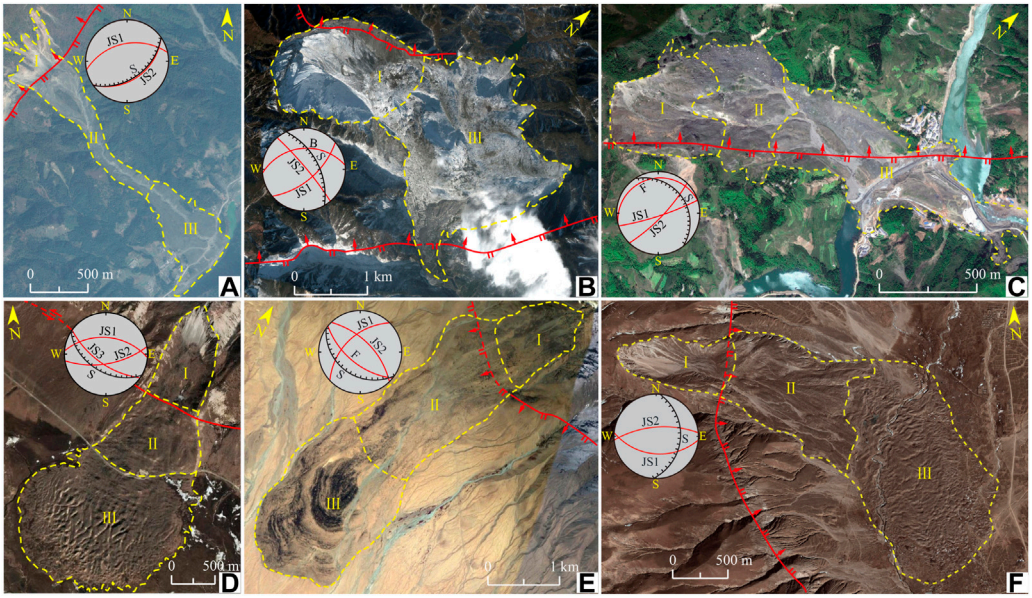

FIGURE 2
Remote images of the Xiejiadianzi **(A)**, Daguangbao **(B)**, Donghekou **(C)**, Luanshibao **(D)**, Tagarma **(E)**, and Nyixoi Chongco **(F)** rock avalanches with the stereographic projections of their source area preferred structures. JS, joints; F, foliation; S, slope; B, bedding plane; I: source area; II: transition zone; III: accumulation zone.

areas are steeper than their transition and accumulation zones. The lithologies of the source areas are different, with one originating in sedimentary rock, three originating in igneous rock, one originating in metamorphic rock, and one originating in mixed layers of sedimentary and metamorphic rock (Table 1). Highly fractured preferred structures are widely developed in their source areas (Figure 2), controlling failures of the bedrock. Unlike the source areas, the transition and accumulation zones are characterized by relatively planar topographies, with their substrates mainly consisting of quaternary deposits, including glacial moraine deposits, alluvial deposits, pluvial deposits, residual deposits, and talus.

Methods

Field investigation

Field investigations are the main method for examining the deposited characteristics of these rock avalanches, and these were performed based on Google Earth images, 1:200,000-scale geological maps, and 1:100,000-scale geomorphological maps. During the field investigations, high resolution cameras were employed to record these surficial and internal sedimentary structures, with a handheld Magellan global positioning system, a TruPulse200X laser rangefinder, and a compass used to confirm location, orientation, and size. 1:1,000-scale aerial images of the Nyixoi Chongco and Tagarma rock avalanches were acquired using fixed-wing unmanned aerial vehicles. The resolution of the aerial images is high enough to observe the surficial landforms of the avalanche carapace facies. Additionally, an area-by-area technique and sieve analyses were used to quantify the inverse grading features revealed by their internal vertical profiles.

Experimental setup

To explore the differential fragmentation in rock avalanche propagation, analogue model tests were also designed and conducted, with an overview of the experimental system given in Figure 3A. The experimental apparatus consists of an inclined flume (2.0 m long and 0.1 m wide), with its dip angle being 45°, a horizontal flume (2.4 m long and 0.1 m wide), and a material releasing box (0.4 m long and 0.1 m wide). Both of the side walls of the flumes are made of 0.8 cm thick plexiglass. To control the release of the material, a releasing gate was installed, as shown in Figure 3B.

To simulate the fragmentation process of avalanche masses in small-scale experiments, fragmentable analog material with relatively low strength was prepared using the scaling law based on the material properties of the Xiejiadianzi and Luanshibao rock avalanches. The main parameters used for the design of the analog material are σ (stress), E (elastic modulus), ϵ (strain), C

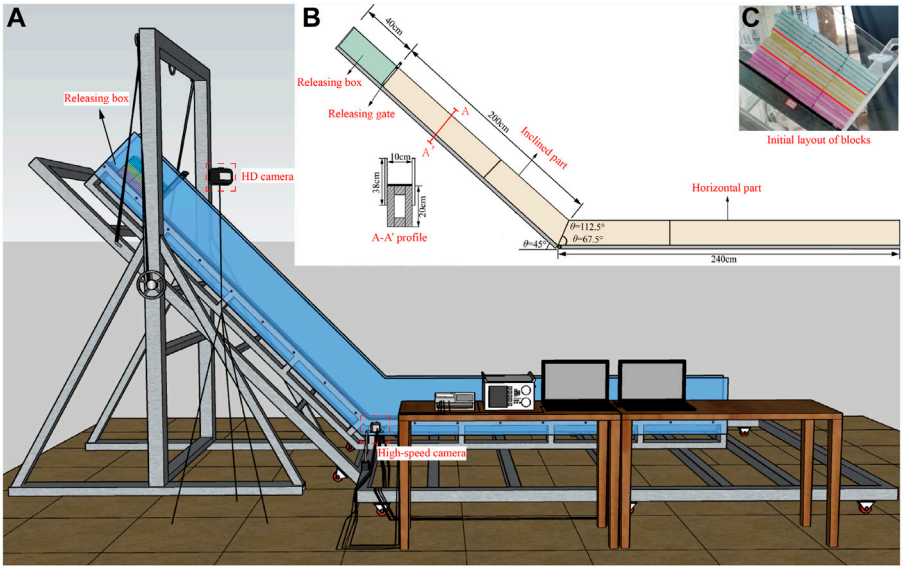

FIGURE 3
Schema of the experimental setup **(A,B)** and initial layout of blocks **(C)**.

TABLE 2 Parameters used for similarity analysis of the protype and similar materials.

	Bulk density/g/cm^3	Internal friction angle/°	Cohesion/MPa	Compressive strength/MPa	Elastic modulus/GPa
Symbol	ρ	φ	C	σ	E
Dimension	ML^{-3}	$M^0L^0T^0$	$ML^{-1}T^{-2}$	$ML^{-1}T^{-2}$	$ML^{-1}T^{-2}$
Scale ratio	1:1	1:1	1:600	1:600	1:600
Protype material	2.4–3.1	45–60	30–50	100–379	50–100
Similar materials	2.4–3.1	45–60	0.05–0.08	0.17–3.5	0.08–0.17

(cohesion), ϕ (internal friction angle), L (dimension), ρ (density), and g (gravitational acceleration), with the scaling law being as follows:

$$f(\sigma, E, \epsilon, C, \phi) = f(l, \rho, g) \quad (1)$$

Referring to Lin et al. (2020), the scaling ratios of length, gravity, and material solid density were selected as the base dimensions, with their values being 600:1, 1:1, and 1:1, respectively. The values of the parameters used for the preparation of analogue material are listed in Table 2, and are according to dimensional analysis (Bolster et al., 2011; Iverson, 2015). Using the calculated values listed in Table 2, raw materials, including barite, quartz, gypsum, sodium silicate, sodium carboxymethyl cellulose, and glycerol were chosen to produce the fragmentable analog blocks, following the preparation process in Lin et al. (2020). The size of the analogue blocks was 100 * 100 *10 mm^3, with the compressive strength, elastic modulus, cohesion, internal friction angle, and bulk density being 0.42 MPa, 106.56 MPa, 48.05 kPa, 29.39°, and 1.83 g cm^{-3}, respectively. The total weight of each test was 7.8 kg. To ensure the reproducibility of each test, three repeat tests were conducted.

For data collection, a high-speed camera (850 f/s) with 0.3 megapixels was used to record the fragmentation and propagation processes of the detached mass when it slid onto the horizontal plane, as shown in Figure 3. A 1080 p high-definition camera (HD camera), was employed to record the initial releasing process to make sure the release steps of each test were consistent. After the deposition of the detached mass in each test, the oblique photography technique was employed to obtain the final deposited characteristics (Li et al., 2021). The grain size distribution of each fragmented detached mass was calculated to quantify the degree of fragmentation.

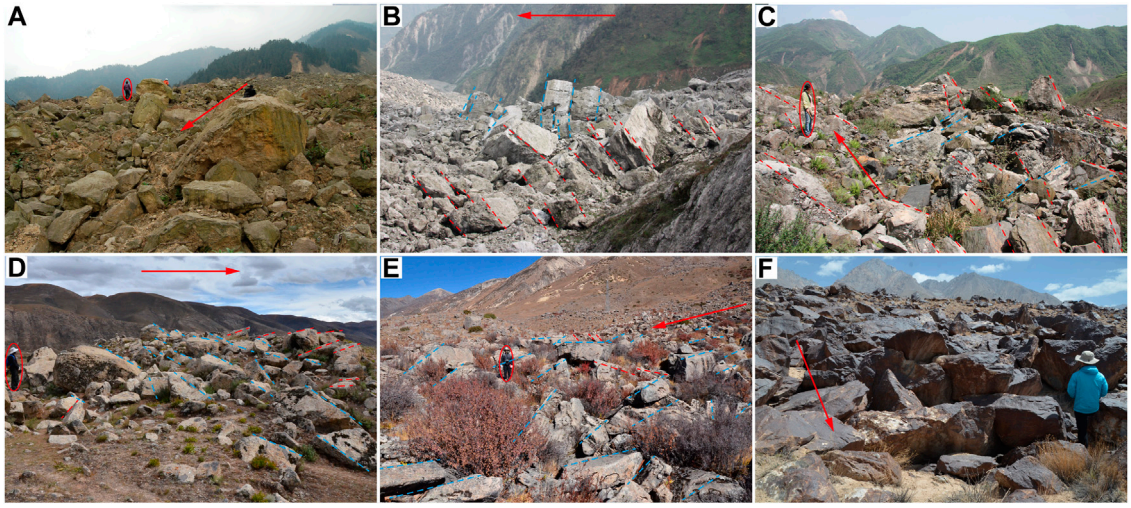

FIGURE 4
Clast-supported structures composed of blocks in the carapace facies of the Xiejiadianzi **(A)**, Daguangbao **(B)**, Donghekou **(C)**, Nyixoi Chongco **(D)**, Luanshibao **(E)**, and Tagarma **(F)** rock avalanches. The red arrow in each subfigure indicates the main movement direction of the avalanche masses with these dashed lines marking the preferred inclinations of fragmented blocks.

Depositional characteristics

The detached rock masses of the studied rock avalanches are characterized by variable volumes (3.5–750 × 10^6 m^3), runouts (2.0–5.4 km), and drop heights (500–1,500 m). It is calculated that their Fahrböschung values fall into the range of 0.19–0.41 (Table 1), indicating the high mobility of the mass propagations. Series of variable surficial characteristics were observed along their traveling paths, including ridges in varying shapes, scales, and orientations, toreva blocks, hummocks, jigsaw structures, and preserved bedrock sequences (Sun et al., 2011; Huang et al., 2012; Wang et al., 2012, 2018, 2019, 2020). Vertically, inverse grading was revealed, with three facies presented from bottom to top, i.e., basal facies, body facies, and carapace facies. In each facies, different sedimentary features were revealed. In the following, detailed descriptions of the depositional characteristics of the investigated cases are presented.

Depositional characteristics of the carapace facies

The carapace facies are characterized by wide distributions in particle size, ranging from micrometers to tens of meters, and mainly composed of blocks with clast-supported structures (Figure 4). Most blocks are irregular and angular, with very sharp edges, retaining their original fractured shapes. Controlled by internal structures, in most of the investigated rock avalanches blocks are mainly present in tabular shapes of varying thickness. Their top and bottom surfaces are usually planar and smooth, especially in the Daguangbao, Donghekou, and Tagarma rock avalanches, with well-developed bedding or foliated structures.

As shown in Figures 4B–F, 5A, imbricate structures consisting of platy-shaped blocks (i.e., clusters of superimposed blocks fragmented to different extents) are commonly distributed, especially in the Daguangbao and Tagarma rock avalanches. The top surfaces of some imbricate structures face upstream (i.e., blocks marked by red dashed lines in Figures 4B–E) with the rest facing downstream (i.e., blocks marked by red dashed lines in Figures 4B–E). Figure 5A is an enlarged view showing the imbricate structures in the Tagarma rock avalanche with the top surface facing downstream. As exhibited in Figure 5A, the surface of each block is smooth and planar, indicating the control of foliation. Additionally, jigsaw structures are observed in the carapace facies, especially in the Daguangbao, Nyixoi Chongco, and Tagarma rock avalanches. Figure 5B shows one jigsaw structure observed in the Tagarma rock avalanche, with fragmented sub-blocks also presenting an imbricate structure, which is consistent with the structures of the source scar (Wang et al., 2020). Figures 5C–E show some jigsaw structures deposited in the Daguangbao rock avalanche, which are characterized by varying degrees of fragmentation. In the jigsaw structures shown in Figures 5C,D, original lithological sequences are well preserved with minor disturbance after fragmentation, indicating an extremely low disturbance in the propagation. Figure 5F shows one jigsaw structure observed in the Nyixoi Chongco rock avalanche.

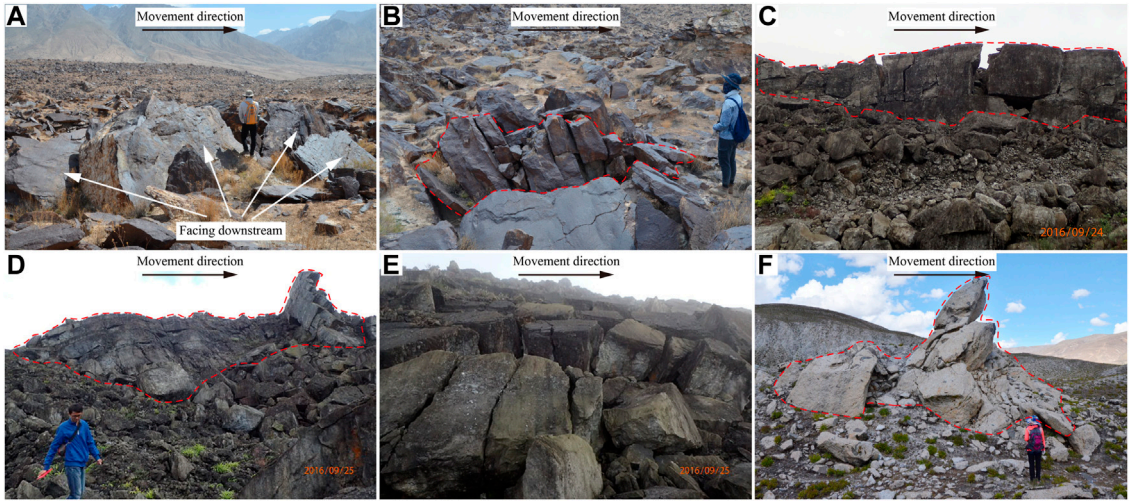

FIGURE 5
Photos showing imbricate structures **(A)** and jigsaw structures **(B–F)** deposited in the carapace facies of the Tagarma **(A,B)**, Daguangbao **(C–E)**, and Nyixoi Chongco **(F)** rock avalanches.

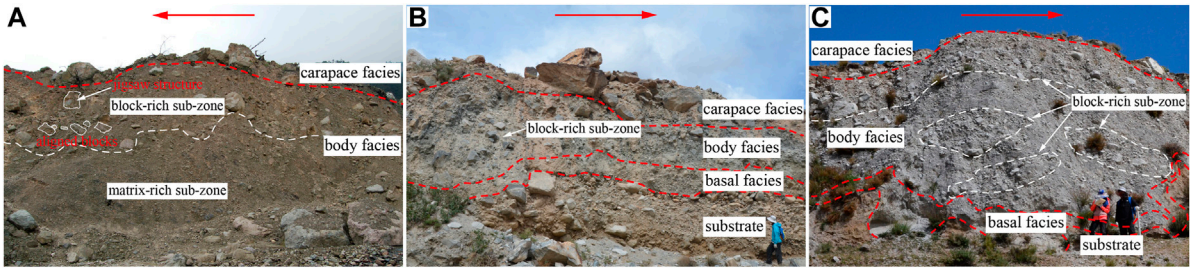

FIGURE 6
Deposited profiles of the Xiejiadianzi **(A)**, Tagarma **(B)**, and Nyixoi Chongco **(C)** rock avalanches. Red arrows indicate the movement directions of the avalanche mass.

Depositional characteristics of the body facies

Due to post-avalanche erosion, some well-preserved outcrops are revealed in the studied cases, providing opportunities to observe their internal sedimentary structures. As the outcrops reveal, the thicknesses of the body facies vary greatly versus runout under the control of underlying topographies, especially for the Nyixoi Chongco rock avalanche (Wang et al., 2012, 2019, 2020; Zeng et al., 2019). Figure 6 shows the deposited profiles of the Xiejiadianzi, Tagarma, and Nyixoi Chongco rock avalanches photographed during field surveys. The body facies are mainly composed of highly fragmented, angular clasts, ranging from micrometer to decimeter scales in diameter, which are obviously finer than those of the carapace facies. As the main part of rock avalanches, a series of internal sedimentological structures are observed, such as fine matrix-rich sub-zones, block-rich sub-zones, jigsaw structures, and inner shear bands (Wang et al., 2018, 2019, 2020).

As shown in Figure 6A, the body facies of the Xiejiadianzi rock avalanche can be further divided into a block-rich sub-zone with directionally aligned blocks and jigsaw structures, and a matrix-rich sub-zone mainly composed of micrometer to centimeter grains. In the outcrops of the Tagarma and Nyixoi Chongco rock avalanches, block-rich sub-zones are also observed, with directionally aligned clasts distributed as shown in Figures 6B,C. Grain sizes in the block-rich sub-zones mainly range in the dozens of decimeters along long axes.

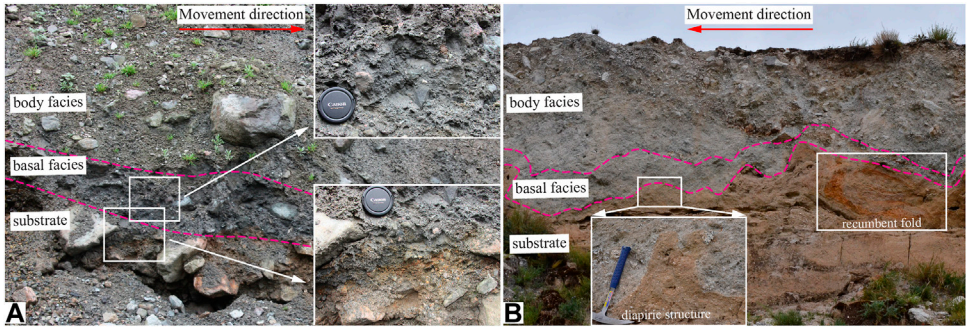

FIGURE 7
Layouts of the basal facies of the Xiejiadianzi **(A)** and Nyixoi Chongco **(B)** rock avalanches.

Depositional characteristics of the basal facies

The basal facies is the lowest zone of rock avalanches in direct contact with the substrate, and is the thinnest zone compared with the upper facies. It is usually less than 1 m in thickness. Due to the intensive interaction between the avalanche mass and the substrate, the fragmentation degree of this facies is obviously higher than the upper avalanche mass, with grains mainly finer than a centimeter in the long axes (Wang et al., 2012, 2015, 2019, 2020). Coarse clasts larger than several centimeters can also be observed occasionally. Figure 7 shows the layout of both outcrops of the Xiejiadianzi and Nyixoi Chongco rock avalanches. As shown in Figure 7A, grains in this facies also have angular shapes with low roundness, and are obviously different from the underlying rounded alluvial deposits. Additionally, intensively deformed shear structures can be observed in this facies and substrate (Figure 7B), including diapiric structures, convoluted laminations, faults, and basal décollements.

Experimental results

Figures 8A–F show the propagated process of the detached mass, with snapshots during 0.35–0.48 s presented in Figures 8G–J to reveal some detailed information about the propagation. From Figures 8A–F, it can be seen that the detached mass mainly behaves as a laminar flow during the whole propagation process with differential fragmentation in the vertical dimension. The snapshots shown in Figures 8G,H further prove the low disturbance of the detached mass in propagation, as the lines marked in red and yellow highlight the lamina flow. As the blocks circled by the red lines indicate, the ones on the top surface display a low fragmentation degree with its initial sequence preserved. The block marked by the yellow lines is fragmented into small clasts, but still preserves its relationship with the upper blocks. Finally, a stratified internal structure, as observed in the source area, is generated in the final deposit (Figure 9A). Such a propagated model was already proposed by Strom in 2006. As exhibited in Figure 9A, a "multilayered" deposit is finally generated, due to pervasive fragmentation of differing extents during propagation, and similar to the inverse grading observed in rock avalanche deposits. According to the propagated features and final deposited sequence, the detached mass can be divided into three zones from rear to front, i.e., the tensional zone, compressional zone, and spreading zone (Figure 9A), which is consistent with the propagated processes proposed in some rock avalanches (Wang et al., 2018, 2019). The frontal spreading zone is relatively thin with clasts deposited relatively sparsely. The deposit in the middle compressional zone is thickest, with some compressed features present, such as folds. Furthermore, some deposited structures, including clast-supported (Figure 9A) and jigsaw structures (Figures 9B,C), can be observed.

To give a more direct sense of the vertical differential fragmentation of the detached mass, the deposited mass was divided into three layers from top to bottom, i.e., the upper, middle, and lower layers, as shown in Figures 9B–D. It can be seen that the upper layer is mainly composed of non-fragmented and low-fragmented blocks. In the propagation, they were mainly fragmented along the pre-existing, fully persistent discontinuities among blocks. Imbricate structures and retained original stratigraphic structures, similar to those observed in the Tagarma and Daguangbao rock avalanches, are widely distributed in the upper layer. The fragmentation degree of the middle layer increases obviously, with most blocks fragmented into clasts of centimeter size. Although the fragmentation degree increases, jigsaw structures are commonly developed in this layer, which is similar to that observed in the

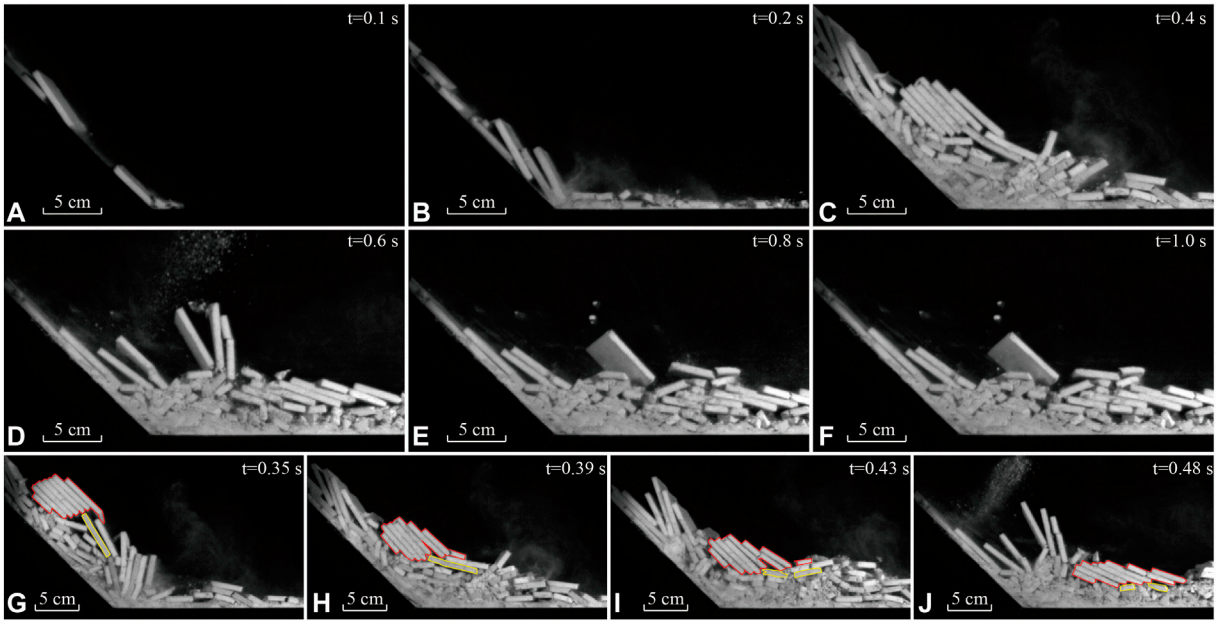

FIGURE 8
Photos recording the propagated process of the detached mass **(A–F)** with snapshots during t = 0.35–0.48 s. The red and yellow lines in **G–J** mark the distribution of preserved block sequence.

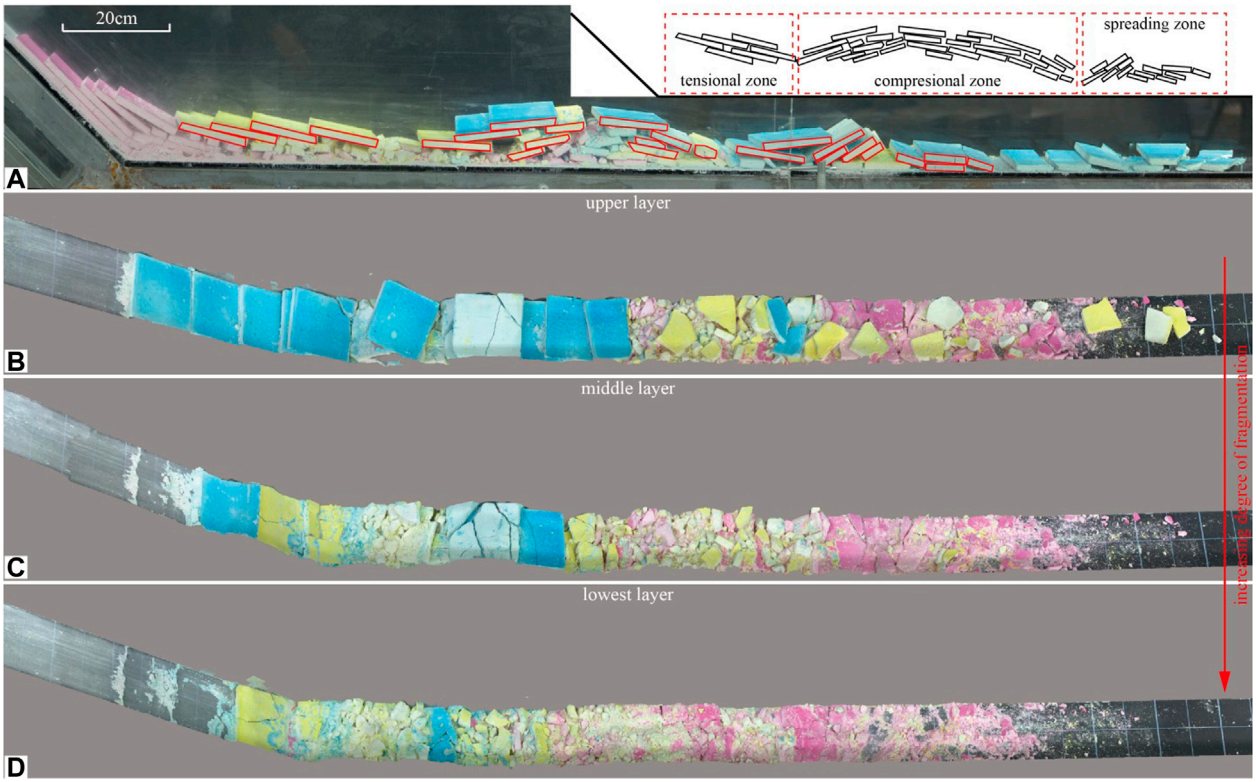

FIGURE 9
Final deposit of the detached mass **(A)** with vertical layering of the deposit from top to bottom **(B–D)**.

avalanche cases. The lowest layer is completely composed of fragmented blocks, with the most fragmented in millimeter size.

Discussion

As described above, the deposit of the experimental study presents an inverse grading feature with a clast-supported structure, retained original stratigraphic structure, imbricate structure, jigsaw structure, and folds, which is similar to that observed in natural rock avalanches. As argued by Strom (1994, 1999), retained original stratigraphic structures are commonly distributed in rock avalanches that occurred in the Pamir and Tian-Shan Mountains and are suggested as indicators of a slight disturbance in avalanche propagation (Strom, 1994, 1999). Jigsaw structures commonly observed in rock avalanches have also been regarded as indicators of a slight internal disturbance in the propagation of an avalanche mass (Paguican et al., 2014; Dufresne et al., 2016b; Wang et al., 2019). Hence, we believe the high consistency between the experimental results and the field observations further proves that a relatively steady movement, with differential fragmentation and slight internal disturbance, should be considered the main propagation form of rock avalanches.

During the propagation, the detached mass in the carapace facies is in a relatively sparse state, with clasts mainly suffering a relatively low stress level dominated by collisions. Fragmentation in the carapace facies is mainly controlled by the breakage of pre-existing fully persistent discontinuities with low stress levels that already existed in the bedrock when detaching from the source area (Charrière et al., 2016; Wang et al., 2020). Furthermore, fragmentation associated with breakages of rock bridges of less persistent structures also occurs, due to continued dynamic interactions among blocks. The body and basal facies are in a relatively dense state with intensive fragmentation occurring. Fragmentation in the body and basal facies is associated with the breakages of rock bridges of less-persistent structures or the generation of new fractures. The stress level suffered by the body and basal facies is higher than that of the carapace facies.

Conclusion

To understand the differential fragmentation and propagation mechanisms of rock avalanches, the sedimentological features of several natural cases were investigated here in detail along their entire travel paths. Furthermore, an analogue model study was conducted to verify the ideas based on the field investigated data. The main findings are as follows:

1) The carapace facies is a commonly observed sedimentological unit in rock avalanche deposits, featuring large blocks armoring the depositional surface. Clasts in this facies are deposited in a relatively sparse state, with a series of complex sedimentological structures, including conservation of stratigraphic sequences, clast-supported structures, imbricate structures, and jigsaw structures. Compared with the carapace facies, the body and basal facies display in a dense state with higher fragmentation.
2) The analogue model results reveal that the detached mass mainly behaves as a laminar flow during propagation with stratified internal structures, as observed in the source area generated in the final deposit. In the propagation, pervasive fragmentation of differing extents occurs in the vertical dimension, with the formation of a “multilayered” deposit. The mass near the top surface is in a sparse state during propagation, and is mainly dominated by impact collisions with the lower main body, and presenting a dense flow.
3) Based on the high consistency of the sedimentological structures obtained from the field investigations and analogue model, we propose that rock avalanches should display in a laminar-dominated propagation with vertical differential fragmentation. The carapace facies should propagate in a sparse state, dominated by impact collisions. During propagation, the facies is characterized by minor disturbance and pervasive dynamic fragmentation. The dynamic fragmentation process is mainly controlled by the breakage of pre-existing, fully persistent structures with low stress levels. The body and basal facies should propagate in a dense state dominated by shearing. During intensive shearing, abundant new fractures are generated, resulting in a higher degree of fragmentation.

Through detailed field investigations and a primary analogue model study of the propagated and deposited features of rock avalanches, possible explanations of their propagation mechanisms are proposed in this study. With this study, we hope to provide more field evidence and laboratory data that can be used in further studies of rock avalanches.

Data availability statement

The original contributions presented in the study are included in the article/Supplementary Material, and further inquiries can be directed to the corresponding author.

Author contributions

Y-FW contributed to all the work related to the manuscript; Q-GC contributed to the field investigation and manuscript writing; Q-WL and KL contributed to the field investigation; and Y-DJ contributed to the experimental study.

Funding

This work was supported by the National Natural Science Foundation of China (Grant nos 41877237, 41761144080, and 41530639), the Second Tibetan Plateau Scientific Expedition and Research Program (STEM) (Grant no. 2019QZKK0906) and the National Key Research and Development Program of China (Grant no. 2017YFC1501000).

Acknowledgments

We would like to thank Springer Nature for English language editing. The data presented in this paper are available on request from the corresponding author.

Conflict of interest

The authors declare that the research was conducted in the absence of any commercial or financial relationships that could be construed as a potential conflict of interest.

Publisher's note

All claims expressed in this article are solely those of the authors and do not necessarily represent those of their affiliated organizations, or those of the publisher, the editors, and the reviewers. Any product that may be evaluated in this article, or claim that may be made by its manufacturer, is not guaranteed or endorsed by the publisher.

References

Aaron, J., and McDougall, S. (2019). Rock avalanche mobility: The role of path material. *Eng. Geol.* 257, 105126. doi:10.1016/j.enggeo.2019.05.003

Blair, T. C. (1999). Form, facies, and depositional history of the north long john rock avalanche, owens valley, California. *Can. J. Earth Sci.* 36 (6), 855–870. doi:10.1139/e99-024

Bolster, D., Hershberger, R. E., and Donnelly, R. J. (2011). Dynamic similarity, the dimensionless science. *Phys. Today* 64 (9), 42–47. doi:10.1063/pt.3.1258

Cagnoli, B., and Piersanti, A. (2015). Grain size and flow volume effects on granular flow mobility in numerical simulations: 3-D discrete element modeling of flows of angular rock fragments. *J. Geophys. Res. Solid Earth* 120 (4), 2350–2366. doi:10.1002/2014jb011729

Charrière, M., Humair, F., Froese, C., Jaboyedoff, M., Pedrazzini, A., and Longchamp, C. (2016). From the source area to the deposit: Collapse, fragmentation, and propagation of the frank slide. *GSA Bull.* 128 (1-2), 332–351. doi:10.1130/B31243.1

Crosta, G. B., Frattini, P., and Fuis, N. (2007). Fragmentation in the val pola rock avalanche, Italian alps. *J. Geophys. Res. Earth Surf.* 112 (F1). doi:10.1029/2005JF000455

Cruden, D. M., and Hungr, O. (1986). The debris of the Frank slide and theories of rockslide-avalanche mobility. *Can. J. Earth Sci.* 23 (3), 425–432. doi:10.1139/e86-044

Davies, T. R. H., McSaveney, M. J., and Hodgson, K. A. (1999). A fragmentation-spreading model for long-runout rock avalanches. *Can. Geotech. J.* 36 (6), 1096–1110. doi:10.1139/t99-067

Davies, T. R. H., and McSaveney, M. J. (2009). The role of rock fragmentation in the motion of large landslides. *Eng. Geol.* 109 (1-2), 67–79. doi:10.1016/j.enggeo.2008.11.004

Davies, T. R. H. (1982). Spreading of rock avalanche debris by mechanical fluidization. *Rock Mech.* 15 (1), 9–24. doi:10.1007/bf01239474

De Blasio, F. V., and Crosta, G. B. (2015). Fragmentation and boosting of rock falls and rock avalanches. *Geophys. Res. Lett.* 42, 8463–8470. doi:10.1002/2015gl064723

Dufresne, A., Bösmeier, A., and Prager, C. (2016b). Sedimentology of rock avalanche deposits – case study and review. *Earth. Sci. Rev.* 163, 234–259. doi:10.1016/j.earscirev.2016.10.002

Dufresne, A., and Dunning, S. A. (2017). Process dependence of grain size distributions in rock avalanche deposits. *Landslides* 14, 1555–1563. doi:10.1007/s10346-017-0806-y

Dufresne, A., and Geertsema, I. M. (2020). Rock slide-debris avalanches: Flow transformation and hummock formation, examples from British columbia. *Landslides* 17, 15–32. doi:10.1007/s10346-019-01280-x

Dufresne, A., Prager, C., and Bösmeier, A. (2016a). Insights into rock avalanche emplacement processes from detailed morpho-lithological studies of the Tschirgant deposit (Tyrol, Austria). *Earth Surf. Process. Landf.* 41 (5), 587–602. doi:10.1002/esp.3847

Dunning, S. A. (2006). The grain size distribution of rock-avalanche deposits in valley-confined settings. *Italian J. Eng. Geol. Environ.* 1(S1), 117–121. doi:10.4408/IJEGE.2006-01.S-15

Evans, S. G., Guthrie, R. H., Roberts, N. J., and Bishop, N. F. (2007). The disastrous 17 february 2006 rockslide-debris avalanche on leyte island, Philippines: A catastrophic landslide in tropical mountain terrain. *Nat. Hazards Earth Syst. Sci.* 7, 89–101. doi:10.5194/nhess-7-89-2007

Fan, X. M., Xu, Q., Scaringi, G., Dai, L. X., Li, W. L., Dong, X. J., et al. (2017). Failure mechanism and kinematics of the deadly June 24th 2017 xinmo landslide, maoxian, sichuan, China. *Landslides* 15, 2129–2146. doi:10.1007/s10346-017-0907-7

Friele, P., Millard, T. H., Mitchell, A., Allstadt, K. E., Menounos, B., Geertsema, M., et al. (2020). Observations on the may 2019 joffre peak landslides, British columbia. *Landslides* 17, 913–930. doi:10.1007/s10346-019-01332-2

Ghaffari, H., Griffith, W., and Barber, T. (2019). Energy delocalization during dynamic rock fragmentation. *Geophys. J. Int.* 217 (2), 1034–1046. doi:10.1093/gji/ggz064

Habib, P. (1975). Production of gaseous pore pressure during rock slides. *Rock Mech.* 7 (4), 193–197. doi:10.1007/bf01246865

Haug, Ø. T., Rosenau, M., Leever, K., and Oncken, O. (2016). On the energy budgets of fragmenting rockfalls and rockslides: Insights from experiments. *J. Geophys. Res. Earth Surf.* 121, 1310–1327. doi:10.1002/2014jf003406

He, S. M., Liu, W., and Wang, J. (2015). Dynamic simulation of landslide based on thermo-poro-elastic approach. *Comput. Geosciences* 75, 24–32. doi:10.1016/j.cageo.2014.10.013

Heim, A. (1932). *Landslides and human lives*. Vancouver: Bitech Publishers, 1–203.

Hewitt, K., Clague, J. J., and Orwin, J. F. (2008). Legacies of catastrophic rock slope failures in mountain landscapes. *Earth-Science Rev.* 87 (1-2), 1–38. doi:10.1016/j.earscirev.2007.10.002

Hewitt, K. (2002). Styles of rock avalanche depositional complexes conditioned by very rugged terrain, Karakoram Himalaya, Pakistan. *Rev. Eng. Geol.* 15, 345–377. doi:10.1130/reg15-p345

Hu, W., Huang, R. Q., McSaveney, M., Yao, L., Xu, Q., Feng, M. S., et al. (2019). Superheated steam, hot CO_2 and dynamic recrystallization from frictional heat jointly lubricated a giant landslide: Field and experimental evidence. *Earth Planet. Sci. Lett.* 510, 85–93. doi:10.1016/j.epsl.2019.01.005

Huang, R. Q., Pei, X. J., Fan, X. M., Zhang, W. F., Li, S. G., and Li, B. L. (2012). The characteristics and failure mechanism of the largest landslide triggered by the Wenchuan earthquake, May 12, 2008, China. *Landslides* 9 (1), 131–142. doi:10.1007/s10346-011-0276-6

Hungr, O., and Evans, S. G. (2004). Entrainment of debris in rock avalanches: An analysis of a long run-out mechanism. *Geol. Soc. Am. Bull.* 116 (9/10), 1240–1252. doi:10.1130/b25362.1

Iverson, R. M., George, D. L., Allstadt, K., Reid, M. E., Collins, B. D., Vallance, J. W., et al. (2015). Landslide mobility and hazards: Implications of the 2014 oso disaster. *Earth Planet. Sci. Lett.* 412, 197–208. doi:10.1016/j.epsl.2014.12.020

Iverson, R. M., Logan, M., and Denlinger, R. P. (2004). Granular avalanches across irregular three-dimensional terrain: 2. Experimental tests. *J. Geophys. Res.* 109 (F1). doi:10.1029/2003jf000084

Iverson, R. M., and Ouyang, C. J. (2015). Entrainment of bed material by Earth-surface mass flows: Review and reformulation of depth-integrated theory. *Rev. Geophys.* 53 (1), 27–58. doi:10.1002/2013rg000447

Iverson, R. M. (2015). Scaling and design of landslide and debris-flow experiments. *Geomorphology* 244 (SI), 9–20. doi:10.1016/j.geomorph.2015.02.033

Knapp, S., and Krautblatter, M. (2020). Conceptual framework of energy dissipation during disintegration in rock avalanches. *Front. Earth Sci. (Lausanne).* 8, 263. doi:10.3389/feart.2020.00263

Larson, K. M., Roland, B., Bilham, R., and Freymueller, J. T. (1999). Kinematics of the India-Eurasia collision zone from GPS measurements. *J. Geophys. Res.* 104 (B1), 1077–1093. doi:10.1029/1998jb900043

Li, K., Wang, Y. F., Cheng, Q. G., Lin, Q. W., Wu, Y., and Long, Y. M. (2022). Insight into granular flow dynamics relying on basal stress measurements: From experimental flume tests. *JGR. Solid Earth* 127 (3). doi:10.1029/2021jb022905

Li, K., Wang, Y. F., Lin, Q. W., Cheng, Q. G., and Wu, Y. (2021). Experiments on granular flow behavior and deposit characteristics: Implications for rock avalanche kinematics. *Landslides* 18 (5), 1779–1799. doi:10.1007/s10346-020-01607-z

Lin, Q. W., Cheng, Q. G., Li, K., Xie, Y., and Wang, Y. F. (2020). Contributions of rockmass structure to the emplacement of fragmenting rockfalls and rockslides: Insights from laboratory experiments. *J. Geophys. Res. Solid Earth* 125 (4). doi:10.1029/2019jb019296

Lin, Q. W., Cheng, Q. G., Xie, Y., Zhang, F. S., Li, K., Wang, Y. F., et al. (2021). Simulation of the fragmentation and propagation of jointed rock masses in rockslides: DEM modeling and physical experimental verification. *Landslides* 18 (3), 993–1009. doi:10.1007/s10346-020-01542-z

Locat, P., Couture, R., Locat, J., Leroueil, S., and Jaboyedoff, M. (2006). Fragmentation energy in rock avalanches. *Can. Geotech. J.* 43 (8), 830–851. doi:10.1139/t06-045

Lucas, A., Mangeney, A., and Ampuero, J. P. (2014). Frictional velocity-weakening in landslides on Earth and on other planetary bodies. *Nat. Commun.* 5 (9), 3417. doi:10.1038/ncomms4417

Manzella, I., and Labiouse, V. (2009). Flow experiments with gravel and blocks at small scale to investigate parameters and mechanisms involved in rock avalanches. *Eng. Geol.* 109 (1-2), 146–158. doi:10.1016/j.enggeo.2008.11.006

Melosh, H. J. (1979). Acoustic fluidization: A new geological process? *J. Geophys. Res.* 84 (B13), 7513–7520. doi:10.1029/jb084ib13p07513

Mergili, M., Frank, B., Fischer, J. T., Huggel, C., and Pudasaini, S. P. (2018). Computational experiments on the 1962 and 1970 landslide events at Huascarán (Peru) with r.avaflow: Lessons learned for predictive mass flow simulations. *Geomorphology* 322, 15–28. doi:10.1016/j.geomorph.2018.08.032

Paguican, E. M. R., van Wyk de Vries, B., and Lagmay, A. F. M. (2014). Hummocks: How they form and how they evolve in rockslide-debris avalanches. *Landslides* 11 (1), 67–80. doi:10.1007/s10346-012-0368-y

Pollet, N., and Schneider, J. L. M. (2004). Dynamic disintegration processes accompanying transport of the holocene flims sturzstrom (Swiss alps). *Earth Planet. Sci. Lett.* 221 (1-4), 433–448. doi:10.1016/s0012-821x(04)00071-8

Pudasaini, S. P., and Hutter, K. (2007). *Avalanche dynamics: Dynamics of rapid flows of dense granular avalanches*. Verlag Berlin Heidelberg: Springer, 1–602.

Pudasaini, S. P., and Krautblatter, M. (2021). The mechanics of landslide mobility with erosion. *Nat. Commun.* 12, 6793. doi:10.1038/s41467-021-26959-5

Pudasaini, S. P., and Miller, S. A. (2013). The hypermobility of huge landslides and avalanches. *Eng. Geol.* 157, 124–132. doi:10.1016/j.enggeo.2013.01.012

Reznichenko, N. V., Andrews, G. R., Geater, R. E., and Strom, A. (2017). Multiple origins of large hummock deposits in alai valley, northern Pamir: Implications for palaeoclimate reconstructions. *Geomorphology* 285, 347–362. doi:10.1016/j.geomorph.2017.02.019

Shea, T., and Vries, B. W. (2008). Structural analysis and analogue modeling of the kinematics and dynamics of rockslide avalanches. *Geosphere* 4 (4), 657–686. doi:10.1130/ges00131.1

Strom, A., and Abdrakhmatov, K. (2018). *Rockslides and rock avalanches of central asia*. Netherlands: Elsevier, 1–424.

Strom, A. 1994. Mechanism of stratification and abnormal crushing of rockslide deposits. In: Proceedings of the 7th International IAEG Congress 3. Balkema, Rotterdam, 9 September, 1994, pp. 1287–1295.

Strom, A. (1999). The morphology and internal structure of large rockslides as indicators of their formational mechanisms. *Dokl. Akad. Nauk.* 369 (1), 1079–1081.

Sun, P., Zhang, Y. S., Shi, J. S., and Chen, L. W. (2011). Analysis on the dynamical process of Donghekou rockslide-debris flow triggered by 5.12 Wenchuan earthquake. *J. Mt. Sci.* 8 (2), 140–148. doi:10.1007/s11629-011-2112-9

Tapponnier, P., Xu, Z. Q., Roger, F., Meyer, B., Arnaud, N., Wittlinger, G., et al. (2001). Oblique stepwise rise and growth of the Tibet plateau. *Science* 294 (5547), 1671–1677. doi:10.1126/science.105978

Van Gassen, W., and Cruden, D. M. (1989). Momentum transfer and friction in the debris of rock avalanches. *Can. Geotech. J.* 26 (4), 623–628. doi:10.1139/t89-075

Wang, Y. F., Cheng, Q. G., Lin, Q. W., Li, K., and Yang, H. F. (2018). Insights into the kinematics and dynamics of the Luanshibao rock avalanche (Tibetan Plateau, China) based on its complex surface landforms. *Geomorphology* 317, 170–183. doi:10.1016/j.geomorph.2018.05.025

Wang, Y. F., Cheng, Q. G., Shi, A. W., Yuan, Y. Q., Qiu, Y. H., and Yin, B. M. (2019). Characteristics and transport mechanism of the Nyixoi Chongco rock avalanche on the Tibetan Plateau, China. *Geomorphology* 343, 92–105. doi:10.1016/j.geomorph.2019.07.002

Wang, Y. F., Cheng, Q. G., Yuan, Y. Q., Wang, J., Qiu, Y. H., Yin, B. M., et al. (2020). Emplacement mechanisms of the Tagarma rock avalanche on the pamir-western himalayan syntaxis of the Tibetan plateau, China. *Landslides* 17, 527–542. doi:10.1007/s10346-019-01298-1

Wang, Y. F., Cheng, Q. G., and Zhu, Q. (2012). Inverse grading analysis of deposit from rock avalanches triggered by Wenchuan earthquake. *Chin. J. Rock Mech. Eng.* 31 (6), 1089–1106. in Chinese. doi:10.3969/j.issn.1000-6915.2012.06.002

Wang, Y. F., Cheng, Q. G., and Zhu, Q. (2015). Surface microscopic examination of quartz grains from rock avalanche basal facies. *Can. Geotech. J.* 52 (2), 167–181. doi:10.1139/cgj-2013-0284

Wang, Y. F., Dong, J. J., and Cheng, Q. G. (2017). Velocity-dependent frictional weakening of large rock avalanche basal facies: Implications for rock avalanche hypermobility? *J. Geophys. Res. Solid Earth* 122 (3), 1648–1676. doi:10.1002/2016jb013624

Weidinger, J. T., Korup, O., Munack, H., Altenberger, U., Dunning, S., Tipelt, G., et al. (2014). Giant rockslides from the inside. *Earth Planet. Sci. Lett.* 389, 62–73. doi:10.1016/j.epsl.2013.12.017

Yuan, Z. D., Chen, J., Owen, L. A., Hedrick, K. A., Caffee, M. W., Li, W. Q., et al. (2013). Nature and timing of large landslides within an active orogen, eastern Pamir, China. *Geomorphology* 182, 49–65. doi:10.1016/j.geomorph.2012.10.028

Zeng, Q. L., Zhang, L. Q., Davies, T., Yuan, G. X., Xue, X. Y., Wei, R. Q., et al. (2019). Morphology and inner structure of Luanshibao rock avalanche in Litang, China and its implications for long-runout mechanisms. *Eng. Geol.* 260, 105216. doi:10.1016/j.enggeo.2019.105216

Zhang, M., and McSaveney, M. (2017). Rock avalanche deposits store quantitative evidence on internal shear during runout. *Geophys. Res. Lett.* 44 (17), 8814–8821. doi:10.1002/2017gl073774

Zhang, M., Yin, Y. P., and McSaveney, M. (2016). Dynamics of the 2008 earthquake-triggered Wenjiagou creek rock avalanche, Qingping, Sichuan, China. *Eng. Geol.* 200, 75–87. doi:10.1016/j.enggeo.2015.12.008

Zhang, P. Z., Shen, Z., Wang, M., Gan, W. J., Bürgmann, R., Molnar, P., et al. (2004). Continuous deformation of the Tibetan Plateau from global positioning system data. *Geol.* 32 (9), 809–812. doi:10.1130/g20554.1

Zhang, Y. B., Xing, A. G., Jin, K. P., Zhuang, Y., Bilal, M., Xu, S. M., et al. (2020). Investigation and dynamic analyses of rockslide-induced debris avalanche in Shuicheng, Guizhou, China. *Landslides* 17, 2189–2203. doi:10.1007/s10346-020-01436-0

Zhao, T., Crosta, G. B., Utili, S., and De Blasio, F. V. (2017). Investigation of rock fragmentation during rockfalls and rock avalanches via 3-D discrete element analyses. *J. Geophys. Res. Earth Surf.* 122 (3), 678–695. doi:10.1002/2016jf004060

Zhao, W. H., Wang, R., Liu, X. W., Ju, N. P., and Xie, M. L. (2020). Field survey of a catastrophic high-speed long-runout landslide in jichang town, shuicheng county, guizhou, China, on july 23, 2019. *Landslides* 17 (6), 1415–1427. doi:10.1007/s10346-020-01380-z

Zhu, Y. Q., Xu, S. M., Zhuang, Y., Dai, X. J., Lv, G., and Xing, A. G. (2019). Characteristics and runout behaviour of the disastrous 28 August 2017 rock avalanche in Nayong, Guizhou, China. *Eng. Geol.* 259, 105154. doi:10.1016/j.enggeo.2019.105154

frontiers | Frontiers in Earth Science

TYPE Original Research
PUBLISHED 23 September 2022
DOI 10.3389/feart.2022.964055

OPEN ACCESS

EDITED BY
Wen Zhang,
Jilin University, China

REVIEWED BY
Yuanjun Jiang,
Chinese Academy of Sciences (CAS), China
Xiaoyi Fan,
Southwest Petroleum University, China

*CORRESPONDENCE
Binbin Zhao,
zhaobinbin@163.com

SPECIALTY SECTION
This article was submitted to Geohazards and Georisks, a section of the journal Frontiers in Earth Science

RECEIVED 08 June 2022
ACCEPTED 12 August 2022
PUBLISHED 23 September 2022

CITATION
Zhao B, Zhang Y, Liu Y, Kong X, Liu C, Xu X and Deng Y (2022), Calibration of effective interface friction angle in granular flow impact experiment. *Front. Earth Sci.* 10:964055. doi: 10.3389/feart.2022.964055

Calibration of effective interface friction angle in granular flow impact experiment

Binbin Zhao[1,2]*, Yingtian Zhang[3], Yi Liu[2], Xiaoang Kong[2], Chang Liu[2], Xiyu Xu[2] and Yuanjing Deng[2]

[1]Faculty of Engineering, China University of Geosciences, Wuhan, China, [2]China Electric Power Research Institute Co., Ltd, Beijing, China, [3]State Grid Smart Internet of Vehicles Co., Ltd, Beijing, China

By using the normal and tangential forces measured in experiments of granular flow impact against a retaining wall, the effective interface friction angle of the wall was calculated in the dynamic phase and the static phase respectively, designated as δ_{ec} and δ_{es}, and both of them are smaller than the interface friction angle measured by laboratory test (δ_2). It is found δ_{ec} shows an increasing trend against inclination angle (β), which is opposite to that of δ_{es}; and δ_{ec} has an underestimation of effective interface friction angle. By comparing the calculated normal forces of static phase and of dynamic phase with the measured values, it is found the lower bound relation between δ_{es}/δ_2 and β obtained from regression analysis could well calibrate the effective interface friction angle for both the wall and flume base. It is also noted that the increasing trend of δ_{ec} against β may be explained by the higher proportion of gravity-friction force at lower inclination angle, i.e., the higher proportion of drag force at higher inclination angle.

KEYWORDS

granular flow, interface friction angle, retaining wall, impact, calibration

1 Introduction

A granular flow impact, such as a landslide or a rock avalanche impinging against a retaining wall or other structures, could generate tremendous impact force on the structures against its flow (Sovilla et al., 2008; Faug et al., 2011). As concluded by Faug et al. (2009) and Jiang et al. (Jiang and Towhata., 2013; Jiang et al., 2015) in a granular flow impact event for both impact modes, see Figure 1, the force exerted on a retaining wall is basically composed of three force components: a drag force (F_d) (Buchholtz and Pöschel, 1998) and a passive earth force (F_p) (Savage and Hutter, 1989), both of them are produced by the flowing or inertial layer; and a gravity-and-friction induced force (F_{gf}) generated by the stagnant zone formed in front of the wall(Jiang and Towhata, 2013). According to the average velocity (v) and depth of flowing layer (h), and the weight of stagnant zone (G), the three force components could be calculated by the Eqs. 1–3.

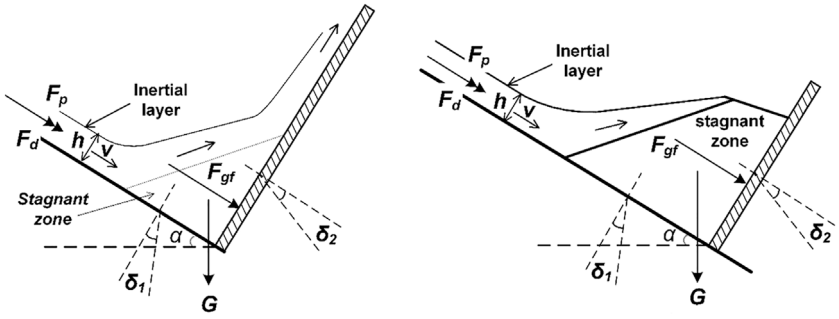

FIGURE 1
Drag force (F_d), passive earth force (F_p) and gravity-and-friction force (F_{gf}) respectively produced by inertial layer and stagnant zone in a granular flow impact event for two kinds of impact mode. δ_1 and δ_2 are respectively the interface friction angles of the flume base and the retaining wall.

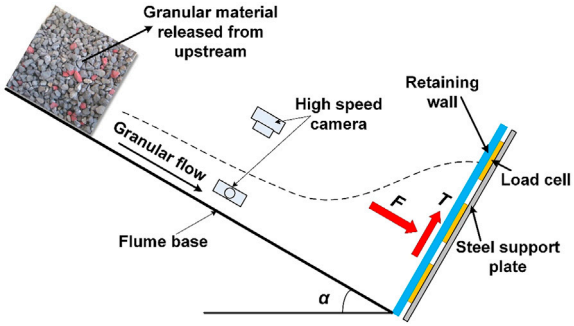

FIGURE 2
Experimental setup of granular material, flume and retaining wall model.

$$F_d = \frac{1}{2}\rho v^2 C_d h \tag{1}$$

In which $C_d = aFr^{-n} = a\left(\frac{v}{\sqrt{gh}}\right)^{-n}$

$$F_p = \frac{1}{2}k_p \rho g h^2 \cos\alpha \tag{2}$$

In which $k_p = \frac{\cos\alpha + \sqrt{\cos^2\alpha - \cos^2\varphi}}{\cos\alpha + \sqrt{\cos^2\alpha - \cos^2\varphi}}$

$$F_{gf} = G\frac{\sin(\alpha - \delta_1)}{\cos(\delta_1 + \delta_2)}\cos\delta_2 \tag{3}$$

In the previous research Bryant et al. (2014) reported that in a granular flow the actual basal friction is smaller than what measured in laboratory interface friction tests. While for a granular flow impact process Jiang et al. (2015) found for the stagnant zone the actual value of friction angle between granular material and the interface of retaining wall (δ_2 in Eq. 3) is also significantly smaller than the value measured by laboratory interface friction tests; also compared with δ_2, the reduction of δ_1.more significantly increases the value of F_{gf} calculated by Eq. 3. As a further extension of Jiang's previous work, this paper provides a more detailed study of the reduction of interface friction angle and a calibration of the effective interface friction angles for impact force calculation.

2 Experimental methodology

As shown in Figure 2, the height and width of the flume were 0.35 m, and 0.3 m, respectively. In order to simulate a granular flow impact process, a mass of limestone particles (named as *Particle1*) were released on the upstream of the flume with an inclination of α. There was a trigger gate in front face of the moving particles to control the release of the particles. After flowing a distance of 2.19 m, it impacted the retaining wall installed at the downstream of the flume. In the experiments the impact force exerted on the retaining wall was measured in both normal and tangential directions by an array of load cells. The total normal force (F) and total tangential force (T) could be deduced from the load cells records. The current methodology neglected the influence of non-uniform normal forces measured from the load cells and ignored the development of interface friction as a function of relative movement between the soil and the interface material. The motion of impact process and the surface velocity of granular flow were recorded by high speed cameras installed at the downstream of the flume. Each model test was named according to the length (L) and height (H) of the initial deposition, and the inclination angle of flume base (α), such as "*Particle1-L44-H20-α45*," which indicates an experiment of *Particle1* with an initial length and height of 44 and 20 cm, and a inclination angle of 45°. By changing initial length, height and inclination angle 64 tests were done in total.

By referring to Burkalow (1945), Pudasaini et al. (2007) and Jiang and Towhata (2013), the interface friction angles of *Particle1* with flume base, retaining wall and side wall were measured by laboratory tests. In the tests a paper cylinder with a diameter of more than 10 times of mean particle diameter (D_{50}) and a height of more than 5 times of D_{50}, was

TABLE 1 Physical properties of particle.

Property	Value
Minimum dry unit weight, γmin (kN/m3)	13.5
Maximum dry unit weight, γmax (kN/m3)	15.4
Mean particle diameter, D50 (mm)	14.1
Maximum particle diameter, Dmax (mm)	25.4
Minimum particle diameter, Dmin (mm)	1.68
Uniformity Coefficient, Cu	1.5
Dynamic internal friction angle, φ (°)	45
Basal friction angle, δ1 (°)	25
Friction angle of retaining wall, δ2 (°)	21
Friction angle of side wall, δ3(°)	15

friction. Then by slowly tilting the plate until the cylinder started to move, the inclination angle was recorded as the interface friction angle between *Particel1* and the plate. Physical properties of *Particle1* are listed in Table 1.

3 Results analysis

3.1 Reduction of interface friction

In order to calculate the effective interface friction angle in a granular flow impact process, first of all, the time history of the total normal force (F) and total tangential force (T) were plotted in Figure 3A. The force history could be categorized into two

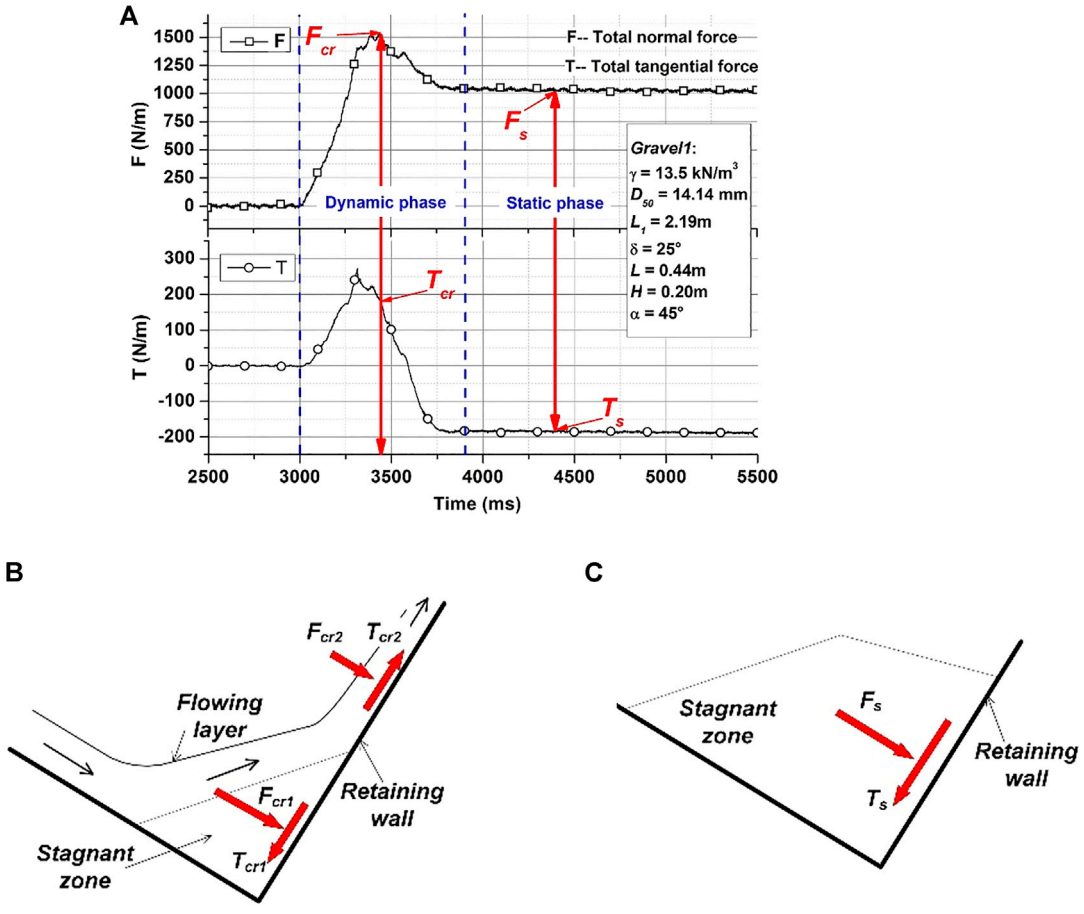

FIGURE 3
(A) Total normal and tangential forces history composed of dynamic and static phases, **(B)** Force generation mode in dynamic phase, **(C)** Force generation mode in static phase.

filled with *Particle1* and placed on the plate which is the same material as flume base or retaining wall or side wall. A gap of half D_{50} was kept between paper cylinder and the plate to avoid

phases: one is the dynamic phase, in which granular flow interacts with the retaining wall, both the flowing layer and the stagnant zone determine the force on the wall (Figure 3B); the

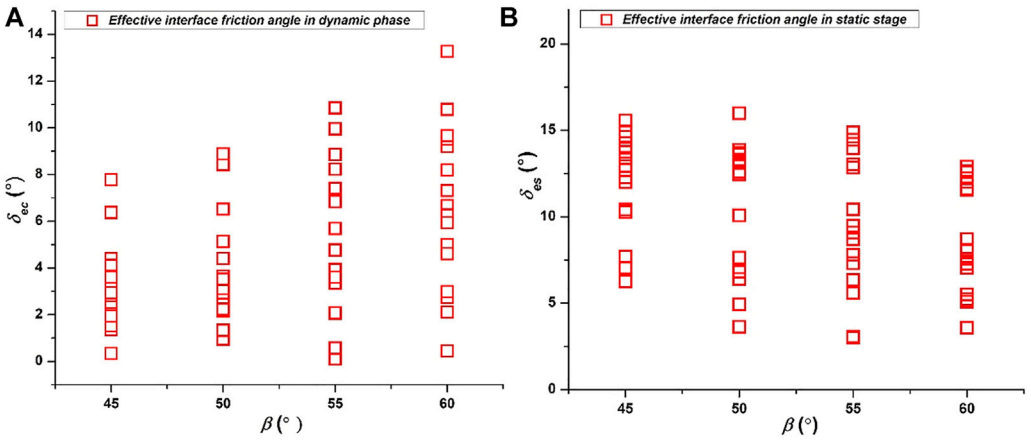

FIGURE 4
Variation of δ_{ec} and δ_{es} with interface inclination angle (β).

other is the static phase, in which granular flow ceases, only the stagnant zone generates force on the wall (Figure 3C). For the dynamic phase the forces were deduced at the time when maximum F occurred, and the corresponding normal and tangential forces are defined as F_{cr} and T_{cr}; while for the static phase, since both normal and tangential forces are constant, therefore, they were deduced at any time and defined as F_s and T_s.

F_{cr}, T_{cr}, F_s, and T_s were deduced for all the 64 experiments, thereafter, the effective interface friction angle of the dynamic phase was calculated by $\delta_{ec} = \arctan(|T_{cr}/F_{cr}|)$; and the effective interface friction angle of the static phase was calculated by $\delta_{es} = \arctan(|T_s/F_s|)$. In Figures 4A,B δ_{ec} and δ_{es} were respectively plotted against inclination angle of wall ($\beta = 90°-\alpha$) instead of inclination angle (α). In Figure 4A the maximum value of δ_{ec} is less than 14°, and in Figure 4B the maximum value of δ_{es} is less than 17°, which obviously indicates that both δ_{ec} and δ_{es} have a significant reduction from the laboratory measured δ_2 (21°). However, Figure 4A shows δ_{ec} increases with β, which is totally opposite to the decreasing trend of δ_{es} against β in Figure 4B. This divergence will be discussed in the last part of the paper.

As shown in Figure 3B in the dynamic phase the flowing layer produced a normal sub-force (F_{cr1}) and a tangential sub-force (T_{cr1}); meanwhile, the stagnant zone produce another pair of normal sub-force (F_{cr2}) and tangential sub-force (T_{cr2}). It is clear that the two tangential sub-forces are opposite in direction, which means the resultant tangential force is smaller than either T_{cr1} or T_{cr2}, i.e., the effective interface friction angle calculated from $\delta_{ec} = \arctan(|(T_{cr1} - T_{cr2})/(F_{cr1} + F_{cr2})|)$ is smaller than its actual value. While in Figure 3C there is only one tangential sub-force, i.e. the effective interface friction angle could be correctly calculated by $\delta_{es} = \arctan(|T_s/F_s|)$. Therefore, it is rational to assess the effective interface friction angle based on the normal and tangential forces in the static phase.

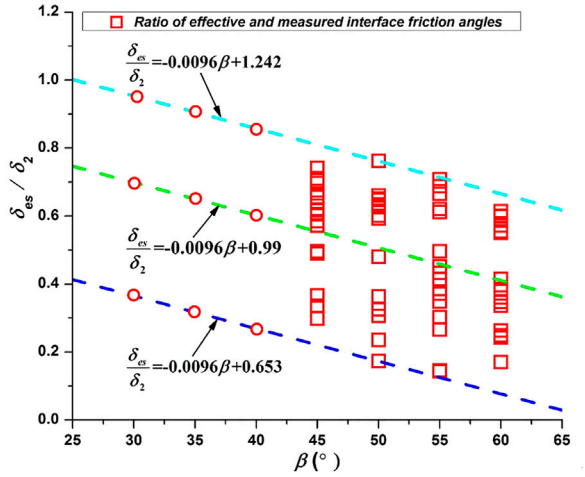

FIGURE 5
Relation of reduction rate of interface friction angle (δ_{es}/δ_2) and inclination angle (β); the red circle is where the value of δ_{es} will be calculated for flume base.

3.2 Calibration of effective interface friction angle

In Figure 4B the effective interface friction angle (δ_{es}) was calculated for the wall, however, from Figure 1 and Eq. 3 it is known that the normal force on the wall is determined by both the frictions of the wall and flume base. Therefore, it is also necessary to evaluate the effective interface friction angle of flume base. Since the laboratory measured interface friction angles of the wall and the flume base are close (Table 1), therefore, authors assume the reduction law for the wall and the flume base is the same; and if a relation between δ_{es} and β could be obtained from

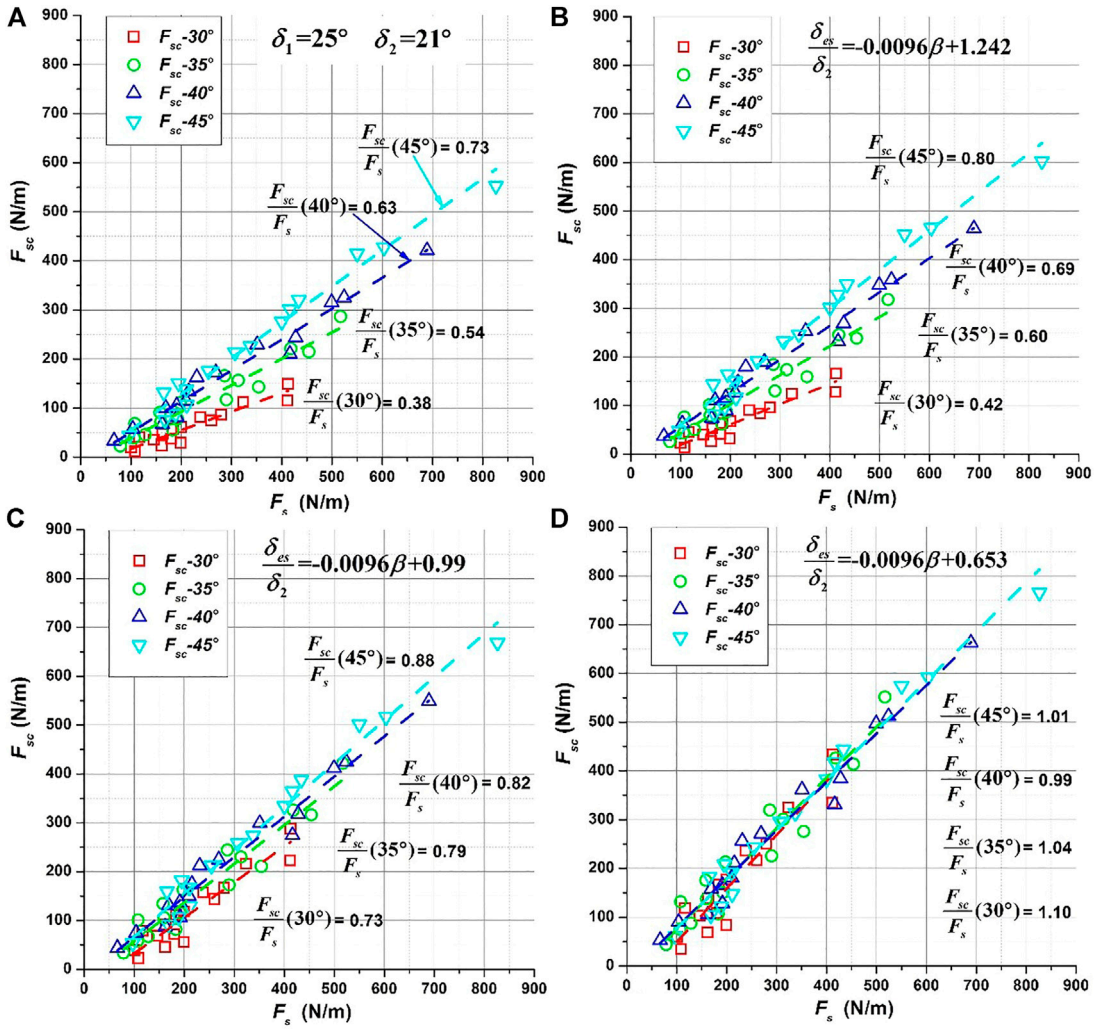

FIGURE 6
Comparison of calculated normal force of static phase (F_{sc}) with normal force of experimental measurement (F_s).

Figure 4B, it will be also applicable to the calibration of the effective interface friction angle of flume base.

In order to obtain one proper relation to calibrate δ_{es}, first, δ_{es} was normalized by δ_2 and plotted against β in Figure 5. The green dash line is the fitting of the data and defined as intermediate relation. Since for each β the value of δ_{es}/δ_2 has a wide scope, therefore, by offsetting the green line to the greatest and lowest bounds of δ_{es}/δ_2, an upper bound (light blue dash line) and a lower bound (deep blue dash line) relationships were found. According to the β of flume base and wall, the corresponding δ_{es} will be calculated. Consequently, it is going to be verified that if any of the relations could well calibrate δ_{es}.

In Figure 6, the normal force in static phase was calculated by Eq. 3 and designated as F_{sc}, and plotted against experimentally measured F_s. From Figures 6A–D the interface friction angles were either set as δ_1 and δ_2 or calculated by the three fitting relations in Figure 5.

Different colors was used to differentiate the results of different inclination angle. In Figure 6A it is clear that using δ_1 = 25° and δ_2 = 21° the calculated F_{sc} were smaller than the measured F_s; and with inclination angle (α) decreasing, the ratio of F_{sc} over F_s decreases from 0.73 to 0.38, i.e., the smaller the inclination angle is, the greater F_{sc} deviates from F_s.

From Figure 6B and Figure 6D, the ratio of F_{sc}/F_s get greater from upper bound relation to intermediate relation and to lower bound relation. As shown in Figure 6D for all the inclination angles the ratios of F_{sc}/F_s are close to 1.0, i.e., the lower bound relation gives the most accurate calibration of δ_{es}. As a second validation, the normal impact force of dynamic phase was calculated by summation of Eqs. 1,3 and designated as F_{sum}. In Figures 7A,B F_{sum} were respectively calculated by using the interface friction angle measured by laboratory test and that calibrated by lower bound relation, and were plotted

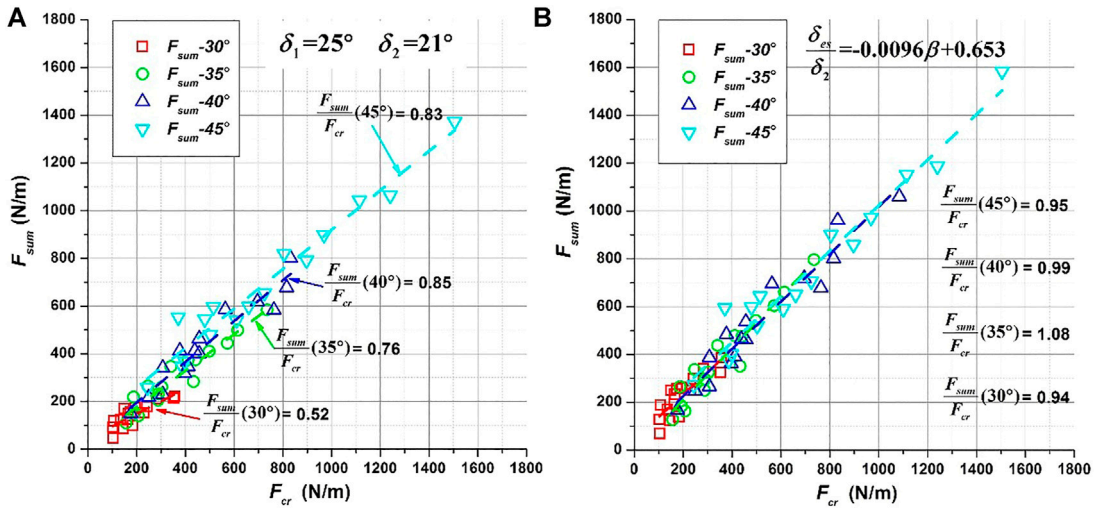

FIGURE 7
Comparison of calculated normal force of dynamic phase (F_{sum}) with normal force of experimental measurement (F_{cr}).

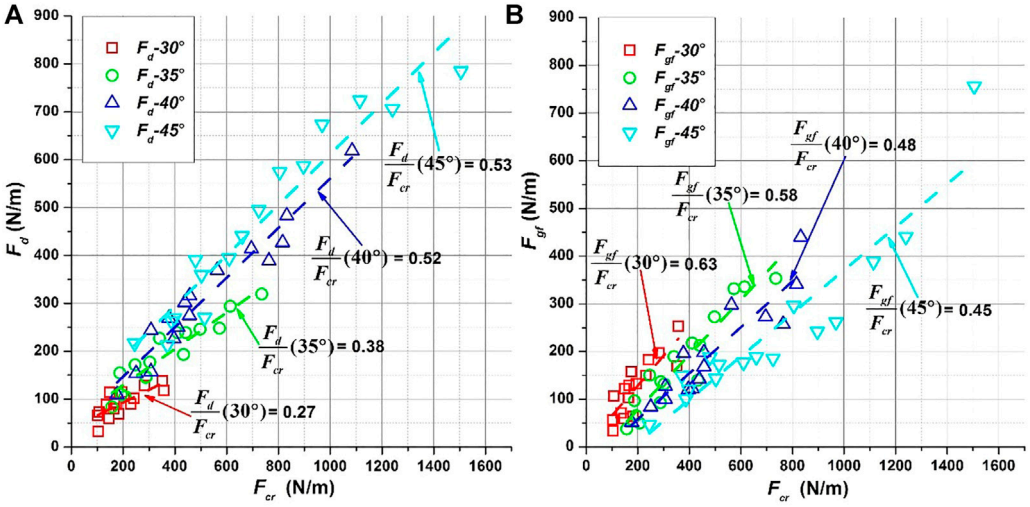

FIGURE 8
Dominant force component variation with inclination angle.

against the experimentally measured impact force (F_{cr}). In Figure 7A it is clear before calibration the ratio of F_{sum}/F_{cr} is always smaller than 1.0, and also decreases with inclination angle; for inclination angle of 30° the F_{sum} is only half of F_{cr}. After calibration for all the inclination angles the ratio of F_{sum}/F_{cr} is very close to 1.0, which once again indicates that the lower bound relation is suitable for the calibration of effective interface friction angle.

4 Discussion

In Section 3, Figures 4A,B present two opposite trends between δ_{es} and β. Since Figure 4B is already validated to be the correct representation of effective interface friction angle, hereby, the reason for the decreasing trend between δ_{ec} and β in Figure 4A is going to be discussed. First, the two main force components, F_d and F_{gf}, were respectively plotted against F_{cr}

in Figure 8, in which Figure 8A shows for higher inclination angle the proportion of F_d is higher; and Figure 8B shows for lower inclination angle the proportion of F_{gf} is higher. For higher inclination angle where the drag force is in domination (Figure 8A), the relatively thicker flowing layer (Figure 1A) produces more upward tangential sub-force; vice versa, for lower inclination angle where the gravity-and-friction force is dominating (Figure 8B), the flowing layer is thinner (Figure 1B), and less upward tangential sub-force is produced. Consequently, for higher inclination angle the resultant tangential force is relatively smaller, the effective friction angle calculated by $\delta_{ec} = \arctan(|(T_{cr1} - T_{cr2})/(F_{cr1} + F_{cr2})|)$ is accordingly smaller, which accounts for the trend in Figure 4A.

5 Conclusion

The effective interface friction angle of the wall calculated for the dynamic phase and the static phase (δ_{ec} and δ_{es}) are smaller than the laboratory measured δ_2. It is found δ_{ec} shows an increasing trend against inclination angle (β), which is opposite to that of δ_{es}; and δ_{ec} has an underestimation of effective interface friction angle. By using regression analysis an upper bound relation, an intermediate relation and a lower bound relation were obtained for δ_{es}/δ_2 and β. It is found the lower bound relation could well calibrate the effective interface friction angle for both the wall and flume base. It is also noted that the increasing trend of δ_{ec} against β in Figure 4A may be explained by the higher proportion of gravity-friction force at lower inclination angle, i.e., the higher proportion of drag force at higher inclination angle.

Data availability statement

The raw data supporting the conclusion of this article will be made available by the authors, without undue reservation.

Author contributions

BZ contributed to conception and investigation of the study and wrote the first draft of the manuscript. All authors contributed to manuscript revision, read, and approved the submitted version.

Funding

This study was funded by the National Key R&D Program of China, grant number 2018YFC0809400.

Conflict of interest

Authors BZ, YL, XK, CL, XX and YD were employed by China Electric Power Research Institute Co., Ltd. Author YZ was employed by State Grid Smart Internet of Vehicles Co., Ltd.

Publisher's note

References

Bryant, S. K., Take, W. A., and Bowman, E. T. (2014). Observations of grain-scale interactions and simulation of dry granular flows in a large-scale flume. *Can. Geotech. J.* 52, 638–655. Published on the web 19 September 2014. doi:10.1139/cgj-2013-0425

Buchholtz, V., and Pöschel, T. (1998). Interaction of a granular stream with an obstacle. *Granul. Matter* 1, 33–41. doi:10.1007/pl00010908

Burkalow, A. (1945). Angle of repose and angle of sliding friction: An experimental study. *Geol. Soc. Am. Bull.* 56 (6), 669–707. doi:10.1130/0016-7606(1945)56[669:aoraao]2.0.co;2

Faug, T., Beguin, R., and Chanut, B. (2009). Mean steady granular force on a wall overflowed by free-surface gravity-driven dense flows. *Phys. Rev. E* 80, 021305. doi:10.1103/physreve.80.021305

Faug, T., Caccamo, P., and Chanut, B. (2011). Equation for the force experienced by a wall overflowed by a granular avalanche: Experimental verification. *Phys. Rev. E* 84, 051301. doi:10.1103/physreve.84.051301

Jiang, Y.-J., and Towhata, I. (2013). Experimental study of dry granular flow and impact behavior against a rigid retaining wall. *Rock Mech. Rock Eng.* 46 (4), 713–729. doi:10.1007/s00603-012-0293-3

Jiang, Y. J., Zhao, Y., Towhata, I., and Liu, D.-X. (2015). Influence of particle characteristics on impact event of dry granular flow. *Powder Technol.* 270, 53–67. doi:10.1016/j.powtec.2014.10.005

Pudasaini, S. P., Hutter, K., Hsiau, S-S., Tai, S-C., Wang, Y., and Katzenbach, R. (2007). Rapid flow of dry granular materials down inclined chutes impinging on rigid walls. *Phys. Fluids (1994).* 19 (5), 053302. doi:10.1063/1.2726885

Savage, S. B., and Hutter, K. (1989). The motion of a finite mass of granular material down a rough incline. *J. Fluid Mech.* 199, 177–215. doi:10.1017/s0022112089000340

Sovilla, B., Schaer, M., Kern, M., and Bartelt, P. (2008). Impact pressures and flow regimes in dense snow avalanches observed at the vallée de la sionne test site. *J. Geophys. Res.* 113 (F1), F01010.

Glossary

a Empirical constant

T Total tangential force, N/m

g Gravitational acceleration, m/s^{-2}

T_{cr} Total tangential forces of dynamic phase, N/m

h Flow thickness, m

T_{cr1} Tangential sub-force of dynamic phase, N/m

k_p Passive earth pressure coefficient

T_{cr2} Tangential sub-force of dynamic phase, N/m

n Empirical constant

T_s Total tangential force of static phase, N/m

v Depth-averaged velocity, m/s

D_{min} Minimum particle diameter, mm

C_d Empirical drag coefficient

α Inclination angle of flume base, °

D_{50} Mean particle diameter, mm

β Inclination angle, °

D_{max} Maximum particle diameter, m

γ_{min} Minimum dry unit weight, kN/m^3

Fr Froude number

γ_{max} Maximum dry unit weight, kN/m^3

F Total normal force, N/m

δ_1 Interface basal friction angle, °

F_{cr} Total normal force of dynamic phase, N/m

δ_2 Interface friction angle of retaining wall, °

F_{cr1} Normal sub-force of dynamic phase, N/m

δ_3 Interface friction angle of side wall, °

F_{cr2} Normal sub-force of dynamic phase, N/m

δ_{ec} Equivalent interface friction angle of dynamic phase, °

F_s Total normal force of static phase, N/m

δ_{es} Equivalent interface friction angle of static phase, °

F_{sum} Total normal force calculated by equation, N/m

θ Angle of repose, °

G Weight of the stagnant zone, N/m

ρ Density of granular flow, kN/m^3

H Height of the initial deposit, m

φ Dynamic internal friction angle, °

L Length of the initial deposit, m

Fd Drag force, N/m

Fp, Passive earth force, N/m

Fgf Gravity-and-friction-induced force, N/m

Kp Passive coefficient

frontiers | Frontiers in Earth Science

TYPE Original Research
PUBLISHED 27 September 2022
DOI 10.3389/feart.2022.970550

OPEN ACCESS

EDITED BY
Xiaojun Guo,
Institute of Mountain Hazards and Environment (CAS), China

REVIEWED BY
Haijun Qiu,
Northwest University, China
Xinghua Zhu,
Chang'an University, China
Yuanjun Jiang,
Institute of Mountain Hazards and Environment (CAS), China

*CORRESPONDENCE
Xin Qu,
xqu1987@163.com

SPECIALTY SECTION
This article was submitted to Geohazards and Georisks, a section of the journal Frontiers in Earth Science

RECEIVED 16 June 2022
ACCEPTED 11 August 2022
PUBLISHED 27 September 2022

CITATION
Qu X and Diao F (2022), Stability assessment for hard anti-inclined bedded rock slopes using a limit equilibrium method.
Front. Earth Sci. 10:970550.
doi: 10.3389/feart.2022.970550

Stability assessment for hard anti-inclined bedded rock slopes using a limit equilibrium method

Xin Qu [1]* and Fangfang Diao [2]

[1]School of Civil and Architecture Engineering, Anyang Institute of Technology, Anyang, Henan, China, [2]School of Foreign Languages, Anyang Institute of Technology, Anyang, Henan, China

The failure mechanism of hard anti-inclined bedded rock slopes with the possibility of undergoing flexural toppling is very complex so that it is difficult to effectively perform their stability assessment. In this study, an attempt was made to accurately predict the stability factor and the failure surface of such slopes: establishing a new failure zone model and developing a limit equilibrium method based on this model. In this model, the failure zones of such a slope were divided strictly according to the failure mechanisms of the rock layers. In the presented method, the failure surface was considered to be a bilinear-type surface as observed in field investigations and laboratory tests, and the non-dimensional parameter indicating the position of application of the interlayer force was revised by deriving the distribution and the equivalent substitution of interlayer force. Then, a comparative study on Yangtai slope was performed to prove the presented method, and the effect of the non-dimensional parameter on the stability was also investigated. The results reveal that the presented method can accurately determine the failure surface and precisely evaluate the slope stability factor. In addition, the presented method has higher predictive accuracy compared with other analytical methods. With the decrease of the non-dimensional parameter, the stability of the slope is reinforced, but the larger landslide with more serious damage effect will occur if the slope undergoes the overall failure.

KEYWORDS

anti-inclined bedded rock slope, stability assessment, flexural toppling, limit equilibrium method, position of application of the interlayer force

Introduction

Toppling, being as a primary failure mode of anti-inclined bedded rock slopes, widely exists in natural and engineering slopes (Chen et al., 2020; Franziska et al., 2019; Gu and Huang, 2016). This failure can be generally divided into three kinds, i.e., flexural toppling, blocky toppling and block-flexure toppling (Goodman and Bray, 1976). If an anti-inclined bedded rock slope involves a dominant parallel joint set dipping steeply into the slope face, the majority of the rock layers are likely to bend toward open space under self-weight or external force. This phenomenon that usually occurs in the slopes composed of slates, phyllites and schists (Radko, 1995), is called flexural toppling (see Figure 1A). If such a slope contains another set of approximately orthogonal joints, most of the rock layers are

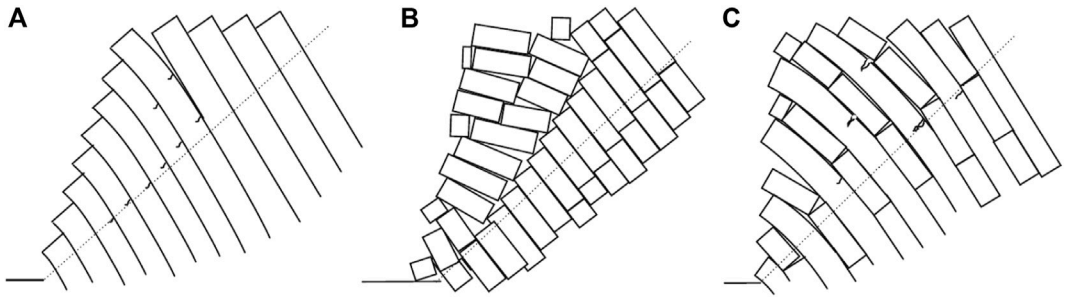

FIGURE 1
Anti-inclined bedded rock slopes: **(A)** flexural-toppling; **(B)** blocky-toppling; **(C)** block-flexure-toppling.

considered to rotate about a fixed point at or near the base under self-weight or external forces (see Figure 1B). This phenomenon that occurs mostly in the slopes composed of thick-bedded sandstone or limestone, as well as in columnar jointed volcanic (Radko, 1995), is called blocky toppling. The difference between the above two failure modes judged from geology is different discontinuities developed in rock masses, while the difference judged from mechanism lies in whether the rock column has bending or tensile resistance. In natural anti-inclined bedded rock slopes, some rock layers have a potential of undergoing blocky toppling while the others may undergo flexural toppling (see Figure 1C). This failure is generally called block-flexure toppling. Typical slopes subjected to block-flexure toppling are composed of bedded chert and shale, bedded sandstone and shale, and thin-bedded limestone (Radko, 1995). As the mechanism of blocky toppling failure is relatively simple, scholars have found numerous significant investigations and established the correspondingly theoretical analysis methods (Liu et al., 2008; Alejano et al., 2019; Recep and Ulamiş, 2020; Sarfaraz, 2021). On the contrary, flexural toppling failure is more complicated as the failure surfaces are often diverse and complex (Zhao et al., 2020; Ning et al., 2021). Fortunately, the existing advanced technologies (optical remote sensing, InSAR, LiDAR, etc.) enable people to accurately identify the geological structure of anti-inclined bedded rock slopes (Cai et al., 2022; Liu et al., 2022; Zhou et al., 2022). Combined with some advanced methods (the intelligence algorithm, LEM, UDEC, DDA, etc.), researchers have found many valuable investigations on this failure mechanism (Fan, 2015; Zheng et al., 2020; Zheng et al., 2021a; Zheng et al., 2021b; Liu et al., 2021; Su et al., 2021) as well.

According to field investigations, experimental studies, theoretical analyses and numerical simulations (Aydan and Kawamoto, 1992; Adhikary et al., 1997; Zuo et al., 2005; Adhikary and Dyskin, 2007; Lu et al., 2012; Cai et al., 2014; Zheng et al., 2015; Su et al., 2017; Zheng et al., 2018a; Zheng et al., 2018b; Lian et al., 2018; Qu and Diao, 2020), after the anti-inclined bedded rock slopes underwent flexural toppling failure, their failure surfaces can be classified into two primary types: linear-type plane and bilinear-type surface (see Figure 2). A linear-type failure plane is generally present in soft anti-inclined bedded rock slopes. This kind of failure plane across the toe of a slope was first proposed by Aydan and Kawamoto (Aydan and Kawamoto, 1992) performing base friction tests, and they discovered that this failure plane was perpendicular to the joints. After that, scholars perfected and improved Aydan and Kawamoto's investigation, which can be summarized as: repositioning the failure planes and establishing other methods. For example, Adhikary et al. (Adhikary et al., 1997) and Adhikary and Dyshin (Adhikary and Dyskin, 2007) found that the failure plane was a linear-type plane with an orientation of 10° above the plane perpendicular to the joints through centrifuge tests. Zheng et al. (Zheng et al., 2015; Zheng et al., 2018a) concluded that the angle between the plane perpendicular to the joints and the potential failure plane was about 13°. The above conclusions are suitable for specific cases, while further verification is required for other cases. The methods for searching the linear-type plane are mainly based on the limit equilibrium principle or discontinuous media theory. Among them, representative methods are the minimum stability factor method (Su et al., 2017), optimal limit equilibrium methods (Zheng et al., 2015; Qu and Diao, 2020), UDEC Trigon approach (Zheng et al., 2018a) and distinct lattice spring model (Lian et al., 2018). According to the relevant literatures (Zheng et al., 2015; Su et al., 2017; Zheng et al., 2018a; Lian et al., 2018; Qu and Diao, 2020), these methods can accurately determine the linear-type failure plane.

A bilinear-type failure surface is often present in hard anti-inclined bedded rock slopes. This kind of failure surface was first found by Zuo (Zuo et al., 2005) through several groups of physical model tests. Thereafter, the shape and position of the bilinear-type failure surface were refined by many scholars. For example, Lu et al. (Lu et al., 2012) considered that the bilinear-type surface was a combination of the plane obtained by Adhikary et al. (Adhikary et al., 1997) and the fracture surface induced by self-weight. Cai et al. (Cai et al., 2014) believed that

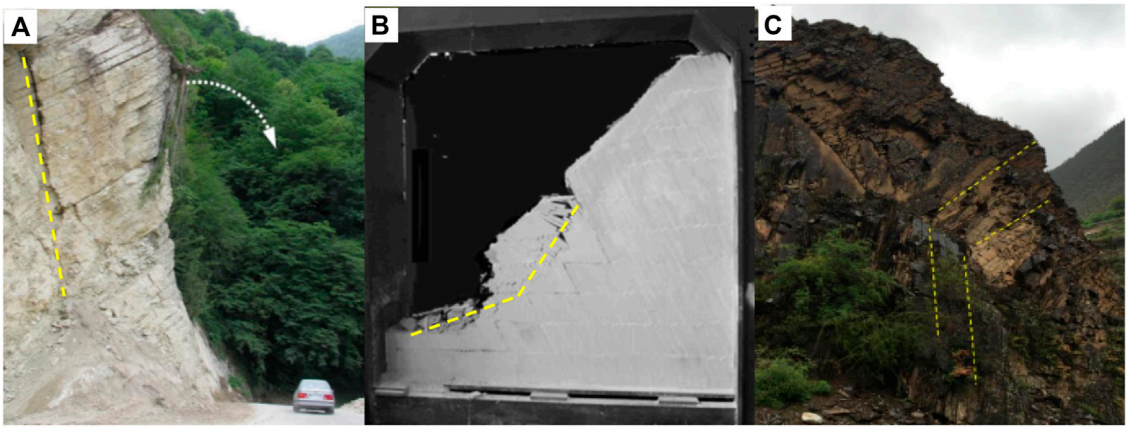

FIGURE 2
Flexural-toppling failures observed in field investigations and laboratory tests: **(A)** Galandrood mine slope; **(B)** the model slope; **(C)** Bank slope of Zhala Hydropower Station.

the total failure surface is formed by the fracture depth of each rock layer derived through a "reference surface" theory. Zheng et al. (Zheng et al., 2018b; Zheng et al., 2020; Zheng et al., 2021a) and Liu et al. (Liu et al., 2021) concluded that the failure plane of superimposed rock layers was a plane perpendicular to the joints, and the failure surface of cantilevered rock layers was multi-planar. Su et al. (Su et al., 2021) took cross joints into account and found that the bilinear-type failure surface was composed of three parts: the shear sliding failure surface at an angle above the plane perpendicular to the joints, the flexural toppling failure surface of superimposed rock layers parallel to the plane perpendicular to the joints, and the fracture failure surface of cantilevered rock layers parallel to the plane perpendicular to the joints. The above studies, mainly based on the limit equilibrium theory, further improve the basic theory of bilinear-type surfaces. However, there are still some issues needed to be resolved. When we employ the limit equilibrium method to assess the slope stability, the non-dimensional parameter indicating the position of application of the interlayer force should not be considered as a constant, but should be a variable varying with the distributions of interlayer forces. Furthermore, the bilinear-type failure surfaces obtained with current analytical methods are in disagreement with those observed in field investigations and physical experiments. Last but not the least, the stability factors of such slopes are not accurately evaluated.

To address these problems, the distribution and the equivalent substitution of the interlayer force were derived through the static equilibrium condition. Moreover, a new calculation formula was established to revise the non-dimensional parameter indicating the position of application of the interlayer force. Then, based on a new failure zone model, a limit equilibrium method was established to determine the bilinear-type failure surfaces and evaluate stability factors of hard anti-inclined bedded rock slopes with the possibility of undergoing flexural toppling. Finally, comparisons with other studies were performed to verify the solutions' validity and accuracy by taking Yangtai slope, and the effect of the non-dimensional parameter was also investigated.

Failure mechanism and failure zone model of hard anti-inclined bedded rock slopes

At the initial stage of the deformation evolvement of hard anti-inclined bedded rock slopes, the overlying rock layers undergo the flexural toppling deformation while the underlying rock layers at the toe of the slope are fiercely squeezed due to the little deformation space. Then, the toppling deformation of the overlying rock layers progressively enlarges, and the stress concentration of the underlying rock layers rapidly increases. The rock layers with a small slenderness ratio are more likely to undergo shear sliding failure, although most rock layers have a potential of undergoing flexural toppling failure (Cai et al., 2014; Zheng et al., 2018b; Zheng et al., 2020; Zheng et al., 2021a; Liu et al., 2021; Su et al., 2021). Once the shear stress reaches the shear strength of the rock layers, the shear sliding failure starts at the toe of a slope and the cracks progresses backwards. After the rock layers susceptible to either shear sliding failure or flexural toppling failure separate from their overlying rock layers, secondary toppling failure occurs under self-weight. However, several rock layers on the top of the slope will be stable if their tensile stresses yield to the tensile strength of the rock layer.

From the above analysis, the slope can be classified into four zones: shear sliding zone, flexural toppling zone, secondary

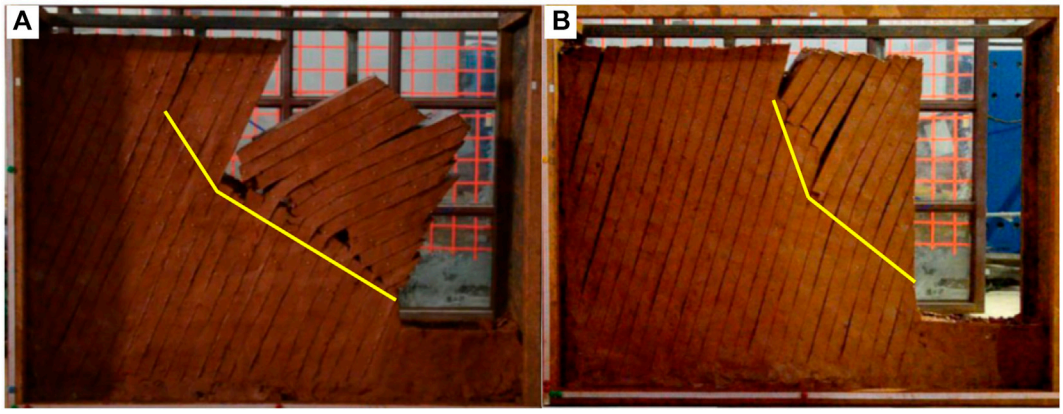

FIGURE 3
Failure surfaces of different models obtained by Ding et al. (Ding et al., 2021): **(A)** β=85, η=65; **(B)** β=85, η=75. Note: β is the inclination of the slope face, η is the inclination of the rock layer.

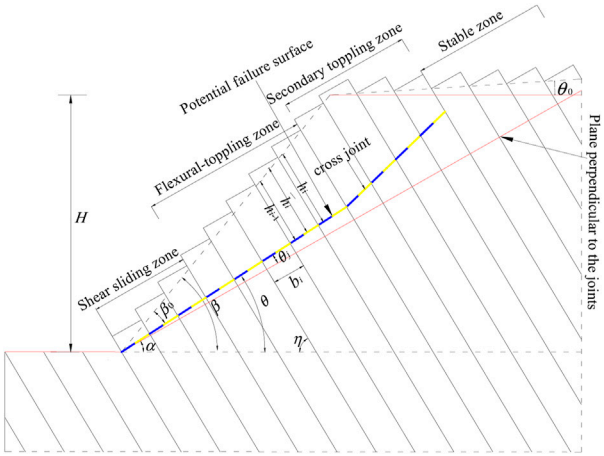

FIGURE 4
Failure zone model of a hard anti-inclined bedded rock slope.

toppling zone and stable zone. The shear sliding zone is composed of all rock layers with the possibility of undergoing shear sliding failure. The flexural toppling zone is composed of all rock layers with the possibility of undergoing flexural toppling failure under self-weight and interlayer forces, and these rock layers are considered to be superimposed cantilever beams. The secondary toppling zone is composed of all rock layers with the possibility of undergoing secondary toppling failure under self-weight, and these rock layers are considered to be independent cantilever beams.

The latest results on the failure surface obtained by Ding et al. (Ding et al., 2021) performing the physical model tests and several assumptions adopted in the previous studies (Zheng et al., 2018b; Su et al., 2021) are also valid in presented framework.

(1) In the shear sliding and flexural toppling zones, a linear-type plane at an angle above the plane perpendicular to the joints is considered to be the total failure surface (see Figure 3) (Ding et al., 2021).
(2) In the secondary toppling zone, for each rock layer, a linear-type failure plane parallel to the plane perpendicular to the joints is supposed to be the failure surface, which was supported by Su et al. (Su et al., 2021) and Zheng et al. (Zheng et al., 2018b).
(3) In each rock layer, a cross joint is supposed to develop on the upslope side of the failure surface, which was supported by Su et al. (Su et al., 2021).

Consequently, a new failure zone model of such slopes was established as shown in Figure 4, where α is the inclination of the plane perpendicular to the joints, β is the inclination of the slope face, β_0 is the angle between the plane perpendicular to the joints and the slope face, η is the inclination of the rock layer, θ_0 is the natural slope angle, θ is the inclination of the potential failure surface, θ_j is the angle between the plane perpendicular to the joints and the potential failure surface, b_i is the thickness of rock layer i, H is the slope height, h_i is the height of the right side of rock layer i, and $\bar{h}_i$ is the equivalent height of rock layer i. $h_{i\text{-}1}$ is the height of the right side of rock layer i-1, which is also equal to the height of the left side of rock layer i. The cross joints are represented by the yellow lines in Figure 4. The rock layers are numbered from the toe to the top. According to geometrical conditions, we can obtain Eq. 1.

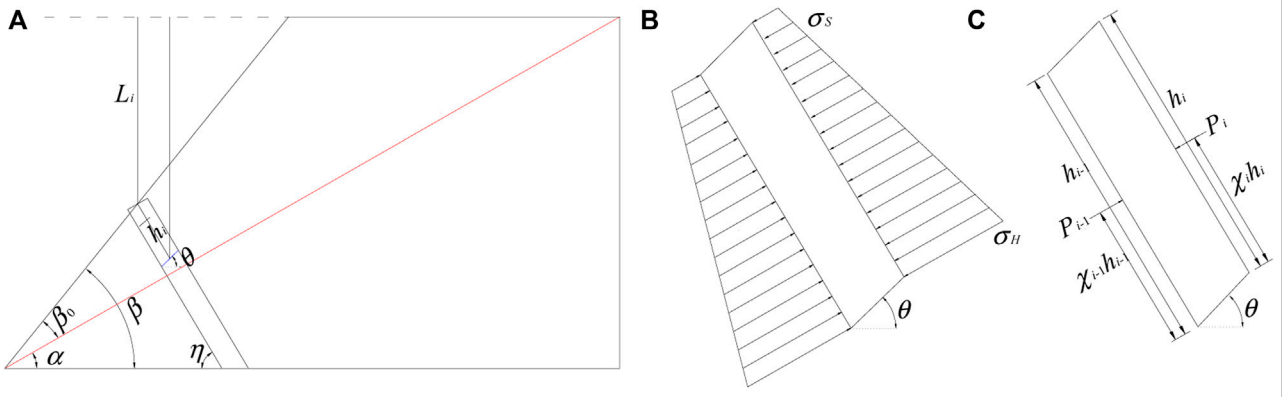

FIGURE 5
Anti-inclined bedded half space infinite slope: **(A)** mechanical model; **(B)** distribution of the interlayer force; **(C)** static equivalent substitution of the interlayer force.

$$\begin{cases} \alpha = \pi/2 - \eta \\ \beta_0 = \beta - \alpha \\ \theta = \alpha + \theta_j \end{cases} \tag{1}$$

Derivation of the non-dimensional parameter χ_i

When we employ the limit equilibrium method to assess the stability of anti-inclined bedded rock slopes subjected to flexural toppling, the interlayer forces exerting on the left side and the right side of the rock layers are considered to be acting on two points, $\chi_i h_i$ and $\chi_{i-1} h_{i-1}$, respectively, where χ_i is the non-dimensional parameter indicating the position of application of the interlayer force. Most researchers considered that χ_i was a constant and they obtained different values about χ_i. Aydan and Kawamoto (Aydan and Kawamoto, 1992) suggested that χ_i was equal to 0.5 as they found that the total side forces were more likely to be acting on the midpoint of the side through their base friction tests. Zheng et al. (Zheng et al., 2018a) verified this conclusion by using a new UDEC Trigon approach. Adhikary et al. (Adhikary et al., 1997) recommended that χ_i was 0.6 according to the centrifuge collapse data. Zheng at al. (Zheng et al., 2015), Qu and Diao (Qu and Diao, 2020) and Su et al. (Su et al., 2021) testified Adhikary's investigation from the perspective of theoretical analysis. However, the distributions of the interlayer forces are different. The non-dimensional parameter χ_i is not a constant, but varies with the distributions of interlayer forces. Based on the principle of static equivalent substitution, the non-dimensional parameter χ_i can be derived through the following analysis.

Figure 5A shows the mechanical model of an anti-inclined bedded half space infinite slope. The vertical load exerting on the top of rock layer i can be written as follows:

$$G_S = \gamma L_i \tag{2}$$

where γ is the unit self-weight, L_i, indicating the distance from the top of rock layer i to the top of slope, can be calculated with Eq. 3.

$$L_i = \begin{cases} H - \left[\sum_{ii=1}^{ii=i-1} b_{ii} + b_i/2\right] \sin\beta/\cos\beta_0 & i < n\_tp \\ 0 & i \geq n\_tp \end{cases} \tag{3}$$

where the first rock layer on the top of the slope is recorded as n_tp.

The vertical unloading exerting on slope face can be derived through static equilibrium condition:

$$G_S' = \gamma L_i \sin^2\beta \tag{4}$$

The lateral pressure exerting on the top of rock layer i can be calculated with Eq. 5.

$$\sigma_S = k\gamma L_i (1 - \sin^2\beta) \tag{5}$$

where k is the lateral pressure coefficient.

The lateral pressure exerting on the base of rock layer i can be calculated with Eq. 6.

$$\sigma_H = k\gamma \left[L_i (1 - \sin^2\beta) + \overline{h_i} \cos\theta \right] \tag{6}$$

Figures 5B,C respectively display the distribution and the static equivalent substitution of the interlayer force. Then, the non-dimensional parameter χ_i can be calculated with Eq. 7.

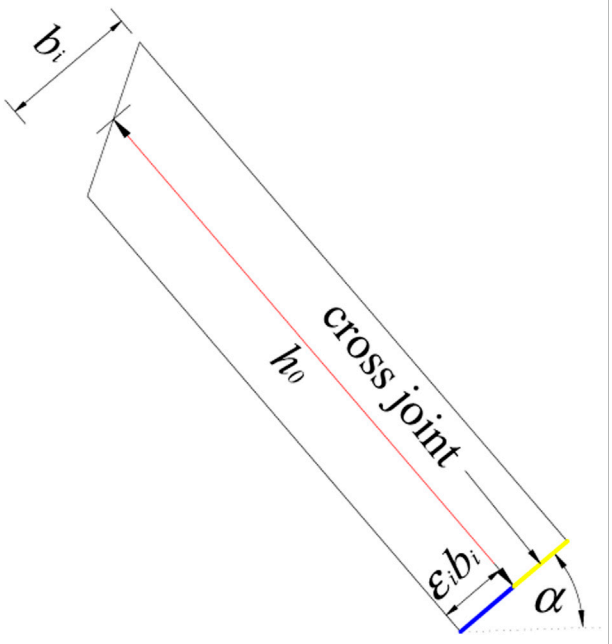

FIGURE 6
Critical height of rock layer *i* under self-weight.

$$\chi_i = \begin{cases} \dfrac{3L_i\left(1-\sin^2\beta\right)+\overline{h_i}\cos\theta}{6L_i\left(1-\sin^2\beta\right)+3\overline{h_i}\cos\theta} & i<n\_tp \\ \dfrac{1}{3} & i\geq n\_tp \end{cases} \tag{7}$$

From Eq. 7, it can be found that the value of χ_i is smaller than 0.5, and is greater than or equal to 1/3. Obviously, the previous studies have overestimated the value of χ_i.

Stability analysis of hard anti-inclined bedded rock slopes

Possible groups of the rock layers with a potential of undergoing the overall failure

Given the value of the searching angle θ_j through Eq. 8, the height of the right side of rock layer *i*, h_i, and its equivalent height, $\overline{h}_i$, can be respectively calculated with Eqs 10, 11.

$$\theta_j = (j-1)\Delta\theta_r,\ 1\leq j\leq nm \tag{8}$$

$$\Delta\theta_r = \beta_0/nm \tag{9}$$

$$h_i = \begin{cases} \sum_{k=1}^{k=i} b_k\left(\tan\beta_0-\tan\theta_j\right) & 1\leq i<n\_tp \\ \sum_{k=1}^{k=i} b_k\left(\tan\beta_0-\tan\theta_j\right)-\left(\sum_{k=1}^{k=i} b_k-\dfrac{H\cos\beta_0}{\sin\beta}\right)\left(\tan\beta_0+\cot\left(\beta_1\right)\right) & i\geq n\_tp \end{cases} \tag{10}$$

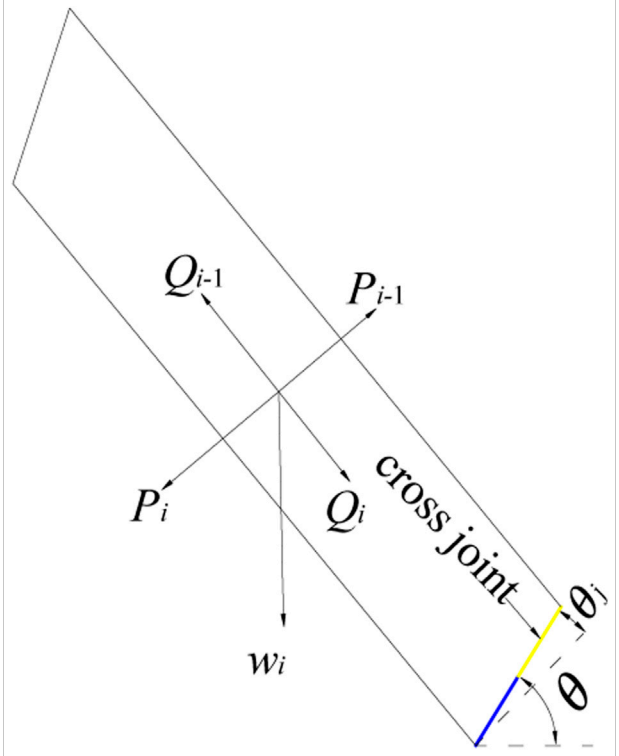

FIGURE 7
Analysis of rock layer *i* with the possibility of undergoing shear sliding failure.

$$\overline{h_i} = (h_i + h_{i-1})/2 \tag{11}$$

where *nm* and $\triangle\theta_r$ are the total number of searching times, and the size of the searching step, respectively. $\beta_1 = \eta+\theta_0$.

For the last rock layer with the possibility of undergoing flexural toppling failure, as the forces exerting on it are only composed of the resistant force and self-weight, the equivalent height of this rock layer, $\overline{h}_i$, must be larger than the critical height, h_0. The critical height of a single rock layer prior to toppling failure under self-weight (see Figure 6), h_0, can be calculated with Eq. 12.

$$h_0 = \frac{(3-2\epsilon_i)b_i\cos\alpha+\sqrt{(3-2\epsilon_i)^2b_i^2\cos^2\alpha+12\epsilon_i^2b_i\sigma_t\sin\alpha/\gamma}}{6\sin\alpha} \tag{12}$$

where ε_i and σ_t are the continuous ratio and the tensile strength of rock layer *i*, respectively.

The first and last rock layers with the possibility of undergoing flexural toppling failure are respectively recorded as *n_start* and *n_end*. Thus, rock layers {1, 2, . . ., *n_start*-1, *n_start*}, {1, 2, . . ., *n_start*, *n_start*+1}, . . ., {1, 2, . . ., *n_end*-1,

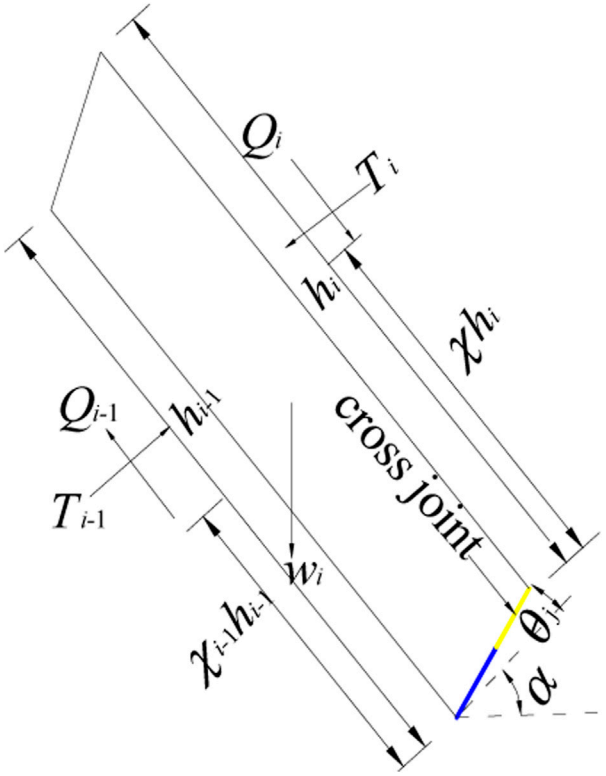

FIGURE 8
Analysis of rock layer *i* with the possibility of undergoing flexural toppling failure.

n_end} are the possible groups of the rock layers with a potential of undergoing the overall failure.

Failure modes of the rock layers located in the shear sliding and flexural toppling zones

In the shear sliding zone, all rock layers have a potential of undergoing shear sliding failure. Accordingly, the stress of each rock layer must meet the Mohr-Coulomb criterion (Su et al., 2021). In this case, the static equilibrium condition of resultant force is rigorously satisfied. Thus, the external force prompting rock layer *i* to undergo shear sliding failure (see Figure 7), P_i, can be determined with Eq. 13.

$$P_i = \frac{\begin{array}{c}\left(\epsilon_i \tan\varphi + (1-\epsilon_i)\tan\varphi_i\right)\left(\cos\theta \sum_{ii=1}^{i} w_{ii} + \cos\theta_j c_i (h_i - h_1)\right) \\ -\sin\theta \sum_{ii=1}^{i} w_{ii} + c_i \sum_{ii=1}^{i} b_{ii}\epsilon_{ii} \Big/ \cos\theta_j - \sin\theta_j c_i (h_i - h_1)\end{array}}{\begin{array}{c}\cos\theta_j\left(1+\tan\varphi_i \tan\theta_j\right) + \cos\theta_j\left(\tan\theta_j - \tan\varphi_i\right) \\ \left(\epsilon_i \tan\varphi + (1-\epsilon_i)\tan\varphi_i\right)\end{array}} \quad (13)$$

where c is the rock layer cohesion, c_i is the joint cohesion, φ is the rock layer friction angle, φ_i is the joint friction angle. If P_i<0, it demonstrates that rock layer *i* has the possibility of undergoing shear sliding failure without any downslope thrusts.

In the flexural toppling zone, all rock layers have the possibility of undergoing flexural toppling failure. Accordingly, the stress of each rock layer must meet the maximum tensile stress theory (Su et al., 2021). In this case, the static equilibrium condition of resultant moment is rigorously satisfied. Thus, the external force prompting rock layer *i* to undergo flexural toppling failure (see Figure 8), T_i, can be determined with Eq. 14.

$$T_i = \frac{\begin{array}{c}T_{i-1}\left(6\chi_{i-1}h_{i-1} + 2\epsilon_i b_i \tan\varphi_i\right) + \left(\epsilon_i^2 b_i^2 \sigma_t \Big/ \cos^2\theta_j\right. \\ \left. + b_i w_i \cos\alpha(3-2\epsilon_i) - 3\overline{h_i} w_i \sin\alpha + 2c_i b_i \left(h_i(6-2\epsilon_i) + h_{i-1}\epsilon_i\right)\right)\end{array}}{6\chi_i h_i - (6-2\epsilon_i) b_i \tan\varphi_i} \quad (14)$$

where T_{i-1} is the external force prompting rock layer *i*-1 to undergo flexural toppling failure. If T_i < 0, it indicates that rock layer *i* has the possibility of undergoing flexural toppling failure without any downslope thrusts.

Failure surface of the rock layers in the shear sliding and flexural toppling zones

In the secondary toppling zone, all rock layers are only subjected to self-weight. Thus, the external force prompting the rock layers in the shear sliding and flexural toppling zones to undergo the overall failure is the final external force prompting the slope to undergo the overall failure. As described in the minimum principle of Pan Jiazheng (Su et al., 2021), once a hard anti-inclined bedded rock slope has the possibility of undergoing the overall failure, the slope will slide or topple along the potential failure surface with the minimum resistant force. In other words, the most dangerous failure surface must be the potential failure surface with the minimum external force prompting the slope to undergo the overall failure.

The external force prompting each group of the rock layers to undergo the overall failure is calculated using a step by step method. Among these external forces, the minimum one is considered to be the external force prompting rock layers 1−*nn* to undergo the overall failure under the searching angle θ_j, recorded as $f_{nn}^{\ j}$. Then, changing the searching angle constantly, the external forces $\{f_{nn}^{\ 1}, f_{nn}^{\ 2}, \ldots, f_{nn}^{\ nm}\}$ are obtained, and the minimum one is considered to be the final external force prompting the slope to undergo the overall failure, recorded as *F*. The corresponding potential failure surface and the rock layers with a potential of undergoing the overall failure are the most dangerous. Obviously, the above problem can be regarded as an optimal problem with the searching angle, θ_j, as the variable parameter, which can be expressed as follows:

$$F = min\left(f_{nn}^{j}\left(\theta_j\right)\right) \quad n\_start \le nn \le n\_end \quad (15)$$

$$f_i^j\left(\theta_j\right) = \begin{cases} P_i\left(\theta_j\right) & 1 \le i \le nst \\ T_i\left(\theta_j\right) & nst < i \le nn \end{cases} \quad (16)$$

where *min* denotes the minimum function. The last rock layer with the possibility of undergoing shear sliding failure is recorded as *nst*, while the first rock layer with the possibility of undergoing flexural toppling failure under self-weight is recorded as *nn*.

The shear sliding zone is composed of rock layers 1–*nst*, which can be determined with inequation (17).

$$\begin{cases} P_{nst} \le T_{nst} \\ P_{nst+1} > T_{nst+1} \end{cases} \tag{17}$$

During the calculation process, $f_{nn} \le 0$ shows that rock layer *nn* has a potential of undergoing flexural toppling failure under self-weight, and thus, the corresponding flexural toppling zone is composed of rock layers *nst*+1–*nn*. The corresponding searching angle is recorded as θ_r.

Failure surface of the rock layers in the secondary toppling zone

Once the rock layers located in the shear sliding and flexural toppling zones separate from their overlying rock layers, rock layers *nn*+1–*nt* have the possibility of undergoing secondary toppling failure if the equivalent height of each of those rock layers is larger than the critical height h_0. The number of fracture stages for rock layer *nn*+1, n_1, can be calculated with Eq. 18.

$$n_1 = \begin{cases} \left\lfloor \left(\sum_{i=1}^{i=nn+1} b_i \tan\beta_0 - \sum_{i=1}^{i=nn} b_i \tan\theta_r \right) \Big/ h_0 \right\rfloor & 1 \le nn+1 < n\_tp \\ \left\lfloor \left(\sum_{i=1}^{i=nn+1} b_i \tan\beta_0 - \left(\sum_{i=1}^{i=nn+1} b_i - (H/\sin\beta)\cos\beta_0 \right) \right. \right. & \\ \left. \left. (\tan\beta_0 + \cot(\beta_1)) - \sum_{i=1}^{i=nn} b_i \tan\theta_r \right) \Big/ h_0 \right\rfloor & n\_tp \le nn+1 \le n\_end \end{cases} \tag{18}$$

where $\lfloor\ \rfloor$ denotes the function rounded towards zero. The total number of the rock layers with the possibility of undergoing all kinds of failures is recorded as *nt*.

According to the detailed analysis conducted by Su et al. (Su et al., 2021), the positions of the potential failure surfaces of the underlying rock layers must be lower than those of the overlying rock layers, and thus, the number of fracture stages for rock layer *nn*+*ii*, n_{ii}, can be calculated with Eq. 19.

$$n_{ii} = \begin{cases} \lfloor (b_{nn+ii}\tan\beta_0 + n_{ii-1}h_0)/h_0 \rfloor & 1 \le nn+ii < n.tp \\ \left\lfloor \left(b_{nn+ii}\tan\beta_0 + n_{ii-1}h_0 - \left(\sum_{i=1}^{i=nn+ii} b_i - (H/\sin\beta)\cos\beta_0 \right) \right. \right. & \\ \left. \left. (\tan\beta_0 + \cot\beta_1) \right) \Big/ h_0 \right\rfloor & nn+ii = n.tp\ (2 \le ii \le t) \\ \lfloor (n_{ii-1}h_0 - b_{nn+ii}\cot\beta_1)/h_0 \rfloor & n.tp < nn+ii \le n.end \end{cases} \tag{19}$$

where the total number of the rock layers with the possibility of undergoing secondary toppling failure under self-weight is recorded as *t*. Additionally, inequation (20) must be satisfied.

$$\begin{cases} \left(b_{nn+t+1}\tan\beta_0 + n_t h_0 - \left(\sum_{i=1}^{i=nn+t+1} b_i - (H/\sin\beta)\cos\beta_0 \right) \right. & \\ \left. (\tan\beta_0 + \cot\beta_1) \right) < h_0 & nn+t+1 = n\_tp \\ (n_t h_0 - b_{nn+t+1}\cot\beta_1) < h_0 & n\_tp < nn+t+1 \le n\_end+1 \end{cases} \tag{20}$$

Stability criterion

From the above analysis, we can find that the sign of *F* can be regarded as an indicator of the stability of a hard anti-inclined bedded rock slope with the possibility of undergoing shear sliding failure and flexural toppling failure: 1) *F*<0, unstable; 2) *F*=0, at the limit equilibrium state; 3) *F*>0, stable. By reducing the strength parameters with the reduction criterion (see Eq. 21) (Su et al., 2021) to make the external force *F* equal to zero, we can obtain the stability factor of the slope *Fs*.

$$\begin{cases} c_t' = \dfrac{c_i}{F_S} \quad c' = \dfrac{c}{F_S} \quad \sigma_t' = \dfrac{\sigma_t}{F_S} \\ \tan\varphi' = \dfrac{\tan\varphi}{F_S} \quad \tan\varphi_t' = \dfrac{\tan\varphi_i}{F_S} \end{cases} \tag{21}$$

Case study

Yangtai slope is a large ancient landslide triggered by rainstorm, which is located in Yangtai Village of Xiuning County, Anhui province, China (see Figure 9) (Liu, 2012). As depicted in Figure 10, the leading edge of the slope is located at an elevation of approximately 350 m, and the trailing edge is located at an elevation of around 620 m. The length of the slope along the river is about 360 m, and the longitudinal length is about 690 m. Due to the long-term rain erosion and surface water erosion, four typical deep gullies are formed on the surface of the slope (see Figure 9). The trailing edge of the landslide is bounded by "ring" steep rock cliffs, while the upstream and downstream are bounded by 4# and 1# gullies respectively (see Figure 9). Due to the strong erosion of Yangtai River, the leading edge of the landslide moves constantly. Multistage creep and tension cracks develop significantly at the leading edge of the slope, and the slope undergoes multiple secondary failures along the secondary sliding surfaces. About 4.3 million cubic meters of residual deposits lay on the side of the road (see Figure 11). The main sliding direction is 195°. Landslide deposits are mainly composed of pebbly silty soil and gravel soil. The composition of gravel soil is mainly highly weathered phyllitic slate, while the composition of silty soil is mainly sub-clay. The sliding bed is mainly composed of sandy slates (Pt2b). The beds strike NW30°–35°, and dip into the slope at approximately 63°. The average thickness of the rock layers is about 4 m. Figure 12 and Table 1 respectively present the calculation model diagram and the softened parameters of rock mass (Liu, 2012).

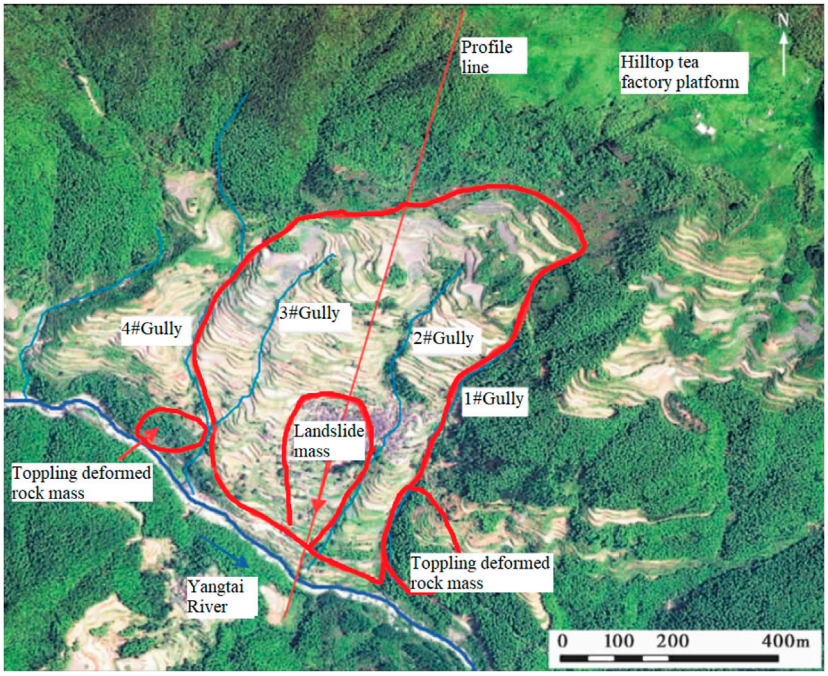

FIGURE 9
Remote sensing image of Yangtai slope.

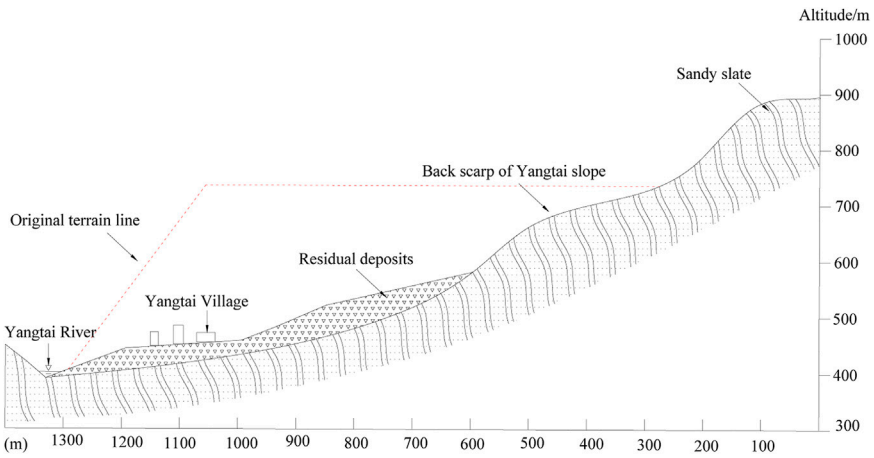

FIGURE 10
Engineering geological profile of Yangtai slope.

The results calculated using the presented method are presented in Table 2, and we can clearly conclude that Yangtai slope is subjected to toppling failure, which is in good agreement with field investigations. Figure 13A shows the non-dimensional parameters χ_i obtained with the presented method. It presents almost a smooth curve in this figure except for the point (26, 0.35), and the reason is that the distribution of the interlayer force between rock layers 27 and 28 changes greatly compared with that of the other interlayer forces. The value of χ_i decreases monotonously as the number of the rock layers increases, and the maximum and the minimum values are 0.498 and 0.333, respectively. Figure 13B shows that the

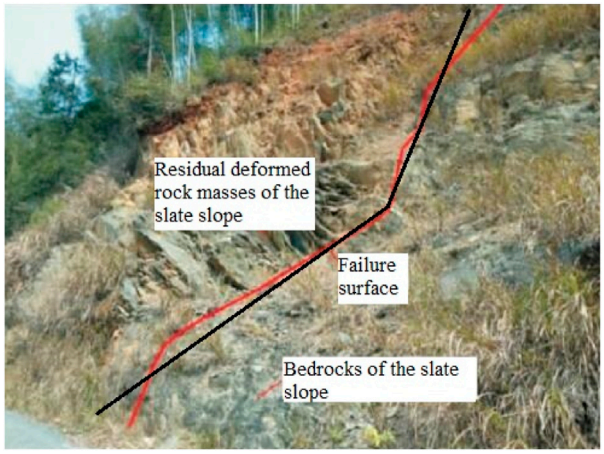

FIGURE 11
Residual deposits of Yangtai slope observed in field investigations.

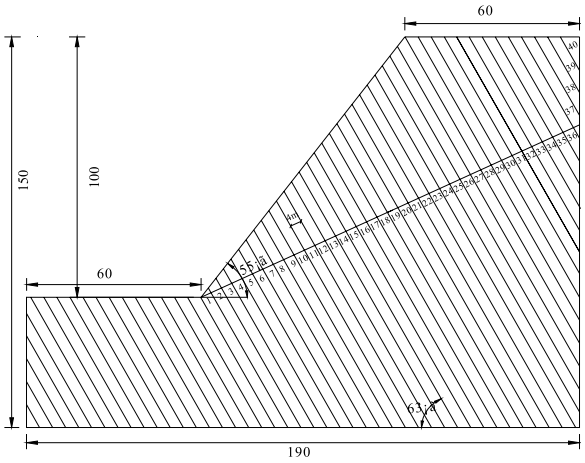

FIGURE 12
Calculation model diagram of Yangtai slope.

failure depths of the rock layers h_i obtained with the presented method, increase first and then decrease. The maximum one, 42.16 m, occurs in rock layer 27, while the minimum one, 1.57 m, occurs in rock layer 1. The external forces prompting rock layers 1–28 to undergo shear sliding failure P_i shown in Figure 14A, and the external forces prompting rock layers 3–28 to undergo flexural toppling failure T_i shown in Figure 14B, increase first and then decrease, as well. As depicted in Figure 15, the shear sliding zone marked in red is composed of rock layers 1–6, the flexural toppling zone marked in blue rock layers 7–28, the secondary toppling zone marked in green rock layers 29–31, and the stable zone marked in yellow rock layers 32–40. By using the method put forward by Su et al. (Su et al., 2021), the shear sliding zone is composed of rock layers 1–13, the flexural toppling zone rock layers 14–28, the secondary toppling zone rock layers 29–31, and the stable zone rock layers 32–40. By using the method put forward by Zheng et al. (Zheng et al., 2018b), the shear sliding zone is composed of rock layers 1–2, the flexural toppling zone rock layers 3–20, the secondary toppling zone rock layers 21–29, and the stable zone rock layers 30–40. By using the method put forward by Lu et al. (Lu et al., 2012), the flexural toppling zone is composed of rock layers 1–12, the secondary toppling zone rock layers 13–27, and the stable zone rock layers 28–40. The failure angles obtained with the above four methods are 7.96°, 14.97°, 0° and 10°, respectively. The failure surfaces obtained with these four methods are plotted in Figure 16. The external forces prompting the slope to undergo the overall failure obtained with the presented method and the method put forward by Su et al. (Su et al., 2021) are −2.72 MN and −1.52MN, respectively, while the stability factors of the slope obtained with these two methods, Majdi and Amini's method (Majdi and Amini, 2011) and Aydan and Kawamoto's method (Aydan and Kawamoto, 1992) are 0.78, 0.68, 0.54 and 093, respectively. By using Aydan and Kawamoto's method (Aydan and Kawamoto, 1992), the residual sliding force is 4.68 MN (see Table 3).

The failure surface of Yangtai slope calculated using the presented method (see Figure 17) is similar with that reported by Liu (Liu, 2012) using UDEC (see Figure 18A) and FLAC3D (see Figure 18B), and is consistent with the actual failure surface observed in field investigations (see Figure 11). Obviously, the presented failure surface (see Figure 17) is more accurate than that obtained using the methods proposed by Lu et al. (Lu et al., 2012), Zheng et al. (Zheng et al., 2018b) and Su et al. (Su et al., 2021). Yangtai slope had undergone the overall failure before the damage developed to the plane perpendicular to the joints, and thus, Aydan and Kawamoto's method (Aydan and Kawamoto, 1992) substantially overestimated the slope stability. Majdi and Amini (Majdi and Amini, 2011) neglected the effects of the mechanical parameters on the stability of hard anti-inclined

TABLE 1 Softened parameters of rock mass of Yangtai slope (Liu, 2012).

H (m)	b (m)	n	ε_i	β (°)	η (°)	θ_0 (°)	φ (°)	φ_i (°)	c (MPa)	c_i (MPa)	γ (kN·m^{-3})	σ_t (MPa)
100	4	40	0.6	55	63	0	45	18	0.4	0.01	27	1.5

TABLE 2 Results of Yangtai slope calculated using the presented method.

Rock layers	χ_i (10^{-1})	P_i (MN)	T_i (MN)	n_{ii}	h_i (m)	Failure modes
1	4.98	1.09	-	-	1.57	Shear sliding
2	4.95	2.19	5.54	-	3.14	Shear sliding
3	4.91	3.29	4.46	-	4.71	Shear sliding
4	4.88	4.40	4.98	-	6.28	Shear sliding
5	4.84	5.51	5.79	-	7.85	Shear sliding
6	4.80	6.63	6.71	-	9.42	Shear sliding
7	4.76	7.75	7.69	-	10.99	Flexural toppling
8	4.72	8.82	8.62	-	12.56	Flexural toppling
9	4.67	9.75	9.44	-	14.13	Flexural toppling
10	4.63	10.58	10.14	-	15.70	Flexural toppling
11	4.58	11.28	10.73	-	17.27	Flexural toppling
12	4.53	11.88	11.20	-	18.84	Flexural toppling
13	4.48	12.35	11.56	-	20.41	Flexural toppling
14	4.42	12.71	11.79	-	21.98	Flexural toppling
15	4.37	12.95	11.90	-	23.55	Flexural toppling
16	4.31	13.07	11.89	-	25.12	Flexural toppling
17	4.24	13.06	11.74	-	26.69	Flexural toppling
18	4.18	12.92	11.45	-	28.26	Flexural toppling
19	4.11	12.63	11.01	-	29.83	Flexural toppling
20	4.03	12.20	10.41	-	31.40	Flexural toppling
21	3.96	11.60	9.64	-	32.97	Flexural toppling
22	3.87	10.83	8.67	-	34.54	Flexural toppling
23	3.79	9.87	7.49	-	36.11	Flexural toppling
24	3.70	8.69	6.07	-	37.67	Flexural toppling
25	3.60	7.28	4.38	-	39.24	Flexural toppling
26	3.50	5.59	2.37	-	40.81	Flexural toppling
27	3.33	3.59	1.58×10^{-3}	-	42.16	Flexural toppling
28	-	1.18	−2.73	-	39.57	Flexural toppling
29	-	-	-	3	31.12	Secondary toppling
30	-	-	-	2	20.75	Secondary toppling
31	-	-	-	1	10.37	Secondary toppling
32	-	-	-	-	-	Stable
33	-	-	-	-	-	Stable
34	-	-	-	-	-	Stable
35	-	-	-	-	-	Stable
36	-	-	-	-	-	Stable
37	-	-	-	-	-	Stable
38	-	-	-	-	-	Stable
39	-	-	-	-	-	Stable
40	-	-	-	-	-	Stable

Note: "-" indicates that the above analysis is not suitable for the corresponding rock layer.

bedded rock slopes, and thus, their method may yield an inaccurate stability factor of Yangtai slope. The non-dimensional parameter indicating the position of application of the interlayer force was considered to be a constant in the method put forward by Su et al. (Su et al., 2021), and the corresponding value was larger than its reasonable one. So, Su et al. (Su et al., 2021) underestimated the slope stability. Consequently, the presented failure surface of Yangtai slope is rational and the corresponding stability factor is credible.

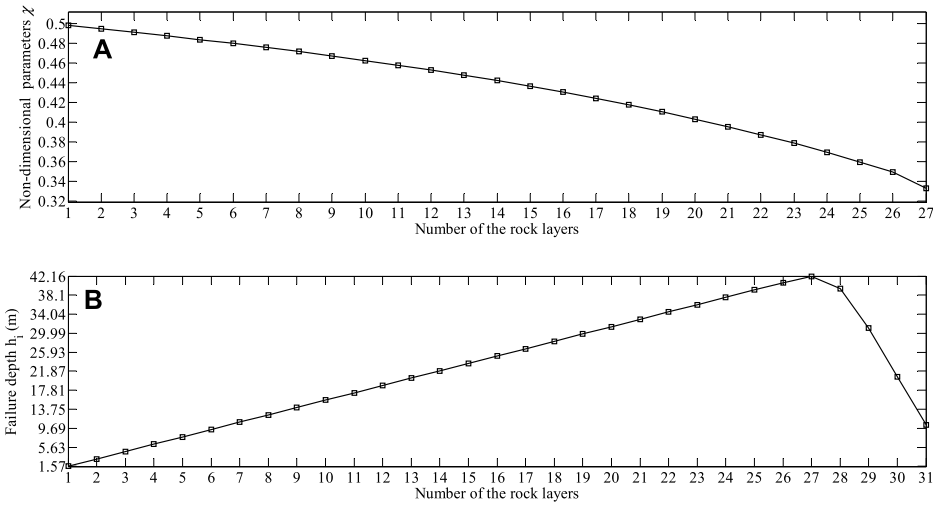

FIGURE 13
Results obtained with the presented method: **(A)** the non-dimensional parameters χ_i; **(B)** the failure depths of rock layers h_i.

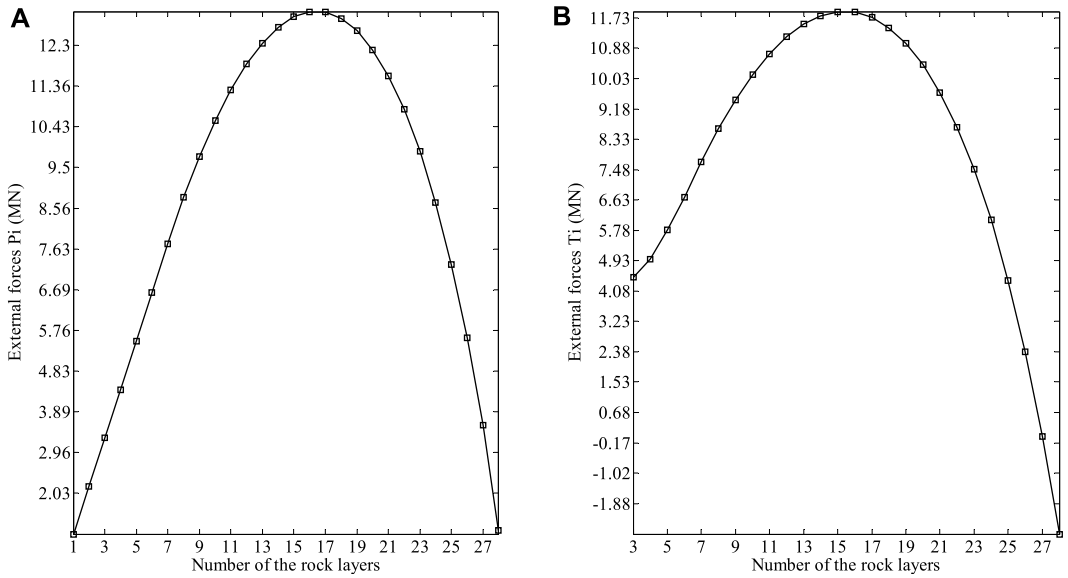

FIGURE 14
Results obtained with the presented method: **(A)** the external forces prompting rock layers 1–28 to undergo shear sliding failure P_i; **(B)** the external forces prompting rock layers 3–28 to undergo flexural toppling failure T_i.

Effect of the non-dimensional parameter χ on the stability of yangtai slope

The values of the non-dimensional parameter χ in previous studies were recommended to be 1/3 (Amini et al., 2012), 0.5 (Aydan and Kawamoto, 1992) and 0.6 (Adhikary et al., 1997). To investigate the effect of the non-dimensional parameter χ on the stability of Yangtai slope, χ is set to the above values and χ_i proposed in presented study, respectively. The presented framework is also valid in this section. The corresponding external forces prompting the rock layers to undergo shear sliding failure and flexural toppling failure, the failure depths and the failure modes of the rock layers are presented in Table 4. The corresponding shear failure angles, the

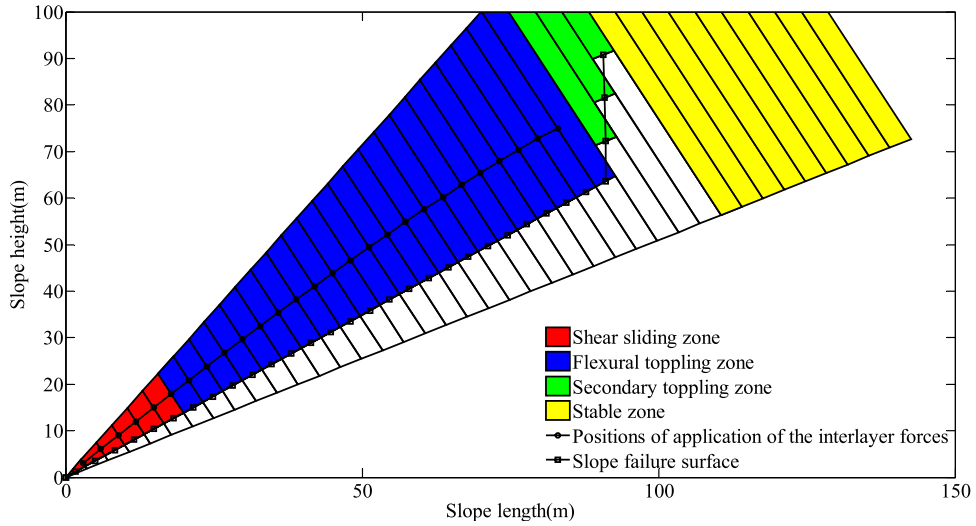

FIGURE 15
Different zones, different positions of application of the interlayer forces and slope failure surface obtained using the presented method.

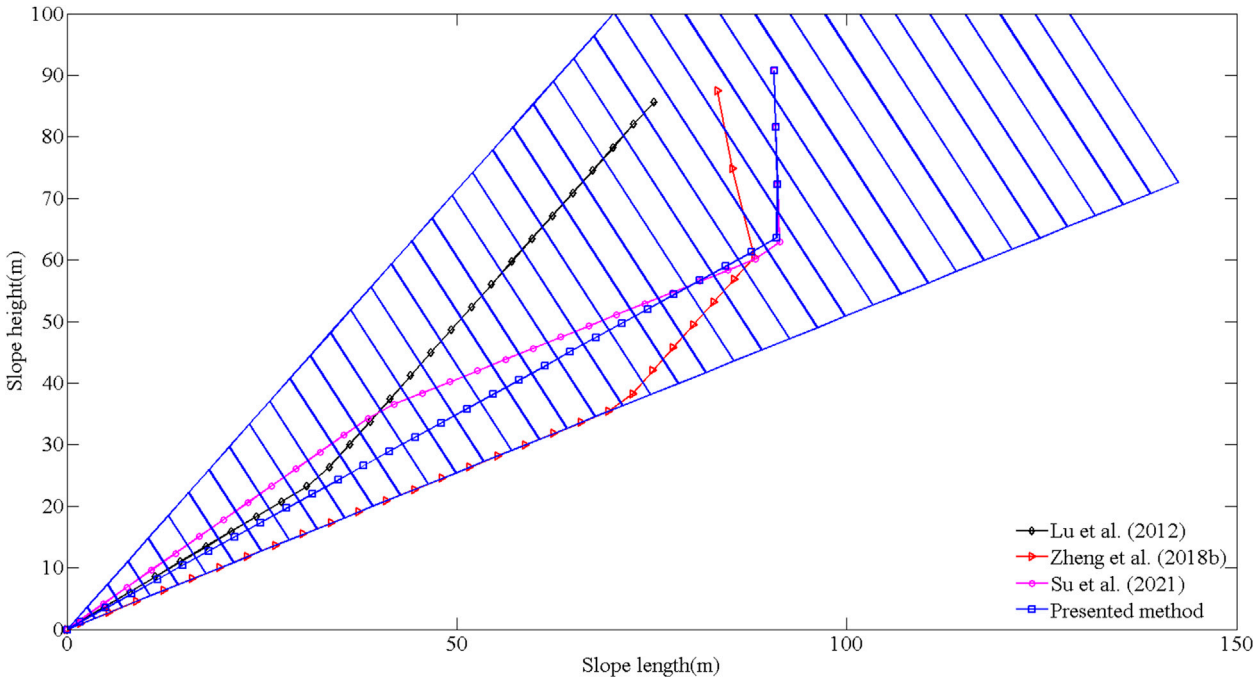

FIGURE 16
The failure surfaces of Yangtai slope obtained using different methods.

total number of the rock layers with a potential of undergoing shear sliding failure or flexural toppling failure, the total number of the rock layers with a potential of undergoing the overall failure, the external force prompting the slope to undergo the overall failure, and the stability factor are listed in Table 5. The failure depths of rock layers h_i, the external forces prompting the rock layers to undergo shear sliding failure P_i, the external forces prompting the rock layers to undergo flexural toppling failure T_i, and the slope failure surfaces,

TABLE 3 Results of Yangtai slope calculated using different methods.

Methods	*nt*	θ_r (°)	*nst*	*nn*	*t*	*F* (MN)	*FS*
Presented method	31	7.93	6	28	3	−2.73	0.78
Majdi and Amini (2011)	-	-	-	-	-	-	0.54
Su et al. (2021)	31	14.57	13	28	3	−1.52	0.68
Aydan and Kawamoto (1992)	40	0	0	40	0	4.68	0.93
Lu et al. (2012)	27	10	0	12	15	-	-
Zheng et al. (2018b)	29	0	2	20	9	-	-

Note: "-" denotes that no specific values are given.

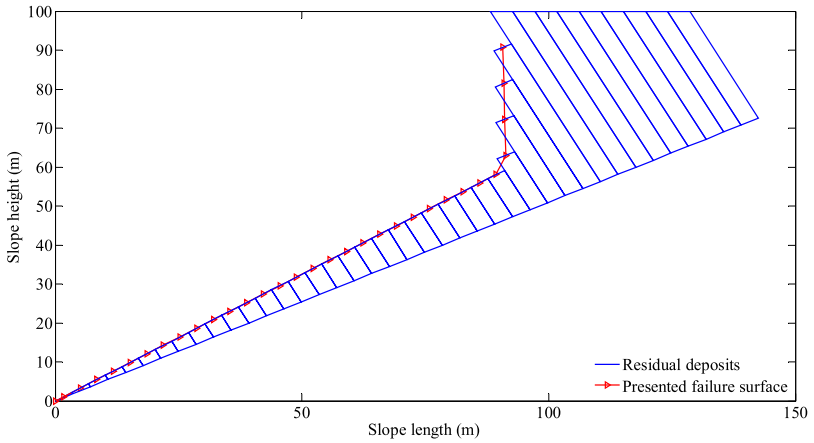

FIGURE 17
Residual deposits and the failure surface of Yangtai slope calculated using the presented method.

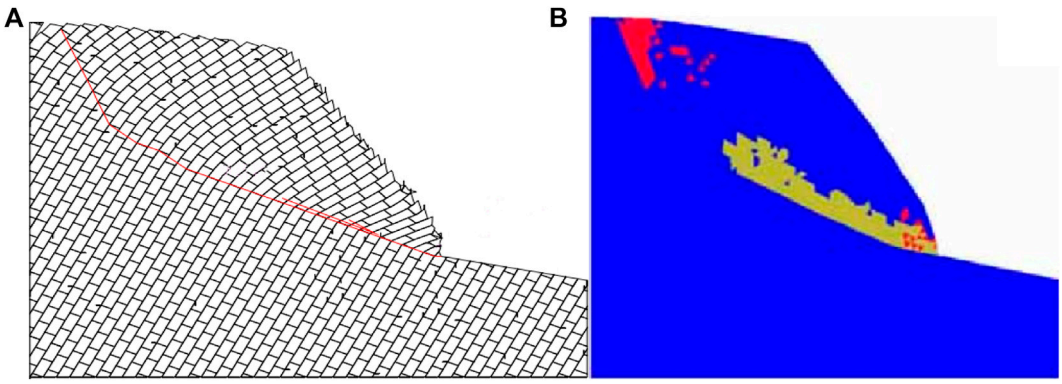

FIGURE 18
Results of Yangtai slope obtained by Liu (Liu, 2012): **(A)** the failure surface using UDEC; **(B)** distribution of plastic zone using FLAC3D.

TABLE 4 The external forces prompting the rock layers to undergo shear sliding failure and flexural toppling failure, the failure depths and the failure modes of the rock layers obtained through the presented framework for different values of χ.

i	χ =1/3			Failure modes	χ =0.5			Failure modes	χ =0.6			Failure modes
	P_i (MN)	T_i (MN)	h_i (m)		P_i (MN)	T_i (MN)	h_i (m)		P_i (MN)	T_i (MN)	h_i (m)	
1	1.13	-	1.70	Shear sliding	1.08	-	1.52	Shear sliding	1.06	-	1.44	Shear sliding
2	2.28	27.42	3.41	Shear sliding	2.16	5.81	3.05	Shear sliding	2.11	4.24	2.87	Shear sliding
3	3.45	7.33	5.11	Shear sliding	3.25	4.47	4.57	Shear sliding	3.17	3.83	4.31	Shear sliding
4	4.62	6.73	6.82	Shear sliding	4.33	4.92	6.10	Shear sliding	4.22	4.43	5.75	Shear sliding
5	5.82	7.72	8.52	Shear sliding	5.42	5.68	7.62	Shear sliding	5.27	5.23	7.18	Flexural toppling
6	7.02	7.94	10.23	Shear sliding	6.51	6.55	9.15	Shear sliding	6.28	6.07	8.62	Flexural toppling
7	8.24	8.83	11.93	Shear sliding	7.61	7.47	10.67	Flexural toppling	7.12	6.77	10.06	Flexural toppling
8	9.48	9.80	13.63	Shear sliding	8.57	8.28	12.19	Flexural toppling	7.81	7.33	11.50	Flexural toppling
9	10.72	10.83	15.34	Shear sliding	9.38	8.93	13.72	Flexural toppling	8.37	7.76	12.93	Flexural toppling
10	11.99	11.89	17.04	Flexural toppling	10.04	9.45	15.24	Flexural toppling	8.80	8.09	14.37	Flexural toppling
11	13.16	12.87	18.75	Flexural toppling	10.56	9.83	16.77	Flexural toppling	9.12	8.30	15.81	Flexural toppling
12	14.15	13.65	20.45	Flexural toppling	10.94	10.07	18.29	Flexural toppling	9.33	8.41	17.24	Flexural toppling
13	14.95	14.42	22.16	Flexural toppling	11.18	10.18	19.81	Flexural toppling	9.44	8.41	18.68	Flexural toppling
14	15.54	14.46	23.86	Flexural toppling	11.29	10.16	21.34	Flexural toppling	9.44	8.32	20.12	Flexural toppling
15	15.90	14.71	25.56	Flexural toppling	11.27	10.01	22.86	Flexural toppling	9.34	8.13	21.55	Flexural toppling
16	16.06	14.62	27.27	Flexural toppling	11.12	9.72	24.39	Flexural toppling	9.15	7.84	22.99	Flexural toppling
17	15.98	14.28	28.97	Flexural toppling	10.84	9.31	25.91	Flexural toppling	8.86	7.46	24.43	Flexural toppling
18	15.66	13.71	30.68	Flexural toppling	10.43	8.78	27.44	Flexural toppling	8.48	6.99	25.86	Flexural toppling
19	15.10	12.90	32.09	Flexural toppling	9.90	8.11	28.96	Flexural toppling	8.00	6.43	27.30	Flexural toppling
20	14.30	11.83	34.09	Flexural toppling	9.24	7.33	30.48	Flexural toppling	7.44	5.77	28.74	Flexural toppling
21	13.25	10.51	35.79	Flexural toppling	8.45	6.41	32.01	Flexural toppling	6.78	5.03	30.17	Flexural toppling
22	11.94	8.93	37.49	Flexural toppling	7.54	5.38	33.53	Flexural toppling	6.04	4.20	31.61	Flexural toppling
23	10.38	7.10	39.20	Flexural toppling	6.51	4.22	35.06	Flexural toppling	5.20	3.28	33.05	Flexural toppling
24	8.56	5.00	40.90	Flexural toppling	5.34	2.93	36.58	Flexural toppling	4.28	2.27	34.49	Flexural toppling
25	6.47	2.63	42.61	Flexural toppling	4.07	1.53	38.10	Flexural toppling	3.27	1.18	35.92	Flexural toppling
26	4.12	3.07×10^{-5}	44.31	Flexural toppling	2.66	8.88×10^{-4}	39.63	Flexural toppling	2.18	6.39×10^{-4}	37.36	Flexural toppling
27	1.50	−2.92	45.79	Flexural toppling	1.14	−1.66	40.93	Flexural toppling	0.99	−1.27	38.58	Flexural toppling
28	-	-	41.49	Secondary toppling	-	-	31.12	Secondary toppling	-	-	31.12	Secondary toppling
29	-	-	31.12	Secondary toppling	-	-	20.75	Secondary toppling	-	-	20.75	Secondary toppling
30	-	-	20.75	Secondary toppling	-	-	10.37	Secondary toppling	-	-	10.37	Secondary toppling
31	-	-	10.37	Secondary toppling	-	-	-	Stable	-	-	-	Stable
32	-	-	-	Stable	-	-	-	Stable	-	-	-	Stable
33	-	-	-	Stable	-	-	-	Stable	-	-	-	Stable
34	-	-	-	Stable	-	-	-	Stable	-	-	-	Stable
35	-	-	-	Stable	-	-	-	Stable	-	-	-	Stable
36	-	-	-	Stable	-	-	-	Stable	-	-	-	Stable
37	-	-	-	Stable	-	-	-	Stable	-	-	-	Stable
38	-	-	-	Stable	-	-	-	Stable	-	-	-	Stable
39	-	-	-	Stable	-	-	-	Stable	-	-	-	Stable
40	-	-	-	Stable	-	-	-	Stable	-	-	-	Stable

Note: "-" indicates that the above analysis is not suitable for the corresponding rock layer.

TABLE 5 The results obtained through the presented framework for different values of χ

χ	*nt*	θ_r (°)	*nst*	*nn*	*t*	*F* (MN)	*FS*
1/3	31	6.03	9	27	4	−2.92	0.84
χ_i	31	7.93	6	28	3	−2.73	0.78
0.5	30	8.57	6	27	3	−1.66	0.74
0.6	30	9.79	4	27	3	−1.27	0.68

obtained through the presented framework for different values of χ, are plotted in Figures 19, 20A,B, 21, respectively.

From Table 4 and Figures 19, 20, we can find that, as the non-dimensional parameter χ increases, the failure depth of each one of rock layers 1–31 h_i (see Figure 19) decreases. The same applies to the external force prompting each one of rock layers 1–27 to undergo shear sliding failure P_i (see Figure 20A), and the external force prompting each one of rock layers 2–25 to undergo flexural toppling failure T_i (see Figure 20B). This indicates that the failure

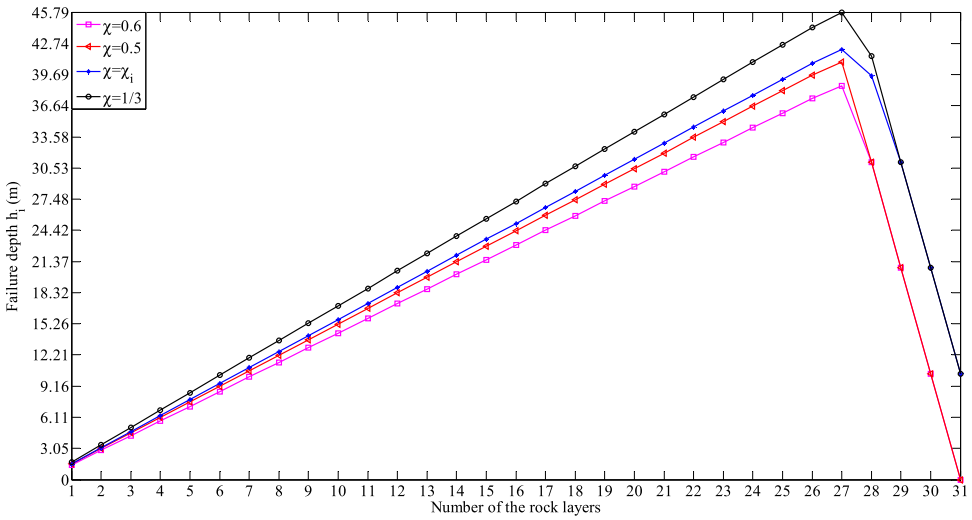

FIGURE 19
Failure depths of the rock layers h_i obtained through the presented framework for different values of χ.

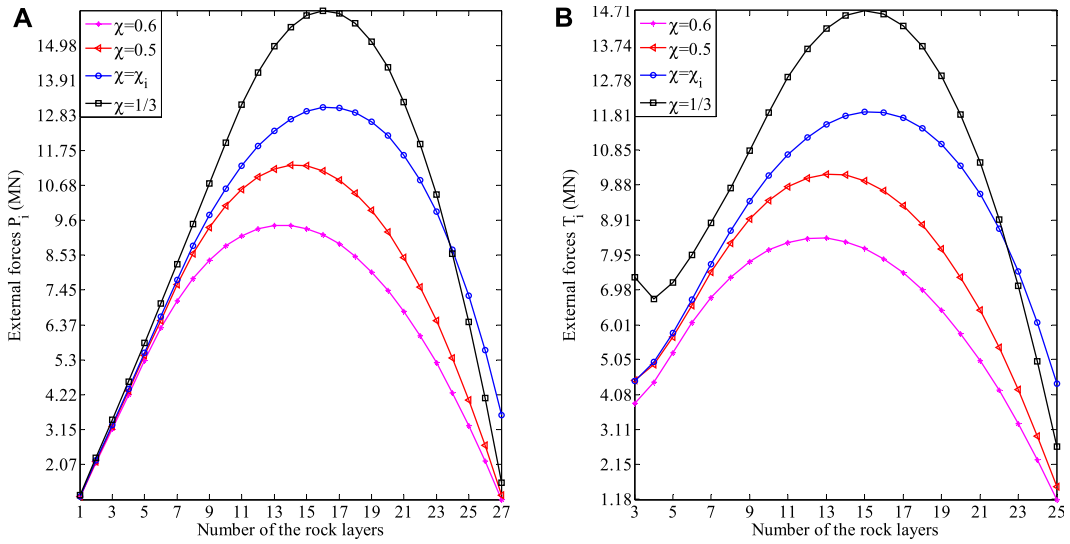

FIGURE 20
Results obtained through the presented framework for different values of χ: **(A)** the external forces prompting the rock layers to undergo shear sliding failure P_i; **(B)** the external forces prompting the rock layers to undergo flexural toppling failure T_i.

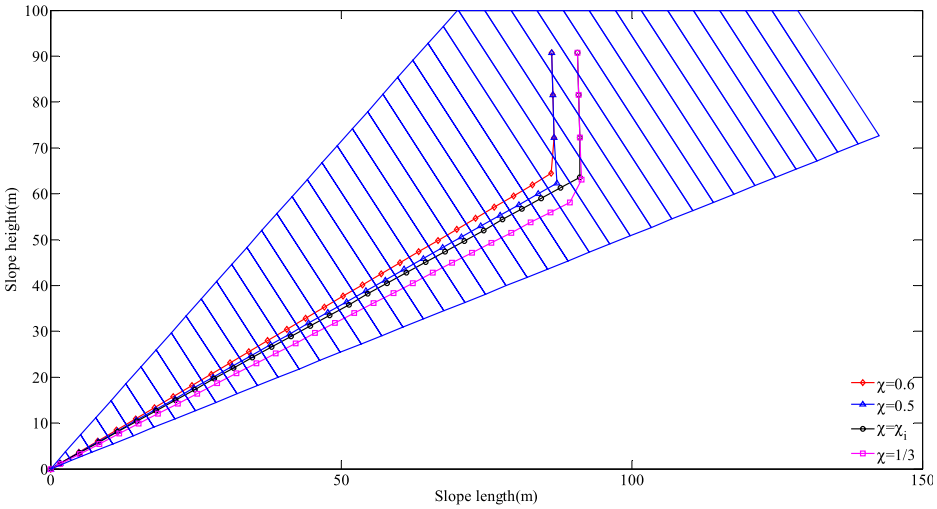

FIGURE 21
Slope failure surfaces obtained through the presented framework for different values of χ.

is more likely to occur in these rock layers. As the distribution of the interlayer force between rock layers 27 and 28 changes greatly, the above conclusion is no longer suitable for the external force prompting each one of rock layers 26–27 to undergo flexural toppling failure. In addition, even with the different non-dimensional parameters χ, there will always be same changing trends in the failure depths of the rock layers $\{h_1, h_2, \ldots, h_{31}\}$, the external forces prompting the rock layers to undergo shear sliding failure $\{P_1, P_2, \ldots, P_{27}\}$, and the external forces prompting the rock layers to undergo flexural toppling failure $\{T_3, T_4, \ldots, T_{27}\}$, which can be summarized as: 1) the values increase first and then decrease; 2) the maximum failure depth occurs in rock layer 27.

From Table 5 and Figure 21, we can conclude that, as the non-dimensional parameter χ decreases, the total number of the rock layers with a potential of undergoing shear sliding failure, and the stability factor, increase significantly, while the shear failure angle, and the external force prompting the slope to undergo the overall failure, decrease dramatically. The slope failure surfaces gradually develop to the deep (see Figure 21), which indicates that the slope becomes more stable as it will take longer time to trigger the overall failure. The greater support resistance is needed at the toe to keep the slope stable prior to overall failure (see Table 5), which indicates that it will cause more serious impact effect after slope failure. But surprisingly, there is little change in the total number of the rock layers with a potential of undergoing the overall failure, as well as the total number of the rock layers with the possibility of undergoing secondary toppling failure. In short, the stability of the slope is reinforced, but once the failure surface is penetrated, the larger landslide with more serious damage effect will occur.

The above conclusions can be verified from the physical mechanism. The external forces prompting rock layers to undergo shear sliding failure and flexural toppling failure, are produced by rock layers squeezing each other due to toppling deformation. If the non-dimensional parameter χ decreases, the larger external forces are required to trigger the above two failures. In this case, the deformation time of rock layers becomes longer, and the deformation depth increases. As a result, the slope failure surfaces develop to the deep, and the stability of the slope is considered to be reinforced because it will take longer time to trigger the overall failure. However, it will cause more serious damage effect as the larger landslide will occur after the failure surface is penetrated.

Conclusion

This study aims to address the problems that the failure surfaces of many hard anti-inclined bedded rock slopes obtained with current analytical methods are inconsistent with those observed in field investigations and the stability factors of such slopes are not accurately evaluated. According to the failure mechanism of the rock layers in such slopes, the slope was classified into four zones: shear sliding zone, flexural toppling zone, secondary toppling zone and stable zone. The non-dimensional parameter indicating the position of application of the interlayer force was revised by deriving the distribution and the equivalent substitution of interlayer force. Then, based on the new failure zone model, a limit equilibrium method was established to assess the stability of such slopes. Comparative analyses of Yangtai slope obtained with the presented approach, Majdi and Amini's method (Majdi and Amini, 2011), Aydan and Kawamoto's method (Aydan and Kawamoto, 1992), UDEC (Liu, 2012),

FLAC3D (Liu, 2012), and the methods developed by Su et al. (Su et al., 2021), Lu et al. (Lu et al., 2012), and Zheng et al. (Zheng et al., 2018b) were performed to testify the solutions' validity and accuracy. Finally, the presented method was extended to investigate the effect of the non-dimensional parameter on the stability of the slope. Several conclusions can be drawn.

(1) The non-dimensional parameter varies with the distribution of interlayer forces. The value of the non-dimensional parameter is smaller than 0.5, and is greater than or equal to 1/3.
(2) The presented method is suitable for evaluating the stability of hard anti-inclined bedded rock slopes. In addition, compared with other analytical methods, the presented method has higher predictive accuracy.
(3) When the non-dimensional parameter decreases, the slope stability is reinforced. However, the larger landslide with more serious damage effect will occur if the slope undergoes the overall failure.

It is important to note that the results presented in this work, which can be employed as the supportive data for the preliminary stability evaluation, is only suitable for the final failure state of hard anti-inclined bedded rock slopes with the possibility of undergoing shear sliding failure and flexural toppling failure.

Data availability statement

The original contributions presented in the study are included in the article/Supplementary Material, further inquiries can be directed to the corresponding author.

Author contributions

XQ: conceptualization, investigation, writing—original draft, writing—review and editing. methodology, resources, project administration, funding acquisition. FD: formal analysis, writing—review and editing, supervision.

Funding

This study has been financially supported by the Natural Science Foundation of Henan (No. 202300410011) and the National Natural Science Foundation of China (No. 42107195).

Conflict of interest

The authors declare that the research was conducted in the absence of any commercial or financial relationships that could be construed as a potential conflict of interest.

Publisher's note

All claims expressed in this article are solely those of the authors and do not necessarily represent those of their affiliated organizations, or those of the publisher, the editors and the reviewers. Any product that may be evaluated in this article, or claim that may be made by its manufacturer, is not guaranteed or endorsed by the publisher.

References

Adhikary, D. P., and Dyskin, A. V. (2007). Modelling of progressive and instantaneous failures of foliated rock slopes. *Rock Mech. Rock Eng.* 40 (4), 349–362. doi:10.1007/s00603-006-0085-8

Adhikary, D. P., Dyskin, A. V., Jewell, R. J., and Stewart, D. P. (1997). A study of the mechanism of flexural toppling failure of rock slopes. *Rock Mech. Rock Eng.* 30 (2), 75–93. doi:10.1007/bf01020126

Alejano, L. R., Veiga, M., Perez-Rey, I., Castro-Filgueira, U., Arzua, J., and Castro-Caicedo, A. J. (2019). Analysis of a complex slope failure in a granodiorite quarry bench. *Bull. Eng. Geol. Environ.* 78 (2), 1209–1224. doi:10.1007/s10064-017-1160-y

Amini, M., Majdi, A., and Veshadi, M. A. (2012). Stability analysis of rock slopes against block-flexure toppling failure. *Rock Mech. Rock Eng.* 45 (4), 519–532. doi:10.1007/s00603-012-0220-7

Aydan, O., and Kawamoto, T. (1992). The stability of slopes and underground openings against flexural toppling and their stabilisation. *Rock Mech. Rock Eng.* 25 (3), 143–165. doi:10.1007/bf01019709

Cai, J. S., Yan, E. C., Wang, Z. Q., Yang, J. G., and Tang, R. X. (2014). Study of cantilever beam limit equilibrium model of anti-inclined layered rock slopes. *Rock Soil Mech.* 35, 15–28.

Cai, J. H., Zhang, L., Dong, J., Dong, X. J., Li, M. H., Xu, Q., et al. (2022). Detection and characterization of slow-moving landslides in the 2017 Jiuzhaigou earthquake area by combining satellite SAR observations and airborne Lidar DSM. *Eng. Geol.* 305, 106730. doi:10.1016/j.enggeo.2022.106730

Chen, M. L., Lv, P. F., Nie, W. Z., Tan, C. M., Bai, Z. H., Liao, Y., et al. (2020). The role of water and lithology on the deformation and failure of an anaclinal rock slope in a hydropower reservoir. *Adv. Civ. Eng.* 2020, 1–13. doi:10.1155/2020/8852227

Ding, B. D., Zhang, H. Z., Zhang, G. C., Beng, X. T., and Yang, Y. C. (2021). Flexural toppling mechanism and stability analysis of an anti-dip rock slope. *Rock Mech. Rock Eng.* 54, 3721–3735. doi:10.1007/s00603-021-02435-w

Fan, F. S. (2015). *Toppling failure and rock burst analysis using the improved NMM and DDA simulation techniques*. Fukuoka: Kyushu University Institutional Repository.

Franziska, G., Simon, L., Andrea, M., and Jordan, A. (2019). From toppling to sliding: Progressive evolution of the moosfluh landslide, Switzerland. *J. Geophys. Res. Earth Surf.* 124 (12), 2899–2919. doi:10.1029/2019jf005019

Goodman, R. E., and Bray, J. W. (1976). "Toppling of rock slopes," in Proceedings of the Specialty Conference on Rock Engineering for Foundations and Slopes ASCE./Boulder Geotechnical Engineering Division of ASCE, Colorado, 1976, August 15-18, 201–243.

Gu, D. M., and Huang, D. (2016). A complex rock topple-rock slide failure of an anaclinal rock slope in the Wu Gorge, Yangtze River, China. *Eng. Geol.* 208 (24), 165–180. doi:10.1016/j.enggeo.2016.04.037

Lian, J. J., Li, Q., Deng, X. F., Zhao, G. F., and Chen, Z. Y. (2018). A numerical study on toppling failure of a jointed rock slope by using the distinct lattice spring model. *Rock Mech. Rock Eng.* 51 (2), 513–530. doi:10.1007/s00603-017-1323-y

Liu, C. H., Jaksa, M. B., and Meyers, A. G. (2008). Improved analytical solution for toppling stability analysis of rock slopes. *Int. J. Rock Mech. Min. Sci.* 45 (8), 1361–1372. doi:10.1016/j.ijrmms.2008.01.009

Liu, T. T., Ding, L. Y., Meng, F., Li, X. P., and Zheng, Y. (2021). Stability analysis of anti-dip bedding rock slopes using a limit equilibrium model combined with bi-directional evolutionary structural optimization (BESO) method. *Comput. Geotechnics* 134, 104116. doi:10.1016/j.compgeo.2021.104116

Liu, Y., Qiu, H. J., Yang, D. D., Liu, Z. J., Y Ma, S., Pei, Y. Q., et al. (2022). Deformation responses of landslides to seasonal rainfall based on InSAR and wavelet analysis. *Landslides* 19, 199–210. doi:10.1007/s10346-021-01785-4

Liu, H. J. (2012). *Research on the toppling deformation mechanism of counter-tilt slate slope in the mountainous zone of southern Anhui*. Chengdu: Chengdu University of Technology.

Lu, H. F., Liu, Q. S., and Chen, C. X. (2012). Improvement of cantilever beam limit equilibrium model of counter-tilt rock slopes. *Rock Soil Mech.* 33 (2), 577–584.

Majdi, A., and Amini, M. (2011). Analysis of geo-structural defects in flexural toppling failure. *Int. J. Rock Mech. Min. Sci.* 48 (2), 175–186. doi:10.1016/j.ijrmms.2010.11.007

Ning, Y. B., Tang, H. M., Zhang, G. C., Smith, J. V., Zhang, B. C., Shen, P. W., et al. (2021). A complex rockslide developed from a deep-seated toppling failure in the upper Lancang River, Southwest China. *Eng. Geol.* 293, 106329. doi:10.1016/j.enggeo.2021.106329

Qu, X., and Diao, F. F. (2020). An optimization of the analytical method for determining the flexural toppling failure plane. *Adv. Civ. Eng.* 2020, 1–12. doi:10.1155/2020/5732596

Radko, B. (1995). *Toppling failure in rock slopes*. Edmonton: University of Alberta.

Recep, K., and Ulamiş, K. (2020). Toppling and sliding in volcanic bimrocks around Bayrakli (Izmir, Turkey). *J. Mt. Sci.* 17 (2), 492–500. doi:10.1007/s11629-019-5648-8

Sarfaraz, H. (2021). An analytical solution for analysis of block toppling failure using approach of fictitious horizontal acceleration. *J. Min. Sci.* 57 (2), 202–209. doi:10.1134/s1062739121020046

Su, L. J., Qu, X., and Zhang, C. L. (2017). *A new calculation method to flexural toppling failure of anti-inclinedped rock slope"//the workshop on world landslide forum*. Cham: Springer, 483–488.

Su, L. J., Qu, X., Zhang, C. L., Iqbal, J., Wang, S. Y., Xu, X. Q., et al. (2021). An optimal method for searching failure surfaces of hard thin-layered anaclinal rock slopes with cross joints. *Arab. J. Geosci.* 14, 1422. doi:10.1007/s12517-021-07814-9

Zhao, W., Wang, R. Q., and Nian, T. K. (2020). Stability analysis of anti-dip rock slopes with flexural toppling failure based on deformation compatibility. *Rock Mech. Rock Eng.* 53 (4), 3207–3221. doi:10.1007/s00603-020-02098-z

Zheng, Y., Chen, C. X., Liu, X. M., Liu, T. T., Zhou, Y. C., Xia, K. Z., et al. (2015). Investigation on calculation method of layered counter-tilt slope for flexural toppling failure. *Chin. J. Rock Mech. Eng.* 34, 4252–4261.

Zheng, Y., Chen, C. X., Liu, T. T., Zhang, H. N., Xia, K. Z., and Liu, F. (2018a). Study on the mechanisms of flexural toppling failure in anti-inclined rock slopes using numerical and limit equilibrium models. *Eng. Geol.* 237, 116–128. doi:10.1016/j.enggeo.2018.02.006

Zheng, Y., Chen, C. X., Liu, T. T., Xia, K. Z., and Liu, X. M. (2018b). Stability analysis of rock slopes against sliding or flexural-toppling failure. *Bull. Eng. Geol. Environ.* 77 (4), 1383–1403. doi:10.1007/s10064-017-1062-z

Zheng, Y., Chen, C. X., Meng, F., Liu, T. T., and Xia, K. Z. (2020). Assessing the stability of rock slopes with respect to flexural toppling failure using a limit equilibrium model and genetic algorithm. *Comput. Geotechnics* 124, 103619. doi:10.1016/j.compgeo.2020.103619

Zheng, Y., Chen, C. X., Liu, T. T., and Ren, Z. H. (2021a). A new method of assessing the stability of anti-dip bedding rock slopes subjected to earthquake. *Bull. Eng. Geol. Environ.* 80, 3693–3710. doi:10.1007/s10064-021-02188-4

Zheng, Y., Wang, R. Q., Chen, C. X., Sun, C. Y., Ren, Z. H., and Zhang, W. (2021b). Dynamic analysis of anti-dip bedding rock slopes reinforced by pre-stressed cables using discrete element method. *Eng. Analysis Bound. Elem.* 130 (4), 79–93. doi:10.1016/j.enganabound.2021.05.014

Zhou, W. Q., Qiu, H. J., Wang, L. Y., Pei, Y. Q., Tang, B. Z., Ma, S. Y., et al. (2022). Combining rainfall-induced shallow landslides and subsequent debris flows for hazard chain prediction. *Catena* 213, 106199. doi:10.1016/j.catena.2022.106199

Zuo, B. C., Chen, C. X., Liu, X. W., and .Shen, Q. (2005). Modeling experiment study on failure mechanism of counter-tilt rock slope. *Chin. J. Rock Mech. Eng.* 24 (19), 3505–3511.

frontiers | Frontiers in Earth Science

TYPE Original Research
PUBLISHED 29 September 2022
DOI 10.3389/feart.2022.982332

OPEN ACCESS

EDITED BY
Xiaojun Guo,
Institute of Mountain Hazards and Environment (CAS), China

REVIEWED BY
Lin Zhang,
Hohai University, China
Po Ning,
Institute of Mountain Hazards and Environment (CAS), China

*CORRESPONDENCE
Binbin Zhao,
123zhaobinbin@163.com

SPECIALTY SECTION
This article was submitted to Geohazards and Georisks, a section of the journal Frontiers in Earth Science

RECEIVED 30 June 2022
ACCEPTED 30 August 2022
PUBLISHED 29 September 2022

CITATION
Zhao B, Cheng Y, Liu Y, Kong X, Yang Z, Tong R, Xu X and Deng Y (2022), Investigation of the numerical simulation of debris flow fluid with concern of phase transition. *Front. Earth Sci.* 10:982332. doi: 10.3389/feart.2022.982332

Investigation of the numerical simulation of debris flow fluid with concern of phase transition

Binbin Zhao[1,2]*, Yongfeng Cheng[1], Yi Liu[1], Xiaoang Kong[1], Zhi Yang[1], Ruiming Tong[1], Xiyu Xu[1] and Yuanjing Deng[1]

[1]China Electric Power Research Institute Co., Ltd., Beijing, China, [2]Faculty of Engineering, China University of Geosciences, Wuhan, China

From a variety of yield stress fluid models, an elastoviscoplastic Herschel-Bulkley (EVPHB) model written in 3D is selected and coupled with a Finite Element Method with Lagrangian Integration Points (FEMLIP) to solve boundary value problems with large deformation process. By tracing the historical variables of a material point, it is verified that in a time-independent flow the elastic strain and viscous strain rate could be accurately reproduced by EVPHB model. For a time-dependent flow, because of the addition of elasticity, the EVPHB model makes the material experience a deformation process which is significantly distinctive from that produced by a pure regularized Herschel-Bulkley model. Benchmarks also show that in FEMLIP the yielded and unyielded zones could be easily defined by EVPHB model according to the stress of a material point. Lastly, it is shown that EVPHB model also induces a stress relaxation process for materials under constant strain. The suitability of FEMLIP to model elastoviscoplastic fluid is verified.

KEYWORDS

debris flow, fluid, phase transition, numerical simulation, yield stress

1 Introduction

Yield stress fluids are widely encountered in our surroundings, such as landslides, mud-debris flows and lava flows in mountain hazards; foams, emulsions, polymer pastes and chocolate in industries (Takeshi and Sekimoto, 2005; Ancey, 2007; Marmottant and Graner, 2007; Bénito et al., 2008; Balmforth et al., 2014). The fundamental feature of a yield stress fluid is that it behaves like a fluid once the yield stress is exceeded but deforms in a finite way like a solid if the material is not sufficiently stressed. In the history of constitutive models' development for yield stress fluids, these materials were firstly treated as viscoplastic fluids, and thereafter, with the addition of elasticity, described by several types of elastoviscoplastic models.

1.1 Elastoviscoplasticity of yield stress fluid

Current popular viscoplastic models generally include Bingham (Bingham, 1922; Sousa and Voight, 1991; Whipple and Dunne, 1992), Herschel-Bulkley (Herschel and Bulkley, 1926; Laigle and Coussot, 1997) and bilinear rheological models (Locat, 1997). Bingham model (linear viscoplastic model) was the first model used to describe the viscoplastic behavior of yield stress fluids, in which the material behaves like a rigid solid and the magnitude of symmetric rate-of-strain tensor ($|\dot{\varepsilon}|$) is zero when shear stress (τ) is lower than a yield stress (τ_0), (Eq. 1), whereas when stress is greater than yield stress, stress is a function of shear strain rate ($\dot{\varepsilon}$) with a viscosity η (Eq. 2). As a further improvement, large number of laboratory rheological tests indicate that real yield stress fluids are generally better described, over a wide range of shear rates, by Herschel-Bulkley model (nonlinear viscoplastic model) in which a nonlinear relation is postulated above the yield stress in terms of a consistency coefficient k and a flow index n (Eq. 3) (Coussot and Piau, 1994; Huang and García, 1999; Chambon et al., 2009, 2014).

when

$$|\tau| < \tau_0,\ |\dot{\varepsilon}| = 0 \tag{1}$$

when

$$|\tau| \geq \tau_0,\ \tau = \eta\dot{\varepsilon} + \tau_0\frac{\dot{\varepsilon}}{|\dot{\varepsilon}|}\ (\text{Bingham model}) \tag{2}$$

when

$$|\tau| \geq \tau_0,\ \tau = k(\dot{\varepsilon})^n + \tau_0\frac{\dot{\varepsilon}}{|\dot{\varepsilon}|}\ (\text{Herschel} - \text{Bulkley model}) \tag{3}$$

Because the original Bingham or Herschel-Bulkley models present a sharp discontinuity at the yield stress which is difficult to handle in numerical methods, Papanastasiou (Papanastasiou, 1987) proposed a regularization of Bingham model which eliminates the need for explicit yield-surface tracking (Papanastasiou model). Further developments of this approach were achieved by Mitsoulis et al. (Mitsoulw et al., 1993) and Papanastasiou and Boudouvis (Papanastasiou and Boudouvis, 1997), they proposed a regularized HB model by combining the original Herschel–Bulkley and Papanastasiou models, as shown in Eq. 4 in which the effective viscosity η_{eff} is a function of k, n, τ_0, $|\dot{\varepsilon}|$, and of a regularization parameter m introduced to smooth the transition between fluid and solid behaviors. Other methods, such as the Augmented Lagrangian Method (ALM), were also developed to locate the yield surface more precisely by decoupling the computation of the nonlinearity introduced by the complex rheological behavior of viscoplastic models from that of the velocity (Liu and Barrett, 1994). However, the ALM requires more complicated iterative schemes (Huilgol and You, 2005; Roquet and Saramito, 2008; Fernández-Nieto et al., 2014).

Regularized Herschel-Bulkley model (RHB):

$$\tau = \left(k(|\dot{\varepsilon}|)^{n-1} + \frac{\tau_0\left[1 - \exp(-m|\dot{\varepsilon}|)\right]}{|\dot{\varepsilon}|}\right)\dot{\varepsilon} = \eta_{eff}\dot{\varepsilon} \tag{4}$$

As an additional complexity, many yield stress fluids were proven to be elastoviscoplastic, with elastic deformations below the yield stress and a combination of recoverable (elastic) and unrecoverable (viscous) deformation above the yield stress (Yano and Daido, 1965; Luu and Forterre, 2009). The most widely used elastoviscoplastic model is the Perzyna model (Perzyna, 1962; Perzyna, 1966), and similar models were also proposed for different applications (Luu and Forterre, 2009; Cheddadi et al., 2012). The difference lies in the behavior of the viscous element, which is related to the second invariant of elastic strain tensor, follows either Bingham (linear) or Herschel-Bulkley (exponential) laws. A one-dimensional illustration of this class of models is shown in Figure 1A: before yielding the model behaves like an elastic solid (Eq. 5); and once stress is above yield stress, the model is a Maxwell fluid with a Bingham or Herschel-Bulkley viscosity (Eq. 6). In Eqs. 5, 6, μ is the elastic shear modulus; ε is the shear strain; $\dot{\tau}$ is the shear stress rate; η' is the apparent viscosity. For a Bingham model, η' is a function of τ_0 and η, while for Herschel-Bulkley model it is a function of τ_0, k and n. A more general elastoviscoplastic model was proposed by Saramito (Saramito, 2007, 2009), as shown in Figure 1B, under the form of a three-dimensional combination of the viscoelastic Oldroyd-B model (Oldroyd, 1950) and a viscoplastic Bingham (or viscoplastic Herschel-Bulkley) model. Before yielding Saramito's model is a Kelvin-Voigt fluid, in which total stress (σ) is the sum of elastic stress (τ) and a solvent viscous stress ($\eta_s\dot{\varepsilon}$); after yielding it is a coupling of Bingham model or Herschel-Bulkley model with a Kelvin-Voigt model. Besides Saramito's model, Isayev and Fan (Isayev and Fan, 1990), Puzrin and Houlsby (Puzrin and Houlsby, 2003) also proposed other elastoviscoplastic models.

when

$$|\tau| < \tau_0,\ \tau = \mu\varepsilon \tag{5}$$

when

$$|\tau| \geq \tau_0,\ \frac{\dot{\tau}}{\mu} + \frac{\tau}{\eta'} = \dot{\varepsilon} \tag{6}$$

1.2 Numerical simulation method

Yield stress fluids have been intensively modelled by conventional numerical methods, such as Finite Volume Method (FVM) (de Souza Mendes et al., 2007; Turan et al., 2012; Syrakos et al., 2013), Finite Difference Method (FDM) (Olshanskii, 2009; Muravleva et al., 2010) and Finite Element Method (FEM) (Adams et al., 1997; Blackery and Mitsoulis, 1997; Alexandrou et al., 2001; Saramito and Roquet, 2001). FVM and FDM are also categorized into Eulerian FEM, and are suitable for

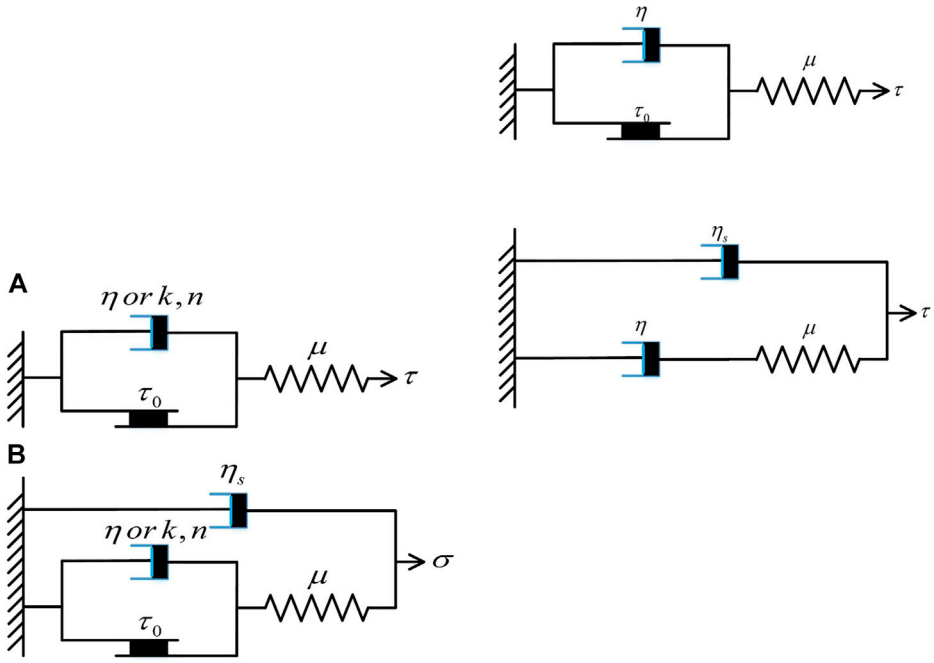

FIGURE 1
(A) Perzyna's model or Cheddadi's model or Luu and Forterre's model, **(B)** Saramito's elastoviscoplastic model.

handling large deformations of history-independent materials without the problem of mesh distortion. However, these methods generally present severe numerical diffusion at the interfaces between different materials (Lenardic and Kaula, 1993; Van Keken et al., 1997), and render also difficult to track material-dependent properties. The conventional FEM, that is also categorized into Lagrangian FEM, is ideal for tracking history-dependent variables of a specified material point, such as stress, strain, displacement and so on. However, it presents severe mesh distortion for extremely large deformations.

To benefit from the capability of handling large deformation of Eulerian FEM and the tracking ability of historical properties of Lagrangian FEM, a lot of efforts were paid to develop new methods, such as Arbitrary Lagrangian-Eulerian method (Hirt et al., 1974; Donea et al., 1982), Material Point Method (Sulsky et al., 1994, 1995), Particle Finite Element Method-second generation (Idelsohn et al., 2013) and Finite Element Method with Lagrangian Integration Points (Moresi and Solomatov, 1995; Moresi et al., 2003). Arbitrary Lagrangian-Eulerian method (ALE) is the most classical method that attempts to capture the advantages of both the Lagrangian and the Eulerian methods in modelling large deformation problems by allowing the mesh in the interior of the domain to move independently of the material. However, this requires an additional remeshing algorithm and computational cost (Margolin, 1997; Knupp et al., 2002). Besides, ALE cannot handle properly very large deformation and history variable tracking in the same setting. The Material Point Method (MPM) (Sulsky et al., 1994, 1995) is an extension of the Particle-in-Cell (PIC) method (Harlow, 1964) which takes advantage of the combined Eulerian-Lagrangian approach. In MPM the material is represented as a collection of material points and their displacements are determined by Newton's laws of motion, while the computational nodes are on a background mesh. MPM use linear shape functions which cause cell crossing noise in large deformation problems. Bardenhagen aned Kober (Bardenhagen and Kober, 2004) proposed to use higher-dimensional shape functions to improve the original MPM and developed the Generalized Interpolation Material Point Method (GIMP), which requires greater computational time. Particle Finite Element Method-second generation (PFEM-2) uses two approaches to communicate particle and mesh data. The first one is called Moving Mesh, which follows the original idea of PFEM (Idelsohn et al., 2004) creating a new mesh using the new position of the particles as nodes. This Moving Mesh approach leads to the evaluation of the mesh distortions and re-meshing processes which are always computationally expensive. The second version, named Fixed Mesh, projects the particle states to nodes while preserving the initial background mesh (Idelsohn et al., 2014), which avoids the remeshing at each time step.

In this paper we refer to a method that is quite similar to the PFEM-2 of Fixed Mesh version. It was firstly introduced by Moresi and Solomatov (Moresi and Solomatov, 1995) and named as Finite Element Method with Lagrangian Integration Points (FEMLIP). Similar to MPM or PFEM-2, FEMLIP is based on a kinematic

dissociation between the Lagrangian material points and the computational nodes of the finite element Eulerian mesh. For a given material configuration, the material points are used as integration points on one element. The resolution of the equilibrium equations at the nodes gives a velocity field, and at the end of each step the velocity is interpolated from the nodes to the material points which are sequentially moved throughout the fixed mesh to a new configuration. This enables the use of standard, proven, structured grid solvers, and also enables the modelling of numerous, interacting materials, without the concern of numerical diffusion (Lenardic and Kaula, 1993; Van Keken et al., 1997). Historical variables of a material point or particle, such as strain, strain rate, or stress could be easily traced, which alleviates problems with the standard Eulerian formulation. The particularity of FEMLIP is its fast-implicit solution method and various particle-reweighting steps. At each time step, the particle weights are varied in order to obtain the correct integral for a given element and improve the accuracy in large fluid deformations (Moresi et al., 2003; Dufour and Pijaudier-Cabot, 2005). The Eulerian-Lagrangian dual traits of FEMLIP makes it well-suited for dealing with large transformations, and meanwhile tracking internal variables during material movement (Moresi et al., 2003; Dufour and Pijaudier-Cabot, 2005; Cuomo et al., 2013; Prime et al., 2014).

Due to their ability to deal both with small, solid-like, and large, fluid-like, deformations, coupled Eulerian-Lagrangian numerical methods appear attractive to model yield stress materials. Yet, the aforementioned state of art discloses that elastoviscoplastic models, which are currently the most advanced to represent the constitutive behavior of these materials, have rarely been implemented in such numerical approaches. In this paper, we investigate the interplay of elasticity, viscosity and plasticity in an elastoviscoplastic Herschel-Bulkley model (EVPHB for short) shown in Figure 1A in the framework of FEMLIP. Through several boundary value problems and demonstrative simulations, the implementation of EVPHB in FEMLIP will be verified by tracking the historical variables and the yielded and unyielded zones.

2 Implementation of herschel-bulkley and RHB models in finite element method with lagrangian integration points

2.1 Three dimensional constitutive model

For the simplicity of numerical implementation, Eqs. 5, 6 are unified into Eq. 7, where the total strain rate ($\dot{\varepsilon}$) is the sum of elastic strain rate ($\dot{\varepsilon}_e$) and viscous strain rate ($\dot{\varepsilon}_v$). Eq. 7 has the form of Maxwell model for stresses below or above yield stress. When stress is below yield stress, the apparent viscosity (η') tends to be infinite, and the model returns to pure elasticity. In the numerical implementation, a numerical viscosity (η_∞) with a large value greater than 10^{10} Pa·s is used in this solid regime. When stress is greater than yield stress, the apparent viscosity is a function of τ_0, k and n, the specific form of which stemming from the Herschel-Bulkley model (Eq. 3).

$$\frac{\dot{\tau}}{\mu} + \frac{\tau}{\eta'} = \dot{\varepsilon}_e + \dot{\varepsilon}_v = \dot{\varepsilon} \tag{7}$$

when $|\tau| < \tau_0$, $\eta' = \eta_\infty$; when $|\tau| \geq \tau_0$, $\eta' = f(k, n\cdots)$

In addition, referring to, e.g., Oldroyd (Oldroyd, 1950) and Mitsoulis (Papanastasiou and Boudouvis, 1997), equations are generalized to three-dimensions by introducing the deviatoric stress tensor (τ_{ij}), its rate ($\dot{\tau}_{ij}$) and the rate of viscous strain tensor $(D_v)_{ij}$. Eq. 7 is transformed into Eq. 8 by introducing the second invariant of the stress tensor ($J_{2\sigma}$) and the second invariant of the viscous strain rate tensor (J_{2_Dv}) defined in Eqs. 11, 12. The Herschel-Bulkley model in Eq. 3 is finally written into a three-dimensional form in Eq. 9, Finally, as shown in Eq. 10, the effective viscosity η' is expressed as a function of k, n, τ_0 and J_{2_Dv}.

$$\frac{\dot{\tau}_{ij}}{2\mu} + \frac{\tau_{ij}}{2\eta'} = (D_e)_{ij} + (D_v)_{ij} = (D)_{ij} \tag{8}$$

when

$$\begin{aligned} |\tau| \geq \tau_0,\ \tau_{ij} &= \tau_0 \frac{\tau_{ij}}{J_{2\sigma}} + k(2D_v)^n_{ij} = \tau_0 \frac{(D_v)_{ij}}{J_{2\_Dv}} + k(2D_v)^n_{ij} \\ &= 2\eta'(D_v)_{ij} \end{aligned} \tag{9}$$

where

$$\eta' = \frac{\tau_0}{2J_{2\_Dv}} + k(2J_{2\_Dv})^{n-1} \tag{10}$$

$$J_{2\sigma} = \left(\frac{1}{2} \sum_{i=1}^{2} \sum_{j=1}^{2} (\tau_{ij})^2 \right)^{1/2} \tag{11}$$

$$J_{2\_Dv} = \left(\frac{1}{2} \sum_{i=1}^{2} \sum_{j=1}^{2} (D_v)^2_{ij} \right)^{1/2} \tag{12}$$

In order to compare this elastovisoplastic Herschel-Bulkley model (EVPHB) with a Herschel-Bulkley model without elasticity, we also introduce the three-dimensional tensorial form of the regularized Herschel-Bulkley model (RHB) introduced in Eq. 4 (Papanastasiou and Boudouvis, 1997):

$$\begin{aligned} \tau_{ij} &= 2\left(k(2J_{2\_Dv})^{n-1} + \frac{\tau_0 \left[1 - \exp(-2mJ_{2\_Dv})\right]}{2J_{2\_Dv}} \right)(D_v)_{ij} \\ &= 2\eta_{eff}(D_v)_{ij} \end{aligned} \tag{13}$$

2.2 Implementation in finite element method with lagrangian integration points

The Stokes equations solved in FEMLIP are shown in Eqs. 14, 15 in strong form, in which f_{ext} is the external force vector, $p$is the

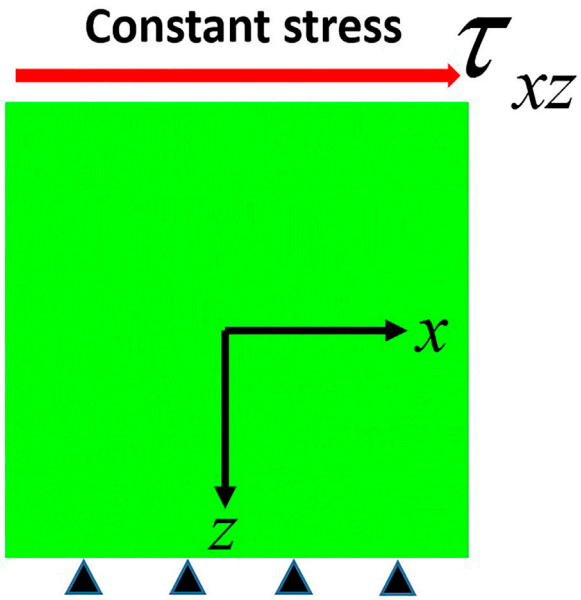

FIGURE 2
Sketch of an infinite shear layer.

pressure and v is the velocity vector. In FEMLIP, all the constitutive laws should be written into the form of a relation between the stress and rate of strain tensors, $\tau_{ij} = 2\eta_{eff}(D_v)_{ij}$(Moresi et al., 2003; Dufour and Pijaudier-Cabot, 2005; Prime et al., 2014). The RHB model is already written in this form, as shown in Eq. 13, and therefore immediate to implement in FEMLIP. To implement the EVPHB model, the deviatoric stress rate ($\dot{\tau}_{ij}$) in Eq. 8 is firstly discretized from the current time t using an elastic timestep (Δt^e) which captures the relevant timescale of the changes in elastic stresses, see Eq. 16 (Moresi et al., 2003). This timestep Δt^ecould, in fact, differ from the advection timestep (Δt) that is chosen for updating the particle positions. In Eq. 16, W is the rotation tensor introduced in the definition of the Jaumann derivative of the stress tensor. Inserting Eq. 16 into Eq. 8, the time-discretized EVPHB model has a form shown in Eq. 17, in which η_{eff} is the effective viscosity. Accordingly the time-discretization at time$t + \Delta t^e$ of the momentum conservation relation Eq. 14 yields the form of Eq. 18, where all the terms that depend on the previous timestep have been gathered in an elastic force term (f_{ext}), Eq. 19 represents the EVPHB model implemented in FEMLIP.

$$\left(f_{ext}\right)_i + \tau_{ij,j} - p_{,i} = 0 \tag{14}$$

$$v_{i,j} = 0 \tag{15}$$

Time discretization:

$$\dot{\tau}_{ij}^{t+\Delta t^e} = \frac{\tau_{ij}^{t+\Delta t^e} - \tau_{ij}^{t}}{\Delta t^e} + \tau_{ij}^{t} W_{ij}^{t} - W_{ij}^{t}\tau_{ij}^{t} \tag{16}$$

$$\tau_{ij}^{t+\Delta t^e} = \eta_{eff}\left(2\left(D^{t+\Delta t^e}\right)_{ij} + \frac{\tau_{ij}^{t}}{\mu\Delta t^e} + \frac{W_{ij}^{t}\tau_{ij}^{t} - \tau_{ij}^{t}W_{ij}^{t}}{\mu}\right) \tag{17}$$

where $\eta_{eff} = \eta' \frac{\mu\Delta t^e}{\mu\Delta t^e + \eta'}$

$$\left(f_{ext}^{t+\Delta t^e}\right)_i + 2\eta_{eff}\left(D^{t+\Delta t^e}\right)_{ij,j} + \left(f_e^{t+\Delta t^e}\right)_i - p_{,i}^{t+\Delta t^e} = 0 \tag{18}$$

where $\left(f_e^{t+\Delta t^e}\right)_i = \eta_{eff}\left(\frac{\tau_{ij,j}^{t}}{\mu\Delta t^e} + \frac{\tau_{ij,j}^{t}W_{ij,j}^{t} - W_{ij,j}^{t}\tau_{ij,j}^{t}}{\mu}\right)$

3 Analysis and validation of EVPHB model

In order to investigate the traits of EVPHB model, as well as to see its difference from a Herschel-Bulkley model without elasticity (RHB), several numerical simulations were performed with FEMLIP. Figure 2 shows the sketch of the shear test of an infinite layer simulated in FEMLIP, in which a square of yield-stress material with a length of 0.03 m is fixed at the bottom while a constant deviatoric stress (τ_{xz}) is applied on the top, with periodic boundary conditions in the horizontal direction (x). The zone of interest has an 80 × 80 mesh density. Material parameters were chosen after Luu and Forterre (Luu and Forterre, 2009) who reported several sets of elastoviscoplastic parameters for different materials such as Carbopol, Bentonite and Kaolin. As shown in Table 1, parameters representative of a Kaolin slurry (K55) with a concentration of 55% were selected for the following analysis. In the following simulations the particle convection timestep Δt and elastic timestep $\Delta t^e$are set to be equal. Since Δt^e is included in EVPHB model, the influence of this parameter on the results will be systematically investigated. In the following, for these shear tests with homogenous stress or strain distribution in z direction, a value of $m = 10^{20}$ is used for the regularization parameter. In this particular configuration, the effective viscosity is everywhere the same, and m could therefore be chosen arbitrarily large value without causing any ill-conditioned matrix for numerical solution.

3.1 Simple shear test with constant applied stress

3.1.1 Shear stress boundary condition lower than yield stress

A constant shear stress (80 Pa) smaller than the yield stress of the material (91 Pa), is applied on the top boundary of shear layer (Figure 2). From Eq. 6, it is known that strain rate induced by a stress is composed of an elastic part and a viscous part, and this even when the stress is smaller than yield stress since the numerical viscosity $\eta' = \eta_\infty$produces a very small viscous deformation. Therefore, the strain rate produced by EVPHB model will generically be named as total strain rate.

TABLE 1 Properties of elastoviscoplastic fluids.

Fluid	Concentration (%)	τ_0 (Pa)	k (Pa s^n)	n	μ (Pa)	ρ (kg m^{-3})
Kaolin						
K55	55	91	68	0.36	69,000	1630

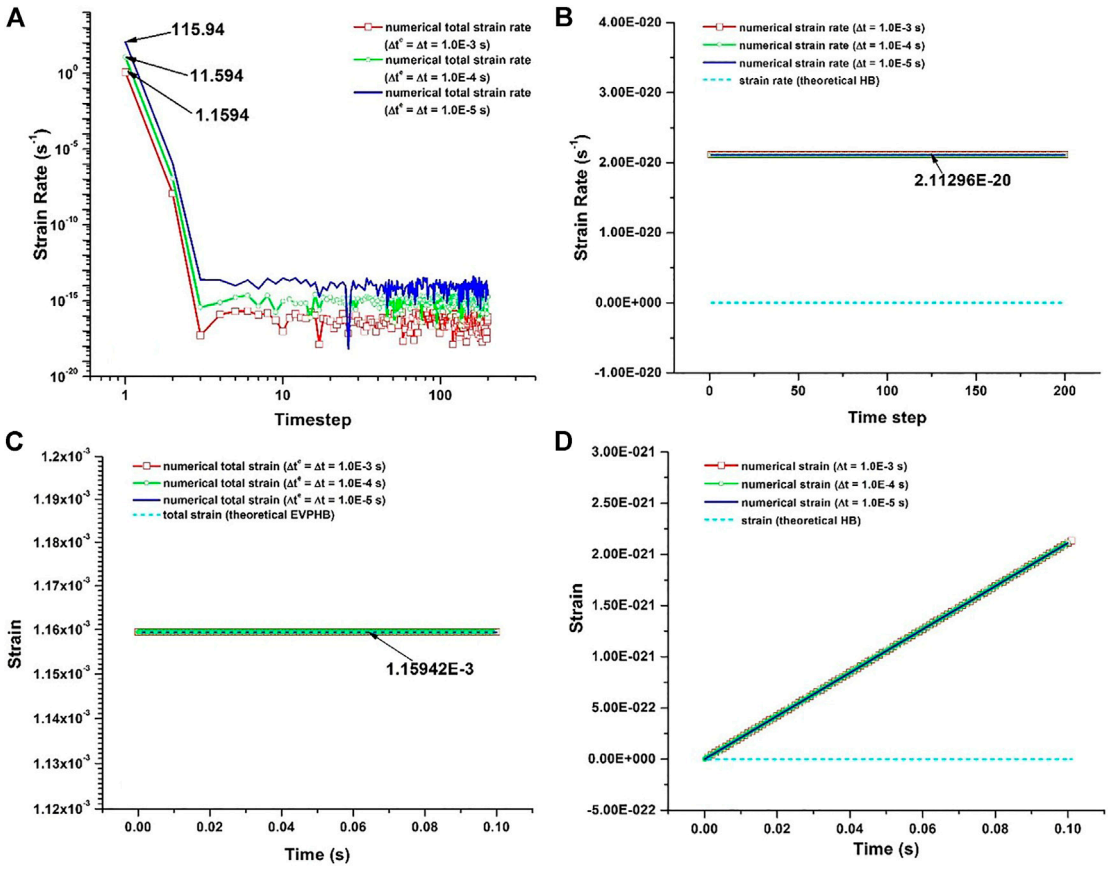

FIGURE 3
Shear stress lower than yield stress. The total shear strain rate and strain produced by EVPHB model were separately plotted in **(A)** and **(C)**, the shear strain rate and strain produced by RHB model were separately plotted in **(B)** and **(D)**.

As shown in Figure 3A, EVPHB model produces a very high total shear strain rate in the first timestep. This is explained by the abrupt boundary stress change from 0 to 80 Pa in the first timestep which produces a great elastic strain rate (see Eq. 6) and, consequently, a great jump of the total strain rate. For the same applied stress change, larger timestep causes smaller stress rate, which is why in Figure 3A the elastic strain rate increase from 1.1594 s^{-1} to 11.594 s^{-1} and 115.94 s^{-1} for timestep values of 10^{-3} s, 10^{-4} s and 10^{-5} s, respectively. Theoretically, Eq. 5 implies that for a constant stress condition, the strain is also constant, i.e. the corresponding strain rate should be 0. However, Figure 3A shows that after the first timestep, the strain rate sharply decreases to a level smaller than 10^{-13} s^{-1} and then oscillates around this value. This oscillation around small value is expected anyway due to numerical viscosity ($\eta' = \eta_\infty$), but in the computations shown, the extremely small value of this strain rate appears to be in fact mainly controlled by numerical noise. Practically, however, the integration of this error in each step is smaller than 10^{-16}, and its influence on total strain is negligible compared to the elastic deformation, as shown in Figure 3C. This numerical error is therefore negligible and the EVPHB model precisely produces the expected elastic strain when stress

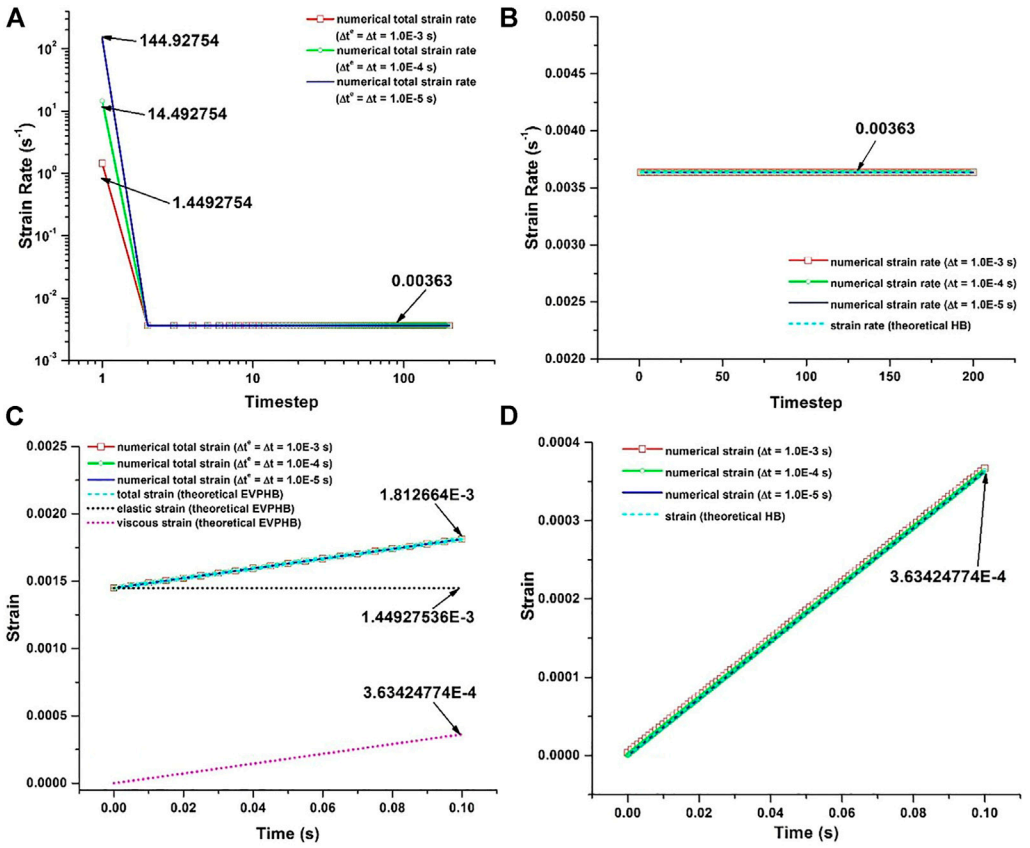

FIGURE 4
Shear stress larger than yield stress. The total shear strain rate and strain produced by EVPHB model were separately plotted in **(A)** and **(C)**, shear strain rate and strain produced by RHB model were separately plotted in **(B)** and **(D)**.

condition is below yield stress since the strain value in Figure 3C is exactly the applied stress divided by the elastic shear modulus.

RHB model also produces a very small shear strain rate of value about 10^{-20} s^{-1} (Figure 3B), which is very close to the 0 value expected for a pure Herschel-Bulkley model, and which is caused in this case by the regularization. This small value integrated over 0.1 s (Figure 3D) only produces a strain increment about 3.1×10^{-21}, and the fluid under yield stress can effectively be considered as rigid with the very large value of regularization parameter m used here, in contrary to the EVPHB model for which the total strain is finite and due to elasticity.

3.1.2 Shear stress boundary condition larger than yield stress

For a constant boundary stress (100 Pa) which is larger than the yield stress of the studied material (91 Pa), the shear strain rate initiates with a very high value in the first timestep, and reaches the theoretical shear strain rate (0.00363 s^{-1}) from the second step regardless of the timestep value (Figure 4A). The cause for the initial jump of shear strain rate is the same as in Figure 3A, due to the initial stress change from 0 Pa to 100 Pa which produce a great elastic strain rate in the EVPHB model. As previously, it is also observed that the length of timestep influences the initial shear strain rate which decreases from 144.92754 s^{-1} to 1.4492754 s^{-1} for different timesteps from 10^{-5} s to 10^{-3} s. After the first time step, the stress is constant (stress rate is 0) and therefore, according to Eq. 6, only a viscous strain rate (of theoretical value 0.00363 s^{-1}) is produced from the second timestep on. Hence, as expected, the elastic strain (black dot) is formed in the first timestep and thereafter keeps constant as shown in Figure 4C. Since the constant stress produces a constant viscous strain rate, the corresponding viscous strain (pink dot) increases linearly in time. It is also clear that regardless of the timestep value, the numerical strain produced by EVPHB model is the same as the theoretical value, which validates the proper implementation of EVPHB model in FEMLIP.

For RHB model (Figure 4B), a purely viscous strain rate with a value perfectly agreeing with the theoretical value (0.00363 s^{-1}) calculated from Eq. 3 is obtained, irrespective of the length of the timestep. Accordingly the viscous strain linearly increased in Figure 4D, and for different timesteps the numerical strain is exactly the same as the theoretical prediction. It is also found that

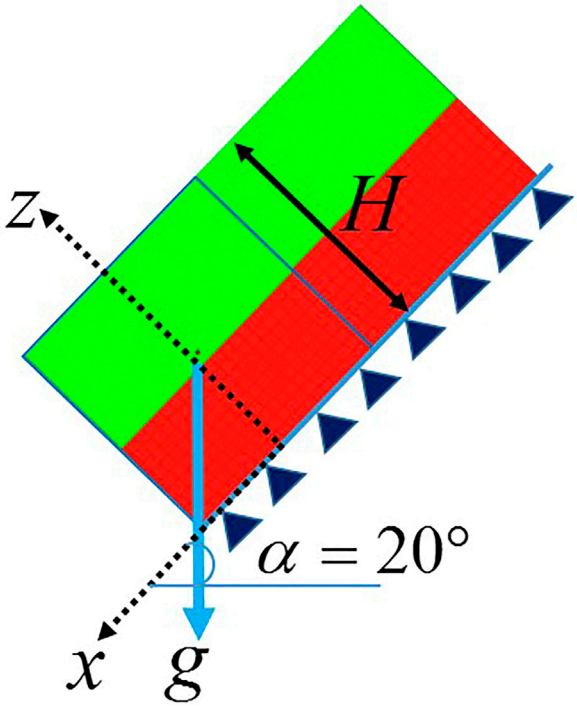

FIGURE 5
Flow of infinite layer under gravity on a slope. The green (resp. red) area represents the plug (resp. sheared) layer in the steady solution, as computed with the EVPHB model.

for the same stress condition, the strain produced by RHB model is much smaller than that produced by EVPHB model, due to the absence of elastic behavior in the former.

3.1.3 Heterogeneous shear layer in a gravity-driven flow

A second benchmark was designed to verify the implementation of the EVPHB model. It consists of an infinite layer of material of thickness H flowing in steady regime under gravity on a slope of angle α as shown in Figure 5. This configuration is characterized by heterogeneous stress, strain and strain rate distributions in the depth direction. In Figure 5 the green part represents the unsheared plug layer where the shear stress τ is lower than the yield stress τ_0, while the red part is the sheared layer where $\tau > \tau_0$. In the simulations, a square of material with a length of H is defined, and the effect of infinite length is produced by periodic boundaries in x direction. The distribution of shear stress in the depth of the flow layer is linear, and can be calculated by Eq. 19, in which (H-z) is the depth in z direction. The condition at the base of the flow is supposed to be non-slip. Associated with the equations of Herschel-Bulkley model (Eqs. 1–3) and with a straightforward integration, the theoretical distributions of velocity, strain rate and strain in the depth direction can be calculated: see Eqs. 20–23, where h_0 is the thickness of the plug layer at the top of the flowing layer and $v(z)$ is the velocity at depth (H-z).

$$\tau(z) = \rho g (H - z) \sin\alpha \tag{19}$$

$$v(z) = \frac{n}{n+1}\left(\frac{\rho g \sin\alpha}{k}\right)^{\frac{1}{n}}\left[(H-h_0)^{\frac{n+1}{n}} - (H-z-h_0)^{\frac{n+1}{n}}\right]$$

when

$$z < H - h_0 = H - \frac{\tau_0}{\rho g \sin\alpha} \tag{20}$$

$$v(z) = \frac{n}{n+1}\left(\frac{\rho g \sin\alpha}{k}\right)^{\frac{1}{n}}(H-h_0)^{\frac{n+1}{n}}, \text{ when } z > = H - h_0 \tag{21}$$

$$\dot{\varepsilon} = \left(\frac{\tau - \tau_0}{k}\right)^{\frac{1}{n}} \tag{22}$$

$$\varepsilon = \dot{\varepsilon} t \tag{23}$$

Using the parameters of K55 in Table 1, we considered an infinite layer with a depth of $H = 0.03$ m flowing on a slope of 20°, and $\Delta t^e = \Delta t = 10^{-5}$s. For RHB model, a value of 10^5 was chosen for the regularization parameter m. In this configuration with heterogeneous strain rate distribution, a larger value of m could cause the ratio of maximum effective viscosity over minimum effective viscosity to become too large, resulting in ill-conditioned matrices for the solution. In the current FEMLIP code, it is found that the value $m = 10^5$ is optimized for numerical solution. Which is the same with the result of Burgos et al. (Burgos et al., 1999) that the regularized Herschel-Bulkley model is most approximate with the ideal Herschel-Bulkley model when $m = 10^5$.

In Figure 6 the stress, velocity, shear strain rate and strain were sampled in the depth direction (z) after 1000 timesteps (at time 0.01 s). The theoretical thicknesses of plug and sheared layers are also indicated. First, Figure 6A shows the linear increase of stress in depth direction: for both EVPHB and RHB models the numerical results are identical to theoretical predictions. From this distribution, the depth of plug layer is calculated to be 0.01336 m according to value of the yield stress (91Pa). In Figures 6B,C the velocity and shear strain rate produced by EVPHB and RHB models also seem perfectly collapse onto the results calculated by Eqs. 21–23. In the plug layer or solid zone, the velocity is uniformly distributed, while in the sheared layer or fluid zone the velocity in the vicinity of yield surface first has a very slow decrease and after a short distance rapidly decreases to zero at the bottom. Similar plug shape is also observed in Figure 6C for the shear strain rate distribution, where it is clear that in the plug layer shear strain rate is 0, and increases to its maximum in the sheared layer at the bottom. In Figure 6D the strain produced by EVPHB model is greater than those of RHB and theoretical HB, due to the elastic deformation accounted for in EVPHB model. For RHB and theoretical HB models, the strain in the solid zone is zero and exponentially increases in the fluid zone.

In Figure 6 because of the linear coordinate system, the layer thicknesses obtained with EVPHB and RHB have nearly negligible difference. A specific comparison of the plug layer

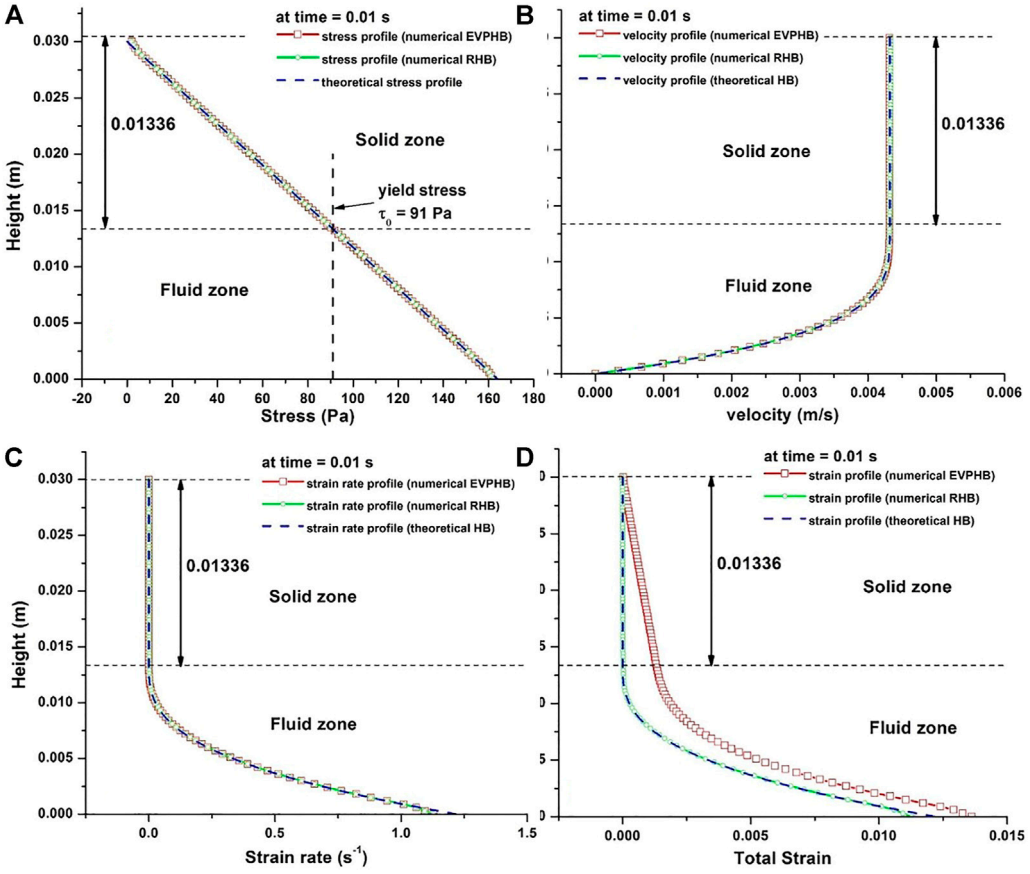

FIGURE 6
(A) Stress distribution in depth direction, **(B)** Velocity distribution in depth direction, **(C)** Shear strain rate distribution in depth direction, **(D)** Strain distribution in depth direction.

thickness obtained with EVPHB and RHB model is portrayed in a logarithm coordinate system in Figure 7.

Since in FEMLIP the stress state of each particle can be tracked, it is natural for EVPHB model to define the solid or fluid state of a particle according to the yield stress criterion, and to derive the plug thickness accordingly. Particle was in solid state when its stress was within the yield stress. Then all the particles in solid state can be obtained to calculate the plug thickness. As expected, in Figure 7, the plug thickness obtained with EVPHB model is therefore in excellent agreement with the theoretical value. On the contrary, with RHB model, an arbitrary threshold on strain rate has to be chosen, which is generally not very accurate due to the smooth shape of the profiles at the transition. For instance the apparent yield surfaces respectively determined by a strain rate of 10^{-5}, 10^{-4}, 10^{-3} and 10^{-2} s^{-1} with RHB model are shown in Figure 7, all of them lying apart from the theoretical plug layer interface. The more accurate tracking of the plug zone through a stress criterion here clearly appears as an advantage of EVPHB model over RHB model.

It is also worthy of note that the strain rate in the plug layer produced by EVPHB model is here smaller than that produced by RHB model, unlike what was observed in Figures 3A,B for the homogeneous shear test. These non-negligible strain rate values produced here by RHB model are clearly related to the value of the regularization parameter m, which cannot be chosen arbitrarily large for the sake of avoiding ill-conditioned matrix. In other words, for a practical simulation, such as any free surface simulations, to insure the priority of successful and accurate numerical solution, EVPHB model has more advantage over RHB model.

From the evolutions of stress, strain rate and strain sampled in the depth direction, the relations between stress and strain, and between stress and strain rate can be reconstructed (Figures 8A,B). As shown in Figure 8A, in the solid zone the stress and strain produced by EVPHB model are linearly dependent (red square line), and consistent with the theoretical elastic constitutive law (blue dash line), i.e. EVPHB model is effectively capable to describe elastic deformation when stress is below yield stress. On the contrary, nearly no strain is produced

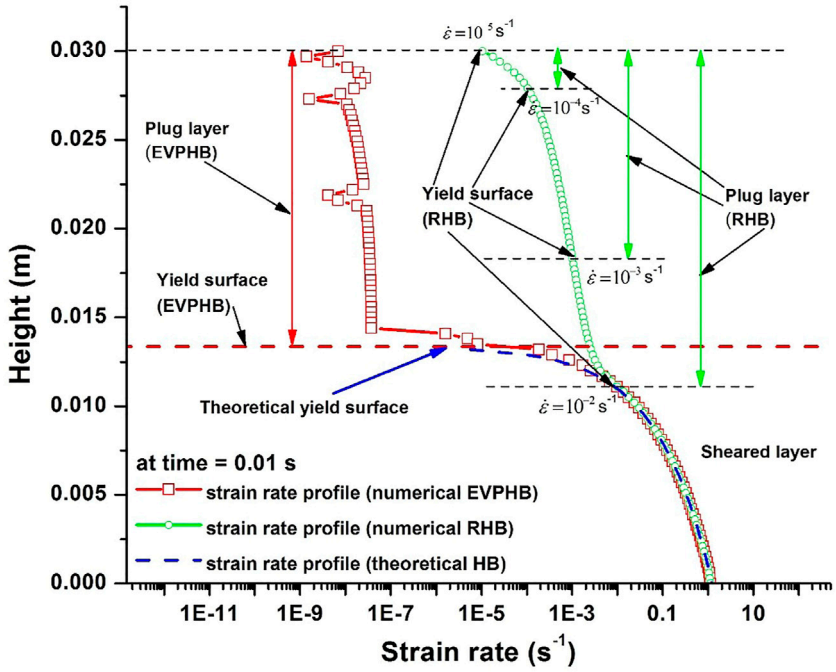

FIGURE 7
Yield surface determined with EVPHB and RHB models. For RHB model, the apparent yield surface corresponding to different strain rate threshold are indicated.

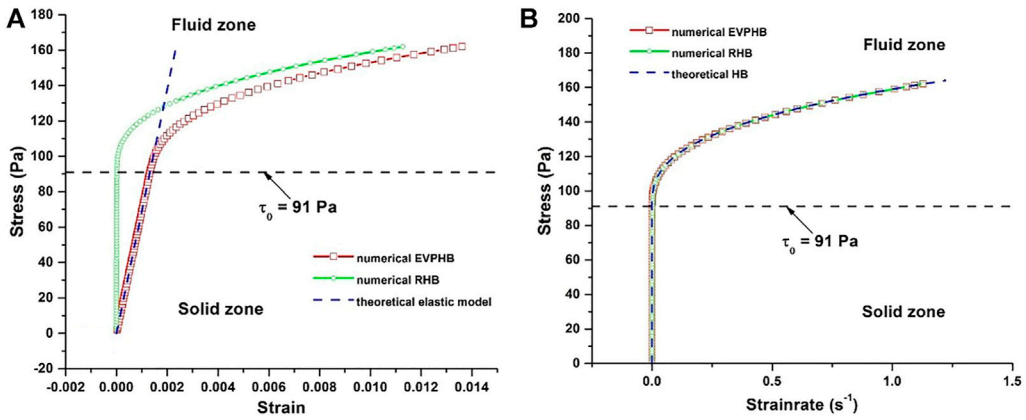

FIGURE 8
(A) Stress and strain relation in depth direction, **(B)** Stress and shear strain rate relation in depth direction.

by RHB model in the solid zone (green square line); in other words, this model treats the material as nearly rigid when stress is below yield stress. In the fluid zone, because of elasticity the two EVPHB and RHB models produce different strains.

In Figure 8B, in the fluid zone the stress and shear strain rate curves produced by both EVPHB and RHB models well collapse onto the theoretical HB constitutive curve, which indicates that both models can represent Herschel-Bulkley relation. In the solid zone, in spite of the stress changes, the strain rate is nearly zero. Therefore, from Figures 8A,B it is again reasonable to conclude that the EVPHB model is capable to accurately describe both elastic (linear stress and strain relation) and viscous (nonlinear stress and strain rate relation)

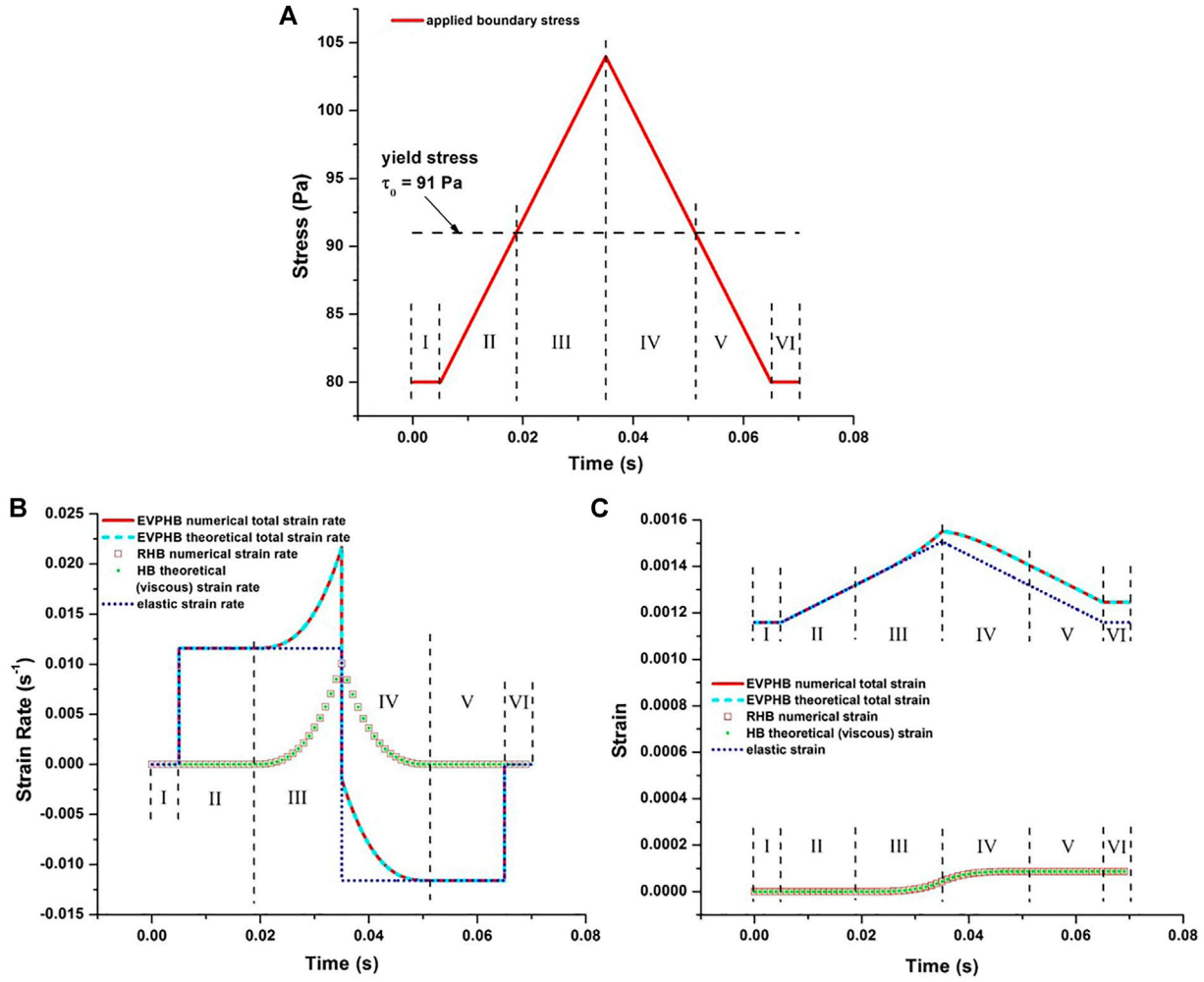

FIGURE 9
(A) Boundary stress development in a time-dependent shear flow, **(B)** Strain rate development produced by both EVPHB and RHB models, **(C)** Strain development produced by both EVPHB and RHB models.

deformations in a flow and that there are remarkable differences between EVPHB and RHB models.

3.2 Simple shear test with time-dependent boundary conditions

3.2.1 Varying shear stress boundary condition

Previous analyses indicate that for a constant stress condition, the elastoviscoplastic traits of a yield stress fluid could be well represented. In this section the response of EVPHB model to a variable stress condition is investigated by continuously changing the boundary stress shown in Figure 2. In Figure 9A, the whole boundary stress variation process is divided into 6 segments numbered from I to VI. The stress increases from 80 Pa to 104 Pa at a rate of 10 Pa/s, and then decreases back at the same rate. The boundary stress in segments I and VI is constant, variable but below the yield stress in segments II and V, and above the yield stress in segments III and IV.

For different stress and stress rate values, the corresponding strain rate and strain are produced by EVPHB and RHB models in different ways, as demonstrated in Figures 9B,C. For EVPHB model, the numerical total strain rate (red line) fully collapses onto the theoretical total strain rate (shallow blue dash line) calculated from Eqs. 5, 6. For RHB model the numerical strain rate (red square) also well collapses onto the theoretical (HB) viscous strain rate (green dot) calculated from Eqs. 1, 3. It is noteworthy that when stress is below the yield stress, the strain rate produced by RHB model is negligible, which indicates that by choosing a proper regularization parameter in Eq. 4, the RHB model can represent an almost rigid material. Similarly, Figure 9C shows that the numerical total strain produced by EVPHB (red line) and RHB models (red square) well agree with

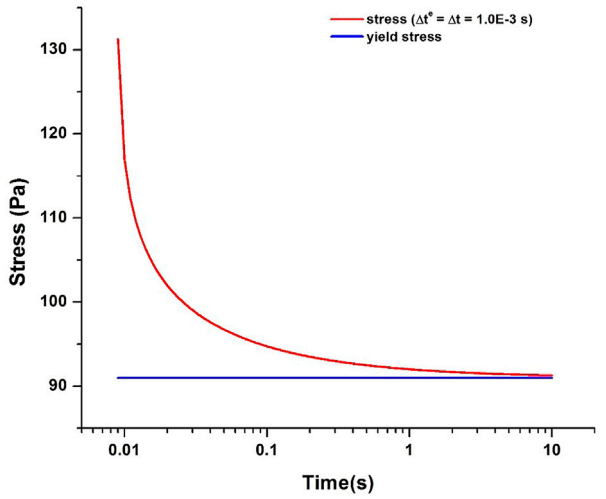

FIGURE 10
Stress relaxation under constant boundary strain produced by EVPHB model.

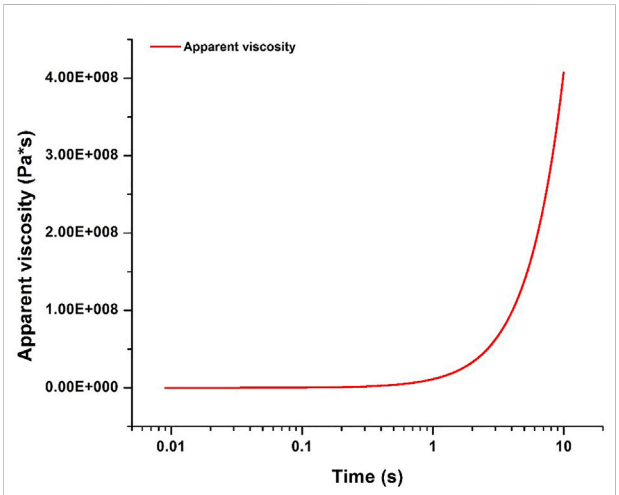

FIGURE 11
Apparent viscosity variation produced by EVPHB model.

the corresponding theoretical values (shallow blue dash line and green dots, respectively).

The most significant difference between EVPHB and RHB models is the addition of elasticity, which makes EVPHB model produce both elastic and viscous deformations. In order to show this difference, the theoretical elastic strain and strain rate are calculated according to the corresponding boundary stress and separately plotted in Figures 9B,C (blue dots). As expected, regardless of whether the stress is below or above the yield stress, as soon as it is it is not constant the elasticity always produces an elastic strain rate in Figure 9B, and consequently an elastic strain in Figure 9C. What is also clearly portrayed by Figure 9B is that for EVPHB model the total strain rate (red line or shallow blue dash line) is the sum of elastic (blue dot) and viscous (green dot) components, which is also true for the strain in Figure 9C.

3.2.2 Relaxation under constant strain

From Eq. 6, it is seen that when stress is above yield stress, EVPHB model is basically a Maxwell model. In other words, under a constant boundary strain condition, EVPHB model is expected to result in a stress relaxation process. This is verified by applying a constant boundary strain (2.33333×10^{-3}) on the top of the square shown in Figure 2. In this shear test, the constant boundary strain was achieved by applying a constant boundary velocity (0.007 m/s) for 0.009 s, after which the boundary velocity is set to be 0. Figure 10 shows the corresponding stress response, characterized by a sharp decrease from a value greater than 130 Pa–91 Pa (yield stress) in less than 10 s, unlike in a classical Maxwell-type stress relaxation, the final stress keeps constant after reaching the yield stress. This is because once the stress is below the yield stress, EVPHB model reduces to a pure elastic model, i.e. only when stress is above the yield stress does EVPHB model show time-dependent behavior. The characteristic relaxation time cannot be theoretically calculated since the apparent viscosity of EVPHB model (η' in Eq. 6) is strain-rate-dependent, and thus here time-dependent, as shown in Figure 11. At the beginning of stress relaxation, the apparent viscosity is almost relatively small, and then sharply increases with time since the strain rate progressively gets smaller as the stress gets closer to the yield stress.

4 Conclusion

On the basis of a comprehensive review of the current viscoplastic models and elastoviscoplastic models proposed for yield stress fluids, a complete elastoviscoplastic Herschel-Bulkley model was considered in this numerical study. The three-dimensional form of the elastoviscoplastic Herschel-Bulkley model (EVPHB) was derived, and the resolution of EVPHB model in Finite Element Method with Lagrangian Integration Points was developed. As a comparison, a regularized Herschel-Bulkley model (RHB) was also implemented in FEMLIP to demonstrate how the elasticity makes the EVPHB model distinctive. The conclusions are summarized as follows:

1) Finite Element Method with Lagrangian Integration Points (FEMLIP) method is suitable for the solution of elastoviscoplastic Herschel-Bulkley model, as well as for regularized Herschel-Bulkley model. The implementation of EVPHB and RHB models are verified to be correct by using four boundary value problems. FEMLIP approach makes the difference over classical numerical method since elastic stresses stored on material points must be carried out over a long distance.
2) In the simple shear tests with constant applied stress and the heterogeneous gravity-driven flow test, the EVPHB model

could reproduce the theoretical elastic strain and stress-strain constitutive relation when stress is below yield stress; when stress is above yield stress, it could reproduce a Herschel-Bulkley stress - strain rate constitutive relation.

3) Since FEMLIP provides the tracing of particle stress and other historical variables and EVPHB model could define the solid or fluid state of a particle according to stress criteria, EVPHB model shows the capability of a more accurate tracking of plug zones over RHB model. For practical simulations, such as free surface simulations, the regularization parameter used in RHB model could not be chosen too large to avoid ill-conditioned matrix, which impedes the accurate determination of plug zones.
4) For a time-dependent boundary stress, the elasticity included in the EVPHB model makes the material under shear experience a deformation process which is significantly distinctive from the deformation process produced by the RHB model. The strain and strain rate produced by EVPHB model includes both elastic and viscous components. EVPHB model also results in a stress relaxation process for materials under constant strain conditions. In this relaxation process, with time going on, the stress first sharply decreases from its initial value above the yield stress, and then slowly reaches the yield stress.

Data availability statement

The original contributions presented in the study are included in the article/supplementary material, further inquiries can be directed to the corresponding author.

Author contributions

BZ contributed to conception and investigation of the study and wrote the first draft of the manuscript. All authors contributed to manuscript revision, read, and approved the submitted version.

Funding

This study was funded by the National Key R&D Program of China, grant number 2018YFC0809400.

Conflict of interest

Authors BZ, YC, YL, XK, ZY, RT, XX and YD were employed by China Electric Power Research Institute Co., Ltd.

Publisher's note

All claims expressed in this article are solely those of the authors and do not necessarily represent those of their affiliated organizations, or those of the publisher, the editors and the reviewers. Any product that may be evaluated in this article, or claim that may be made by its manufacturer, is not guaranteed or endorsed by the publisher.

References

Adams, M. J., Aydin, İ., Briscoe, B. J., and Sinha, S. K. (1997). A finite element analysis of the squeeze flow of an elasto-viscoplastic paste material. *J. Nonnewt. Fluid Mech.* 71, 41–57. doi:10.1016/s0377-0257(96)01546-7

Alexandrou, A. N., McGilvreay, T. M., and Burgos, G. (2001). Steady Herschel–Bulkley fluid flow in three-dimensional expansions. *J. Nonnewt. Fluid Mech.* 100, 77–96. doi:10.1016/s0377-0257(01)00127-6

Ancey, C. (2007). Plasticity and geophysical flows: A review. *J. Nonnewt. Fluid Mech.* 142, 4–35. doi:10.1016/j.jnnfm.2006.05.005

Balmforth, N. J., Frigaard, I. A., and Ovarlez, G. (2014). Yielding to stress: Recent developments in viscoplastic fluid mechanics. *Annu. Rev. Fluid Mech.* 46, 121–146. doi:10.1146/annurev-fluid-010313-141424

Bardenhagen, S. G., and Kober, E. M. (2004). The generalized interpolation material point method. *Comput. Model. Eng. Sci.* 5, 477–496.

Bénito, S., Bruneau, C. H., Colin, T., Gay, C., and Molino, F. (2008). An elasto-visco-plastic model for immortal foams or emulsions. *Eur. Phys. J. E* 25, 225–251. doi:10.1140/epje/i2007-10284-2

Bingham, E. C. (1922). *Fluidity and plasticity*. McGraw-Hill.

Blackery, J., and Mitsoulis, E. (1997). Creeping motion of a sphere in tubes filled with a Bingham plastic material. *J. Nonnewt. Fluid Mech.* 70, 59–77. doi:10.1016/s0377-0257(96)01536-4

Burgos, G. R., Alexandrou, A. N., and Entov, V. (1999). On the determination of yield surfaces in Herschel–Bulkley fluids. *J. Rheol. (N. Y. N. Y).* 43, 463–483. doi:10.1122/1.550992

Chambon, G., Ghemmour, A., and Laigle, D. (2009). Gravity-driven surges of a viscoplastic fluid: An experimental study. *J. Nonnewt. Fluid Mech.* 158, 54–62. doi:10.1016/j.jnnfm.2008.08.006

Chambon, G., Ghemmour, A., and Naaim, M. (2014). Experimental investigation of viscoplastic free-surface flows in a steady uniform regime. *J. Fluid Mech.* 754, 332–364. doi:10.1017/jfm.2014.378

Cheddadi, I., Saramito, P., and Graner, F. (2012). Steady Couette flows of elastoviscoplastic fluids are nonunique. *J. Rheol. (N. Y. N. Y).* 56, 213–239. doi:10.1122/1.3675605

Coussot, P., and Piau, J. M. (1994). On the behavior of fine mud suspensions. *Rheol. Acta* 33, 175–184. doi:10.1007/BF00437302

Cuomo, S., Prime, N., Iannone, A., Dufour, F., Cascini, L., and Darve, F. (2013). Large deformation FEMLIP drained analysis of a vertical cut. *Acta Geotech.* 8, 125–136.

de Souza Mendes, P. R., Naccache, M. F., Varges, P. R., and Marchesini, F. H. (2007). Flow of viscoplastic liquids through axisymmetric expansions–contractions. *J. Nonnewt. Fluid Mech.* 142, 207–217. doi:10.1016/j.jnnfm.2006.09.007

Donea, J., Giuliani, S., and Halleux, J.-P. (1982). An arbitrary Lagrangian-Eulerian finite element method for transient dynamic fluid-structure interactions. *Comput. Methods Appl. Mech. Eng.* 33, 689–723. doi:10.1016/0045-7825(82)90128-1

Dufour, F., and Pijaudier-Cabot, G. (2005). Numerical modelling of concrete flow: Homogeneous approach. *Int. J. Numer. Anal. methods Geomech.* 29, 395–416. doi:10.1002/nag.419

Fernández-Nieto, E. D., Gallardo, J. M., and Vigneaux, P. (2014). Efficient numerical schemes for viscoplastic avalanches. Part 1: The 1D case. *J. Comput. Phys.* 264, 55–90. doi:10.1016/j.jcp.2014.01.026

Harlow, F. H. (1964). The particle-in-cell computing method for fluid dynamics. *Methods comput. Phys.* 3, 319–343.

Herschel, W. H., and Bulkley, R. (1926). Measurement of consistency as applied to rubber-benzene solutions. *Am. Soc. Test. Proc.* 16, 621–633.

Hirt, C. W., Amsden, A. A., and Cook, J. L. (1974). An arbitrary Lagrangian-Eulerian computing method for all flow speeds. *J. Comput. Phys.* 14, 227–253. doi:10.1016/0021-9991(74)90051-5

Huang, X., and García, M. H. (1999). Modeling of non-hydroplaning mudflows on continental slopes. *Mar. Geol.* 154, 131–142. doi:10.1016/S0025-3227(98)00108-X

Huilgol, R. R., and You, Z. (2005). Application of the augmented Lagrangian method to steady pipe flows of Bingham, Casson and Herschel-Bulkley fluids. *J. Nonnewt. Fluid Mech.* 128, 126–143. doi:10.1016/j.jnnfm.2005.04.004

Idelsohn, S. R., Marti, J., Becker, P., and Oñate, E. (2014). Analysis of multifluid flows with large time steps using the particle finite element method. *Int. J. Numer. Methods Fluids* 75, 621–644. doi:10.1002/fld.3908

Idelsohn, S. R., Nigro, N. M., Gimenez, J. M., Rossi, R., and Marti, J. M. (2013). A fast and accurate method to solve the incompressible Navier-Stokes equations. *Eng. Comput. Swans.* 30, 197–222. doi:10.1108/02644401311304854

Idelsohn, S. R., Onate, E., and Del Pin, F. (2004). The particle finite element method: A powerful tool to solve incompressible flows with free-surfaces and breaking waves. *Int. J. Numer. Methods Eng.* 61, 964–989. doi:10.1002/nme.1096

Isayev, A. I., and Fan, X. (1990). Viscoelastic plastic constitutive equation for flow of particle filled polymers. *J. Rheol. (N. Y. N. Y).* 34, 35–54. doi:10.1122/1.550113

Knupp, P., Margolin, L. G., and Shashkov, M. (2002). Reference Jacobian optimization-based rezone strategies for arbitrary Lagrangian Eulerian methods. *J. Comput. Phys.* 176, 93–128. doi:10.1006/jcph.2001.6969

Laigle, D., and Coussot, P. (1997). Numerical modeling of mudflows. *J. Hydraul. Eng.* 123, 617–623. doi:10.1061/(asce)0733-9429(1997)123:7(617)

Lenardic, A., and Kaula, W. M. (1993). A numerical treatment of geodynamic viscous flow problems involving the advection of material interfaces. *J. Geophys. Res.* 98, 8243–8260. doi:10.1029/92jb02858

Liu, W. B., and Barrett, J. W. (1994). Quasi-norm error bounds for the finite element approximation of some degenerate quasilinear elliptic equations and variational inequalities. *ESAIM Math. Model. Numer. Anal.* 28, 725–744. doi:10.1051/m2an/1994280607251

Locat, J. (1997). "Normalized rheological behaviour of fine muds and their flow properties in a pseudoplastic regime," in *Debris-flow hazards mitigation: Mechanics, prediction, and assessment (ASCE)* (Rotterdam, Netherlands: Millpress Science Publishers), 260–269.

Luu, L. H., and Forterre, Y. (2009). Drop impact of yield-stress fluids. *J. Fluid Mech.* 632, 301–327. doi:10.1017/S0022112009007198

Margolin, L. G. (1997). Introduction to "An arbitrary Lagrangian-Eulerian computing method for all flow speeds. *J. Comput. Phys.* 135, 198–202. doi:10.1006/jcph.1997.5727

Marmottant, P., and Graner, F. (2007). An elastic, plastic, viscous model for slow shear of a liquid foam. *Eur. Phys. J. E* 23, 337–347. doi:10.1140/epje/i2006-10193-x

Mitsoulw, E., Abdali, S., Fluid, C., and Unit, D. (1993). Flow simulation of herschel-bulkley fluids through extrusion dies. *Can. J. Chem. Eng.* 71, 147–160. doi:10.1002/cjce.5450710120

Moresi, L., Dufour, F., and Mühlhaus, H.-B. (2003). A Lagrangian integration point finite element method for large deformation modeling of viscoelastic geomaterials. *J. Comput. Phys.* 184, 476–497. doi:10.1016/s0021-9991(02)00031-1

Moresi, L., and Solomatov, V. S. (1995). Numerical investigation of 2D convection with extremely large viscosity variations. *Phys. Fluids* 7, 2154–2162. doi:10.1063/1.868465

Muravleva, L., Muravleva, E., Georgiou, G. C., and Mitsoulis, E. (2010). Numerical simulations of cessation flows of a Bingham plastic with the augmented Lagrangian method. *J. Nonnewt. Fluid Mech.* 165, 544–550. doi:10.1016/j.jnnfm.2010.02.002

Oldroyd, J. G. (1950). On the formulation of rheological equations of state. *Proc. R. Soc. Lond. Ser. A. Math. Phys. Sci.* 200, 523–541.

Olshanskii, M. A. (2009). Analysis of semi-staggered finite-difference method with application to Bingham flows. *Comput. Methods Appl. Mech. Eng.* 198, 975–985. doi:10.1016/j.cma.2008.11.010

Papanastasiou, T. C., and Boudouvis, A. G. (1997). Flows of viscoplastic materials: Models and computations. *Comput. Struct.* 64, 677–694. doi:10.1016/S0045-7949(96)00167-8

Papanastasiou, T. C. (1987). Flows of materials with yield. *J. Rheol. (N. Y. N. Y).* 31, 385–404. doi:10.1122/1.549926

Perzyna, P. (1966). Fundamental problems in viscoplasticity. *Adv. Appl. Mech.* 9, 243–377.

Perzyna, P. (1962). The constitutive equations for rate sensitive plastic materials. *Q. Appl. Math.* 20, 321–332. doi:10.1090/qam/144536

Prime, N., Dufour, F., and Darve, F. (2014). Unified model for geomaterial solid/fluid states and the transition in between. *J. Eng. Mech.* 140. doi:10.1061/(asce)em.1943-7889.0000742

Puzrin, A. M., and Houlsby, G. T. (2003). Rate-dependent hyperplasticity with internal functions. *J. Eng. Mech.* 129, 252–263. doi:10.1061/(asce)0733-9399(2003)129:3(252)

Roquet, N., and Saramito, P. (2008). An adaptive finite element method for viscoplastic flows in a square pipe with stick-slip at the wall. *J. Nonnewt. Fluid Mech.* 155, 101–115. doi:10.1016/j.jnnfm.2007.12.003

Saramito, P. (2007). A new constitutive equation for elastoviscoplastic fluid flows. *J. Nonnewt. Fluid Mech.* 145, 1–14. doi:10.1016/j.jnnfm.2007.04.004

Saramito, P. (2009). A new elastoviscoplastic model based on the Herschel–Bulkley viscoplastic model. *J. Nonnewt. Fluid Mech.* 158, 154–161. doi:10.1016/j.jnnfm.2008.12.001

Saramito, P., and Roquet, N. (2001). An adaptive finite element method for viscoplastic fluid flows in pipes. *Comput. Methods Appl. Mech. Eng.* 190, 5391–5412. doi:10.1016/s0045-7825(01)00175-x

Sousa, J., and Voight, B. (1991). Continuum simulation of flow failures. *Geotechnique* 41, 515–538. doi:10.1680/geot.1991.41.4.515

Sulsky, D., Chen, Z., and Schreyer, H. L. (1994). A particle method for history-dependent materials. *Comput. Methods Appl. Mech. Eng.* 118, 179–196. doi:10.1016/0045-7825(94)90112-0

Sulsky, D., Zhou, S.-J., and Schreyer, H. L. (1995). Application of a particle-in-cell method to solid mechanics. *Comput. Phys. Commun.* 87, 236–252. doi:10.1016/0010-4655(94)00170-7

Syrakos, A., Georgiou, G. C., and Alexandrou, A. N. (2013). Solution of the square lid-driven cavity flow of a Bingham plastic using the finite volume method. *J. Nonnewt. Fluid Mech.* 195, 19–31. doi:10.1016/j.jnnfm.2012.12.008

Takeshi, O., and Sekimoto, K. (2005). Internal stress in a model elastoplastic fluid. *Phys. Rev. Lett.* 95, 108301–108304. doi:10.1103/PhysRevLett.95.108301

Turan, O., Chakraborty, N., and Poole, R. J. (2012). Laminar Rayleigh-Bénard convection of yield stress fluids in a square enclosure. *J. Nonnewt. Fluid Mech.* 171, 83–96. doi:10.1016/j.jnnfm.2012.01.006

Van Keken, P. E., King, S. D., Schmeling, H., Christensen, U. R., Neumeister, D., and Doin, M. (1997). A comparison of methods for the modeling of thermochemical convection. *J. Geophys. Res.* 102, 22477–22495. doi:10.1029/97jb01353

Whipple, K. X., and Dunne, T. (1992). The influence of debris-flow rheology on fan morphology, Owens Valley, California. *Geol. Soc. Am. Bull.* 104, 887–900. doi:10.1130/0016-7606(1992)104<0887:TIODFR>2.3.CO;2

Yano, K., and Daido, A. (1965). Fundamental study on mud-flow. *Bull. Disaster Prev. Res. Inst.* 14, 69–83.

frontiers | Frontiers in Earth Science

TYPE Original Research
PUBLISHED 06 January 2023
DOI 10.3389/feart.2022.993975

OPEN ACCESS

EDITED BY
Wen Zhang,
Jilin University, China

REVIEWED BY
Jiewei Zhan,
Chang'an University, China
Yifei Cui,
Tsinghua University, China
Yuanjun Jiang,
Institute of Mountain Hazards and Environment (CAS), China

*CORRESPONDENCE
Zhenlei Wei,
1025332814@qq.com

SPECIALTY SECTION
This article was submitted to Geohazards and Georisks, a section of the journal Frontiers in Earth Science

RECEIVED 14 July 2022
ACCEPTED 15 September 2022
PUBLISHED 06 January 2023

CITATION
Zhao Y, Huang Z, Wei Z, Zheng J and Konagai K (2023), Assessment of earthquake-triggered landslide susceptibility considering coseismic ground deformation.
Front. Earth Sci. 10:993975.
doi: 10.3389/feart.2022.993975

Assessment of earthquake -triggered landslide susceptibility considering coseismic ground deformation

Yu Zhao[1,2], Zeng Huang[1,3], Zhenlei Wei[4]*, Jun Zheng[1] and Kazuo Konagai[5]

[1]College of Civil Engineering and Architecture, Zhejiang University, Hangzhou, China, [2]MOE Key Laboratory of Soft Soils and Geoenvironmental Engineering, Zhejiang University, Hangzhou, China, [3]Powerchina Zhongnan Engineering Corporation Limited, Changsha, China, [4]College of Environment and Civil Engineering, Chengdu University of Technology, Chengdu, China, [5]International Consortium on Landslides, Kyoto, Japan

The distance to the surface rupture zone has been commonly regarded as an important influencing factor in the evaluation of earthquake-triggered landslide susceptibility. However, the obvious surface rupture zones usually do not occur in some buried-fault earthquake cases, which means information about the distance to the surface rupture is lacking. In this study, a new influencing factor named coseismic ground deformation was added to remedy this shortcoming. The Mid-Niigata prefecture earthquake was regarded as the study case. To select a more suitable model for generating the landslide susceptibility map, three commonly used models named logistic regression (LR), artificial neural network (ANN), and support vector machine (SVM) were also conducted to assess landslide susceptibility. The performances of these three models were evaluated with the receiver operating characteristic curve. The calculated results showed that the ANN model has the highest area under the curve (AUC) value of 0.82. As the earthquake triggered more landslides in the epicenter area, which makes it more prone to landslides in further earthquakes, the susceptibility analysis at two different mapping scales (the whole study area and the epicenter area) was also applied.

KEYWORDS

earthquake-triggered landslides, landslide susceptibility mapping, coseismic ground deformation, machine learning, buried-fault earthquakes, Mid-Niigata earthquake

Introduction

Earthquake-triggered landslides are commonly seen in the earthquake disaster chain. The landslides not only bring loss of life and property but also seriously affect the post-earthquake rescue. By summarizing the data of 40 historical earthquake events in the world, Keefer (1984) discovered that the earthquake-triggered landslide was the main reason for the loss of life and property. More than 60 people were killed and nearly 100,000 people were displaced due to the Mid-Niigata earthquake in 2004 (Bandara and

Ohtsuka, 2017). In 2008, the Wenchuan earthquake triggered nearly 200,000 landslides, killing about 20,000 people (Xu et al., 2012b). At present, numerous researchers regard susceptibility mapping as an effective way to hazard mitigation and disaster management, and several models have been used to generate landslide susceptibility maps.

At present, one type of commonly used method to evaluate the susceptibility of landslides is the physical-based method. For this type of method, the study area is usually divided into slope units and then LEM or FEM is applied to calculate the safety factor (FS) of each slope unit (Saade et al., 2016). However, the physical mechanism of the landslide is often very complicated, especially for the landslides caused by earthquakes. Due to the difficulty of obtaining enough parameters for slope dynamic analysis, it still is a tough job to assess landslide susceptibility with physical-based models in large-scale areas.

The statistical learning method was another important method for landslide susceptibility assessment. This type of method is based on the assumption that future landslides would easily occur under similar conditions to those of the previous landslides. By analyzing the characteristics of the current landslides, a set of influencing factors is usually selected to implement statistical learning and evaluate the landslide susceptibility map (Nguyen et al., 2019; Zhao et al., 2019; Nsengiyumva and Valentino, 2020; Vojteková and Vojtek, 2020). At present, many statistical learning methods are being used successfully to calculate the landslide susceptibility index (LSI) and generate earthquake-triggered landslide susceptibility maps (Xu et al., 2012a; Pham et al., 2016; Hong et al., 2017; Abeysiriwardana and Gomes, 2022). For example, Yang et al. (2015) established the susceptibility map of seismic landslides for the Lushan earthquake in Sichuan Province with an artificial weighting method. Shrestha and Kang (2019) used a maximum entropy model to produce the landslide susceptibility map of the central region of the Nepal Himalayas. However, the relatively good performance of these methods highly relies on local geo-environment factors and self-features of the methods. For different study areas, the most accurate method is also different. Thus, it is necessary to make comparisons between various methods for selecting a more suitable method which produces a more reliable landslide susceptibility map (Bui et al., 2016).

Gorum et al. (2011) pointed out that the influencing factors of seismic landslides should include seismic correlation parameters, geology parameters, and topography parameters. Ding and Hu (2014) conducted the cluster analysis and the maximum possible classification method to study seismic landslide susceptibility of Beichuan County in the Wenchuan earthquake. Influencing factors which include land-use type, seismic intensity, and annual rainfall were selected to produce a reasonable susceptibility map. Since earthquake-triggered landslides tend to occur frequently near the surface rupture zone (Xu et al., 2012b; Xu, 2014), numerous scholars took the distance to the surface rupture zone as an influencing factor in the evaluation of landslide susceptibility (Xu et al., 2012b; Xu, 2014). However, it is worth noting that some buried-rupture earthquakes often do not have obvious surface rupture zones, and the buried-rupture earthquakes can also trigger abundant landslides (Xu, 2014). The evaluation accuracy of landslide susceptibility for buried-rupture earthquakes is affected by a lack of the factor of the distance to rupture (Regmi et al., 2016). Therefore, it is necessary to improve the accuracy of landslide susceptibility assessment for buried-rupture earthquakes by introducing new influencing factors.

The Mid-Niigata earthquake, which occurred in 2004, has become an important case for studying landslides due to good seismography and a rich collection of seismic landslides. Wang et al. (2007) detected the relationship of landslide occurrence with geological, geomorphological conditions, slope geometry, and earthquake parameters for the Mid-Niigata earthquake. Bandara and Ohtsuka (2017) used the landslide occurrence ratio (LOR) to determine the correlation between the occurrence of earthquake-triggered landslides and geological attributes for the Mid-Niigata earthquake.

In this study, based on GIS technology, three statistical methods and two different scales are evaluated to assess the landslide susceptibility caused by the Mid-Niigata earthquake. First of all, we selected lithology, elevation, slope, slope aspect, surface curvature, distance from the road, and the peak value of earthquake acceleration as the influencing factors to evaluate the susceptibility of seismic landslides in the whole affected zone (large-scale area). For a large-scale area, three different statistical learning methods (Logistic regression (LR), support vector machine (SVM), and artificial neural network (ANN)) are utilized and compared to make reasonable seismic landslide susceptibility maps. As the epicenter area has a higher landslide frequency more prone to earthquake-triggered landslides, the seismic landslide susceptibility in this area is further evaluated. Finally, given the fact of very short surface ruptures, the Mid-Niigata earthquake was regarded as a buried-rupture earthquake (Maruyama et al., 2007). Coseismic ground deformation decomposed from high-resolution DEM is added as an influencing factor to improve the evaluation accuracy of the seismic landslide susceptibility for the epicenter area.

Study site and material

Study site

The Mid-Niigata earthquake occurred on 23 October 2004. The Japan Meteorological Agency (JMA) measured the magnitude of the mainshock as 6.8, the epicenter is located at 37°18′16.56″N, 138°50′10.32″E, and the focal depth is about 13.1 km (Chigira and Yagi, 2006; Kokusho et al., 2011). Within 3 days after the mainshock, more than 900 landslides

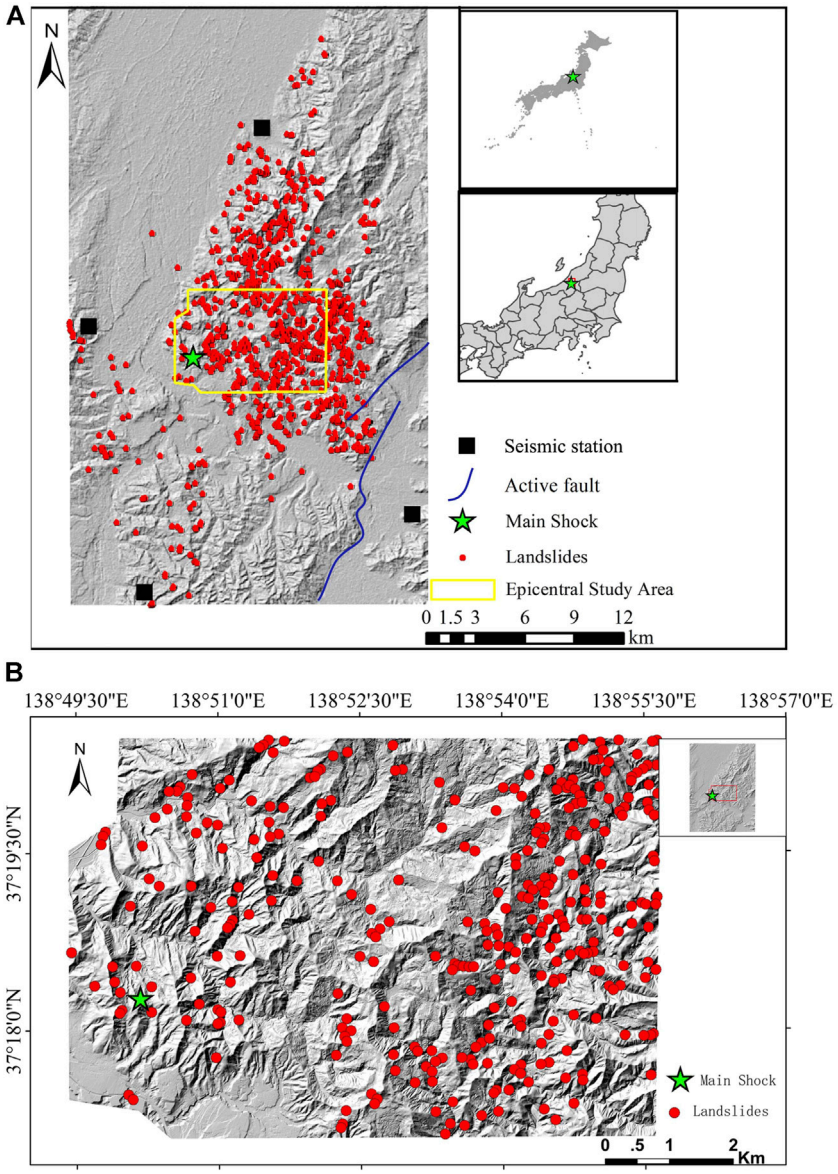

FIGURE 1
Locations of landslides in the study area: **(A)** large-scale area; **(B)** epicenter area.

were induced by the earthquake (Chigira and Yagi, 2006; Kokusho et al., 2014). After the earthquake sequences, a very small surface rupture was found along a previously unmapped northern extension fault zone. The length of the surface rupture was about 1 km (Maruyama et al., 2007). The surface slip of the Mid-Niigata earthquake event was also very small (<20 cm of vertical displacement). In addition, the surface rupture zone is also far away from the epicenter zone, where seismic landslides have concentrated distribution (Sato et al., 2005), i.e., the study area of seismic landslide susceptibility did not contain the surface rupture zone. So in this study, we consider that the surface rupture zone has little effect on the formation of seismic landslides and regard the earthquake as a buried-rupture earthquake.

Landslide inventory

In this study, the assessment of seismic landslide susceptibility is performed on two scales, the large area and the epicenter area. As shown in Figure 1, the large-scale area is 22 km wide (east to west) and 40 km long (north to south). The

TABLE 1 Scales of the landslide-influencing factors.

Spatial database	Data layers	Scale/resolution
Landslides	Landslide points	
Geological map	Lithology types	1:50,000
Road map	Distance from roads	1:10,000
DEM	Slope	30×30 m
	Aspect	
	Elevation	
	Surface curvature	
Seismic factors	PGA	350×350 m
Coseismic ground deformation	Magnitude of deformation	50×50 m

total area of the large-scale area is about 880 km^2. The epicenter area is 7 km long (north to south) and 9 km wide (west to east). The total area is about 56 km^2. The epicenter area is located in the bordering area between Nagaoka City and Ojiya City.

Many methods have been utilized to set up landslide inventory maps, including satellite image interpretation, aerial photography, field survey, and historical landslide records (Vařilová et al., 2015). In this research, the landslide inventory map was interpreted from satellite image data and then checked by field survey data (Kokusho 2008; Kokusho et al., 2009). As shown in Figure 1A, a total of 957 landslide locations were recorded in the large-scale area, most of which are distributed in the mountainous area around the epicenter area and spread to the northeastern mountainous area. There are also some landslides located in the eastern and southern mountain areas. The landslide inventory map of the epicenter area is also shown in Figure 1B.

Landslide influencing factors

The factors that affect the occurrence of earthquake-triggered landslides usually include geology, topography, hydrology, climate, human activities, and earthquake-related parameters. Based on the availability of data and impacted factors used in previous studies (Reichenbach et al., 2018), seven landslide influencing factors (lithology, elevation, slope, slope aspect, surface curvature, peak ground acceleration, and the distance from the road) were taken into consideration for landslide susceptibility analysis for the large-scale area. In the later analysis in the epicenter area, coseismic ground deformation was added as an influencing factor. The scales of the landslide influencing factors are shown in Table 1.

Lithology directly determines the physical and mechanical properties of the slope, which have a direct impact on slope stability. The lithology maps in the large area and the epicenter area are shown in Figure 2A and Figure 3A. The elevation also affects the occurrence of seismic landslides (Hasegawa et al., 2009). The elevation has been regarded as a key factor determining the gravitational potential energy of the terrain. Elevation also indicates the amplification effect of seismic-induced landslides. The elevation maps of the large-scale area and the epicenter area are shown in Figure 2B and Figure 3B, respectively. The slope angle has a direct impact on slope stability that determines the ratio of the anti-sliding force to sliding force. The slope angle maps of the large-scale area and epicenter area are shown in Figure 3C and Figure 3C, respectively. According to previous studies (Xu et al., 2012a; Pham et al., 2016; Hong et al., 2017), the slope aspect is divided into nine groups. The slope aspect maps of the large study area and the epicenter area are shown in Figure 2D and Figure 3D, respectively, and the P and FL mean the flat area. The surface curvature distributions in the large-scale and epicenter areas are shown in Figure 2E and Figure 3E, respectively.

The peak ground acceleration (PGA) of an earthqauke is the maximum absolute value of the acceleration of the surface soil in the earthquake (Tian et al., 2019; Xu and Xu, 2013; Xu et al., 2013; Li et al., 2013; Xu et al., 2012a,b). The PGA was obtained from inversion analysis based on the K-NET and KiK-net observations. The resolution of PGA data is 350 m. The distribution of peak accelerations in the large-scale area and the epicenter area is shown in Figure 2F and Figure 3F, respectively. Human activities have also greatly impacted the topography features. Road construction not only produced a new steep cutting slope but also caused great disturbance to the original slope. Therefore, the distance to the road is taken into account in the assessment of landslide susceptibility. In this study, the locations of high-grade roads like expressways were interpreted from the satellite image. The distances to the road map were divided into seven classes (0–50, 50–100, 100–200, 200–300, 300–400, 400–500, and >500 m). The distances to road maps of the large-scale area and the epicenter area are shown in Figure 2G and Figure 3G, respectively.

For earthquakes with surface ruptures, previous research studies show that there is a clear connection between

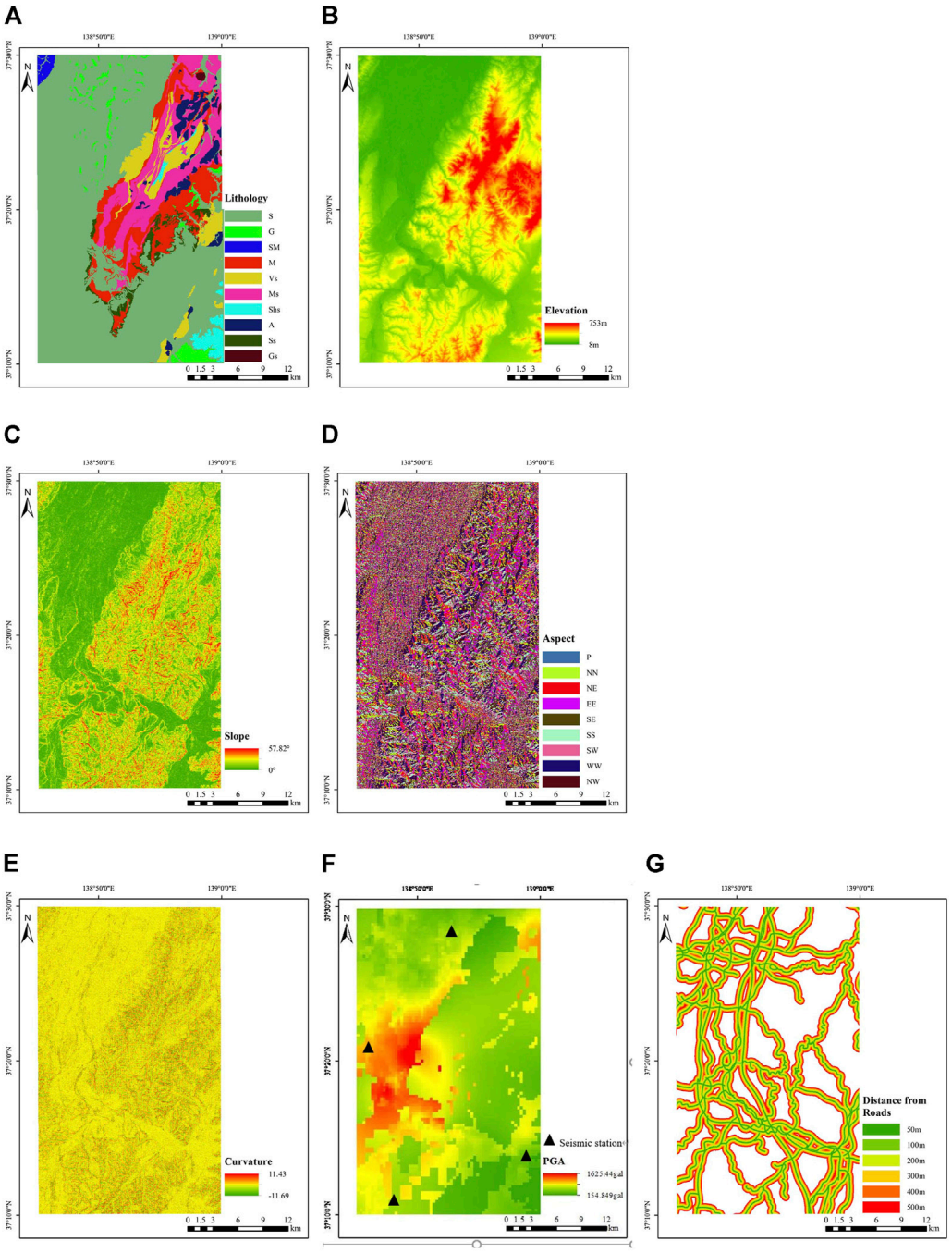

FIGURE 2
Landslide-controlling factors of the large area: **(A)** lithology; **(B)** elevation; **(C)** slope degree; **(D)** aspect; **(E)** profile curvature; **(F)** PGA; and **(G)** distance to roads.

landslide distribution and the distance to the rupture zone (Xu et., al 2012b; Xu, 2014), which means the distance to the surface rupture could be used as an influencing factor. However, for buried-rupture earthquakes, as very short or no surface rupture is exposed, it is difficult to establish the relationship between the distribution of landslides and surface rupture. Therefore, it is necessary to introduce new influencing factors to improve the accuracy of landslide susceptibility analysis for buried-rupture earthquakes.

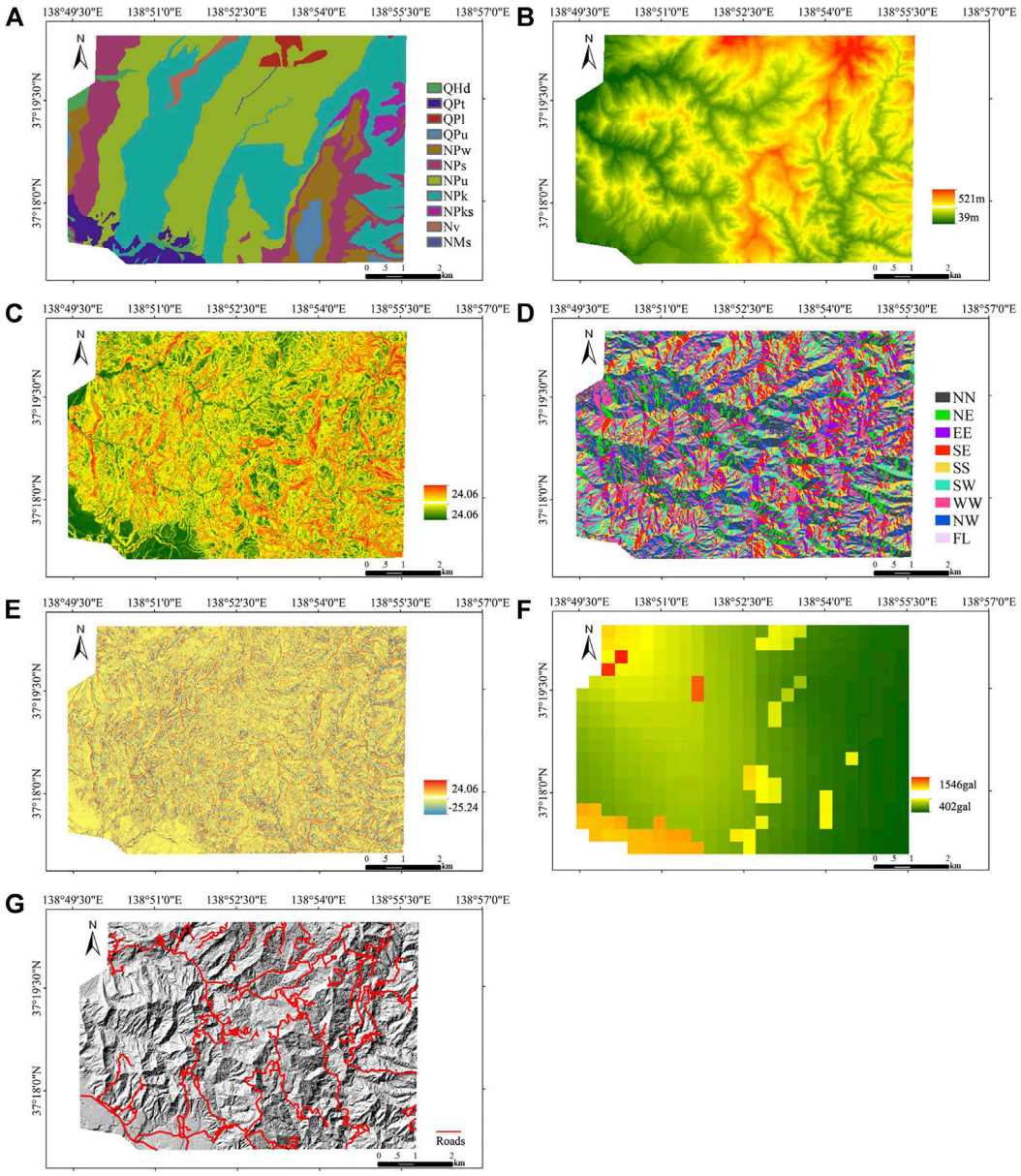

FIGURE 3
Landslide-controlling factors of the epicenter area: **(A)** lithology; **(B)** elevation; **(C)** slope degree; **(D)** aspect; **(E)** profile curvature; **(F)** PGA; and **(G)** distance to roads.

Coseismic ground deformation characterizes the absolute permanent ground deformation before and after the earthquake, and it has been demonstrated that there is a good correlation between landslide distribution and the values of coseismic ground deformation (Chang et al., 2005; Zhao et al., 2014). Therefore, coseismic ground deformation could make up for the disadvantage of losing surface rupture in the assessment of seismic landslide susceptibility to a certain extent. Coseismic ground deformation can be obtained by decomposed high-resolution DEM before and after the earthquake (Zhang et al., 2010; Zhao et al., 2012). Figure 4 shows the description of landform changes in Lagrangian and Eulerian manners. Supposing that a small patch i of the ground surface with one particular node mapped on it is inclined in East-West (x) and North-South (y) directions, Δz_i^e is expressed in terms of the Lagrangian vector $\{\Delta x_i^l\ \Delta y_i^l\ \Delta z_i^l\}$ of the movement of the patch as

$$\Delta_{Z_i}^e = \begin{Bmatrix} t_{X,i} & t_{y,i} & 1 \end{Bmatrix} \cdot \begin{Bmatrix} \Delta X_i^l & \Delta y_i^l & \Delta Z_i^l \end{Bmatrix}^T, \quad (1)$$

where $t_{x,i}$ and $t_{y,i}$ are tangents of the patch plane in the x and y directions, respectively. Taking three adjacent patches, i1, i2, and

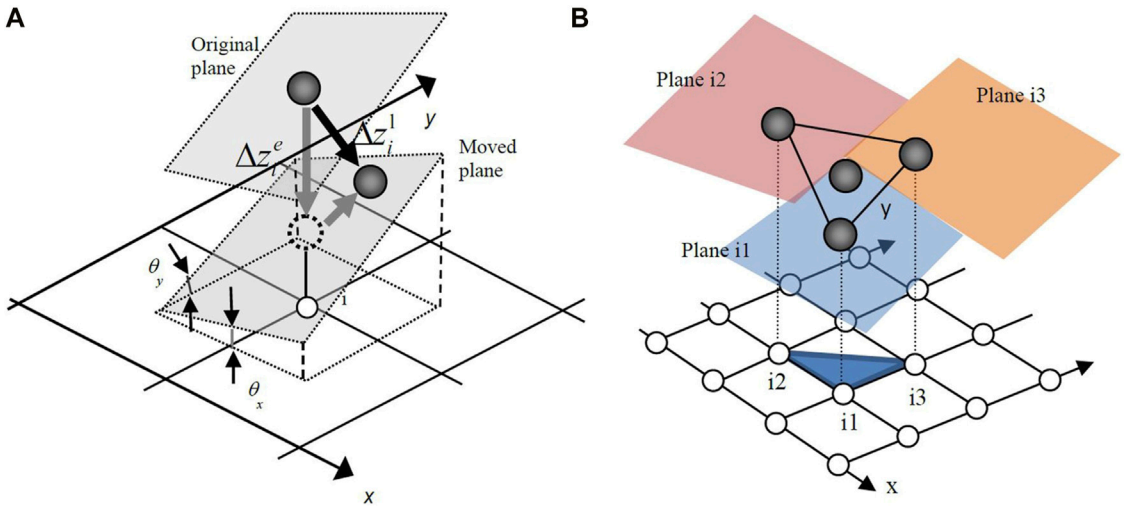

FIGURE 4
Description of landform changes in the Lagrangian and Eurlaian manners: **(A)** scheme of one point and **(B)** scheme of three-point (adopted from Zhao et al., 2012).

i3 in a triangle and using the displacement of its center $\{\Delta x_i^l\ \Delta y_i^l\ \Delta z_i^l\}$ as the representative displacement vector of the triangle, the following simultaneous equations are to be satisfied:

$$\begin{Bmatrix} \Delta z_{i1}^e \\ \Delta z_{i2}^e \\ \Delta z_{i2}^e \end{Bmatrix} = \begin{bmatrix} t_{x,i1} & t_{x,i1} & 1 \\ t_{x,i1} & t_{x,i1} & 1 \\ t_{x,i1} & t_{x,i1} & 1 \end{bmatrix} \begin{Bmatrix} \Delta x_i^l \\ \Delta x_i^l \\ \Delta x_i^l \end{Bmatrix} = T \bullet \begin{Bmatrix} \Delta x_i^l \\ \Delta x_i^l \\ \Delta x_i^l \end{Bmatrix}. \quad (2)$$

An assumption that the triangle undergoes a rigid body translation is used in the aforementioned formulation. The inclination of the moving plane (plane i1) is essential for calculating $t_{x,i}$ and $t_{y,i}$. Suppose the equation of the moving plane is expressed as

$$z = ax + by + c, \quad (3)$$

where a= $t_{x,i1}$=tan$\theta_{x,i1}$ and b= $t_{y,i1}$=tan$\theta_{y,i1}$

Zhao et al. (2012) provided a more rigorous solution method, including the definition of a nominal plane, the improvement of DEM comparability, and matrix condition test. In this study, we used the method proposed by Zhao et al. (2012) to calculate coseismic ground deformation. It is to be noted that the decomposition algorithm requires high-resolution (2 m) DEM. Thus, coseismic ground deformation is added as an influencing factor for the epicenter area only. The DEMs before the earthquake were derived from aerial photos shot by the Geospatial Information Authority of Japan in 1975 and 1976. Triangulation points prepared for road construction in 1986 were then used to orthogonalize and digitize these photos by Aero Asahi (2004). The standard deviation of the digitized aero photos from the triangulation data is 0.589 and 0.517 m in the horizontal and vertical directions, respectively. The DEMs after the earthquake were prepared by airborne LiDAR scanning conducted by Nakanihon Air Service on 24 Oct 2008, the second day of the mainshock and three major aftershocks. After scanning and post-processing standard courses, calibration courses were performed. The average differences for the x coordinate, y coordinate, and elevation are 0.09, 0.2, and 0.06 m respectively, showing good repeatability of scanning. Both sets of DEMs have a resolution of 2 m×2 m. Since the two sets of DEMs were prepared in different ways, it is not appropriate to directly compare them in the calculation. The contour line

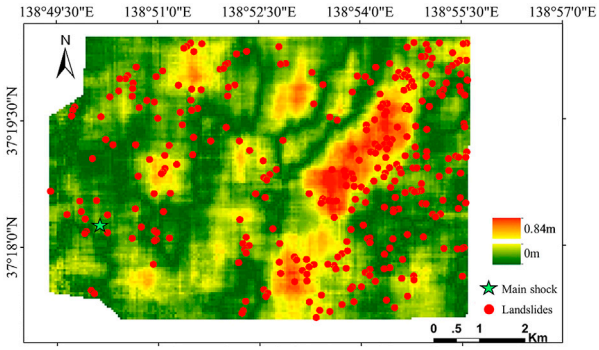

FIGURE 5
Distribution of coseismic ground deformation in the epicenter area.

derived from the 1975 DEMs is quite smooth while that from the 2004 DEMs is curly and tilted owing to the high spatial frequency components. Therefore, we used smoothed elevations instead of the original ones for the 2004 DEMs by substituting the x and y coordinates of each point into the equation of its nominal plane. Given that three adjacent points undergo a rigid body translation movement, their coseismic deformation can be decomposed by solving simultaneous equations. A cut-off window was selected according to regional geology to obtain the tectonic displacements. The properly defined nominal plane could also fully or partially eliminate terrain changes owing to human activities during the time gap between two sets of DEMs since the size of the smooth window is larger than all man-made changes. In addition, to verify the accuracy of the calculated coseismic ground deformation, the calculated displacements were also compared with those at points of triangulation. In total, 11 available triangulation points buried on roads were used. The compared results showed that the difference between the observed displacement and calculated displacement was small, which demonstrated that the calculated coseismic ground deformation is accurate. Details can also be found in the studies by Konagai et al. (2009) and Zhao et al. (2012). The distribution of coseismic ground deformation in the epicenter area is shown in Figure 5.

The orientation of the computed coseismic ground deformation could be divided into two directions: lateral components and vertical components. Zhao et al. (2012) compared the location of earthquake-triggered landslides with the displacement field of lateral components and vertical components, respectively. The results showed that landslide clusters were found within large lateral deformation regions, while landslides seem to be off where the vertical displacement is large. Therefore, in this study, only lateral deformation is used. Figure 5 also shows the distribution of the absolute value of the lateral ground deformation.

Landslide data preparation

In this study, the numbers of landslide points and non-landslide points are sampled at a ratio of 1:1.2 for the large-scale area. A total of 1,117 non-landslide points' data were randomly selected in the non-landslide area. Subsequently, 70% of the landslide points and non-landslide points were selected randomly from the landslide inventory map as the training dataset, with the rest as the testing dataset. To obtain optimum results, we randomly selected the sample points (landslides points and non-landslide points) 10 times, respectively. For different selections, the training and testing samples are different, but the numbers of sample points are the same. In the epicenter area, as the used method to calculate coseismic ground deformation needs high-resolution DEM, the whole epicenter area was converted into 2 m pixels. The total number of pixels is 555,324, and the number of seismic landslide pixels is 45,852. Similarly, 70% of the landslide pixels and non-landslide pixels were selected randomly as the training dataset, with the remaining 30% as the testing dataset.

Methodology

Logistic regression

Logistic regression is suitable for describing the relationship between the categorical outcome (landslide or non-landslide) and input variables (landslide-affecting factors). The principle of the LR is to analyze the spatial relationship between the landslide-affecting factors and the occurrence of a landslide. The results of the regression usually can be interpreted as the probability which is constrained in the interval between 0 and 1.

The LR is indicated by an equation of the form

$$Y = f(P) = \ln\left(\frac{P}{1-P}\right) = \beta_0 + \beta_1 X_1 + \beta_2 X_2 + \cdots + \beta_n X_n, \quad (4)$$

where Y represents outcome variables (landslide or non-landslide), $X = X_1, X_2 \ldots Xn$ represents input variables, n is the *nth* landslide-affecting factor, β_0 is the intercept condition, and $\beta_1, \beta_2 \ldots \beta_n$ are the regression coefficients (Tu, 1996).

The SPSS 10.0 was used to conduct the LR analysis to predict the correlation between the occurrence of landslides and landslide-affecting factors. The regression coefficients were then obtained.

The probability of a landslide event (P) can be determined from the following equation:

$$P = P(Y/X) = \frac{e^{\beta_0+\beta_1 X_1+\beta_2 X_2+\cdots+\beta_n X}}{1+e^{\beta_0+\beta_1 X_1+\beta_2 X_2+\cdots+\beta_n X}}. \quad (5)$$

The probability values change from 0 to 1, with 0 indicating a 0% probability of landslide occurrences and one indicating a 100% probability.

Artificial neural networks

An ANN model has many advantages compared with other models (Yılmaz, 2009a). An ANN could process imprecise and fuzzy data without any assumptions. The ANN model with the most frequently used back-propagation BP algorithm (Pradhan and Lee, 2010b) is used in this study.

The model mainly consists of one input layer, several hidden layers, and an output layer. There are usually two stages for using an ANN, the training stage and classifying stage. During the training stage, the hidden and the input layer neurons handle

their inputs by a corresponding weight, sum the product, and then deal with the sum using a nonlinear transfer function to generate a result. During the classification period, the ANN predicts a target value by adjusting the weights in accordance with the errors between the actual output values and the target output ones and makes the difference minimum.

In this study, the number of hidden layer nodes is calculated by the following equation (Yılmaz, 2009a):

$$N_h = 2N_i + 1, \tag{6}$$

where N_i is the number of input nodes and N_h is the number of hidden nodes.

Then, a three-layer network with one input layer (7 neurons), one hidden layer (15 neurons), and one output layer was used in the large-scale area. In the epicenter area, a three-layer network consisting of one input layer (8 neurons), one hidden layer (17 neurons), and one output layer was utilized. It is important to decide the initial weight range influencing the convergence of the model. In this study, the initial weights were randomly selected from a small range of [-0.25 to 0.25] as proposed by Yılmaz, 2009b. For the hidden layer, the activation function is the hyperbolic tangent, and the activation function is the softmax function for the output layer. We did not use an optimization algorithm for the ANN model.

Support vector machine

The SVM model employs nonlinear transformations of the covariates into a higher dimensional feature space. The two main principles of the SVM are the optimal classification hyperplane and the use of a kernel function (Yao et al., 2008).

The details of a two-class SVM model are described as follows. Given a set of linear separable training vectors x_i (i=1,2 ... n) that consist of two categorical outcomes (landslide or non-landslide denoted as y= ±1), the purpose of the SVM is to find an n-dimensional hyperplane differentiating the two categories by the maximum gap.

Mathematically, the gap $\frac{1}{2}\|w\|^2$could be a minimized subject to the following constraints:

$$y_i((w \cdot x_i) + b) \geq 1, \tag{7}$$

where $||w||$ is the norm of the normal of the hyperplane, b is a scalar base, and $(\cdot)$ denotes the scalar product operation. Using the Lagrangian multiplier, the cost function can be defined as

$$L = \frac{1}{2}\|w\|^2 - \sum_{i=1}^{n}\lambda_i(y_i((w \bullet x) + b)) \geq 1, \tag{8}$$

where λ_i is the Lagrangian multiplier. The solution can be obtained by the dual minimization of Eq. (8) with respect to w and b

In this study, the two-class SVM method was used due to its good performance in landslide susceptibility analysis (Yao et al., 2008; Yılmaz, 2010).

Results

Training and validating the statistical models for the large-scale area

In this study, the performances of the three models (LR, ANN, and SVM) for the large-scale area were validated using a receiver operating characteristic (ROC) curve. The area under the curve (AUC) indicates how good the statistical model is. It means the model has perfect performance when the AUC value equals to 1. A higher AUC value indicates better performance of the statistical model.

Because each sample dataset is selected randomly, the landslide susceptibility calculated by the same model is not the same. To determine the best model, the models are utilized 10 times for analysis of randomly selected datasets, respectively. For different analyses, the training and testing samples are different. For the same analyses, the training samples and testing samples are the same for all three models. The area under the ROC curve (AUC) of each analysis was compared to explore the difference between the three methods. The results are shown in Table 2.

Table 2 shows that the ANN model performed the best among the three models with the highest AUC value and the accuracy of the SVM model was the worst. Based on the maximum AUC values of 10 simulations, the ANN simulation result was also the best (83.6%). The average value and variance of the ANN model were 82.5 and 0.44%, respectively, which was better than those of the LR and SVM models. It means the robustness of the ANN model is better than that of the LR and SVM models.

Yılmaz (2009a) used three models including frequency ratio (FR), ANN, and LR to generate the landslide susceptibility maps of Kat County (Tokat–Turkey). The result showed that the ANN model performed better than the other models. Yılmaz (2010) utilized four different models, namely, conditional probability (CP), LR, ANN, and SVM models to assess the landslide susceptibility of Koyulhisar (Sivas, Turkey). The results also showed that the performance of the ANN model was the best. Some other research studies also showed that the ANN model performed more accurately than the other models (Gómez and Kavzoglu, 2005; Yesilnacar and Topal 2005). We consider the ANN model performed better than the other models because it has a good global searching ability and can learn the near-optimum solution without the gradient information of error functions. As there are about a total of 2,000 samples in the calibration and validation sets, large numbers of samples in the calibration stage will lead to sufficient training of the model and establish an appropriate structure of the ANN model. So the ANN model performs well on the condition that those large numbers of samples were available. For any algorithm, the quantity and quality of samples have key impacts on the accuracy of the predicted results the algorithm makes.

TABLE 2 AUC values of different models in the large-scale area.

Number	1	2	3	4	5	6	7	8	9	10	Statistical value	
Model	%	%	%	%	%	%	%	%	%	%	Average value	Variance value
LR	82.0	81.6	82.3	80.2	81.4	80.2	81.4	80.7	81.6	82.0	81.3	0.49
ANN	83.3	82.4	83.6	81.3	82.1	82.0	82.1	82.3	82.8	83.1	82.5	0.44
SVM	80.8	80.9	81.8	80.1	80.7	79.4	80.4	80.5	80.5	81.8	80.7	0.47

TABLE 3 Distribution of different classes obtained by different methods.

Model	Class	Area (km^2)	Time of landslide occurrence	Percentage of each susceptible class area (%)	Percentage of landslides in each susceptible class (%)	Landslide density (times/km^2)
LR	Very high	87.61	387	9.95	40.44	4.42
	High	175.55	350	19.95	36.57	1.99
	Moderate	263.60	171	29.95	17.87	0.65
	Low	353.35	49	40.15	5.12	0.14
SVM	Very high	87.71	473	9.97	49.43	5.39
	High	175.95	286	19.99	29.89	1.63
	Moderate	264.16	126	30.01	13.17	0.48
	Low	352.28	72	40.03	7.52	0.20
ANN	Very high	87.60	402	9.95	42.01	4.59
	High	175.54	352	19.95	36.78	2.01
	Moderate	263.60	171	29.95	17.87	0.65
	Low	353.37	32	40.15	3.34	0.09

Development of landslide susceptibility maps for the large-scale area

In this study, all three models have been used to calculate the landslide susceptibility index (LSI) and then generate the landslide susceptibility maps. There are several mathematical methods including quantiles, natural breaks, standard deviation, equal intervals, and descending area percentage to be reclassified in the LSI (Ayalew et al., 2004). Among the aforementioned methods, the descending area percentage technique is the most widely used. In this study, the descending area percentage technique was used. The landslide susceptibility maps were constructed into four classes: low (40%), moderate (30%), high (20%), and very high (10%). The landslide density was used to assess the performance of landslide susceptibility maps. The landslide density (LD) is defined as the ratio of the number of landslides and the area of each susceptible class.

The calculated landslide densities by using the three different models are shown in Table 3. It can be observed that all maps present good spatial predictions of landslides as landslide density is ascending from very low to very high class (Yīlmaz, 2009b). The results using the ANN model show that the very high class contains 42.01% of the total landslides; however, it only covers 9.95% of the total study area, and the LD of the very high class was 4.59. In comparison, the low classes only contain 3.34% landslides; however, it covers 40.15% area and the LD of the low class was 0.09. This indicates that the ANN model performed well in susceptibility classification as it fits well with the landslide inventories.

The landslide susceptibility maps of different methods are shown as Figure 6. The analysis results of LR, SVM, and ANN models are very close. The epicenter area is a very high susceptible area, the northeast and the southwest mountain areas are high and very high susceptible areas, respectively, and the northern plains area is distributed with the low susceptible class. The susceptibility map of the ANN model shows that the high susceptible areas and low susceptible areas are more concentrated into blocks, and zonation produced by the SVM and LR are more dispersed. Overall, all three models could generate reasonable landslide susceptibility maps.

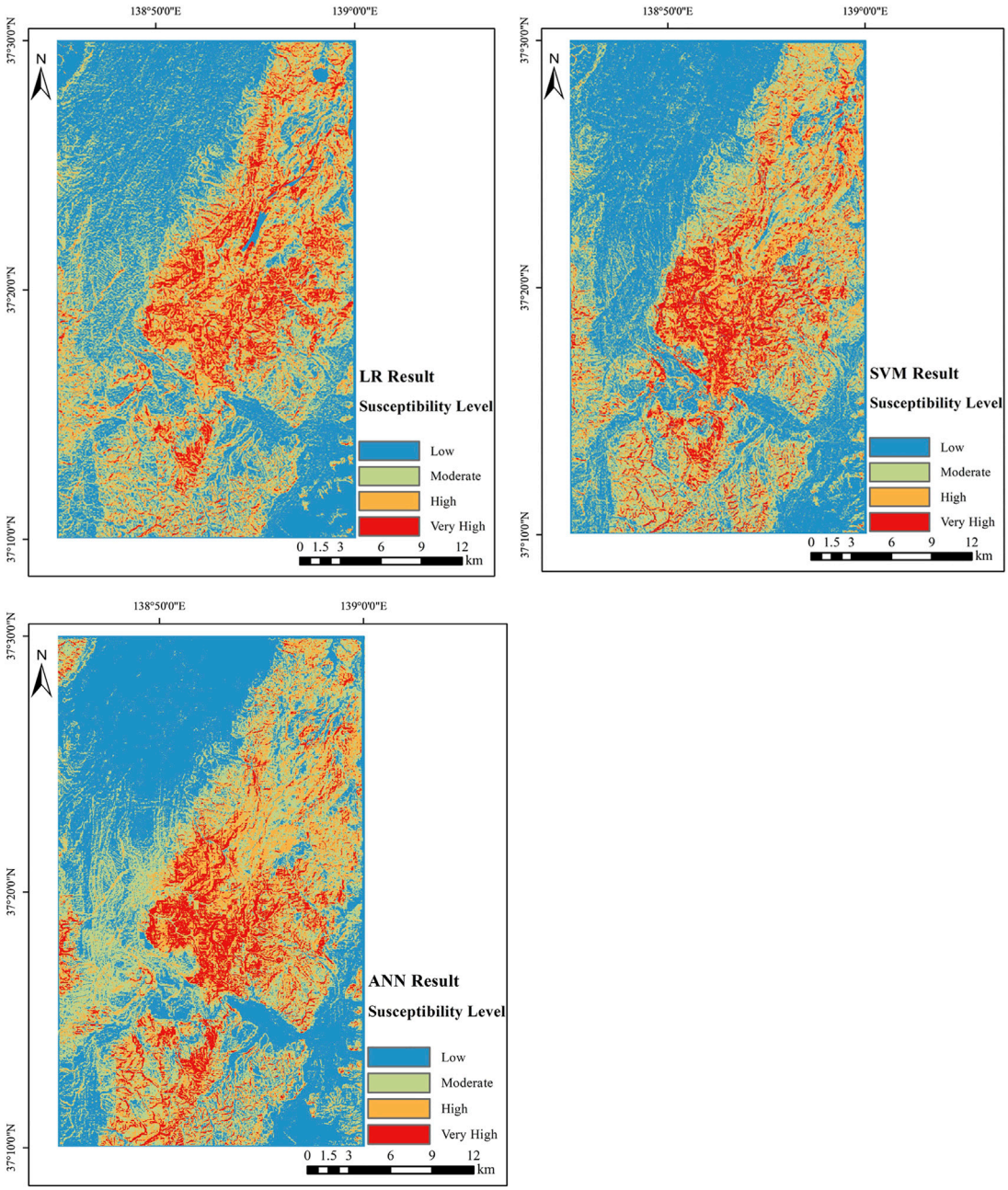

FIGURE 6
Landslide susceptibility maps using different models for the large area. **(A)** LR model. **(B)** SVM model. **(C)** ANN model.

Model performance validation for the epicenter area

From the landslide susceptibility map of the large-scale area, it is known that the susceptibility level in the epicenter area is generally high. Since it is still too costly to remediate all slopes in the approximately 60 km^2 area, it is necessary to further evaluate the landslide susceptibility in the epicenter area. It can be seen in Section 4.1 that the ANN model is the most suitable model for landslide susceptibility assessment in this area. Therefore, we only use the ANN model to analyze and evaluate the landslide susceptibility in the epicenter area.

First, to evaluate the significance of landslide susceptibility analysis by considering different scales, the values of the AUC for the epicenter area are calculated in two different conditions. First,

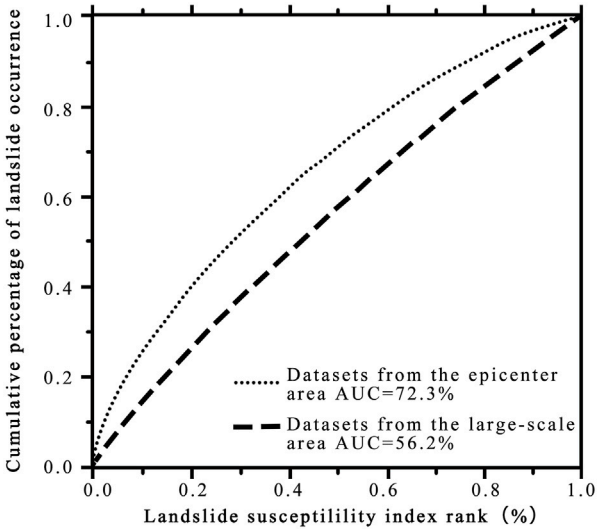

FIGURE 7
Analysis of the ROC curve under different scales.

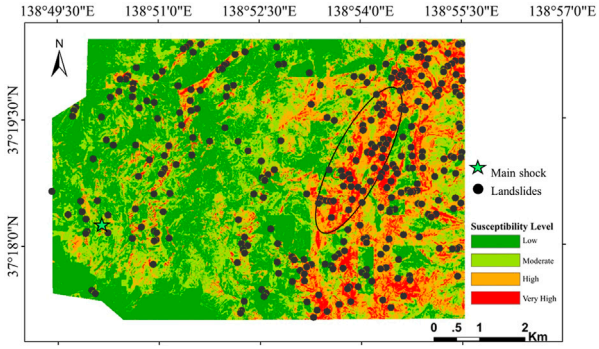

FIGURE 8
Landslide susceptibility map of the epicenter area.

we calculate the values of the AUC based on the corresponding calculated LSI of the epicenter area from the large-scale (whole affected area) datasets. Then, the values of the AUC are calculated based on the calculated LSI from the epicenter area datasets. The values of the AUC of the two different conditions are shown in Figure 7. The results show that the AUC is 56.2% based on the calculated LSI from the large-scale datasets, in contrast, the AUC is 72.3% based on the calculated LSI from the epicenter area solely. The results show that it is necessary to assess landslide susceptibility under different scales.

Subsequently, the landslide density and landslide susceptibility map of the epicenter area were obtained as shown in Table 4 and Figure 8. The results show that the very high class contains 40.44% of the total landslides; however, it only covers 8.6% of the epicenter area and the LD of the very high class was 26.54. In comparison, the low classes contain only 5.12% landslides; however, it covers 40.15% area and the LD of the low class was only 0.73. The landslide density increases gradually between the low class and very high class. This indicates that the landslide susceptibility map fits well with the landslide inventories.

As shown in Figure 8, the very high-class area is mainly distributed along the long axis of the ellipse in the east of the study area, and a large amount of deep-seated landslides occurred in this area. The high-susceptibility area is also distributed in the northwestern area. The occurrence possibility of landslides in the central area and southwest plain area is relatively low. Compared with the epicenter area parts in the landslide susceptibility map of the large-scale area, the landslide susceptibility maps obtained by the epicenter area research have a better discrimination degree, which can meet the key prevention and control requirements in the small area.

Discussion

It is important to select suitable influenced factors in landslide susceptibility mapping. The analysis of the predictive importance for the input variables in the large-scale analysis is also conducted. The predictive importance of the input variables in the large-scale analysis is calculated by the variance method. The predictive importance of the influence factors in the large-scale analysis is shown in Table 5.

TABLE 4 Distribution of different classes in the epicenter area.

	Class	Area (km^2)	Landslide occurrence	Percentage of each susceptible class area (%)	Percentage of landslides in each susceptible class (%)	Landslide density (times/km^2)
ANN	Very high	4.7853	127	8.6	40.44	26.54
	High	10.8605	115	19.51	36.57	10.57
	Moderate	18.089	56	32.5	17.87	3.10
	Low	21.9236	16	39.39	5.12	0.73

TABLE 5 Predictive importance of different influencing factors in the large-scale analysis.

Number	Influencing factor	Predictive importance
1	Elevation	100
2	PGA	95.84
3	Slope	91.74
4	Lithology	82.76
5	Curvature	70.95
6	Slope aspect	64.86
7	Distance to roads	48.12

TABLE 6 Predictive importance of different influencing factors in the epicenter area.

Number	Influencing factor	Predictive importance
1	Lithology	0.213
2	Slope	0.207
3	PGA	0.169
4	Curvature	0.125
5	Coseismic ground deformation	0.093
6	Elevation	0.086
7	Slope aspect	0.057
8	Distance to roads	0.048

As shown in Table 5, elevation has the greatest impact on the occurrence of earthquake landslides and the impact of other factors is in order of peak earthquake acceleration, slope, lithology, curvature, aspect, and distance from the road. As all values are positive, it means all the selected influencing factors make a positive contribution to the assessment of landslide susceptibility in large-scale analysis.

Influencing factors including lithology, elevation, slope, slope aspect, surface curvature, peak ground acceleration, the distance from the road, and coseismic ground deformation were considered in the small-scale analysis. Since the contribution of these factors to landslide models might be different, it is necessary to quantify the effects of influential factors on the assessment of landslide susceptibility. The analysis of variance method has been utilized to evaluate the predictive capability of these factors in the small-scale analysis. The factors with higher variance values indicate a higher contribution to landslide models and *vice versa*. The predictive capability of eight landslide-affecting factors is shown in Table 6.

As Table 6 shows, lithology has the greatest impact on the occurrence of earthquake landslides and the impact of other factors is in order of slope, peak earthquake acceleration,

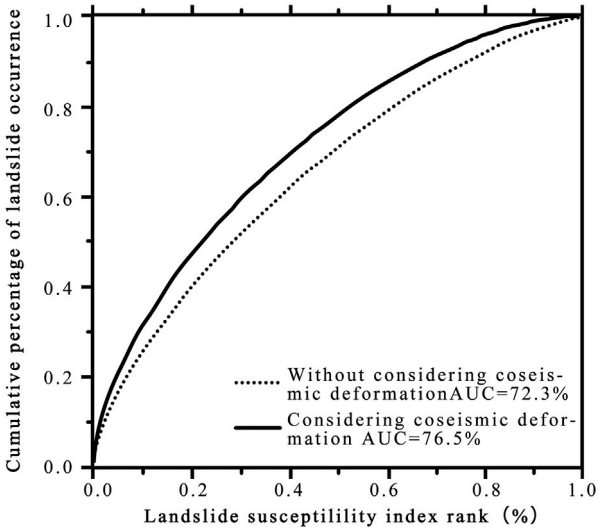

FIGURE 9
Analysis of the ROC curve considering coseismic surface deformation or not.

curvature, coseismic ground deformation, elevation, aspect, and distance from the road. As all values are positive, it means all the selected influenced factors make a positive contribution to the assessment of landslide susceptibility. Reichenbach et al. (2018) critically reviewed the statistically-based landslide susceptibility assessment literature by systematically searching for and then compiling an extensive database of 565 peer-review articles from 1983 to 2016. The results showed that elevation, aspect, and distance from the road are commonly chosen as influencing factors in the assessment of landslide susceptibility. The importance of coseismic surface deformation is higher than the elevation, aspect, and distance from the road. It means that coseismic ground deformation should be regarded as an important factor in the assessment of landslide susceptibility.

Then, to evaluate the effects of the new factor coseismic ground deformation on the assessment of landslide susceptibility, two different situations are considered. One situation regards coseismic deformation as an influencing factor, whereas the other does not. Figure 9 shows the values of the AUC by considering coseismic surface deformation or not. From Figure 9, it can be seen that the AUC is 72.3% without considering coseismic surface deformation, in contrast, the AUC is 76.5% by considering coseismic surface deformation. It means that coseismic surface deformation has a positive effect on the assessment of landslide susceptibility.

In addition, there are other several advantages to regarding coseismic ground deformation as an important

factor in landslide mapping. Coseismic ground deformation will help to reveal hidden subsurface damage. It should be noted that not all deformation will directly lead the landslides. However, the area with large coseismic surface deformation often indicates that the movement of the rock mass may be further developed and the integrity of the rock mass is reduced, which renders slopes prone to landslip in future earthquakes again. Zhao et al. (2012) explored the localized coseismic deformation in Kizawa (a small village), Japan, after the earthquake. The results showed that the calculated coseismic deformation in Kizawa is relatively large but the landslides are sparse. However, after a detailed investigation, it was found that underground structures such as tunnels and wells were severely damaged. The road alignment of the Kizawa tunnel, which was buried 30 m beneath the ground surface, was shifted sideways 1–1.5 m in the east-to-southeast direction. Furthermore, two irrigation wells were dislocated at 30 and 20 m, beneath the ground, respectively. Therefore, it is highly possible that the ground underwent some subsurface damage at locations with large coseismic deformation. Although the deformation did not form landslides at these locations in the 2004 Mid-Niigata earthquake, as there was accumulated deformation within the rock and soil, a landslide will easily occur in the next earthquake event. Therefore, especially in the case of buried-fault earthquakes, coseismic surface deformation can be considered an important influencing factor in the assessment of earthquake landslide susceptibility.

However, it should be noted that some limitations still existed in this study. The spatial resolution of the PGA map in the epicenter area is relatively low. The PGA map of the epicenter area is the result of back-analysis from sparse seismic station data. It is to be noted that the used PGA map is also the highest resolution map that the authors could get and most back-analyses can offer. It also inferred that the low resolution of the PGA map is also the main reason that causes the relatively lower value of the AUC (0.72) in the epicenter area, as the value of the AUC in the large-scale area is 0.82 for the ANN model. However, in other words, the low value of the AUC also demonstrated the urgent demand for introducing new factors to improve the assessment of landslide susceptibility.

Conclusion

In this study, the LR, ANN, and SVM models are applied to generate landslide susceptibility maps based on the 2004 Mid-Niigata earthquake-triggered landslide inventories. A total of seven impact factors, namely, lithology, elevation, slope, aspect, surface curvature, peak acceleration, and the distance from the road are selected as the influenced factors. The ROC curve evaluation results clearly demonstrate that the map obtained from the ANN model performed the best among the three models. The variance of the AUC for randomly selected datasets by the ANN is also the smallest, which means that the ANN model has excellent robustness.

Therefore, the ANN model can be used for the assessment and development of landslide susceptibility maps. Then, the significance of landslide susceptibility analysis considering different scales is also evaluated. The results show that the AUC is 56.2% based on the datasets from the large-scale, in contrast, the AUC is 72.3% based on the datasets from the epicenter area solely. The results show it is necessary to assess landslide susceptibility under different scales. At the same time, we included coseismic ground deformation as the influencing factor for landslide susceptibility in the epicenter area. The AUC increased from 0.723 to 0.765 after considering the newly added factor. The predictive capability of eight landslide-affecting factors also showed that the importance of coseismic surface deformation is higher than the elevation, aspect, and distance from the road. Therefore, for the buried-rupture earthquake, coseismic surface deformation can be considered an important factor to evaluate the susceptibility of landslides.

Data availability statement

The raw data supporting the conclusion of this article will be made available by the authors, without undue reservation.

Author contributions

YZ, ZH, and ZW conceived this research. YZ, JZ, and KK designed the methodology and performed the experiments. YZ and ZW analyzed the results and wrote the manuscript. All authors contributed to the preparation of this manuscript.

Funding

This research was supported financially by the National Natural Science Foundation of China (Grant No. 52178359 and Grant No 51988101), the Fundamental Research Funds for the Central Universities (2019FZJD002) and the Natural Science Foundation of Sichuan Province (Grant No. 2022NSFSC1129).

Acknowledgments

The authors appreciate Fuchu Dai in the Beijing University of Technology for his advice on improving the study.

Conflict of interest

ZH was employed by the company Powerchina Zhongnan Engineering Corp. Ltd.

The remaining authors declare that the research was conducted in the absence of any commercial or financial relationships that could be construed as a potential conflict of interest.

Publisher's note

References

Abeysiriwardana, H. D., and Gomes, P. I. A. (2022). Integrating vegetation indices and geo-environmental factors in GIS-based landslide-susceptibility mapping: Using logistic regression. *J. Mt. Sci.* 19, 477–492. doi:10.1007/s11629-021-6988-8

Ayalew, L., Yamagishi, H., and Ugawa, N. (2004). Landslide susceptibility mapping using GIS-based weighted linear combination, the case in Tsugawa area of Agano River, Niigata Prefecture, Japan. *Landslides* 1 (1), 73–81. doi:10.1007/s10346-003-0006-9

Bandara, S., and Ohtsuka, S. (2017). Spatial distribution of landslides induced by the 2004 Mid-Niigata prefecture earthquake, Japan. *Landslides* 14 (6), 1877–1886. doi:10.1007/s10346-017-0819-6

Bui, D. T., Nguyen, Q. P., Hoang, N. D., and Klempe, H. (2016). A novel fuzzy K -nearest neighbor inference model with differential evolution for spatial prediction of rainfall-induced shallow landslides in a tropical hilly area using GIS. *Landslides* 14 (1), 1–17. doi:10.1007/s10346-016-0708-4

Chang, K. J., Taboada, A., and Chan, Y. C. (2005). Geological and morphological study of the Jiufengershan landslide triggered by the Chi-Chi Taiwan earthquake. *Geomorphology* 71 (3), 293–309. doi:10.1016/j.geomorph.2005.02.004

Chigira, M., and Yagi, H. (2006). Geological and geomorphological characteristics of landslides triggered by the 2004 Mid Niigta prefecture earthquake in Japan. *Eng. Geol.* 82 (4), 202–221. doi:10.1016/j.enggeo.2005.10.006

Ding, M., and Hu, K. (2014). Susceptibility mapping of landslides in Beichuan County using cluster and MLC methods. *Nat. Hazards (Dordr).* 70 (1), 755–766. doi:10.1007/s11069-013-0854-0

Gómez, H., and Kavzoglu, T. (2005). Assessment of shallow landslide susceptibility using artificial neural networks in Jabonosa river basin, Venezuela. *Eng. Geol.* 78 (1–2), 11–27. doi:10.1016/j.enggeo.2004.10.004

Gorum, T., Fang, X. M., Westen, C. J. V., Huang, R. Q., Xu, Q., Tang, C., et al. (2011). Distribution pattern of earthquake-induced landslides triggered by the 12 May 2008 Wenchuan earthquake. *Geomorphology* 133 (3–4), 152–167. doi:10.1016/j.geomorph.2010.12.030

Hasegawa, S., Dahal, R. K., Nishimura, T., Nonomura, A., and Yamanaka, M. (2009). DEM-based analysis of earthquake-induced shallow landslide susceptibility. *Geotech. Geol. Eng. (Dordr).* 27 (3), 419–430. doi:10.1007/s10706-008-9242-z

Hong, H., Liu, J. Z., Zhu, A. X., Shahabi, H., Pham, B. T., Chen, W., et al. (2017). A novel hybrid integration model using support vector machines and random subspace for weather-triggered landslide susceptibility assessment in the Wuning area (China). *Environ. Earth Sci.* 76 (19), 652. doi:10.1007/s12665-017-6981-2

Keefer, D. K. (1984). Landslides caused by earthquakes. *Geol. Soc. Am. Bull.* 95 (4), 406. doi:10.1130/0016-7606(1984)95<406:lcbe>2.0.co;2

Kokusho, T. Ishizawa, T., and Hara, T. (2009). Slope failures during the 2004 niigataken chetsu earthquake in Japan. *Earthquake geotechnical case histories for performance-based design*. Balkema: CRC Press, 47–70.

Kokusho, T., Ishizawa, T., and Koizumi, K. (2011). Energy approach to seismically induced slope failure and its application to case histories. *Eng. Geol.* 122 (1-2), 115–128. doi:10.1016/j.enggeo.2011.03.019

Kokusho, T., Koyanagi, T., and Yamada, T. (2014). Energy approach to seismically induced slope failure and its application to case histories –Supplement. *Eng. Geol.* 181, 290–296. doi:10.1016/j.enggeo.2014.08.019

Kokusho, T. (2008). *Report of the 2004 niigataken chuetsu earthquake slope disaster database*. Tokyo: Chuo University. (In Janpanese).

Konagai, K., Fujita, T., Ikeda, T., and Takatsu, S. (2009). Tectonic deformation buildup in folded mountain terrains in the October 23, 2004, Mid-Niigata earthquake. *Soil Dyn. Earthq. Eng.* 29, 261–267. doi:10.1016/j.soildyn.2008.01.013

Li, W. L., Huang, R. Q., Tang, C., Xu, Q., and Westen, C. V. (2013). Co-Seismic landslide inventory and susceptibility mapping in the 2008 wenchuan earthquake disaster area, China. *J. Mt. Sci.* 10 (3), 339–354. doi:10.1007/s11629-013-2471-5

Maruyama, T., Iemura, K., Azuma, T., Yoshioka, T., Sato, M., and Miyawaki, R. (2007). Paleoseismological evidence for non-characteristic behavior of surface rupture associated with the 2004 Mid-Niigata Prefecture earthquake, central Japan. *Tectonophysics* 429 (1), 45–60. doi:10.1016/j.tecto.2006.09.008

Nguyen, H., Mehrabi, M., Kalantar, B., Moayedi, H., and Abdullahi, M. M. (2019). Potential of hybrid evolutionary approaches for assessment of geo-hazard landslide susceptibility mapping. *Geomatics, Nat. Hazards Risk* 10, 1667–1693. doi:10.1080/19475705.2019.1607782

Nsengiyumva, J. B., and Valentino, R. (2020). Predicting landslide susceptibility and risks using GIS-based machine learning simulations, case of upper Nyabarongo catchment. *Geomatics, Nat. Hazards Risk* 11, 1250–1277. doi:10.1080/19475705.2020.1785555

Pham, B. T., Pradhan, B., Tien Bui, D., Prakash, I., and Dholakia, M. B. (2016). A comparative study of different machine learning methods for landslide susceptibility assessment: A case study of uttarakhand area (India). *Environ. Model. Softw.* 84, 240–250. doi:10.1016/j.envsoft.2016.07.005

Pradhan, B., and Lee, S. (2010a). Landslide susceptibility assessment and factor effect analysis: Backpropagation artificial neural networks and their comparison with frequency ratio and bivariate logistic regression modelling. *Environ. Model. Softw.* 25 (6), 747–759. doi:10.1016/j.envsoft.2009.10.016

Pradhan, B., and Lee, S. (2010b). Regional landslide susceptibility analysis using back-propagation neural network model at Cameron Highland, Malaysia. *Landslides* 7 (1), 13–30. doi:10.1007/s10346-009-0183-2

Regmi, A. D., Dhital, M. R., Zhang, J. Q., Su, L, J., and Chen, X. Q. (2016). Landslide susceptibility assessment of the region affected by the 25 April 2015 Gorkha earthquake of Nepal. *J. Mt. Sci.* 3 (11), 1941–1957. doi:10.1007/s11629-015-3688-2

Reichenbach, P., Rossi, M., Malamud, D. B., Mihir, M., and Guzzetti, F. (2018). A review of statistically-based landslide susceptibility models. *Earth. Sci. Rev.* 180, 60–91. doi:10.1016/j.earscirev.2018.03.001

Saade, A., Abou-Jaoude, G., and Wartman, J. (2016). Regional-scale co-seismic landslide assessment using limit equilibrium analysis. *Eng. Geol.* 204, 53–64. doi:10.1016/j.enggeo.2016.02.004

Sato, H. P., Sekiguchi, T., Kojiroi, R., Suzuki, Y., and Iida, M. (2005). Overlaying landslides distribution on the earthquake source, geological and topographical data: The Mid niigata prefecture earthquake in 2004, Japan. *Landslides* 2 (2), 143–152. doi:10.1007/s10346-005-0053-5

Shrestha, S., and Kang, T. S. (2019). Assessment of seismically-induced landslide susceptibility after the 2015 Gorkha earthquake, Nepal. *Bull. Eng. Geol. Environ.* 78 (3), 1829–1842. doi:10.1007/s10064-017-1191-4

Tian, Y. Y., Xu, C., Hong, H. Y., Zhou, Q., and Wang, D. (2019). Mapping earthquake-triggered landslide susceptibility by use of artificial neural network (ANN) models: An example of the 2013 minxian (China) mw 5.9 event. *Geomatics, Nat. Hazards Risk* 10, 1–25. doi:10.1080/19475705.2018.1487471

Tu, J. V. (1996). Advantages and disadvantages of using artificial neural networks versus logistic regression for predicting medical outcomes. *J. Clin. Epidemiol.* 49 (11), 1225–1231. doi:10.1016/s0895-4356(96)00002-9

Vařilová, Z., Kropáček, J., Zvelebil, J., Šťastný, M., and Vilímek, V. (2015). Reactivation of mass movements in Dessie graben, the example of an active landslide area in the Ethiopian Highlands. *Landslides* 12 (5), 985–996. doi:10.1007/s10346-015-0613-2

Vojteková, J., and Vojtek, M. (2020). Assessment of landslide susceptibility at a local spatial scale applying the multi-criteria analysis and GIS: A case study from Slovakia. *Geomatics, Nat. Hazards Risk* 11, 131–148. doi:10.1080/19475705.2020.1713233

Wang, H. B., Sassa, K., and Xu, W. Y. (2007). Analysis of a spatial distribution of landslides triggered by the 2004 Chuetsu earthquakes of Niigata Prefecture, Japan. *Nat. Hazards (Dordr).* 41 (1), 43–60. doi:10.1007/s11069-006-9009-x

Xu, C., Dai, F., Xu, X., and Yuan, H. L. (2012a). GIS-based support vector machine modeling of earthquake-triggered landslide susceptibility in the Jianjiang River watershed, China. *Geomorphol. (Amst).* 145–146 (2), 70–80. doi:10.1016/j.geomorph.2011.12.040

Xu, C. (2014). Do buried-rupture earthquakes trigger less landslides than surface-rupture earthquakes for reverse faults? *Geomorphology* 216, 53–57. doi:10.1016/j.geomorph.2014.03.029

Xu, C., and Xu, X. (2013). Controlling parameter analyses and hazard mapping for earthquake-triggered landslides: An example from a square region in beichuan county, sichuan Province, China. *Arab. J. Geosci.* 6, 3827–3839. doi:10.1007/s12517-012-0646-y

Xu, C., Xu, X., Dai, F., and Saraf, A. K. (2012b). Comparison of different models for susceptibility mapping of earthquake triggered landslides related with the 2008 Wenchuan earthquake in China. *Comput. Geosciences* 46 (3), 317–329. doi:10.1016/j.cageo.2012.01.002

Xu, C., Xu, X., and Yu, G. (2013). Landslides triggered by slipping-fault-generated earthquake on a plateau: An example of the 14 april 2010, ms 7.1, yushu, China earthquake. *Landslides* 10, 421–431. doi:10.1007/s10346-012-0340-x

Yang, Z. H., Lan, H. X., Gao, X., Li, L. P., Meng, Y. S., and Wu, Y. M. (2015). Urgent landslide susceptibility assessment in the 2013 Lushan earthquake-impacted area, Sichuan Province, China. *Nat. Hazards (Dordr).* 75 (3), 2467–2487. doi:10.1007/s11069-014-1441-8

Yao, X., Tham, L. G., and Dai, F. C. (2008). Landslide susceptibility mapping based on support vector machine: A case study on natural slopes of Hong Kong, China. *Geomorphology* 101 (4), 572–582. doi:10.1016/j.geomorph.2008.02.011

Yesilnacar, E., and Topal, T. (2005). Landslide susceptibility mapping: A comparison of logistic regression and neural networks methods in a medium scale study, hendek region (Turkey). *Eng. Geol.* 79 (3–4), 251–266. doi:10.1016/j.enggeo.2005.02.002

Yilmaz, I. (2009b). A case study from Koyulhisar (Sivas-Turkey) for landslide susceptibility mapping by artificial neural networks. *Bull. Eng. Geol. Environ.* 68 (3), 297–306. doi:10.1007/s10064-009-0185-2

Yilmaz, I. (2010). Comparison of landslide susceptibility mapping methodologies for koyulhisar, Turkey: Conditional probability, logistic regression, artificial neural networks, and support vector machine. *Environ. Earth Sci.* 61 (4), 821–836. doi:10.1007/s12665-009-0394-9

Yilmaz, I. (2009a). Landslide susceptibility mapping using frequency ratio, logistic regression, artificial neural networks and their comparison: A case study from Kat landslides (tokat-Turkey). *Comput. Geosciences* 35 (6), 1125–1138. doi:10.1016/j.cageo.2008.08.007

Zhang, Y. S., Yao, X., Xiong, T. Y., Ma, Y. S., Hu, D. G., Yang, N., et al. (2010). Rapid identification and emergency investigation of surface ruptures and geohazards induced by the m_s 7.1 yushu earthquake. *Acta Geol. Sin. Ed.* 84 (6), 1315–1327.

Zhao, Y., and Konagai, K. (2014). Evidence of a hidden landslide slip surface beneath a mountain hamlet. *Environ. Earth Sci.* 71 (10), 4615–4624. doi:10.1007/s12665-014-3078-z

Zhao, Y., Konagai, K., and Fujita, T. (2012). Multi-scale decomposition of Co-seismic deformation from high resolution DEMs: A case study of the 2004 mid-niigata earthquake. *Acta Geol. Sin. - Engl. Ed.* 86 (4), 1013–1021. doi:10.1111/j.1755-6724.2012.00725.x

Zhao, Y., Wang, R., Jiang, Y. J., Liu, H. J., and Wei, Z. L. (2019). GIS-based logistic regression for rainfall-induced landslide susceptibility mapping under different grid sizes in Yueqing, Southeastern Chinaerent grid sizes in Yueqing, Southeastern China. *Eng. Geol.* 259, 105147. doi:10.1016/j.enggeo.2019.105147

APPENDIX TABLE A1 Lithological distribution in the large-scale area.

The lithology data used in this paper are redrawn from the 1: 50,000 geological map of Nagaoka and Ojiya by the Geological Survey of Japan's Ministry of International Trade and Industry. There are 10 different lithology groups in the large-scale area (Appendix Table A1) and 11 different lithology groups in the epicenter area (Appendix Table A2).

Category	Lithology
S	Conglomerate with mudstone
G	Conglomerate with sandstone
SM	Sandstone with silt
M	Sandstone with mudstone
Vs.	Volcanic rock
Ms	Mudstone
Shs	Shale
A	Residual soil
Ss	Sandstone
Gs	Conglomerate

APPENDIX TABLE A2 Lithological distribution in the epicenter area.

The elevation data used in this paper are generated from the 30 m resolution DEM data obtained from the ASTER Global Digital Elevation Model (ASTER GDEM). The slope angle in the study area ranges from 0° to 57.82° for the large area. A 0° slope angle means a flat area. The west part of the large-scale area is an almost flat area, whereas the mountains mainly spread from the NE direction to the SW direction. The influence of the slope aspect on the stability of the slope is multifaceted. Different slope directions have different influences of solar radiation and rainfall on the slopes that control the moisture of the terrain that affects landslide occurrences. Surface curvature determines the pooling and dispersion of surface water and affects the strength and stability of rocks and soils. In addition, there is a strong correlation between soil thickness and surface curvature due to soil sedimentation caused by the water flow. Since the inertia forces generated by earthquakes are important causes of earthquake-triggered landslides, the PGA is generally chosen as the impact factor of landslide susceptibility. It has been acknowledged that the slope stability is affected not only by the PGA of the mainshock but also by that of aftershocks. However, introducing more influencing factors of the same types will also lead to overfitting problems. Therefore, at present, almost all studies only considered the PGA map of mainshock as influencing factors regardless of the effect of aftershocks on the assessment of landslide susceptibility, and the concluded landslide susceptibility mappings were also reliable.

Category	Lithology
QHd	Accumulation of Holocene
QPt	Accumulation of Pleistocene
QPl	Ancient landslide deposits of Pleistocene
QPu	Conglomerate of Pleistocene
NPw	Conglomerate of Pliocene
NPs	Sandy mudstone of Pliocene
NPu	Mudstone of Pliocene
NPk	Mudstone with sandstone of Pliocene
Nv	Volcanic rock of Pliocene
NMs	Shale of Miocene

frontiers | Frontiers in Earth Science

TYPE Original Research
PUBLISHED 10 January 2023
DOI 10.3389/feart.2022.977246

OPEN ACCESS

EDITED BY
Wen Zhang,
Jilin University, China

REVIEWED BY
Ming Chang,
Chengdu University of Technology, China
Guisheng Hu,
Chinese Academy of Sciences (CAS), China

*CORRESPONDENCE
Weilin Xu,
xuwl@scu.edu.cn

†These authors have contributed equally to this work

SPECIALTY SECTION
This article was submitted to Geohazards and Georisks, a section of the journal Frontiers in Earth Science

RECEIVED 24 June 2022
ACCEPTED 28 September 2022
PUBLISHED 10 January 2023

CITATION
Niu Z, Meng C, Xu W, Di B, Long Y and Yang H (2023), Experimental study on whole process of river blockage and dam break under different hydrodynamic conditions. *Front. Earth Sci.* 10:977246. doi: 10.3389/feart.2022.977246

Experimental study on whole process of river blockage and dam break under different hydrodynamic conditions

Zhipan Niu[1,2†], Chuke Meng[1†], Weilin Xu[2*], Baofeng Di[1], Yi Long[1] and Hang Yang[1]

[1]Institute for Disaster Management and Reconstruction, Sichuan University, Chengdu, China, [2]State Key Laboratory of Hydraulics and Mountain River Engineering, Sichuan University, Chengdu, China

River blockage and dam break usually occur in mountainous areas with many valleys, and are frequent and extremely harmful natural disasters. With the construction of infrastructures in mountainous areas, the demand for disaster prevention and control has been further increased. Based on an innovative flume model for simulating whole process of river blockage and dam break, the present study carried out eight groups tests under different inflow rates. In the analysis, the whole process of river blockage and dam break was divided into four stages: ESBA (Early stage of blockage), LSBA (Late stage of blockage), ESBK (Early stage of breaking) and LSBK (Late stage of breaking). By analyzing the relationship between Q_{in} and Q_{max}, it is found that Q_{max} shows an overall trend of increase with the increase of Q_{in} while some contrarily decreasing Q_{max} cases exist when Q_{in} slightly increases. The cases of irregularities may come from the inflow condition impact and randomness during the dam formation process. In addition, the slope of the curve Q_{in}–Q_{max}/Q_{in} parameter shows a decreasing trend with the increase in the median particle size of the soil. The present study proposes a new method for model experiments, providing new ideas for subsequent model experiments. Furthermore, these conclusions can provide reference for disaster prevention and mitigation in mountainous areas.

Abbreviations: *a*, a fitting parameter in Equation 6; *B*, partial regression coefficient; *Beta*, standard regression coefficient; d_{50}, the particle size when the cumulative particle size distribution percentage reaches 50%; H_d, Dam height, the dam's geometry is random due to particle collision and other reasons during the sliding movement of the soil, and there are slight differences in dam height under different initial parameters; k_d, downstream slope ratio; k_u, upstream slope ratio; L_d, Dam length; L_{max}, The highest water level in front of the dam; *P*, Significance; Q_{in}, Inflow rate, initial parameter manually set at the beginning of a test; Q_{max}, The maximum discharge of the breach; *Std. Error*, standard error; t_0, The moment when the landslide slides into the main channel just after it stabilizes; t_1, The moment when the flow just overtops; t_2, After the dam breaks, the upstream water level just drops to 8 cm, which refers to the end of breaking; *T*, results of *t*-test on regression coefficients; T_b, Breaking time, the breaking time is the difference between t_2 and t_1, and the formula to calculate this is $T_b = t_2 - t_1$; T_s, Water storage time, the water storage time is the difference between the time when the water flow just overtops and the time when the landslide just stabilizes after sliding into the main channel, and the formula to calculate this is $T_s = t_1 - t_0$; V_l, the maximum volume of the dam lake; V_d, Dam volume; *VIF*, Variance Inflation Factor; W_d, Dam width.

KEYWORDS
landslide dam, inflow rate, breach discharge, dam geometry, river blockage, dam break

Introduction

Due to natural disasters, such as earthquakes, rainstorms, typhoons and melting glaciers, destructive landslides or debris flows can easily form near mountain valleys (Coussot and Meunier, 1996; Cruden, 2005; Sassa, 2007; Chae et al., 2017; Chen et al., 2022). These material sources would very likely block river channels, causing these to stop flowing and form natural dams (Costa and Schuster, 1988; Fan et al., 2020; Zhong et al., 2021). The water volume of these resulting dammed lakes would gradually increase over time, and the threat to downstream human infrastructures and life would be self-evident.

Research on whole process of river blockage and dam break has been the basis and focus for solving the above problems. Research in this area has been mainly carried out from the perspective of field observation, model test, numerical simulation and theoretical analysis. Present studies generally divide the continuous process of river blockage and dam break into independent researches on the formation process of blocked rivers and its process of breaking. Recent developments in the field of formation process of river blockage have led to a renewed interest in the statistical analysis of field research data. Fan et al. (2014) developed an empirical method to predict coseismic landslide dam formation using landscape parameters obtained from digital elevation models. Chen and Wu. (2018) take Xinmo landslide for example, studied the post-failure behavior of the landslide using two-dimensional discontinuous deformation analysis (2D DDA). Li et al. (2020) proposed a discrete element simulation model to predict the geometry and formation process of landslide dams. In addition, Zhao et al. (2019b) and Wu et al. (2020) have explored the formation mechanism through model tests and numerical simulations. However, the results in this regard remains relatively lacking. For researches on whole process of river blockage and dam break, a large part of these researches adopt the method of combining the model test and theoretical analysis. The reason is because the model test can reproduce the actual block and break process in a small-scale model, allowing researchers to summarize the physical mechanism similar to the prototype. Rapid progress has been taken in the recent 30 years in the field of the experimental study on landslide dams. Coleman et al. (2002) made a detailed exploration of the overtopping process of homogeneous noncohesive embankments using model test. Awal (2008) identified the mechanism of landslide dams failure under different breaking modes through model tests. Schmocker and Hager. (2009) carried out a series of overtopping breach tests and indicated definite minimum dimensions for both the dike height and width, sediment diameter and overtopping discharge. Nian et al. (2020) proposed a dimensionless River Blockage Criterion (RBC) to judge the formation of landslide dams based on a series of model tests. And (Peng et al., 2021) investigated the breaching mechanisms of landslide dams composed of different materials under surge waves. However, the forming or breaking mechanism presents to be heterogeneous and highly test condition dependent, which greatly restricts the extrapolation. Although there are many reports in the above literature on the outcome of simple flume experiment, most are restricted to geometric similarity. Therefore, in recent years, there are a large number of published studies (Hanson et al., 2002; Höeg et al., 2004; Morris et al., 2007; Sheng-shui et al., 2014; Zhao et al., 2019; Li et al., 2021) that describe the landslide dam' failure mechanism using large-scale field models or centrifugal models. Although the cost of this kind of experiment is high, this can better meet similar conditions, and the obtained test results are more similar to the prototype phenomenon, making this a better research method. Other approaches were performed through the establishment of the mathematical and physical model of a dam, and a high-performance computer simulates the dam breaking process, including the evolution process of breaches and floods (Cristofano, 1973; Fread, 1988; Chang and Zhang, 2010; Liu, 2018; Luo et al., 2019; Ruan et al., 2021; Tian et al., 2021; Zhang et al., 2021). However, these models have high simulation accuracy only when the input parameters are sufficiently large and accurate (Zhong et al., 2021).

In view of all that has been mentioned so far, one may suppose that a phenomenon or mechanism of river blockage or dam break is explained in depth. However, the above research has tended to focus on only one part of the whole process of river blockage and dam break rather than the continuous whole process. These studies have not able to convincingly confirm the relevance between model and prototype. The key issue is that the actual whole process of river blockage and dam break contains a number of uncertainties. First, the uncertainty of the occurrence time of natural disasters can lead to the triggering of landslides or debris flow that block the river, and this uncertainty puts forward more urgent time requirements for the prevention and control of such disasters. Second, after a landslide or debris flow forms, it is difficult to accurately predict whether and how the river would be blocked. Third, after the dam is formed, the breaking mode and the location of the breach have strong randomness. Finally, under the action of these above-mentioned random events, the outburst flood process would cause great changes. These suggests that a more realistic and continuous model test may lead to a more consistent

conclusion with the actual prototype. Therefore, we developed a model that simulates the whole process in order to explore more valuable conclusions.

In addition, the impact of river flow on dam formation and break is a critical and interesting issue. The impact of the inflow on whole process of river blockage and dam break has strong uncertainties. For the same river, the flow may greatly vary at different time points of the year. For example, in the Jinsha River in China, where river blockage events frequently occur, the flood season from June to October accounts for 74–81% of the annual water volume (Wang et al., 2022). As a results, the consequences and prevention methods of river blockage events in different periods would be quite different. And the flow rate and water depth of the river would also affect the size of the formed dam (Chen et al., 2019). Therefore, considering only the inflow rate, there are a number of uncontrollable factors involved in the overall blockage and breakage process, and it would be difficult to fully grasp the key mechanism of the inflow rate on the whole process of river blockage and dam break. However, in recent years, some scholars have investigated the influence mechanism of inflow rate on the breaking process of natural dams through small-scale model tests. Xu et al. (2013) considered that the upstream inflow is the main factor that impacts the dam-break process through model tests with three groups of different inflow rates. Yang et al. (2015) investigated the change process of a breach under four different inflow rates. Zhou M. et al. (2019) concluded the relationship between the inflow rate and peak discharge of a breach through three groups of different inflow rates. These studies have carried out in-depth explorations on the impact of different flow rates on the breaking process, but the initial conditions were set too ideally. For example, the shape of the dam body have a fixed shape, the gradation was uniform, and

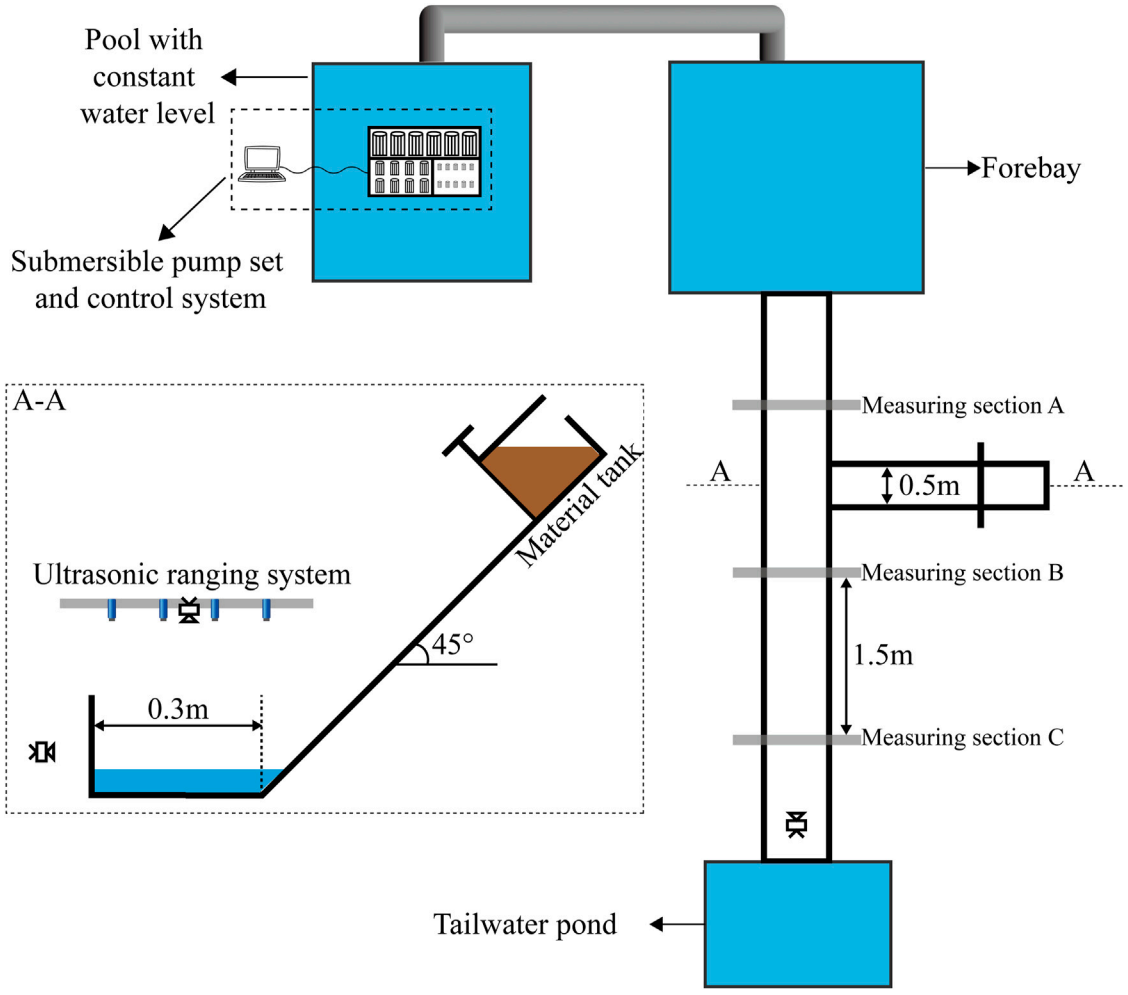

FIGURE 1
Experimental setup.

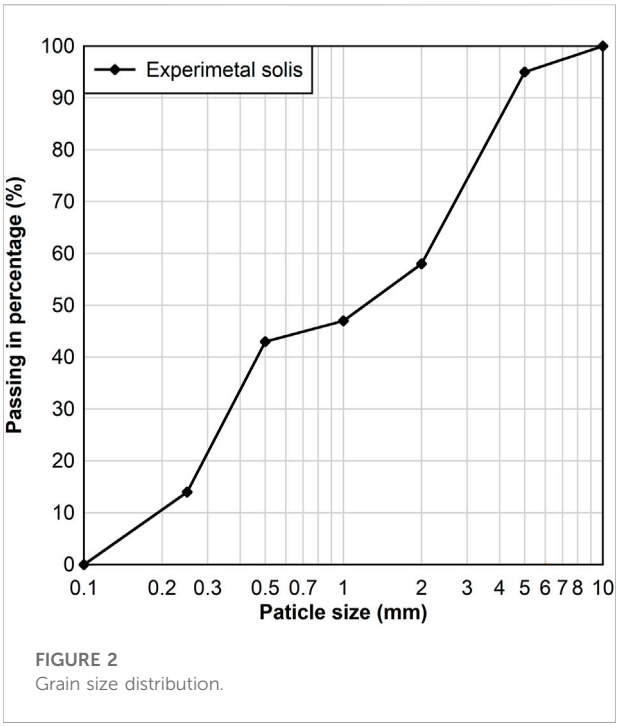

FIGURE 2
Grain size distribution.

the influence of water flow on the formation of the dam body was ignored. Based on some defects in the above tests, conducting the whole-process tests under different inflow rates are not only helpful to verify the reliability of previous research conclusions, but also to further explore the mechanism from a new perspective.

In summary, there are many uncertain factors in whole process of river blockage and dam break. Considering that the initial input quantity, such as initial hydrodynamic conditions, topographic conditions and provenance conditions, can be regarded as a definite initial quantity, the breaking flood flow and the change process of upstream and downstream water levels are correlated to the risk of this disaster chain. The present study used the newly developed model for the whole process of river blockage and dam break to explore new research methods for whole process of river blockage and dam break. In addition, under the condition of changing the initial inflow rate, the present study investigated the influence and internal mechanism of input parameters (inflow, topography, provenance, *etc.*) on output parameters (breach discharge, water level, *etc.*).

Methods

Model design

The experimental model is presented in Figure 1. The width and slope of the main channel, and the width and slope of the slope channel was adjusted according to the requirements. For the main channel, the length was 10.0 m, the height was 0.8 m, the width was adjusted between 0.1 m and 1.5 m, and the slope was adjusted between 1° and 15°. In the present experiment, the width was 30 cm and the slope was 1° for the main channel, while the width was 0.5 m, the height was 0.6 m, the length was 3.5 m, and the slope range was adjusted within 20°–70° for the slope channel. Furthermore, in the present experiment, the slope was 45°, the landslide material was stored in the material tank on the slope channel, and the maximum storage volume of the material tank was 0.3 m^3. Furthermore, the mass of the landslide source was fixed at 80.0 kg. The water supply system included the laboratory water supply facilities, a pool with a constant water level, a forebay, a submersible pump set, and a control system. The storage capacity of the pool with a constant water level was 10.0 m^3, and the maximum storage capacity of the forebay can reach up to 5.0 m^3. When the laboratory water supply facility filled the pool up to the constant water level, the excess water flowed back to the large underground pool of the water supply facility after filling. Hence, the water level of the flat pool remained unchanged. The submersible pump set included three types of submersible pumps: six large water pumps with a maximum flow rate of 2 L/s, eight medium water pumps with a maximum flow rate of 1 L/s, and eight small water pumps with a maximum flow rate of 0.5 L/s. The pump set was fixed at the central position of the forebay, and the control system was used to integrate and control the switches of each water pump. The designed output flow range was 0.5–24.0 L/s. Due to the energy loss in the pumping process, the output flow was attenuated by 40%, and the actual output flow range was within 0.3–14.4 L/s.

During the experiment, the water level was measured using an ultrasonic ranging system. The ultrasonic wave was reflected after encountering the water surface. The measurement accuracy was high, and the maximum measurement frequency was 60 Hz. The phenomenon of the whole process of blocking and breaking was captured using a high-speed camera, as presented in Figure 1.

Materials

Grain size distribution has a great influence on whole process of river blockage and dam break. In order to make the gradation as consistent as possible with the actual situation, a wide-graded soil was used. Furthermore, in order to prevent more serious seepage phenomenon, fine particles were also present in the soil to fill the pores, allowing the experimental soil to have low permeability. The grain size distribution for the present experiment is presented in Figure 2.

In traditional dam model experiments, researchers usually design the shape of the dam (dam height, dam width, *etc.*) in advance, and most of these are two-dimensional models. In order to achieve the design effect, the compaction of the dam body may

FIGURE 3
Comparison of experimental landslide dams and prototypes: **(A)** manual stacked dam; **(B)** natural sliding dam in this paper; **(C,D)** are photographs of landslides blocking river.

be unintentionally affected, and the stacking method used is usually manual stacking or simple tool-assisted stacking, resulting in some errors. In the present study, the project of building a dam was abandoned in the experiment, and the initial parameters (mass, gradation, *etc.*) of the soil were entered to the designed landslide device. The landslide dam was formed by the sliding soil from the slope channel, which had authenticity and three-dimensionality. For example, the designed dam body is often a trapezoid or triangle with clear edges and corners (Figure 3A), but the actual accumulation geometry is irregular (Figures 3C,D). Comparing Figures 3B–D, we can see that the geometry of the naturally sliding landslide dam is more consistent with the prototype while the artificial dam is not.

For the random phenomenon of dam formation during the test, the dam geometry was calibrated in advance. The dam geometries measured in three tests under the same conditions are presented in Table 1. The dam's geometry in the three pretests is presented in Figure 4. It can be observed that the change in shape was relatively small. Furthermore, since the dam's geometry has influence on the experiment, and the dam height is an important parameter to control the process for breaking, the influence of the dam's height on the dam's geometry on the whole process of blocking and breaking was considered for the present study.

Costa and Schuster (1988) reported that the potential energy of water is an important parameter that affects dam breakage and flooding, and is correlated to the storage capacity of the impoundment (V_l). After field investigations, Korup (2004) considered that dam height (H_d) and dam volume (V_d) are the two key variables that can be used to assess the dam stability, and determine whether this would induce flood risk. Subsequently, Peng and Zhang (2012) proposed a set of dimensionless numbers, ($\frac{H_d}{W_d}$, $\frac{V_d^{1/3}}{H_d}$ and $\frac{V_l^{1/3}}{H_d}$), which can be used to define the geometric features of landslide dams and lakes. In order to verify whether experimental model dams can represent real landslide dams, Zhou G. G. D. et al. (2019) counted the dimensionless coefficients of 80 landslide dams from different regions of the world, and proposed that when the dimensionless numbers of a model experiment are close to the

TABLE 1 Dam body parameters.

	H_d (m)	W_d (m)	L_d (m)	V_d (m^3)	V_l (m^3)	k_u	k_d	$\frac{H_d}{W_d}$	$\frac{V_d^{1/3}}{H_d}$	$\frac{V_l^{1/3}}{H_d}$
1	0.1900	1.2250	0.30	0.03	0.0684	0.59	0.53	0.16	1.64	0.33
2	0.1950	1.3000	0.30	0.03	0.0702	0.50	0.43	0.15	1.59	0.32
3	0.1720	1.1950	0.30	0.03	0.0619	0.53	0.60	0.14	1.81	0.33
Mean	0.1857	1.2400	0.30	0.03	0.0669	0.54	0.52	0.15	1.67	0.33

actual, the experiment models can be considered to represent real landslide dams. This conclusion helps to check whether the dimensions in the model experiment can meet the actual situation. Jiang et al. (2020) applied this conclusion in his research, proving that his model can satisfy the scale effect.

Therefore, the model designed for the present experiment comprehensively considered these parameters, and these key parameters were measured in multiple pre-experiments. The specific parameters are presented in Table 1. All parameters were within the feasible range (Zhou M. et al., 2019). This shows that the model, material and hydraulic properties of the present experiment can meet the actual situation.

Experimental procedure

The only initial variable in the present experiment is the inflow rate of the main channel. In order to simulate whole process of river blockage and dam break, the present experiment did not carry out human intervention after setting the initial

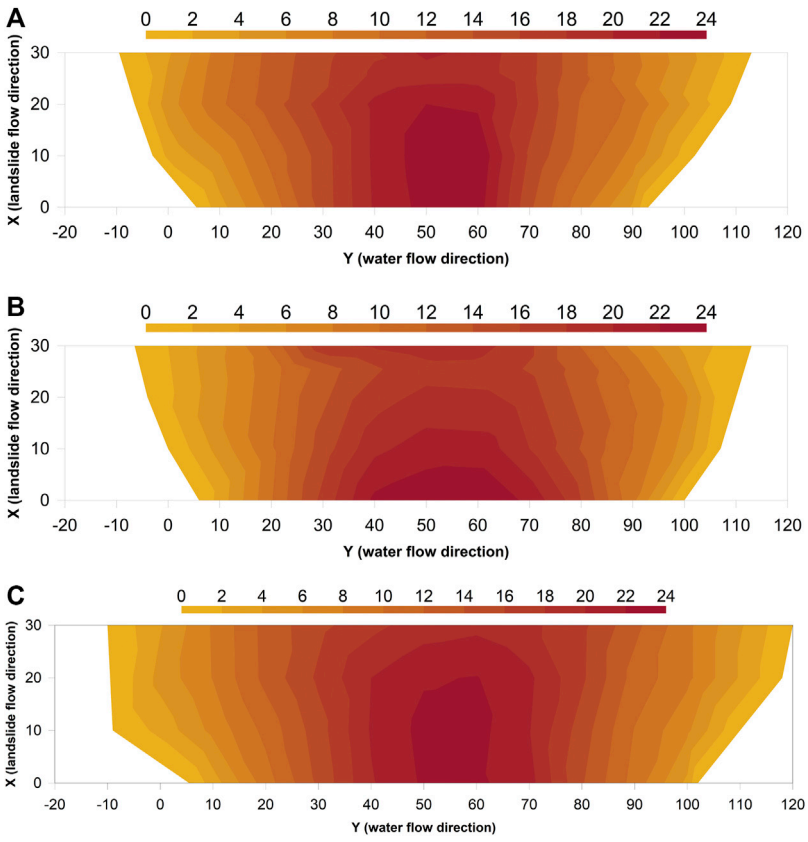

FIGURE 4
Dam geometry comparison: **(A-C)** are dam geometry obtained in three pre-experiments under the same conditions. All units are in centimeters. The sliding direction of the landslide along the horizontal direction is the same as the positive direction of the *x*-axis, the water flow direction is the same as the positive direction of the *y*-axis, and the exit position of the landslide into the main channel is between y = 50 and y = 60.

TABLE 2 Test arrangements and results.

Test number	Q_{in} (L/s)	H_d (m)	T_s (s)	T_b (s)	L_{max} (m)	Q_{max} (L/s)
1	1.18	0.1700	350	193	0.1869	7.13
2	1.81	0.1678	219	114	0.1811	9.75
3	2.47	0.1650	146	169	0.1918	8.83
4	3.00	0.1745	132	97	0.1912	13.15
5	3.68	0.1681	94	116	0.1939	10.61
6	4.26	0.1900	101	129	0.2139	15.73
7	4.89	0.1761	76	142	0.2048	14.21
8	5.16	0.1842	73	120	0.2112	16.67

parameters. The specific implementation process for the present experiment is, as follows:

(1) Clarify the initial conditions of the test;
(2) Initially place the preset landslide soil into the bearing device of the side slope, and turn on the pump set to make the river flow meet the preset flow;
(2) Arrange ultrasound sensors in the river to measure the upstream and downstream water levels;
(4) Arrange high-speed cameras around the model to measure the process of the landslide movement, the blocking process of the dam body, and the breaking process of the dam;
(5) After the measuring device is arranged and the river flow is stable, release the landslide;
(6) Wait for the end of the test, the sign at the end of the test is, the dam height is reduced to 1/2 of the maximum dam height.

Results and discussion

General description of whole process of river blockage and dam break

The test arrangements and results are presented in Table 2. In determining the breaking flow, the water balance equation is usually used to calculate the breach discharge, especially in model experiments and numeral calculations (Zhong et al., 2021). The simplified calculation equation used for the present study is, as follows:

$$Q_{out} = -A\frac{dL_w}{dt} + Q_{in} \quad (1)$$

where Q_{out} refers to the flow discharge, and can be considered as the breach discharge (due to the characteristics of the dam material, the influence of the seepage discharge on the calculation is ignored); Q_{in} refers to the inflow rate; A refers to the lake area; L_w refers to the upstream water level. Since the slope of the main channel is 1°, the variation of A with time is relatively low. In order to simplify the calculation in the absence of large errors, A is regarded as a constant. L_w can be obtained by the ultrasonic sensor, Q_{in} is a designed constant quantity, then the breach discharge can be calculated according to Eq. 1.

The variation process of the upstream water level and breach discharge with time is presented in Figure 5. According to the upstream water level, breach discharge, and actual observation results, the whole process of blocking and breaking was divided into four stages.

(1) **Early stage of blockage (ESBA)**: At this time, the landslide has not blocked the main channel, the upstream flow is stable, and the water level at the measuring point remains unchanged, as shown in Figure 6A;
(2) **Late stage of blockage (LSBA)**: At this time, the landslide just blocks the river, there is no discharge for the time being, and the upstream water level gradually increases, as shown in Figure 6B;
(3) **Early stage of breaking (ESBK)**: At this time, the overtopping water flow gradually erodes the dam crest, forming a breach, which gradually expands, and the breach discharge gradually increases and reaches a peak value, as shown in Figure 6C;
(4) **Late stage of breaking (LSBK)**: At this time, the shape of the landslide dam slightly changes, and the breach discharge gradually decreases to the initial inflow rate, as shown in Figure 6D.

Effect of Q_{in} on Q_{max}

The relationship between Q_{in} and Q_{max} was drawn, as shown in Figure 7, and the test data was fitted. The fitting formula is, as follows:

$$Q_{max} = 4.92 + 2.15Q_{in} \quad (2)$$

where Q_{in} refers to the inflow rate (L/s) and Q_{out} refers to the breach discharge (L/s). In the formula, R^2=0.81, indicating that Q_{max} and Q_{in} have a high linear correlation. In the whole process, Q_{max} increased with the increase in Q_{in}.

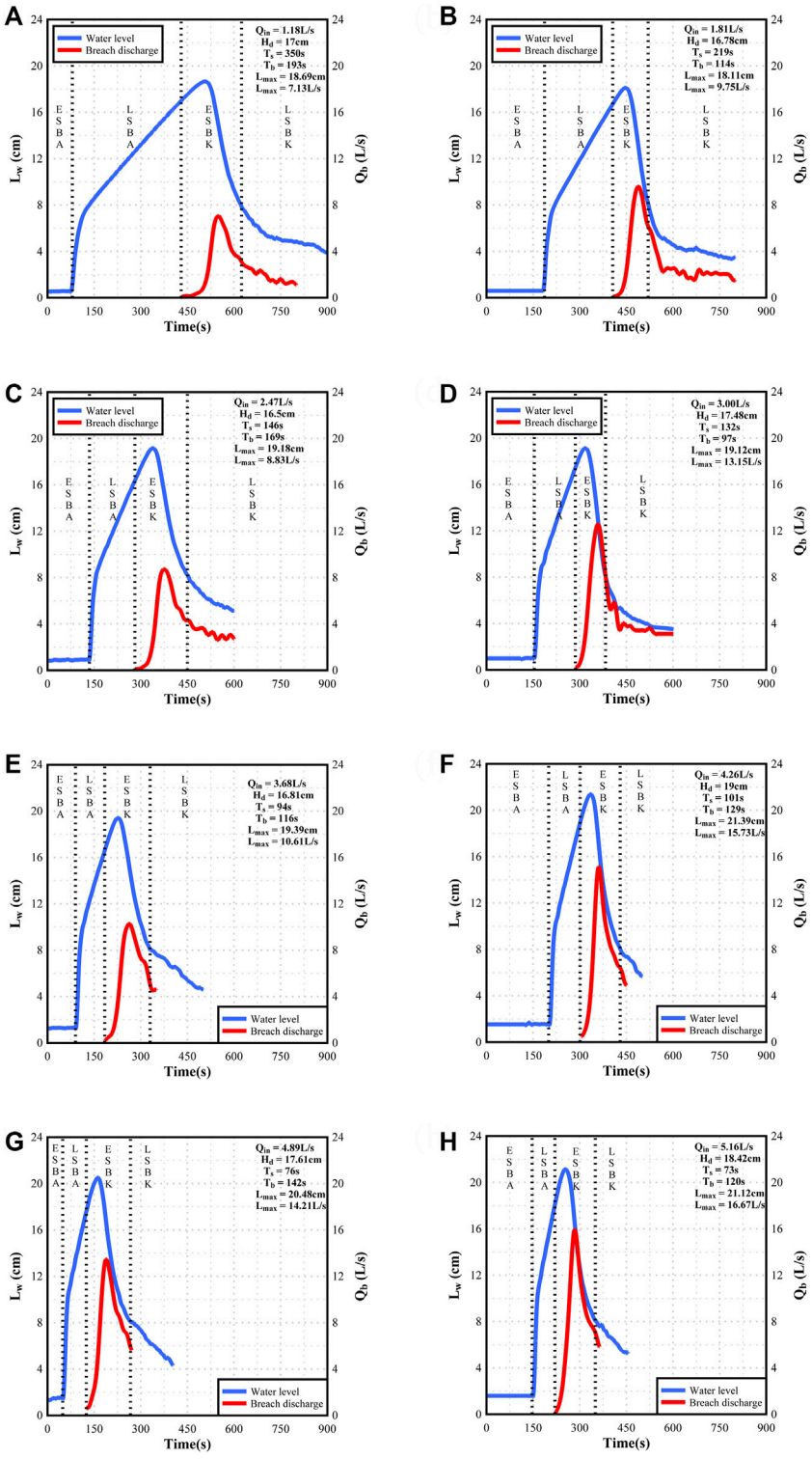

FIGURE 5
The upstream water level curve and the breach discharge curve at different stages: **(A-H)** expressed the water level and breach discharge process under different flow rates, respectively.

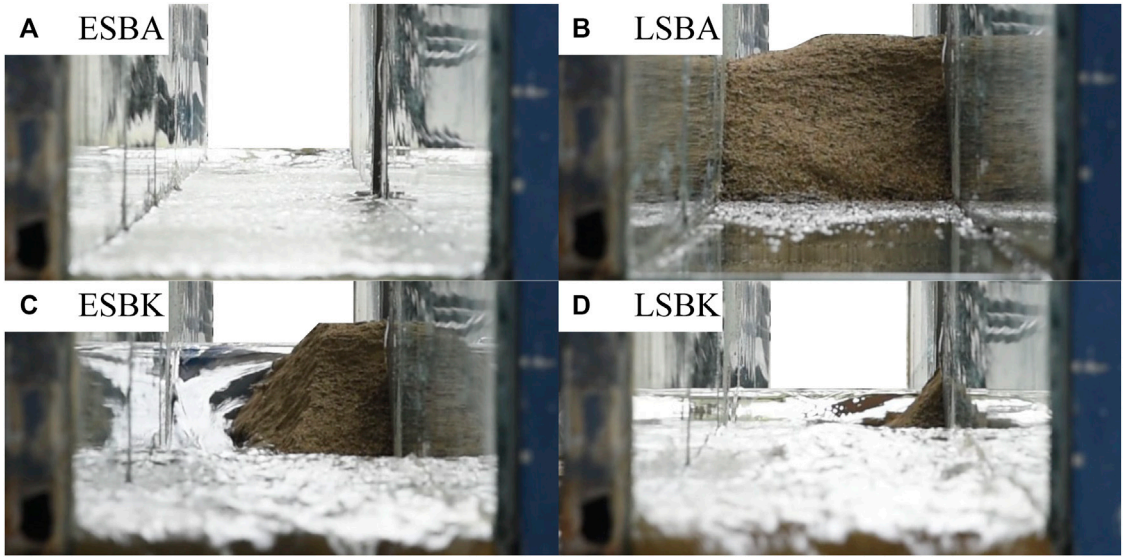

FIGURE 6
The four stages of the whole process of river blockage and dam breaking: **(A)** early stage of blockage; **(B)** Late stage of blockage; **(C)** Early stage of breaking; **(D)** Late stage of breaking.

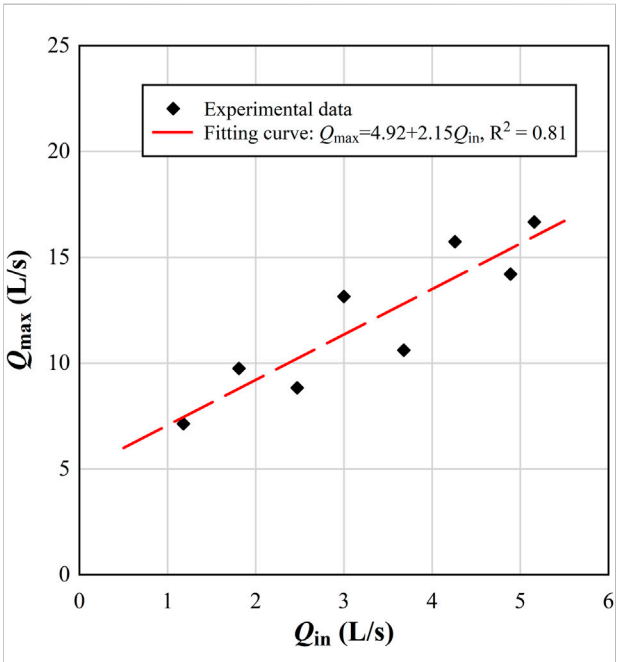

FIGURE 7
The relationship between Q_{in} and Q_{max}.

The relational expression of L_w' can be obtained from Eq. 1:

$$L_w^{'} = \frac{dL_w}{dt} = \frac{Q_{in} - Q_{out}}{A} \quad (3)$$

where L_w refers to the upstream water level (cm) and $L_w^{'}$ refers to the upstream water level growth rate (cm/s). In Eq. 3, it can be observed that the overall reason for the increase in Q_{max} with the increase in Q_{in} is that a larger Q_{in} can increase $L_w^{'}$. This causes in the water level to be flow faster as it rises and flow slower as it falls.

A larger Q_{in} would cause the upstream water level at have a higher value when the flow just overtops, and this would have a higher flow area during the rising stage of the water level at ESBK. For the soil erosion rate in Eq. 4 (Hanson and Simon, 2001), it can be observed that a larger flow area would speed up the erosion process of the dam body, thereby shortening the breaking duration.

$$E = K_d(\tau - \tau_c) \quad (4)$$

where E refers to the soil erosion rate (mm^3/m^2-s), K_d refers to the material property of the soil, and τ refers to the water flow shear force. The magnitude of the water flow shear force is positively correlated to the wet circumference.

Due to the rapid widening of the breach and slow drop in water depth, the outflow area would rapidly increase and become larger. According to experience and based on Eq. 5, this is often used to calculate the breach discharge in a dam breach model (Singh and Scarlatos, 1988). It can be observed that this case tends to have a larger peak discharge.

$$Q_{out} = 1.7[B + h_b \tan\alpha]h_b^{3/2} \quad (5)$$

where: B refers to the width of the bottom of the breach, h_b refers to the depth of the breach, and α refers to the angle of the side slope. B, h_b and α would gradually change with the erosion of the

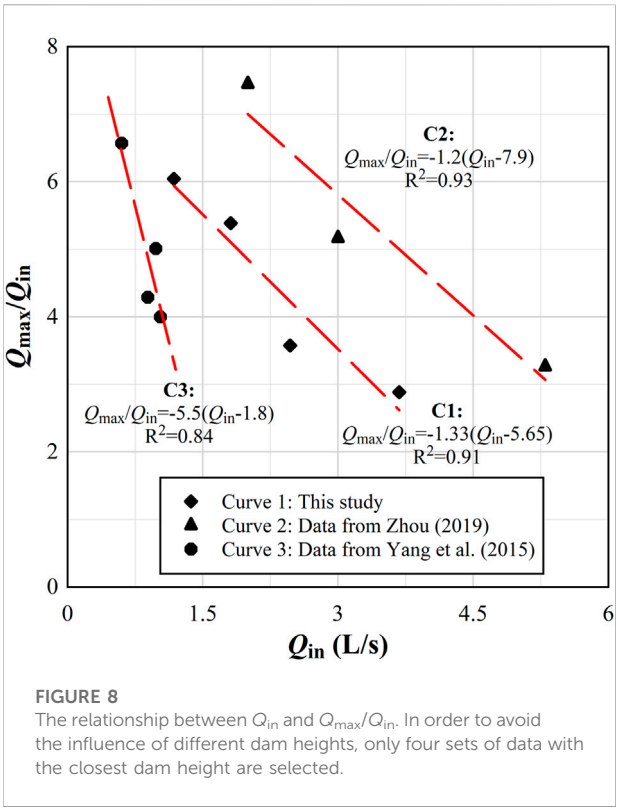

FIGURE 8
The relationship between Q_{in} and Q_{max}/Q_{in}. In order to avoid the influence of different dam heights, only four sets of data with the closest dam height are selected.

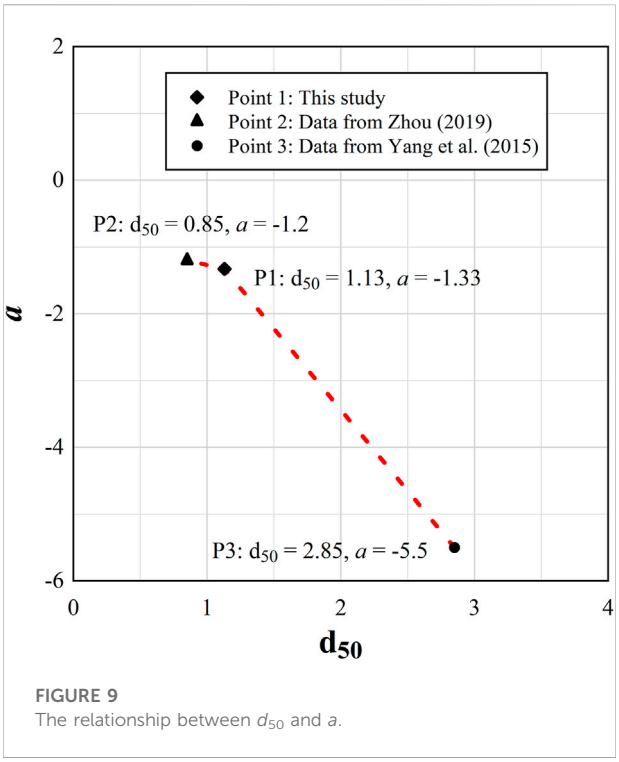

FIGURE 9
The relationship between d_{50} and a.

breach through the overtopping water flow. This is the fundamental reason that drives the change in breach discharge.

In summary, the influence of the increase in Q_{in} in the whole process mainly lies in two aspects. On one hand, the upstream water level at the beginning of ESBK would have a high value, resulting to a higher flow area during the rising stage before breaking. On the other hand, a larger flow area would accelerate the erosion process. In addition, Walder et al. (2015) explained that Q_{max} is an increasing function of initial water level through some theoretical analysis on a series of model tests. Therefore, combined with the experimental phenomenon, it can be observed that a higher water level and a faster erosion process causes the peak discharge to arrive earlier and become larger.

The investigators also considered that this is what contributed to the conclusion that the dimensionless peak discharge (Q_{max}/Q_{in}) decreases with the inflow rate (Zhou M. et al., 2019). In the present study, the investigators fitted the relationship between Q_{in} and Q_{max}/Q_{in}, and compared this with previous studies. The fitting equation is presented in Eq. 6, and the fitting result is presented in Figure 8.

$$Q_{max}/Q_{in} = a(Q_{in} - b) \quad (6)$$

where a and b represent the fitting parameters, respectively. It was found that parameter a is correlated to d_{50}. As observed in Figure 9, a decreased as d_{50} increased. This shows that the breach evolution of soil with a larger d_{50} would be more sensitive to the influence of the inflow rate. For example, for Curve3 in Figure 8, the Q_{max}/Q_{in} decreased more when the same Q_{in} increased.

Effect of Q_{in} and H_d on Q_{max}

Although Q_{max} increased with the increase in Q_{in} in the whole process, it was observed in Figure 7 that when the inflow rate only changed within a small range and Q_{in} increased, Q_{max} did not necessarily increase. This result was mainly caused by the randomness of friction and collision during the movement of soil particles during the sliding of the landslide. The short-term process of a landslide blocking the main channel to form a dam is shown in Figure 10. Dams with different shapes would lead to different subsequent processes. Hence, Q_{max} may not necessarily increase with the increase in inflow rate. However, the above phenomenon would only occur when the inflow rate changes in a relatively small range, because the dam height changes caused by randomness are limited. Therefore, when the inflow rate increases to a sufficient level, Q_{max} would increase with the increase in Q_{in}.

It would be relatively one-sided to only analyze the effect of Q_{in} on Q_{max}. Furthermore, it is given that multiple linear regression can help to analyze the relationship between multiple independent variables and dependent variables (Andrews, 1974; Aiken et al., 2003; Uyanık and Güler, 2013). In order to explain the influencing factors of Q_{max}, multiple linear regression was used to determine the effect of

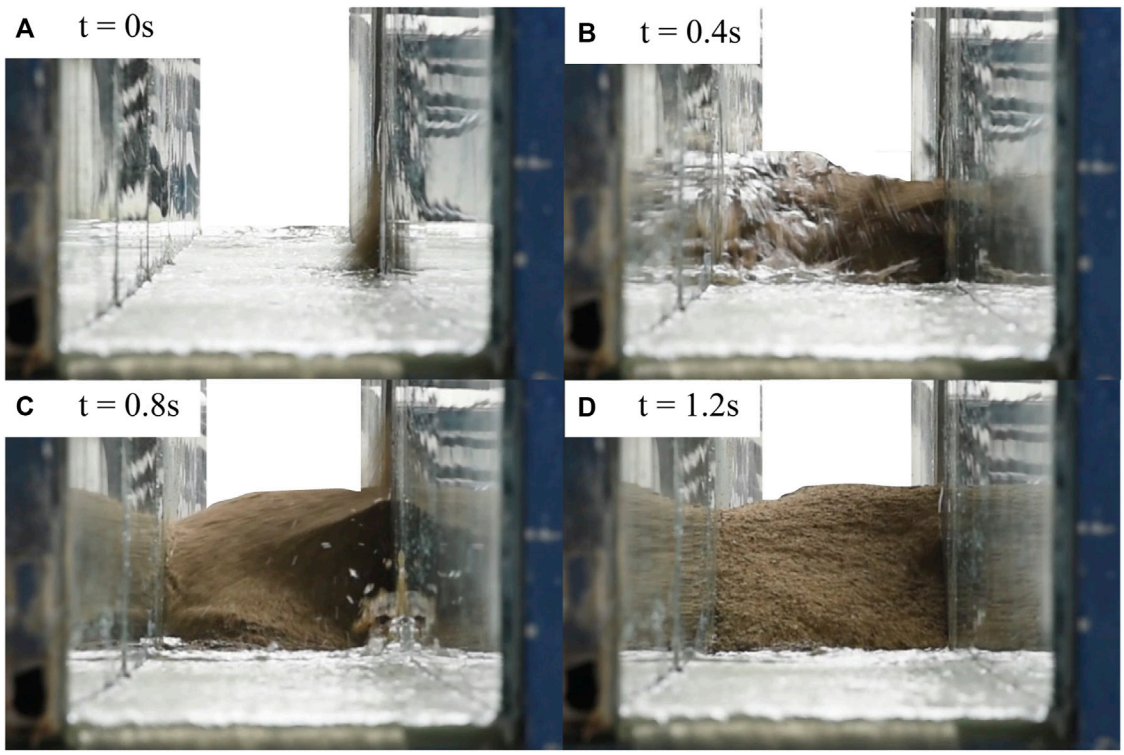

FIGURE 10
Short-term process of landslide blocking the main channel to form a dam: **(A)** At t = 0 s, the landslide is about to reach the channel; **(B)** At t = 0.4 s, the landslide just blocked the river; **(C,D)** the landslide dam is formed.

TABLE 3 Multiple linear regression results.

	B	*Std. Error*	*Beta*	*t*	*p*	*Tolerance*	*VIF*
Constant	−25.254	10.325		−2.446	0.058		
Inflow rate	1.366	0.387	0.573	3.529	0.017	0.529	1.890
Dam height	1.877	0.639	0.477	2.936	0.032	0.529	1.890
R = 0.95, R^2 = 0.93							

Q_{in} and H_d on Q_{max}. The analysis results are presented in Table 3, and the regression equation is presented in Eq. 7:

$$Q_{max} = -25.25 + 1.37Q_{in} + 1.88H_d \quad (7)$$

in this model, the interpretation degree of Q_{in} and H_d to Q_{max} is R^2=0.93, which is higher than the interpretation degree for Q_{in} to Q_{max}. It is noteworthy that Q_{in} and H_d can predict Q_{max} very well. The coefficient of H_d was 1.88, and the coefficient of Q_{in} was 1.37, indicating that the increase in Q_{max} per unit of increase in H_d was higher, when compared to that of Q_{max} for each increase in unit of increase.

The absolute value of Beta indicates the order of importance of the independent variables. As presented in Table 3, it can be observed that the Beta value of Q_{in} is slightly larger than the Beta value of H_d. This means that the independent value Q_{in} contributes more to the model, when compared to H_d. Although the significance of the constant was slightly larger than 0.05, the significance p for all three variables was less than 0.06. This means that the independent variable coefficient is statistically significant. The variance increase factors VIF in the present model were all lower than 10, as shown in Table 3. This means that there are no multiple correlations among variables.

Conclusion

The whole process of river blockage and dam break under different hydrodynamic conditions was investigated in a flume model for a range of inflow rates between 1.18 and 5.16 L/s. The phenomenon and process of river blockage and dam break were preliminarily demonstrated and the mechanism of how the inflow rate influences the whole process was explored. The main conclusions are summarized as follows:

Four stages including ESBA, LSBA, ESBK, and ESBK, can be distinguished during the whole process of river blockage and dam break due to significant differences in hydraulic properties. ESBA occurs at the initial stage of blockage and gradually evolves to LSBA when the soil accumulated dam cut off the river. It develops to ESBK as the stored water overtops and expands breaches. Followed by LSBK, the breach flow decreases after the peak breach flow. Among these stages, ESBK is the most violent period, Breaking flooding occurs at this time, and its duration and peak flow are important factors in assessing the risk; LSBK is the final stage in the whole process during when the change of the dam body becomes relatively slow, and the breaking process slows down.

The impact of Q_{in} on Q_{out} was explained theoretically. As is expected, the increase in Q_{in} will cause a relatively high upstream water level at the beginning of ESBK and accelerate the erosion process. Q_{max} shows an overall trend of increase with the increase of Q_{in} while some contrarily decreasing Q_{max} cases exist when Q_{in} slightly increases. The multiple regression analysis for Q_{in} and H_d on Q_{max} explained the cases of irregularities may come from the inflow condition impact and randomness during the dam formation process.

The present study investigated the effect of Q_{in} on Q_{max}/Q_{in}. The development trend of Q_{in}-Q_{max}/Q_{in} in this paper is consistent with that in the previous dam break flume experiment. By analyzing the soil gradation adopted in previous flume model experiments, we found that the slope of the curve Q_{in}-Q_{max}/Q_{in} parameter shows a decreasing trend with the increase in the median particle size of the soil.

The multiple regression equation for Q_{in} and H_d on Q_{max} was obtained. Q_{in} and H_d fits the Q_{max} multiple regression extremely well, and the goodness of fit reached 93%. And we found that when compared to the increase in Q_{max} per increase unit Furthermore, the increase in Q_{max} per increase unit of H_d was higher, when compared to the increase in Q_{max} per increase unit.

Data availability statement

The original contributions presented in the study are included in the article/Supplementary Materials, further inquiries can be directed to the corresponding authors.

Author contributions

XW-L, NZ-P, DB-F, and MC-K contributed significantly to the conception of the study; MC-K, LY, and YH performed the experiment; NZ-P and MC-K contributed to analysis and manuscript preparation; XW-L and DB-F reviewed the original draft; NZ-P, MC-K, XW-L, DB-F, LY, and YH helped perform the analysis with constructive discussions.

Funding

This research was supported by the National Key Research and Development Plan of China (Grant No.2019YFC1510704-01) and CAS Light of West China Program (No. 2021160160).

Conflict of interest

The authors declare that the research was conducted in the absence of any commercial or financial relationships that could be construed as a potential conflict of interest.

Publisher's note

References

Aiken, L. S., West, S. G., and Pitts, S. C. (2003). Multiple linear regression. *Hand. book. Psychol.*, 481–507. doi:10.1007/978-1-59745-530-5_9

Andrews, D. F. (1974). A robust method for multiple linear regression. *Technometrics* 16, 523–531. doi:10.1080/00401706.1974.10489233

Awal, R. (2008). *Study on landslide dam failure due to sliding and overtopping.* Kyoto, Japan: Kyoto University.

Chae, B.-G., Park, H.-J., Catani, F., Simoni, A., and Berti, M. (2017). Landslide prediction, monitoring and early warning: A concise review of state-of-the-art. *Geosci. J.* 21, 1033–1070. doi:10.1007/s12303-017-0034-4

Chang, D., and Zhang, L. (2010). Simulation of the erosion process of landslide dams due to overtopping considering variations in soil erodibility along depth. *Nat. Hazards Earth Syst. Sci.* 10, 933–946. doi:10.5194/nhess-10-933-2010

Chen, H., Ruan, H., Chen, J., Li, X., and Yu, Y. (2022). Review of investigations on hazard chains triggered by river-blocking debris flows and dam-break floods. *Front. Earth Sci.* 10, 830044. doi:10.3389/feart.2022.830044

Chen, K.-T., Chen, X.-Q., Hu, G.-S., Kuo, Y.-S., and Chen, H.-Y. (2019). Effects of river flow velocity on the formation of landslide dams. *J. Mt. Sci.* 16, 2502–2518. doi:10.1007/s11629-018-5319-1

Chen, K.-T., and Wu, J.-H. (2018). Simulating the failure process of the Xinmo landslide using discontinuous deformation analysis. *Eng. Geol.* 239, 269–281. doi:10.1016/j.enggeo.2018.04.002

Coleman, S. E., Andrews, D. P., and Webby, M. G. (2002). Overtopping breaching of noncohesive homogeneous embankments. *J. Hydraul. Eng.* 128128, 8299–8838. doi:10.1061/(asce)0733-9429(2002)128:9(829)

Costa, J. E., and Schuster, R. L. (1988). The formation and failure of natural dams. *Geol. Soc. Am. Bull.* 100, 1054–1068. doi:10.1130/0016-7606(1988)100<1054:tfafon>2.3.co;2

Coussot, P., and Meunier, M. (1996). Recognition, classification and mechanical description of debris flows. *Earth-Science Rev.* 40, 209–227. doi:10.1016/0012-8252(95)00065-8

Cristofano, E. A. (1973). *Method of computing erosion rate for failure of earthfill dams*. Denver, CO, United States: US Department of the Interior, Bureau of Reclamation, Engineering and Research Center. 727.

Cruden, D. (2005). Debris-flow hazards and related phenomena. *Can. Geotech. J.* 42, 1723. doi:10.1139/t05-075

Fan, X., Dufresne, A., Siva Subramanian, S., Strom, A., Hermanns, R., Tacconi Stefanelli, C., et al. (2020). The formation and impact of landslide dams – state of the art. *Earth-Science Rev.* 203, 103116. doi:10.1016/j.earscirev.2020.103116

Fan, X., Rossiter, D. G., van Westen, C. J., Xu, Q., and Görüm, T. (2014). Empirical prediction of coseismic landslide dam formation: Coseismic landslide dam formation. *Earth Surf. Process. Landforms* 39, 1913–1926. doi:10.1002/esp.3585

Fread, D. (1988). *BREACH, an erosion model for earthen dam failures*. NOAA: Hydrologic Research Laboratory, National Weather Service.

Hanson, G., Cook, K., and Temple, D. (2002). Research results of large-scale embankment overtopping breach tests. *ASDSO Annu. Conf.*

Hanson, G. J., and Simon, A. (2001). Erodibility of cohesive streambeds in the loess area of the midwestern USA. *Hydrol. Process.* 15, 23–38. doi:10.1002/hyp.149

Höeg, K., Løvoll, A., and Vaskinn, K. (2004). Stability and breaching of embankment dams: Field tests on 6 m high dams. *Int. J. Hydropower. Dams* 11, 88

Jiang, X., Wörman, A., Chen, P., Huang, Q., and Chen, H. (2020). Mechanism of the progressive failure of non-cohesive natural dam slopes. *Geomorphology* 363, 107198. doi:10.1016/j.geomorph.2020.107198

Korup, O. (2004). Geomorphometric characteristics of New Zealand landslide dams. *Eng. Geol.* 73, 13–35. doi:10.1016/j.enggeo.2003.11.003

Li, D., Nian, T., Wu, H., Wang, F., and Zheng, L. (2020). A predictive model for the geometry of landslide dams in V-shaped valleys. *Bull. Eng. Geol. Environ.* 79, 4595–4608. doi:10.1007/s10064-020-01828-5

Li, L., Yang, X., Zhou, J., Zhang, J., and Fan, G. (2021). Large-scale field test study on failure mechanism of non-cohesive landslide dam by overtopping. *Front. Earth Sci.* 9, 660408. doi:10.3389/feart.2021.660408

Liu, W., and He, S. (2018). Dynamic simulation of a mountain disaster chain: Landslides, barrier lakes, and outburst floods. *Nat. Hazards (Dordr).* 19, 757–775. doi:10.1007/s11069-017-3073-2

Luo, J., Xu, W., Tian, Z., and Chen, H. (2019). Numerical simulation of cascaded dam-break flow in downstream reservoir. *Proc. Institution Civ. Eng. - Water Manag.* 172, 55–67. doi:10.1680/jwama.15.00088

Morris, M. W., Hassan, M. A. A. M., and Vaskinn, K. A. (2007). Breach formation: Field test and laboratory experiments. *J. Hydraulic Res.* 45, 9–17. doi:10.1080/00221686.2007.9521828

Nian, T., Wu, H., Li, D., Zhao, W., Takara, K., and Zheng, D. (2020). Experimental investigation on the formation process of landslide dams and a criterion of river blockage. *Landslides* 17, 2547–2562. doi:10.1007/s10346-020-01494-4

Peng, M., Ma, C.-Y., Chen, H.-X., Zhang, P., Zhang, L.-M., Jiang, M.-Z., et al. (2021). Experimental study on breaching mechanisms of landslide dams composed of different materials under surge waves. *Eng. Geol.* 291, 106242. doi:10.1016/j.enggeo.2021.106242

Peng, M., and Zhang, L. M. (2012). Breaching parameters of landslide dams. *Landslides* 9, 13–31. doi:10.1007/s10346-011-0271-y

Ruan, H., Chen, H., Wang, T., Chen, J., and Li, H. (2021). Modeling flood peak discharge caused by overtopping failure of a landslide dam. *Water* 13, 921. doi:10.3390/w13070921

K. Sassa (Editor) (2007). *Progress in landslide science* (Berlin: Springer).

Schmocker, L., and Hager, W. H. (2009). Modelling dike breaching due to overtopping. *J. Hydraulic Res.* 47, 585–597. doi:10.3826/jhr.2009.3586

Sheng-shui, C., Xu-shun, F., Qi-ming, Z., and Yun-hui, L. (2014). Centrifugal model tests and numerical simulations for break of earth-rock dams due to overtopping. *Chin. J. Geotech. Eng.* 36, 922–932. doi:10.11779/CJGE201405017

Singh, V. P., and Scarlatos, P. D. (1988). Analysis of gradual earth-dam failure. *J. Hydraul. Eng.* 1141141, 21–42. doi:10.1061/(asce)0733-9429(1988)114:1(21)

Tian, Z., Yang, H., Wang, W., and Cao, D. (2021). Numerical analysis of sand bed degrading and sediment transport rate under tailings dam break. *Front. Earth Sci.* 9, 686277. doi:10.3389/feart.2021.686277

Uyanık, G. K., and Güler, N. (2013). A study on multiple linear regression analysis. *Procedia - Soc. Behav. Sci.* 106, 234–240. doi:10.1016/j.sbspro.2013.12.027

Walder, J. S., Iverson, R. M., Godt, J. W., Logan, M., and Solovitz, S. A. (2015). Controls on the breach geometry and flood hydrograph during overtopping of noncohesive earthen dams: DAM-BREACH hydraulics and hydrographs. *Water Resour. Res.* 51, 6701–6724. doi:10.1002/2014WR016620

Wang, F., Bao, K., Huang, C., Liu, R., Han, W., Yi, C., et al. (2022). Distribution, characteristics, and research status of microplastics in the trunk stream and main lakes of the yangtze river: A review. *China Geol.* 5, 1–15. doi:10.31035/cg2022002

Wu, H., Nian, T., Chen, G., Zhao, W., and Li, D. (2020). Laboratory-scale investigation of the 3-D geometry of landslide dams in a U-shaped valley. *Eng. Geol.* 265, 105428. doi:10.1016/j.enggeo.2019.105428

Xu, F., Yang, X., Zhou, J., and Hao, M. (2013). Experimental research on the dam-break mechanisms of the jiadanwan landslide dam triggered by the wenchuan earthquake in China. *Sci. World J.*, 1–13. doi:10.1155/2013/272363

Yang, Y., Cao, S., Yang, K., and Li, W. (2015). Experimental study of breach process of landslide dams by overtopping and its initiation mechanisms. *J. Hydrodyn.* 27, 872–883. doi:10.1016/S1001-6058(15)60550-9

Zhang, J., Wang, W., Tian, Z., and Li, Y. (2021). An investigation of the characteristics of dam-break flood in a confluence channel based on the lattice Boltzmann method. *AIP Adv.* 11, 045320. doi:10.1063/5.0045256

Zhao, T., Chen, S., Fu, C., and Zhong, Q. (2019). Centrifugal model test on the failure mechanism of barrier dam overtopping. *KSCE J. Civ. Eng.* 23, 1548–1559. doi:10.1007/s12205-019-0375-9

Zhong, Q., Wang, L., Chen, S., Chen, Z., Shan, Y., Zhang, Q., et al. (2021). Breaches of embankment and landslide dams - state of the art review. *Earth-Science Rev.* 216, 103597. doi:10.1016/j.earscirev.2021.103597

Zhou, G. G. D., Zhou, M., Shrestha, M. S., Song, D., Choi, C. E., Cui, K. F. E., et al. (2019a). Experimental investigation on the longitudinal evolution of landslide dam breaching and outburst floods. *Geomorphology* 334, 29–43. doi:10.1016/j.geomorph.2019.02.035

Zhou, M., Zhou, G. G. D., Cui, K. F. E., Song, D., and Lu, X. (2019b). Influence of inflow discharge and bed erodibility on outburst flood of landslide dam. *J.Mt. Sci.* 16, 778–792. doi:10.1007/s11629-018-5312-8

frontiers | Frontiers in Earth Science

TYPE Methods
PUBLISHED 11 January 2023
DOI 10.3389/feart.2022.1004400

OPEN ACCESS

EDITED BY
Changdong Li,
China University of Geosciences
Wuhan, China

REVIEWED BY
Ruilin Fan,
Aecom United States, United States
Luigi Lombardo,
University of Twente, Netherlands
Subodh Chandra Pal,
University of Burdwan, India

*CORRESPONDENCE
Qiang Yao,
yaoqiang777@scu.edu.cn

SPECIALTY SECTION
This article was submitted to
Geohazards and Georisks,
a section of the journal
Frontiers in Earth Science

RECEIVED 27 July 2022
ACCEPTED 20 October 2022
PUBLISHED 11 January 2023

CITATION
Xu G, Ji J, Luo D, Qi S, Li H,
Dembele MDM and Yao Q (2023),
Discrimination of debris flow in narrow-
steep type and wide-gentle type gullies
in Wenchuan meizoseismal area.
Front. Earth Sci. 10:1004400.
doi: 10.3389/feart.2022.1004400

Discrimination of debris flow in narrow-steep type and wide-gentle type gullies in Wenchuan meizoseismal area

Guoqing Xu[1,2], Jiejie Ji[3], Dengze Luo[4], Shunchao Qi[1,2], Hongtao Li[1,2], Molobaly Dit Mahamadou Dembele[1,2] and Qiang Yao[1,2]*

[1]State Key Laboratory of Hydraulics and Mountain River Engineering, Sichuan University, Chengdu, China, [2]College of Water Resource and Hydropower, Sichuan University, Chengdu, China, [3]Sichuan Water Resources and Hydroelectric Investigation & Design Institute Co, Ltd, Chengdu, China, [4]Yalong River Hydropower Development Company, Ltd, Chengdu, China

The debris flow disasters in the Wenchuan meizoseismal area are dominantly triggered by the gully-type debris flow. Research on its classification method can be of great theoretical value and practical significance for developing targeted prevention measures. The current empirical classification method has some disadvantages, such as inconsistent discrimination criteria and poor practicability. In this paper, in order to overcome these drawbacks, the topography, rainfall, and source characteristics data of 176 gully-type debris flows in the Wenchuan "5.12" meizoseismal area since 2008 were collected and divided into the narrow-steep, transitional, and wide-gentle types based on field investigation. The narrow-steep type gullies are mainly concentrated in small catchments with severe erosion. In contrast, the wide-gentle type gullies are often characterized by big catchments, gentle vertical slopes, and debris flows movement dominated by deposition. An empirical discrimination method for debris flow gullies is proposed based on the characters of the gullies in the meizoseismal area, and a mathematical discrimination model named Gully Geomorphology Index (GGI) is also constructed. The results from existing cases indicated that both methods were accurate to discriminate between the narrow-steep and wide-gentle debris flow gullies. According to the empirical discrimination method, among the 176 channel-type debris flows, the numbers of narrow-steep, transitional, and wide-gentle channel types are 105 (59.66%), 12 (6.82%), and 59 (33.52%), respectively. While for the GGI method, the value 0.05 and 0.10 were defined as the threshold of the three types, and the distribution of the results is 104 (59.09%) for the narrow-steep type, 16 (9.09%) for the transitional type, and 56 (31.82%) for the narrow-steep type, which can better classify the transitional type gullies and is more practical. We hope that the discrimination methods proposed in this paper will help better understand the disaster-causing mechanism and improve the prevention measures of debris flow in the Wenchuan meizoseismal area.

KEYWORDS

debris flow, narrow-steep gully, wide-gentle gully, discrimination method, gully geomorphological index

1 Introduction

Since the 2008 "5.12" earthquake, mega flash floods and debris flows have occurred in Wenchuan, Dujiangyan, Mianzhu, and other strong seismic regions for many years, causing huge losses to local people's lives and properties (Fan et al., 2018). Debris flow is one of the main types of post-earthquake secondary disasters, of which abundant source material was produced and the critical rainfall threshold was consequently reduced by the activating effect of the earthquake (Koi et al., 2008; Wu et al., 2011; Tang et al., 2012; Yin et al., 2015; Qi et al., 2020). Many researchers have studied the area. Lombardo et al. (2019) retrieved the pattern of the ground motion through the landslides the Wenchuan earthquake itself triggered. Loche et al. (2022) studies the post-seismic response of a small area. According to the previous studies, the active period of debris flow after the earthquake will be 5–30 years (Tang et al., 2009; Huang and Li 2014; Zhang et al., 2014; Xiong et al., 2020), so it can be seen that the Wenchuan meizoseismal area is still in the high incidence period of post-earthquake debris flow. Debris flow gully can be generally divided into formation area, circulation area and accumulation area (Qu and Xiao, 2018). As the Wenchuan meizoseismal area is located in China's one and two-step boundary line in the Hengduan mountain range, the valleys are steep, the generation and concentration of runoff are urgent. Therefore, the outbreak of debris flow in this region after the earthquake is likely to be the gully type. Due to the different geomorphological characteristics of different channels, the formation of the channel debris flow disaster-causing mechanism and disaster-causing mode also differ. The current debris flow discrimination method have been unable to meet the requirements for the meizoseismal area debris flow disaster control, so there is an urgent need to effectively identify the type of debris flow to develop different types of prevention engineering in this region.

In past years, debris flow researches mainly focused on two types of debris flows: Slope debris flow and gully debris flow. Debris flows that have occurred after the Wenchuan earthquake in Southwest China have different formation mechanisms, erosion, deposition characteristics, and secondary disaster chain (Han 2016). Several research teams have studied the type of debris flows in this region. Yang et al. (2012) proposed the concept of narrow-steep channel type debris flow after studying 67 mudslide ditches that occurred in five areas of the Wenchuan meizoseismal area from 2008 to 2013 and analyzed their unique management difficulties and corresponding prevention and control countermeasures (Yang et al., 2015; Yang et al., 2020). Based on the characteristics of 13 debris flows along the Duwen Expressway in 2013, Han (2016) divided the channel-type debris flows into two categories, narrow-steep and wide-gentle, and discussed their disaster mechanism. For each of them, the prevention measures were then given by Han et al. (2018). After analyzing the parameters of 145 debris flows that erupted after the Wenchuan Earthquake, Chen et al. (2018) proposed the concept of urgent-steep gully debris flows, summarized their motion and dynamic characteristics, and Li et al. (2020) studied their initiation characteristics through flume experiment. The above-mentioned "narrow-steep" and "urgent-steep" gullies refer to a kind of debris flow gully with a small watershed area, narrow flow channel, and steep channel gradient, in which the debris flow erupts, moves swiftly and violently. The term "narrow" describes the character of the width of the overall watershed and flow channel, while "urgent" and "steep" are used to indicate both the overall and the flow channel gradient. Therefore, we use narrow-steep type to describe this kind of debris flow gully, while the gullies with opposite characteristics are defined as a wide-gentle type.

Accurate classification of gullies in the meizoseismal area can help promote the mechanistic understanding of debris flow further and thus improve engineering management. To date,

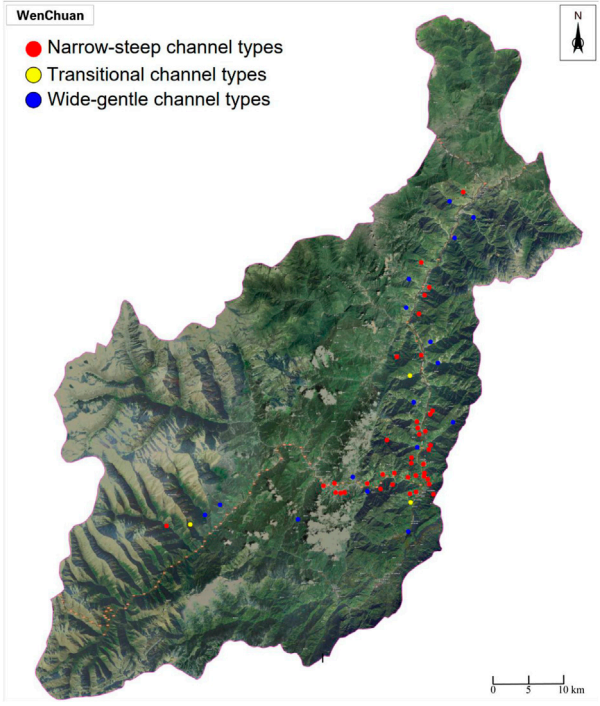

FIGURE 1
Distribution of the 58 debris flow gullies in Wenchuan.

the identification of gully-type debris flows in the meizoseismal area is mainly based on the empirical methods proposed by different scholars. The main defects associated with these methods include the inconsistent selection of indicators and the conflicting identification rules. In addition, the gully-type debris flows in seismic regions are mainly divided into two categories: "narrow-steep/urgent-steep/steep" and "wide-gentle." However, field investigations found that the current empirical methods could not identify debris flows with characteristics in between. Hence, in order to address the deficiencies of the empirical discrimination method in the selection of indicators, discrimination criteria, classification, method operation, and other aspects, several improvements are made on the empirical discrimination method in this paper by combining the characteristics of the indicators of 176 debris flows in the meizoseismal areas. During the "5·12″ earthquake, Wenchuan was the area most affected by the earthquake and also had a high incidence of debris flows. Figure 1 shows the distribution of the 58 debris flow gullies in the Wenchuan area. On this basis, a gully geomorphological index (GGI) discrimination model is proposed. The results show that the model has good operability and accuracy and is of significant guidance to further research on the mechanism of disaster and its prevention and control.

2 Analysis of debris flow discriminant indicator

The quantitative indicators to describe the topography of debris flow gullies are divided into the planimetric indicators and spatial elevation indicators (Liao et al., 2011). The main indicators that can describe the feature of "narrow" are planimetric indicators, such as watershed area, watershed length, average watershed width, watershed integrity coefficient, average channel width, and main channel length. These metrics can be accessed through GIS (Chowdhuri et al., 2020; Pal et al., 2020; Roy et al., 2020). The main indicators that can describe the feature of "steep" are spatial elevation indicators, such as the relative elevation of the watershed, the average vertical slope of the catchment, and the slope of both sides of the trench. The meaning of the indicators is shown as follow:

(1) Drainage area F: The drainage area is the area enclosed by the watershed and represents the catchment capacity of the watershed. Its scale reflects the extent of debris flow gully development. If the other conditions remain invariant, the larger the watershed area, the greater the catchment capacity, the more sources of loose solids the watershed contains, and the greater the size and destructive capacity of the resulting debris flows (Li et al., 2014).

(2) Watershed length, average width, and watershed integrity factor: watershed length refers to the axial length of the watershed, which is generally the same as the main gully length when studying the debris flows (Wang et al., 2020). Since the watershed is mostly irregular in shape, the width characteristic is often expressed as the average watershed width B, which is determined as $B = F/L$, where L is the main channel length. The watershed integrity coefficient reflects the morphological characteristics of the watershed, which is determined as $\delta = F/L^2$. The smaller the coefficient, the narrower the watershed. The watershed integrity coefficient is very closely related to the formation of debris flows. When $\delta < 1$, the shape of the watershed is narrow and the river slope is steep, which can easily lead to side slope collapse and accumulation in the riverbed, providing the material source conditions for debris flow generation (Zhou 1991; Chang et al., 2009).

(3) Average channel width: The average channel width is mainly dependent on the watershed's shape and the average width; it is positively correlated to the latter. The bottom width is usually measured to calculate the average width. However, most of the narrow steep debris flow gully has a profile for the V-shaped section, and the actual channel width under this section varies with the scale of the debris flow. The larger the scale, the greater the average channel width. Thus, it is difficult to determine the width of the flow channel in the event of a debris flow and unreasonable to use only the bottom width as the proxy for the average channel width. Therefore, the average watershed width is selected to represent the width information.

(4) Relative elevation difference of the catchment: the relative height difference of the watershed quantitatively reflects the spatial height variation of the debris flow gully. The more significant the difference in elevation, the greater the potential energy converted into kinetic energy, and the stronger the athletic ability for debris flow (Wang et al., 2020).

(5) Average vertical slope of the channel I: vertical slope reflects the steepness of the gully, generally using the average longitudinal ratio of the original area and circulation area to represent (Li et al., 2014; Wang et al., 2020). The high average vertical slope indicates that the gully is in the formative-developmental stage in geomorphological development. With narrow gully and severe erosion, debris flow frequently occurs (Wang et al., 2020).

In summary, we selected the watershed area, the average watershed width, the watershed integrity coefficient, and the main channel length to represent the character of width. The relative elevation of the watershed and the average vertical slope of the catchment are selected to represent the character of the slope.

TABLE 1 The existing empirical discrimination methods for channel-type debris flow in the meizoseismal area.

Type of gully	Watershed area (km^2)	Watershed integrity coefficient	Average channel width(m)	Relative elevation difference of catchment(m)	Average vertical slope of the channel (‰)	References
Narrow-steep	≤5	≤0.4	—	≥1000	≥300	Yang et al. (2015)
	<10	—	<30	—	>300	Han (2016), Han et al. (2018)
	<3.5			767–2238	>400	Li et al. (2020)
	<5	<0.4	—	—	>300	Chen et al. (2018)
Wide-gentle	>10	—	>50	—	<200	Han (2016)

3 Topographical features of the debris flow gully in the meizoseismal area

Table 1 summarizes previous studies' existing empirical discrimination methods for debris flow gullies. Still, for many gullies, like Anjia gully (F=9.17km^2, I= 434‰, δ=0.28, the width in circulation area: 10–30 m) and Bayi gully (F=8.63 km^2, I=366‰, δ=0.44), they have a typical character of narrow-steep gullies such as large longitudinal gradient and narrow circulation area. Although they are not fully meeting the specific parameters given in Table 1, they should also be classified as narrow-steep gullies (Zhao et al., 2021). In addition, the different indicators and criteria proposed by other investigators may result in the same gully being classified as different types by using different empirical discrimination methods. Due to different types of gullies having different disaster-causing mechanisms, this discriminant bias will significantly impact the later theoretical research and engineering control. For instance, wide-gentle gullies are always dominated by siltation, and the treatment engineering measures are often adopted as intercepting sources in the upstream and drainage in the downstream.

In contrast, for the narrow-steep gullies, erosion is the main disaster. Consolidating the slope and bed of the gully and building a retaining dam at the gully outlet are effective methods for disaster control (Han 2016). Using treatment measures without considering the gully type may cause severe damage. Taking the Wenjia gully (F=7.81 km^2, L=3.25 km, H=1519 m) for example, it built many check dams to prevent the debris flow, while the debris flow occurred on 13 August 2010 filled many check dams and eventually destroyed the dams at the outlet, which caused 7 casualties, 39 injured, and 497 houses buried (Liu et al., 2017). Therefore, in order to discriminate the type of gullies more precisely, the topographical features of gullies are analyzed from six indicators based on the 176 cases.

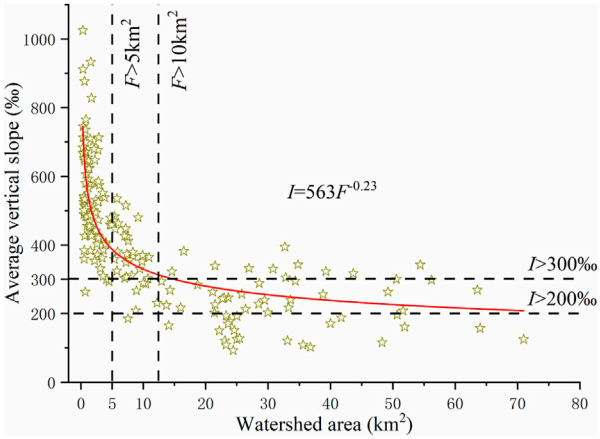

FIGURE 2
Average vertical slope versus watershed area of 176 channel-type debris flow gullies in the meizoseismal areas.

3.1 Watershed area

The watershed area distribution of the 176 cases is shown in Figure 2, The gullies with $F < 5km^2$, $5 \le F \le 10km^2$ and $F > 10km^2$ are accounting for 48.30%, 15.91%, and 35.80%, respectively, suggesting that one of the characteristics of channel-type debris flow in the meizoseismal area is tended to be a small watershed. This is because the meizoseismal area is located in middle-high gorge areas, where the topography is presented to be eroded landform and small-scale gullies densely distributed. Plenty of sources generated after the earthquake contributed to the transformation of these small-scale gullies into debris flow gullies (Ni et al., 2014). Table 1 shows that the gullies have been divided into two groups in previous studies, i.e., the wide-gentle gullies and the narrow-steep gullies (Yang et al., 2015; Chen et al., 2018), according to the value of the watershed area F. However, different investigators have used different F values to distinguish these two gullies types,

e.g., F = 5km^2 was suggested by Yang and Chen et al., while F = 10km^2 was preferred by Han (2016). Qu and Xiao (2018) also proposed that the range of watershed area of narrow-steep gullies area is between 0.3 and 10 km^2 and with an average value of 3 km^2 based on collected 145 gullies in the meizoseismal. There is a common view that narrow-steep gullies have watershed areas lower than 10 km^2, and the smaller the watershed area, the better it fits the features of narrow-steep gullies. Therefore, the condition $F < 5$km^2 can reflect more the character of the narrow-steep type. While for the gullies with a watershed area between 5 and 10 km^2 often have characters between wide-gentle and narrow-steep, defined as a transitional type. Thus, we propose that the corresponding threshold values of watershed area for the narrow-steep, transitional, and wide-gentle gully debris flows are $F < 5$km^2, $5 \le F \le 10$km^2, and $F > 10$km^2, respectively.

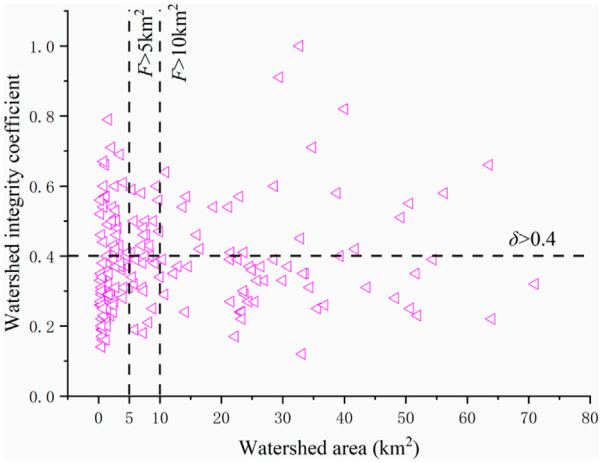

FIGURE 3
Watershed integrity coefficients versus watershed area of 176 channel-type debris flow gullies in the meizoseismal areas.

3.2 Average vertical slope of the channel

The average vertical slope of the channel is the key indicator controlling the formation and movement of debris flow. Takahashi (1980) found that when the vertical slope of the gully in the original area is above 286‰, the rainwater collected in the catchment area plays a more significant role in the occurrence of debris flows. The Institute of Mountain Hazards and Environment (IMHE) investigated the debris flow along Chengdu-Kunming railway and presented that the steep gully can be defined when the average vertical slope is greater than 250‰ (Chengdu Institute of mountain hazards and environment and Chinese Academy of Sciences, 1989); Specification of Geological Investigation for Debris Flow Stabilization (DZ/T2006) stipulates that a gully bed with a vertical slope greater than 12° (213‰) is highly susceptible to debris flow (resources 2006). Among the 176 cases in the meizoseismal area, 67.61% have an average vertical slope greater than 300‰, indicating that most debris flow gullies are steep, which endowed the debris flow a large amount of kinetic and potential energy, causing large-scale scouring and deposition. The Scholars (Chen et al., 2018; Han et al., 2018) often used the average vertical slope $I > 300$‰ as a criterion to determine narrow-steep channel debris flows (Table 1), while Han et al. proposed that the average vertical slope $I < 200$‰ is likely to generate wide-gentle channel debris flow. So in this study, we adopted the existed views and defined that the average vertical slope between 200‰ and 300‰ belongs to transitional type gullies.

Figure 2 shows that the gully average vertical slope tends to decrease with the increasing watershed area, and their relationship satisfies the curvilinear distribution of the dimensionless power function (Qu and Xiao 2018; Lyu et al., 2022). 68.91% of the gullies with the average vertical slop $I > 300$‰ are gathered in the watershed area $F < 5$km^2,

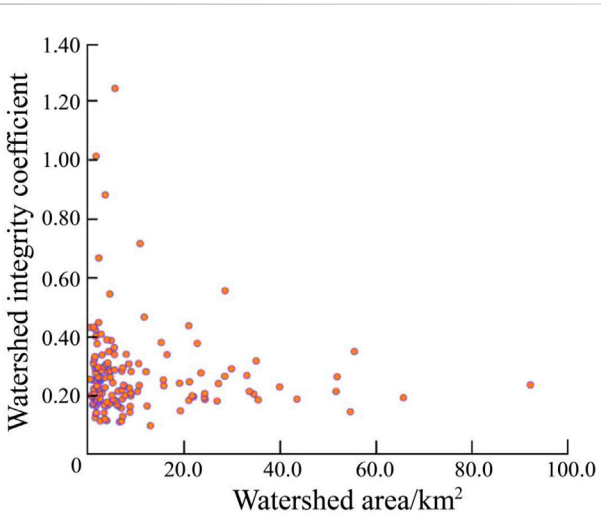

FIGURE 4
Watershed integrity factor and catchment area of 145 channel-type debris flows in the meizoseismal area (Chen et al., 2018).

representing the narrow-steep debris flow gully. 95.65% of gullies with the average vertical slop $I < 300$‰ are clustered in the watershed area $F > 10$km^2, representing wide-gentle gullies. This phenomenon can be explained as when the watershed area is small, the gully is in the formation-development stage, the effect of water flow downcutting erosion is severe, shaping high slope gradients and gully-bed ratios; With the increasing of the catchment area, the gullies evolution comes to an end, the degree of channel incision decreases, making it hard to satisfy the hydrodynamic conditions required to initiate a debris flow.

3.3 Watershed integrity coefficient

Previous studies often used $\delta < 0.4$ as a condition to verdict narrow-steep gullies (Yang et al., 2015). Figure 3 plots the watershed integrity coefficients against a catchment area for all the cases. 60.80% of the 176 gullies have watershed integrity coefficients less than 0.4. From the aspect of the watershed area, there are 85 debris flow gullies with a catchment area $F < 5\text{km}^2$, of which 63.53% (i.e., 54) had a watershed integrity coefficient $\delta < 0.4$; and of the 63 debris flow ditches with a watershed area $F > 10\text{km}^2$, 65.08% (i.e., 41) had a catchment integrity factor $\delta < 0.4$. So, it can be seen that regardless of the size of the watershed, the watershed integrity coefficients in the meizoseismal area showed a predominance of less than 0.4. In addition, Chen et al. (2018) analyzed the relationship between the watershed integrity coefficient and the watershed area for 145 channel-type debris flow gullies in the meizoseismal area. The results are replotted in Figure 4. which shows that the watershed integrity coefficient $\delta < 0.4$ is accounting for 75%; Qu and Xiao (2018) also found that the watershed integrity coefficient of channel-type gullies in the meizoseismal area is gathered between 0.1 and 0.4 and with an average value of 0.26, which indicates that $\delta < 0.4$ in strong seismic areas is a common phenomenon, there is no clear relationship between the watershed integrity coefficient and the watershed area, using this condition to represent the feature of "narrow" is inadequate. Thus, this study only used the watershed integrity coefficient as a reference index.

3.4 Relative elevation difference of catchment

Yang et al. used the condition $H > 1000\text{m}$ to discriminate the character of narrow-steep gullies. However, 139 out of the 176 watersheds have a relative height difference $H > 1000\text{m}$, accounting for 78.98%. This indicates that this condition is a common characteristic of channel-type debris flows in the meizoseismal area. Qu and Xiao (2018) proposed that the relative height difference range of narrow-steep gullies is between 896m and 2586 m where $H > 1000\text{m}$ could represent the characteristic of "steep" However since the meizoseismal area belongs to the alpine-gorge area., many wide-gentle gullies also present high relative elevation differences (e.g., Taoguan gully, watershed area: 50.86 km^2, relative elevation difference:2901 m). Thus, since this condition does not distinguish well between the two types of gullies, it is therefore used as a reference in the discrimination method.

3.5 Main channel length and average watershed width

The length of the main channel determines the flow length of the debris flow and the volume of erosion sources along the way, reflecting its energy and destructive power. From the 176 cases, 109 (61.9%) have a main gully length less than 5 km, showing the short gully is the main feature of the debris flow gullies in the meizoseismal area. Figure 5 indicates that the main channel length and watershed area satisfies a linear distribution with a positive correlation (R^2=0.84). Their control effect on debris flow outbreaks is similar. With the decrease of the watershed area, the main channel length gets short, making it unfavorable to store loose material while conducive to debris flow initiation. Under the condition of narrow-steep gully F<5 km^2, the main gully length satisfies L<5 km. Since the main gully length strongly correlates with the watershed area, L<5 km is used in this paper as a secondary discriminant condition.

The equation B=F/L can calculate the average watershed width because the main channel length is consistent with the watershed length. Figure 5 shows 63.6% (112) gullies are satisfied with condition B<2 km, indicating that the long-narrow basin form is typically characteristic of gullies in the meizoseismal area. The relationship of watershed area and average watershed width satisfy a linear distribution (R^2=0.83) and under the condition of F<5 km^2 for narrow-steep gullies, the average basin widths all satisfy B<2 km, so B<2 km is used as a secondary discriminant.

4 Rainfall and source characteristics

Wenchuan meizoseismal area belongs to tectonically eroded mid-alpine landscapes, and the topography significantly influences the climate. When encountering mountains, the air current lift results in clouds and rainfall, so the precipitation and rainy days increase with mountain elevation (Gu et al., 2005). Local heavy rainfall is mainly concentrated in the debris flow gullies catchment area. Therefore, the heavy rainfall that triggers debris flow is characterized by concentrated precipitation areas, rapid confluence, and uneven spatial distribution, which are highly favorable to the occurrence of debris flows (Zhang et al., 2014).

The rainfall in Wenchuan meizoseismal area is abundant. The average annual precipitation for the last 56 years is 719. 70 mm, with a large inter-annual variation and an oscillating upward trend. Statistics show that the average annual rainfall before the earthquake was about 716 mm, and the average annual rainfall from 2008 to 2017 after the earthquake was 752. 61 mm, which has increased by 5. 17% compared with the pre-earthquake period. With more precipitation, the loose hills are more prone to geological hazards (Guo et al., 2017). As shown in Figure 6, precipitation during the year was mainly concentrated between June and September. Approximately 70% of precipitation occurs in this period (Tang et al., 2016). Previous studies found that the critical rainfall intensity of debris flow is between 15.8 and 56.5 mm/h in the Wenchuan meizoseismal area. Also, the annual thresholds for debris flows have increased each year over the past years loose vegetation recovered (Guo et al., 2016).

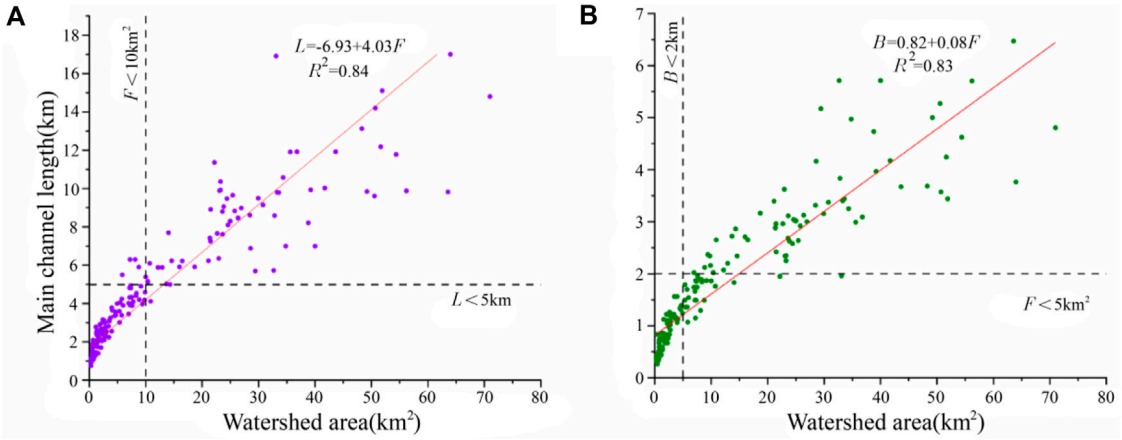

FIGURE 5
(A) Main channel length versus Watershed area **(B)** Average watershed width versus Watershed area.

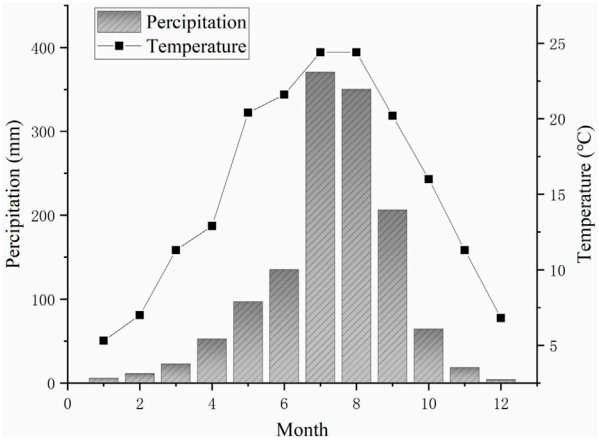

FIGURE 6
Average temperature and precipitation in the meizoseismal area from 1965 to 2015.

Debris flow outbreaks result from the combined effect of the previously accumulated rainfalls and the recent rainfalls (Jiang et al., 2021; Li et al., 2021). The short duration with high-intensity rainfall plays a decisive role in triggering debris flows. This precipitation process can rapidly form larger flood peaks within a certain range of the debris flow basin, which induces the loose deposits to be piled up in the gully or washed out. Besides, the continuous light rainfall that often occurs during the rainy season in the meizoseismal areas saturates the water content of loose soil, increases its volume weight, reduces its shear strength and stability, resulting in a reduction in the critical rain intensity required to trigger debris flow, which facilitates debris flow activity.

The sources in the study area are mainly divided into landslide accumulation sources, channel accumulation sources, and slope erosion sources. Due to the increase in adverse geological phenomena caused by the strong earthquake, both the landslide deposit and channel deposit sources increased significantly. The proportion of dynamic storage also increased, providing a large amount of loose material for debris flow formation, resulting in a significant increase in the risk of channel-type debris flow in the meizoseismal area (Chen et al., 2012). In addition, during the earthquake, the mountain body was cracked and loosened under seismic waves, resulting in many critical slope bodies that were cracked but not slippery. Under the action of rainfall and self-weight, those potential sources will be disintegrated and piled up in the gully, recharging the sources in stages.

In terms of the source distribution, gully-type debris flow in the meizoseismal area has a concentrated source distribution, mainly accumulating in the gully, which is unstable. Compared to the wide-gently gullies, the narrow-steep gullies have a smaller catchment area but a larger storage capacity per unit area. For example, compared with Qipan gully, which has a watershed area of 54.2 km^2 and a dynamic storage capacity of 130,000 m^3/km^2 of loose material per unit area, the narrow-steep Maliu gully has a watershed area of 1.6 km^2 and a dynamic storage capacity of 940,000 m^3/km^2 of loose material per unit area, and the “7.10” debris flow washed out 100.58 million m^3 of solid material at one time (Zhang et al., 2012).

Five typical gully-type debris flows gullies were selected from the two massive debris flows in Yingxiu Township, Mianhao Township, and Yinxing Township in the Wenchuan meizoseismal area 2010.08.13 and 2013.07.10. The screening experiment was carried out on these gullies, and the gradation curves were obtained as shown in Figure 7. The gradation of solid particles from the deposition

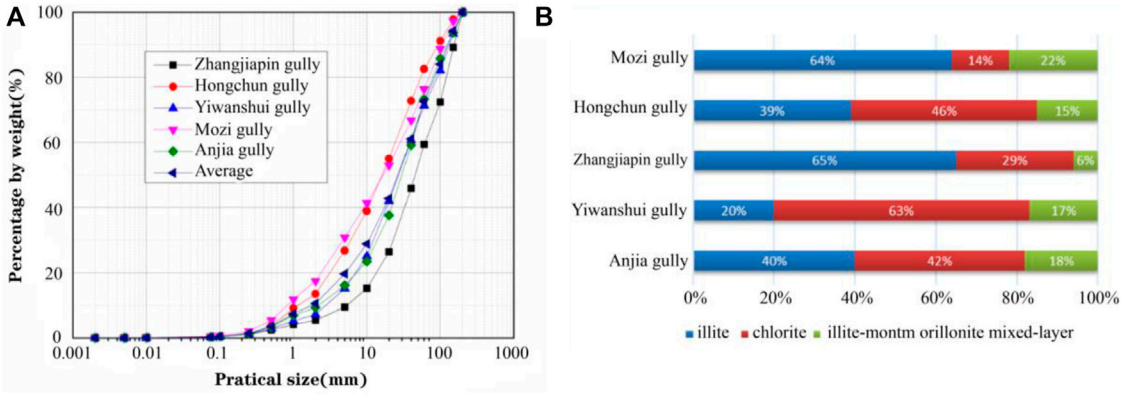

FIGURE 7
(A) The gradation curves of five gullies **(B)** Clay mineral composition of the deposit source in the meizoseismal area.

sources in the meizoseismal area is widely distributed and has good continuity. The gradation curves have an inhomogeneity coefficient greater than 5 and a curvature coefficient between 0.95 and 3, with no missing particle groups. The content of fine particles less than 0.075 mm is less than 0.5%, and the content of sticky particles less than 0.005 mm is less than 0.11%, with slight differences between different gullies. Most of the source particle size is smaller than pre-earthquake, and the loose solid material is mainly the mixture of block gravel and soil. The proportion of rock blocks is large, while the total amount of less than 200 mm blocks is also relatively large, which is easy to initiate.

Webb et al. (2008) investigated the relationship between the clay mineralogy and major-cation chemistry of fine-grained bedrock units and the occurrence of debris flows on the entire Colorado Plateau, finding that the debris flow producers are uniformly low in montmorillonite (5%) and high in illite and kaolinite (71%); conversely, fine-grained bedrock that does not produce debris flows has lower illite and kaolinite (25%) and higher montmorillonite (51%) content. Analysis of the clay mineral composition of the deposit source in the meizoseismal area by X-ray diffraction experiments revealed that it is mainly composed of three clay minerals (Figure 7): illite, chlorite, and illite-montmorillonite mixed-layer, with an average content of 45.6%, 38.8%, and 15.6% respectively. The total contents of illite and chlorite are over 75%, while the contents of illite-montmorillonite mixed-layer are below 25%, which indicates the clay mineral composition in the meizoseismal area is favorable to the formation of debris flow.

5 Discrimination method of gully-type debris flows in the meizoseismal area

Identifying the gullies type plays a vital role in understanding the mechanism of debris flow and designing corresponding prevention engineering. The existing discrimination methods are always empirical and have defects such as inconsistent selection of indicators and conflicting identification rules. Based on the topographic feature of the 176 gullies in the meizoseismal area, the research for the discrimination method of debris flow gullies was carried out in this section.

The watershed area and average vertical slope of the channel, which reflect the character of width and slope, are selected as the main discrimination indicators in empirical discrimination. The average watershed width and main channel length are selected as secondary discrimination indicators. Table 2 shows the discrimination method. When the two main indexes belong to the same category, they can be discriminated directly. When one main index belongs to transitional, while the other one belongs to the other type, it can be discriminated to be narrow-steep or wide-gentle type. When there is a conflict between the two main indexes, comprehensive empirical discrimination should be made based on the specific values of the two indicators combined with the secondary index.

In using the empirical discriminant method to discriminate channel-type debris flows in the meizoseismal areas, the traditional empirical method needs to rely on the subjective human experience to make comprehensive judgments, particularly for cases where the results of two discriminant indicators are inconsistent. Take the Banqiao gully (watershed area: 26.96 km^2, average vertical slope: 332‰) as an example. It has the characteristics of “steep” as the slope exceeds 300‰; however, its watershed area is much larger than 10 km^2, which indicates the “wide” characteristic is more prominent, so it is categorized as the wide-gentle type. Although the empirical discrimination method can identify the gully type, it relies on subjective experience because of the terrain complexity, which reduces the applicability of the method. Therefore, based on the empirical discriminant method, a novel mathematical discriminant model is proposed by further analyzing and selecting the key discriminant indicators.

TABLE 2 Improved empirical discrimination model.

Indicators	Narrow-steep type	Transitional type	Wide-gentle type
Watershed area (km^2)	≤5	5–10	>10
Average vertical slope of the channel (‰)	>300	200–300	<200
average watershed width (km)	<2		>2
main channel length (km)	<5		>5

TABLE 3 Verification of Discrimination Results of Empirical method and GGI.

Name	L/ km	F/ km^2	B/ km	Factor	H/ m	I/‰	GGI	Empirical method	GGI	Han (2016)
Taoguan gully	14.20	50.86	3.58	0.25	2901	197.00	0.02	WG	WG	WG
Qipan gully	15.10	54.20	3.59	0.24	3050	192.00	0.02	WG	WG	WG
Chutou gully	8.90	21.70	2.44	0.27	2952	184.00	0.06	WG	T	WG
Xinqiao gully	5.00	14.30	2.86	0.57	2110	267.90	0.05	WG	T	WG
Yanglin gully	5.50	7.95	1.45	0.26	2124	386.00	0.18	NS	NS	NS
Sucun gully	4.25	5.79	1.36	0.32	2275	455.00	0.29	NS	NS	NS
Anjia gully	4.90	9.17	1.87	0.38	2350	417.00	0.14	NS	NS	NS
Lianshandaqiao gully	1.34	0.60	0.45	0.33	1159	483.00	4.31	NS	NS	NS
Huaxi gully	5.15	10.39	2.02	0.39	1897	287.00	0.09	T	T	WG
Mozi gully	4.00	7.40	1.85	0.46	1696	424.00	0.12	NS	NS	NS
Wayao gully	2.78	1.21	0.44	0.16	1796	646.04	3.41	NS	NS	NS
Futang gully	1.30	1.12	0.86	0.66	851	654.62	0.88	NS	NS	NS
Zhangjiapin gully	2.20	1.71	0.78	0.35	937	425.91	0.71	NS	NS	NS

Note: NS: narrow-steep channel debris flow; WG: wide-gentle channel debris flow; T: transitional channel debris flow.

There are two functional relations in the four indicators describing the width of the gully (including watershed area, average watershed width, watershed integrity coefficient, and main channel length), displayed as $\delta = F/L^2$ and $B = F/L$. So, any two indicators can deduce all the massages of the width of the gully. Similarly, a functional relationship exists between the average vertical slope of the channel and the relative elevation difference of catchment (i.e., I=H/L). So, we use two width indicators and one slope indicator to construct the mathematical function. Previous studies (Qu and Xiao 2018) found that the smaller the watershed area and the bigger the relative elevation difference, the more it fits the characteristics of narrow-steep gullies. When the area is fixed, the smaller the average width of the watershed, the more it fits the narrow-steep gullies. Therefore, the gully geomorphic index (GGI) is defined as the coefficient of discrimination, as shown in Eq. 1.

$$\mathrm{GGI} = \frac{1}{F} * \frac{H}{B} = \frac{HL}{F^2} \tag{1}$$

From the classification criteria of the improved empirical discrimination method, the narrow-steep gullies have characteristics of $F < 5\mathrm{km}^2$, $B < 2\mathrm{km}$ and $H > 1000\mathrm{m}$, while the wide-gentle gullies have characteristics of $F > 10\mathrm{km}^2$, it is possible to define $GGI > 0.10$ as the narrow-steep channel debris flow. The same token $GGI < 0.05$ is used for the wide-gentle channel debris flow and $0.05 \leq GGI \leq 0.10$ the transition channel.

Han et al. (2018) investigated 13 debris flows gullies outbreaking along the Duwen expressway on 10 July 2013, and classified them into two categories: wide-gentle and narrow-steep type by analyzing their characteristics. Table 3 verified the accuracy of the two discrimination methods proposed in this paper by applying them to the 13 gullies. For narrow-steep gullies (e.g., Mozi gully, Anjia gully), both methods can identify them well, while for wide-gentle gullies, there are a few differences between the discriminant method and the results from Han, et al. The inconsistence gullies like Huaxi gully (main channel length: 5.15 km, watershed area: 10.39 km^2, average vertical slope: 287%) are charactered by medium-scale watershed area and relative gentle slope, which is defined as a transitional type. The discrimination methods proposed in this paper can better reflect the overall characteristics of gullies, then facilitates the targeting of prevention engineering.

The discrimination methods are applied to the 176 cases, and the results are shown in Tab X. For the empirical discrimination method, the number of narrow-steep channel type, transitional channel type, and wide-gentle channel type is 105 (59.66%), 12

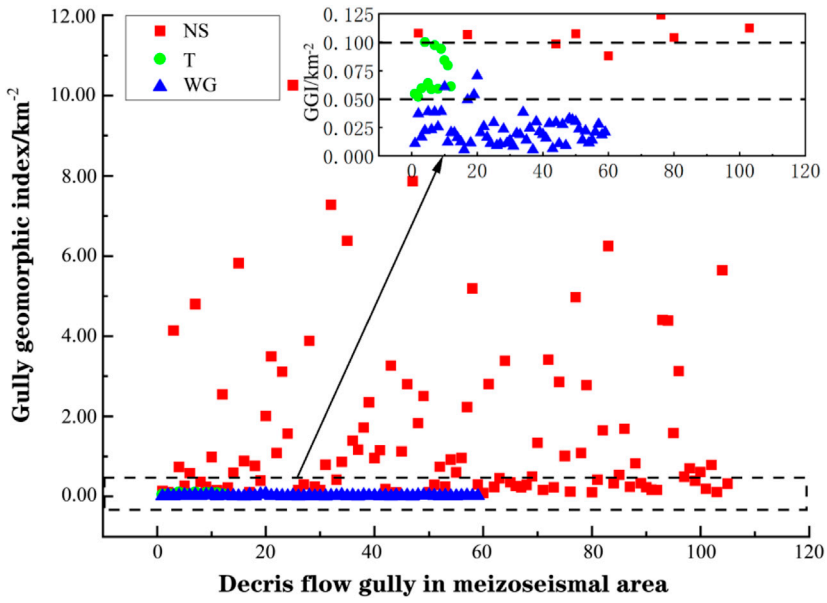

FIGURE 8
The classification results of 176 gullies by the two methods.

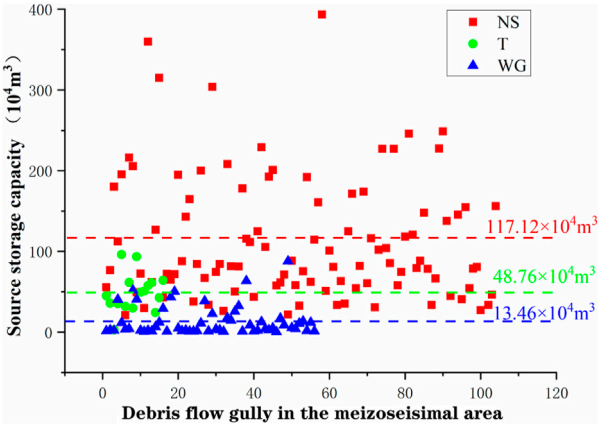

FIGURE 9
The source reserves of the three types of debris flow gully.

(6.82%), and 59 (33.52%), respectively. While for GGI, the distribution of the result is 104 (59.09%), 16 (9.09%), and 56 (31.82%), respectively. Figure 8 shows the classification results of 176 gullies by the two methods, which is essentially in agreement.

Figure 9 shows the amount of source storage per km^2 for three types of debris flow gullies. The average volume of narrow-steep, transitional, and wide-gentle debris flow gully are 117.12×10^4 m^3/km^2, 48.76×10^4 m^3/km^2, and 13.46×10^4 m^3/km^2, respectively. The source storage capacity per unit area of narrow-steep debris flow gully is 8.7 times greater than that of the wide-gentle type, which indicates the narrow-steep gully is more prone to debris flow occurrence.

6 Discussion

Narrow-steep debris flow gullies are always taking the shape of “V”, characterized by small watershed area (F < 5 km^2), large longitudinal slope (I>300‰), significant relative height difference (H>1000), and the main channel length is generally less than 5 km (Figure 10). The bank slope is steep, leading the runoff generation and concentration rapidly and the source transport fast, thus the debris flow outbreaks suddenly. Due to the narrow width of the gully (5–30 m), it is more likely to erode the bank slope (Lyu et al., 2017), which further enhances the destructive capacity of debris flow. In the aspect of movement characteristic, the narrow-steep type debris flow is characterized by downward erosion and retrogressive erosion owing to the steep terrain, with no chance for deposition. Therefore, the focus of management should be on the control of undercutting and anadromous erosion of the gully.

Wide-gentle debris flow gullies are mostly “U” shaped, with characters of big watershed area (F>10 km^2), gentle longitudinal gradient (I<200‰), and long main channel length (Figure 10). Generally, this type has broad gully bottom and multiple tributary ditches, which tend to form cascade failure under heavy rainfall. The movement characteristic of wide-gentle type debris flow is mainly deposition. The scale of the outflow

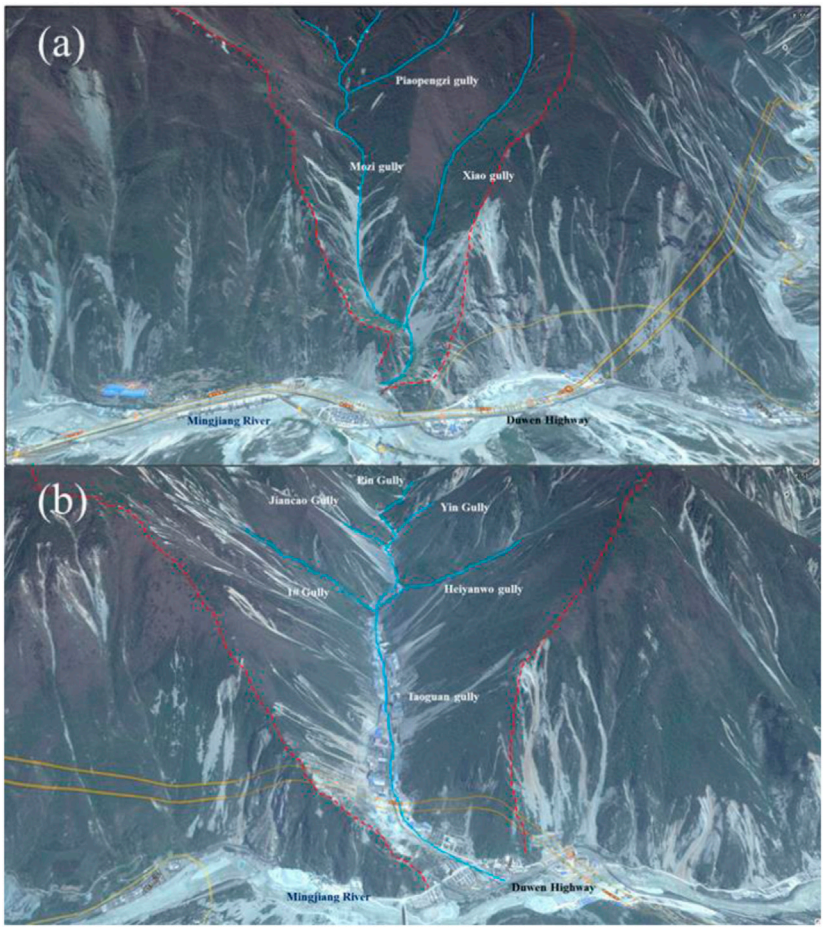

FIGURE 10
The typical narrow-steep and wide-gentle debris flow gullies: **(A)** The typical narrow-steep debris gully: Mozi gully (the watershed area: 7.4 km^2, the average vertical slope: 424‰, with "V" shaped section) **(B)** The typical wide-gentle debris gully: Taoguan gully (the watershed area: 50.86 km^2, the average vertical slope: 197‰, with "U" shaped section).

is huge, so it permanently blocks the river and forms barrier lakes. The multi-stage dam can effectively prevent the formation of barrier lakes and reduce the risk of collapse.

The current large-scale debris flow with a large watershed area, long main channel length, and gentle longitudinal slope are the future development trend of some small-scale debris flow with a small watershed area, short main gully length, and steep longitudinal slope. Lyu et al. (2022) found that the frequency of debris flow occurrence is closely related to the stage of gully evolution. As the watershed area grows, the frequency gradually increases until the watershed area reaches medium scale, which is assumed to be the morphologically most active gullies with the highest growth and incision rate. Then, as the watershed area further grows, the watershed morphology gradually stabilizes, and the mudflow frequency decreases affected by the milder gully gradient (Stock and Dietrich, 2006). From the perspective of the gully evolution stage, the narrow-steep debris flow gully is currently in its young-adult stage. With the strong downward erosion, lateral erosion, and retrogressive erosion, the gully gradually becomes longer and wider, reflecting the characteristics of transitional debris flow gully as the gully evolution enters its late stage, the debris flow gully evolute to wide-gentle debris flow gully with low frequency of debris flow occurrence.

Comparing the results of the mathematical model and empirical discriminating method on 176 samples, it was found that for all three types of gullies, the results from these two methods were generally consistent with each other. Several inconsistent cases (Table 4) were found at the boundaries of the discriminant criteria, which have a character between narrow-steep and wide-gentle types. It can be seen that compared with the empirical discriminating method, the mathematical model (GGI) can

TABLE 4 The inconsistent gullies with the two methods.

Name	Main channel length (km)	Watershed area (km^2)	Average channel width (km)	Watershed integrity factor	Relative elevation difference of catchment(m)	Average vertical slope of the channel (‰)	Gully geomorphic index	Improved empirical discrimination
Shilong Gully	3.91	7.3	1.87	0.48	1200	307	T	NS
Huaxi Gully	5.15	10.39	2.02	0.39	1478	287	T	WG
Dongguacao Gully	5.88	12.92	2.20	0.37	1730	294	T	WG
Hualin Gully	5.88	12.2	2.07	0.35	1360	231	T	WG

better classify the transitional type gullies. And form the aspect of operativity, the mathematical model is more practical and thus can be better used in the later remediation of debris flows in the meizoseismal area.

The preventive measures taken for different types of debris flow gullies are also different. For the wide-gentle gully type of debris flow, the management concept of "stopping mainly, supplemented by drainage" is used. For the narrow-steep type gully debris flows, the management concept of "consolidating the source and slope in the gully and stopping the siltation at the mouth of the gully" is used (Han 2016). For transitional mudslides, the above engineering measures can be chosen according to the actual situation.

In this paper, the proposed methods for classifying the gullies type in the meizoseismal area are based on the geomorphological perspectives. The sample quantity and study area restrict them. Further research should be conducted by expanding the sample size, combining DEM data with deep learning neural network algorithm (Chowdhuri et al., 2021; Saha et al., 2021; Chakrabortty et al., 2022).

7 Conclusion

Debris flow is a natural disaster that is widely distributed in some areas of the world with special topography and geomorphological conditions. Different types of debris flows should be subject to different control measures. Therefore, the study of mudslide discrimination methods is crucial. This paper collected 176 channel-type debris flow events in the meizoseismal area since 2008. Based on the analysis of gully character, two discrimination methods were proposed, and the following conclusions can be drawn:

(1) The gully-type debris flows in the meizoseismal area are characterized by small watershed areas, long strips, and steep longitudinal slopes, most of which have relative height differences greater than 1000 m, making them highly susceptible to debris flow. The short-duration, high-intensity rainfall in concert with continuous light rainfall is more conducive to debris flow formation. Besides, due to the earthquake disturbance, the sources in the meizoseismal area have increased significantly compared to the pre-earthquake period, and the clay mineral composition is favorable to the formation of debris flow.

(2) The debris flow gullies in meizoseismal area are classified as narrow-steep, transitional and wide-gentle types based on the topographical features. Narrow-steep debris flow gullies are mostly "V" shaped, with a small watershed area, steep channel slope, and narrow circulation channels. The debris flow moves fast in the channel, making it easy to form downward and lateral erosion. Wide-gentle debris flow gullies are mostly "U shape, with a larger basin area and gentler channel slope, the debris flow is easy to deposit in the channel, forming cascade failure and blocking the river. As the transitional stage of gully evolution, the transitional debris flow gully showed scour and deposition characteristics simultaneously. The source storage capacity per unit area of narrow-steep debris flow gully is 8.7 times greater than that of the wide-gentle type, indicating the narrow-steep gully is more prone to debris flow occurrence.

(3) The mathematical discrimination model named Gully Geomorphology Index (GGI) was constructed, and the value 0.05 and 0.10 were defined as the threshold of Narrow-steep, transitional and wide-gentle type gullies. Empirical method was applied to the 176 cases, showing the number of narrow-steep channel type, transitional channel type, and wide-gentle debris flow gullies are 105 (59.66%), 12 (6.82%), and 59 (33.52%), respectively. While for GGI, the distribution of discrimination results is 104 (59.09%), 16 (9.09%), and 56 (31.82%), which can better classify the transitional type gullies and is more practical.

At present, the world is encountering extreme climate and frequent natural disasters. The rapid identification of natural disasters is conducive to establishing a prevention and control system faster, and is of great significance to disaster prevention and reduction projects. The discrimination methods of narrow steep gully type debris flow and wide gentle gully type debris flow proposed in this paper greatly improve the speed of debris flow type discrimination, and the existing data show that these two methods have high reliability. We can use these two methods to construct numerical or experimental models of different debris flow gullies to further investigate their movement mechanisms and control measures. So as to promote the development of disaster prevention and reduction projects.

Data availability statement

The datasets presented in this study can be found in online repositories. The names of the repository/repositories and accession number(s) can be found in the article/supplementary material.

Author contributions

GX, DL, JJ, and QY planned the campaign; DL and JJ collected and analyzed the data; DL and MM wrote the manuscript draft; SQ, HL and QY reviewed and edited the manuscript.

Funding

This work is supported by the National Key R&D Program of China (2018YFC1505402), Sichuan Provincial International Science and Technology Collaboration & Innovation Project (2022YFH0078), National Natural Science Foundation of China (No. 51809188).

Conflict of interest

JJ was employed by Sichuan Water Resources and Hydroelectric Investigation and Design Institute Co., Ltd, China. DL was employed by Yalong River Hydropower Development Company, Ltd, China.

The remaining authors declare that the research was conducted in the absence of any commercial or financial relationships that could be construed as a potential conflict of interest.

Publisher's note

All claims expressed in this article are solely those of the authors and do not necessarily represent those of their affiliated organizations, or those of the publisher, the editors and the reviewers. Any product that may be evaluated in this article, or claim that may be made by its manufacturer, is not guaranteed or endorsed by the publisher.

References

Chakrabortty, R., Pal, S. C., Santosh, M., Roy, P., and Chowdhuri, I. (2022). Gully erosion and climate induced chemical weathering for vulnerability assessment in sub-tropical environment. *Geomorphol. (Amst).* 398, 108027–555X. doi:10.1016/j.geomorph.2021.108027

Chang, T. C., Wang, Z. Y., and Chien, Y. H. (2009). Hazard assessment model for debris flow prediction. *Environ. Earth Sci.* 60 (8), 1619–1630. doi:10.1007/s12665-009-0296-x

Chen, M., Tang, C., Gan, W., and Cai, Y. (2018). Characteristics and dynamical process of debris flow at urgent steep gully in the earthquake areas—Illustrated with case of wayao gully in wenchuan. *J. J. Yunnan Univ.* 40 (2), 272–278. doi:10.7540/j.ynu.20170495

Chen, N-S., Hu, G-S., Deng, M-F., Zhou, W., Yang, C-L., Han, D., et al. (2012). Impact of earthquake on debris flows — A case study on the wenchuan earthquake. *J. Earthq. Tsunami* 05 (05), 493–508. doi:10.1142/S1793431111001212

Chengdu Institute of mountain hazards and environmentChinese Academy of Sciences (1989). *Research and control of debris flow*. Sichuan: M. Sichuan Science and Technology Press.

Chowdhuri, I., Pal, S. C., Arabameri, A., Saha, A., Chakrabortty, R., Blaschke, T., et al. (2020). Implementation of artificial intelligence based ensemble models for gully erosion susceptibility assessment. *Remote Sens. (Basel).* 12 (21), 3620. doi:10.3390/rs12213620

Chowdhuri, I., Pal, S. C., Saha, A., Chakrabortty, R., and Roy, P. (2021). Evaluation of different DEMs for gully erosion susceptibility mapping using *in-situ* field measurement and validation. *J. Ecol. Inf.* 65, 101425. doi:10.1016/j.ecoinf.2021.101425

Fan, X., Juang, C. H., Wasowski, J., Huang, R., Xu, Q., Scaringi, G., et al. (2018). What we have learned from the 2008 wenchuan earthquake and its aftermath: A decade of research and challenges. *Eng. Geol.* 241, 25–32. doi:10.1016/j.enggeo.2018.05.004

Gu, X., Tian, N., and Pan, P. J. (2005). "Climatic characteristics of rainstorms in Qian southeast China in the last 40 years and its topographic influence on the distribution of rainstorms," in Proceedings of the 2005 Annual Meeting of the Chinese Meteorological Society, October 2005, Suzhou, China, 6529–6535.

Guo, X., Cui, P., Li, Y., Fan, J., Yan, Y., and Ge, Y. (2016). Temporal differentiation of rainfall thresholds for debris flows in Wenchuan earthquake-affected areas. *Environ. Earth Sci.* 75 (2), 109. doi:10.1007/s12665-015-5031-1

Guo, X., Cui, P., Marchi, L., and Ge, Y. (2017). Characteristics of rainfall responsible for debris flows in Wenchuan Earthquake area. *Environ. Earth Sci.* 76 (17), 596. doi:10.1007/s12665-017-6940-y

Han, M. (2016). *Hazard mechanism research of wide-gentle and narrow-steep channels debris flow in wenchuan earthquake region*. Sichuan Chengdu: D. Southwest Jiaotong University.

Han, M., Hu, X., and Hu, K. (2018). Comparative study between debris flow of wide-gentle and narrow-steep channel based on numerical simulation and prevention measures. *J. Nepal Geol. Soc.* 55, 167–172. doi:10.3126/jngs.v55i1.22808

Huang, R., and Li, W. (2014). Post-earthquake land sliding and long-term impacts in the Wenchuan earthquake area, China. *Eng. Geol.* 182, 111–120. doi:10.1016/j.enggeo.2014.07.008

Jiang, Z., Fan, X., Siva Subramanian, S., Yang, F., Tang, R., Xu, Q., et al. (2021). Probabilistic rainfall thresholds for debris flows occurred after the Wenchuan earthquake using a Bayesian technique. *Eng. Geol.* 280, 105965. doi:10.1016/j.enggeo.2020.105965

Koi, T., Hotta, N., Ishigaki, I., Matuzaki, N., Uchiyama, Y., and Suzuki, M. (2008). Prolonged impact of earthquake-induced landslides on sediment yield in a mountain watershed: The Tanzawa region, Japan. *Geomorphol. (Amst).* 101 (4), 692–702. doi:10.1016/j.geomorph.2008.03.007

Li, L., Yu, B., Zhu, Y., Chu, S., and Wu, Y. (2014). Topographical factors in the formation of gully-type debris flows in Longxi River catchment, Sichuan, China. *Environ. Earth Sci.* 73 (8), 4385–4398. doi:10.1007/s12665-014-3722-7

Li, N., Tang, C., Gong, L., Yang, C., Chen, M., and Gan, W. (2020). An experimental study of starting characteristics of steep-channel debris flow: A case study of the flow: A case study of the futang gully in the wenchuan county. *J. Acta Geol. Sin.* 94 (02), 634–647. doi:10.19762/j.cnki.dizhixuebao.2019146

Li, Y., Liu, X-n., Gan, B-r., Wang, X-k., Yang, X-g., Li, H-b., et al. (2021). Formation-evolutionary mechanism analysis and impacts of human activities on the 20 August 2019 clustered debris flows event in wenchuan county, southwestern China. *Front. Earth Sci. (Lausanne).* 9, 616113. doi:10.3389/feart.2021.616113

Liao, F. W., Liu, X., and Liu, P. (2011). Comprehensive mathematical evaluation on risk of debris flow. *Adv. Mat. Res.* 368-373, 829–833. doi:10.4028/www.scientific.net/AMR.368-373.829

Liu, F. Z., Xu, Q., Dong, X. J., Yu, B., and Frost, J. D. Li H. J. (2017). Design and performance of a novel multi-function debris flow mitigation system in Wenjia Gully, Sichuan. *Landslides* 14 (6), 2089–2104. doi:10.1007/s10346-017-0849-0

Loche, M., Scaringi, G., Yunus, A. P., Catani, F., Tanyaş, H., Frodella, W., et al. (2022). Surface temperature controls the pattern of post-earthquake landslide activity. *Sci. Rep.* 12 (1), 988–1011. doi:10.1038/s41598-022-04992-8

Lombardo, L., Bakka, H., Tanyas, H., van Westen, C., Mai, P. M., and Huser, R. (2019). Geostatistical modeling to capture seismic-shaking patterns from earthquake-induced landslides. *J. Geophys. Res. Earth Surf.* 124 (7), 1958–1980. doi:10.1029/2019JF005056

Lyu, L., Wang, Z., Cui, P., and Xu, M. (2017). The role of bank erosion on the initiation and motion of gully debris flows. *Geomorphol. (Amst).* 285, 137–151. doi:10.1016/j.geomorph.2017.02.008

Lyu, L., Xu, M., Wang, Z., Cui, Y., and Blanckaert, K. (2022). A field investigation on debris flows in the incised Tongde sedimentary basin on the northeastern edge of the Tibetan Plateau. *Catena (Amst).* 208, 105727. doi:10.1016/j.catena.2021.105727

Ni, H., Tang, C., Zheng, W., Xu, R., Tian, K., and Xu, W. (2014). An overview of formation mechanism and disaster characteristics of post-seismic debris flows triggered by subsequent rainstorms in wenchuan earthquake extremely stricken areas. *Acta Geol. Sin. - Engl. Ed.* 88 (4), 1310–1328. doi:10.1111/1755-6724.12290

Pal, S. C., Arabameri, A., Blaschke, T., Chowdhuri, I., Saha, A., Chakrabortty, R., et al. (2020). Ensemble of machine-learning methods for predicting gully erosion susceptibility. *Remote Sens. (Basel).* 12 (22), 3675. doi:10.3390/rs12223675

Qi, S., Chen, X., Simms, P., Zhou, J., and Yang, X. (2020). New method for determining the permeability function parameters of soft soils considering synchronous sedimentation and consolidation. *Comput. Geotechnics* 127, 103781. doi:10.1016/j.compgeo.2020.103781

Qu, Y., and Xiao, J. (2018). The preliminary study on characteristics of urgent steep-channel debris flows in meizosismal area. *J. Chang. Inst. Tech.(Nat. Sci. Edi.)* 19 (4), 57–61. doi:10.3969/j.issn.1009-8984.2018.04.014

Roy, P., Chakrabortty, R., Chowdhuri, I., Malik, S., Das, B., and Pal, S. C. (2020). "Development of different machine learning ensemble classifier for gully erosion susceptibility in gandheswari watershed of West Bengal, India," in *Machine learning for intelligent decision science. Algorithms for intelligent systems*. Editors J. Rout, M. Rout, and H. Das (Singapore: Springer). doi:10.1007/978-981-15-3689-2_1

Saha, A., Pal, S. C., Arabameri, A., Chowdhuri, I., Rezaie, F., Chakrabortty, R., et al. (2021). Optimization modelling to establish false measures implemented with *ex-situ* plant species to control gully erosion in a monsoon-dominated region with novel *in-situ* measurements. *J. Environ. Manage.* 287, 112284–114797. doi:10.1016/j.jenvman.2021.112284

Stock, J. D., and Dietrich, W. E. (2006). Erosion of steepland valleys by debris flows. *Geol. Soc. Am. Bull.* 118 (9-10), 1125–1148. doi:10.1130/B25902.1

Takahashi, T. (1980). Debris flow on prismatic open channel. *J. Hydr. Div.* 106 (3), 381–396. doi:10.1061/jyceaj.0005381

Tang, C., van Asch, T. W. J., Chang, M., Chen, G. Q., Zhao, X. H., and Huang, X. C. (2012). Catastrophic debris flows on 13 August 2010 in the Qingping area, southwestern China: The combined effects of a strong earthquake and subsequent rainstorms. *Geomorphol. (Amst).* 139-140, 559–576. doi:10.1016/j.geomorph.2011.12.021

Tang, C., Van Westen, C. J., Tanyas, H., and Jetten, V. G. (2016). Analyzing post-earthquake landslide activity using multi-temporal landslide inventories near the epicentral area of the 2008 Wenchuan earthquake. *Nat. Hazards Earth Syst. Sci.* 16 (12), 2641–2655. doi:10.5194/nhess-16-2641-2016

Tang, C., Zhu, J., Li, W. L., and Liang, J. T. (2009). Rainfall-triggered debris flows following the Wenchuan earthquake. *Bull. Eng. Geol. Environ.* 68 (2), 187–194. doi:10.1007/s10064-009-0201-6

Wang, Y., Nie, L., Zhang, M., Wang, H., Xu, Y., and Zuo, T. (2020). Assessment of debris flow risk factors based on meta-analysis—cases study of northwest and southwest China. *Sustainability* 12 (17), 6841. doi:10.3390/su12176841

Webb, R. H., Griffiths, P. G., and Rudd, L. P. (2008). Holocene debris flows on the Colorado Plateau: The influence of clay mineralogy and chemistry. *Geol. Soc. Am. Bull.* 120 (7-8), 1010–1020. doi:10.1130/B26055.1

Wu, S. R., Shi, J. S., and Wang, H. B. (2011). Analysis of activity intensity for landslides triggered by the Wenchuan earthquake, Sichuan Province, China. *Environ. Earth Sci.* 65 (4), 1021–1028. doi:10.1007/s12665-011-0952-9

Xiong, J., Tang, C., Chen, M., Zhang, X., Shi, Q., and Gong, L. (2020). Activity characteristics and enlightenment of the debris flow triggered by the rainstorm on 20 August 2019 in Wenchuan County, China. *Bull. Eng. Geol. Environ.* 80, 873–888. doi:10.1007/s10064-020-01981-x

Yang, D. X., Chen, X. Q., and You, Y. (2012). The debris flow development trend in xiaogangjian gully in Mianzhu county, wenchuan earthquake zone. *J. J. Mt. Sci.* 30 (06), 701–708. doi:10.3969/j.issn.1008-2786.2012.06.010

Yang, D., You, Y., Chen, X., Zhao, W., Shi, S., and Xie, Z. (2015). Typical characteristics and mitigation of debris flow in narrow-steep gullies in the Wenchuan earthquake areas. *J. HYDROGEOLOGY Eng. Geol.* 42 (01), 146–153. doi:10.16030/j.cnki.issn.1000-3665.2015.01.25

Yang, D., You, Y., Zhao, W., Huang, H., Sun, H., and Liu, Y. (2020). Abrasion behavior and anti-wear measures of debris flow drainage channel with large gradient. *Water* 12 (7), 1868. doi:10.3390/w12071868

Yin, Y., Cheng, Y., Liang, J., and Wang, W. (2015). Heavy-rainfall-induced catastrophic rockslide-debris flow at sanxicun, dujiangyan, after the wenchuan ms 8.0 earthquake. *Landslides* 13 (1), 9–23. doi:10.1007/s10346-015-0554-9

Zhang, Ning, Yao, Leihua, and Wang, Qing (2012). "Study on one-dimensional movement model of Maliu gully debris flow," in International Symposium on Geomatics for Integrated Water Resource Management, Lanzhou, 19-21 Oct. 2012, 1–6. doi:10.1109/GIWRM.2012.6349611

Zhang, Y., Cheng, Y., Yin, Y., Lan, H., Wang, J., and Fu, X. (2014). High-position debris flow: A long-term active geohazard after the wenchuan earthquake. *Eng. Geol.* 180, 45–54. doi:10.1016/j.enggeo.2014.05.014

Zhao, B., Yu, B., Chang, M., and Yang, L. (2021). Characteristics of debris flow in narrow-steep channel. *J. J. Sediment Res.* 46 (5), 61–67. doi:10.16239/j.cnki.0468-155x.2021.05.010

Zhou, B. F. (1991). *Mitigation and prevention guidebook of debris flow*. Beijing: M, Scientific Press.

Frontiers in Earth Science

Investigates the processes operating within the major spheres of our planet

Advances our understanding across the earth sciences, providing a theoretical background for better use of our planet's resources and equipping us to face major environmental challenges.

Discover the latest Research Topics

See more →

Frontiers

Avenue du Tribunal-Fédéral 34
1005 Lausanne, Switzerland
frontiersin.org

Contact us

+41 (0)21 510 17 00
frontiersin.org/about/contact